Formation des P-bodies et régulations post-transcriptionnelles associées à leurs facteurs d'assemblage dans les cellules humaines

Clémentine Bossevain

Sorbonne-Université

Ecole Doctorale 515-Complexité du vivant

Laboratoire de Biologie du Développement CNRS-Sorbonne-Université UMR 7622

Equipe Compartimentation et trafic intracellulaire des mRNPs

Formation des P-bodies & régulations post-transcriptionnelles associées à leurs facteurs d'assemblage dans les cellules humaines

Par Clémentine BOSSEVAIN

Thèse de doctorat de BIOCHIMIE ET BIOLOGIE MOLECULAIRE

Dirigée par Dr. Dominique WEIL et Dr. Maïté COUREL

Présentée et soutenue le 30 Septembre 2020

Devant un jury composé de :

Mme. Catherine-Laure TOMASETTO, DR	Rapportrice
M. Olivier NAMY, DR	Rapporteur
Mme. Julia MORALES, DR	Examinatrice
M. Frank MARTIN, DR	Examinateur
Mme. Dominique WEIL, DR	Directrice de thèse
Mme. Maïté COUREL, MC	Co-directrice de thèse

Résumé/Abstract

Résumé

Les P-bodies (PB) sont des granules ribonucléoprotéiques concentrant des milliers d'ARNm particulièrement riches en AU, et une centaine de protéines. Parmi celles-ci, 3 répresseurs de la traduction : DDX6, LSM14A et 4E-T sont indispensables à l'assemblage des PB. Dans une 1ère partie, nous nous sommes intéressés au mécanisme d'assemblage des PB. Nous avons identifié par une approche de TAP-tag et de spectrométrie de masse les partenaires de LSM14A, de son paralogue LSM14B et de 4E-T. Le croisement de leurs interactomes avec ceux, déjà connus, de DDX6 et des PB révèle 8 nouveaux candidats d'assemblage des PB. Nous montrons que l'un d'eux, ILF3, contribue au maintien des PB. Nous montrons par ailleurs qu'une fraction de LSM14A est associée au complexe d'initiation de la traduction. La 2nde partie porte sur l'influence du contenu en GC sur les régulations post-transcriptionnelles. Nous avons cherché : si DDX6, LSM14A et 4E-T ont des préférences de liaison à l'ARN expliquant l'accumulation préférentielle d'ARNm riches en AU dans les PB, quelles informations apporte la localisation des cibles des miARN dans/hors des PB sur le mécanisme de régulation des ARNm par les miARN, et quels autres paramètres que le contenu en GC influenceraient la localisation des ARNm aux PB. Nos analyses montrent : que 4E-T est la seule des 3 protéines d'assemblage des PB à manifester une préférence de liaison pour les ARNm riches en AU, que la localisation dans les PB des cibles des miARN est associée à une répression de leur traduction dépendante de DDX6, et que la rétention d'ARNm riches en AU sur les membranes et les ribosomes concurrence leur recrutement aux PB.

Abstract

P-bodies (PBs) are ribonucleoprotein granules where thousands of mRNAs especially AU-rich, and hundreds of proteins concentrate. Among these proteins, three repressors of translation: DDX6, LSM14A and 4E-T are required to assemble PBs. In a first part, we looked at PB assembly mechanism. We identified by a TAP-tag approach coupled to mass spectrometry analysis protein partners of LSM14A, its paralog LSM14B and 4E-T. Crossing their interactomes with already known DDX6 and PB interactomes revealed 8 new PB assembly candidates. We demonstrate that one of them, ILF3, contributes to PB maintenance. Concerning LSM14A, we show that a fraction of LSM14A associates to the initiation complex. In a second part, related to the influence of GC content on post-transcriptional regulations, we asked: if DDX6, LSM14A and 4E-T have a RNA-binding preference that could explain accumulation of AU-rich mRNAs in PBs, how global localization of miRNA targets in/out PB is informative in regards to mRNA regulation mechanism by miRNAs, and which other parameters apart from mRNA GC content could influence mRNA localization to PBs. Our analyses show: that out of the 3 PB assembly factors, only 4E-T has a preference for AU-rich mRNAs, that localization to PBs of miRNA targets is correlated to their translational repression by DDX6 and that retention of AU-rich mRNAs on membranes and ribosomes competes with their localization to PBs.

Remerciements

Je remercie en premier lieu les membres de mon jury de thèse : le Dr. Catherine-Laure Tomasetto et le Dr. Olivier Namy pour avoir accepté d'être mes rapporteurs, le Dr Julia Morales et le Dr Frank Martin pour avoir bien voulu examiner ce travail.

J'adresse ensuite ma plus profonde reconnaissance à ma directrice de thèse, Dominique Weil. Dominique, un immense merci pour m'avoir permis de réaliser ce doctorat dans ton laboratoire. Merci pour le temps investi dans chaque aspect de cette formation, pour ton encadrement à la fois exigeant et bienveillant, et ce que cela m'a permis d'apprendre, tant sur le plan scientifique qu'humain. J'espère en faire bon usage.

Maïté Courel, si j'en suis venue à travailler sur les P-bodies, c'est initialement grâce à toi... Merci pour ta disponibilité, tes conseils avisés et relectures rigoureuses. Ce fut une chance de t'avoir pour co-encadrante.

Michèle Ernoult-Lange, merci pour tous tes conseils pratiques qui m'ont efficacement orientée au jour le jour à la paillasse et ce tout au long de ce projet.

Marianne Bénard, merci d'avoir pris le temps de discuter de mes résultats, répondu à mes questions… et de m'avoir supportée comme voisine de paillasse pendant ces 3 ans…

Michel Kress, je te remercie pour tes conseils et ton aide « bio-info-related », ainsi que pour l'ambiance bien particulière que tu apportes au labo en collaboration directe avec Michèle.

Marie Noelle Benassy et Catherine Ségalas, merci pour tout ce que vous réalisez au quotidien. Par ailleurs, sans nos cafés matinaux les journées de labo n'auraient pas démarré d'aussi bon pied…

Je remercie également les membres de mon comité de suivi, Micheline Fromont-Racine, Juliette Leymarie et Hervé Le Hir, pour leurs conseils et questions pertinentes qui ont contribué à l'amélioration de cette thèse.

Enfin, j'adresse mes plus sincères remerciements à mes proches, spécialement mes parents pour leur amour inconditionnel et leur soutien sans lesquels je ne me trouverais pas en train d'écrire ces lignes aujourd'hui.

A toutes et à tous : « Merci. »

.

SOMMAIRE

Liste des Figures

INTRODUCTION

RESULTATS PARTIE 1

Liste des Tableaux

Liste des Abréviations

43S: complexe de pré-initiation

48S: 43S associé à l'ARNm

4E-BP: eIF4E Binding Protein

4E-IP: eIF4E Interacting Protein

4E-T: eIF4E Transporter

aa: acide aminé

ADN: Acide DésoxyriboNucléique

ARE: AU-Rich Element

ARE-BP: AU-Rich Element-Binding Protein

ARNm: Acide RiboNucléique messager

ARNt: ARN de transfert

ATP: Adenosine Triphosphate

CCR4-NOT: Catabolite Carbon Repressor 4-Negative regulator of Transcription

CPE: Cytoplasmic Polyadenylation Element

CPEB: CPE-Binding Protein

DCP1,2: Decapping Enzyme 1,2

DDX6: DEAD box helicase 6

eEFs: eukaryotic Elongation Factor

eIF4F: complexe d'eIF4A-eIF4E-eIF4G-eIF4B

eIFs: eukaryotic Initiation Factors

EJC: Exon Junction Complex

ER: Reticulum Endoplasmique

FC: Fold Change

GAP: GTPase Activating Protein

GDI: GDP Dissociation Inhibitor

GDP: Guanosine Diphosphate

GEF: Guanine nucleotide Exchange Factor

GFP: Green Fluorescent Protein

GO: Gene Ontology

GTP: Guanosine Triphosphate

hnRNP: heterogeneous nuclear RiboNucleoProtein

IRES: Internal Ribosome Entry Site

m^7GTP: 7-Méthylguanosine 5'-triphosphate

miRNA: micro ARN

miRNP: microRNA RiboNucleoParticle

(m)RNP: (messenger) RiboNucleoProtéine

MS: Mass Spectrometry

NMD: Nonsense Mediated-Decay

nt: nucléotides

PABP: Poly(A)-Binding Protein

PAN3: Poly(A) Nucléase 2 et 3

PARN: Poly(A) RNase

PB: P-bodies/Processing bodies

PTB: Polypyrimidine Tract Binding protein

PTC: Premature Terminaison Codon

PTM: Post-Translational Modification

RBD: RNA-Binding Domain

RBP: RNA-binding Protein

RISC: RNA-Induced Silencing Complex

Rluc: Renilla luciférase

RNA seq: RNA sequencing

SG: Stress Granule

siRNA: small interfering RNA

sm(i)FISH: single molecule (inexpensive) Fluorescent In Situ Hybridization

INTRODUCTION

Partie 1 : mRNPs & régulations post-transcriptionnelles cytoplasmiques chez les eucaryotes

Dans un organisme eucaryote pluricellulaire, toutes les cellules ne remplissent pas les mêmes fonctions ni ne sont exposées aux mêmes variations environnementales. Dans ces conditions, il est vital pour les cellules de pouvoir exprimer sélectivement dans l'espace et dans le temps, les gènes adéquats afin d'adapter le niveau de protéines aux circonstances (Sokabe and Fraser, 2018). Si, historiquement, les régulations transcriptionnelles ont été considérées comme les protagonistes quasi exclusifs du contrôle de base de l'expression génique (*i.e*. dans des conditions environnementales stables), il est aujourd'hui admis que la coordination globale de l'expression génique dépend également largement des régulations post-transcriptionnelles (Figure1). La première analyse quantitative et à large échelle des contributions relatives des différentes étapes de l'expression génique sur le niveau de protéines a été réalisée en 2011 sur des fibroblastes de souris (Schwanhäusser et al., 2011). Les mesures des demi-vies de 5000 ARNm par marquage métabolique ainsi que d'abondance de ces ARNm et de leurs protéines correspondantes dans une population de cellules asynchrones ont montré, après révision des calculs dans (Li et al., 2014), que la transcription explique 38 % de la variation des niveaux de protéines. La dégradation de l'ARN en explique 18%, la traduction 30% et la dégradation des protéines 14%, ce qui confirme l'importance des régulations post-transcriptionnelles dans le contrôle de l'expression génique.

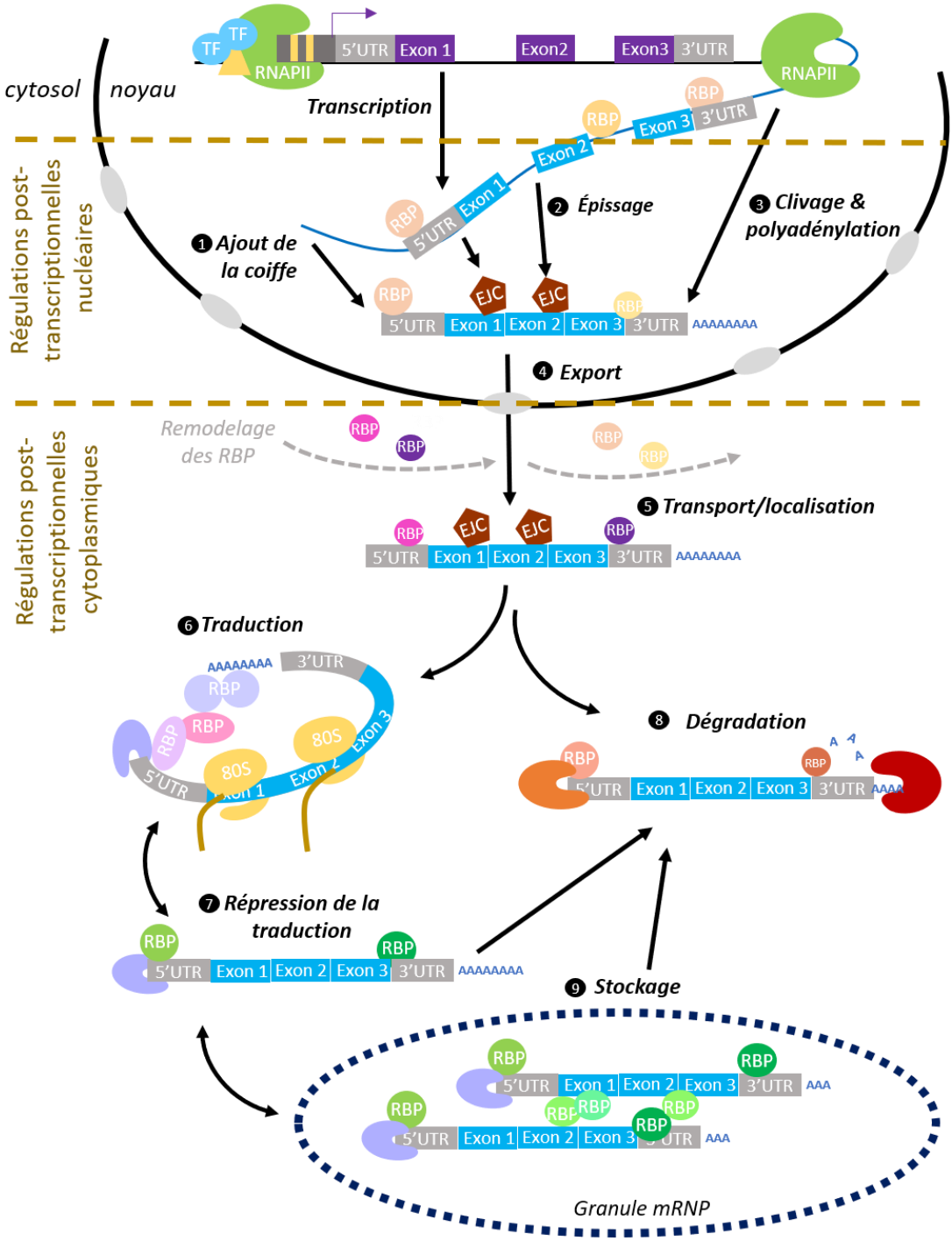

Figure 1. Principales régulations post-transcriptionnelles eucaryotes

Après que l'ARN est transcrit dans le noyau par l'ARN Pol II assistée de facteurs de transcription généraux et spécifiques, des RBP se lient au transcrit pré-messager et catalysent l'addition d'une coiffe 7 méthylguanosine (1), l'épissage des introns et le dépôt de l'EJC (2) ainsi que l'ajout d'une queue poly(A) (3). L'ARN mature est exporté dans le cytoplasme via les pores nucléaires (4). Le mRNP est remodelé par l'ajout/retrait de RBP spécifiques contribuant à orienter son devenir cytoplasmique. Après transport éventuel (5), l'ARNm peut être traduit (6), réprimé en traduction (7) et/ou puis dégradé (8). Les mRNPs dont la traduction est réprimée peuvent également se condenser dans des granules mRNPs où ils sont transitoirement stockés (9). (Modifié d'après Chin and Lécuyer, 2017).

Dans le cadre de cette introduction, nous traiterons des régulations post-transcriptionnelles cytoplasmiques, c'est-à-dire celles qui s'appliquent au contrôle de la traduction de l'ARNm et de sa stabilité. Après avoir rappelé les mécanismes moléculaires d'initiation de la traduction ainsi que les mécanismes de dégradation de l'ARNm nous ferons le point sur les principales régulations de ces processus. Les exemples et références choisis concernerons prioritairement le modèle mammifère sans exclure toutefois des références ponctuelles à d'autres organismes modèles eucaryotes lorsque cela s'avèrera nécessaire.

1. ***Traduction de l'ARNm : mécanisme moléculaire de l'étape d'initiation et principes de régulation***

La traduction de l'ARNm chez les eucaryotes se décompose en quatre phases successives : initiation, élongation, terminaison et recyclage du ribosome (Sokabe and Fraser, 2018). En pratique, l'initiation de la traduction consiste à activer en parallèle la sous-unité 40S et l'extrémité 5' de l'ARNm, à recruter le 40S sur l'ARNm, à sélectionner le codon d'initiation et à y assembler le ribosome afin de pouvoir démarrer la synthèse protéique (Figure 2). Toutes ces étapes requièrent l'intervention coordonnée d'une multiplicité d'acteurs moléculaires : treize facteurs d'initiation de la traduction canoniques (eIFs) (Tableau 1), plusieurs facteurs auxiliaires tels que la PABP (Poly(A) Binding Protein) et l'hélicase DHX29, auxquels s'ajoutent les ribosomes, les ARN de transfert (ARNt) et l'ARNm. Avec des taux d'initiation estimés par des approches d'imagerie *in vivo* sur molécule unique entre 1,4 et 3,6 évènements d'initiation/min selon les transcrits considérés (Morisaki et al., 2016; Yan et al., 2016) et comparés à des taux d'élongation estimés entre 3,1 et 4,9 codons/s par les mêmes approches, l'étape d'initiation de la traduction est considérée comme relativement lente même s'il existe des hétérogénéités de cinétique entre ARNm d'une même cellule. Il s'agit de l'étape limitante et par conséquent la plus étroitement régulée du processus de traduction. Pour la majorité des ARNm eucaryotes, l'initiation de la traduction fait intervenir la coiffe de l'ARNm dans le recrutement et l'assemblage des sous-unités ribosomales sur l'ARNm (von der Haar et al., 2004), selon un mécanisme dit « coiffe-dépendant » que nous détaillons ici.

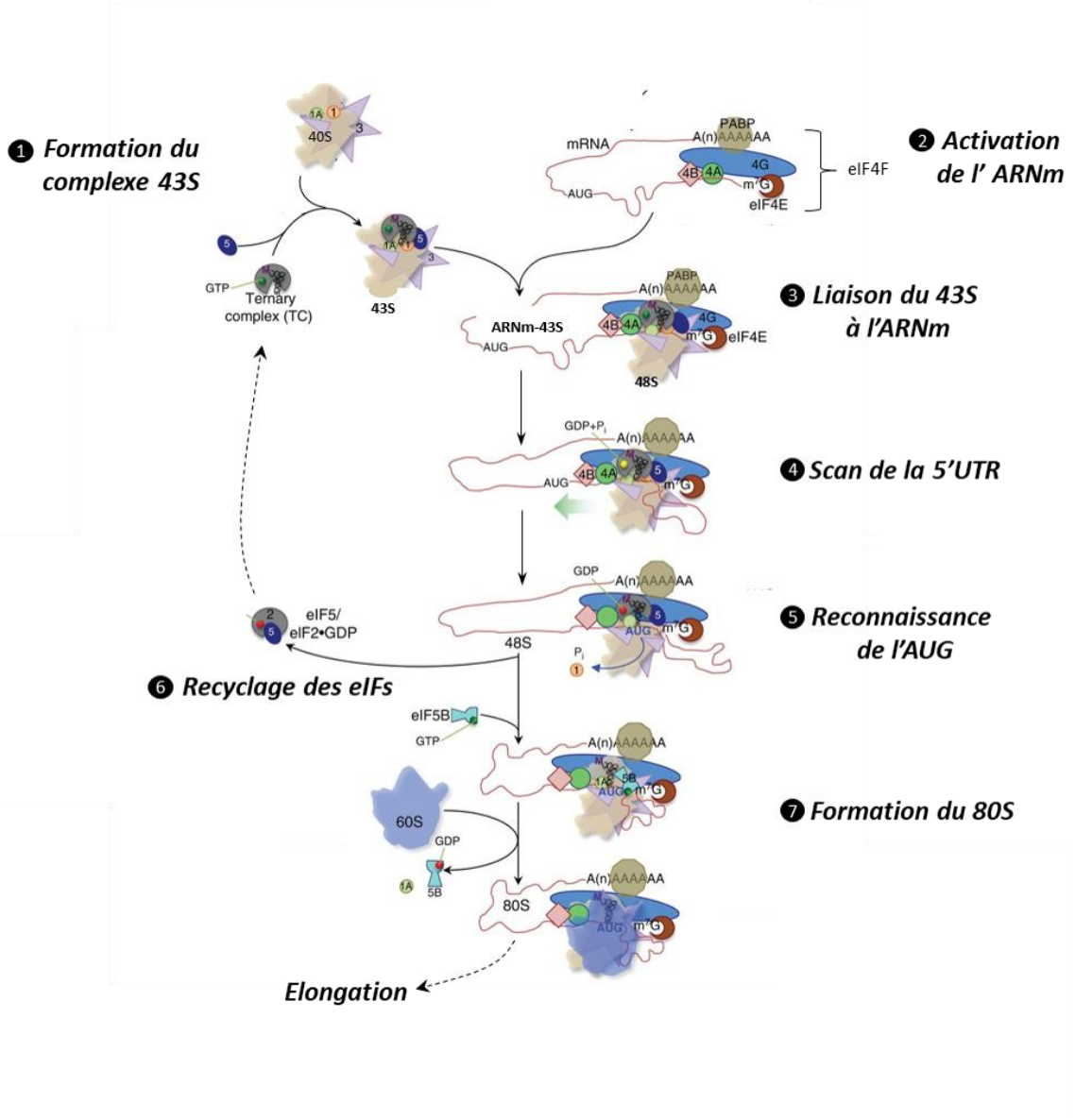

Figure 2 L'initiation de la traduction coiffe-dépendante.

Le complexe ternaire comportant l'ARNt initiateur, chargé en méthionine et d'eIF2 chargé en GTP, s'associe à la petite sous-unité ribosomale (40S), portant déjà eIF1A, eIF3 et eIF5 pour former le complexe 43S (1).En parallèle de (1), le complexe eIF4F comportant eIF4A/eIF4E/eIF4G et eIF4B se forme, par interaction de la protéine de liaison à la coiffe eIF4E et de la protéine plateforme eIF4G. PABP permet la circularisation de l'ARNm lié à eIF4E ce qui facilite la traduction (2).L'association des complexes 43S et eIF4F forme le complexe 48S, complexe actif de l'initiation de la traduction (3). Celui-ci scanne la région 5'UTR de l'ARNm (4) jusqu'à atteindre le codon AUG initiateur. (5) A l'atteinte de l'AUG, les facteurs d'initiation de la traduction se dissocient pour être recyclés (6) et la grande sous-unité ribosomale (60S) s'associe à la petite pour former le ribosome (7). Cette étape signe la fin de l'initiation et le début de l'élongation de la traduction. (Modifié d'après Merrick and Pavitt, 2018).

Nom	Sous-unité	Masse moléculaire (kDa)	Fonction
eIF1	1	13	Stimule la liaison du TC au 40S/favorise le balayage/contribue à la fidélité de sélection de l'AUG
eIF1A	1	17	Stimule la liaison du TC au 40S/lie le 43S au complexe eIF4F/empêche la liaison du 60S avant la reconnaissance de l'AUG
eIF2	3	36/38/51	formation du TC
eIF2B	5	34/39/50/60/80	réalise l'échange GDP-GTP pour eIF2
eIF3	13	total 800	Stimule la liaison du TC au 40S/lie le 43S au complexe eIF4F/empêche la liaison du 60S avant la reconnaissasnce de l'AUG
eIF4A	1	165	ARN hélicase déroulant les structures secondaires du 5'UTR préalablement au balayage
eIF4B	1	69,3	activateur de eIF4A
eIF4E	1	25	lie la coiffe m^7 GTP de l'ARNm/export de l'ARNm du noyau
eIF4G	1	176	formation du complexe eIF4F en liant eIF4E, eIF4A, eIF4B/ formation du 48S en liant eIF3/ conformation closed-loop en liant PABP
eIF5	1	49	GAP spécifique d'eIF2-GTP hydrolysant le GTP en GDP lors de la reconnaissance de l'AUG
eIF5B	1	139	GTPase.association des deux s.u ribosomales
eIF6	1	27	empêche une association prématurée en tre le 60S et le 40S
DHX29	1	155	déroule les structures secondaires de la 5' UTR
ABCE1	1	67	empêche l'association prématurée des deux sous-unité ribosomales

Tableau 1. Récapitulatif des fonctions des facteurs d'initiation de la traduction eucaryotes

(Modifié d'après Jackson et al., 2010)

1.1 Initiation de la traduction coiffe-dépendante

1.1.1 Formation du complexe 43S

La première étape de l'initiation de la traduction consiste à mettre en contact la petite sous-unité ribosomale (40S) avec un ARNt initiateur chargé en méthionine (ARNt-Met), sous une forme capable d'être recrutée sur l'ARNm. En pratique, ceci implique l'assemblage d'un complexe 43S PIC (Pre Initiation Complex) contenant le complexe ternaire (TC), les facteurs d'initiation eIF1, eIF1A et eIF3 et le 40S.

Le complexe ternaire inclut le facteur d'initiation eIF2, l'ARNt-Met et du GTP. Il permet d'acheminer l'ARNt-Met jusqu'à la petite sous-unité du ribosome (Dever et al., 2016; Hinnebusch, 2014) grâce à l'action de eIF2 qui, sous sa forme eIFI2-GTP, est capable de lier à

la fois le 40S *via* sa sous-unité eIF2α (Hashem et al., 2013) et l'ARNt-Met (Hinnebusch and Lorsch, 2012). Après hydrolyse du GTP et relargage du phosphate, eIF2-GDP perd son affinité pour l'ARNt-Met et quitte le PIC (Algire et al., 2005). Si la forme eIF2-GTP possède dix fois plus d'affinité pour l'ARNt-Met que la forme eIF2-GDP, il s'agit également de la forme la moins stable (Kapp and Lorsch, 2004). Ainsi, la formation du complexe ternaire nécessite la conversion d'eIF2-GDP en sa forme active liée au GTP. Cette activation repose sur l'action combinée d'un GEF (guanine nucléotide exchange factor) : eIF2B (Pavitt, 2005), et d'une GAP/GDI (GTPase Activating Protein/ GDP Dissociation Inhibitor) : eIF5 (Jennings and Pavitt, 2010), (Figure 3).

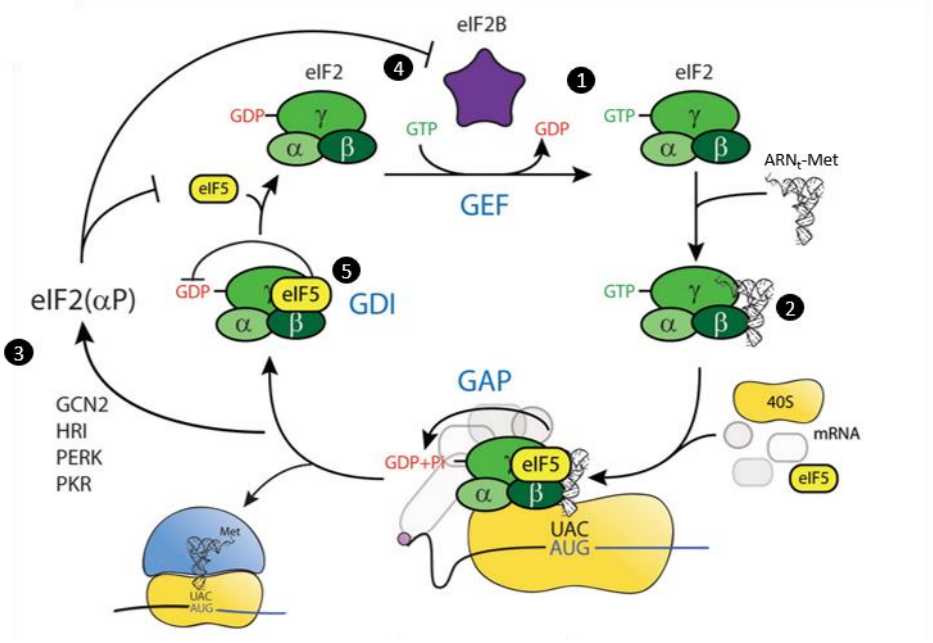

Figure 3 Cycle d'activation du facteur d'initiation eIF2

eIF2-GDP est activée par l'action de eIF2B. eIF2B est un GEF (Guanine exchange factor) qui dissocie le GDP de eIF2 pour y permettre la liaison du GTP (1) et faciliter la liaison du Met-ARNt à eIF2 (2). En conditions de stress, la sous-unité α de eIF2 est phosphorylée sur sa sérine 51 par différentes kinases telles GCN2, HRI, PERK, PKR (3). Sous sa forme phosphorylée, eIF2(αP) inhibe l'activité de eIF2B et conséquemment l'initiation de la traduction (4) (revu en détail dans Proud, 2018 ; Wek, 2018). L'action de GDI (GDP Dissociation Inhibitor) de eIF5 stabilise la liaison du GDP à eIF2 et empêche la dissociation de eIF2 qui pourrait autrement échapper à la régulation par eIF2B. eIF5 a aussi une fonction GAP (GTPase Activating Protein) intervenant après de la reconnaissance de l'AUG (5). (Modifié d'après Jennings and Pavitt, 2014)

Le recrutement du TC au 40S fait intervenir trois facteurs additionnels : eIF1, eIF1A et eIF3. Les facteurs eIF1 et eIF1A se lient de manière coopérative à la sous-unité 40S, du côté de la face non exposée au solvant (Sokabe and Fraser, 2014). Selon deux études par coupure dirigée avec des radicaux hydroxyles, eIF1 occupe le site P du 40S (Lomakin et al., 2003) et eIF1A le site A du 40S (Yu et al., 2009). Leur liaison au 40S induit un changement de conformation de ce dernier, qui adopte alors une conformation ouverte à laquelle peut se lier le TC (Merrick and Pavitt, 2018b). Cette conformation ouverte sera également importante pour l'étape de scanning (*cf* partie 1 paragraphe 1.1.4). Deux études successives de cryo-microscopie électronique (cryo-EM) ont permis de résoudre la structure du complexe 43S-DHX29 de mammifère à 11,6 Å puis 6 Å et ont montré qu'eIF3 possède plusieurs points de contact avec la sous-unité 40S (des Georges et al., 2015; Hashem et al., 2013). eIF3 établit trois points de contact avec le 40S : (1) sur la face exposée au solvant *via* les interactions de eIF3a avec les protéines ribosomales S1/S26/S7 et de eIF3c avec S27, S15 et S7 ; (2) à l'entrée du canal ARNm *via* les interactions de eIF3b avec S4 ; (3) à la sortie du canal ARNm *via* les interactions de eIF3d avec RPS28, RPS7 et RPS9 (Figure 4). eIF3 joue aussi un rôle dans la stabilisation du TC au 40S du fait d'un contact entre eIF3d et le domaine D1-eIF2α (des Georges et al., 2015). (Figure 5). Une étude récente basée sur l'analyse des profils de sédimentation sur gradients de sucrose des différents eIFs crosslinkés à l'ARNm a montré que la suppression de eIF3d par ARN interférence empêche la formation d'un complexe 43S, ce qui appuie l'importance d'eIF3d dans l'association d'eIF3 au 40S (Herrmannová et al., 2020)

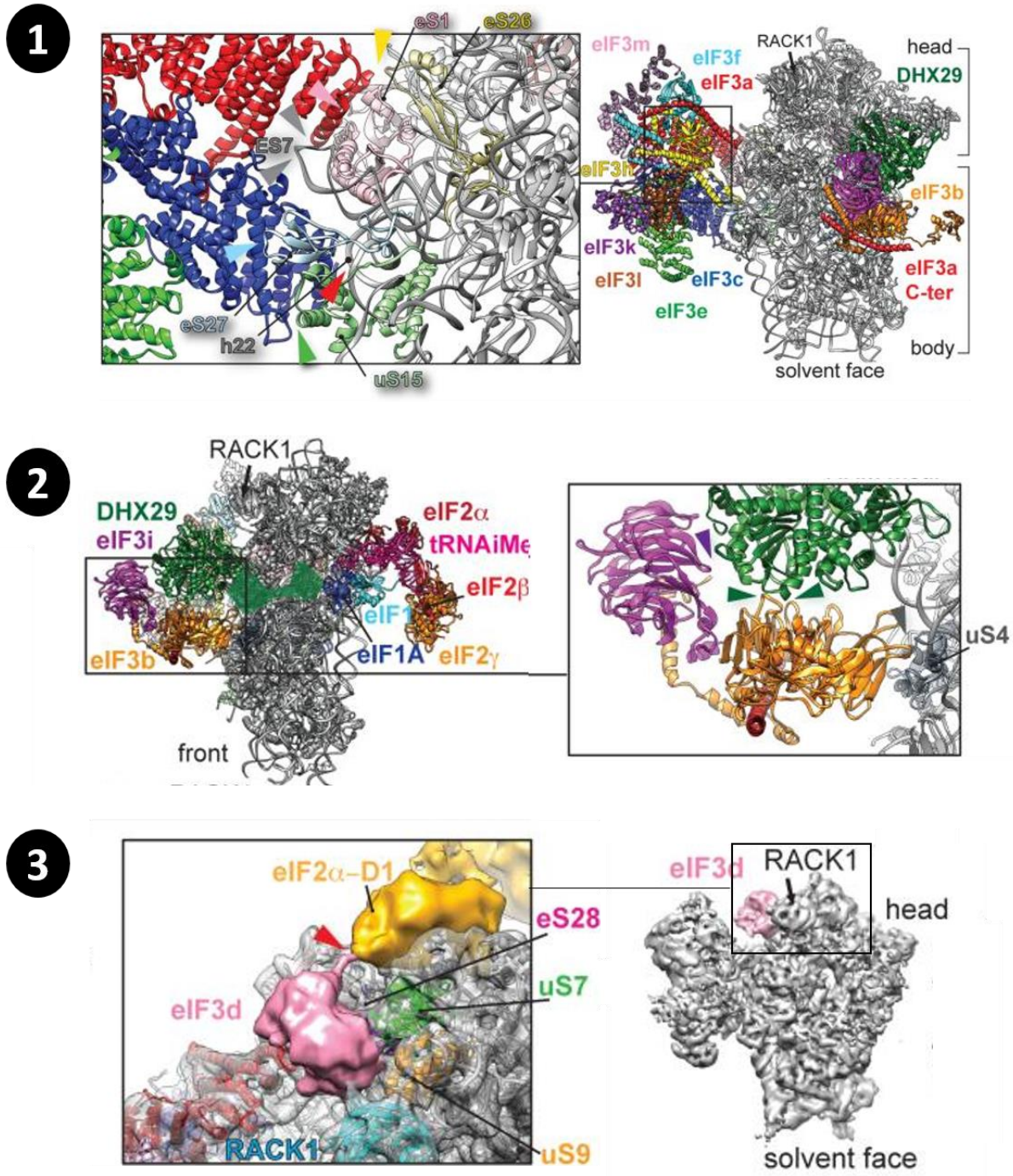

Figure 4 Contacts de eIF3 avec la sous-unité 40S au sein du complexe 43S

(1) et (3) sont des vues depuis la face exposée au solvant des interactions entre eIF3 et le 43S et (2) est une vue depuis la face inter sous-unités. Les rectangles noirs représentent une vue détaillée des interactions de la sous-unité eIF3a avec les protéines ribosomales RPS1/RPS26/RPS7 et de eIF3c avec RPS27, RP S15 et RPS7 (1); de eIF3b avec RPS4 à l'entrée du canal ARNm (2); de eIF3d avec RPS28, RPS7, RPS9 à la sortie du canal ARNm (3).(Modifié d'après des Georges et al., 2015)

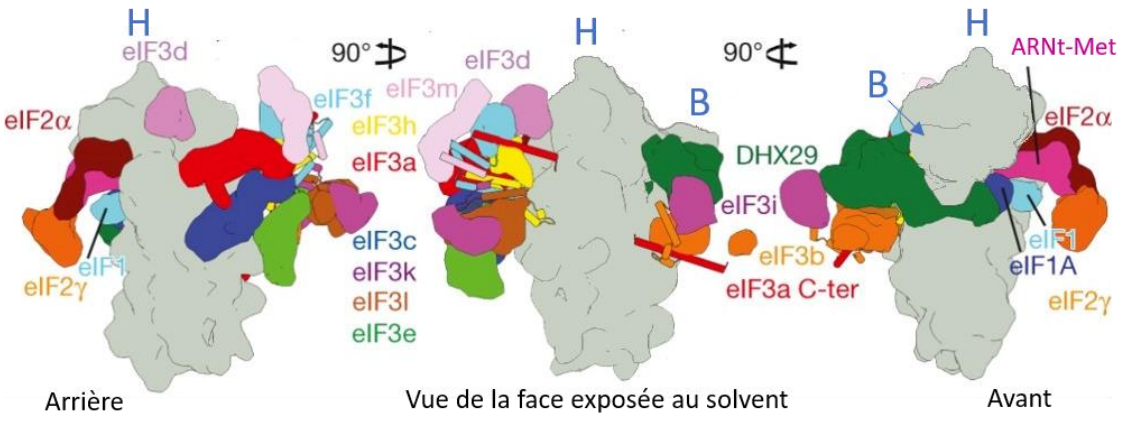

Figure 5 Schéma de la structure du complexe 43S-DHX29 mammifère.

Le complexe 43S lié à l'hélicase DHX29 est représenté successivement depuis l'arrière, la face exposée au solvant, l'avant. Le 40S est représenté en gris tandis que les sous-unités des différents eIFs ainsi que DHX29 sont en couleur. H indique la tête du 40S et B le bec. eIF3 possède trois régions d'interaction avec le 40S. L'ensemble des sous-unités (eIF3f/h/a/c/k/l/e) se lie du côté exposé au solvant du 40S à l'opposé de la plateforme via eIF3a et eIF3c. Le module eIF3b/i/g est en contact avec l'entrée du canal ARNm via eIF3b. eIF3d est situé à côté du canal de sortie de l'ARNm. eIF1 et eIF1A sont positionnés sur la face non exposée au solvant et occupant respectivement les sites A et P. eIF2. (Modifié d'après des Georges et al., 2015)

1.1.2 Assemblage du complexe eIF4F sur l'ARNm

Pour pouvoir recruter le 43S, l'ARNm doit être activé grâce à la formation du complexe eIF4F à l'extrémité de la 5'UTR. Le complexe eIF4F se compose de la protéine de liaison à la coiffe eIF4E, de la protéine plateforme eIF4G, de l'ARN-hélicase eIF4A et de sa protéine activatrice eIF4B. eIF4E se lie à la coiffe (Sonenberg et al., 1978, 1979) en entourant le m^7 GTP par les orbitales π de deux résidus tryptophane (Marcotrigiano et al., 1997). En parallèle, eIF4E s'associe à la protéine eIF4G par un motif consensus Tyr-XXXX-Leu-Φ (avec X a.a variable, ϕ acide aminé portant un radical hydrophobe) ce qui renforce l'affinité d'eIF4E pour la coiffe (Grüner et al., 2016). L'association d'eIF4E à la coiffe est également stabilisée par la liaison directe d'eIF4G à l'ARNm (Yanagiya et al., 2009) et sensible à la phosphorylation de la sérine 209 (Wang et al., 1998). En conditions de stress, cette sérine est phosphorylée par la kinase MNK (Scheper et al., 2002) ce qui dissocie eIF4E de la coiffe.

La formation du complexe eIF4F (Figure 6) entraîne deux réarrangements de l'ARNm : le

déroulement des structures secondaires de la 5'UTR et le rapprochement des extrémités 5'et 3' selon une conformation circulaire dite en « boucle fermée » (closed-loop). Le facteur eIF4G joue un rôle clef dans ces deux réarrangements. eIF4G lie eIF4A associée à eIF4B, ceci active la fonction ARN hélicase de eIF4A et lui permet de dérouler des structures secondaires et/ou de déplacer des complexes ARN-protéines susceptibles de gêner le recrutement d'un ARN simple brin dans le canal ARN du 43S PIC (García-García et al., 2015; Ozes et al., 2011). Dans certains cas, d'autres ARN-hélicases telles que DDX3 (Soto-Rifo et al., 2012) ou DHX29 pour les ARNm très structurés (Dhote et al., 2012; Pisarev et al., 2008) contribuent également au déroulement des structures secondaires de la 5'UTR .En parallèle de son interaction à eIF4A, eIF4G s'associe également à la PABP (Imataka et al., 1998). Selon les données structurales, l'interaction entre ces deux protéines est directe et concerne les résidus 178-203 d'eIF4G ainsi que le domaine RRM2 (RNA Recognition Motif 2) de PABP (Safaee et al., 2012). Cette interaction est au cœur du modèle en boucle fermée. Selon ce modèle, la chaîne d'interactions directes m^7GTP-eIF4E-eIF4G-PABP-queue poly(A) rapproche les extrémités 5' et 3' de l'ARNm et permet de recruter le 40S sur l'ARNm ainsi que de faciliter le recyclage du ribosome (Hinnebusch, 2014; Jackson et al., 2010; Kahvejian et al., 2001; Mangus et al., 2003; Wells et al., 1998). Ce modèle expliquerait la synergie observée *in vivo* au cours de la traduction, entre la coiffe 5' et la queue poly A (Gallie, 1991). Les interactions à la base du modèle closed-loop ont été initialement démontrées à partir de systèmes de traduction *in vitro* (Imataka et al., 1998; Preiss and Hentze, 1998; Tarun and Sachs, 1995; Tarun et al., 1997). Ultérieurement, des approches plus physiologiques ont complété ces études. Notamment, les facteurs eIF4E, eIF4G et PAB1 crosslinkés aux extrémités 5' et 3' de plusieurs transcrits endogènes associés aux polysomes ont été co-purifiés par affinité chez la levure *S.cerevisiae*, démontrant ainsi la réalité de cette chaîne d'interaction *in vivo* sur des transcrits pouvant être activement traduits (Archer et al., 2015). Également, la mesure de la traduction *in situ* d'ARNm rapporteurs luciférase dans un système de traduction mammifère montre que la proximité des extrémités 5' et 3' d'un ARNm facilite le démarrage d'un nouveau cycle de traduction sur la même molécule d'ARNm à partir d'un ribosome venant de terminer la traduction (Alekhina et al., 2020). Notons toutefois que la visualisation en smFISH (single molecule Fluorescent In Situ Hybridation) d'ARNm en cours de traduction ne montre pas de co-localisation des extrémités 5' et 3', suggérant que la conformation closed-loop est une étape transitoire de l'étape d'initiation (Adivarahan et al., 2018).

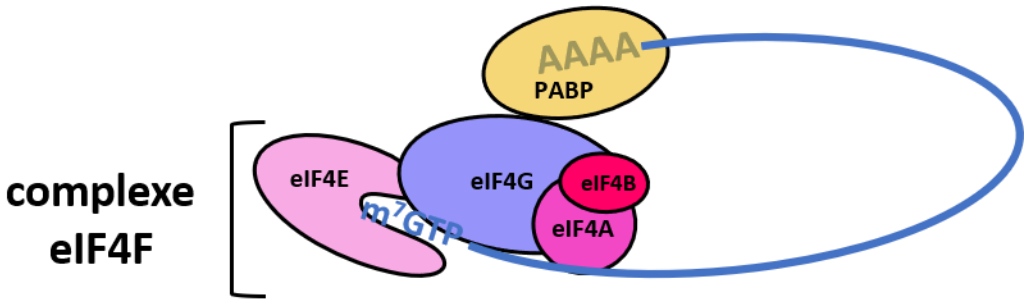

Figure 6 Organisation schématique du complexe eIF4F

Le complexe eIF4F est composé des facteurs d'initiation de la traduction eIF4G, eIF4A, eIF4B et eIF4E. eIF4E interagit directement avec la coiffe m^7GTP de l'ARNm ainsi qu'avec eIF4G. eIF4G se lie directement à eIF4E, à l'hélicase eIF4A ainsi qu'à PABP.

1.1.3 Recrutement du 43S sur l'ARNm

Le complexe 43S est recruté sur l'ARNm *via* le complexe eIF4F. D'après la structure du complexe 48S humain résolue par cryo-EM, les contacts entre eIF4F et le 43S reposent sur l'interaction directe du facteur eIF4G avec les sous-unités eIF3c, eIF3d et eIF3e du complexe 43S à côté du canal de sortie de l'ARNm ainsi que sur l'interaction directe de eIF4B avec la protéine ribosomale RPS3 et l'ARNr 18S à l'entrée du canal ARN (Eliseev et al., 2018).

La manière dont s'insère l'ARNm dans le canal ARN du ribosome reste imprécise. Des expériences ayant reconstitué un système d'initiation de traduction mammifère appuient le modèle selon lequel l'association eIF4E–eIF4G–eIF3–40S positionne eIF4E sur le bord antérieur du ribosome et où l'ARNm s'insérerait alors dans le canal ARNm de sorte à pouvoir être scanné à partir du premier nucléotide (Kumar et al., 2016). Un mécanisme alternatif envisage le déplacement de eIF4F du canal d'entrée vers le canal de sortie de l'ARNm. Au cours de ce déplacement eIF4F resterait lié à la coiffe et l'ARNm serait ainsi entraîné dans le canal ARN (Pelletier and Sonenberg, 2019), (Figure7). Une étude récente basée sur le RCPseq (Ribosome Complex Profiling sequencing)[1] a permis d'évaluer la dynamique de recrutement des ribosomes à l'ARNm et suggère que l'attachement de l'ARNm au ribosome s'effectue

[1] Le RCPseq consiste à crosslinker *in vivo* sur l'ARNm le 80S et les RNP ne contenant que la petite sous-unité ribosomale. Les ARN et particules ribosomales crosslinkés sont séparés sur gradient de sucrose et les ARN extraits des différentes fractions sont séquencés à haut débit. Cette technique permet de mesurer la vitesse et le mode de recrutement du 40S au niveau de la coiffe, la processivité du 40S lors du scanning du 5'UTR et la vitesse d'initiation de la traduction.

plutôt selon le premier modèle décrit ci-dessus, par l'enfilement de l'ARNm à travers le 40S (Giess et al., 2020).

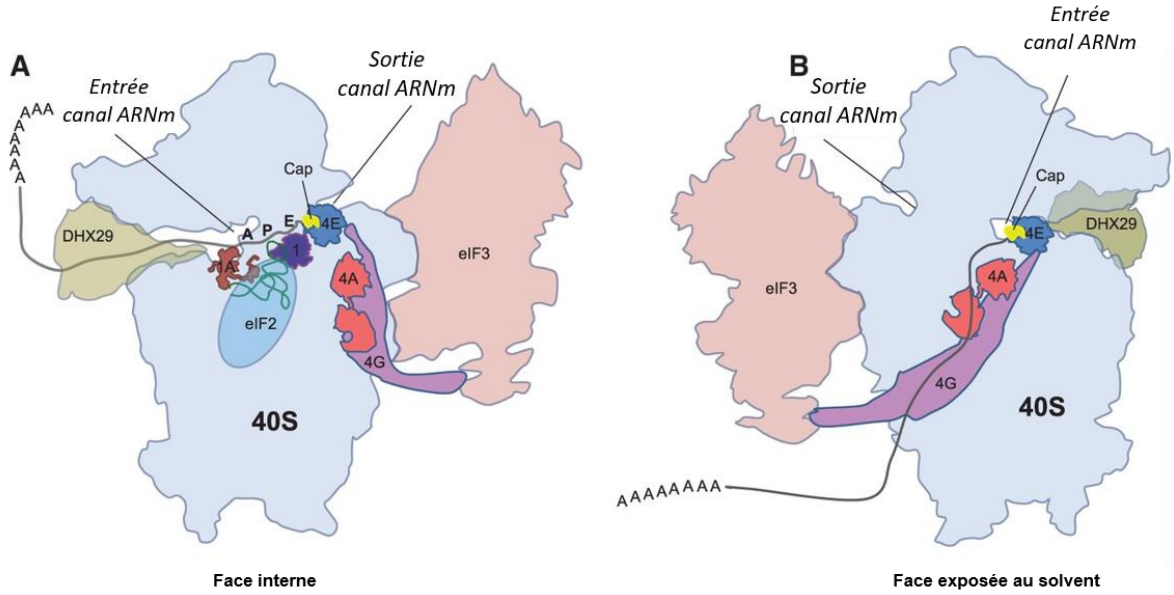

Figure 7 Deux modèles d'association du complexe 43S sur l'ARNm médié par le complexe eIF4F

*Modèle A : eIF4E est localisé à côté du site E de la sous-unité 40S. Le 40S s'attache légèrement en aval de l'extrémité 5' de l'ARNm et l'ARNm s'insère alors directement dans le canal ARNm. Modèle B : eIF4E est localisé à côté du site A du 40S et l'ARNm est « enfilé » dans le canal ARNm et scanné à partir du premier nucléotid*e. *(Modifié d'après Kumar et al., 2016).*

1.1.4 Du balayage de la 5'UTR à la formation du 80S

Après avoir lié l'ARNm, le 43S PIC scanne la 5'UTR dans le sens 5'->3' jusqu'à ce que l'anticodon de l'ARNt-Met reconnaisse un codon AUG initiateur. Généralement, le premier AUG rencontré lors du balayage est utilisé comme codon initiateur sous réserve qu'il se situe dans un contexte de séquence favorable. Chez les mammifères la séquence GCCPuCC**AUG**G, appelée séquence consensus de Kozak, favorise la reconnaissance de l'AUG (Kozak, 1986, 1987) Si le contexte de séquence de l'AUG en diffère significativement, le codon AUG n'est pas retenu pour commencer l'élongation (phénomène de « leaky scanning »).

D'après la résolution par cryo-EM du complexe 48S purifié dans des réticulocytes de lapin, plusieurs changements de conformation se produisent au cours du scanning (Figure 8 et Figure 9), notamment une re-localisation de eIF3b à partir de la face exposée au solvant vers la face interne du 40S (Simonetti et al., 2016). La structure du complexe 48S humain montre qu'eIF4A

et eIF4G sont physiquement associés dans le 48S et que eIF4B est physiquement associé au 40S (Eliseev et al., 2018). Ceci laisse supposer qu'eIF4A activée par eIF4B déroule les structures secondaires au cours du scanning. De manière intéressante, eIF4E est le seul composant du complexe eIF4F n'ayant pas été retrouvé associé au 48S, ce qui suggère qu'il se dissocie du complexe d'initiation de la traduction lors de l'insertion du transcrit dans le canal ARNm (Kumar et al., 2016). Cette analyse est cohérente avec une étude ultérieure montrant par des approches de co-immunoprécipitation et de pulldown que l'étape de scanning implique un changement de complexe eIF4G1/eIF4E vers un complexe eIF4G/eIF1 (Haimov et al., 2018)

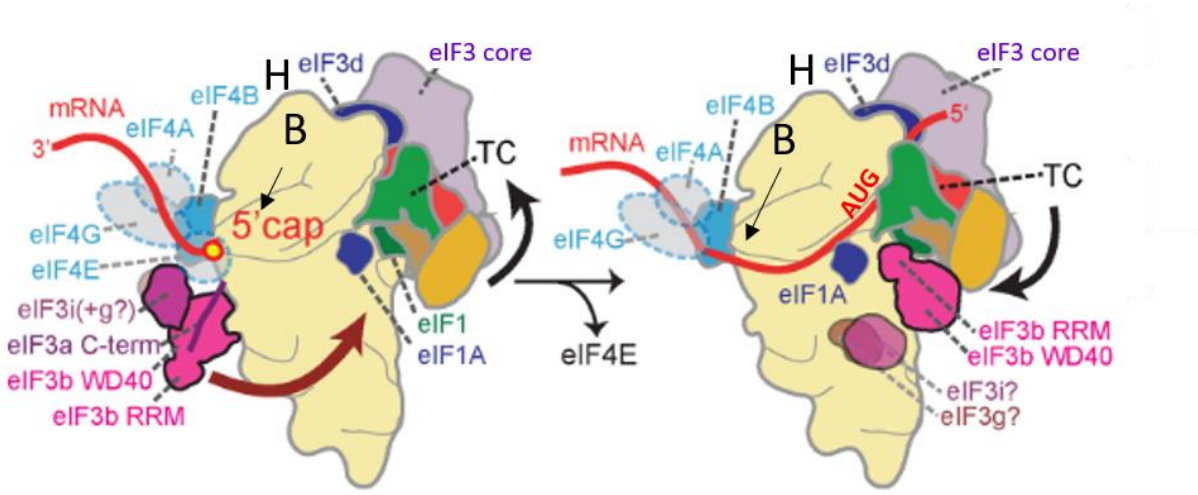

Figure 8 Réarrangements structuraux du complexe 48S au cours du balayage de la 5'UTR

L'association du complexe eIF4F (bleu) au complexe 43S permet d'insérer l'ARNm dans le canal ARN du 40S et forme ainsi le 48S. La re localisation de eIF3b vers la face interne du 40S facilite le balayage de la 5'UTR dans le sens 5'->3'. La reconnaissance de l'AUG provoque un réarrangement du complexe ternaire (TC) suite auquel les eIFs se dissocieront successivement du complexe d'initiation (non représenté). B=bec du 40S ; H=tête du 40S. NB : Dans la structure du complexe 48S à l'origine de ce schéma, les densités n'ont pas été associées avec certitude à eIF3i et eIF3g en raison d'une résolution insuffisante. (Eliseev et al., 2018)

Lorsque le codon AUG est reconnu, un duplex se forme entre l'ARNm et l'ARNt-Met et est stabilisé par eIF1A (Lomakin and Steitz, 2013). Les eIFs se dissocient ensuite séquentiellement. Le GTP contenu dans eIF2 est hydrolysé par sa sous-unité eIF2γ ce qui diminue son affinité pour l'ARNt-Met (Algire et al., 2005) et le dissocie du complexe d'initiation, eIF1 se dissocie du site P du ribosome (Zhang et al., 2015) et est remplacé par eIF5 (Orr et al., 2020) (Llácer et al., 2018). eIF3 reste quant à lui attaché au 40S jusqu'à la fin de

l'élongation (Beznosková et al., 2015). Le facteur ABCE1 qui était directement lié au 40S tout au cours de l'initiation pour empêcher une association précoce du 60S (Mancera-Martínez et al., 2017; Simonetti et al., 2020) est remplacé par la GTPase eIF5B ce qui permet aux deux sous-unités ribosomales de s'assembler en un complexe 80S (Fernández et al., 2013). Enfin, la dissociation de eIF5B-GDP et de eIF1A signe la fin de l'étape d'initiation. A ce stade, le 80S est attaché à l'ARNm avec l'ARNt-Met apparié au codon initiateur AUG dans le site P du ribosome : tout est en place pour que la réaction de synthèse peptidique et la phase d'élongation commencent.

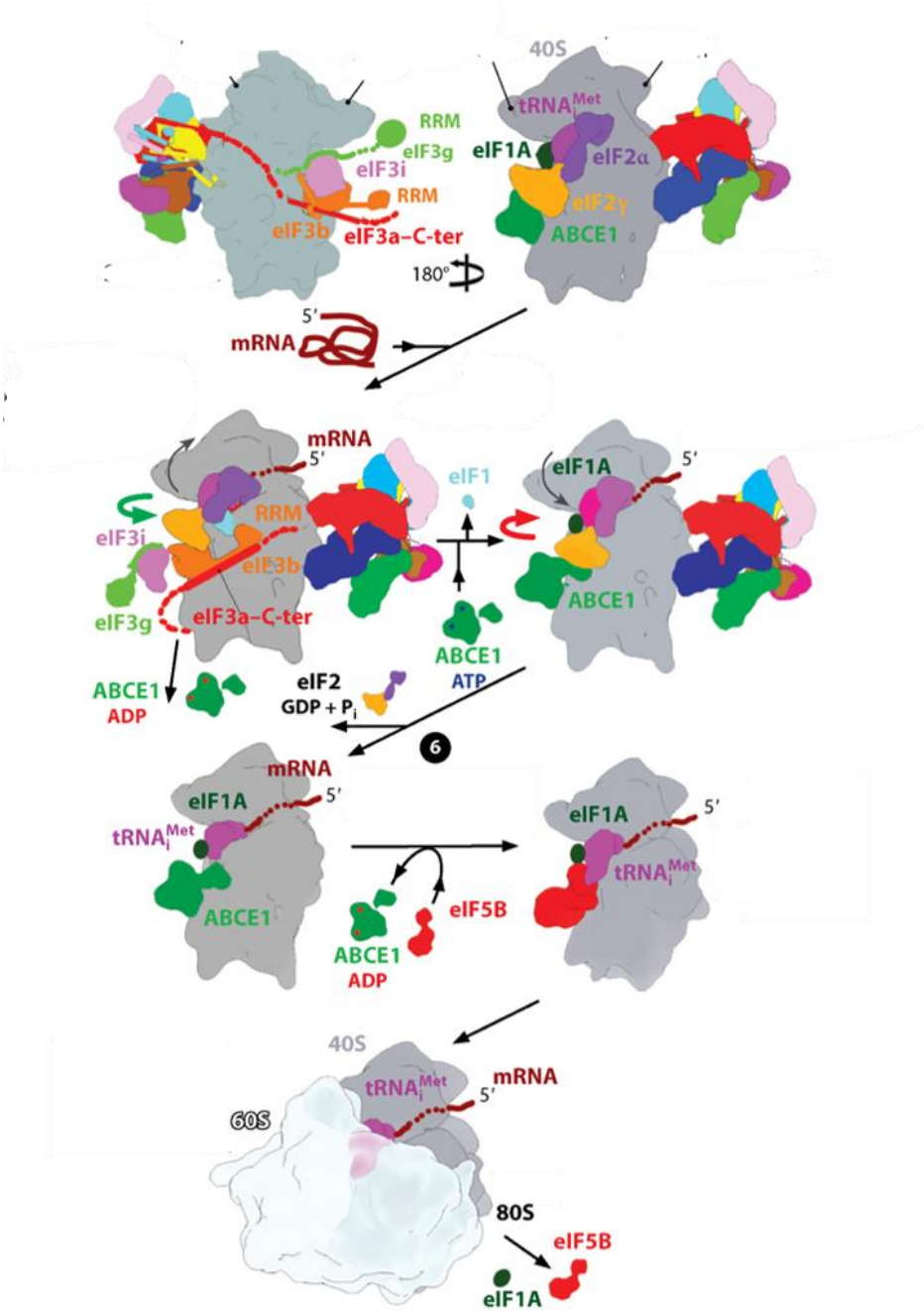

Figure 9 Du balayage de la 5'UTR à la formation du 80S

L'attachement de l'ARNm au 43S (1), déclenche la relocalisation des sous-unités eIF3b-i-g vers la face interne du 40S (flèche verte) ce qui déplace ABCE1, change la conformation du complexe ternaire (TC) et facilite le balayage (2). Une fois le codon initiateur reconnu, eIF1 se dissocie du 48S et eIF3b-i-g sont à nouveau délocalisés (flèche rouge) ce qui dégage le site de liaison de ABCE1(3). eIF5 stimule l'hydrolyse du GTP par eIF2 et le relargage du Pi (phosphate inorganique) facilite la dissociation de ces facteurs d'initiation du 48S (4). Le moment exact où eIF3 quitte le 48S n'est pas connu avec précision mais plusieurs études suggèrent qu'il reste présent pendant l'élongation (Hashem and Frank, 2018). La dissociation de eIF2 permet à eIF5B de lier à l'extrémité CCA de l'ARNt-Met (5) et de stimuler la jonction

des deux sous-unités (6). Le départ de eIF5B et eIF1A signe la fin de l'initiation de la traduction coiffe-dépendante.

Note : ABCE1 (ATP binding cassette E1) avait été à tort attribué à eIF3i et eIF3g dans des modèles antérieurs, l'erreur a été corrigée dans (*Mancera-Martínez et al., 2017) et confirmée par plusieurs études structurales (Kiosze-Becke et al., 2016 ; Heuer et al., 2017).(Modifié d'après Guca and Hashem, 2018)*

1.2 Principales régulations de la traduction

La traduction fait partie des voies de biosynthèse cellulaires les plus coûteuses en énergie (Rolfe and Brown, 1997) : chaque réaction d'estérification d'un ARNt avec un a.a nécessite l'hydrolyse des deux liaisons phosphate d'une molécule d'ATP, la formation de chaque liaison peptidique requiert l'hydrolyse de deux molécules de GTP et à cela s'ajoute le coût de production des composants de la machinerie de traduction. Dans ces conditions, il s'avère plus efficace pour la cellule de réguler la traduction en amont de ces dépenses énergétiques c'est-à-dire au niveau de l'étape d'initiation.

Différents principes de régulation de la traduction existent selon qu'ils s'appliquent à un ARNm, à un groupe d'ARNm ou à la majorité du transcriptome (Figure 10). La régulation globale de la traduction repose généralement sur l'activation ou l'inhibition de composants de la machinerie de traduction et fait fréquemment intervenir des modifications post-traductionnelles de facteurs d'initiation de la traduction (Jackson et al., 2010; Proud, 2018). En comparaison, la plupart des régulations ciblées de la traduction impliquent la reconnaissance d'éléments de séquence *cis* présents sur l'ARNm par des facteurs *trans* incluant des RBP (Hershey et al., 2019) et/ou des petits ARN non codant comme les miARN (Duchaine and Fabian, 2019). Ces différentes régulations peuvent se cumuler sur un même transcrit et de leur combinaison résulte le taux de synthèse du transcrit considéré. Dans ce paragraphe les régulations globales de la traduction sont abordées à travers l'exemple des facteurs d'initiation eIF4E et eIF2. Sont également décrites sans exhaustivité les principales régulations ciblées basées sur des éléments de séquence de l'ARNm ou sur sa localisation intracellulaire. Les régulations médiées par les miARN font l'objet d'une description à part (*cf* partie 1 paragraphe 3).

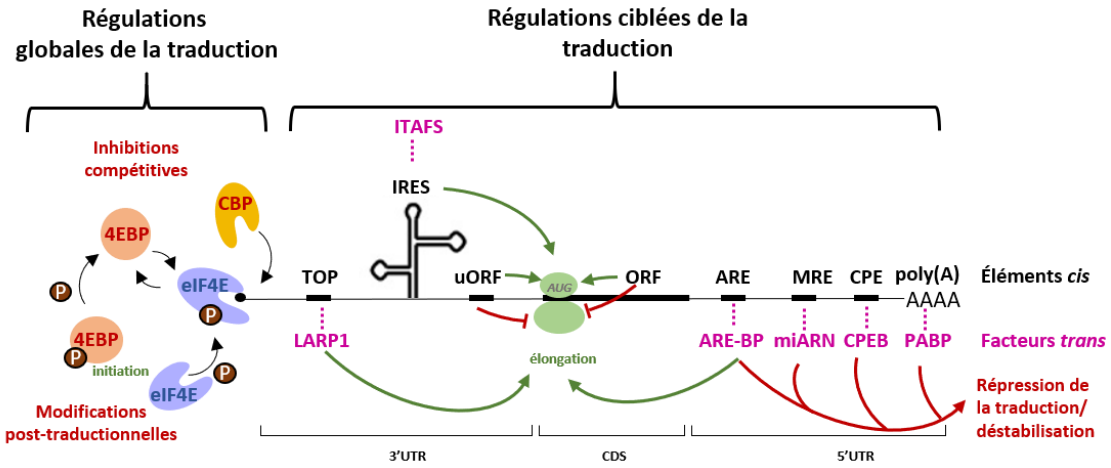

Figure 10 Principes de régulations de la traduction eucaryote.

La régulation de la traduction peut être ciblée lorsqu'elle concerne un groupe d'ARNm spécifiques ou générale quand elle s'applique à la majorité des transcrits. Dans le cas des régulations ciblées, des éléments cis de séquence de l'ARNm (en noir gras) sont reconnus par des facteurs trans (en rose) qui activent ou répriment la traduction (flèches rouges et vertes). Les régulations globales de la traduction font intervenir des inhibiteurs compétitifs des facteurs d'initiation et/ ou des modifications post-traductionnelles modulant l'activité des facteurs d'initiation de la traduction. Abréviations : CBP : Cap Binding Protein ; TOP : Terminal OligoPyrimidine motif ; ITAFS : Interacting Trans Activating Factors ; (u)ORF : (upstream) Open Reading Frame ; ARE (BP) : AU-Rich Element (Binding Protein) ; MRE : miRNA Responsive Element ; CPE Cytoplasmic Poly(A)denylation Element. NB : Les régulations affectant l'élongation se répercutent sur l'initiation de la traduction car il s'agit de l'étape limitante et les régulations ciblant l'initiation empêchent l'élongation. (Modifié d'après Harvey et al., 2018).

1.2.1 Régulation globale de la traduction par inhibition compétitive pour la formation du complexe d'initiation de la traduction

- <u>Régulation de la formation du complexe eIF4F par séquestration d'eIF4E</u>

Par son activité de liaison à la coiffe et d'activation d'eIF4A (Feoktistova et al., 2013), eIF4E est un acteur indispensable de la formation du complexe eIF4F. Conséquemment, il représente une cible de régulation globale de la traduction privilégiée (Merrick and Pavitt, 2018). La régulation de l'activité d'eIF4E fait intervenir les protéines inhibitrices 4E-IP (eIF4E-Interacting Protein) (Figure 11). Le groupe des 4E-IP inclut chez les mammifères les protéines 4E-BP 1,2,3, (eIF4E-Binding Protein 1,2,3), différant principalement par leur distribution tissulaire (Joshi et al., 2004; Pause et al., 1994), CYFIP qui inhibe la traduction des cibles de FMRP (Napoli et al., 2008), 4E-T (Dostie et al., 2000a) et Angel 1 (Gosselin et al., 2013). Tous

ces inhibiteurs se lient à eIF4E *via* la même séquence consensus $YX_4L\Phi$ qu'eIF4G (Mader et al., 1995; Rhoads, 2009). A la différence de eIF4G, les 4E-IP possèdent un motif de liaison supplémentaire à eIF4E (Gosselin et al., 2013 ; Grüner et al., 2016; Peter et al., 2015), qu'elles utilisent pour se lier aux complexes eIF4E-eIF4G, déplacer et prendre la place d' eIF4G sur la surface dorsale d'eIF4E et ainsi empêcher la formation du complexe eIF4F (Igreja et al., 2014)

L'affinité des 4E-BP pour eIF4E est contrôlée par des modifications post-traductionnelles de phosphorylation s'inscrivant dans la voie de de signalisation FRAP/mTOR. (FKBP12 Rapamycin Associated Protein / mammalian Target Of Rapamycin) (Gingras et al., 1999). 4E-BP 1,2,3 portent quatre sites de phosphorylation : Ser 65, Thr 37, Thr 46 et Thr 70. Lorsque ces sites ne sont pas phosphorylés, les 4E-BP entrent en compétition avec eIF4G pour la liaison à eIF4E, ce qui inhibe la traduction. En conditions d'hyperphosphorylation, les 4E-BP adoptent une conformation ne leur permettant plus de se lier à eIF4E lequel s'associe alors à eIF4G (Bah et al., 2015). Cette régulation s'inscrit dans une boucle de rétrocontrôle plus large permettant d'adapter la traduction au niveau d'expression d'eIF4E. 4E-BP1 est hypophosphorylée lorsque le niveau d'expression de eIF4E est faible. Ceci induit la liaison de 4E-BP 1 à eIF4E ainsi que l'ubiquitination et la dégradation de 4E-BP 1 (Yanagiya et al., 2012)

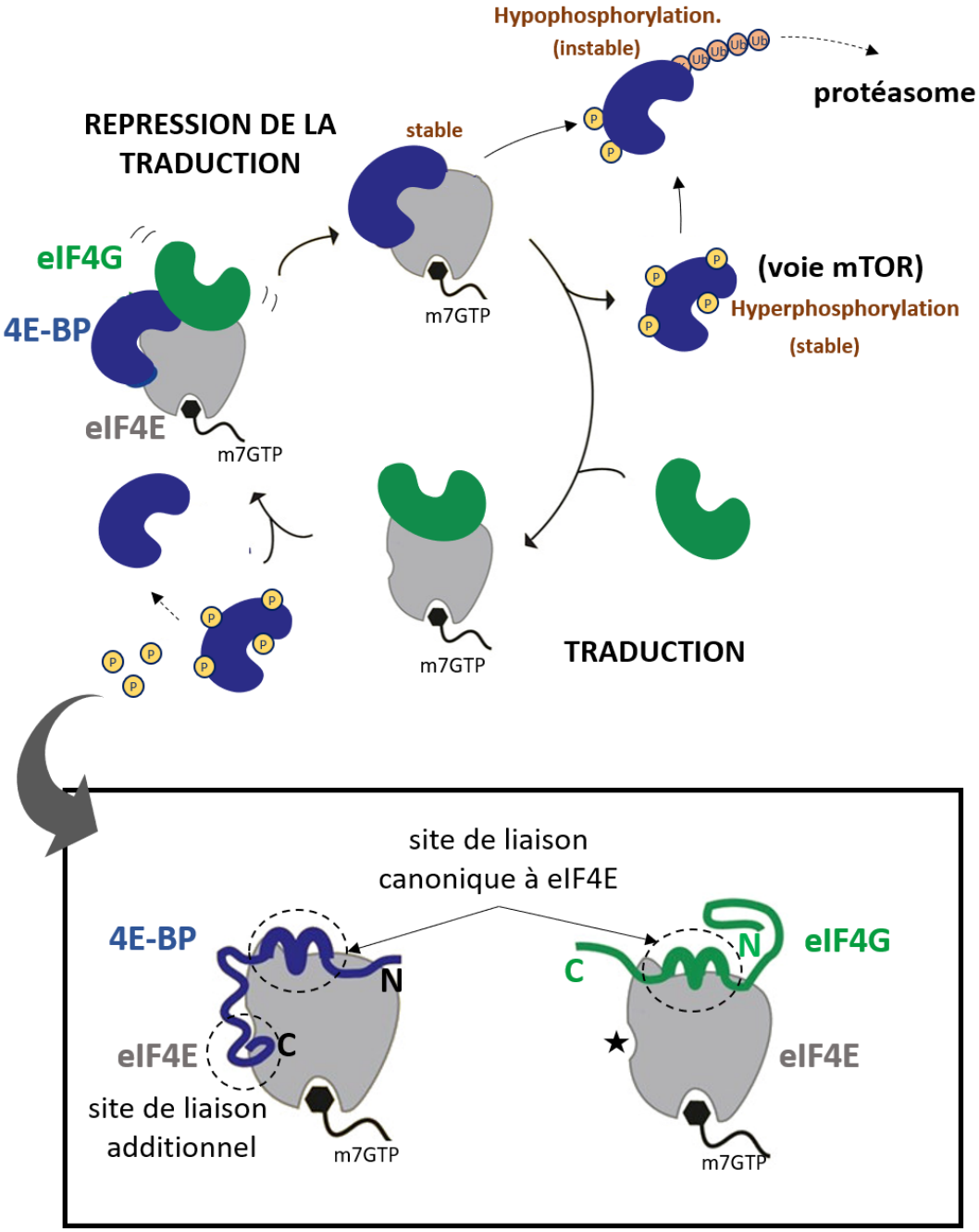

Figure 11 Modèle de régulation de la formation du complexe eIF4F par les 4E-IP

eIF4G se lie à une région dorsale de eIF4E via le motif conservé $YX_4L\Phi$ (avec Y : Tyrosine, X : a.a, L : Leucine, et Φ : a.a à résidu hydrophobe) également présent sur les 4E-IP. eIF4E possède de plus un site de liaison latéral auquel s'attachent les 4E-IP quand eIF4G occupe le site de liaison dorsal. L'attachement des 4E-IP au site latéral de eIF4E accroît leur affinité pour eIF4E d'un facteur 3 ce qui déplace eIF4G du site de liaison dorsal au profit des 4E-IP. La traduction est alors inhibée.

La stabilité et l'association de 4E-IP à eIF4E sont sous contrôle du statut de phosphorylation des 4E-IP. Les 4E-IP doivent être déphosphorylées pour s'associer à eIF4E. Sous forme hypophosphorylée ils sont ubiquitinés et dégradés par le protéasome. Leur hyperphosphorylation permet de les stabiliser lorsqu'ils ne sont pas liés à eIF4E. (Modifié d'après Peter et al., 2015; Yanagiya et al., 2012)

- Régulation de la disponibilité du complexe ternaire par phosphorylation d'eIF2.

Une autre régulation globale bien connue de la traduction s'applique au facteur eIF2. (Figure 12). Hors condition de stress, eIF2B permet à eIF2 d'échanger une molécule de GDP pour une molécule de GTP, forme sous laquelle eIF2 assemble le complexe ternaire et initie la traduction. En conditions de stress, par exemple suite à une infection virale, un choc thermique ou un déficit nutritionnel (Clemens, 2001), l'une des quatre kinases HRI (Haem-Regulated-Inhibitor), GCN2 (General Control Nondepressible 2), PKR (Protéine Kinase activée par l'ARN double brin) ou PERK (PKR-like Endoplasmic Reticulum Kinase) est activée, ce qui phosphoryle la sérine 51 de la sous-unité α du facteur eIF2-GDP. Cette phosphorylation accroît l'affinité de eIF2B pour la forme eIF2-GDP et empêche sa dissociation. Ceci inhibe la formation du complexe ternaire et réduit l'efficacité générale de la traduction (Proud, 2018). Cette régulation s'inscrit dans le cadre de la voie de réponse intégrée au stress (Pakos-Zebrucka et al., 2016). Notons qu'il existe un couplage entre plusieurs modifications post-traductionnelles de eIF2 dont sa méthylation par PRMT7 sur la sérine 51 de la sous-unité α : l'absence de PRMT7 diminue la phosphorylation de eIF2α tandis que sa surexpression l'accroît (Haghandish et al., 2019)

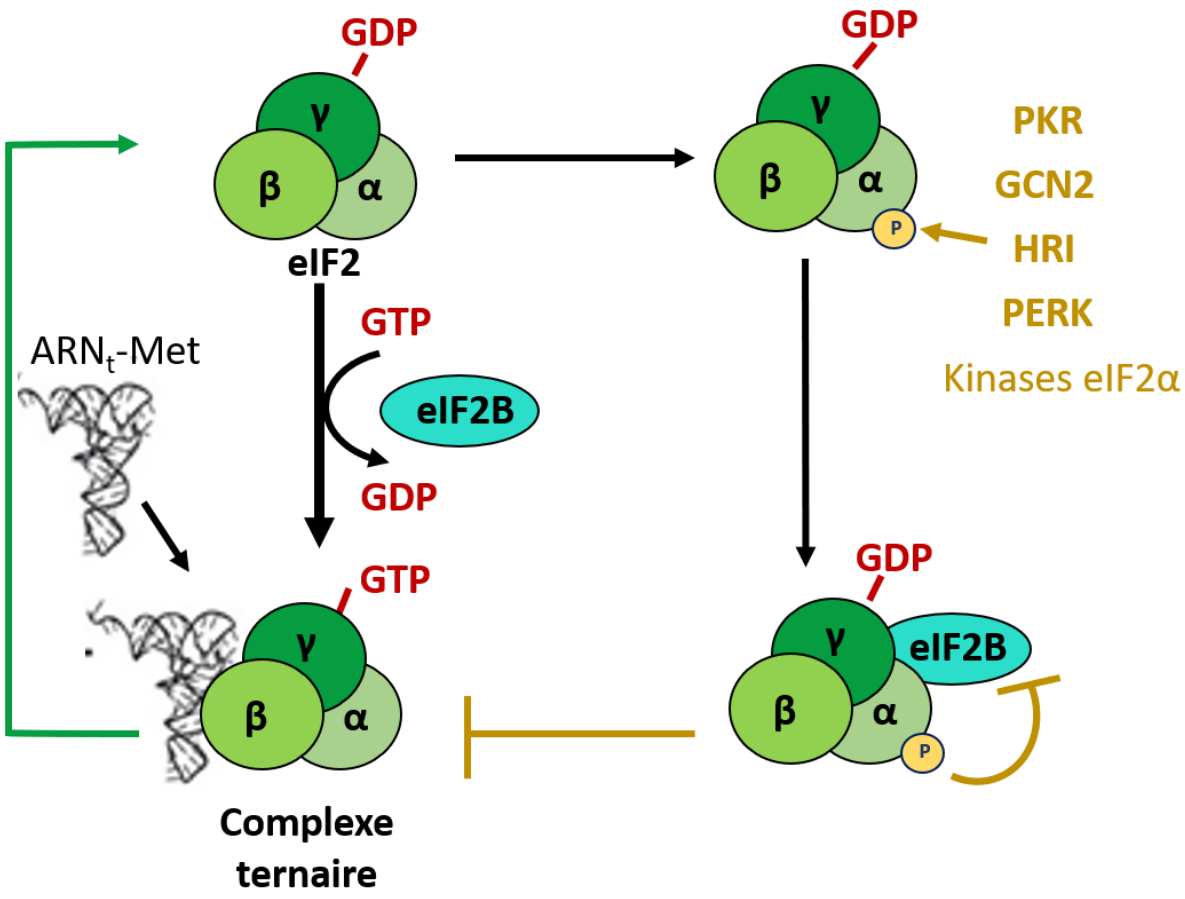

Figure 12 Régulation de la formation du complexe ternaire par phosphorylation d'eIF2

En conditions de stress, plusieurs kinases peuvent phosphoryler la sérine 51 de la sous-unité α de eIF2-GDP.La phosphorylation de eIF2 séquestre eIF2B et l'empêche d'échanger le GDP en GTP sur eIF2. Ceci inhibe la formation du complexe ternaire, indispensable à l'initiation de la traduction. (Modifié d'après Jennings et al., 2017).

1.2.2 Régulations ciblées via la reconnaissance d'éléments de séquence ou de structure dans les UTR

- <u>Régulation de la traduction de l'ORF principale par la traduction d'une uORF</u>

La reconnaissance d'un codon initiateur AUG situé dans un contexte de séquence favorable initie la traduction de l'ORF principale. Il arrive toutefois que ce processus soit perturbé lorsque le 48S rencontre au cours du scanning un codon AUG (uAUG) ou un codon initiateur alternatif (par exemple UUG, CUG) situé en amont du codon initiateur de l'ORF principale. Si cet uAUG est suivi d'un codon stop, le cadre de lecture entre ces deux éléments

constitue une uORF (upstream Open Reading Frame) pouvant être traduite. Ces éléments de séquence sont fréquents à l'échelle du transcriptome : selon des analyses *in silico,* 50% des ARNm mammifères contiendraient au moins une uORF (Calvo et al., 2009). Une grande partie de ces uORF potentielles ont effectivement été retrouvées associées *in vivo* à des ribosomes suite à des expériences de ribosome profiling[2] (Chew et al., 2016; Ingolia et al., 2009; Johnstone et al., 2016). De manière intéressante, la position des uTIS (upstream *Translation Initiation Site)* se trouve évolutivement conservée chez les mammifères : sur 12945 gènes orthologues communs à la souris et à l'homme 85% des uTIS sont conservées (Daubner et al., 2013; Mackereth and Sattler, 2012), ce qui suggère une réelle importance fonctionnelle de la traduction de ces uORF.

Peu de peptides codés par les uORF ont été détectés en spectrométrie de masse (Slavoff et al., 2013), peut-être en raison de leur dégradation rapide et/ou de leur petite taille les rendant techniquement difficiles à détecter (Orr et al., 2020). Ceci suggère néanmoins que l'effet régulateur observé sur la traduction de l'ORF principale est dû à la traduction des uORF plutôt qu'au produit de leur traduction.

La comparaison des niveaux d'ARNm et de protéine issus de plusieurs transcriptomes et protéomes de mammifères montre que les ARNm contenant au moins une uORF ont une expression protéique de l'ORF principale plus faible que les transcrits sans uORF. (Calvo et al.,2009 ; Ye et al., 2015). La comparaison dans plusieurs jeux de données de ribosome profiling des efficacités de traduction du CDS d'ARNm contenant des uORF par rapport aux ARNm sans uORF montre que la présence d'uORF est associée à une répression de la traduction (Johnstone et al., 2016). Cet effet répresseur est confirmé à l'échelle du transcrit individuel puisque l'insertion d'uORF sur des ARNm rapporteurs réduit leur expression protéique de 30 à 80 % en comparaison à un transcrit rapporteur sans uORF, tout en affectant modestement (5%) les niveaux d'ARNm (Calvo et al., 2009; Johnstone et al., 2016).

[2] Le ribosome profiling est une technique de mesure à large échelle et quantitative de la traduction consistant à cartographier les sites d'interaction des ribosomes sur les ARNm en cours de traduction. En pratique, la progression de la traduction est bloquée par l'ajout d'inhibiteurs de la traduction comme la cycloheximide. Les lysats cytoplasmiques sont séparés sur gradient de sucrose. Une partie des ARNm extraits des fractions séparées sur gradient est séquencée à haut débit tandis qu'une autre partie est incubée avec des ribonucléases (souvent la RNAse I) dégradant toutes les régions d'ARN accessibles à l'exception de celles associées à des RBP ou aux ribosomes. Les fragments obtenus après digestion à la RNAse I sont ensuite séquencés. La combinaison des résultats des deux séquençages parallèles permet de déterminer la position exacte de chaque ribosome associé à un ARNm et pour un ARNm donné, la quantité de ribosomes effectivement en train de le traduire.

Les uORFs régulent la traduction de l'ORF principale selon plusieurs mécanismes. (Figure 13). Dans un premier cas de figure, initialement démontré sur l'ARN GCN4 chez la levure (Hinnebush et al., 2005), la traduction de l'uORF entraine le recyclage rapide des facteurs d'initiation et des ribosomes à l'extrémité 5' dès que le codon STOP de l'uORF est atteint, ce qui empêche la machinerie de traduction d'accéder à l'ORF principale.

Alternativement, la traduction de l'uORF peut ralentir les ribosomes ; ceux-ci font alors obstacle aux 48S ne s'étant pas arrêtés sur l'uAUG et empêchent la traduction de l'ORF. Dans cette seconde configuration, l'accumulation des ribosomes au niveau de l'uORF peut induire le recrutement d'UPF1 et induire la dégradation de l'ARNm par la voie du NMD (Nonsense Mediated Decay) (Hinnebusch et al., 2016).

Plusieurs paramètres additionnels affectent l'activité régulatrice des uORF parmi lesquels la longueur de l'uORF, sa position sur la 5'UTR, sa composition en codons, la composition de la séquence autour du codon stop de l'uORF (Wethmar, 2014).

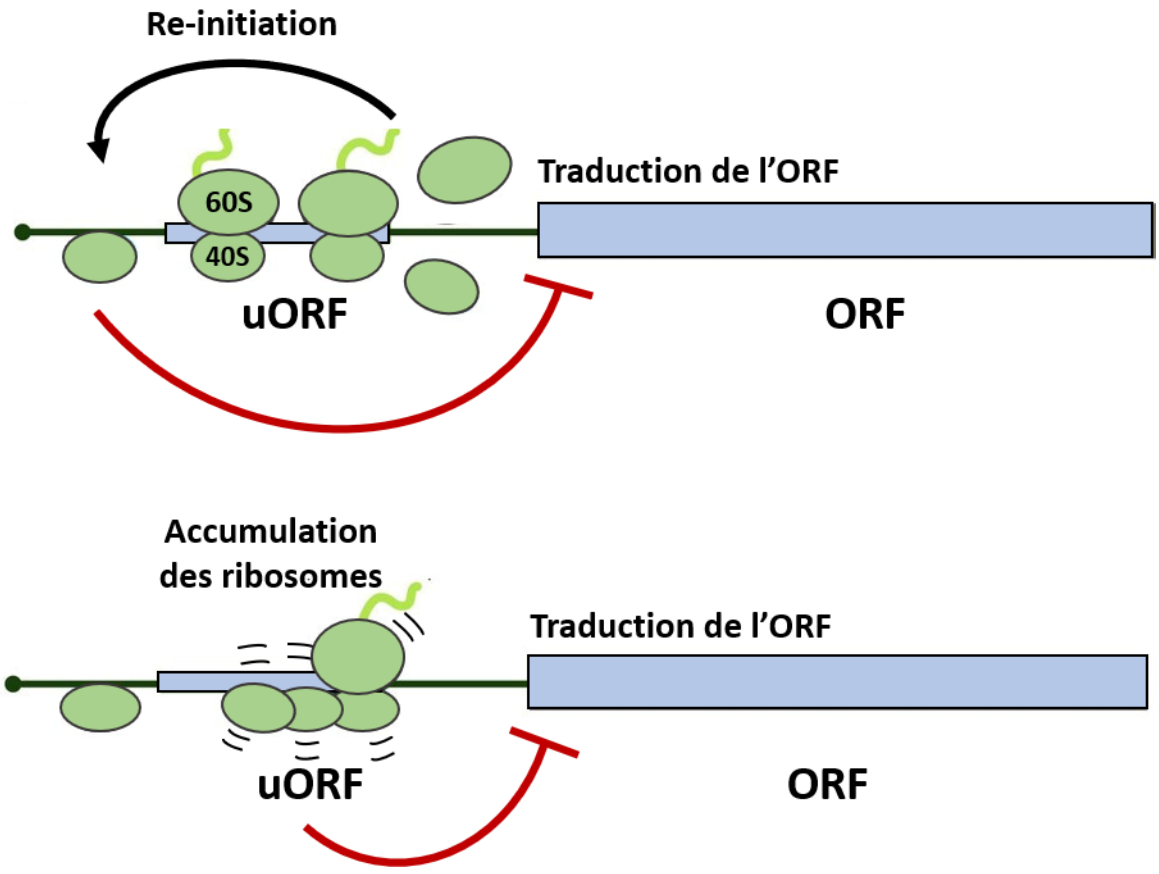

Figure 13 Contrôle de la traduction de l'ORF principale par les uORF

La traduction de l'uORF inhibe la traduction de l'ORF principale selon deux mécanismes. Une première possibilité est que les ribosomes soient recyclés et réadressés à l'extrémité 5' de l'ARNm

immédiatement après la terminaison de la traduction de l'uORF, ils ne peuvent donc pas accéder à l'ORF principale. Alternativement, la traduction de l'uORF peut gêner le scanning par les 48S PIC ne s'étant pas arrêtés à l'uAUG. (Modifié d'après Hinnebusch et al., 2016).

- La reconnaissance par des RBP d'éléments de séquence spécifiques dans les UTR

Un moyen de régulation de la traduction de l'ARNm de manière ciblée fait intervenir le recrutement de facteurs *trans* par des éléments de séquence *cis* localisés dans les UTR. Les facteurs *trans* concernés sont le plus souvent des RBP (RNA Binding Proteins) se liant à l'ARNm *via* des RBD (RNA Binding Domains). Le plus souvent les RBD sont des domaines globulaires permettant de reconnaître des séquences ou structures d'ARN spécifiques et de réguler leur expression de manière ciblée (Hentze et al., 2018). Actuellement plus de 1000 RBP ont été identifiées *in vivo* dans les cellules humaines par des approches de protéomique (Baltz et al., 2012; Beckmann et al., 2015; Castello et al., 2016; He et al., 2016) . Une quarantaine de RBD sont actuellement annotés (Müller-McNicoll and Neugebauer, 2013). Les plus fréquemment rencontrés chez les mammifères incluent les RRM (RNA Recognition Motif), les domaines KH (K-Homology) ; les domaines ZnF (Zinc Finger binding domain) (Corley et al., 2020). Il a été récemment observé que les IDR (Intrinsically Disordered Region) de nombreuses RBP peuvent également servir de domaines de liaison à l'ARN. (Hentze et al., 2018; Järvelin et al., 2016).

Individuellement, les RBP se lient à de courts segments d'ARN (~4-6nt) avec une faible affinité et de manière séquence et/ou structure-spécifique (Änkö et al., 2012; Ascano et al., 2012). *In vivo*, les RBP modulent leur spécificité de liaison à l'ARN ainsi que leur affinité de liaison afin de réguler leurs cibles de manière spécifique. Ceci implique la multimérisation de RBD. Il peut s'agir de plusieurs copies du même RBD (exemple 4 RRM dans les PTB, Sawicka et al., 2008) ou de la combinaison de plusieurs types de RBD comme c'est le cas des protéines CPEB utilisant deux RRM et un ZnF pour lier leurs cibles (Afroz et al., 2015). (Figure 14)

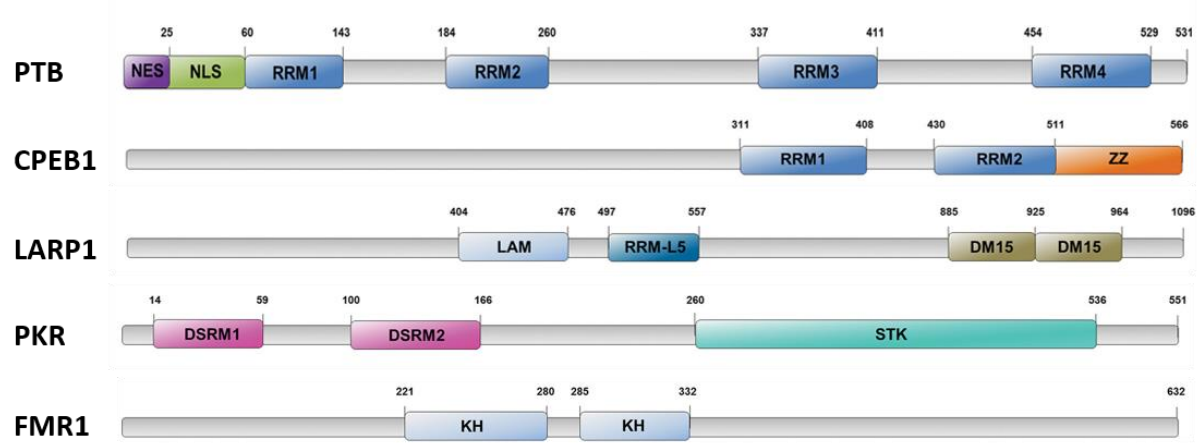

Figure 14 Comparaison de RBP régulatrices de la traduction et de leurs RBD

Les RBD des RBP suivantes est représentée : PTB (Polypyrimidine Tract-Binding protein 1) ; CPEB1 (Cytoplasmic Polyadenylation Element-Binding Protein 1) ; LARP1 (LA-Related Protein 1) ; PKR (double-stranded RNA-activated protein kinase) ; FMR1 (Fragile X Mental Retardation Protein 1).

Domaines de liaison à l'ARN : RRM (RNA Recognition Motif) ; MLLE (Met-Leu-Leu-Glu motif) ; NES (Nuclear Export Sequence) ; NLS (Nuclear localisation Sequence) ; ZZ (ZZ-type zinc finger domain) ; LAM (La motif) ; RRM-L5 (RRM-like motif 5) ; DSRM (Double-Stranded RNA-binding Motif) ; STK (Ser-Thr Kinase domain) ; KH (K Homology RNA-binding domain). (Modifié d'après Harvey et al., 2018)

La traduction de plusieurs groupes d'ARNm incluant les ARNm à motif TOP, les IRES, les CPEs est régulée par ce processus.

Les ARNm portant un motif TOP (Terminal OligoPyrimidine) sont caractérisés par un nucléotide C invariant suivi d'une série pyrimidine de 4-15 nt et d'une région riche en GC directement en aval du motif TOP (Meyuhas and Kahan, 2015). Les ARNm à motif TOP incluent à ce jour 93 transcrits codant majoritairement des protéines impliquées dans la traduction : 79/80 des protéines ribosomales, les cinq facteurs d'élongation de la traduction (EEF1A1, EEF1B2, EEF1D, EEF1G, and EEF2) et des facteurs d'initiation de la traduction (eIF3e, eIF3f, eIF4B et eIF3h). L'extrémité 5' des ARNm TOP est reconnue par le domaine DM15 de la protéine LARP-1 (Lahr et al., 2017) (Figure 14) qui réprime leur traduction par compétition avec eIF4F (Fonseca et al., 2015). L'activité régulatrice de LARP1 sur la traduction des ARNm TOP est sous contrôle de la voie de signalisation mTOR (Philippe et al., 2018) permettant d'adapter la traduction des TOP mRNA aux conditions de croissance (Nandagopal and Roux, 2015).

Un autre motif ARN fréquent est le motif CPE (Cytoplasmic Poly(A)dénylation Element) constitué d'une séquence consensus 5' UUUUAUU 3'présente dans la 3'UTR de 20 à 30% des transcrits chez les vertébrés (Piqué et al., 2008). Les CPE sont reconnus par des protéines CPEB (Cytoplasmic Poly(A)dénylation Elements Binding Protein) qui contrôlent la traduction de leur ARNm cibles par répression ou activation de la poly(A)dénylation (Ivshina et al., 2014). Chez les vertébrés, il existe quatre protéines CPEB (CPEB1-4) divisées en deux sous-familles : CPEB1 et CPEB2-4. Les quatre CPEB ont en commun une région C terminale contenant deux RRM et un ZnF (Afroz et al., 2015) leur permettant de reconnaître les même transcrits contenant des CPE mais avec des affinités différentes (Harvey et al., 2018a). Leur extrémités N-terminales diffèrent par la présence de domaines régulateurs cibles de modifications post-traductionnelles lesquelles combinées à l'action d'autres éléments *cis* déterminent les différentes activités des RBP régulatrices qui s'y lient (Fernández-Miranda and Méndez, 2012). L'activité biochimique des CPEB a initialement été caractérisée sur la protéine CPEB1 dans des ovocytes de Xénope (Figure 15). CPEB1 y remplit deux fonctions : elle réprime la traduction des ARNm maternels portant des CPE dans leur 3'UTR puis active leur traduction dans les œufs matures en induisant la poly(A)dénylation. La répression de la traduction par CPEB1 requiert un arrangement particulier de CPEs sur le transcrit cible avec au moins 2 CPEs espacés par moins de 50 nucléotides (Piqué et al., 2008). Une fois CPEB1 recrutée sur ces CPE, elle inhibe l'interaction {coiffe- eIF4E-eIF4G -PABP-queue poly A} à deux niveaux. D'une part en empêchant l'association de PABP avec la queue poly(A) *via* le recrutement par CPEB1 de la déadénylase PARN (Kim and Richter, 2006) ; et d'autre part en empêchant l'interaction entre eIF4E et eIF4G *via* le recrutement par CPEB1 soit de la protéine 4E-Tqui interagit avec eIF4E et bloque le recrutement de eIF4G soit par le recrutement de 4E-T qui lie eIF4E1b (isoforme d'eIF4E spécifique des ovocytes de Xénope ayant une plus faible affinité pour le m^7GTP et pour eIF4G) et forme un complexe répresseur de la traduction avec DDX6, PAT1 et LSM14B (Andrei, 2005; Minshall et al., 2007a). Chez l'homme, PAT1B et LSM14A, LSM14B, 4E-T sont bien détectées comme partenaires de DDX6 mais pas CPEB1, possiblement en raison de sa faible expression dans ces cellules (Ayache et al., 2015).

L'activation de la traduction dépendant de CPEB1 est déclenchée par une stimulation hormonale à la progestérone induisant la phosphorylation de CPEB1 par la kinase Aurora B, un réarrangement du complexe CPEB permettant la poly(A)dénylation du transcrit par la

poly(A)dénylase GLD2 et l'activation conséquente de la traduction (Kim and Richter, 2006; Mendez and Richter, 2001). Les autres protéines CPEB régulent également la traduction de transcrits portant les motifs CPE mais font intervenir des mécanismes différents .Par exemple CPEB2 agit dans les cellules somatiques sur l'élongation de la traduction qu'il réprime *via* son interaction avec le facteur d'élongation eEF2 tandis que CPEB3 régule la traduction de ses cibles dans les neurones *via* un stockage dans les PB dépendant des conditions d'activité synaptiques et régulée par sumoylation (Ford et al., 2019; Huang et al., 2006; Mendez and Richter, 2001)

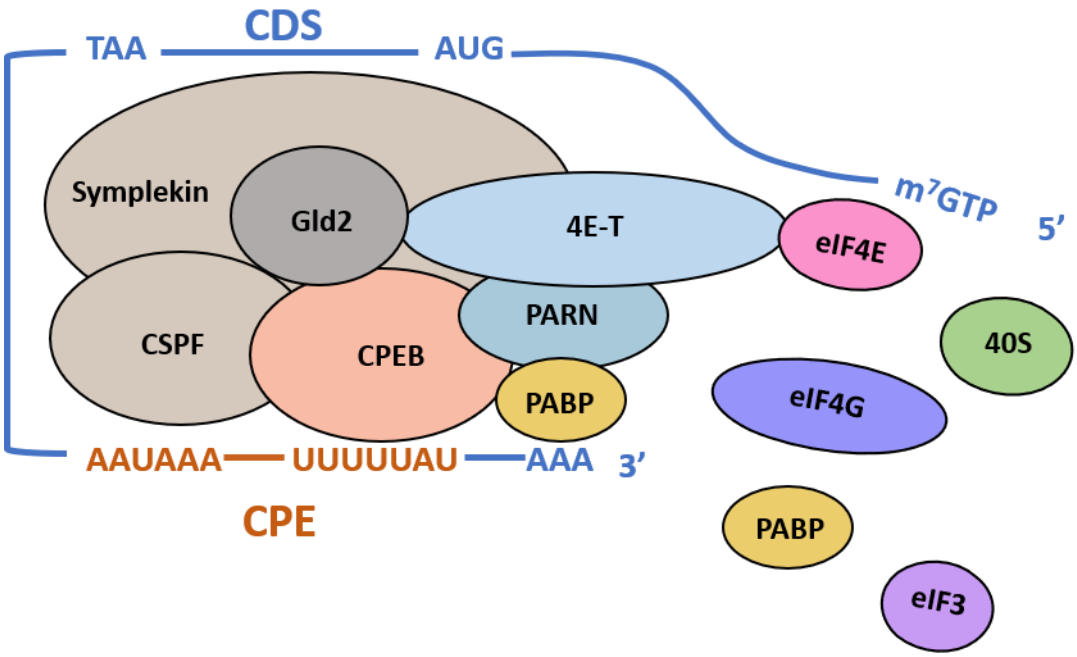

Figure 15 Régulation de la traduction par le complexe CPEB (modèle Xénope)

Dans le noyau des ovocytes de Xénope, les protéines CPEB1 et CSPF (Cleavage and Polyadenylation Specificity Factor) reconnaissent une séquence spécifique dans la 3'UTR de l'ARNm. Le mRNP ainsi formé est exporté dans le cytoplasme où il s'associe avec le facteur d'assemblage, Symplekin, les polymérases Gld2 et PAPB, la déadénylase PARN et 4E-T. Dans les ovocytes de Xénope, PARN étant plus active que Gld2, les ARNm peuvent être déadénylés, ce qui favorise la répression de la traduction. De plus, 4E-T lie simultanément CPEB et eIF4E ce qui empêche la formation du complexe d'initiation de la traduction. Lorsque l'ovocyte est mature, la phosphorylation de CPEB1 par la kinase Aurora B entraîne l'expulsion de PARN du complexe CPEB, ce qui active Gld2 et la traduction. (Modifié d'après Ivshina et al., 2014)

- Régulation de la traduction par des éléments de structure du 5'UTR

La séquence 5'UTR de certains ARNm contient des structures secondaires pouvant intervenir dans le contrôle de la traduction. Nous illustrons ce concept à travers l'exemple des IRES. D'autres structures secondaires telles les G-quadruplexes ou des structures tertiaires telles les pseudoknots sont également impliquées dans la régulation de la traduction (revues dans Leppek et al., 2018).

Entre 10 et 15 % des ARNm mammifères contiennent dans leur 5'UTR une structure localisée juste en amont du codon d'initiation appelée IRES (Internal Ribosome Entry Site) (Weingarten-Gabbay et al., 2016). Cette structure leur permet de recruter directement le complexe d'initiation sur l'ARNm. La traduction par les IRES intervient également dans des conditions où la traduction coiffe-dépendante est compromise, par exemple dans les situations de stress du réticulum endoplasmique, d'hypoxie ou lors de la différenciation cellulaire. De manière intéressante, un grand nombre des ARNm contenant des IRES codent des protéines impliquées dans la protection contre différents stress ou dans l'induction de l'apoptose. (Komar and Hatzoglou, 2011).

Les IRES cellulaires se répartissent en deux classes selon leur mécanisme de recrutement du 40S (Figure 16) : les IRES de type I interagissent avec le 40S *via* des ITAF (IRES Trans-Acting Factors) qui se lient à des éléments *cis* par exemple des RBD ou des modifications m6 méthyl-adénosine (Meyer et al., 2015; Yang and Wang, 2019). Les IRES de type II contiennent un petit élément *cis* s'associant directement à l'ARNr 18S pour recruter le ribosome (Dresios et al., 2006).

La plupart des ITAF ont pour point commun d'appartenir à la famille des HnRNP (Heterogeneous nuclear RiboNucleoProteins) comme par exemple HnRNP A1, C1/C2, I, E1/E2, K. Ces protéines ont la propriété de transiter entre le noyau et le cytoplasme, ce qui suggère une relation croisée entre la traduction et la transcription ou la maturation de l'ARN. Le mécanisme exact par lequel ces ITAF facilitent la traduction IRES-dépendante n'est pas clairement établi et plusieurs hypothèses ont été émises. Les ITAF pourraient agir comme chaperonnes de l'ARNm (Yang and Wang, 2019) et remodeler les structures autour de l'IRES ou alternativement, servir d'adapteurs moléculaires avec le ribosome et/ou les autres eIFs (King et al., 2010; Stoneley and Willis, 2004).

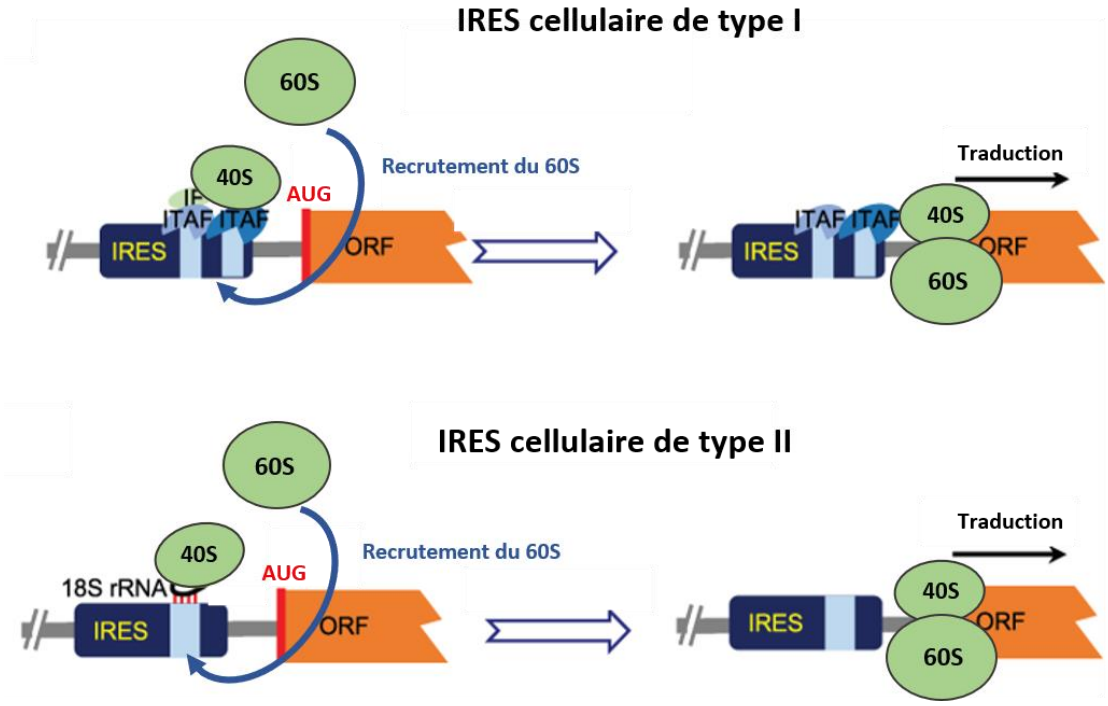

Figure 16 Traduction IRES-dépendante des ARNm cellulaires

Dans les IRES cellulaires de type I, l'élément cis est reconnu par des ITAF qui interagissent directement avec le 40S ou recrutent le 40S indirectement via des facteurs d'initiation (IF). Les IRES de type II contiennent quant à eux un élément cis se liant directement à l'ARNr18S du 40S. (Modifié d'après Yang and Wang, 2019)

1.2.3 Influences de la composition nucléotidique de l'ARNm sur la traduction

Le code génétique comporte 61 codons codant 20 acides aminés. Ceci implique qu'un même acide aminé puisse être codé par plusieurs codons synonymes. Lorsqu'un acide aminé est codé par n codons synonymes il est dit n fois dégénéré (n allant de 2 à 6).

Chez plusieurs espèces comme la levure *S. cerevisiae*, la bactérie *E. coli*, et le poisson zèbre *D. rerio*, des approches par ribosome profiling ont montré que ces codons synonymes ne sont pas uniformément décodés par le ribosome, certains codons se trouvant plus rapidement décodés que d'autres (Ingolia, 2014). Les codons synonymes les plus efficacement décodés sont définis comme « optimaux ». Plusieurs paramètres rendent compte du degré d'optimalité des codons comme par exemple le tAI (ARNt Adaptative Index) défini chez la levure comme l'efficacité avec laquelle l'ARNt correspondant à un codon donné est utilisé par

le ribosome (Zhou et al., 2009). Sur la base de cet indicateur, les codons optimaux ont été définis comme ceux ayant un tAI > 0,47 (Pechmann and Frydman, 2013). Des expériences de ribosome run-off[3] chez la levure montrent que des ARNm rapporteurs enrichis en codons optimaux sont relocalisés dans les fractions sub-polysomales d'un gradient de sucrose suite au run-off alors que les ARNm avec peu de codons optimaux restent sédimentés dans les fractions polysomales (Presnyak et al., 2015). Ces résultats suggèrent que la composition en codons du CDS influence la cinétique locale d'élongation de la traduction. Ceci est cohérent avec les résultats d'expériences de traduction *in vitro* dans lesquelles des vitesses d'élongation plus importantes sont mesurées sur des ARNm enrichis en codons optimaux (Yu et al., 2015). Plusieurs explications rendraient compte du décodage non uniforme des codons synonymes. Elles incluent l'influence des niveaux d'offres et de demandes des ARNt sur le taux d'occupation du ribosome (Hanson and Coller, 2018), les différences de stabilité d'appariement de la wobble base (Stadler and Fire, 2011) et l'influence de la composition de séquence et de la structure de l'ARNm autour du codon initiateur (Pop et al., 2014).

A ceci s'ajoute le constat que les codons synonymes ont un usage biaisé c'est-à-dire qu'ils ne sont pas uniformément représentés dans le transcriptome. Pour expliquer la corrélation observée entre le biais d'usage de codons et le niveau d'expression protéique, Chu et collaborateurs ont calculé la corrélation entre les niveaux d'expression protéique et plusieurs paramètres influencés par le biais d'usage de codons comme la vitesse d'élongation moyenne sur l'ORF, le contenu en GC, le niveau de structure de l'ARNm et le niveau d'expression de l'ARN. Parmi ces paramètres, la vitesse moyenne d'élongation est le plus fortement corrélé au niveau d'expression protéique (Chu et al., 2014). Le modèle établi chez la levure propose que les ribosomes s'accumulent au niveau des séquences enrichies en codons non optimaux et que ce ralentissement se répercute sur l'étape d'initiation de la traduction en empêchant les ribosomes d'y être recyclés ce qui diminue le rendement en protéine du transcrit considéré (Figure 17)

[3] Le ribosome run-off est une technique à large échelle et quantitative dérivée du ribosome profiling et utilisée pour étudier l'élongation de la traduction *in vivo*. Elle est basée sur l'emploi d'inhibiteurs de la traduction spécifiques tels la harringtonine ou la lactidomycine qui bloquent les ribosomes au niveau du codon initiateur. L'élongation est ensuite bloquée à différents temps après l'ajout des inhibiteurs de l'initiation. Ceci permet de mesurer la distance parcourue par les ribosomes depuis le site d'initiation et ainsi de déterminer la vitesse d'élongation et les sites de pause du ribosome.

Dans le transcriptome humain, nous avons observé une corrélation forte (rs= 0,46) entre le nombre de codons peu fréquents (prenant en compte la fréquence d'usage de chaque codon et la longueur des CDS) et le rendement protéique (Courel et al., 2019). Nous reviendrons sur ce point dans la partie résultats.

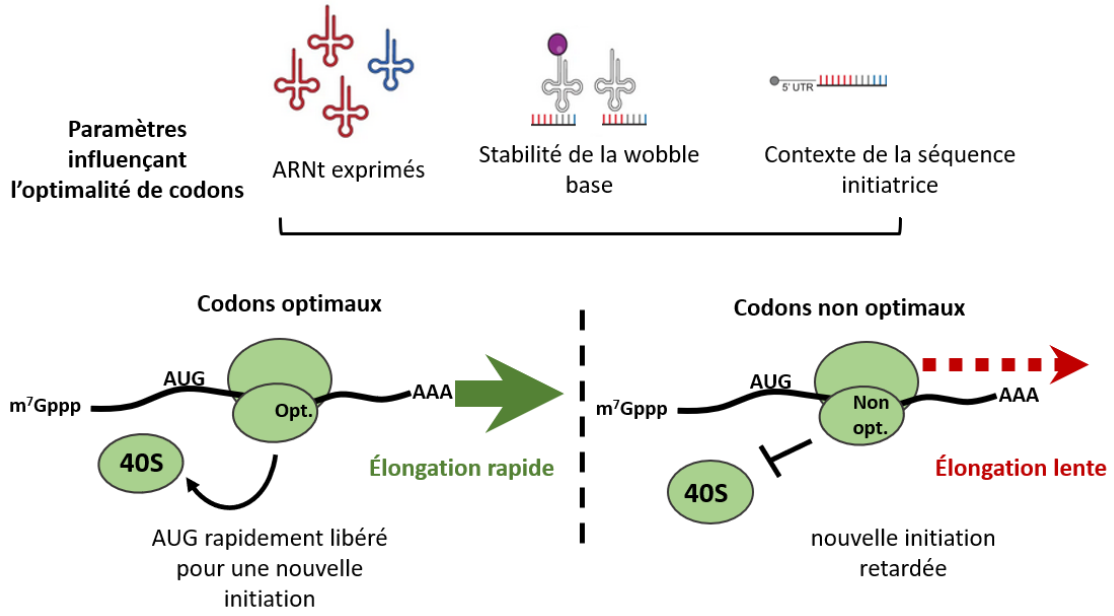

Figure 17 Influence de la composition en codons du CDS sur la traduction

Les CDS contenant des codons non optimaux ont une phase d'élongation plus lente que les CDS contenant des codons optimaux. Cette différence d'élongation affecte le taux de synthèse du transcrit lorsqu'elle se répercute sur l'étape d'initiation en retardant la libération du 40S. Plusieurs paramètres tels que le niveau d'expression des ARNt, la stabilité d'appariement de la wobble base et la composition de la séquence autour du codon initiateur influencent l'efficacité avec laquelle les ribosomes décodent les codons. (Modifié d'après Wu et al., 2019).

1.2.4 La traduction localisée

Certains ARNm sont traduits localement à des endroits précis de la cellule. Souvent cette traduction spatialement délimitée repose sur la localisation de l'ARNm dès lors qu'il est plus efficace de transporter des ARNm puis de les traduire *in situ* plutôt que de transporter une à une des protéines sur leur lieu d'action (Hilliker, 2014). La traduction localisée entre en jeu dans de nombreux processus biologiques comme par exemple la polarisation embryonnaire, ou la plasticité synaptique (Buxbaum et al., 2015). Dans cette introduction nous nous limitons

aux traductions localisées aux membranes en nous basant sur l'exemple du Réticulum Endoplasmique Rugueux (RER).

La traduction localisée à la membrane du RER, concerne principalement les ARNm codant des protéines membranaires ou sécrétées transitant par le réseau endomembranaire et a été visualisée très tôt en microscopie électronique (Palade, 1975). Le processus commence dans le cytosol où se déroulent les phases d'initiation et le début de l'élongation. Lorsqu'une séquence-signal ou un domaine transmembranaire émerge à l'extrémité du peptide naissant, celui-ci est reconnu par la protéine SRP (Signal Recognition Particle) qui adresse co-traductionnellement l'ensemble {ribosome/ARNm/peptide naissant} à la membrane du réticulum endoplasmique (Noriega et al., 2014) en se fixant au récepteur du SRP (Figure 18). Au fur et à mesure que la traduction se poursuit sur la membrane de l'ER, le peptide naissant est transloqué dans le lumen du RER *via* le canal transmembranaire Sec61. Une fois dans le lumen différentes chaperonnes comme BiP assistent le repliement du peptide.

La traduction localisée au RER couplée avec le transport dans le lumen sert également de traduction auxiliaire dans des conditions de stress (infection virale, hypoxie…) où la traduction cytosolique est inhibée (Lerner and Nicchitta, 2006; Staudacher et al., 2015).

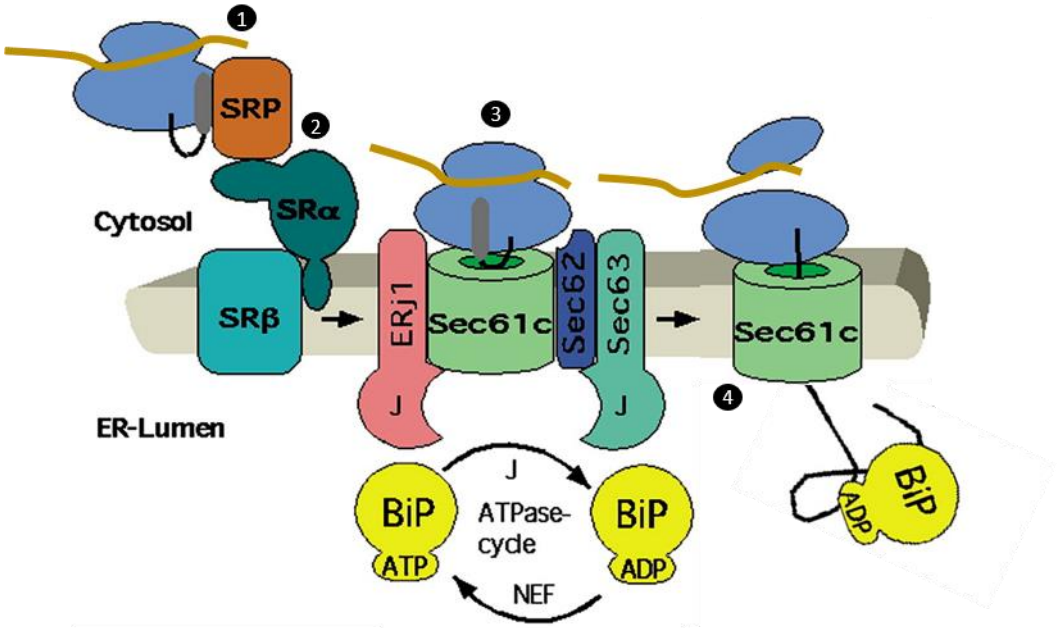

Figure 18 Modèle de traduction localisée à la membrane du réticulum endoplasmique

La séquence signal d'adressage à l'ER présente sur le peptide naissant est reconnue par la protéine SRP (1). La protéine SRP se lie à la sous-unité α du récepteur SRP (2) ce qui amène le ribosome en cours de traduction au contact du canal transmembranaire Sec61 (3). Le peptide naissant est inséré co-traductionnellement dans le lumen où des chaperonnes telles BiP contribuent à son repliement (4). (Modifié d'après Zimmermann et al., 2011)

2. Stabilité des ARNm dans le cytoplasme

2.1 Mécanismes généraux de dégradation de l'ARNm

Dans les cellules mammifères, les demi-vies des ARNm s'étalent sur une gamme allant de la minute à la journée (Ingolia et al., 2011; Schwanhäusser et al., 2011; Tani et al., 2012), ce qui résulte de différents processus de dégradation des ARNm dans le cytoplasme. Dans cette partie nous présentons succinctement les mécanismes de la déadénylation et du decapping, étapes préalables à l'exécution des voies de dégradation générales de l'ARNm par XRN1 ou par l'exosome (Figure 19). Après avoir résumé ces voies de dégradations, nous abordons deux processus de régulation de la stabilité des transcrits : l'usage différentiel de codons et les régulations en *trans* à travers l'exemple des ARE-BP.

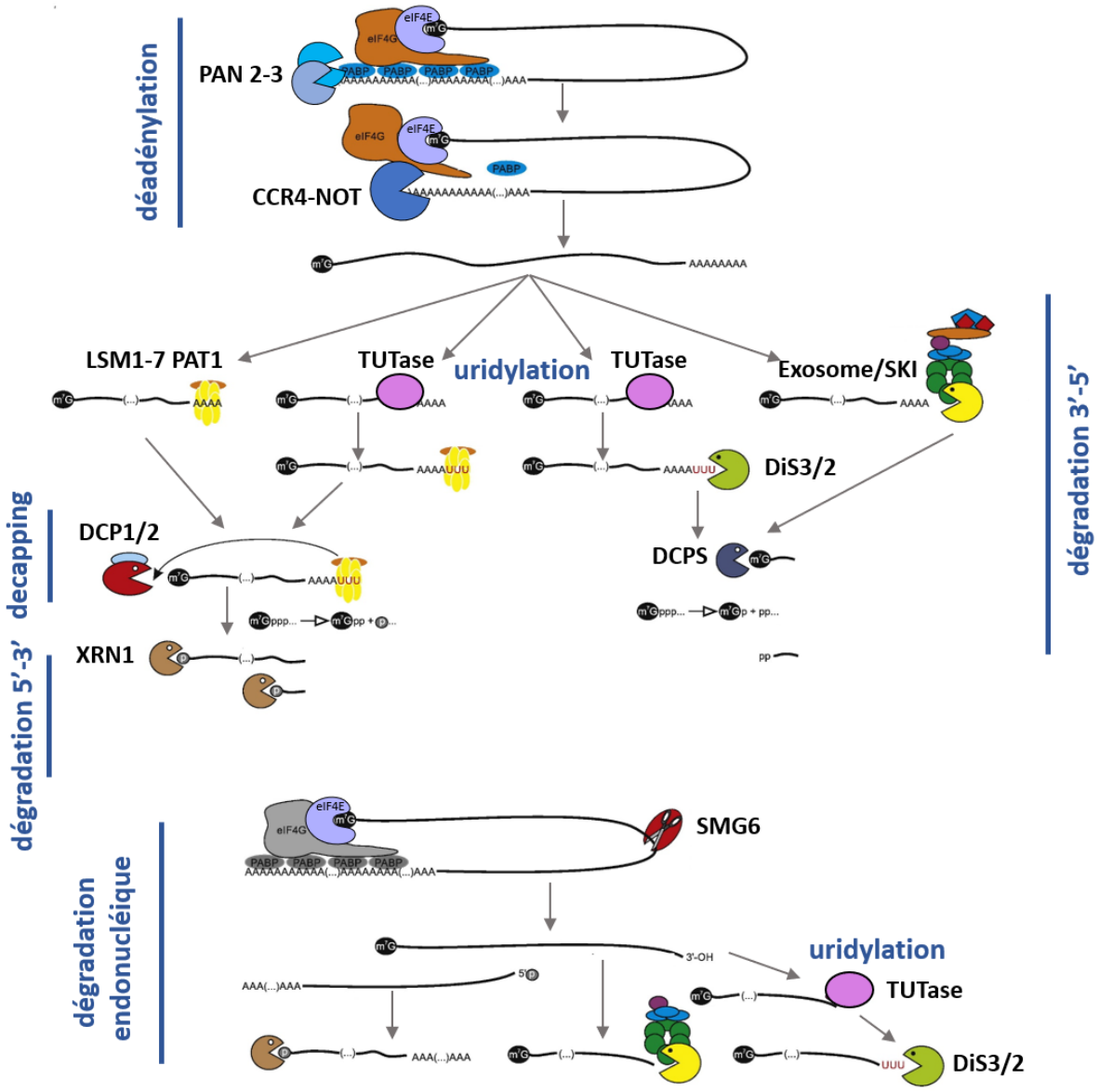

Figure 19 Principales voies cytoplasmiques de dégradation de l'ARNm

La dégradation de l'ARNm commence par la disruption de la structure en boucle fermée de l'ARNm et la déprotection des extrémités 5' et 3' par decapping, déadénylation et uridylation. Après quoi la dégradation a lieu soit à partir de l'extrémité 5' lorsqu'elle est médiée par XRN1 soit à partir de l'extrémité 3' lorsqu'elle fait intervenir l'exosome. Quand la dégradation intervient dans le cadre d'une voie de contrôle de la qualité elle peut être initiée par clivage endonucléolytique. Ceci conduit à l'exposition de fragment 3' et 5' non protégés qui sont alors dégradés par les exonucléases précédemment citées. (Modifié d'après Łabno et al., 2016)

2.1.1 Déadénylation

La déadénylation se déroule à l'extrémité 3' de l'ARNm et consiste en un raccourcissement de la queue poly A (Muhlrad and Parker, 1992). Chez les eucaryotes, deux complexes enzymatiques exécutent la déadénylation cytoplasmique : le complexe CCR4-NOT incluant les déadénylases CCR4 et POP2 (aussi appelée CAF1) et le complexe PAN comprenant les enzymes PAN2 et PAN3 (Poly(A) Nucléase 2 et 3). A ces deux complexes s'ajoute l'activité individuelle d'autres déadénylases telles PARN, Nocturnin ou Angel1/2 (revues dans Godwin et al., 2013).

- Le complexe CCR4-NOT :

Le complexe CCR4-NOT est constitué des deux déadénylases CCR4 et POP2 interagissant l'une avec l'autre ainsi qu'avec les protéines non-enzymatiques CNOT1, CNOT2, CNOT3, CNOT4, CNOT9 et CNOT10. Dans les cellules humaines, CCR4 et POP2 possèdent chacune deux orthologues : CCR4A/CNOT6 et CCR4B/CNOT6L pour CCR4 et CAF1A/CNOT7 et POP2/CNOT8 pour POP2 (Aslam et al., 2009). Les orthologues CNOT7 et CNOT8 diffèrent par la composition des sous-complexes qu'ils forment avec les protéines CNOT (Lau et al., 2009). Concernant l'architecture du complexe CCR4-NOT, la protéine CNOT1 sert d'échafaudage sur lequel les sous-unités additionnelles se lient selon un arrangement dépendant de l'organisme considéré (Wahle and Winkler, 2013). CNOT9 et CNOT2/3 servent de plateforme d'interaction protéine-protéine avec des RBP. Chez l'homme, les 2 sous-unités catalytiques CCR4 et POP2 interviennent de façon complémentaire dans le processus de déadénylation (Figure 19) : POP2 se lie aux segments poly(A) n'étant pas liés à PABP tandis que CCR4 raccourcit les séquences associées à PABP et sur lesquels l'activité de POP2 est bloquée (Yi et al., 2018). CAF1 est également impliquée dans la déadénylation induite par les siARN/miARN (Piao et al., 2010). Les sous-unités CNOT 10 et CNOT 11 interagissent également avec CNOT1 (Lau et al., 2009; Mauxion et al., 2013) sans que leur rôle n'ai été à ce jour précisément caractérisé, ce qui est également le cas de la majorité des sous-unités non enzymatiques de CCR4-NOT. Les sous-unités non enzymatiques serviraient de site de liaison aux RBP capables de recruter CCR4-NOT sur l'ARNm et permettraient ainsi de rendre la déadénylation transcrit-spécifique. A titre d'exemple, les ARNm liés au complexe RISC peuvent recruter CCR4-NOT *via* une interaction physique directe entre CNOT9 et TNRC6 (Mathys et al., 2014). Dans plusieurs autres

organismes des RBP spécifiques telles Nanos (Bhandari et al., 2014; *D.melanogaster*), Pumilio (Webster et al., 2019; *S.cerevisiae*), Smaug (Wahle and Winkler, 2013 *S.cerevisiae*), SMG5/7 (Shoemaker and Green, 2012; *S.cerevisiae*) ou TTP (Bulbrook et al., 2018; HeLa cells), peuvent également recruter CCR4-NOT *via* l'une de ses sous-unités non-enzymatiques.

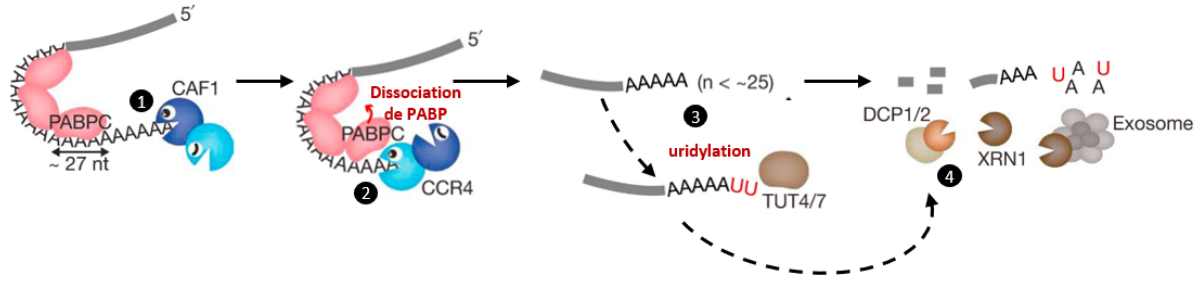

Figure 20 Modèle de déadénylation puis dégradation de l'ARNm dépendant du complexe CCR4-NOT

CCR4 dégrade la partie 3' de la queue poly A non liée à la PABP (1). CNOT dégrade ensuite la partie associée à PABPC par unités de 27nt ce qui dissocie PABP de l'ARNm (2). L'ARNm déadénylé peut être uridylé par des TUTases telles TUT4 ou TUT7 (3). Le départ de PABP engage irréversiblement l'ARNm dans l'une des voies de dégradation 5'-3' ou 3'-5'. (4). (*Modifié d'après* Yi et al., 2018)

- <u>Le complexe PAN</u>

Ce second complexe de déadénylation contient l'enzyme PAN2, responsable de l'activité catalytique ainsi que PAN3, qui régule l'activité de PAN2. Ces deux enzymes catalysent conjointement un raccourcissement partiel de la queue poly(A) d'environ 200 à 110 adénosines chez les mammifères (Uchida et al., 2004; Wahle and Winkler, 2013). Des études de cinétiques de dégradation de l'ARNm codant la β-globine en conditions de surexpression de CCR4 ou PAN2 chez la souris montrent que la déadénylation se réalise séquentiellement : elle est initiée par PAN2 tant que la PABP est présente. Une fois PABP déplacée, PAN2 est inactivée au profit de CCR4 qui achève la déadénylation (Yamashita et al., 2005).

2.1.2 Le Decapping

Dans la perspective où le transcrit sera dégradé à partir de son extrémité 5', sa coiffe protectrice est préalablement clivée de manière irréversible, ce qui constitue l'objet de la phase de decapping. Cette étape peut succéder à la déadénylation mais il arrive également qu'elle se produise indépendamment du raccourcissement de la queue poly A.

Le decapping est orchestré par le complexe DCP1/DCP2 dans lequel l'activité enzymatique est portée par DCP2 (Wang et al., 2002), tandis que DCP1 joue le rôle d'activateur de DCP2. Des mesures de cinétique de dégradation *in vitro* ont montré que d'autres facteurs prennent part à l'activation de DCP2. Les facteurs d'activation évolutivement conservés de la levure à l'homme incluent : le complexe LSM1-7 /PAT1B (Vindry et al., 2017), la protéine EDC3 (Enhancer of decapping 3) (Fromm et al., 2012; Nissan et al., 2010) et l'hélicase DDX6 (Coller and Parker, 2004). Chez la levure, deux facteurs supplémentaires, Edc1 et Edc2, contribuent à activer Dcp2 (Borja et al., 2011). Chez les métazoaires, le facteur EDC4 -inexistant chez la levure, est nécessaire pour assembler le complexe de decapping et activer DCP2 (Łabno et al., 2016).

Concernant le mécanisme d'activation de DCP2 par ses cofacteurs, les données de cristallographie réalisées chez la levure montrent que l'interaction directe de Dcp1 avec Dcp2 fait passer l'enzyme d'une conformation ouverte catalytiquement inactive à une conformation fermée active (She et al., 2008). Des études structurales plus récentes sur le complexe Dcp1-Dcp2-m^7GDP indiquent que Dcp1 stabilise le domaine catalytique NRD de Dcp2 et recrute les deux autres cofacteurs de decapping Edc1 et Edc2. Simultanément, la liaison directe d'Edc3 à Dcp2 accroît l'affinité de Dcp2 pour l'ARNm et stimule son activité catalytique (Charenton et al., 2016). L'interaction Dcp1/Edc1 sert quant à elle à positionner Dcp2 dans une conformation catalytiquement active par rapport à la coiffe de l'ARNm (Mugridge et al., 2018). Les domaines d'interaction entre Dcp1 et Dcp2 sont pas conservés de la levure à l'homme et les interactions directes entre DCP1 et DCP2 y sont de faible affinité. L'activation de DCP2 nécessite chez les métazoaires l'intervention d'EDC4 (Figure 21). Celle-ci sert de plateforme d'assemblage pour le complexe de decapping en liant simultanément DCP1, DCP2 et XRN1 et permet à un trimère DCP1 d'activer DCP2 (Chang et al., 2014).

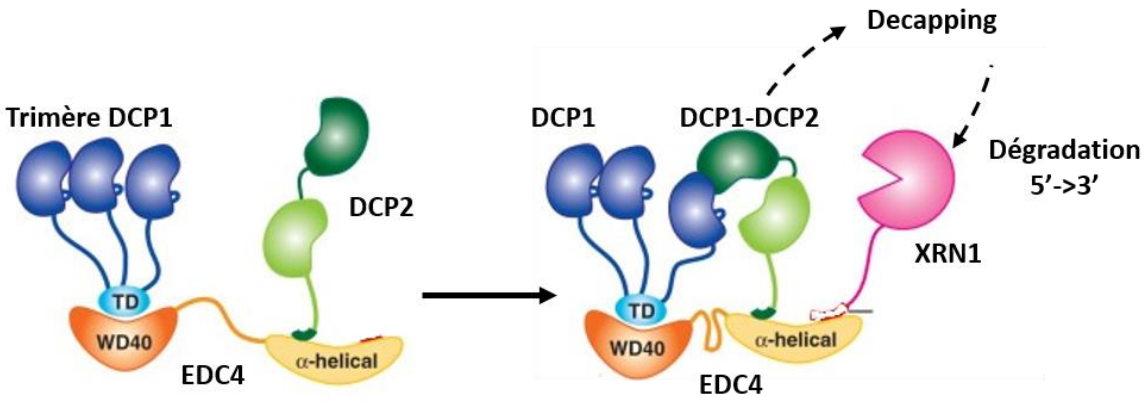

Figure 21 Activation du complexe de decapping humain

DCP1 se lie sous forme de trimère sur le domaine WD40 du cofacteur EDC4. Suite à cette liaison, DCP1 se lie au domaine NRD de DCP2 laquelle adopte alors une conformation fermée, catalytiquement active pour la réaction de decapping. Le recrutement direct de XRN1 sur EDC4 permet aux transcrits dont la coiffe vient d'être clivée par DCP2 d'être dégradés rapidement. (Modifié d'après Chang et al., 2014).

Deux autres cofacteurs de decapping, PAT1B (Pat1 chez la levure) et DDX6 (Dhh1 chez la levure), sont aussi impliqués dans l'activation de DCP2. Pat1 a initialement été décrit comme un activateur de decapping suite à l'observation que des ARNm rapporteurs sont stabilisés sous leur forme coiffée et déadénylée dans des souches *patl1Δ* (Bouveret et al., 2000; Tharun et al., 2000). Sa fonction d'activateur de decapping a également été caractérisée chez l'homme par des expériences de tether assay[4] (Ozgur et al., 2010). De plus, à l'échelle du transcriptome 2221 gènes se trouvent stabilisés après siPAT1B (Vindry et al., 2017) ce qui est cohérent avec un rôle de cette protéine dans la dégradation des ARNm. En termes d'interactions protéiques, PAT1B est co-immunoprécipité avec DCP1/2 et XRN1 (Ozgur et al., 2010) et interagit directement avec LSM1-7 (Sharif and Conti, 2013) ce qui laisse supposer qu'il contribue au decapping en facilitant le recrutement des autres facteurs du decapping sur l'ARNm. De manière intéressante, PAT1B interagit de façon ARN- dépendante avec eIF4E, eIF4G et PABP (Arribas-Layton et al., 2013) et sa surexpression provoque une répression générale de la traduction chez la levure (Coller and Parker, 2004). Cette activité

[4] Le thether est un essai fonctionnel permettant d'étudier *in vivo* le rôle d'une RBP d'intérêt sur la traduction/ la stabilité de ses ARNm cibles indépendamment de la capacité de liaison à l'ARNm de la RBP.

supplémentaire de répresseur de la traduction en remodelant le complexe d'initiation de la traduction faciliterait l'accès de DCP2 à la coiffe m^7GTP.

Un autre cofacteur de decapping : DDX6, interagit avec PAT1B (Ayache et al., 2015) et possède également une activité de répression de la traduction (Minshall et al., 2009). Il sera détaillé ultérieurement dans la seconde partie de cette introduction.

Les mécanismes précis par lesquels PAT1B et DDX6 remodèlent les complexes d'initiation de la traduction et/ou activent le decapping ne sont pas clairement caractérisés. Une étude récente de transcriptomique réalisée sur des levures *Dcp2Δ*, *Pat1Δ*, *Lsm1Δ* ou *Dhh1Δ* a apporté des précisions sur leurs modes d'action respectifs (He et al., 2018). Les profils d'expression issus des différents séquençages indiquent que Pat1, Lsm1 et Dhh1 sont impliqués dans la déstabilisation d'une partie seulement des transcrits ciblés par Dcp2. De plus, les transcrits séquencés se répartissent en deux sous-groupes : d'un côté des transcrits conjointement stabilisés en l'absence de Pat1 ou de Lsm1 (cohérent avec l'existence d'un complexe Pat1- Lsm1-7) et d'un autre côté des transcrits stabilisés en l'absence de Dhh1 et insensibles à Pat1 et Lsm1-7. Ces résultats nuancent l'assertion que ce sont des facteurs « généraux » de decapping (Parker, 2012) et suggèrent que Pat1 et Dhh1 remplissent des fonctions distinctes dans le processus de decapping.

En plus d'être nécessaire à la voie de dégradation générale 5'-3', le complexe de decapping est également requis dans des voies de dégradation particulières telles le NMD (Nonsense Mediated Decay), la dégradation des transcrits portant des éléments ARE (Fenger-Grøn et al., 2005; Yamashita et al., 2005) et la dégradation des cibles de miARN (Behm-Ansmant et al., 2006). Le complexe de decapping est alors recruté par des RBP spécifiques. Par exemple, DDX6 interagit dans les cellules humaines avec les effecteurs de la voie des miARN AGO1 et AGO2 indépendamment de l'ARN. De plus, l'absence de DDX6 diminue la répression d'un ARNm rapporteur cible de miARN (Chu and Rana, 2006). En ce qui concerne les cibles du NMD, c'est le facteur UPF1 qui recrute DCP2 et active le decapping (Lykke-Andersen, 2002).

2.1.3 Deux options de dégradation

- -Dégradation ‘5’ ->3 par l’exonucléase XRN1

Suite au decapping par DCP2, les ARNm possédant une extrémité 5’ monophosphate lient l’exonucléase 5’ 3’ cytoplasmique XRN1 (Jones et al., 2012). Des approches par cristallographie ont montré : que le site catalytique de XRN1 reconnaît l’extrémité 5’ de l’ARNm et que l’ARNm est transloqué nucléotide par nucléotide au fur et à mesure que l’ARNm substrat est hydrolysé. Ce mode de fonctionnement permet notamment à XRN1 de résoudre des structures secondaires sur l’ARN sans consommer d’ATP (Jinek et al., 2011).

Plusieurs interactions impliquant XRN1 sont le support d’un couplage entre la dégradation 5’->3’, le decapping et la déadénylation. Chez la Drosophile et la levure, XRN1 est co-immunoprécipité avec DCP1 indépendamment de la présence d’ARN et la structure de leurs domaines d’interaction a été caractérisée par spectrométrie RMN (Braun et al., 2012). Chez les vertébrés, le domaine d’interaction de XRN1 avec DCP1 n’est pas conservé et le couplage dégradation/decapping s’effectue *via* le cofacteur EDC4 interagissant simultanément avec XRN1 et DCP1 (Braun et al., 2012; Chang et al., 2014) (Figure 21). Concernant le couplage entre dégradation et déadénylation, des approches de co-immunoprécipitation et de purification d’affinité montrent que XRN1 interagit directement avec le complexe CCR4-NOT ainsi qu’avec PAT1B *via* la région peu structurée CIR (C-terminal Interacting R*egion)*, et que ces interactions s’excluent mutuellement (Chang et al., 2019). Plus encore, cette étude a montré que l’interaction XRN1-CCR4-NOT réprime la déadénylation par la sous-unité POP2. Les auteurs suggèrent que la liaison concurrentielle de PAT1B à ce même domaine contribue à coordonner la déadénylation, le decapping et la dégradation 5’->3’.

Dans la plupart des modèles, la dégradation par XRN1 intervient après la traduction de l’ARNm. Toutefois, des expériences basées sur la quantification d’ARNm rapporteur dans des profils de polysome chez la levure suggèrent que la dégradation générale par XRN1 peut avoir lieu co-traductionnellement (Hu et al., 2009). Plus récemment, l’analyse structurale par cryo-EM d’un complexe purifié XRN1/80S/ARN a démontré l’existence d’une interaction stable entre XRN1 et le ribosome. L’interaction directe XRN1/ribosome en couplant la traduction de l’ARNm à sa dégradation contribuerait à accroître l’efficacité du processus de dégradation (Tesina et al., 2019a)

- . Dégradation 3 ‘->5’ par l’exosome

Alternativement à la dégradation 5'-3', les ARN peuvent être dégradés à partir de leur extrémité 3' par un complexe multiprotéique : l'exosome. Ce complexe a initialement été découvert dans le cadre de son intervention dans la voie de biogenèse des ARNr chez la levure (Mitchell et al., 1997). Depuis, des analyses de transcriptomique dans plusieurs organismes modèles ont montré qu'il prend part à la dégradation de nombreuses classes d'ARN incluant les ARNm, des ARN non codant comme les CUTs (Cryptic Unstable Transcripts) et les SUTs (Stable Uncharacterized Transcripts), des précurseurs d'ARNt, des pri-miARN (Chekanova et al., 2007 ; Gudipati et al., 2012 ; Pefanis et al., 2015 ; Schneider et al., 2012)

Structurellement, l'exosome est formé d'un cœur (appelé EXO9) composé de six RNases (RRP41, RRP42, RRP45, RRP46, MTR3 et OIP2) organisées en anneau autour de l'ARN et accompagnées de trois RBP (CSL4, RRP4 et RRP40) (Januszyk and Lima, 2014). Dans le cytoplasme des cellules mammifères, l'exosome s'associe à l'enzyme DIS3 qui porte l'activité endonucléolytique et exonucléolytique (Lebreton et al., 2008)

In vivo, l'activité de l'exosome nécessite la présence d'activateurs spécifiques comme le complexe SKI (SuperKiller), un hétérotétramère incluant les hélicases SKI2 et SKI3 assemblées avec SKI8 selon une stœchiométrie 1 :1 :2. Ce complexe interagit avec l'exosome *via* SKI7 (Araki et al., 2001). La dégradation de l'ARN s'achève par la libération de la coiffe seule, ou liée à quelques nucléotides et qui est alors dégradée par l'enzyme de clivage de la coiffe DCPS (DCP Scavenger) (Bazzini et al., 2016).

2.2 . Eléments de contrôle de la stabilité des ARNm

2.2.1 Composition nucléotidique du CDS

En plus de réguler le taux de traduction, la composition en codons influence également directement la stabilité de l'ARNm. A l'échelle du transcriptome chez la levure, la demi-vie des transcrits corrèle positivement avec l'optimalité des codons : *in vivo* à l'échelle du transcrit, la substitution de codons non optimaux d'un transcrit instable par des codons synonymes optimaux multiplie sa demi-vie par 7 et inversement, la substitution des codons optimaux par

des synonymes non optimaux dans la CDS d'un transcrit stable diminue sa demi-vie d'un facteur 10 (Presnyak et al., 2015).

Plusieurs approches ont été mises en œuvre pour étudier le lien de causalité entre ralentissement l'élongation au niveau des codons non optimaux et déclenchement de la dégradation de l'ARNm chez l'homme. Pour isoler les effets du CDS sur la stabilité de l'ARNm, Narula et collaborateurs ont mesuré les demi-vies d'une collection d'ARNm rapporteurs récapitulant l'ORFeome humain et montrent que les codons les plus lentement traduits d'après des données de ribosome profiling se trouvent préférentiellement dans les ARNm rapporteurs instables de la collection. De plus, cette stabilité corrèle positivement au temps de résidence des codons dans le site A du ribosome (Narula et al., 2019). Une étude encore plus directe a mesuré dans différentes cellules humaines la stabilité de chaque codon et confirmé que la composition en codons (indépendamment de la composition en acides aminés) est un déterminant de la stabilité de l'ARNm (Wu et al., 2019)

Concernant les mécanismes moléculaires sous-jacent, il est observé que l'optimalité des codons influence les taux de déadénylation et de decapping d'ARNm rapporteurs en plus de jouer sur la vitesse d'élongation. Dans le modèle levure (Figure 22), les différences de vitesse d'élongation de la traduction (évaluée par TRAP Translating Ribosome Affinity Purification), dues à la composition en codons sont captées par la machinerie de traduction et entrainent le recrutement de CCR4-NOT, ainsi que de l'activateur de decapping Dhh1 (Radhakrishnan and Green, 2016; Sweet et al., 2012; Webster et al., 2018). Dans ce modèle, une fraction de Dhh1 est physiquement associée aux ribosomes en cours d'élongation et réagit à un ralentissement local de l'élongation au niveau des codons non optimaux en s'accumulant sur l'ARNm ce qui ralentit encore plus l'élongation et oriente le transcrit vers les voies de dégradation (Radhakrishnan and Green, 2016). Ces résultats sont remis en cause par Jacobson et collaborateurs (Jacobson et al., 2018) et nuancés par les résultats de Zeidan et collaborateurs (Zeidan et al., 2018) qui ne mesurent qu'une faible corrélation entre optimalité de codon et changement d'abondance des transcrits l'échelle du transcriptome entres des souches *Dhh1Δ vs* WT. Le croisement de leurs ribosome profiling *Dhh1Δ* et WT avec les données de RIPseq Dhh1 (Miller et al., 2017) confirme toutefois que l'association de Dhh1 s'accroît sur les transcrits dont la stabilité est régulée par Dhh1. Le rôle de DDX6 dans le couplage entre efficacité de l'élongation et stabilité des ARNm n'est pas conservé entre la levure et les

mammifères : dans des cellules embryonnaires de souris où le gène *DDX6* a été inactivé, les transcrits stabilisés par l'absence de DDX6 ne sont pas significativement surreprésentés parmi les transcrit les plus inefficacement traduits et ne sont pas non plus significativement enrichis en codons non optimaux (Freimer et al., 2018). Chez l'homme, notre analyse de différents jeux de données de transcriptomique montre que les transcrits liés par DDX6 contiennent préférentiellement des nucléotides GC, sont régulés de manière prépondérante en stabilité, possèdent peu de codons non optimaux et présentent un rendement protéique élevé (Courel et al., 2019)

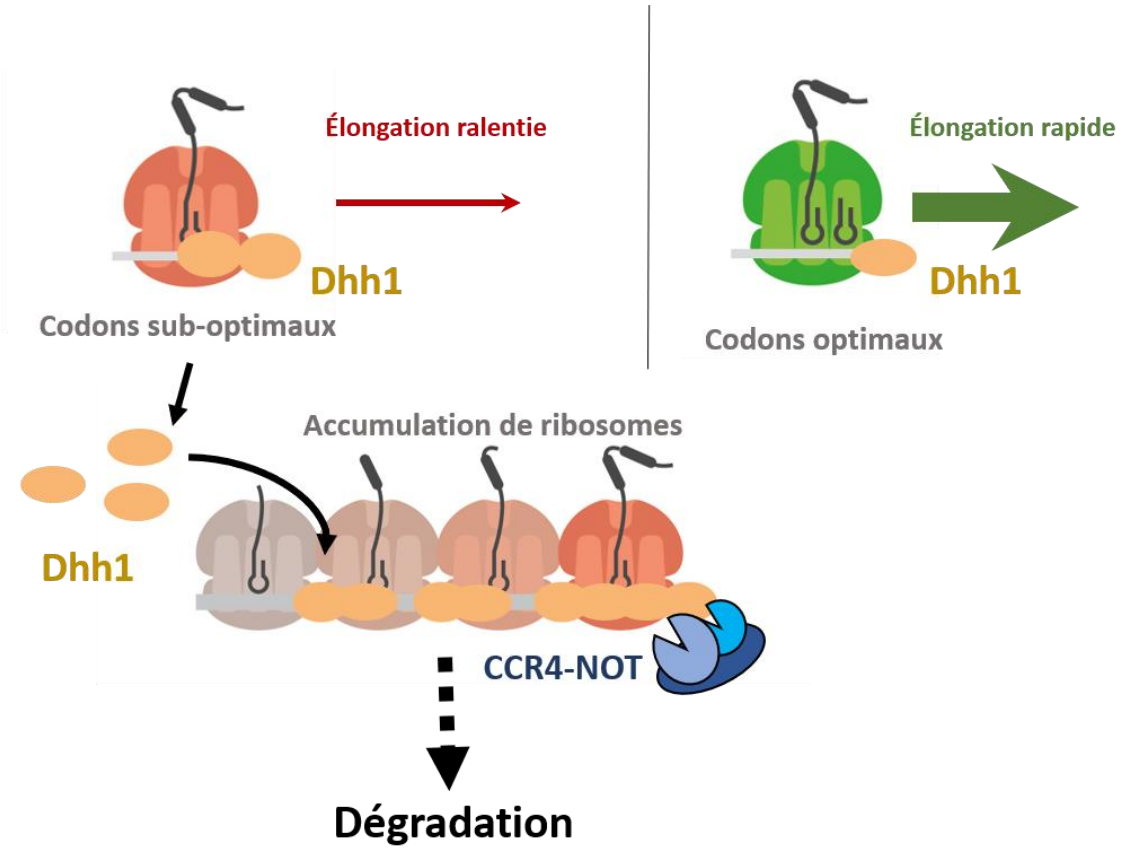

Figure 22 Régulation de la stabilité de l'ARNm (modèle levure)

Les ARNm ayant un CDS enrichi en codons suboptimaux sont décodés plus lentement que les ARNm enrichis en codons optimaux. Dhh1 associée aux ribosomes « capte » la vitesse d'élongation. Lorsque celle-ci est ralentie, des molécules supplémentaires de Dhh1 sont recrutées sur l'ARNm ce qui ralentit d'autant plus la progression des ribosomes sur l'ARNm. L'accumulation de ces derniers déclenche le recrutement du complexe CCR4-NOT et la dégradation subséquente du transcrit. (Modifié d'après Radhakrishnan and Green, 2016).

Chez l'homme, l'identité de la wobble base est fortement corrélée à l'optimalité du codon. En effet, les codons contenant soit un G ou C en troisième position (GC3) ont été identifiés par analyse bio-informatique comme stabilisateurs alors que ceux avec un A ou U en troisième position sont non optimaux. De plus, des transcrits optimisés sur lesquels le cadre de lecture est déplacé restent stables ce qui suggère que le contenu en GC médian du CDS représente à lui seul un proxy de la stabilité du transcrit (Hia et al., 2019).

2.2.2 Régulation de la stabilité de l'ARNm par des éléments de séquence contenus dans la région 3'UTR : exemple des ARNm à ARE

Plusieurs éléments localisés dans les UTR des transcrits contribuent à en réguler la stabilité. Ces éléments sont reconnus par des RBP ou des miARN induisant le recrutement ciblé de la machinerie de dégradation. A titre d'exemple nous traitons ici de la régulation de la stabilité des transcrits portant des ARE par les ARE-BP (ARE Binding Protein).

Les ARE ont été découverts dans la région 3'UTR d'ARNm codant des cytokines (Caput et al., 1986). Les ARNm à ARE se caractérisent par la présence d'une ou plusieurs copies du motif AUUUA dans leur 3' UTR insérée(s) au sein d'une séquence riche en uracile (Helfer et al., 2012). Les ARNm à AREs constituent 9% des ARNm totaux (Barreau et al., 2005). Certaines ARE-BP ont un effet déstabilisateur de l'ARNm ce qui est par exemple de cas d'AUF1, TTP, TIA-1 (Chen and Shyu, 1995) (Tableau 2). Des études ultérieures ont démontré que ces éléments de séquence pouvaient aussi avoir un effet stabilisateur intervenant dans des processus biologiques tels que la prolifération et la différenciation cellulaires, la maturation de certains miARNs, l'épissage alternatif de certains ARN pré-messagers (Otsuka et al., 2019).

Le mécanisme par lequel les séquences AREs régulent la dégradation de l'ARNm implique la fixation de RBP spécifiques appelées ARE-BP (Tableau 2). La plupart des ARE-BP reconnaissent leurs transcrits-cibles grâce à des RBD canoniques comme le RRM, le Znf et le KH domaine (Nicastro et al., 2015).

ARE-BP	RBD	ARNm cibles
AUF1	4 RRMs	TNF-α, IL-1β,c-fos, c-myc, VEGF, COX2
TTP	2 Znf	TNF-α, GM-CSF, IL-10, TTP, HuR
ZFP36L1	2 Znf	CDK6
ZFP36L2	2 Znf	LHR, H3K4, H3K9
KSRP	4 KH domains	Myogenin, c-fos, c-myc, TNF-α
TIA-1	3 RRMs	Cc,TNF-α,VEGF, COX2
HuR	3 RRMs	GAP-43, APP, BACE1, TNFα, VEGF, COX2, c-fos
HuD	3 RRMs	HuR
GAPDH	-	CSF
LDHM	-	

Tableau 2 Principales ARE-BP régulant la stabilité des ARNm

Les ARE-BP déstabilisatrices sont surlignées en bleu, et les ARE-BP stabilisatrices en vert. (Modifié d'après Otsuka et al., 2019)

Les ARE-BP régulent la stabilité de l'ARNm selon différents mécanismes moléculaires (Figure 23). Ils peuvent interférer avec la voie de dégradation miARN dépendante (Jing et al., 2005), activer les voies de dégradation générales 3'-5' (Chen et al., 2001) ou 5'-3' des ARNm (Helfer et al., 2012). Dans ce dernier cas, les ARE-BP fonctionnent comme des adaptateurs connectant les ARNm à ARE avec le complexe de decapping (Lykke-Andersen and Wagner, 2005; Stoecklin et al., 2006) ou la déadénylase CCR4-NOT (Bulbrook et al., 2018).

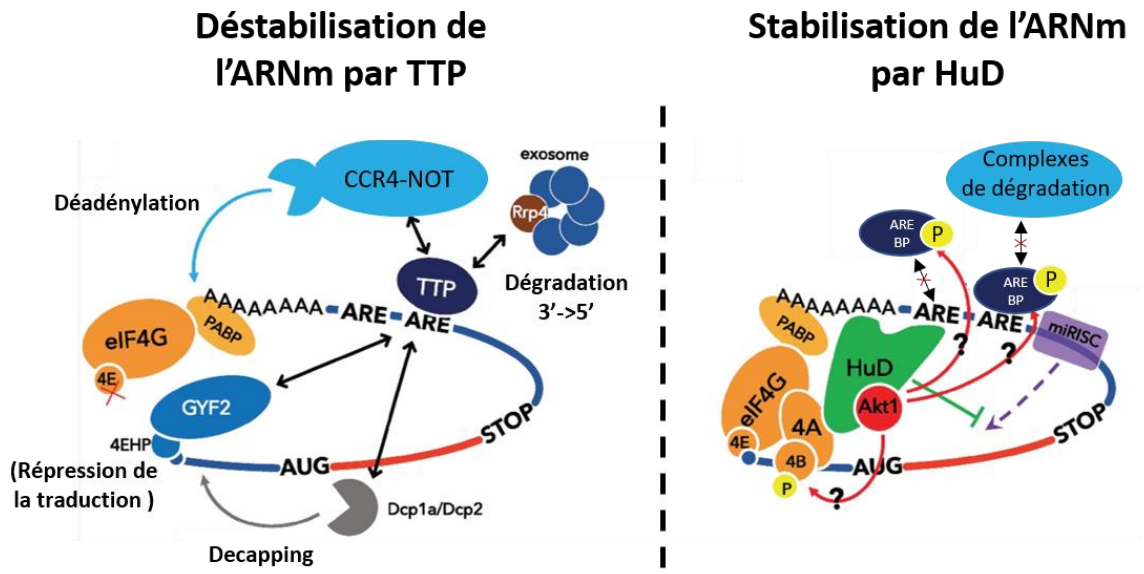

Figure 23 Contrôle de la stabilité de l'ARNm par les ARE-BP TTP et HuD.

Dans ce modèle issu d'études en cellulaires humaines, TTP provoque la dégradation de l'ARNm en recrutant le complexe CCR4-NOT, l'exosome et le complexe de decapping. Il réprime également la traduction de l'ARNm en se liant à GYF2 qui recrute l'inhibiteur 4EHP.

HuD (exclusivement exprimée dans les cellules neuronales) stimule la traduction en interagissant directement avec eIF4A et la queue poly(A). La liaison à eIF4A atténue l'effet inhibiteur des miARN ciblant ce facteur d'initiation (cf. partie 1 paragraphe 3). HuD s'associe également à Akt/PKB. Akt/PKB phosphoryle les ARE-BP déstabilisatrices comme KSRP, TTP, ZFP36L1 ou ZFP36L2 ce qui a pour effet de les inactiver. Elle phosphoryle également eIF4B ce qui stimule l'activité d'eIF4A. (Modifié d'après Otsuka et al., 2019)

2.2.3 Les voies particulières de dégradation : exemple du NMD

Les régulations de la stabilité de l'ARNm sont aussi intégrées dans les voies de contrôle de la qualité des ARNm (RQC). Le RQC sert à éviter l'accumulation d'ARNm dysfonctionnels et la production de peptides anormaux. Dans le cytoplasme le RQC se décline en trois voies de dégradations (Lykke-Andersen and Bennett, 2014) : le NMD (Nonsense-Mediated-Decay), que nous détaillons ultérieurement, dégrade les ARNm portant un codon STOP prématuré (appelé PTC, Premature Terminaison Codon), le NSD (Non-Stop-Decay) dégrade les ARNm sans codon STOP et le NGD (No-Go-Decay) cible les ARNm sur lesquels les ribosomes sont bloqués.

Le NMD est déclenché lorsqu'un ribosome en cours de traduction se retrouve bloqué sur un PTC localisé à plus de 50-55 nucléotides en amont de la dernière jonction exon-exon portant un EJC (Exon Junction Complex) lequel recrute les hélicases UPF2 et UPF3 (Kervestin and

Jacobson, 2012). Le PTC entre dans le site A du ribosome et la fixation des facteurs de terminaison eRF1 et eRF3 y hydrolyse la chaine polypeptidique attachée au site P. UPF1 est alors recrutée par eRF3 au niveau du PTC de même que la protéine kinase SMG1 se liant aux facteurs eRF1 et eRF3 formant ainsi le complexe SURF (SMG1-UPF1-eRF1-eRF3). SMG8 et SMG9 s'associent également au complexe SURF afin de bloquer temporairement la phosphorylation d'UPF1 par SMG1. Le complexe {SURF-SMG8-SMG9} est transloqué du ribosome aux protéines UPF2 et UPF3 associées à l'EJC. Après la translocation, SMG8 et SMG9 se dissocient du complexe ce qui permet à l'ARN hélicase DHX34 de servir de plateforme d'interaction entre UPF1 et SMG1 (Melero et al., 2016). La phosphorylation subséquente d'UPF1 par SMG1 déclenche la dissociation du ribosome de l'ARNm, inhibe l'initiation de la traduction en empêchant l'association d'eIF3, et recrute les protéines SMG5, SMG6 et SMG7, ce qui induit la dégradation du transcrit (Hug et al., 2016) (Figure 24). Chez les mammifères, plusieurs mécanismes peuvent intervenir dans la dégradation de l'ARNm par la voie du NMD. Une première option est que SMG6 agisse comme une endonucléase et produise des fragments dégradés par les exonucléases classiques (Eberle et al., 2009; Huntzinger et al., 2008). Alternativement, l'hétérodimère SMG5–SMG7 peut recruter le complexe CCR4-NOT qui active le decapping et la dégradation 5'->3'. Enfin, il est également envisageable qu'UPF1 recrute directement le complexe de decapping conduisant à la dégradation 5'-3'. (Loh et al., 2013).

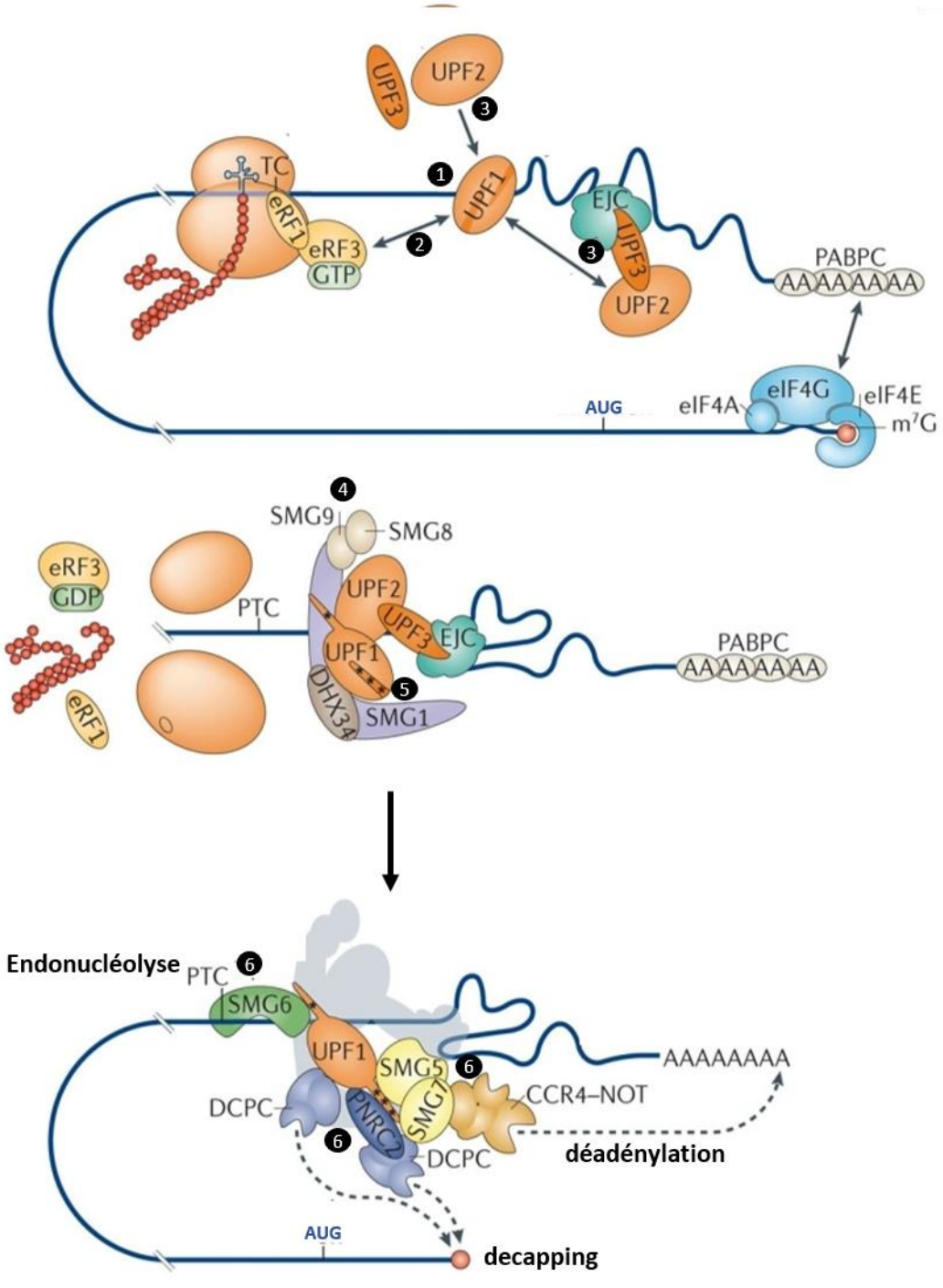

Figure 24 Dégradation de l'ARNm par la voie du NMD

Lorsque l'étape de terminaison est inefficace, par exemple lorsque le ribosome rencontre un PTC (Premature Terminaison Codon), UPF1 peut se lier à l'ARNm de manière non spécifique (1) ou alternativement être recruté par eRF3 (eukaryotic Release Factor 3) (2). UPF1 seul ou assisté de l'EJC recrute ensuite UPF2 et UPF3 (3) ce qui initie l'assemblage d'un complexe activateur du NMD au niveau du PTC. Ce complexe contient UPF1,2,3, SMG1,8,9, DHX34 et l'EJC (4). Lorsque le ribosome se dissocie de l'ARNm, SMG1 phosphoryle UPF1 (5) ce qui entraine le recrutement de l'endonucléase SMG6, du complexe CCR4-NOT via le dimère SMG5– SMG7 et/ou du complexe de decapping (6). Le clivage endonucléolytique ou la déadénylation et le decapping sont suivies de la dégradation complète du

transcrit par les voies générales de dégradation 5'->3' ou 3'->5' (non représenté) (Modifié d'après Lykke-Andersen and Bennett, 2014)

Des études récentes montrent qu'en plus d'intervenir dans le cadre du RQC (Ribosom Quality Control), le NMD constitue une voie de régulation post-transcriptionnelle indépendante, ciblant *via* UPF1 (Imamachi et al., 2017) ainsi que *via* SMG6 (Courel et al., 2019) des transcrits particulièrement riches en GC. Les transcrits possédant un intron en 5' UTR suivi par une uORF ou une longue séquence 3'UTR sont également des cibles privilégiées de cette voie de régulation (Colombo et al., 2017).

3. Les régulations par ARN interférence

Les régulations post-transcriptionnelles cytoplasmiques ciblées de l'expression génique peuvent également être médiées par les voies dites d'ARN interférence. Ces voies de régulations se trouvent partiellement conservées chez les eucaryotes : elles sont en effet présentes chez tous les métazoaires mais ont en revanche disparu de plusieurs organismes unicellulaires tels *S. cerevisiae* , *Trypanosoma cruzi*, *Leishmania major* et *Plasmodium falciparum* (Cerutti and Casas-Mollano, 2006). Ces régulations se subdivisent en trois voies chacune faisant intervenir des petits ARN non codant de nature différente : les siARNs (Small Interfering ARN), les miARNs (MicroARN) et les piARNs (PIWI Interacting ARN). Dans cette introduction nous décrivons les mécanismes moléculaires de la répression de la traduction et de la dégradation dépendant des miARNs. Les miARN sont de petits ARN non codants de 22 nt formés à partir de précurseurs appelés miARN primaires (pri-miARN) (Winter et al., 2009) eux même issus de la transcription de gènes spécifiques par l'ARN Pol II (Lee et al., 2002). Une fois clivés dans le noyau par l'enzyme DROSHA, les précurseurs de miARN sont exportés dans le cytoplasme par l'exportine 5 (Wu et al., 2018) où ils acquièrent leur forme mature suite au clivage par DICER. Pour le détail des étapes de biogenèse des miARN, se référer à (Bartel, 2018).

3.1 Des régulations sélectives ciblant un grand nombre de transcrits

3.1.1 Reconnaissance des cibles

Une fois présents sous leur forme mature dans le cytoplasme, les miARN sont chargés sous forme simple brin sur le complexe miRISC (miARN Induced Silencing Complex) où ils servent de guide pour la reconnaissance des transcrits cibles en s'appariant à des séquences complémentaires localisées dans la 3'UTR et appelées MRE (miARN Response Element). Chez les mammifères, la quasi-totalité des miARN s'apparient à leurs cibles de manière imparfaitement complémentaire, sans faire intervenir l'activité endonucléique des protéines AGO et notamment AGO2 (Bartel, 2018). Des données structurales montrent que les miARN s'apparient à leurs cibles en deux temps : d'abord *via* une portion de séquence de 6 nt appelée «séquence seed» incluant les nucléotides 2 à 7 du miARN ce qui induit un changement de conformation de la protéine AGO et permet ensuite l'appariement du miARN à sa cible par les nucléotides 8 et/ou 13-16. D'autres sites non canoniques supplémentaires sont parfois également impliqués (Schirle et al., 2014). Le dernier nucléotide de la MRE est souvent une adénine ne s'appariant pas directement au miARN mais se liant à la protéine AGO et contribuant à stabiliser le complexe miRISC sur l'ARNm cible (Schirle et al., 2015), (Figure 25).

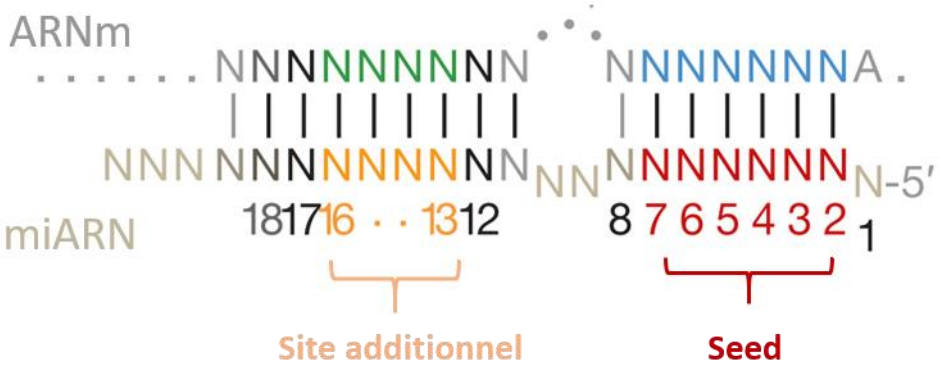

Figure 25 Appariement des miARN à leurs ARNm cibles

Les positions 2 à 7 du miARN (en rouge) constituent la séquence seed par laquelle le miARN s'apparie à sa cible par interactions Watson–Crick. Des sites de liaison additionnels situés entre les nucléotides 13 à 16 (en orange) du miARN peuvent également contribuer à l'appariement avec l'ARNm cible. L'adénine en dernière position du MRE interagit directement avec la protéine AGO2.(Modifié d'après Bartel, 2018).

. Chez l'homme, plus de 4000 miARN possédant chacun entre un à un millier d'ARNm cibles ont été séquencés (miRTarBase 7.0). Ces miARN réguleraient ~60% des ARNm (Friedman et al., 2009), contre 27% et 37% respectivement chez *C. elegans* et *D. melanogaster* (Bartel, 2018). La stratégie de régulation par les miARN se base sur un effet répresseur modeste à chaque MRE, souvent moins de 50% de répression selon une approche combinée de transcriptomique et de protéomique haut débit (Baek et al., 2008; Selbach et al., 2008). L'effet répresseur associé à un MRE donné est d'autant plus important que le MRE se trouve dans un contexte nucléotidique riche en AU et/ou qu'il est proche (8-40 nt) de sites de régulation reconnus par des miARNs co-exprimés permettant un effet coopératif (Grimson et al., 2007).

3.1.2 Régulation de la formation du complexe miRISC

Dans le cytoplasme, l'activité des miARN est régulée par plusieurs modifications post-transcriptionnelles intervenant aux extrémités 5' ou 3' et susceptibles de modifier les interactions miARN/MRE ou miARN/AGO (Bartel, 2018). Par exemple, l'extrémité 3' des pré-miARN peut être oligo-uridylée par les uridyltransférases TUT4 et TUT7 ce qui bloque la progression de l'enzyme DICER responsable du clivage des pre-miARN en miARN. Conséquemment le pré-miARN est dégradé par l'exonucléase DIS3L2 capable de reconnaître les oligo(U) (Faehnle et al., 2014; Ustianenko et al., 2013).

Les protéines AGO font également l'objet de modifications post-traductionnelles influençant la formation et l'activation fonctionnelle du complexe miRISC. Parmi celles-ci, la phosphorylation de la sérine 387 d'AGO2 par la kinase AKT3 documentée *in vitro* ainsi que dans des cellules HeLa diminue l'activité de clivage d'AGO2 et réoriente son activité dans la répression de la traduction associée à la voie des miARN dès lors que la déplétion d'AKT3, de même que l'expression d'un mutant AGO ne pouvant être phosphorylé sur ce site conduisent à la dé-répression d'un ARNm rapporteur Luciférase et à un affaiblissement de l'interaction d'AGO2 avec TNRC6A (Horman et al., 2013). Alternativement, la phosphorylation de la tyrosine 393 d'AGO2 régule négativement l'activité des miARN en les empêchant de se lier à AGO2 (Rüdel et al., 2011).

3.2 Deux modes d'action des miARN sur l'expression des ARNm : répression de la traduction et dégradation de l'ARN

L'interaction entre le complexe miRISC et un ARNm cible inhibe l'expression de cet ARNm. Cette inhibition peut s'expliquer de différentes façons. Dans de très rares cas chez les mammifères, l'ARNm ciblé est clivé par endonucléolyse par la protéine AGO2 (Shin et al., 2010). Plus classiquement, l'ARNm est réprimé en traduction et/ou est dégradé par la voie de dégradation 5'-3 '.

3.2.1. Mécanisme moléculaire de la dégradation de l'ARNm induite par les miARN

A l'échelle du transcriptome la dégradation induite par les miARN concerne 66 à 90 % des régulations dépendantes de miARN (Jonas and Izaurralde, 2015). Concernant le mécanisme moléculaire (Figure 26), les protéines AGO interagissent avec TNRC6 (GW182) directement liée à la PABPC (Jinek et al., 2010; Zekri et al., 2009) et recrute les complexes PAN et CCR4-NOT via PAN3 et NOT1 (Braun et al., 2011). Les ARNm sont alors successivement déadénylés par ces deux complexes (Chen et al., 2009; Wahle and Winkler, 2013). Le complexe CCR4-NOT interagit avec les facteurs de decapping DDX6 (Rouya et al., 2014) et PAT1B, ainsi qu'avec le répresseur 4E-T (Nishimura et al., 2015). Ces protéines recrutent ensuite le complexe de decapping (Chen et al., 2014; Jonas and Izaurralde, 2013; Mathys et al., 2014). Le complexe miRISC peut également recruter directement le complexe de decapping. La coiffe de l'ARNm est alors clivée par DCP2 puis DCP1 et EDC4 recrutent XRN1 qui dégrade l'ARNm cible (Braun et al., 2012).

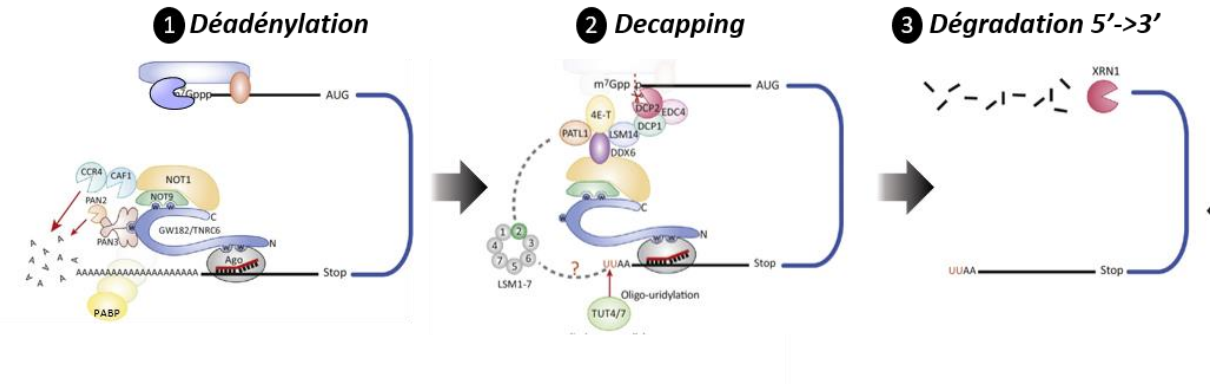

Figure 26 Dégradation de l'ARNm par les miARN

La dégradation de l'ARNm par les miARN se décompose en trois étapes. Les transcrits cibles sont d'abord déadénylés par les complexes CCR4-NOT et PAN ayant été recrutés par TNRC6 (1). Les ARNm déadénylés sont ensuite oligo-uridylés par TUT4/7, ce qui déclenche la dégradation. En plus de recruter les déadénylases, TNRC6 active la dissociation de PABP ce qui accroît l'efficacité de la déadénylation par CCR4-NOT. Des cofacteurs de decapping incluant DDX6 sont ensuite recrutés sur le complexe CCR4-NOT et activent la suppression de la coiffe par DCP2 (2). L'exonucléase XRN1 dégrade ensuite l'ARNm (3). (Modifié d'après Iwakawa and Tomari, 2015)

3.2.2. Mécanismes moléculaires de répression de la traduction miARN -dépendants

Plusieurs études basées sur des analyses biochimiques en cellules humaines suggèrent que la répression de la traduction par les miARN cible la phase d'initiation (Humphreys et al., 2005; Pillai, 2005) et implique la dissociation des facteurs d'initiation dont eIF4G, eIF4A1 et eIF4A2 (Fukao et al., 2014) ainsi que de PABP (Rissland et al., 2017). Deux principaux mécanismes moléculaires de répression de la traduction par les miARN sont décrits à ce jour (Figure 27). Le premier mécanisme implique le recrutement par TNRC6 du complexe CCR4-NOT qui interagit directement avec DDX6 *via* la sous-unité CNOT 1 (Chen et al., 2014a; Kuzuoğlu-Öztürk et al., 2016; Mathys et al., 2014; Rouya et al., 2014). DDX6 lié à CCR4-NOT interagit à son tour directement avec d'autres facteurs de répression de la traduction dont en particulier 4E-T. L'interaction 4E-T/DDX6 est capable de réprimer *in vivo* la traduction d'un ARNm rapporteur ciblé par le miARN let7 (Kamenska et al., 2016). Des résultats d'expériences de tether montrent que 4E-T peut réprimer la traduction de manière eIF4E-indépendante (Kamenska et al., 2014). Concernant la voie des miARN, la répression de la traduction de leurs

cibles fait intervenir la liaison directe de 4E-T avec 4EHP (eIF4E2) qui entre en compétition avec eIF4E pour se lier à la coiffe de l'ARNm (Chapat et al., 2017; Chen and Gao, 2017).

De manière intéressante, des mutations du domaine FDF de DDX6 empêchant son interaction avec 4E-T ainsi qu'avec des facteurs de decapping (EDC3, PAT1B, LSM14A) rendent DDX6 incapable de réprimer la traduction d'un ARNm rapporteur (Kuzuoğlu-Öztürk et al., 2016). De plus, l'absence de 4E-T diminue sans la supprimer totalement la répression de la traduction des cibles des miARN par DDX6 (Kuzuoğlu-Öztürk et al., 2016) ce qui suggère que DDX6 puisse interagir avec d'autres facteurs que 4E-T pour réprimer la traduction des cibles de miARN.

Un modèle alternatif implique l'hélicase eIF4A2 (paralogue de eIF4A1), impliquée dans le recrutement du 43S et le scanning lors de l'initiation de la traduction. eIF4A2 se lie de manière mutuellement exclusive, en compétition avec DDX6, sur la sous-unité CNOT1 du complexe CCR4-NOT (Meijer et al., 2019). Elle fait de plus partie d'un complexe endogène incluant DDX6 et CNOT1 (Wilczynska et al., 2019) et son absence empêche la répression miARN-dépendante d'un ARNm rapporteur (Meijer et al., 2013a). Le mécanisme détaillé par lequel eIF4A2 interfère avec l'initiation de la traduction n'est à ce jour pas clairement établi. Les hypothèses retenues à ce sujet incluent une inhibition de la formation du complexe eIF4F et/ou de l'étape de scanning par le 48S PIC (Fukao et al., 2014).

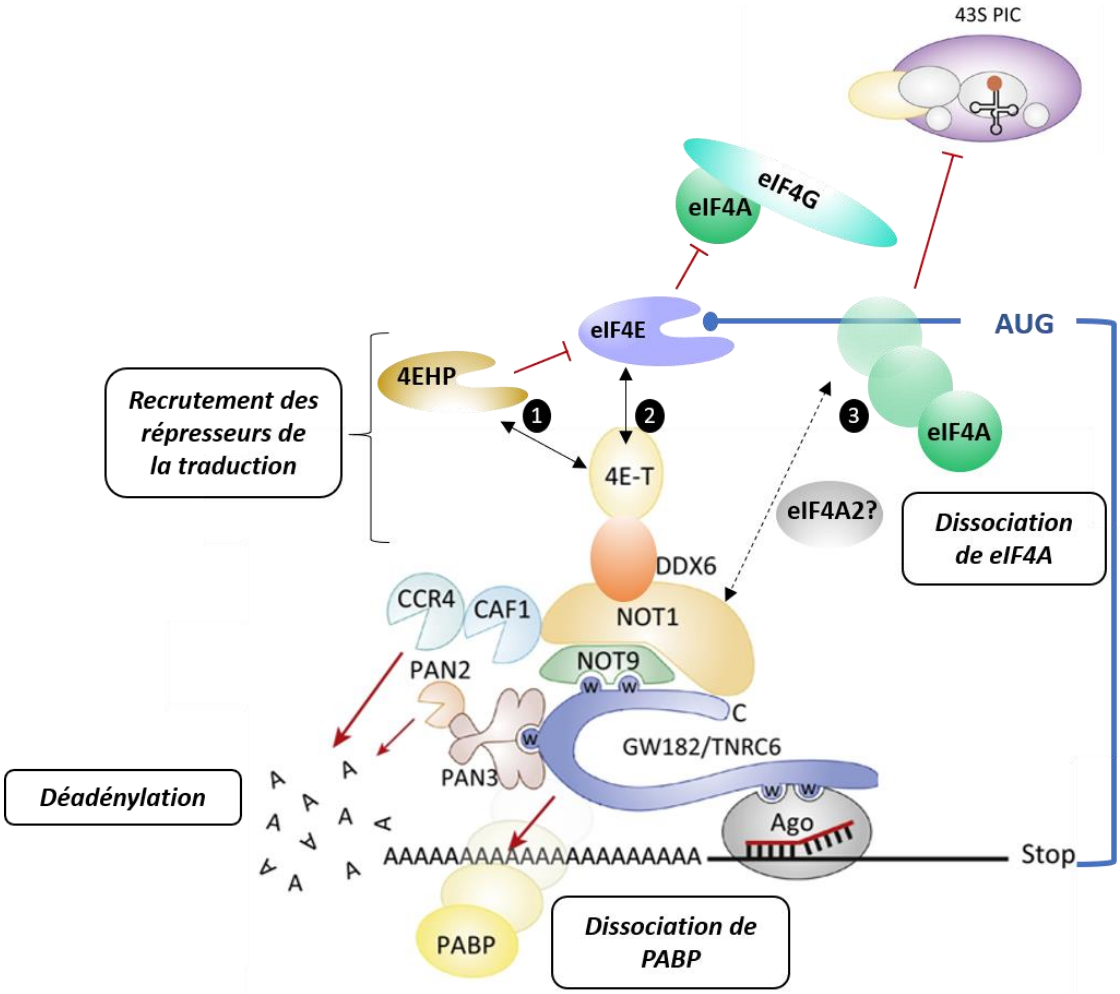

Figure 27 Répression de la traduction par les miARN

TNRC6 dissocie PABP de la queue poly(A) et recrute les complexes CCR4-NOT et PAN via les résidus tryptophane de son domaine N terminal GW. Les complexes CCR4-NOT et PAN orchestrent la déadénylation de l'ARNm (celle-ci n'est toutefois pas indispensable à la répression de la traduction). Le complexe CCR4-NOT recrute des répresseurs de la traduction comme DDX6 et 4E-T via la sous-unité CNOT1. 4E-T peut alors réprimer l'initiation de la traduction de deux manières : (1) soit en interagissant directement avec 4EHP qui empêche eIF4E d'accéder à la coiffe de l'ARNm (1) soit en liant directement eIF4E et en empêchant la formation du complexe eIF4F (2). Les miARN peuvent aussi réprimer la traduction en déplaçant l'hélicase eIF4A du complexe eIF4F, possiblement par l'action de eIF4A2 et selon des mécanismes à ce jour inconnus.(Modifié d'après Iwakawa and Tomari, 2015)

3.2.3. Coordination de la répression de la traduction et de la dégradation miARN-dépendantes

Les contributions relatives de la répression de la traduction et de la dégradation aux régulations miARN-dépendantes constituent l'objet de débats non encore résolus (Iwakawa and Tomari, 2015; Jonas and Izaurralde, 2015) . D'un côté, des expériences de ribosome profiling et de RNA-seq dans des conditions de surexpression ou de délétion de différents miARN montrent que les miARN entrainent plus fréquemment des changements d'abondance de leurs ARNm cibles plutôt qu'ils n'en modifient l'efficacité de la traduction. Ceci suggère qu'à l'échelle du transcriptome l'action des miARN sur la stabilité de leurs cibles serait prépondérante par rapport à leur activité de répression de la traduction (Eichhorn et al., 2014). Il n'est néanmoins pas exclu que la répression de la traduction puisse précéder la dégradation des transcrits cibles, ce que suggèrent des études de cinétique de répression de la traduction de miARN rapporteurs (Béthune et al., 2012; Djuranovic et al., 2012), voire qu'elle soit un prérequis à la dégradation (Radhakrishnan and Green, 2016). Enfin, il semble que la répression de la traduction par les miARN puisse ne pas immédiatement être suivie de la dégradation de l'ARNm cible. A titre d'exemple, l'ARNm CAT1 est réprimé en traduction par miR-122 et peut, en fonction des conditions cellulaires, retourner en traduction sans être immédiatement dégradé (Bhattacharyya et al., 2006).

Des travaux récents de polysome profiling et de marquage métabolique, menés sur deux lignées de cellules embryonnaires de souris où les gènes *Ddx6* et *Dgcr8* ont été inactivés par Crispr Cas9, montrent que l'absence de DGCR8 (facteur indispensable à la biogenèse des miARN) empêche à la fois la répression de la traduction et la dégradation des cibles de miARN tandis que l'absence de DDX6 empêche la répression de la traduction des cibles des miARN sans affecter leur stabilité (Freimer et al., 2018). Ceci suggère que la dégradation miARN-dépendante peut se dérouler indépendamment de la répression de la traduction dans le cas des transcrits ciblés par DDX6.

Un autre élément associé à la coordination de l'activité des miARN est la localisation cellulaire du processus d'ARN interférence. En effet, s'il est admis que les processus d'ARN interférence ont lieu dans le cytoplasme, il est observé en parallèle que les acteurs des voies d'ARN interférence (protéines du miRISC, miARNs et ARNm cibles) s'accumulent également dans des granules de mRNP appelés P-bodies (Jakymiw et al., 2005) (*cf* partie 2). Ces structures semblent impliquées dans les régulations par l'ARN-interférence dès lors que le silencing de TNRC6 inhibe la répression de la traduction d'ARNm rapporteurs ciblés par des miARN, et que

l'expression de mutants AGO ne pouvant être localisés dans les PB perdent leur activité de répression de la traduction même lorsqu'ils se trouvent accrochés artificiellement à leurs ARNm cibles (Bhattacharyya et al., 2006; Eulalio et al., 2007; Liu et al., 2005; Pillai, 2005).

Partie 2 : Les P-Bodies

La compartimentation cellulaire est à l'origine de plusieurs propriétés émergentes contribuant à améliorer l'adaptation des cellules à leur environnement (Gomes and Shorter, 2019). En effet, elle permet : d'accroître les vitesses de réaction en concentrant certains réactants biochimiques, de séquestrer des composants potentiellement dangereux, de stocker des molécules d'intérêt ou encore d'amplifier des voies de signalisation en concentrant récepteurs et molécules de signal (Boeynaems et al., 2018). En termes d'ultrastructure cellulaire, la compartimentation se matérialise par l'existence d'organites membranaires parmi lesquels le noyau, les mitochondries et les organites du réseau endomembranaire (appareil de Golgi, réticulum endoplasmique, endosome, lysosome etc). Elle implique également des organites non membranaires (Hyman and Brangwynne, 2011), appelés MLO (Membrane Less Organelles) (Mélèse and Xue, 1995; Schmidt and Görlich, 2016) ou biocondensats (Banani et al., 2017). Ces derniers peuvent contenir uniquement des protéines comme les PML bodies (ProMyelocytic Leukemia) ou des protéines et des ARN, comme par exemple les P-bodies (Brangwynne, 2013). Certains de ces organites sans membrane se localisent dans le noyau comme les nucléoles, les corps de Cajal, les nuclear speckles, les paraspeckles, les PML bodies. D'autres organites sont cytoplasmiques comme les P-bodies, les granules de stress, les granules germinaux, les granules neuronaux (Figure 28). Ces MLO remplissent des fonctions moléculaires diverses (Tableau 3) et pour certains leur présence dans les cellules dépend des conditions environnementales et/ou du type cellulaire.

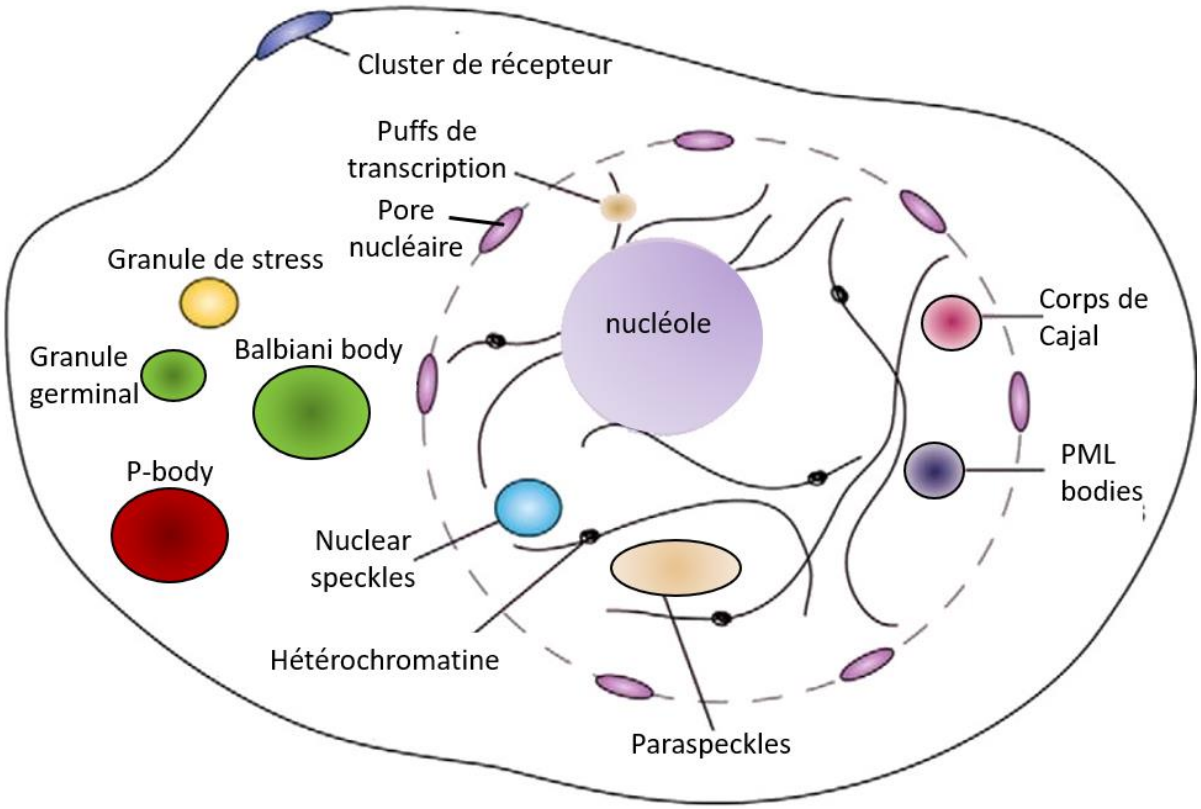

Figure 28 Principaux organites sans membrane des cellules eucaryotes

Les différents organites sans membrane sont schématisés selon leur présence dans le noyau ou dans le cytoplasme des cellules eucaryotes. Plusieurs de ces biocondensats ne se rencontrent que dans certains types cellulaires. Par exemple, les Balbiani bodies et les granules germinaux (en vert) sont spécifiques des cellules germinales. Se référer au tableau 3 pour les fonctions associées à chaque organite. (Modifié d'après Gomes and Shorter, 2019).

P-bodies	stockage d'ARNm réprimés en traduction	Standart & Weil, 2018 ; Luo & Slavoff, 2018
Balbiani bodies	localisation d'ARNm dans les ovocytes	Jamieson-Lucy et al., 2019
granules germinaux	régulation de la traduction dans les cellules germinales	Sengupta & Boag, 2012
granules de stress	stockage d'ARNm bloqués en traduction et de protéines de la machinerie de traduction	Protter & Parker, 2016; Ivanov et al., 2019
complexe du pore nucléaire	import/export nucléaire	Gomes & Shorter, 2018
corps de Cajal	assemblage et maturation des snRNP	Staněk, 2017
nucléole	centre de biogenèse des ribosomes; stabilité du génome	Lindström et al., 2018 ; Tzekrekou et al., 2017
PML bodies	recrutement de protéines impliquées dans divers processus cellulaires (remodelage de la chromatine, modification des télomères, défense antivirale…)	Lallemand-Breitenbach & de Thé, 2018
hétérochromatine	maintien de la stabilité du génome	Allshire &Madhani, 2017
paraspeckles	retention nucléaire d'ARN modifé A->I	Fox & Lamond., 2010
nuclear speckles	stockage de facteurs d'épissage	Galganski et al., 2017

Tableau 3 Fonctions des principaux organites eucaryotes sans membrane

En vert les organites cytoplasmiques, en bleu les organites nucléaires.

Focalisons-nous à présent sur les organites au cœur de notre étude : les P-bodies (Processing-bodies, par la suite abrégés en PB). Les PB désignent des granules de mRNP cytoplasmiques d'environ 0,5 µm de diamètre, conservés chez les eucaryotes de la levure à l'homme et constitutivement présents dans les cellules mammifères à raison de 5 à 10 PB/cellule (Figure 29).

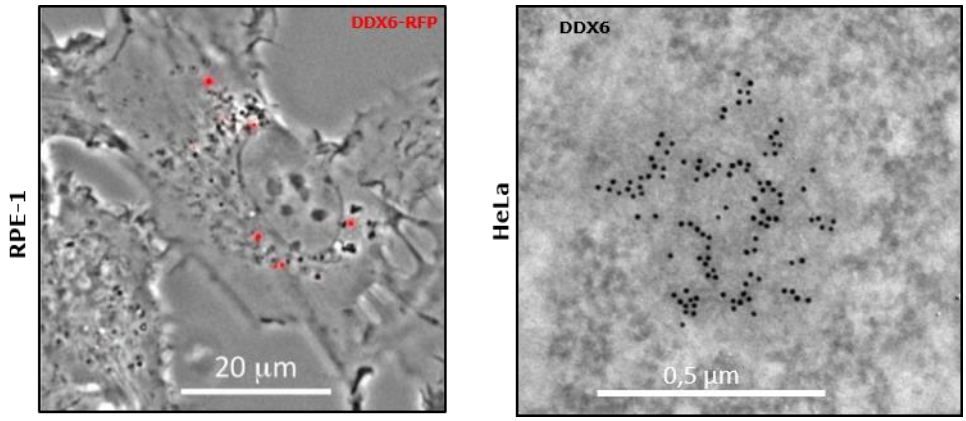

Figure 29 Visualisation des P-bodies marqués par DDX6 dans des cellules épithéliales humaines

Panneau de gauche : localisation de la protéine DDX6-RFP marquant les PB dans des cellules RPE-1 observées par microscopie à contraste de phase sur cellules vivantes. (Standart and Weil, 2018).

Panneau de droite : détail de l'ultrastructure d'un PB observé par immuno-microscopie électronique avec un anticorps dirigé contre la protéine endogène DDX6, et un anticorps secondaire couplé à des grains d'or. (*Modifié d'après Souquere et al., 2009).*

Comme pour d'autres organites disparaissant lors de la mitose, la taille et le nombre de PB varie au cours du cycle cellulaire : en utilisant un co-marquage avec CENP-F (Centromere Protein type F) et PCNA (Proliferating Cell Nuclear Antigen) sur des cellules HeLa synchronisées en phase S Yang et collaborateurs observent des PB moins nombreux en phase G1 et au début de la phase S du cycle cellulaire (Yang et al, 2004). De plus, les PB se décondensent lors de l'entrée en mitose et se réassemblent au cours de la phase G1 du cycle cellulaire.

Bien que les PB aient été découverts il y a plus de vingt ans, leur fonction moléculaire est longtemps restée controversée entre stockage et dégradation d'ARNm, notamment en raison de l'impossibilité de les purifier du fait de leur petite taille et de leur relativement faible

abondance cellulaire. Toutefois, au début de ma thèse, une approche de purification par FAPS (Fluorescent-Activated Particle Sorting) des PB venait d'être mise en œuvre au laboratoire et a permis de déterminer la composition exhaustive en protéines et en ARN des PB dans les cellules humaines (Hubstenberger et al., 2017). Comme nous allons le voir, les résultats de cette étude ont également apporté des éléments de clarification quant à la fonction cellulaire des PB. Actuellement les PB sont décrits comme des lieux de stockage d'ARNm représentant un niveau supplémentaire de régulation impliqué dans la coordination des régulations post-transcriptionnelles (Standart and Weil, 2018).

1. Composition des PB

1.1 Composition protéique

1.1.1 Les protéines identifiées dans les PB par approche gène candidat

XRN1 (Bashkirov et al., 1997), DCP1, DCP2, LSM1-7(van Dijk et al., 2002; Ingelfinger et al.,2002) et TNRC6 (Eystathioy et al., 2003) sont les premières protéines dont la localisation dans des foci cytoplasmiques appelés DCP-bodies ou encore GW bodies a été décrite par microscopie à immunofluorescence sur les protéines endogènes ou sur des protéines de fusion dans des cellules mammifères. Le nom actuel de Processing-bodies est issu de l'étude de ces granules chez *S. cerevisiae* (Sheth and Parker, 2003) ayant montré que plusieurs protéines de la voie de dégradation 5'->3' de l'ARNm dont Dcp1, Dcp2, Lsm1, Pat1, Dhh1 et Xrn1 s'y trouvent concentrés. Par la suite, d'autres protéines liées au métabolisme de l'ARN ont été localisées dans les PB chez différents organismes (Eulalio et al., 2007b; Parker and Sheth, 2007; Wilczynska et al., 2005). Ces protéines se répartissent principalement entre des facteurs de dégradation 5'->3' (XRN1, DCP1, DCP2), cofacteurs de decapping (EDC3, EDC4, PAT1B, LSM1-7), déadénylases (PAN2, PAN3, complexe CCR4-NOT), acteurs des voies d'ARN-interférence (AGO1-4, GW182), facteurs du NMD (UPF1, SMG7, SMG5) et répresseurs de la traduction (DDX6, LSM14A, CPEB1, 4E-T). La liste des composants des PB continue de

s'allonger : parmi les composants récemment identifiés, la micro-protéine Nobody (Non annotated P-body dissociating polypeptide) (D'Lima et al., 2017) ainsi qu'HAX-1 (Zayat et al., 2015) ont été récemment colocalisés avec d'autres protéines canoniques des PB dans les cellules humaines.

Le niveau de surconcentration des protéines des PB par rapport au cytosol a été déterminé expérimentalement pour DDX6 par une approche d'immuno-microscopie électronique dans des cellules humaines. La protéine DDX6 endogène est 170 fois plus concentrée dans les PB que dans le cytosol. Toutefois, en termes de quantité de protéine il est important de considérer que le stockage dans les PB ne concerne qu'une fraction minoritaire (~10%) de la quantité cellulaire totale de DDX6 (Ernoult-Lange et al., 2012). Une approche différente basée sur la comparaison d'intensité de fluorescence dans *versus* hors des PB de la protéine de fusion GFP-AGO2 a estimé un facteur 10 de surconcentration de cette protéine dans les PB par rapport au cytoplasme, et a montré que, là aussi, la localisation aux PB ne concerne qu'une faible proportion (~1%) de la quantité cytoplasmique totale de GFP-AGO2 (Leung et al., 2006). Ces dernières considérations soulignent la difficulté d'étudier les protéines des PB par des approches de seule purification d'affinité.

Chez la levure, une étude récente basée sur une approche de microscopie quantitative à fluorescence montre que la gamme de surconcentrations des composants des PB est large ; un petit nombre de protéines des PB principalement associées à la dégradation de l'ARNm (Dcp2, Edc3, Pat1, Xrn1, Lsm1, Upf1 et Dhh1) sont fortement concentrées dans les PB par rapport au cytoplasme (d'un facteur 30 pour Dhh1 à un facteur 133 pour Dcp2) tandis que les autres protéines des PB n'y sont enrichies que d'un facteur inférieur ou égal à 10 (Xing et al., 2020). Considérant des cellules de 8 µm de diamètre contenant chacune en moyenne 5 PB de 500 nm de diamètre, il est possible d'estimer la proportion des principales protéines des PB comprise entre 3% (Dhh1) et 15% (Dcp2) (Tableau 4).

protéine	coefficient de partition	concentration dans les PB (µM)	concentration cytoplasmique (µM)	proportion de la protéine dans les PB (%)
Dp2	133	15	0,12	15
Edc3	133	12	0,09	16
Pat1	107	12	0,12	12
Xrn1	53	11	0,22	6
Lsm1	52	8,9	0,17	6
Upf1	39	5,1	0,13	5
Dhh1	30	10	0,38	3

Tableau 4 Estimation de la proportion des principales protéines des PB chez S. cerevisiae

Les concentrations dans les PB et cytoplasmiques utilisées pour calculer la proportion de chaque protéine dans les PB sont reprises des résultats de (Xing et al., 2020) obtenus dans des souches S. cerevisiae Dcp1Δ.

1.1.2 Protéome des PB

Notre connaissance actuelle de la composition en protéines des PB de cellules humaines est issue de deux études indépendantes de protéomique à large échelle (Figure 30). La première étude précédemment mentionnée et réalisée au laboratoire repose sur la purification par tri de particules fluorescentes (FAPS) réalisé sur des lysats cytoplasmiques de cellules HEK293, exprimant de manière stable la protéine de fusion GFP-LSM14A utilisée pour marquer les PB, et sur l'identification en spectrométrie de masse des protéines présentes dans les fractions pré-triée et triée (Figure 30). Cette approche identifie 125 protéines significativement enrichies dans les PB dont 15 préalablement connues (Figure 31). Comme attendu, les protéines identifiées sont majoritairement associées au métabolisme de l'ARNm et plus particulièrement à la répression de la traduction, à la voie de régulation par les miARN, à la dégradation générale de l'ARNm et au NMD (Hubstenberger et al., 2017).

La seconde étude (Youn et al., 2018) a utilisé une approche de BioID (Proximity-Dependent Biotinylation (BioID) (Roux, 2013) combinée à une purification d'affinité sur deux protéines des PB : DCP1A et PAT1B portant un double tag BirA*-FLAG. (Figure 30). Suite à la purification d'affinité, 54 et 68 protéines endogènes se recoupant partiellement (7 protéines en communs : AGO1, AGO2, DCP1B, EDC3, EDC4, MARF1 et SMG7 se retrouvant toutes dans le

protéome des PB issu de leur purification par FAPS) ont été identifiées par spectrométrie de masse comme partenaires directs de DCP1A et PAT1B et donc comme potentiels composants des PB. Cette méthode présente l'avantage de mettre en évidence des interactions protéine-protéine (IPP) faibles et/ou transitoires *in vivo*. Toutefois, les données issues de cette approche sont à interpréter avec précaution étant donné que toutes les protéines des PB sont aussi et majoritairement présentes dans le cytoplasme et que par conséquent, les interactions identifiées par BioID pourraient tout à fait avoir lieu en dehors des PB. L'utilisation d'un plus grand nombre de protéines des PB comme appât dans le BioID pourrait améliorer la résolution du réseau d'interactions spécifiques des PB. Notons qu'une étude récente a tenté de purifier des PB de cellules U2OS en conditions de stress (Matheny et al., 2019). Là aussi, l'interprétation se heurte au fait que le résultat de la purification est un mélange de complexes solubles et/ou de PB, ne permettant pas de tirer de conclusions quant aux seuls PB.

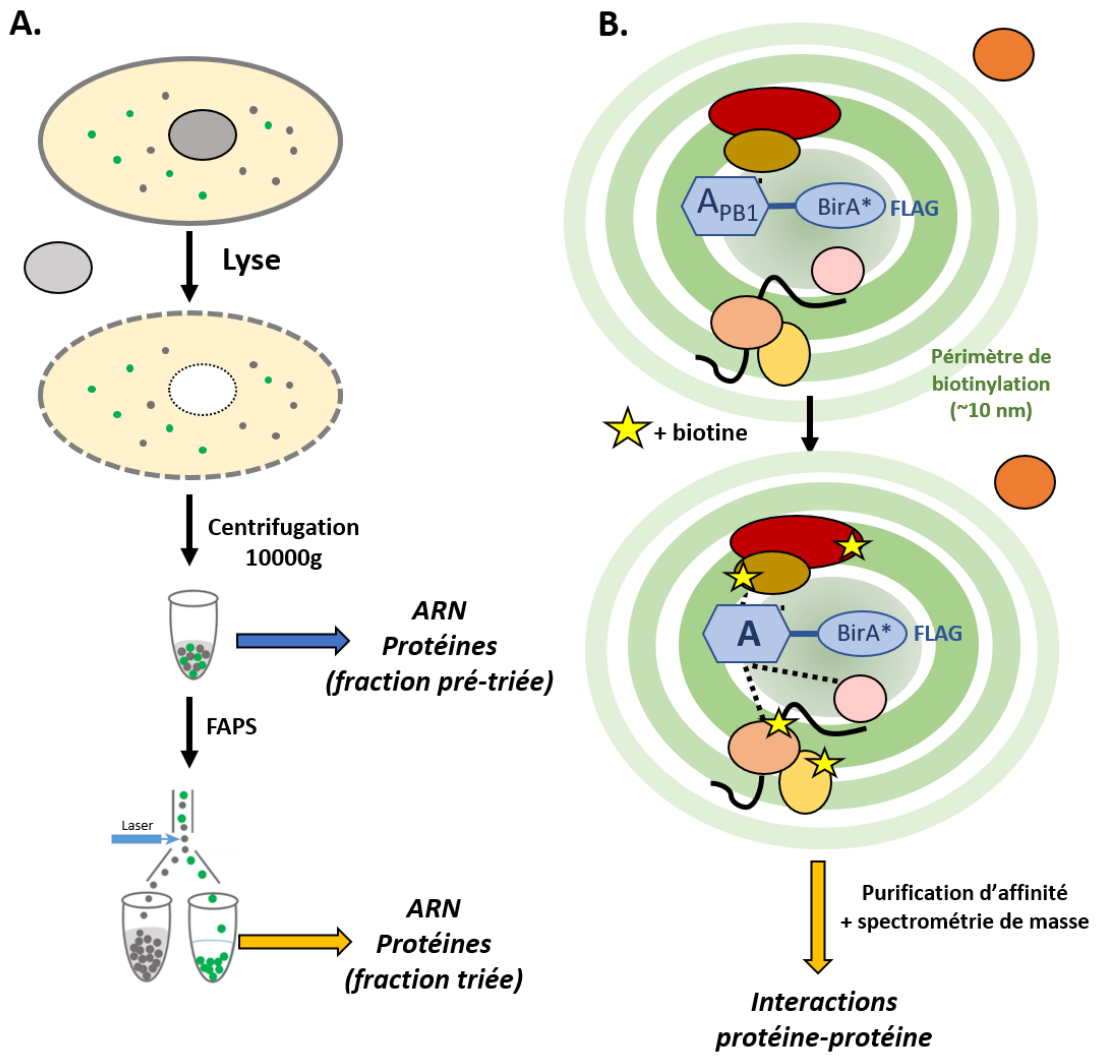

Figure 30 Comparaison de deux stratégies expérimentales d'étude de la composition des PB

A. Purification des PB par FAPS*. Les lysats cytoplasmiques de cellules HEK293 exprimant de manière stable un marqueur fluorescent des P-bodies, la protéine GFP-LSM14A (vert), sont centrifugés à 10000g ce qui constitue la fraction pré-triée. Cette fraction passe ensuite à travers un FACS (Fluorescence-Activated Cell Sorter) afin de récupérer la fraction triée contenant les PB fluorescents. Les protéines des fractions pré-triées et triées sont identifiée par LC-MS/MS (Liquid Chromatography–Tandem Mass Spectrometry). En parallèle, les ARN totaux des fractions pré-triées et triées sont extraits, les librairies d'ADNc préparées à partir de random-primers puis séquencées à haut débit. (Modifié d'après Standart and Weil, 2018).*

B. Identification du réseau d'interactions des PB par marquage de proximité à la biotine. *Une protéine appât A (DCP1A et PAT1B dans Youn et al., 2018) contenue dans les PB et fusionnée à la biotine-ligase BirA* étiquetée avec le peptide FLAG est exprimée transitoirement dans des cellules HEK. L'ajout de biotine au milieu de culture permet à BirA* de biotinyler des protéines environnantes dans un rayon de 10 nm. Les partenaires d'interaction directs sont ensuite purifiés par affinité avec un anticorps dirigé contre le FLAG et identifiés en spectrométrie de masse. Ceci réalisé en parallèle pour plusieurs protéines appât contenues dans les PB, permet en croisant les interactomes d'établir le réseau d'interactions protéiques localisées dans les PB. (Modifié d'après Go et al., 2019 Biorxiv)*

La purification des PB met par ailleurs en évidence une spécificité de composition protéique qui différencie les PB d'autres granules mRNP dont notamment les granules de stress. En effet le croisement du protéome des PB avec celui des granules de stress ne trouve que 25% de protéines communes entre les deux types de granules. Également, les protéines des PB se caractérisent par leur relativement grand nombre de partenaires protéiques (Hubstenberger et al., 2017) ainsi que par la présence d'IDR (Intrinsically Disordered Region) (Uversky, 2017). Deux tiers d'entre elles sont des RBP associées au métabolisme de l'ARN (Hubstenberger et al., 2017). Ces caractéristiques sont importantes pour expliquer l'assemblage des PB que nous détaillerons dans un paragraphe dédié (*cf* Partie 2 paragraphe 2).

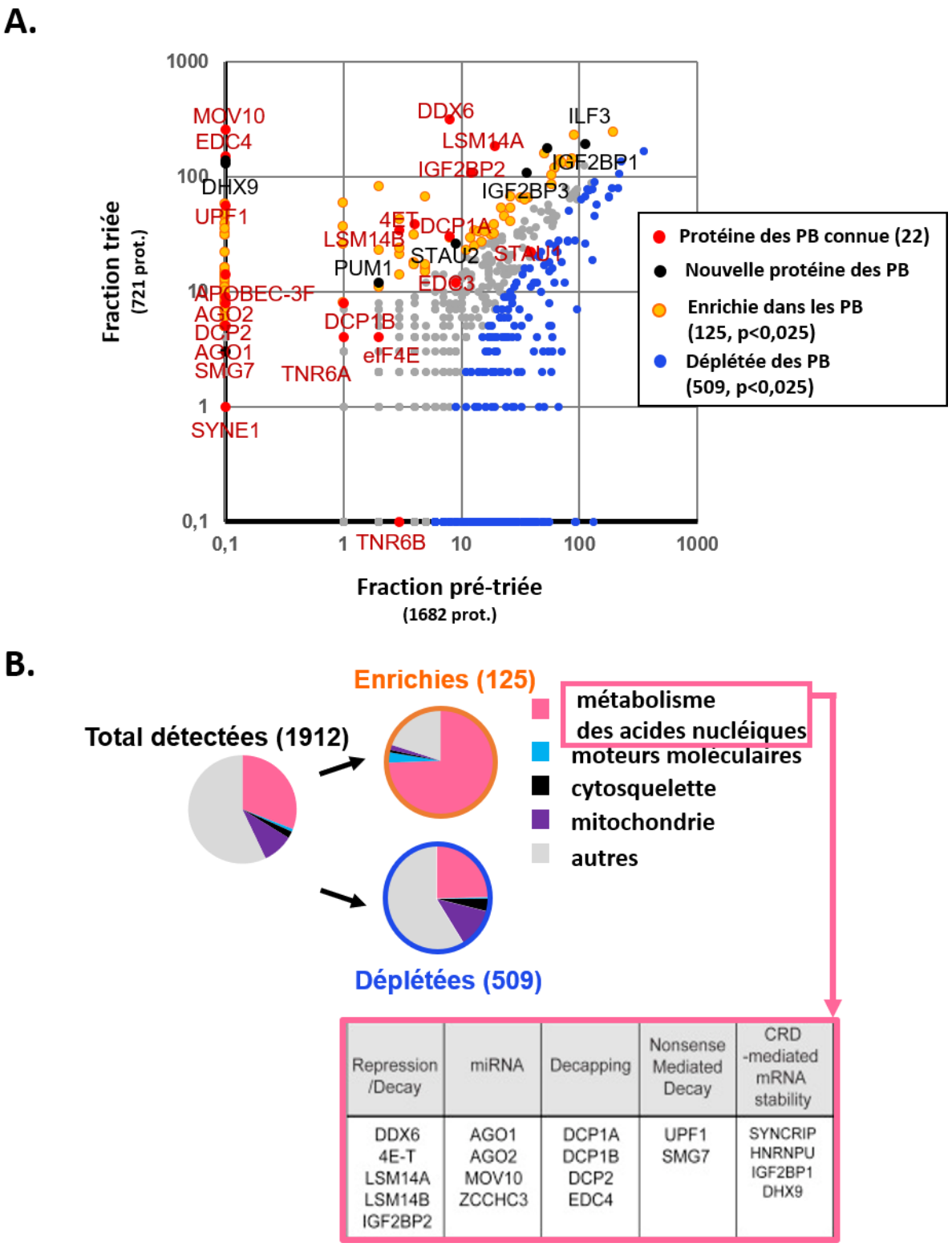

Figure 31 Protéome des PB suite à leur purification par FAPS

(A) *Comparaison des scores de spectrométrie de masse associés aux protéines des fractions pré-triée et triée. En orange les protéines significativement enrichies dans les PB, en bleu celles significativement déplétées.*

(B) Répartition fonctionnelle des protéines enrichies et déplétées des PB. (Modifié d'après Hubstenberger et al., 2017).

1.2. Composition en ARN

1.2.1. Localisation d'ARN dans les PB par approche gène candidat

Avant que les PB ne soient purifiés, des approches d'hybridation fluorescente *in situ* sur molécule unique (smFISH) avaient détecté la présence d'ARNm (CAT-1) et de miARN endogènes (miR122) dans les PB (Bhattacharyya et al., 2006) ainsi que d'ARNm rapporteurs contenant des motifs particuliers tels des MRE (Pillai et al., 2005a), des séquences TOP (Halstead et al., 2015) ou des motifs ARE (Franks and Lykke-Andersen, 2007). Par ailleurs, une approche d'l'immuno-microscopie électronique a montré que les PB sont dépourvus d'ARN ribosomiques (Hubstenberger et al., 2017). Précédemment il avait été observé en immunofluorescence qu'à la différence des granules de stress, les protéines ribosomales ne se localisent pas dans les PB (Kedersha et al., 2005). Ensemble ces observations confirment que les transcrits localisés dans les PB ne sont pas traduits.

Les quantifications réalisées à l'échelle du transcrit individuel montrent que pour un ARN donné il existe une large variabilité intercellulaire de la proportion du transcrit localisée dans les PB. Par exemple pour l'ARNm SPEN la proportion du transcrit contenue dans les PB est de 15% en moyenne mais peut atteindre jusqu'à 30% dans 12 % des cellules (Hubstenberger et al., 2017), elle est comprise entre 1 et 13% pour l'ARNm rapporteur CFP-β-actine-MS2 (Aizer et al., 2014) et oscille entre 11 et 36 % pour un ARNm rapporteur ciblé par let7 (Pillai et al., 2005a).

1.2.2 RNome des PB

Suite à la purification des PB par FAPS présentée précédemment, les ARN totaux contenus dans les fractions pré-triée et triée ont été extraits et séquencés. L'analyse des résultats de séquençage montre que le stockage dans les PB concerne majoritairement des ARNm,

représentant un tiers du transcriptome humain codant. Il s'agit donc d'un phénomène à la fois large et sélectif (Figure 32). Les ARNm des PB ont pour particularité d'être régulés en traduction mais pas en stabilité par DDX6. Ils possèdent un faible rendement protéique, (Hubstenberger et al., 2017) résultant d'un biais de codons (Courel et al., 2019). Enfin, ils se trouvent également enrichis en ARNm cibles de répresseurs de la traduction : par exemple, les ARNm contenant des ARE se trouvent stockés dans les PB (Franks and Lykke-Andersen, 2007).

Chez la levure, les ARNm associés à deux composants des PB (Dcp2 et Scd6 -orthologue de LSM14A) ont été purifiés par cCLAP (chemical Cross-Linking coupled to Affinity Purification) dans trois conditions de stress chacune capable d'induire des PB, et séquencés (Wang et al., 2018). D'après cette étude, le recrutement d'ARNm par Dcp2 et Scd6 (qui inclurait donc le recrutement des ARNm des PB selon le postulat des auteurs) concerne un grand nombre de transcrits (1544 ARNm soit ~1/4 du transcriptome de levure) avec 1/3 des transcrits s'exprimant de façon stress-spécifique. De manière intéressante, la longueur du CDS des transcrits spécifiquement associés aux protéines Dcp2 et Scd6 est fonction de la nature du stress. Nous reviendrons sur ce point lorsque nous aborderons la formation des PB (partie 2 paragraphe 2.2)

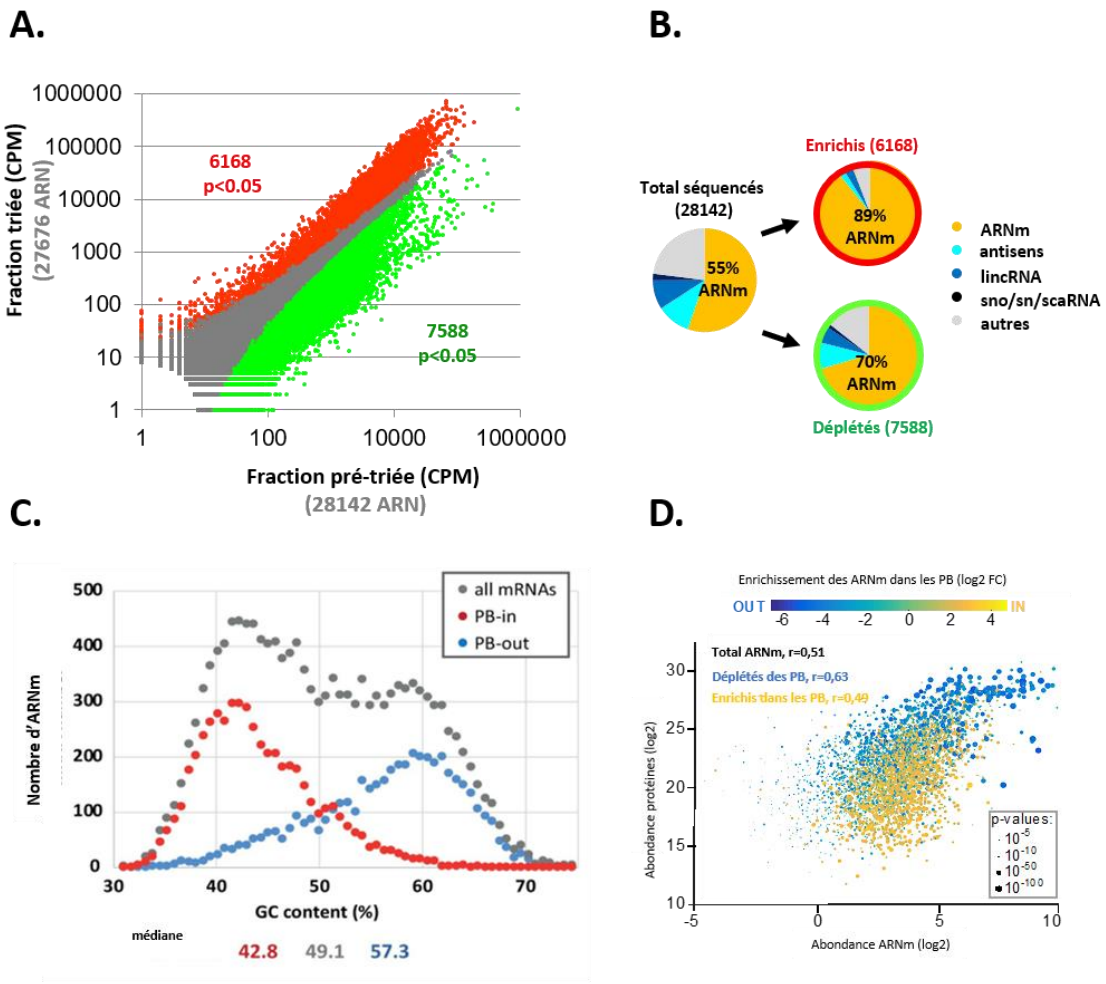

Figure 32 Principales caractéristiques des ARNm enrichis dans les PB

(A) Comparaison des abondances d'ARN entre les fractions triée et pré-triée à partir des données de RNAseq, exprimées en CPM (Count Per Million). En rouge les transcrits significativement enrichis dans les PB et en vert ceux significativement déplétés. Ces données montrent que les PB concentrent jusqu'à un cinquième du transcriptome.

(B) Comparaison des proportions d'ARN codant et non codant enrichis et exclus des PB indiquant que les PB contiennent majoritairement des ARNm.

(C) ARNm du transcriptome humain, enrichis, ou déplétés des PB représentés selon leur contenu en GC. Les pourcentages en GC médians sont précisés en bas. Les PB contiennent majoritairement les ARNm riches en AU du transcriptome.

(D) Comparaison des abondances des protéines et des ARNm qui les codent et colorés selon l'enrichissement des ARNm dans les PB. Pour un niveau d'expression d'ARNm donné, l'abondance des protéines qu'ils codent est d'autant plus faible que ces ARNm sont fortement enrichis dans les PB. (Modifié d'après Courel et al., 2019 ; Hubstenberger et al., 2017)

2. Formation des PB

La première description du comportement liquide des organites sans membrane a été réalisée sur les P-granules de cellules embryonnaires chez *C. elegans* (Brangwynne et al., 2009). Dans cet organisme il a été observé que les P-granules fusionnent, se condensent, se dissolvent, échangent rapidement des composants protéiques avec le cytoplasme et réagissent à la déformation en fluant (*i.e.* en se déformant à une vitesse lente sous l'effet d'une force) et leur viscosité dynamique (Pa.s) a été estimée à 1 Pa.s (pour comparaison $\eta_{\text{eau à 30°C}} = 0{,}8 .10^{-3}$ Pa.s et $\eta_{\text{miel 30\%humidité à 30°C}} \sim 2$ Pa.s (Yanniotis et al., 2006)). Des comportements similaires de gouttelettes visqueuses ont ultérieurement été décrits dans d'autres organites sans membrane tels les granules de stress (SG), les PB, les nucléoles, les speckles nucléaires (Hyman et al., 2014; Li et al., 2018; Shin and Brangwynne, 2017) et constituent autant d'observations suggérant que les organites sans membrane se forment par un processus physique de séparation de phase liquide-liquide (Hyman et al., 2014).

2.1 La séparation de phase liquide-liquide

2.1.1. Principes fondamentaux

La séparation de phase liquide-liquide (LLPS) désigne le partage d'une phase liquide initialement homogène en deux phases distinctes : une phase concentrée et une phase déplétée. Ce phénomène se produit à partir de seuils de concentration et dans des conditions de température (Nott et al., 2015) et de pH (Kaibara et al., 2000; Koga et al., 2011) bien précis récapitulés dans un diagramme de phase (Figure 33). A l'échelle moléculaire, la LLPS se produit dans des conditions où les interactions homotypiques (*i.e.* entre molécules de propriétés similaires) entre composants de la solution deviennent plus fortes que les interactions hétérotypiques ce qui rend le maintien d'une phase liquide unique thermodynamiquement défavorable (Gomes and Shorter, 2019). Notons que la nature des cosolvants ainsi que la concentration en sels peuvent également influencer la formation des condensats *in vitro* en modifiant la force des interactions entre les ARN et protéines entrant en séparation de phase (Nakashima et al., 2019).

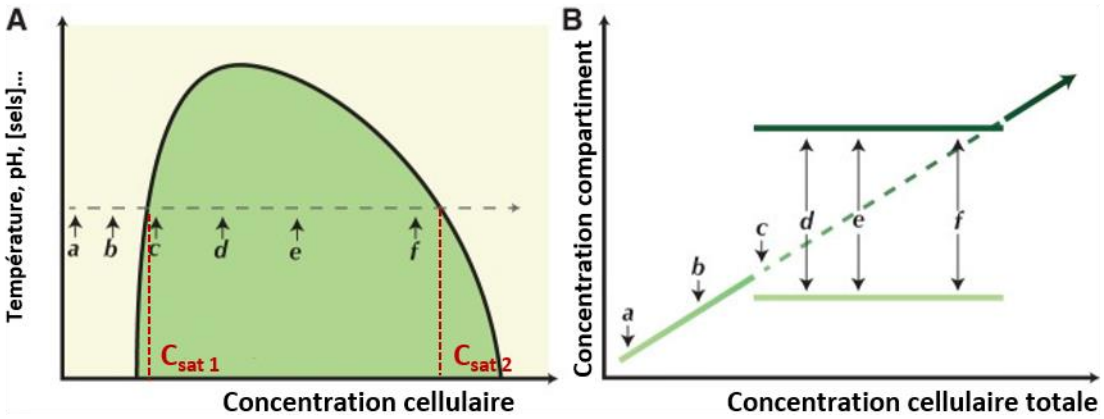

Figure 33 Diagramme de phase et séparation de phase liquide-liquide

***A**. Diagramme de phase théorique montrant les conditions de concentration dans lesquelles le système est sous forme d'une phase homogène (jaune) ou de deux phases séparées (vert). Les pointillés représentent la réponse du système à un accroissement de concentration*

***B.** Un mélange homogène se sépare en deux phases à partir du seuil de concentration (c). Passé ce seuil, la taille de la gouttelette s'accroît sans que sa concentration ne soit modifiée (d), (e) (f). Au-delà du seuil de concentration (f), le système retourne dans un état monophasique (Modifié d'après McSwiggen et al., 2019).*

La valeur du seuil de concentration à partir duquel un composant entre en séparation de phase dépend principalement de deux paramètres moléculaires : la multivalence du composant c'est-à-dire le fait qu'il possède plusieurs sites d'interaction avec d'autres ligands, et l'affinité de chaque site d'interaction pour ses ligands (Peran and Mittag, 2020). L'importance de la multivalence pour la formation des séparations de phase a d'abord été démontrée expérimentalement *in vitro* sur des mélanges de protéines, d'ARN et de protéines/ARN (Boeynaems et al., 2018) puis *in vivo* sur des protéines chimères fluorescentes (Li et al., 2012). Dans cette étude, la co-expression dans des cellules HeLa de la protéine mCherry-$SH3_5$ contenant cinq répétitions du domaine SH3 (SRC Homology 3) avec la protéine eGFP-PRM_5 comportant cinq répétitions du motif ligand de SH3, PRM (Proline Rich Motif), conduit à la formation de granules cytoplasmiques de 0,5 à 2 µm de diamètre. Ceci ne se produit pas lorsque les mêmes protéines sont exprimées seules ou sous des versions contenant un plus petit nombre de modules répétés confirmant ainsi que des interactions multivalentes entre protéines peuvent engendrer des séparations de phase dans les cellules.

En terme de cinétique, la séparation de phase commence par une étape de nucléation où les protéines ayant le seuil de concentration le plus bas, les « scaffolds », se condensent pour former le cœur du granule et recrutent dans un second temps d'autres composants, les clients, dont le seuil de concentration est plus élevé (Alberti, 2017; Lin et al., 2015a; Nott et al., 2015). Les mécanismes *in vivo* du processus de nucléation ne sont pas clairement établis. Toutefois plusieurs études étayent l'idée que la nucléation des organites sans membrane commence par le pré-assemblage de certains composants spécifiques du granule. Par exemple, les nucléoles se forment à partir d'un ARNr (Grob et al., 2014) ou encore les centrosomes à partir d'un centriole (Gönczy, 2012; Zwicker et al., 2014).

En théorie, le recrutement des clients s'effectue par partitionnement ou séquestration. Formellement, le coefficient de partition des molécules clients Kpart (*i.e.* le rapport de leurs concentrations respectives dans la phase surconcentrée et dans le solvant) dépend de la différence d'énergie libre standard (ΔG0) entre ces différentes phases et est donné par la relation $Kpart = e^{-\Delta G0/RT}$ où R est la *constante* des gaz parfaits et T la température. ΔG0 est elle-même décomposée en plusieurs contributions $\Delta G0=\Delta G0_{hphob}+\Delta G0_{charge}+\Delta G0_{Hbond}+\Delta G0_{mesh}$ (Figure 34). Brièvement, $\Delta G0_{hphob}$ est l'énergie libre de solvatation, elle rend compte du fait que la polarité locale à l'intérieur des condensats est plus faible que dans leur environnement aqueux proche ce qui favorise le partitionnement des molécules hydrophobes. $\Delta G0_{charge}$ résulte de l'existence de larges régions chargées dans certaines molécules et explique notamment le partitionnement des IDP (Intrinsically Disordered Protein) sur lesquelles nous reviendrons dans le paragraphe suivant. $\Delta G0_{Hbond}$ rend compte des interactions par liaison hydrogène des molécules partitionnées avec la matrice du condensat. Enfin $\Delta G0_{mesh}$ représente l'énergie nécessaire pour déformer réseau d'interactions à l'intérieur du condensat afin d'y intégrer de nouvelles molécules, il s'agit d'une contribution négative au partitionnement (Nakashima et al., 2019).

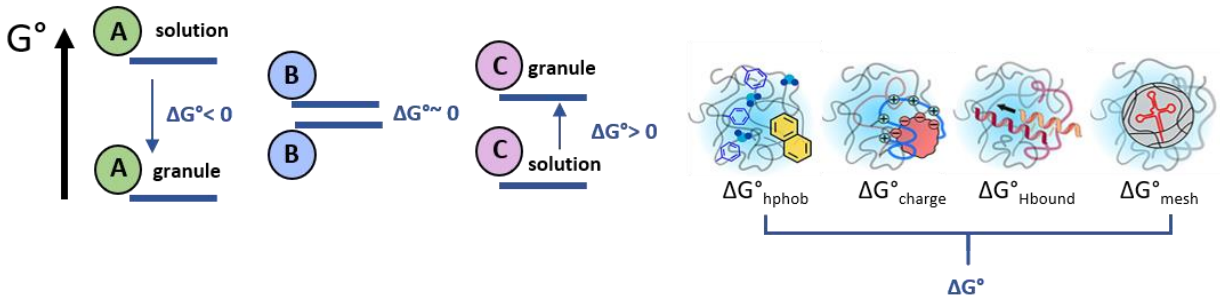

Figure 34 Partitionnement des molécules clients dans les biocondensats

Dans le cas des biocondensats déjà formés les molécules se partitionnent entre le solvant et la séparation de phase selon la différence d'énergie libre entre ces deux phases. La molécule A ayant un ΔG°< 0 est sélectivement recrutée dans le granule, la molécule B n'a pas de comportement déterminé et la molécule C est sélectivement exclue du granule. Plusieurs interactions contribuent à la différence d'énergie libre illustrée à droite (Modifié d'après Nakashima et al., 2019)

2.1.2. Déterminants moléculaires des LLPS

Plusieurs types d'interactions entre ARN et protéines interviennent dans la formation des organites sans membranes. Les domaines repliés des protéines forment des interactions protéines-protéines et/ou protéines-ARN spécifiques (Kato et al., 2012; Li et al., 2012). Les protéines contenant des IDP contribuent également à plusieurs types d'interactions multivalentes. A la différence des domaines globulaires, les IDP n'adoptent pas de conformation tridimensionnelle fixe du fait de la présence de longs éléments de séquence ayant une faible diversité d'a.a et de la composition chimique de ces a.a les empêchant de se replier en domaines structurés, ce qui contribue notamment à maintenir le comportement liquide des biocondensats (Darling et al., 2018). Ces séquences non structurées appelées LCD (Low Complexity Domains) sont souvent enrichies en acides aminés à résidus polaires (glycine, glutamine, asparagine, et serine) et/ou chargés (acide aspartique, acide glutamique, arginine et lysine) (Uversky et al., 2015) se trouvant répétés sous forme de petits motifs FG-, RG-, GY-, KSPEA-, SY, ou formant des régions riches en Q/N (Banani et al., 2017), ce qui les rend particulièrement aptes à former des séparations de phase liquide-liquide (Brangwynne et al., 2015; Nott et al., 2015; Pak et al., 2016). D'ailleurs, *in vitro,* les IDP suffisent à assembler des granules protéiques par LLPS. Ceci a été montré sur des solutions contenant juste une IDP comme par exemple DDX4, une protéine de nuage (*i.e.* de granule germinal) (Nott et al., 2015), la protéine des granules de stress TIA-1 (Gilks et al., 2004) ou encore les régions désordonnées de plusieurs RBP mises en présence d'ARN dans des conditions physiologiques telles eIF4G, Lsm4, TIA1, Fus, hnRNPA1 (Lin et al., 2015a). L'implication des LCD de plusieurs RBP dans la localisation de ces RBP dans les biocondensats s'avère également importante *in vivo*. Par exemple chez la levure, les régions riches en Q/N de Lsm4p (Decker et al., 2007) ainsi que de Ccr4, Pop2, Dhh1 (Reijns et al., 2008) contribuent à l'accumulation de ces protéines dans les

PB en conditions de stress. Chez la souris, les LCD de TIA1 et PUM2 contribuent à l'accumulation de ces protéines dans les granules de stress (Gilks et al., 2004; Vessey et al., 2006). De manière intéressante, les granules de stress mammifères possèdent une organisation sub-granulaire comprenant une région périphérique et un cœur où les concentrations en protéines et en ARN sont plus élevées que dans la périphérie (Jain et al., 2016; Souquere et al., 2009). Une approche de TALM (Tracking And Localisation Microscopy) permettant de localiser des protéines individuelles sur de longues périodes temporelles) a comparé dans des cellules neuronales de rat traitées à l'arsenite, la distribution des coefficients de diffusion de deux versions d'une protéine canonique des granules de stress (G3BP1) : la version entière de G3BP1 contenant 1 RBD et 4 LCD et une version tronquée ($G3BP_C$) contenant 1 RBD et 2 LCD. Selon cette étude, les protéines $G3BP_C$ peuvent être recrutées dans les SG comme la protéine entière mais elles y sont moins mobiles. Ceci suggère que la présence de LCD contribue, à l'intérieur des SG, à la diffusion de G3BP1 et y facilite le passage d'un état interactif et immobile dans le cœur du SG à un état diffusif dans la périphérie. (Niewidok et al., 2018).

Parallèlement aux protéines, l'ARN joue aussi un rôle actif dans la formation des granules mRNP par LLPS. Il peut notamment agir comme « plateforme » de recrutement de RBP. Par exemple, lorsque la traduction est bloquée *in vivo* suite à un stress, ce sont les ARNm qui nucléent la formation des granules de stress (Bounedjah et al., 2014; Van Treeck et al., 2018). Alternativement, les ARN peuvent être recrutés *in vitro* dans des granules déjà pré-nucléés (Nott et al., 2016), notamment *via* des interactions ARN-ARN se produisant à la surface de condensats ARN ou RNP (Tauber et al., 2020). De manière intéressante, il est observé que la taille de granules mRNP artificiels reconstitués à l'intérieur de cellules humaines est directement influencée par la densité des domaines d'interaction avec l'ARN, pouvant en effet conduire à une gêne stérique empêchant le recrutement d'autres briques élémentaires à la surface du condensat (Garcia-Jove Navarro et al., 2019). (Figure 35)

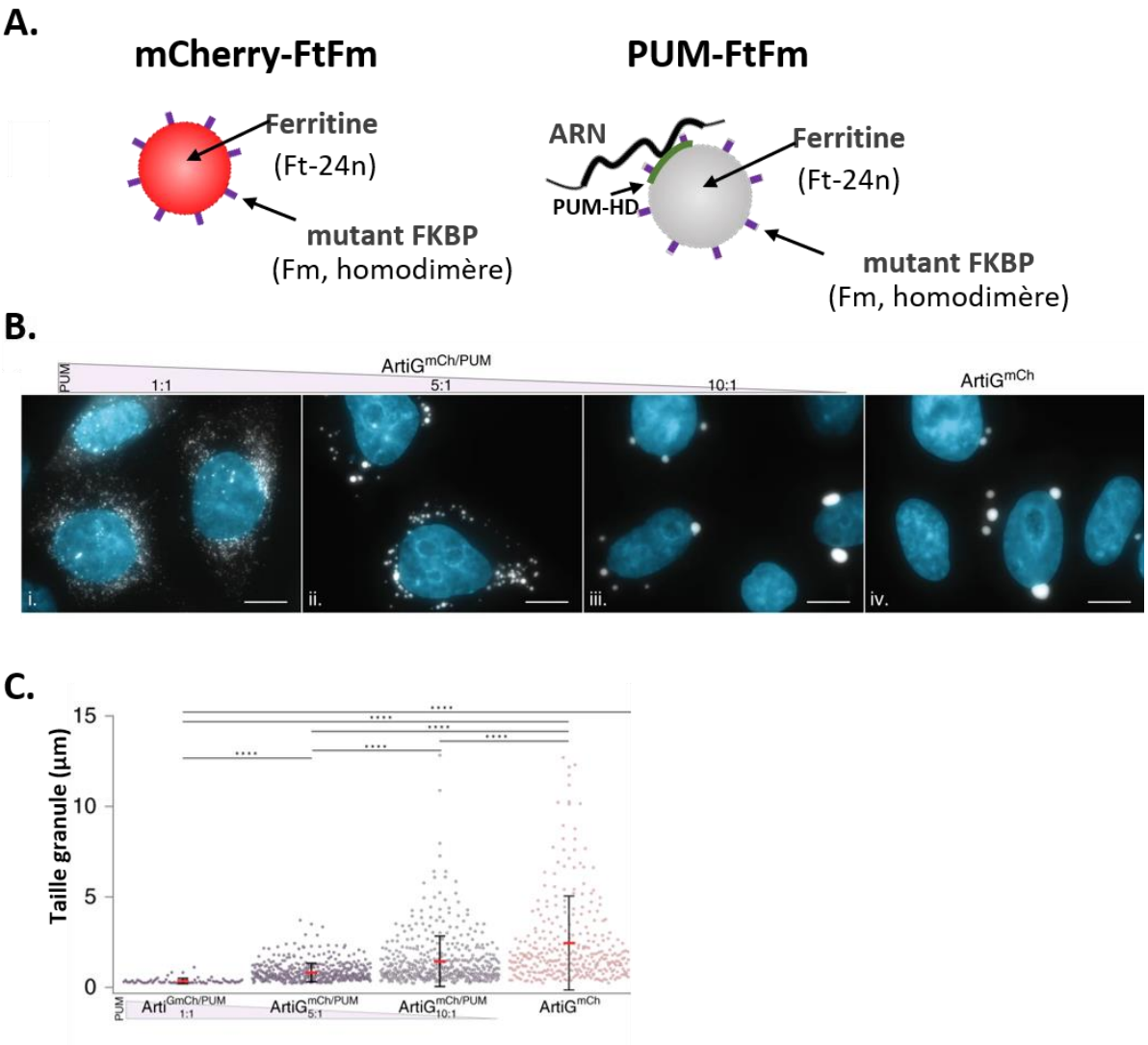

Figure 35 Effet de l'ARN sur la taille de condensats ARN-protéine artificiels recrées dans les cellules humaines

(A) *Des granules ARN-protéines artificiels (ArtiG $^{mCh/PUM}$) sont recrées dans des cellules HeLa en coexprimant les protéines chimères mCherrry-FtFm et PUM-FtFm. FtFm est une protéine chimère composée de 24 répétitions de la ferritine chacune fusionnée à la protéine F36M-FKBP (version mutée de la protéine FKBP ayant la propriété de former des homodimères avec des affinités de l'ordre de 1µM). Dans sa version PUM-FtFm, la FtFm est fusionnée au domaine de liaison à l'ARNm de la protéine Pumilio1 humaine.*

(B) *Les plasmides codant mCherrry-FtFm et PUM-FtFm. sont transfectés dans différents ratios (1 :1, 5 :1, et 10 :1) et la formation des granules est mesurée en microscopie confocale 8-10 h après transfection.*

(C) *Quantification de la taille des granules artificiels (****p < 0.0001).*

(Modifié d'après Garcia-Jove Navarro et al., 2019)

2.1.3. Eléments régulateurs des LLPS in vivo

In vivo, d'autres paramètres peuvent moduler la formation de condensats par LLPS. Certaines modifications post traductionnelles induisent des changements dans les charges des acides aminés des domaines repliés et des LCD des protéines et/ou dans leur distribution. Ceci modifie le nombre ainsi que l'intensité des interactions multivalentes des protéines modifiées et change conséquemment leur capacité à former des séparations de phase (Bah and Forman-Kay, 2016 ; Hofweber and Dormann, 2019). Par exemple, la méthylation des arginines de DDX4X double son seuil de concentration ce qui tend à dissoudre les granules qu'elle forme (Nott et al., 2015).

Certaines protéines agissent également directement sur les séparations de phase liquide liquide. C'est le cas notamment des hélicases à ARN Dhh1 , Ded1, Dbp1, Dbp2 (Hondele et al., 2019) et eIF4A (Tauber et al., 2020), qui, en modulant les structures secondaires de l'ARN et les interactions protéine/ARN, contrôlent activement les propriétés viscoélastiques des granules. Chaque hélicase serait spécifique d'un type de granule particulier (Hondele et al., 2019)

Enfin, signalons que l'activité de protéines chaperonnes peut intervenir dans l'assemblage ou le désassemblage des biocondensats. Par exemple chez *C. elegans*, le complexe CCT (Chaperonin-Containing Tailless *complex* polypeptide 1) contribue à l'assemblage des grP-bodies (Hubstenberger et al., 2015), tandis que chez la levure, une mutation sur le site de liaison à l'ATP de CCT3 conduit à la formation de PB hypertrophiés (Nadler-Holly et al., 2012). Dans les cellules humaines, les deux ATPases RUVBL1/2 prennent part au remodelage des granules de stress, en synergie avec les complexes CCT et MCM (MiniChromosome Maintenance complex) (Jain et al., 2016).

2.2 Le processus de formation des PB in vivo

2.2.1 Recrutement d'ARNm réversiblement exclus de la traduction

Tous les facteurs d'initiation de la traduction sont absents des PB (à l'exception d'eIF4E sans doute en raison de son association avec son répresseur 4E-T (Andrei, 2005; Ferraiuolo et

al., 2005). La quasi-totalité des protéines ribosomales (73/78) est absente des protéines enrichies dans les PB et une approche d'hybridation *in situ* couplée à de l'immuno--microscopie électronique montre que les ARNr 18S et 28S sont exclus des PB (Hubstenberger et al., 2017). Ainsi les ARNm des PB se trouvent exclus du dispositif de traduction. Ne pas être associé à la machinerie de traduction s'avère nécessaire au recrutement des ARNm dans les PB. En effet, lorsque les polysomes sont artificiellement figés sur l'ARNm au moyen de cycloheximide, le nombre de PB décroît et ce quelle que soit la protéine utilisée pour les repérer (Andrei, 2005; Wilczynska et al., 2005). Inversement, lorsque les polysomes sont artificiellement dissociés de l'ARNm par ajout de puromycine, le nombre de PB augmente (Wilczynska et al., 2005). La visualisation des mouvements individuels d'ARNm rapporteurs sortant de la traduction par une approche de NCT (Nascent Chain Tracking)*[5] met en évidence deux types de comportements des ARNm par rapport aux PB. Une partie d'entre eux s'associe transitoirement (entre 6 à 18s) aux PB tandis que d'autres sont maintenus à l'intérieur des PB pour des périodes prolongées (entre 1min30s et 45min) où ils seraient stockés sous forme réprimée (Moon et al., 2019) (Figure 36). Notons que la répression de la traduction des ARNm stockés dans les PB est réversible. Par exemple, supprimer la répression de la traduction de l'ARNm CAT-1 provoque sa délocalisation des PB et son recrutement aux polysomes (Bhattacharyya et al., 2006). Les dynamiques d'interaction des ARN avec les PB ont été visualisées sur d'autres classes d'ARN notamment les miARN (Pitchiaya et al., 2019). Ces derniers présentent également un schéma d'interaction bimodal (*i.e.* interactions stables ou transitoires) avec les PB, influencé par le statut de liaison du miARN à son ARNm cible. En effet, la micro-injection d'un ARNm cible du miARN rapporteur let7 accroît d'un facteur cinq la proportion d'interactions transitoires formées par ce miARN avec son ARNm cible.

[5] Le NCT est une approche basée sur l'utilisation conjointes de tags présentant plusieurs épitopes et de sondes fluorescentes couplées à des anticorps permettant de quantifier les dynamiques de traduction à l'échelle du transcrit individuel.

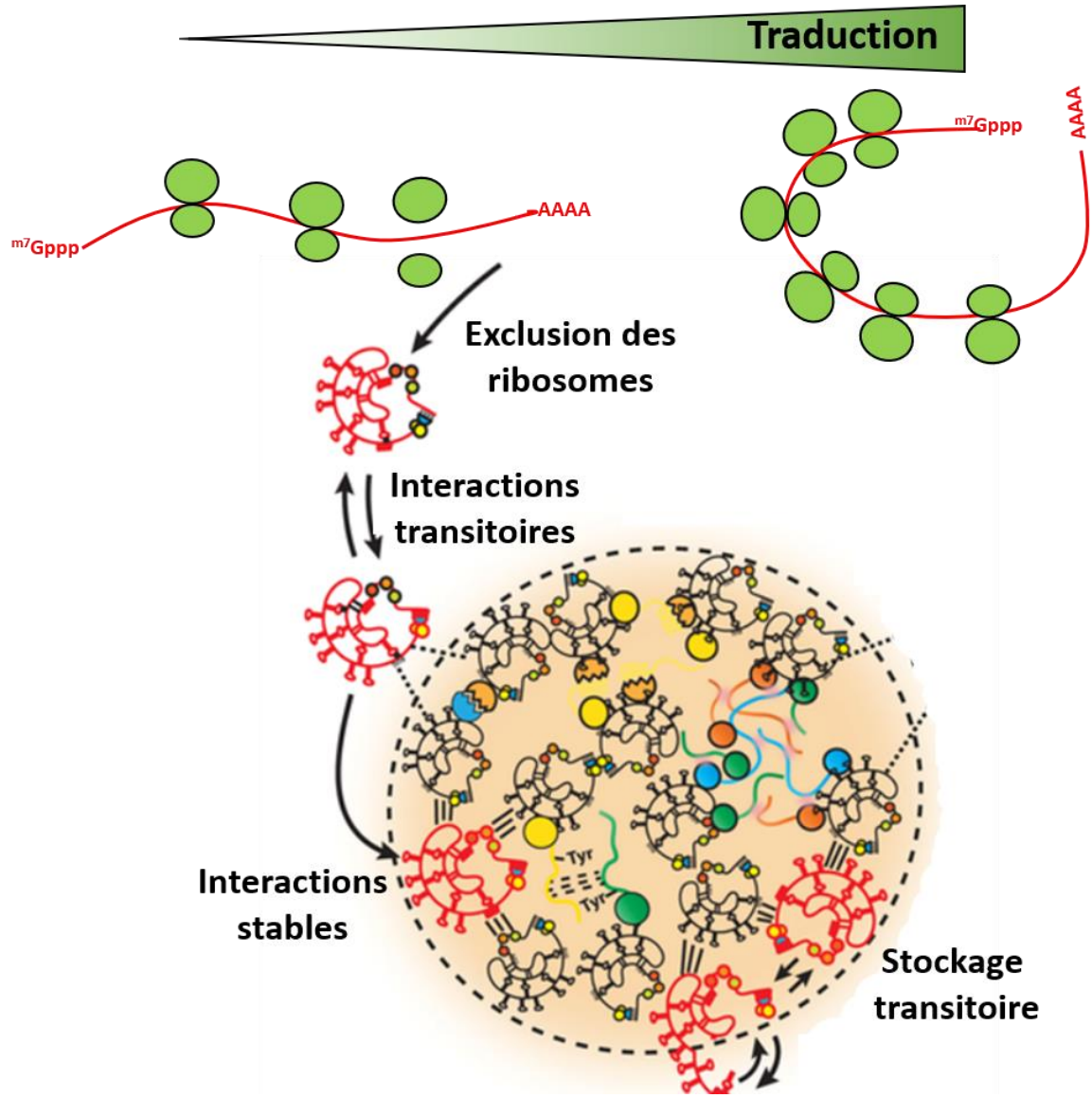

Figure 36 Modèle de recrutement des ARNm aux PB

Suite à la répression de la traduction, les ribosomes se dissocient. Les ARNm diffusent dans le cytoplasme sous forme condensée et interagissent transitoirement avec des composants à la surface du granule (pointillés noirs). Certains ARNm forment des interactions stables et sont engagés dans des interactions multivalentes avec d'autres ARNm ou protéines. (Modifié d'après Moon et al., 2019).

En termes de mécanismes de recrutement des ARNm aux PB, deux déterminants principaux interviennent. D'un côté, une partie des ARNm enrichis dans les PB sont ciblés par des RBP ayant une activité de répresseurs spécifiques de la traduction et enrichis dans les PB. Aussi est-il plausible que la reconnaissance d'un ou plusieurs éléments de séquence dans la 3'UTR des ARNm cibles de ces RBP soit associée au recrutement simultané de leurs transcrits cibles dans les PB (Hubstenberger et al., 2017). Parallèlement, les ARNm des PB possèdent un

biais de codon à l'origine de leur faible rendement protéique (Courel et al., 2019). Hypothétiquement, le fait d'être moins bien traduits en ferait des cibles plus efficacement régulables par répression de la traduction comparé à des ARNm intrinsèquement traduits de manière active, dont l'expression serait plus efficacement contrôlée par dégradation.

2.2.2 Assemblage des PB à partir de complexes mRNP de répression de la traduction

Plusieurs éléments suggèrent que les ARNm sont recrutés dans les PB sous forme de mRNP suite à l'action de répresseurs de la traduction. En effet, la suppression par ARN interférence de l'expression de certains facteurs de répression généraux de la traduction comme 4E-T, LSM1, DDX6 ou CCR4 empêche l'accumulation réciproque de chacun de ces facteurs dans les PB ce qui laisse envisager qu'ils y soient recrutés sous forme de complexes pré-préformés plutôt qu'individuellement (Andrei, 2005). Concernant les complexes de répression de la voie d'ARN interférence, les protéines du complexe RISC, les miARN et leurs ARNm cibles sont présents dans les PB (Pillai et al., 2005a) et la suppression de GW182 par ARN interférence délocalise AGO2 des PB tout en inhibant la répression de la traduction d'ARNm rapporteurs (Liu et al., 2005). Ceci a très tôt suggéré que les ARNm cibles de miARN sont recrutés aux PB sous forme de miRNP déjà réprimés. Enfin, l'interaction 4E-T/DDX6 induit la répression de traduction d'ARNm rapporteur et contribue en partie à la formation des PB (quelques PB peuvent se former après mutation du domaine d'interaction CHD de 4E-T avec DDX6) ce qui montre que l'association de ces deux protéines sur l'ARNm contribue à son recrutement aux PB (Kamenska et al., 2016).

Dans les cellules humaines, plusieurs protéines contribuent au maintien des PB dès lors que leur suppression par ARN interférence entraine une diminution du nombre de PB observables en immunofluorescence. Certaines de ces protéines sont indispensables au maintien des PB quand l'absence de l'une d'entre elles entraine la dissolution complète des PB (Figure 37). Ceci concerne notamment les protéines DDX6, 4E-T, LSM1, CCR4 (Andrei, 2005), LSM14A (Yang, 2006), GW182 (Yang, 2004) et CPEB1 (Serman et al., 2007). Toutefois dans la majorité des cas testés, lorsque les cellules sont soumises à un stress capable d'induire les PB, ces derniers se reforment même en l'absence de l'une des protéines requises pour leur maintien, montrant

ainsi qu'elles ne sont pas indispensables à l'assemblage *de novo* des PB. Trois protéines des PB, DDX6 4E-T et LSM14A, dérogent à ce comportement. Effectivement, en l'absence de l'une de ces trois protéines, il est impossible de reformer des PB après ajout de drogues induisant les PB tels l'arsenite, la vinblastine, soit après exposition des cellules à 30°C (Ayache et al., 2015).

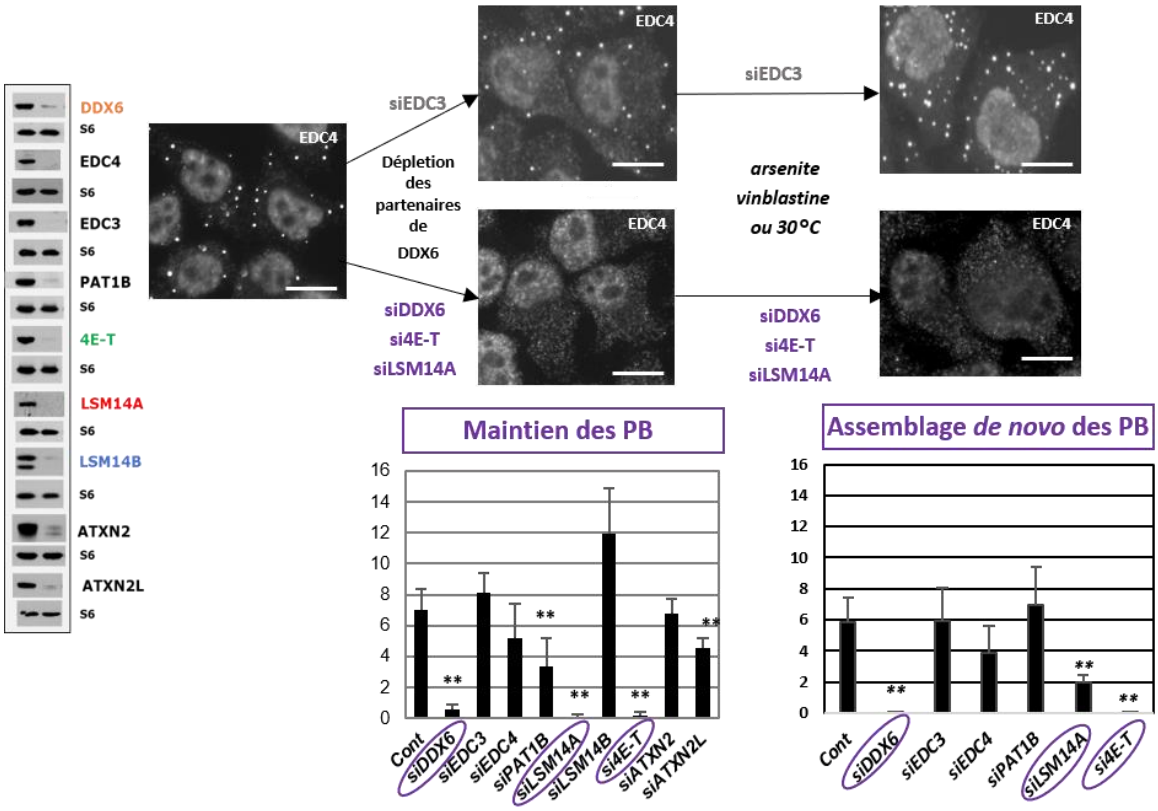

Figure 37 Identification des protéines de maintenance et d'assemblage des PB

*Les cellules HeLa sont transfectées avec les siARN précisés sur la gauche. 48h plus tard, les PB sont analysés en par immunofluorescence avec un anticorps anti-EDC4 (Barre d'échelle 10 µm). Le comptage des PB sur trois expériences indépendantes (**, p < 0.005.) montre que les protéines DDX6, LSM14A et 4E-T sont indispensables au maintien des PB tandis que PAT1B et ATXN2L ne font qu'y contribuer.*

Après traitement à l'arsenite, à la vinblastine ou après un choc thermique, les PB sont réinduits en l'absence de toutes les protéines testées sauf DDX6 LSM14A et 4E-T ce qui démontre le caractère indispensable de ces trois protéines à l'assemblage des PB. (Modifié d'après Ayache et al., 2015)

2.2.3 Formation des PB dans d'autres organismes

Si le principe d'assemblage des PB reposant sur la formation d'un réseau d'interactions entre RBP multivalentes semble conservé parmi les eucaryotes, des différences existent quant aux conditions de formation des PB. Par exemple, alors que les PB sont constitutivement présents dans les cellules mammifères, ils ne se forment chez la levure que dans des conditions restreintes de croissance telles la privation de glucose (Teixeira et al., 2005). Dans ces conditions la majorité de la traduction cellulaire s'arrête et certains ARNm non traduits se condensent avec des facteurs de dégradation et de répression de la traduction sous forme de PB (Brengues et al., 2005; Lui et al., 2014; Sheth and Parker, 2003).

Par ailleurs, la majorité des protéines des PB sont conservées parmi les eucaryotes (avec quelques exceptions préalablement mentionnées *cf* partie 2 paragraphe 1). Toutefois, leur implication relative dans le processus d'assemblage des PB diffère d'un organisme à l'autre. Chez la levure des souches *edc3Δ* ne peuvent pas former de PB suite à la privation de glucose. De plus l'expression de protéines Edc3 dont les domaines d'interaction Lsm ou Yjef-N ont été délétés entraine un défaut d'assemblage des PB marqués par Dcp2 sans affecter le niveau d'expression de Dcp2 (Decker et al., 2007). D'autres approches génétiques chez la levure ont mis en évidence un statut similaire des protéines Dcp2 et Pat1 (Pilkington and Parker, 2008; Teixeira and Parker, 2007). Le rôle prépondérant de ces facteurs de dégradation n'est pas retrouvé pour les PB de cellules humaines (Ayache et al., 2015). Réciproquement, dans les cellules humaines trois protéines : DDX6, LSM14A et 4E-T ont un statut unique dans la formation des PB (Ayache et al., 2015) ne se retrouvant pas chez la levure.

2.3. Focus sur trois protéines d'assemblage des PB : LSM14A, 4E-T et DDX6

2.3.1. Structure primaire et fonctions moléculaires

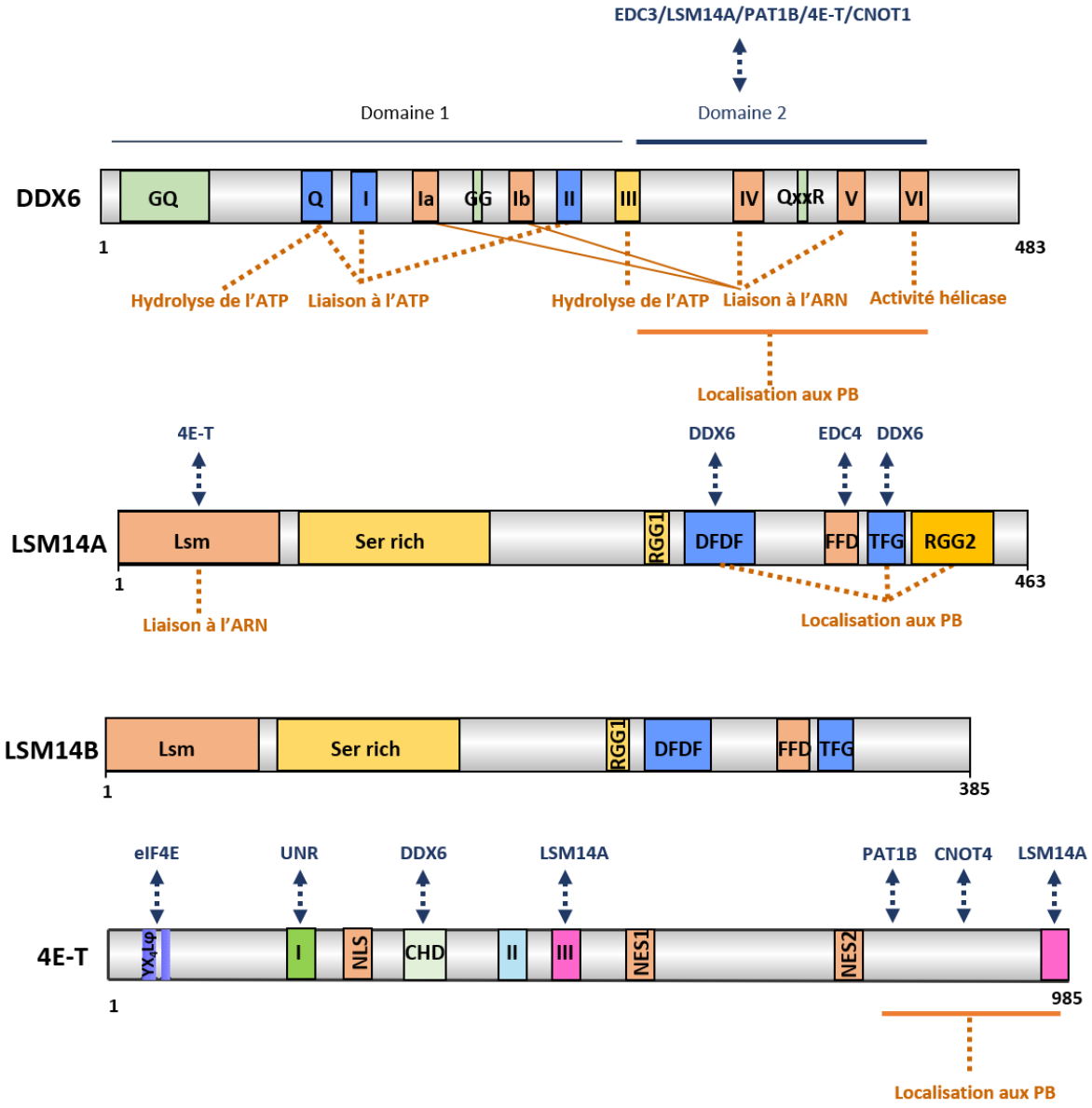

Figure 38 Structure primaire de DDX6, LSM14A, 4E-T et LSM14B

En noir le nom des domaines et motifs protéiques, en bleu les partenaires protéiques directs, en orange les fonctions moléculaires associées.

DDX6 :

La protéine DDX6 est une hélicase à ARN à boîte DEAD (Cordin et al., 2006) évolutivement conservée de la levure à l'homme (Presnyak and Coller, 2013; Weston and Sommerville, 2006) localisée dans le cytoplasme et particulièrement concentrée dans les PB (Minshall et al., 2009). Comme les autres hélicases à motif DEAD, DDX6 possède deux domaines globulaires centraux D1 et D2 contenant chacun le domaine RecA caractéristique des hélicases (Fairman-Williams et al., 2010)(Figure 38). Le domaine D1 contient les motifs Q, I(AKNGTGK), Ia (VPTRELALQ), Ib (TPGR), II (DEAD), et III (SAT). Le domaine D2 contient les motifs IV(IIF),QwwR, V (TRGID). et VI(LHRIGRSGR). Chacun de ces motifs contribue à différents aspects de l'activité biochimique de DDX6 à savoir : la liaison à l'ATP (motifs Q, I et II), l'hydrolyse de l'ATP (motifs Q et III), la liaison à l'ARN (motifs Ia, Ib, IV et V) et l'activité hélicase (motif VI) (Cordin et al., 2006; Nishimura et al., 2015; Tanner et al., 2003).

DDX6 et ses homologues se trouvent particulièrement abondants dans le cytoplasme : dans des cellules HeLa, DDX6 est 7 fois plus abondante que l'ARNm en ratio molaire (Ernoult-Lange et al., 2012), dans les ovocytes de Xénope elle y est 15 fois plus abondante que les ARNm réprimés (Smillie and Sommerville, 2002) et 8 fois plus abondante chez le trypanosome (Kramer et al., 2010)

En termes de propriétés biochimiques, DDX6 se lie avec une grande affinité (K_d= 1 nM) et sans spécificité de séquence à l'ARNm (Dutta et al., 2011; Ernoult-Lange et al., 2012). De plus, elle s'oligomérise *in vitro,* sous forme de dimère et trimère, indépendamment de la présence d'ARN (Ernoult-Lange et al., 2012a).

Dans les cellules humaines, DDX6 possède une activité de répresseur démontrée par une approche de tether (Chu and Rana, 2006). Le domaine D2 est particulièrement important dans cette activité de répression puisque la fixation artificielle de D2 dans la 3'UTR d'un ARNm rapporteur suffit à en réprimer la traduction *in vivo* (Minshall et al., 2009). Le domaine D2 contient également les sites de liaison de DDX6 à plusieurs partenaires protéiques. Plusieurs approches structurales ont co-cristallisé D2 avec différents répresseurs de la traduction et activateurs du decapping : LSM14A, EDC3, PAT1B, CNOT1 et 4E-T. Les interactions entre DDX6 et LSM14A/EDC3/ PAT1B/4E-T sont mutuellement exclusives (Brandmann et al., 2018; Ozgur et al., 2015a; Sharif et al., 2013a; Tritschler et al., 2008, 2009), ce qui expliquerait que DDX6

soit impliquée dans plusieurs complexes protéiques associés à différentes fonctions biologiques que nous détaillons par la suite.

LSM14A :

LSM14A est une RBP appartenant à la famille LSM et conservée des eucaryotes unicellulaires à l'homme (Albrecht and Lengauer, 2004). Chez les vertébrés, LSM14 a évolué en deux protéines paralogues, LSM14A et LSM14B (Marnef et al., 2009). Chez le Xénope, les deux paralogues présentent une expression temporelle différente dans les ovocytes: LSM14B y est exprimée de manière croissante jusqu'au stade II de l'ovogenèse (Minshall et al., 2007) et co-sédimente avec DDX6 sur des ARNm spécifiques, activement traduits à ce moment du développement (Ladomery and Sommerville, 2015). L'expression de LSM14A s'accroît quant à elle progressivement en parallèle de la décroissance d'expression de LSM14B à partir du stade II de l'ovogenèse (Minshall et al., 2007; Tanaka et al., 2006). Chez *A. thaliana,* DCP5 (homologue de LSM14A) est également impliquée dans le développement précoce en régulant la traduction et la stabilité d'ARNm spécifiques impliqués dans la germination (Xu and Chua, 2009). Dans les cellules humaines, LSM14A et LSM14B co-localisent dans les PB de cellules somatiques (Yang, 2006) et ont un statut différent vis-à-vis du maintien des PB : alors que l'absence de LSM14A entraine la disparition des PB, l'absence de LSM14B accroît quant à elle leur formation. Cette dernière observation est à mettre en relation avec l'existence d'une co-régulation entre ces deux protéines : la diminution d'expression de LSM14A stimule l'expression de LSM14B et inversement (Ayache et al., 2015) (Figure 39).

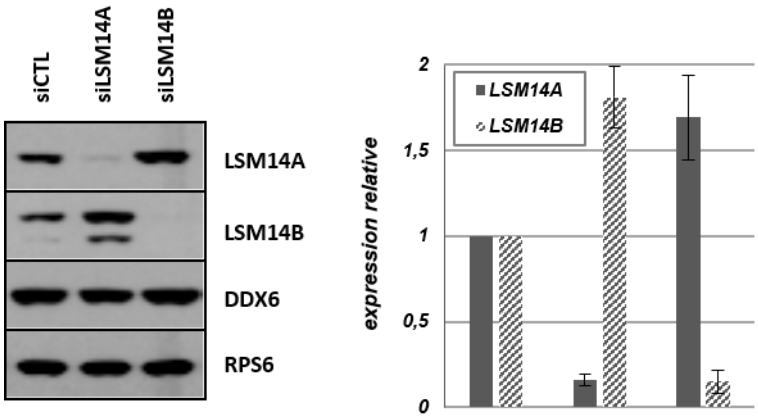

Figure 39 Co-régulation de l'expression de LSM14A et de LSM14B

Après transfection des siLSM14A ou si LSM14B, les protéines sont analysées par WB avec les anticorps indiqués et les signaux quantifiés dans 3 expériences indépendantes. (*Modifié d'après Ayache et al., 2015)*

En termes de structure primaire (Figure 38), la protéine LSM14A se compose du domaine caractéristique LSm pouvant se lier à l'ARN et à 4E-T (Brandmann et al., 2018; Nishimura et al., 2015) , d'une région riche en sérine/thréonine pouvant être modifié post-traductionnellement par phosphorylation, d'un motif FDF (phénylalanine-aspartate-phénylalanine) et de motifs FDF-TFG impliqués dans des interactions protéine-protéine avec DDX6 (Brandmann et al., 2018). Le motif FFD de LSM14A est capable de lier directement EDC4 (Brandmann et al., 2018). Enfin, les deux motifs RGG arginine-glycine-glycine peuvent être méthylés par PRMT1 ce qui contribue à localiser LSM14A dans les PB (Matsumoto et al., 2012). LSM14B diffère structurellement de LSM14A au niveau de sa partie C terminale, plus courte, et ne contenant qu'un seul motif RGG.

L'activité de répression de la traduction de LSM14A a été démontrée *in vivo* par des expériences de tether de la partie N-terminale de LSM14A chez le Xénope (Tanaka et al., 2006a) et du domaine Lsm chez l'homme (Brandmann et al., 2018).

4E-T

4E-T (eIF4E Transporter protein) aussi appelé EIF4ENIF1 (eIF4E Nuclear Import Factor1) est une protéine évolutivement conservée parmi les métazoaires. Elle a initialement été

caractérisée comme une 4E-BP requise pour la localisation d'eIF4E dans le noyau (Dostie et al., 2000b). Si la protéine 4E-T peut être localisée dans le noyau, elle se trouve majoritairement présente dans le cytoplasme et dans les PB (Andrei, 2005; Ferraiuolo et al., 2005).

Comme les autres 4E-BP, la partie N-terminale de 4E-T contient deux motifs de liaison à eIF4E: le motif consensus $YX_4L\varphi$ entrant en compétition avec eIF4G (Sonenberg and Hinnebusch, 2009), et le motif adjacent commun aux 4E-BP mais absent chez eIF4G (Peter et al., 2015). Les séquences NLS (Nuclear localisation Sequence) et NES (Nuclear Export Sequence) sont responsables de l'activité de transporteur nucléaire de 4E-T (Dostie et al., 2000b), (Figure 38).

La comparaison des séquences de 4E-T entre les vertébrés et la Drosophile a identifié quatre motifs conservés : les motifs I (131-161), II (291-316), III (331-346) et CHD. Le motif I lie spécifiquement la protéine UNR, les motifs II et III n'ont pas de rôle connu à ce jour et le domaine CHD se lie à DDX6 (Kamenska et al., 2016). D'après la structure du complexe LSM14A-4E-T, la partie C terminale de 4E-T contient un motif s'associant au domaine Lsm de LSM14A (Brandmann et al., 2018). De plus, une région centrale de 4E-T (résidus 335–490) interagit *in vitro* directement avec le domaine Lsm de LSM14A (Nishimura et al., 2015) ce qui est confirmé *in vivo* par co-immunoprécipitation (Kamenska et al., 2016).

Concernant les fonctions moléculaires de 4E-T, cette protéine possède une activité de répresseur général de la traduction. En effet, sa surexpression diminue la traduction générale, et ce de manière eIF4E-dépendante (Ferraiuolo et al., 2005; Kamenska et al., 2014b). De plus, 4E-T réprime la traduction d'ARNm spécifiques indépendamment de sa liaison à eIF4E. En effet 4E-T réprime la traduction d'un ARNm rapporteur en tether assay même lorsque les motifs d'interaction de 4E-T avec eIF4E sont mutés. Enfin, 4E-T contribue à la répression de la traduction dans le cadre des régulations par les miARN conjointement avec DDX6 (Kamenska et al., 2014b).

2.3.2. Principaux complexes mRNP cytoplasmiques incluant DDX6, LSM14A, 4E-T

DDX6, LSM14A et 4E-T sont des RBP multivalentes pouvant interagir directement l'une avec l'autre et possédant toutes les trois une activité de répression de la traduction. Ces trois protéines et leurs homologues font partie de complexes mRNP pouvant réprimer la traduction

et/ou enlever la coiffe 5'del'ARN selon les partenaires auxquels elles s'associent. Notamment, les trois protéines font partie du complexe de répression de la traduction CPEB initialement caractérisé dans les ovocytes de Xénope. Dans ces cellules se trouvant au stade I/II de l'ovogenèse, la protéine DDX6 co-purifie après filtration sur gel dans les mêmes fractions que CPEB1, 4E-T, PAT1A, LSM14B, eIF4E1b et est également co-immunoprécipitée avec ces protéines (Minshall et al., 2007b, 2009). Dans les cellules humaines, la purification par TAP-tag des complexes mRNP contenant DDX6 a permis d'identifier LSM14A, 4E-T, PAT1B, LSM14B parmi les principaux partenaires protéiques de DDX6 mais pas la protéine CPEB1 sans doute trop faiblement exprimée, de sorte que le complexe de répression qu'ils forment a été appelé « CPEB-like » (Ayache et al., 2015).
DDX6 fait également partie avec 4E-T et CCR4-NOT d'un complexe de répression de la traduction des ARNm ciblés par les miARN. Dans ce complexe, DDX6 interagit avec la sous-unité CNOT1 ce qui stimule l'activité ATPase de DDX6 (Mathys et al., 2014). De plus, des mutations empêchant DDX6 de se lier à NOT1 (Chen et al., 2014b; Mathys et al., 2014; Rouya et al., 2014) ou à 4E-T (Kamenska et al., 2016) inhibent la répression de la traduction d'un ARNm rapporteur cible d'un miARN.

L'association de DDX6 et de LSM14A au sein des complexes de decapping a principalement été étudiée sur leurs homologues chez la levure. Dans cet organisme, Scd6 (homologue de LSM14A) est un activateur direct de l'enzyme de decapping Dcp2. Elle se lie directement au domaine HLM de Dcp2 de même qu'Edc3 avec qui elle entre en compétition. *In vitro* Edc3 et Scd6 stimulent l'activité de Dcp1/Dcp2 mais l'affinité de Scd6 pour Dcp2 étant plus faible qu'Edc3, l'activation du decapping résultant de l'interaction Scd6/Dcp2 est également moins importante (Fromm et al., 2012b).

L'homologue de DDX6, Dhh1, co-immunoprécipite avec plusieurs facteurs de decapping dont Dcp1, Lsm1 et Pat1 (Coller et al., 2001) et co-cristallise avec Edc3 et Pat1 (Sharif et al., 2013). Les interactions directes de Dhh1 avec Pat1 et Edc3 sont mutuellement exclusives et interfèrent avec la capacité de liaison à l'ARN de Dhh1 (Sharif et al., 2013a), ce qui a également été observé chez la Drosophile (Tritschler et al., 2009). De plus, chez des doubles mutants *dhh1Δ/pat1Δ*, la demi-vie d'un ARNm rapporteur est significativement plus longue que chez des mutants de délétion *dhh1Δ* ou *pat1Δ* (Coller and Parker, 2005). Dans les cellules humaines,

DDX6 est également co-immunoprécipitée avec DCP2, DCP1, EDC3, EDC4, PAT1B et LSM14A (Ayache et al., 2015; Fenger-Grøn et al., 2005). L'analyse structurale du complexe LSM14A-DDX6 montre que LSM14A se lie à DDX6 par les motifs FDF et TFG, séparés par un motif FFD lui-même requis pour l'interaction de LSM14A avec EDC4 (Brandmann et al., 2018). Certaines des interactions de LSM14A ne sont pas conservées de la levure à l'homme. Par exemple, EDC4 n'existe pas chez la levure et Scd6 peut directement y recruter le complexe de decapping par interaction directe avec Dcp1. De plus, plusieurs études *in vitro* ont montré que Scd6 peut réprimer la traduction d'un ARNm rapporteur en se liant directement sous sa forme méthylée par PRMT1 à eIF4G (Nissan et al., 2010; Poornima et al., 2016). L'existence d'un mécanisme similaire dans d'autres organismes reste à ce jour inconnu.

2.3.3 Apport des expériences de complémentation sur les fonctions biologiques de LSM14A, 4E-T et DDX6

Des expériences de complémentation montrent que suite à la délétion conjointe des domaines CHD (domaine d'interaction de 4E-T avec DDX6) et du motif I (motif d'interaction de 4E-T avec UNR), 4E-T perd sa capacité à réprimer la traduction d'un ARNm rapporteur ainsi que la traduction d'un ARNm rapporteur ciblé par un miARN. De plus, dans des cellules humaines déplétées de la protéine DDX6 endogène, l'expression d'une protéine DDX6 exogène entière restore l'activité de répression de 4E-T ce qui n'est pas le cas suite à l'expression de mutants ATPase de DDX6 ou du mutant d'interaction de DDX6 avec CNOT1(Kamenska et al., 2016). Ceci suggère que la fonction ATPase de DDX6, elle-même stimulée par la liaison de DDX6 à CNOT1 (Ozgur et al., 2015b), contribue à la répression de la traduction par 4E-T. En termes de localisation aux PB, la délétion du seul domaine CHD diminue de 60% le nombre de PB/cellule en comparaison à la version de 4E-T non mutée, indiquant que l'interaction 4E-T/DDX6 est requise pour la formation des PB (Kamenska et al., 2016). Concernant LSM14A, des expériences similaires où le motif TFG ou FFD est délété (motifs d'interaction de LSM14A avec DDX6) montrent que l'interaction DDX6/LSM14 contribue à la formation des PB (Brandmann et al., 2018). Concernant DDX6, une substitution d'acide aminé sur le motif de liaison de DDX6 à LSM14A et à 4E-T diminue la formation des PB

(Ozgur et al., 2015a; Sharif et al., 2013a; Tritschler et al., 2008), étayant ce faisant le rôle central des interactions DDX6-4E-T et DDX6-LSM14A dans la formation des PB.

3. Fonction moléculaire et importance biologique des PB

3.1 Stockage d'ARNm réprimés plutôt que dégradation d'ARNm

3.1.1 Arguments expérimentaux « pro-dégradation »

Le rôle des PB dans le métabolisme de l'ARNm est longtemps resté controversé entre deux fonctions : la dégradation des ARNm et le stockage de transcrits non traduits. Initialement, les PB ont été assimilés à des sites de dégradation de l'ARNm. En effet, ils contiennent presque tous les facteurs de la voie de dégradation 5'->3' incluant des déadénylases, des facteurs de decapping, l'enzyme XRN1 (van Dijk et al., 2002; Sheth and Parker, 2003), ainsi que plusieurs facteurs de la voie du NMD. De plus, des ARN poly(A) s'accumulent dans les PB après suppression par ARN interférence de XRN1 (Cougot et al., 2004) et la taille ainsi que le nombre de PB augmentent dans des souches de levures *xrn1*Δ ou *dcp1*Δ (Sheth and Parker, 2003). Enfin, une accumulation d'ARNm contenant un codon de terminaison prématuré, donc cibles du NMD, a été observée à la périphérie des PB (Durand et al., 2007). L'ensemble de ces résultats a suggéré que les PB seraient des sites actifs de dégradation de l'ARNm et/ou *a minima* des sites d'accumulation de transcrits en attente de dégradation (Decker and Parker, 2012).

3.1.2 Arguments expérimentaux « pro-stockage »

Néanmoins, plusieurs observations ont invalidé le modèle associant les PB à des sites de dégradation de l'ARNm. D'une part suite à la purification des PB, la distribution des reads du RNAseq est identique entre les fractions pré-triée et triée, ce qui suggère que les PB n'accumulent pas de produits de dégradation. De plus, le croisement de ces données avec le transcriptome siDDX6 réalisé en parallèle sur des cellules HEK293 montre que l'absence de

cette protéine (et donc la dissolution des PB) n'influence pas le niveau d'expression des ARNm enrichis dans les PB. (Hubstenberger et al., 2017). Ces résultats ont été confirmés par une approche de smFISH ayant pour objectif de visualiser l'accumulation d'intermédiaires de dégradation dans les PB au moyen d'un ARN rapporteur bi-fluorescent TREAT (*3*'-RNA End Accumulation during Turnover). Cette étude montre que la dégradation du transcrit rapporteur se produit à l'extérieur des PB (Horvathova et al., 2017). Les conclusions sont similaires en utilisant le système rapporteur MS2-MCP chez *S. cerevisiae* dans des conditions de stress où se forment les PB (Tutucci et al., 2018). L'absence de dégradation des ARNm des PB en dépit de la présence d'enzyme de dégradation dans ces granules pourrait s'expliquer soit par le fait que les enzymes de dégradation s'accumulent dans les PB sous une forme inactive (Schütz et al., 2017) et/ou par le fait que les ARNm des PB puissent être protégés des enzymes de dégradation par exemple grâce à leur association à 4E-T/eIF4E empêchant le recrutement des enzymes de decapping (Räsch et al., 2020). Le consensus actuel est que les PB servent à stocker transitoirement des ARNm réprimés en traduction. En effet, plusieurs répresseurs de la traduction se concentrent dans des PB dont les trois RBP indispensables à leur assemblage DDX6, 4E-T et LSM14A. (Ayache et al., 2015; Hubstenberger et al., 2017). De plus, nos données de polysome profiling montrent que les ARNm enrichis dans les PB sont plus activement traduits en l'absence de DDX6 (donc en l'absence de PB) et suggèrent que ce sont des transcrits préférentiellement régulés en traduction qui s'accumulent dans les PB (Hubstenberger et al., 2017). Également, l'étude des facteurs des voies d'ARN interférence a montré que les composants du complexe RISC s'accumulent conjointement avec des ARNm cibles dont la traduction est inhibée par un miARN dans les PB et que les transcrits réprimés peuvent retourner dans le cytosol pour être traduits lorsque le miARN est inactivé (Bhattacharyya et al., 2006). Ceci est cohérent avec les résultats de l'approche de smFISH précédemment mentionnée, ayant démontré que l'association stable des miRNP aux PB nécessite que le miARN injecté soit fonctionnel pour réprimer la traduction de ses ARNm cibles (Pitchiaya et al., 2019a).

3.2 Homéostasie et adaptation cellulaire

3.2.1 Adaptation rapide et coordonnée du transcriptome

La capacité des PB à stocker conjointement et réversiblement un grand nombre d'ARNm réprimés en traduction représente une opportunité de contrôle supplémentaire de l'expression génique : celle d'intégrer différentes régulations post-transcriptionnelles et donc de pouvoir répondre rapidement aux changements d'environnement cellulaires. Chez la levure, il a été observé que les PB se formant en conditions de stress séquestrent des ARNm rapporteurs très exprimés hors conditions de stress. Dans des souches *edc3Δpatl1Δ* incapables de former des PB, ces ARNm ne peuvent plus être stockés dans les PB et leur expression est alors associée à une léthalité accrue par rapport à des levures WT *(Lavut and Raveh, 2012).* Ceci suggère que le stockage des transcrits dans les PB contribue effectivement à l'adaptation aux conditions environnementales.

Adresser cette question par une approche similaire sur les PB de cellules épithéliales humaines s'avère plus délicat car les PB n'y sont pas indispensables à la viabilité cellulaire en conditions standard de culture. Toutefois, deux observations issues de la purification des PB supportent l'idée que les PB y jouent un rôle de coordinateur de l'expression d'ARNm codant des protéines fonctionnellement voire physiquement associées (Standart and Weil, 2018). Premièrement, les ARNm codant des protéines régulatrices intervenant dans une même fonction cellulaire (cet ensemble d'ARNm est aussi appelé régulon), sont enrichis dans les PB alors que les transcrits codant des protéines effectrices tendent à en être exclus. Par exemple, les ARNm codant les protéines du ribosome, effecteur de la traduction, sont exclus des P-bodies, alors que les ARNm codant des régulateurs de la traduction incluant les protéines des PB eux-mêmes, s'y accumulent. De plus, les ARNm codant des protéines s'assemblant dans les mêmes complexes tendent à avoir le même comportement par rapport aux PB en termes d'enrichissement/ exclusion. Par exemple, les ARNm codant les sous-unités du centrosome et des complexes condensine/cohésine impliqués dans le cycle cellulaire sont stockés dans les P-bodies alors que les ARNm codant les sous-unités du protéasome et des nucléosomes en sont exclus suggérant que les P-bodies soient impliqués dans l'adaptation de la production des protéines individuelles à leur stœchiométrie au sein de complexes protéiques. (Hubstenberger et al., 2017), (Figure 40).

A la lumière du modèle de formation des PB par LLPS, il est envisageable que l'implication des PB à l'adaptation aux conditions environnementales soit basée sur leur capacité à établir un

équilibre dynamique avec le cytoplasme qui permettrait de tamponner les variations de concentration cytoplasmique des composants (ARNm et protéines) se concentrant dans les PB. Les résultats issus de la reconstitution de granules artificiels dans des cellule humaines appuient cette hypothèse. A partir de la phase de nucléation du granule artificiel, il est observé que la concentration cytosolique de la protéine FFm (ici l'élément structural unitaire des granules artificiels) cesse d'augmenter et se maintient à une valeur stationnaire tandis que la concentration de la même protéine dans la phase condensée continue de croître (Garcia-Jove Navarro et al., 2019). Ceci corrobore l'idée qu'*in vivo,* la condensation en granules puisse effectivement maintenir une protéine à une concentration cytoplasmique limite constante.

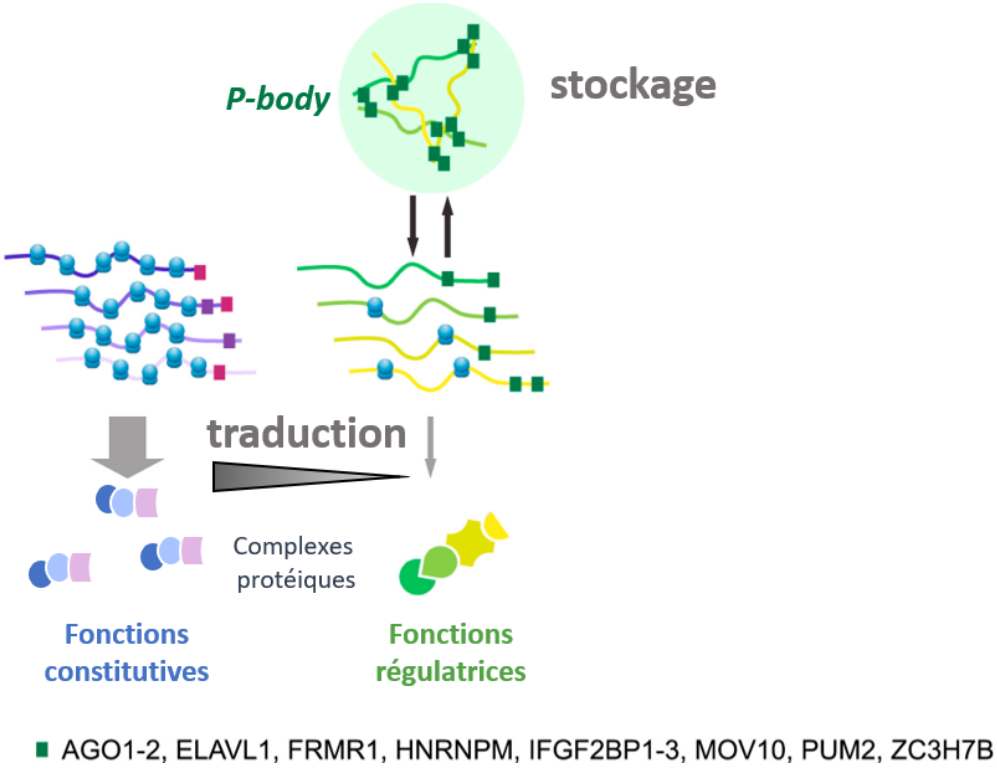

Figure 40 Coordination des régulations post-transcriptionnelles par les PB

Les PB stockent des ARNm peu traduits et codant essentiellement des protéines régulatrices et ayant tendance à s'assembler dans les mêmes complexes protéiques. Parallèlement, les ARNm exclus des PB sont fortement traduits et codent des protéines à fonctions constitutives. Des RBP particulières (carrés verts) localisent les ARNm aux PB par reconnaissance d'un élément cis dans l'UTR des transcrits des PB. (Modifié d'après Hubstenberger et al., 2017).

3.2.2 Rôle des PB au cours du développement

Plusieurs observations suggèrent que les régulations post-transcriptionnelles médiées par les PB interviennent dans différents processus du développement en particulier le neurodéveloppement

Le dernier élément à l'appui de cette idée est apporté par des données de séquençage d'exons à haut-débit ayant identifié cinq mutations *de novo,* faux-sens hétérozygotes sur le gène *DDX6* de patients présentant des signes de déficience intellectuelle ainsi qu'un retard de développement. Les cinq mutations (His372Arg, Arg373Gln, Cys390Arg, Thr391Ile et Thr391Pro) sont localisées dans l'exon 11 de *DDX6*. Cet exon code deux motifs (motif QxxR et le motif V) du domaine RecA2 impliqué dans l'activité ATPase de DDX6, dans sa liaison à l'ARN ainsi qu'à ses partenaires protéiques (*cf.* partie 2 paragraphe 2.3.1). Les fibroblastes issus des patients exprimant les variants Arg373Gln et Cys390Arg de DDX6 à des niveaux similaires à ceux de la protéine non mutée présentent un important défaut d'assemblage des PB. En effet, alors que 70 à 80% des fibroblastes des parents des patients contiennent des PB, seulement 30% des cellules de patients contiennent des PB se trouvant moins nombreux que dans les fibroblastes des parents. De plus, les versions DDX6 mutées exprimées dans des cellules HeLa sont incapables de former *de novo* des PB et ne peuvent pas non plus interagir avec les partenaires principaux habituels 4E-T, LSM14A, PAT1B ni dans une moindre mesure avec EDC3. Enfin, le croisement du transcriptome des fibroblastes du patient portant la mutation Cys390Arg avec les données de CLIP DDX6 et le transcriptome d'une lignée K562 transfectée de manière stable par un shDDX6 dont l'expression a été induite pendant 48h, montre que les ARNm abondants dans les fibroblastes de patients (dont beaucoup codent des facteurs de traduction), le sont aussi dans les jeux de données de CLIP et dans le transcriptome shDDX6 ce qui suggère que ces transcrits sont régulés en stabilité par un mécanisme DDX6-dépendant et impliquant une liaison directe à DDX6 (Balak et al., 2019).

Une autre protéine des PB, 4E-T, est également impliquée dans le contrôle de la neurogenèse (Figure 41). Dans les précurseurs radiaux de cortex de souris, 4E-T s'associe à eIF4E au sein de granules similaires aux PB avec LSM1 et DDX6. Dans ces granules, 4E-T empêche la différenciation en neurones en réprimant la traduction de différents facteurs de transcription

ainsi que de facteurs de différenciation bHLH (basic Helix Loop Helix) tels les Neurogénines 1 et 2 ou NeuroD qui lui sont retrouvés associés par une approche de RIP (RNA Immunoprécipitation) (Yang et al., 2014).

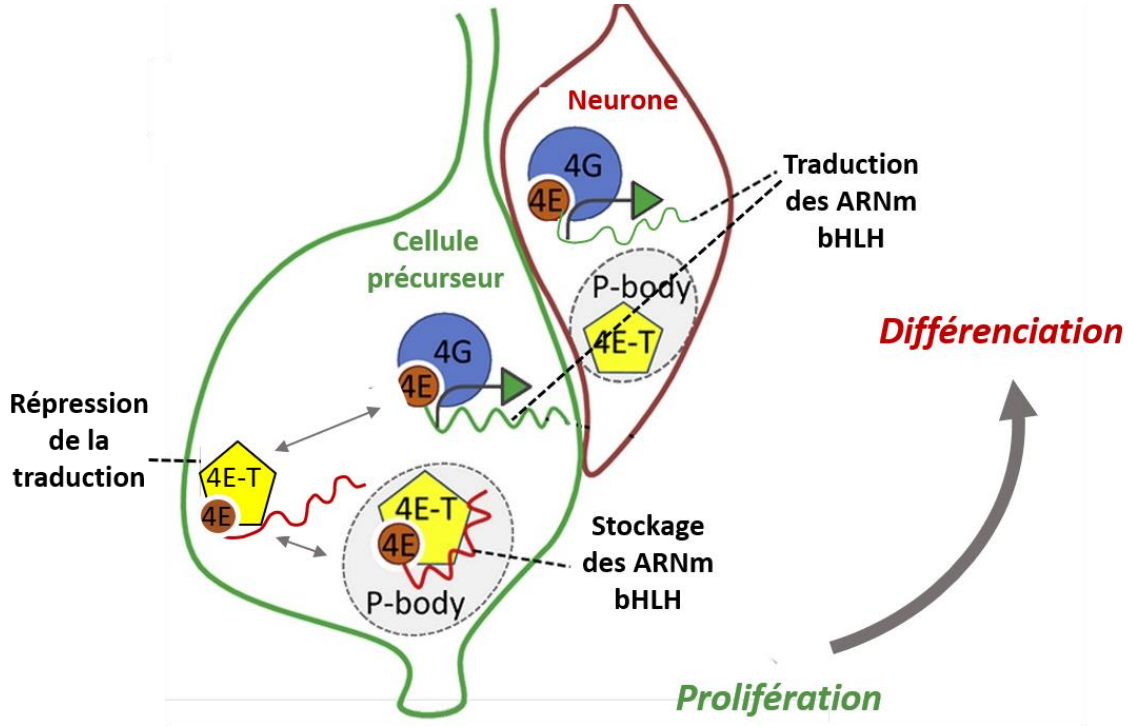

Figure 41 Modèle de contrôle de la neurogenèse par les PB

Les ARNm codant les facteurs de différenciation bHLH ainsi que des facteurs de transcription ont leur traduction réprimée par 4E-T et sont stockés dans les PB. Dans ces conditions, les cellules précurseurs continuent de se diviser. Lorsque ces ARNm sont déstockés des PB et traduits dans le cytoplasme, la différenciation des cellules précurseurs en neurones a lieu. (Modifié d'après Yang et al., 2014).

RESULTATS

Part1 Analysis of PB assembly factors in human cells provides new insight into LSM14A-associated functions

Introduction

Post-transcriptional regulation in the cytoplasm of eukaryotic cells relies on the balance between mRNA translation, storage and decay. Several pathways regulate mRNA translation and contribute to the adaptation of protein production to cellular needs. In metazoan, 4E-BPs (eIF4E Binding Proteins) mediate general inhibition of translation by regulating the eIF4F complex activity during initiation step (Kamenska et al., 2014a; Peter et al., 2015). In addition, miRNAs (micro-RNAs) and other *trans* regulators achieve selective translational inhibition by recognizing *cis* elements such as MRE (miRNA Response Element), ARE (AU-Rich Elements), CPE (Cytoplasmic Polyadenylation Elements) or TOP (Terminal OligoPyrimidine) motifs, embedded in the UTRs of their mRNA targets (Duchaine and Fabian, 2019; Harvey et al., 2018b; Hinnebusch et al., 2016; Iwakawa and Tomari, 2015).

Remarkably, a large number of transcripts translationally repressed by these pathways are able to concentrate into cytoplasmic mRNP granules called P-bodies (PBs) (Hubstenberger et al., 2017). These membrane-less organelles are thought to form by phase separation (Yoshizawa et al., 2020) and to coordinate storage of transcripts encoding regulatory proteins (Hubstenberger et al., 2017; Standart and Weil, 2018). Not to be associated to the translation machinery is required for mRNAs to accumulate into PBs. Indeed, in human cells where polysomes are artificially blocked on mRNAs by cycloheximide, PBs disappear whereas polysomes disruption by puromycin treatment, increases number of PBs (Andrei, 2005; Wilczynska et al., 2005). Also, visualization of different mRNA reporters highlighted that while some of them transiently associate to PBs other stably associate into PBs where they are thought to be stored in a repressed state (Moon et al., 2019).

Interestingly, while repression of translation occurs independently of mRNA accumulation in PBs, molecular actors of PB formation so far characterized in human cells are multitasking repressors of translation, namely the RNA helicase DDX6, the repressor of translation 4E-T (eIF4E-transporter protein), and LSM14A (Ayache et al., 2015).

DDX6 is a general repressor of translation since its silencing stimulates cellular translation (Chu and Rana, 2006) and it translationally represses reporter mRNAs when artificially tethered to their 3'UTR (Minshall et al., 2009). Moreover, DDX6 is a key effector of miRNA silencing in human cells since its depletion releases translational repression conferred by the let-7a miRNA (Chu and Rana, 2006; Eulalio et al., 2007a; Rouya et al., 2014). Structural experiments showed that human DDX6 binds to CNOT1 mIF4G domain (Chen et al., 2014; Mathys et al., 2014) CNOT1. This interaction activates DDX6 ATPase activity (Mathys et al., 2014) and enhances miRNA-mediated silencing (Chen et al., 2014; Rouya et al., 2014). Moreover, crystal structure of CNOT1/DDX6/4E-T complex (Ozgur et al., 2015b) shows that when directly bound to CNOT1, DDX6 can interact with 4E-T but not with its other partners EDC3, LSM14A and PAT1B, all of which directly interact with the RecA2 domain of DDX6 in a mutually exclusive manner (Jonas and Izaurralde, 2013; Ozgur et al., 2015; Sharif et al., 2013; Tritschler et al., 2009).

DDX6 partner, 4E-T, predominantly localizes to PBs in human cells (Andrei, 2005; Ferraiuolo et al., 2005) but can shuttle between nucleus and cytoplasm to localize eIF4E to the nucleus (Dostie et al., 2000). 4E-T acts as a general repressor of translation, partly by sequestering eIF4E from eIF4G (Gingras et al., 1999) but also in an eIF4E-independent way, as shown by tether assays experiments (Kamenska et al., 2014). Actually, 4E-T also binds to 4EHP (eIF4E2) which represses mRNA translation including through the miRNA pathway : knocking down 4EHP in mammalian cells partially inhibits miRNA-mediated silencing (Chapat et al., 2017; Chen and Gao, 2017) and 4E-T knock-down impairs miRNA-mediated silencing of reporter mRNAs (Chapat et al., 2017; Kamenska et al., 2016). Finally, a 4E-T mutant unable to interact with eIF4E is defective in promoting decay of miRNA targeted mRNAs (Nishimura et al., 2015), which suggests that 4E-T is able to promote both early translation repression and repression and decay of miRNA targets.

The third PB assembly factor, LSM14A, is a RBP able to interact directly both with 4E-T and DDX6 in human cells (Brandmann et al., 2018; Nishimura et al., 2015). Its activity in repression of translation has been characterized using the tether assay in human cells (Brandmann et al., 2018), Arabidopsis (Xu and Chua, 2009) and Xenopus oocytes (Fromm et al., 2012; Rajyaguru et al., 2012; Yang, 2006). Of note, ribosome profiling and RNAseq analyses performed in *dcp2Δ, scd6Δ, dhh1Δ, dcp2Δscd6Δ and dcp2Δdhh1Δ* yeast strains in nutrient replete medium conditions showed that Scd6 (LSM14A) and Dhh1 (DDX6) cooperate in repressing translation

and destabilizing a subset of native mRNAs functionally related to carbohydrate metabolism (Zeidan et al., 2018). Scd6 also inhibits assembly of the 48S PIC (Pre Initiation Complex) *in vitro* by binding to eIF4G *via* its methylated RGG motif (Nissan et al., 2010; Poornima et al., 2016; Rajyaguru et al., 2012a). Whether this interaction is conserved in higher eukaryotes is hitherto not known. Interestingly, methylation of the RGG domain of human LSM14A is necessary for the localization of this protein in PBs (Matsumoto et al., 2012).

In Xenopus oocytes, DDX6 coimmunoprecipitates and copurifies in gel-filtration fractions with CPEB1, 4E-T, PAT1B, LSM14B, and eIF4E (Minshall et al., 2007b, 2009), hence forming a CPEB complex required for translation repression of maternal mRNAs. Characterization of DDX6 interactome by TAP tag followed by mass spectrometry analysis in human cells found DDX6 associated with all members of the CPEB complex except CPEB1 -possibly due to its weak expression. Three members of this "CPEB-like complex" : DDX6, LSM14A (paralog of LSM14B which is himself dispensable to PB assembly), and 4E-T are necessary to maintain PBs and also to assemble them *de novo* following specific PB -inducing stresses such as arsenite, vinblastine or mild cold shock (Ayache et al., 2015; Minshall et al., 2009; Serman et al., 2007) . These results are in line with complementation assays demonstrating that 4E-T/DDX6 and LSM14A/DDX6 respective interactions contribute to *de novo* PB assembly since almost no PB can form in cells expressing DDX6 protein mutated for 4E-T interaction (Kamenska et al., 2016) or for LSM14A interaction (Brandmann et al., 2018) in human cells when their endogenous counterpart is silenced.

One hypothesis concerning PB formation includes that they assemble first through translationally repressed mRNPs, which then aggregate into larger structures. In order to address from which mRNP complexes PBs could assemble, we investigated the mRNP complexes containing LSM14A, LSM14B and 4E-T in human epithelial cell lines and that could organize along with DDX6 to assemble PBs. Using a tandem affinity purification TAP-tag strategy coupled to mass spectrometry analysis, we mapped LSM14A, LSM14B and 4E-T respective interactomes in human cells. Top partners included members of the CPEB-like complex and common partners uncovered new candidates for PB assembly. Mass spectrometry results also unexpectedly identified several initiation factors and small ribosomal proteins co purifying with LSM14A which led us to characterize LSM14A association to the translation initiation complex.

Results

1) Purification of LSM14A, LSM14B and 4E-T cytoplasmic complexes identifies a large set of partners related to RNA metabolism

To determine the main mRNP complexes containing either LSM14A, LSM14B or 4E-T, we purified these complexes from epithelial HEK293 using a TAP-tag approach as we previously did for DDX6 (Ayache et al., 2015) (Supplemental Figure 1A). To do so, plasmids encoding either LSM14A, LSM14B or 4E-T fused to FLAG and HA sequences were transiently transfected in HEK293 cells. 48H after transfection, we confirmed by immunofluorescence analysis that the tagged proteins could localize to PBs labelled by anti-EDC4 antibodies (Figure 1A). We also controlled by western blotting analysis that the tagged proteins were expressed at levels similar to their endogenous counterparts (Figure 1B) which overall confirmed that LSM14A, LSM14B and 4E-T transgenes were fully functional in terms of localization to PBs and did not alter cellular mRNP composition.

mRNP complexes containing these proteins were then purified from cytoplasmic lysates treated either with RNAse inhibitor or RNAse to discriminate between RNA-dependent and RNA-independent interactions, first on FLAG and then on HA affinity resins. The same protocol was concomitantly applied to cells transfected with an empty vector as a control. One tenth of the elution was separated on denaturing SDS–PAGE gel and silver-stained to assess the quality of the purification (Figure 1C). Purification quality was deemed satisfactory since tagged proteins were visualized at their expected size and the silver staining pattern was more complex than in the negative control sample (Figure 1C). Complexes purified from both RNAse inhibitor and RNAse-treated lysates and from control lysates treated with RNAse were briefly separated by SDS PAGE (Supplemental Figure 1B). Gel was cut into 5 lanes (each one corresponding to one sample) and each lane was cut into 6 slices that were individually trypsinized. Peptides obtained from each digestion were subsequently analysed by mass spectrometry

Several criteria were applied to ensure high confidence in the identified proteins: a 0.1% FDR (False Discovery Rate) cut-off was used for peptides, and a 0.2% FDR cut-off for proteins. Then we considered proteins identified by at least 2 peptides (see also material and methods). We furthermore removed any protein whose score in the control was higher than or equal to score in samples. Finally, contaminants such as keratins, immunoglobins and several proteins of cytoskeleton were also excluded from the list (Supplemental Table 1).

Once these stringent criteria implemented, mass spectrometric analysis identified between 168 and 238 proteins, specifically interacting with LSM14A, LSM14B or 4E-T and scoring above 20 (arbitrary minimal score set to facilitate dataset analysis) (Figure 2A and Supplemental Table 1). Between 66 and 104 interactions were found both in RNAse and RNAse inhibitor-treated samples. When degrading RNA, between 40 and 63 proteins were no longer detected. Finally, between 52 and 80 proteins were identified exclusively in RNAse treated samples, which at first sight might seem counterintuitive but might be explained by these proteins taking part to complexes where tags are inaccessible in presence of RNA.

Approximately three quarters of the identified interactions occurred in RNAse-treated conditions, indicating RNA-independent interactions (Figure 2A). Functional annotation based on the literature found at least one third of LSM14A, LSM14B and 4E-T partners involved in RNA metabolism, which is consistent with known molecular functions of these proteins (Figure 2B upper panel). Further subclassification revealed that this category mainly included repressors and activators of translation as well as decay factors (Figure 2B, lower panel). Based on the values of spectral counting with normalized total spectra from Scaffold software, LSM14A top scoring partners included DDX6 and other components of the CPEB-like complex, namely LSM14B and 4E-T (Figure 2C, upper panel). Other specific interactions previously documented included the 2 arginine methyltransferases PRMT5 and PRMT1 which is required for LSM14A to localize to PBs (Matsumoto et al., 2012) as well as the repressive regulator of translation FMR1 (Fragile X mental retardation protein) and its partners FXR1 and FXR2 (He and Ge, 2017). A very similar pattern of interactions applied to LSM14B, in line with strong homology and similar localization in PBs of both proteins (Figure 2C, middle panel). Interestingly, all components of 2 chaperonin complexes: the MCM complex (MiniChromosome Maintenance) and the CCT (Chaperonin-containing tailless complex polypeptide 1) were identified amongst LSM14B partners with higher scores than in LSM14A

dataset (supplemental table 1). These complexes are both involved in assembly and disassembly of stress granules in human cells (Jain et al., 2016) and the CCT complex contributes to formation of grPBs in *C.elegans* (Hubstenberger et al., 2015). Concerning 4E-T, its top scoring partners included components of the same repressive complexes as LSM14A/B , 6 tubulins, and the two chaperon proteins RUVBL1 and RUVBL2 (Figure 2C, lower panel). Several components of the CRD-mediated complex, shown to promote stability of the *myc* mRNA (Weidensdorfer et al., 2009) and including HNRNPU, SYNCRIP, YBX1, and DHX9 were also present in the 3 datasets.

Interestingly, we noticed that while proteins of the decapping complex and of repressive complexes were as abundantly found associated with DDX6 (Supplemental Figure 2A), LSM14A, LSM14B and 4E-T partners are mostly related to repressive complexes including the CPEB-like complex and the FMRP complex (Figure 2C). These observations are in accordance with the known functions of LSM14A and 4E-T in repression of translation and their localization to PBs.

We also compared our TAP-tag results with three proteomes available in the literature : proteomes of LSM14A and 4E-T established by proximity-dependant BioID (Biotin Identification) approach (Youn et al., 2018) (Supplemental Figure 2B) and a second proteome of 4E-T obtained by a FLAG-affinity purification strategy (Kamenska et al., 2016) (Supplemental Figure 2C). Mass spectrometry analysis following BioID purification identified 64 proteins as LSM14A significant partners (FDR<0,05). LSM14A partners also present in our LSM14A TAP-tag results included repressors of translation such as components of the CPEB-like complex, members of the FMRP complex (FMR1, FXR2, NUFIP2). LSM14A partners found in the BioID but not in our TAP tag included decapping factors (DCP1A, DCP1B; LSM1, LSM12, EDC3, EDC4), RNA interference factors (AGO1, AGO2, TNRC6A, TNRC6B), CNOT-CCR4 subunits and NMD factors (UPF1, SMG1, SMG8, SMG9). Similar observations applied to 4E-T partners with 21 out of 41 significant interactors also present in our analysis (Supplemental Figure 2B). Interestingly we noted that NOT1 subunit was found in our TAP tag and in the BioID purifications, in agreement with the interaction between 4E-T and NOT1 demonstrated *in vitro* (Räsch et al., 2020). Regarding the 4E-T proteome from (Kamenska et al., 2016), 34 out of 50 4E-T top scoring partners were also present in our TAP tag in RNAse conditions (Supplemental Figure 2C). Common partners notably included repressors of translation such as DDX6, cold shock

domain protein CSDE1 which have been described to facilitate the interaction of AGO2-miRISC to PB components like LSM14A and the decapping factors DCP1-DCP2 (Kakumani et al., 2020). Consistently, STRAP (Serine Threonine kinase receptor associated protein) is the direct partner of CSDE1 was also identified among LSM14A partners. Both DDX6 and CDSE1 were found to directly interact with 4E-T on its motif 1 and CHD domain, respectively (Kamenska et al., 2016). Translation initiation factors like the canonical 4E-T partner eIF4E, 4 eIF3 subunits and 2 ribosomal proteins from the small subunit (RSP3 and RPS4X) were also common to the 2 independent analyses. These observations might be consistent with 4E-T acting at the 5'end of its target mRNAs.

To verify that interactions highlighted by mass spectrometry analysis do not result from the expression of exogenous proteins, we performed immunoprecipitations experiments with anti-LSM14A, anti-LSM14B and anti-4E-T antibodies using cytoplasmic lysates from untransfected HEK293 cells in presence and in absence of RNAse (Supplemental Figure 3). As expected, anti-LSM14A antibodies coimmunoprecipitated endogenous 4E-T and DDX6 proteins as efficiently as LSM14A itself, suggesting that a large fraction of 4E-T and DDX6 proteins interact with LSM14A.

While EDC3 and EDC4 proteins were not detected in LSM14A TAP tag, we found that endogenous EDC3 was weakly co-immunoprecipitated with LSM14A in absence of RNAse and that EDC4 was immunoprecipitated efficiently with LSM14A in both conditions, which is consistent with the interaction domain between EDC4 and LSM14A previously characterized by structural experiments (Brandmann et al., 2018). LSM14B was not immunoprecipitated efficiently by anti-LSM14A antibody nor LSM14A by anti-LSM14B antibody in both presence of RNAse and RNAse inhibitor. Given that LSM14A is ten times more abundant then LSM14B (Supplemental table 3), we cannot exclude that these proteins could interact together but quantities would be too low to be detected. Finally, DDX6 was coimmunoprecipitated weakly with 4E-T in absence of RNAse in agreement with its much higher cellular abundance compared to 4E-T.

Overall, these results provided a consistent dataset showing that the three PB assembly proteins interact in the cell with a large set of factors linked to cytosolic mRNA metabolism.

2) Comparison of LSM14A, 4E-T and DDX6 partners with PB proteome identifies potential new PB assembly factors

The three PB proteins LSM14A, 4E-T and DDX6 were previously shown to be essential for PB maintenance because their individual silencing by RNA interference completely dissolved PBs (Ayache et al., 2015; Chu and Rana, 2006; Ferraiuolo et al., 2005; Yang et al., 2006). They are also required for *de novo* PB assembly following PB induction by various treatments such as arsenite, vinblastine or mild cold shock exposure (Ayache et al., 2015; Minshall et al., 2009; Serman et al., 2007). Structural data evidenced that interactions between 4E-T or LSM14A and DDX6 were mutually exclusive since occurring on the same region of DDX6 RecA2 domain. Moreover, complementation assays with interaction mutants revealed that LSM14A deficient for DDX6 interaction cannot assemble PBs (Brandmann et al., 2018), while DDX6 deficient for LSM14A interaction and 4E-T deficient for DDX6 interaction displayed only reduced ability to assemble PBs (Ayache et al., 2015; Kamenska et al., 2016). On these grounds, DDX6, LSM14A and 4E-T could not associate in a ternary complex to assemble PB. Alternative scenari include possible intervention of a fourth or even several, other PB assembly partner(s).

To specify in which mRNP complexes DDX6, LSM14A and 4E-T take part in PB formation we looked for new PB assembly factors by comparing our LSM14A, LSM14B and 4E-T TAP tag datasets with published DDX6 proteome (Ayache et al., 2015) and PB proteome (Hubstenberger et al., 2017). Indeed, if other PB assembly partners exist, they should be partners of the four proteins LSM14A, LSM14B, 4E-T DDX6 and be localized to PBs. By doing so, we obtained a list of 12 proteins significantly enriched in PBs and able to interact with LSM14A, LSM14B, 4E-T and DDX6 (Figure 3A). These 12 proteins comprised the 4 proteins of the CPEB-like complex DDX6 LSM14A LSM14B and 4E-T. Eight other factors included 3 RBPs: ILF3, DHX9 and HRNPU, 3 mitochondrial proteins: ATAD3A, SLC25A5, SLC25A6 and two proteins from the small ribosomal subunit: RPS3 and RPS4X.

Concerning PB assembly, involvement of DDX6, LSM14A LSM14B and 4E-T in PB formation had already been assessed (Ayache et al., 2015). ATAD3A, SLC25A5, SLC25A6 being mitochondrial proteins, we did not favour the hypothesis that they could be indispensable to PB assembly. Similarly, RPS3 and RPS4X being ribosomal proteins and knowing that the translation machinery is excluded from PBs, we thought major contribution of these proteins to PB

assembly is unlikely. The three other factors ILF3, DHX9 and HNRNPU seemed better candidates. Since ILF3 localization to PBs had previously been confirmed in the lab (Hubstenberger et al., 2017), we started by investigating involvement of this candidate in PB maintenance and assembly. To evaluate ILF3 contribution to PB maintenance, we transiently silenced ILF3 (Supplemental Figure 4A). Cells were fixed 48h after transfection and stained with anti-EDC4, anti-XRN1 or anti-DDX6 antibodies to visualize PBs (Figure 3B). Counting displays a significant 40 % drop in PB number/cells in absence of ILF3 and the observation is identical for the 3 markers used to visualize PBs (Figure 3C). To control that the effect we observed was indeed due to partial PB dissolution by siILF3 and did not result from a decreased expression of the proteins we used to visualize PBs, we ensured by western blotting analysis that EDC4, XRN1 and DDX6 expression levels were unaffected by ILF3 silencing (Supplemental Figure 4B). Wondering next whether partial PB dissolution observed in absence of ILF3 could occur via a decreased expression of PB assembly factors, we assessed their expression in absence of ILF3.We observed that LSM14A, LSM14B, DDX6 and 4E-T protein expression levels were unaffected by the absence of ILF3 (Supplemental Figure 4B).

To assess ILF3 contribution to PB *de novo* assembly, HEK293 cells transiently silenced for ILF3 were treated for 30min with arsenite before fixation. Using three different markers to visualize PBs, immunofluorescence imaging showed that arsenite induced PBs as efficiently in absence of ILF3 as in the control. (Figure 3D). Arsenite treatment increased PB number by ~66% which is consistent with previous observations (Ayache et al., 2015). The same increase was observed in absence of ILF3 and in control for the 3 PB markers (Figure 3E). Collectively, these results show that ILF3 contributes to PB maintenance without being an essential factor and is not involved in PB *de novo* assembly.

3) LSM14A associates *in vivo* with translation initiation complex

Interestingly, several initiation factors were found specifically present in LSM14A complexes, including 12 out of 13 eIF3 subunits, 3 out of 3 eIF2 subunits, eIF4B and eIF4G (Figure 4A upper panel). Also,.17 out of 21 proteins of the small ribosomal subunit but only 11 out of 34 proteins of the large ribosomal subunit were found to interact with LSM14A (Figure 4A lower panel). This observation is reminiscent of interactions occurring in yeast where LSM14A homolog Scd6 interacts *in vitro* with the initiation complex *via* eIF4G, thus preventing association of the 43S

PIC to mRNA (Nissan et al., 2010; Poornima et al., 2016). In order to investigate whether these interactions are conserved *in vivo* in human cells, we assessed the immunoprecipitation of several components of the initiation complex from HEK293 cytoplasmic lysates by anti-LSM14A antibody : eIF4E because of its interaction with the LSM14A partner 4E-T and its localization to PBs, and also eIF3a given its high MS score in our dataset (Figure 4B). LSM14A antibodies specifically immunoprecipitated eIF3a in presence of RNAse inhibitor. Unexpectedly immunoprecipitation was more efficient in presence of RNAse which may be explained by epitopes being more accessible in this condition. Concerning eIF4E, immunoprecipitation efficiency by anti-LSM14A was also weak and enhanced by RNA digestion. Reciprocally, anti-eIF3a antibody immunoprecipitated a fraction of LSM14A as well as RPS6. These observations confirm mass spectrometry results in which eIF3a, eIF4E and RPS6 were found to associate with LSM14A in both conditions RNAse and RNAse out. Moreover, they suggest that besides being mainly involved in repressive complexes like those accumulated in PBs, LSM14A could be implied in control of translation at the initiation step in a complex interacting with eIF3a and the 40S.

In order to assess LSM14A association to mRNA 5'end; we performed cap binding assay on HEK cytoplasmic lysates. In this assay, cytoplasmic lysates are incubated with Agarose beads coupled to m^7GTP, a 5' mRNA cap analogue on which factors involved in the regulation of translation initiation are known to bind. As a negative control we used Agarose beads coupled to GTP, on which initiation factors do not bind. We observed that LSM14A and DDX6 proteins were specifically retained by m^7GTP beads though less efficiently than canonical initiation factor eIF4E and its direct partner 4E-T. This suggests that a fraction of LSM14A and DDX6 could be present in mRNA 5' end-associated complexes.

To complement these results, we analysed the distribution of endogenous LSM14A in polysomal fractions using sucrose gradients. In polysome profiles from 10-50% sucrose gradients centrifuged for 2h45 at 39K RPM, LSM14A was distributed along the entire gradient and a large fraction of the protein was present in sub-polysomal fractions (Supplemental Figure 5A). In a 5-20% sucrose gradient centrifuged for 2h45 at 39K RPM, LSM14A was enriched in 40S fraction, according to both RNA absorbance profile and RPS6 distribution along the profile. (Figure 4D). For comparison, we looked at DDX6 and 4E-T distributions: both were present in all subpolysomal fractions without preferentially co-sedimenting in any

particular fraction. These observations suggest that a fraction of LSM14A associates to 43S and/or 48S complex *in vivo*.

In order to investigate if other components of the CPEB-like complex were involved in LSM14A association to the initiation complex, we repeated these experiments after transiently silencing either DDX6, LSM14A or 4E-T. We noted that neither the absence of LSM14A had an effect on DDX6 distribution across the polysome profile (Supplemental Figure 5B) nor absence of DDX6 on LSM14A distribution across the polysome profile (Supplemental Figure 5C). These observations suggest that LSM14A association to the initiation complex is independent of DDX6.

Interestingly, we noted that in absence of 4E-T, LSM14A was significantly displaced towards sub-40S fraction (Figure 5A). Nonetheless, absence of 4E-T did not influence immunoprecipitation of eIF3a by anti-LSM14A antibody indicating that interaction between LSM14A and eIF3a occurs independently of 4E-T (Figure 5B).

Figures

Figure 1

A.

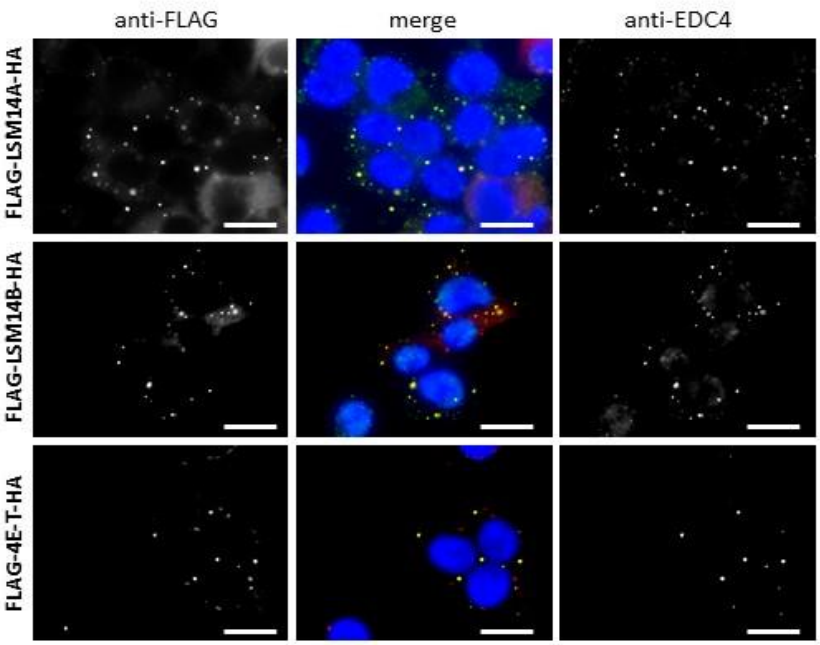
anti-FLAG
merge
anti-EDC4
FLAG-LSM14A-HA
FLAG-LSM14B-HA
FLAG-4E-T-HA

B.

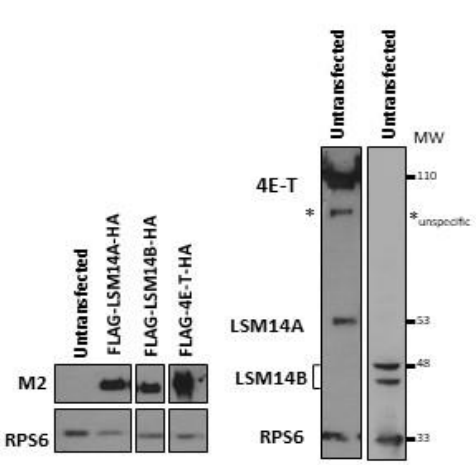
Untransfected
FLAG-LSM14A-HA
FLAG-LSM14B-HA
FLAG-4E-T-HA
M2
RPS6
Untransfected
Untransfected
MW
4E-T
LSM14A
LSM14B
RPS6
110
53
48
33
*unspecific

C.

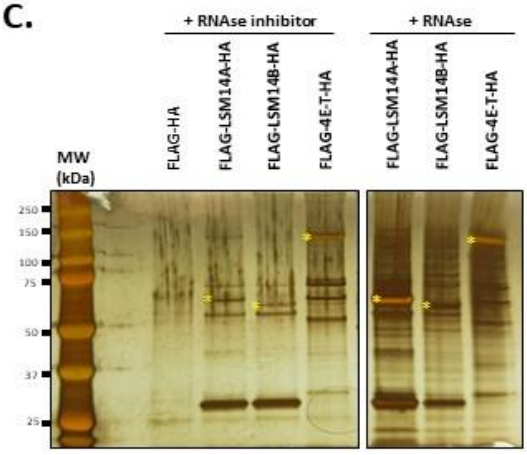
+ RNAse inhibitor
+ RNAse
FLAG-HA
FLAG-LSM14A-HA
FLAG-LSM14B-HA
FLAG-4E-T-HA
FLAG-LSM14A-HA
FLAG-LSM14B-HA
FLAG-4E-T-HA
MW
(kDa)
250
150
100
75
50
37
25

Figure 2

A.

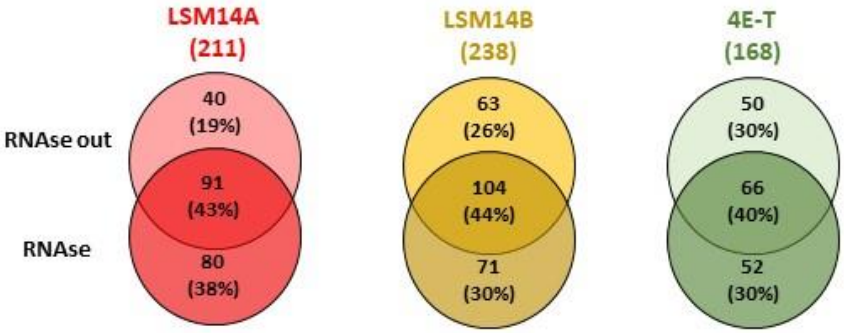
LSM14A
(211)
LSM14B
(238)
4E-T
(168)
RNAse out
RNAse
40
(19%)
91
(43%)
80
(38%)
63
(26%)
104
(44%)
71
(30%)
50
(30%)
66
(40%)
52
(30%)

B.

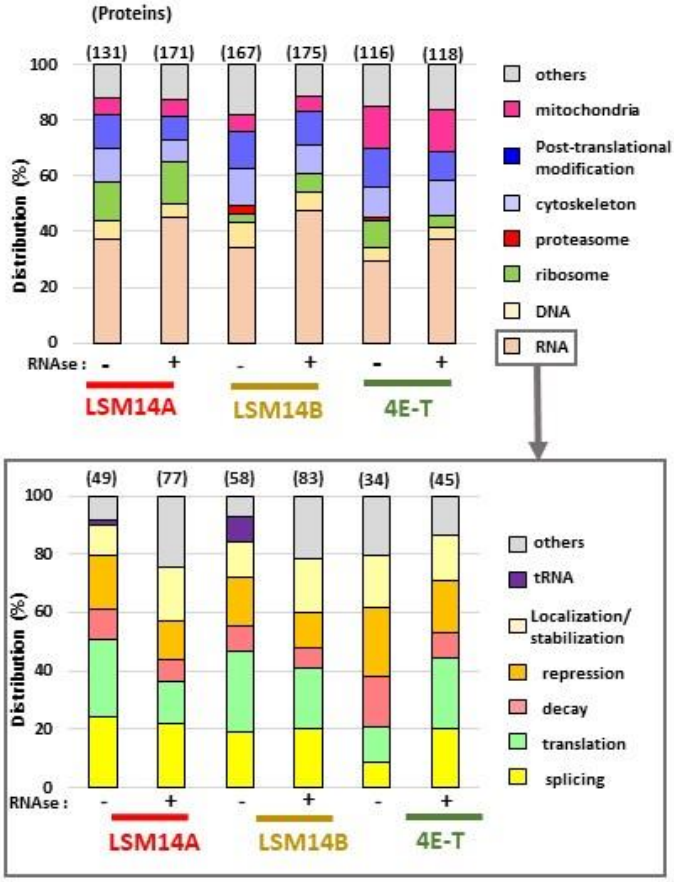
(Proteins)
(131)
(171)
(167)
(175)
(116)
(118)
Distribution (%)
RNAse :
LSM14A
LSM14B
4E-T
others
mitochondria
Post-translational modification
cytoskeleton
proteasome
ribosome
DNA
RNA
(49)
(77)
(58)
(83)
(34)
(45)
tRNA
Localization/ stabilization
repression
decay
translation
splicing

C.

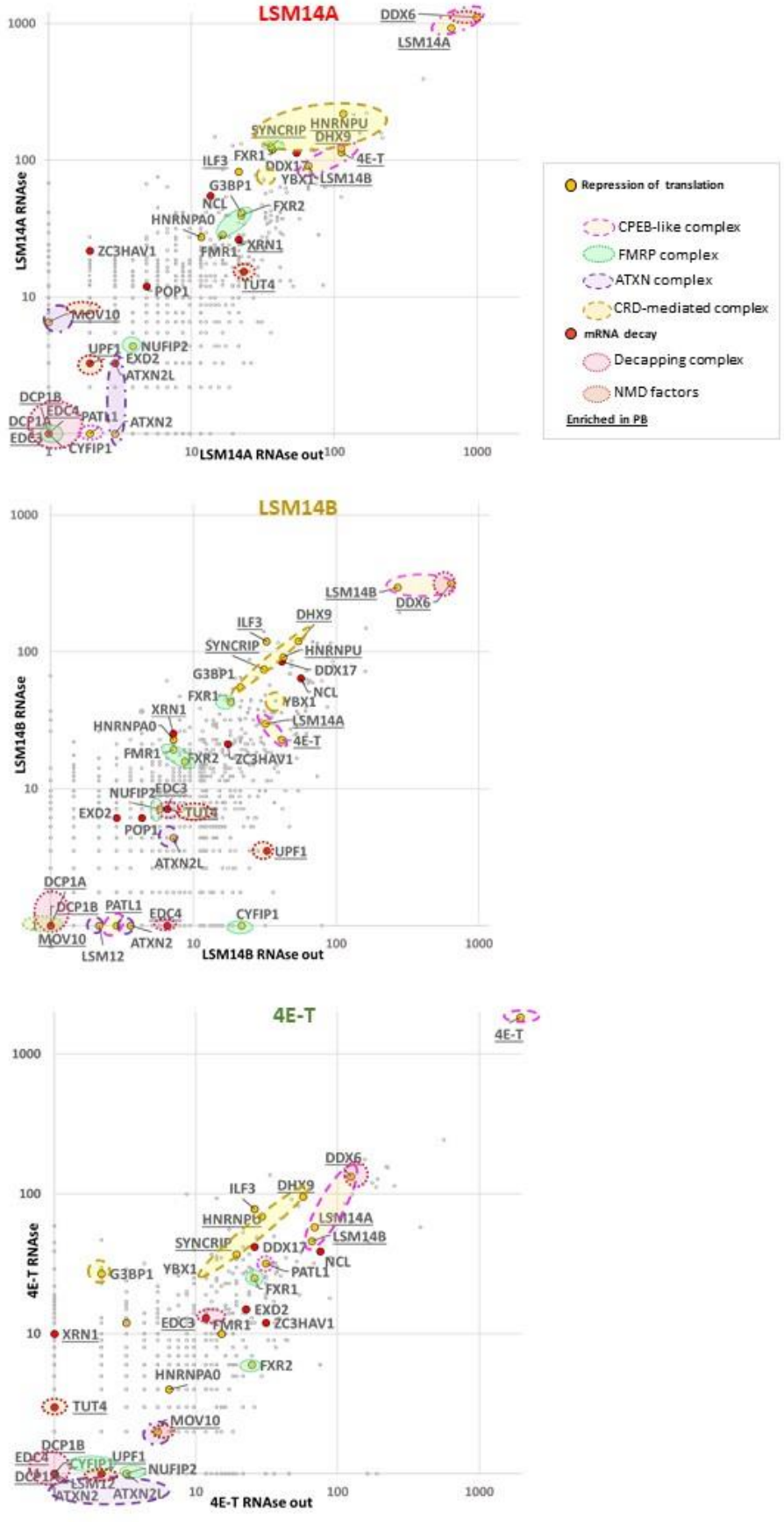
LSM14A
LSM14A RNAse
LSM14A RNAse out
DDX6
LSM14A
SYNCRIP
HNRNPU
DHX9
ILF3
FXR1
DDX17
4E-T
YBX1
LSM14B
G3BP1
NCL
FXR2
HNRNPA0
ZC3HAV1
FMR1
XRN1
TUT4
POP1
MOV10
UPF1
NUFIP2
EXD2
ATXN2L
DCP1B
EDC4
PATL1
DCP1A
ATXN2
EDC3
CYFIP1
Repression of translation
CPEB-like complex
FMRP complex
ATXN complex
CRD-mediated complex
mRNA decay
Decapping complex
NMD factors
Enriched in PB
LSM14B
LSM14B RNAse
LSM14B RNAse out
LSM14B
DDX6
DHX9
ILF3
SYNCRIP
HNRNPU
G3BP1
DDX17
FXR1
NCL
YBX1
XRN1
LSM14A
HNRNPA0
4E-T
FMR1
FXR2
ZC3HAV1
NUFIP2
EDC3
EXD2
TUT4
POP1
UPF1
ATXN2L
DCP1A
DCP1B
PATL1
EDC4
CYFIP1
MOV10
ATXN2
LSM12
4E-T
4E-T RNAse
4E-T RNAse out
4E-T
DDX6
ILF3
DHX9
HNRNPU
LSM14A
SYNCRIP
LSM14B
DDX17
NCL
G3BP1
YBX1
PATL1
FXR1
EXD2
EDC3
FMR1
ZC3HAV1
XRN1
FXR2
HNRNPA0
TUT4
MOV10
DCP1B
EDC4
CYFIP1
UPF1
DCP1A
NUFIP2
LSM12
ATXN2
ATXN2L
1000
100
10
10
100
1000

Figure 3

A.

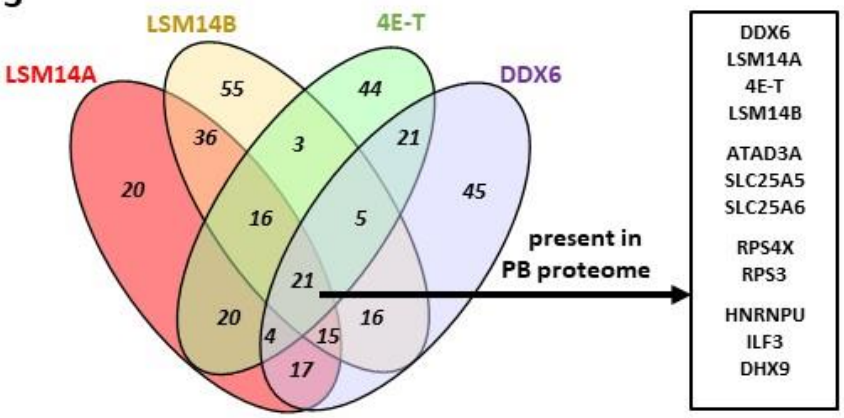
LSM14B
4E-T
LSM14A
DDX6
55
44
36
3
21
20
45
16
5
21
20
4
15
16
17
present in
PB proteome
DDX6
LSM14A
4E-T
LSM14B
ATAD3A
SLC25A5
SLC25A6
RPS4X
RPS3
HNRNPU
ILF3
DHX9

B.

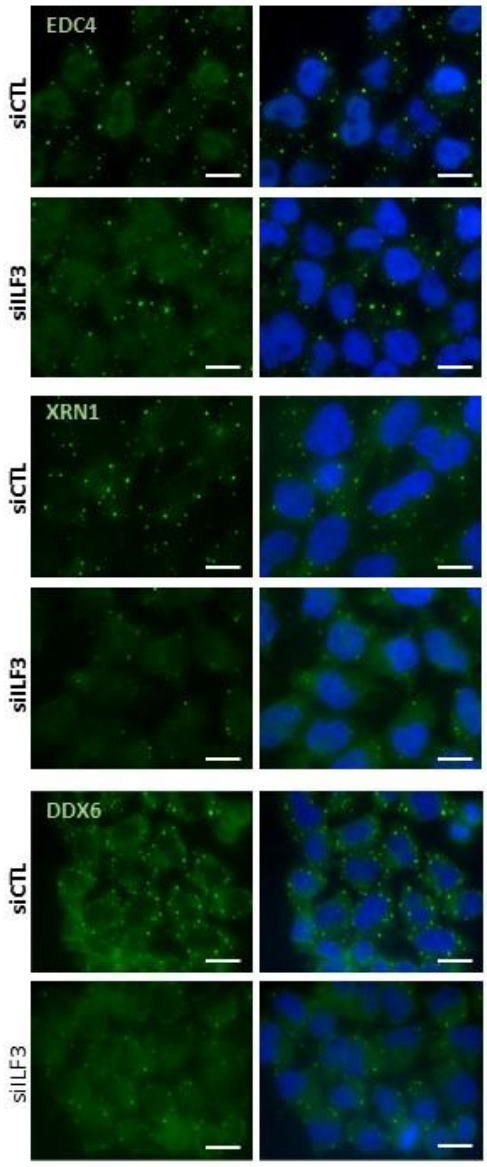
EDC4
siCTL
siILF3
XRN1
siCTL
siILF3
DDX6
siCTL
siILF3

C.

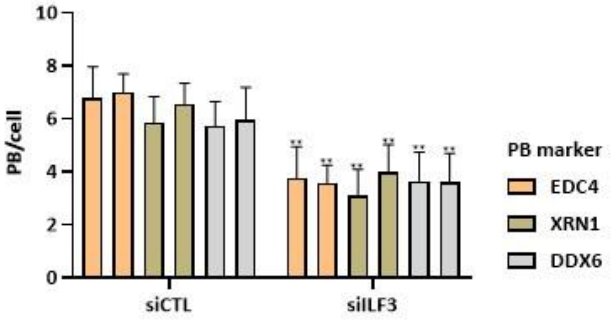
PB/cell
10
8
6
4
2
0
siCTL
siILF3
PB marker
EDC4
XRN1
DDX6

D.

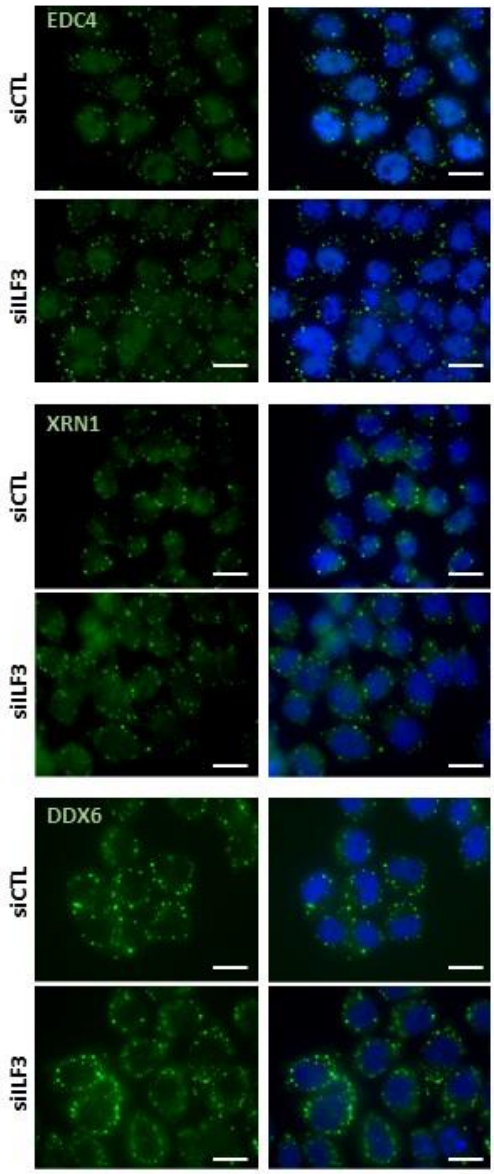
EDC4
siCTL
siILF3
XRN1
siCTL
siILF3
DDX6
siCTL
siILF3

E.

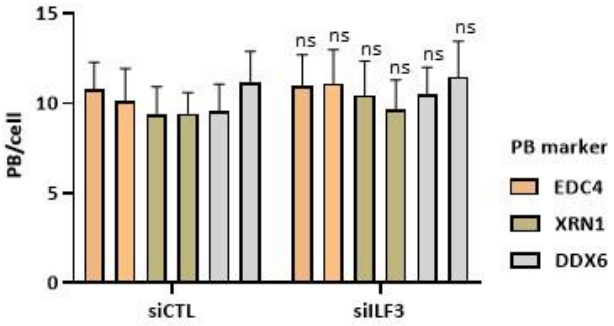
15
10
5
0
PB/cell
ns
ns
ns
ns
ns
ns
siCTL
siILF3
PB marker
EDC4
XRN1
DDX6

Figure 4

A.

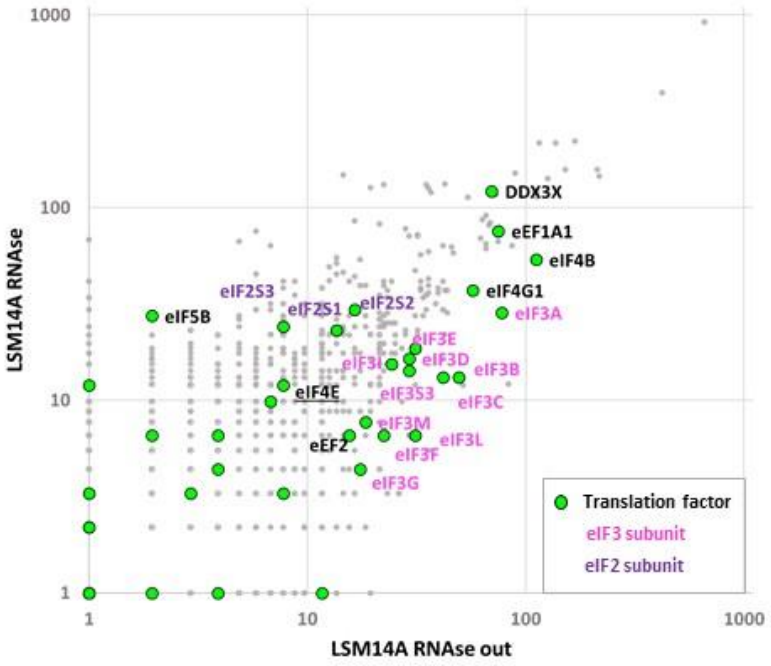

rIbosome sub-unit	rIbosomal proteIns	LSM14A (score > 20)		LSM14B score > 20		4E-T score > 20	
		RNAse out	RNAse	RNAse out	RNAse	RNAse out	RNAse
40S	21	15	17	4	8	5	5
60S	34	4	11	1	4	6	0

B.

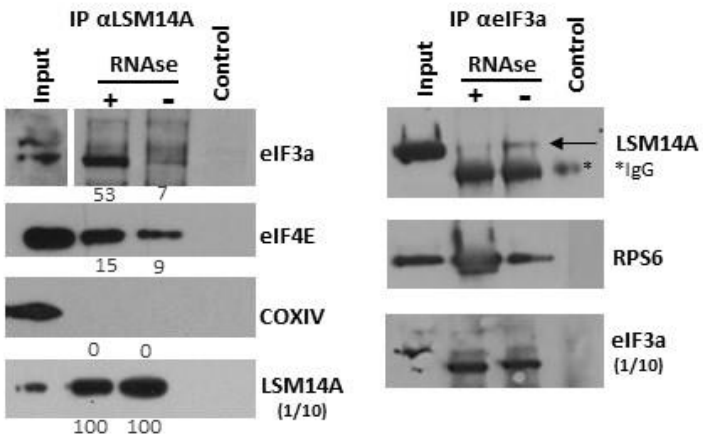

C.

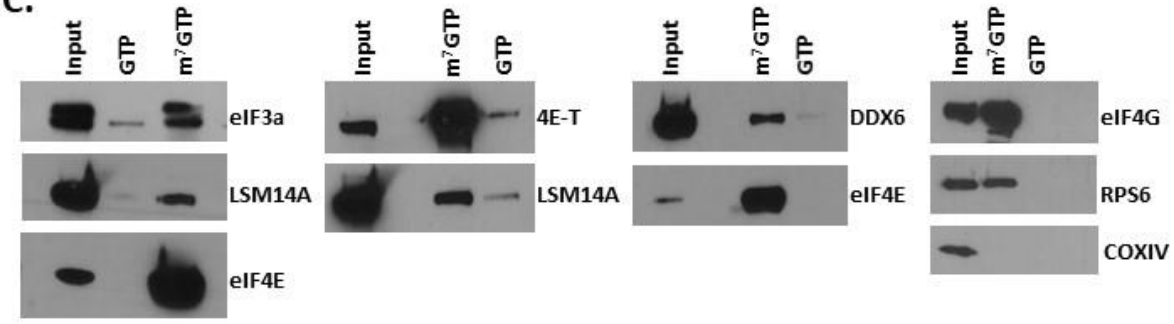

D.

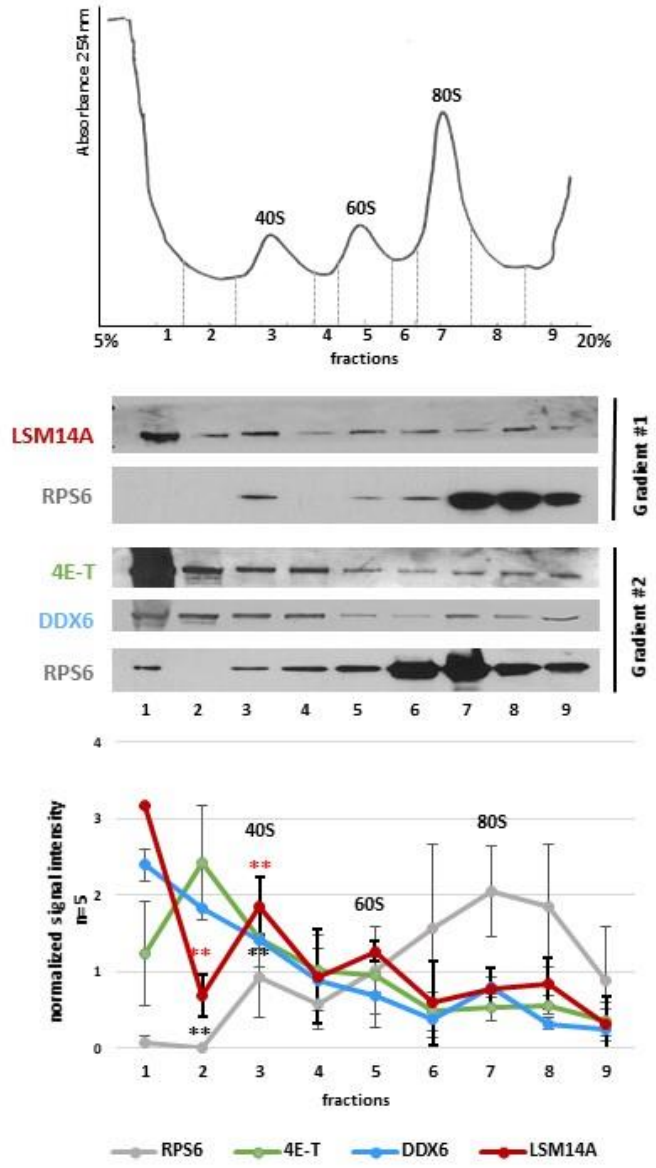
Absorbance 254nm
80S
40S
60S
5%
1
2
3
4
5
6
7
8
9
20%
fractions
LSM14A
RPS6
Gradient #1
4E-T
DDX6
RPS6
Gradient #2
1
2
3
4
5
6
7
8
9
4
3
2
1
0
normalized signal intensity
n=5
40S
80S
60S
**
**
**
**
1
2
3
4
5
6
7
8
9
fractions
RPS6
4E-T
DDX6
LSM14A

.

Figure 5

A.

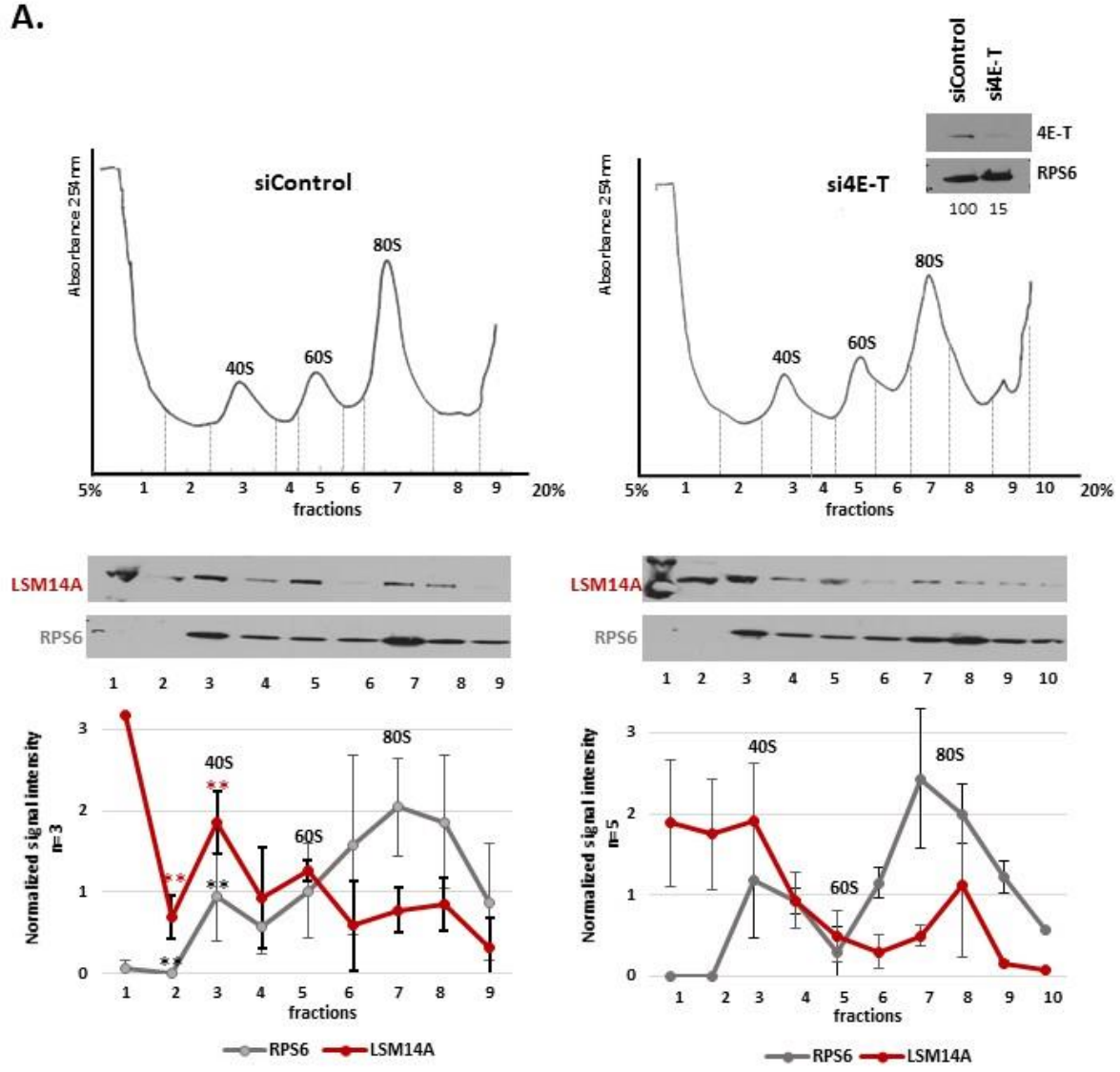
siControl
si4E-T
4E-T
RPS6
100 15
Absorbance 254 nm
40S
60S
80S
5%
20%
fractions
LSM14A
RPS6
Normalized signal intensity
n=3
n=5
RPS6
LSM14A

B.

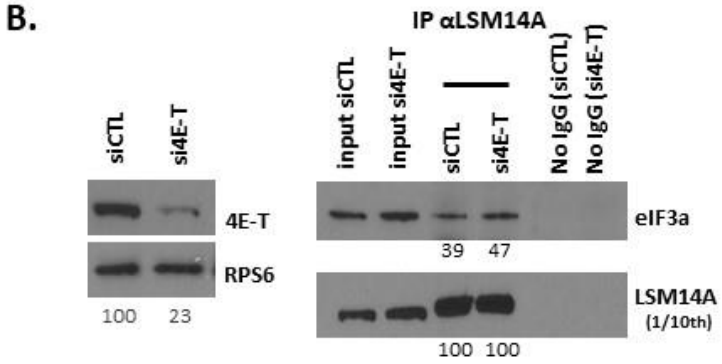
IP αLSM14A
siCTL
si4E-T
input siCTL
input si4E-T
siCTL
si4E-T
No IgG (siCTL)
No IgG (si4E-T)
4E-T
RPS6
100 23
eIF3a
39 47
LSM14A
(1/10th)
100 100

Supplemental Figure 1

A.

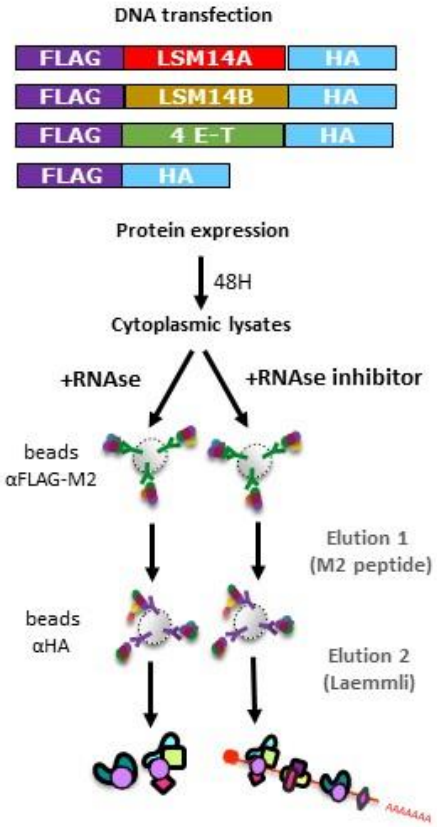

B.

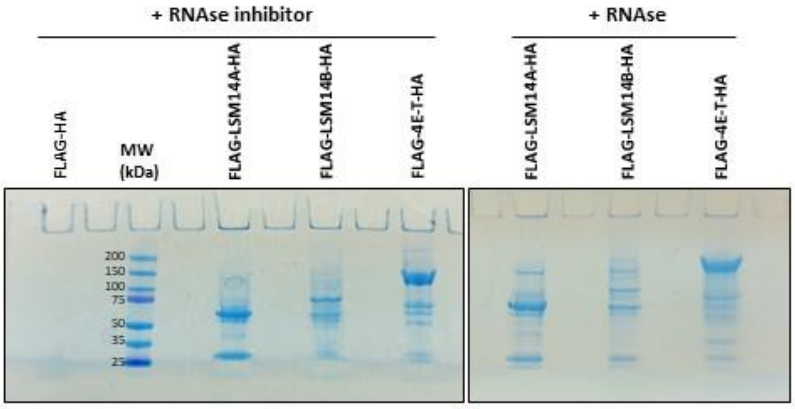

Supplemental Figure 2

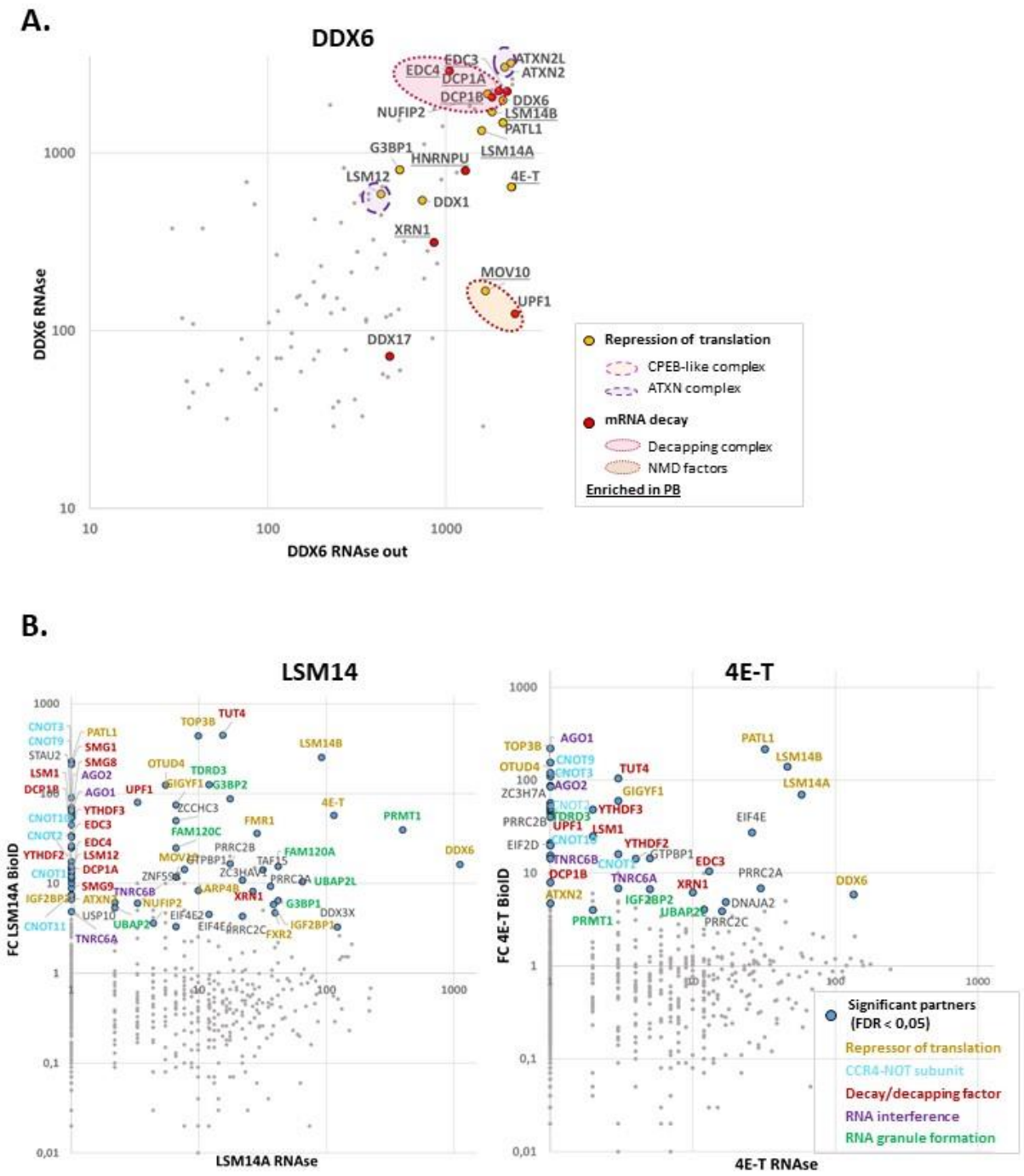

C.

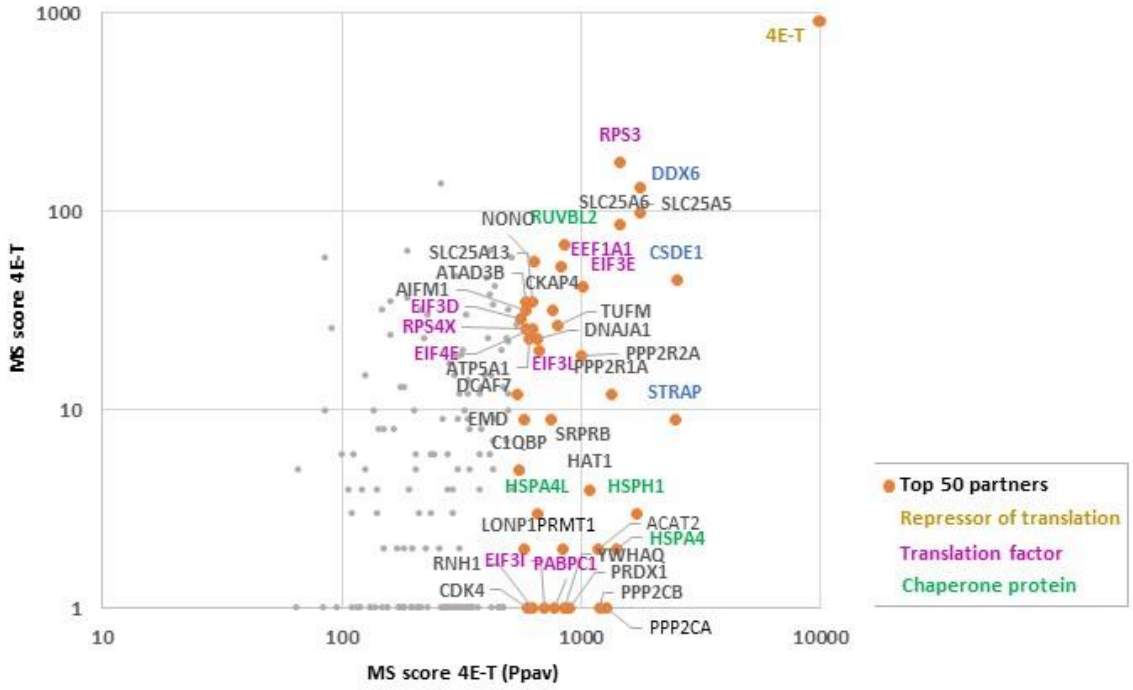
1000
100
10
1
MS score 4E-T
10
100
1000
10000
MS score 4E-T (Ppav)
4E-T
RPS3
DDX6
SLC25A6
SLC25A5
NONO
RUVBL2
SLC25A13
EEF1A1
EIF3E
CSDE1
ATAD3B
AIFM1
CKAP4
EIF3D
TUFM
RPS4X
DNAJA1
EIF4E
EIF3L
PPP2R2A
ATP5A1
PPP2R1A
DCAF7
STRAP
EMD
C1QBP
SRPRB
HAT1
HSPA4L
HSPH1
LONP1
PRMT1
ACAT2
HSPA4
RNH1
EIF3I
PABPC1
YWHAQ
PRDX1
CDK4
PPP2CB
PPP2CA
Top 50 partners
Repressor of translation
Translation factor
Chaperone protein

Supplemental Figure 3

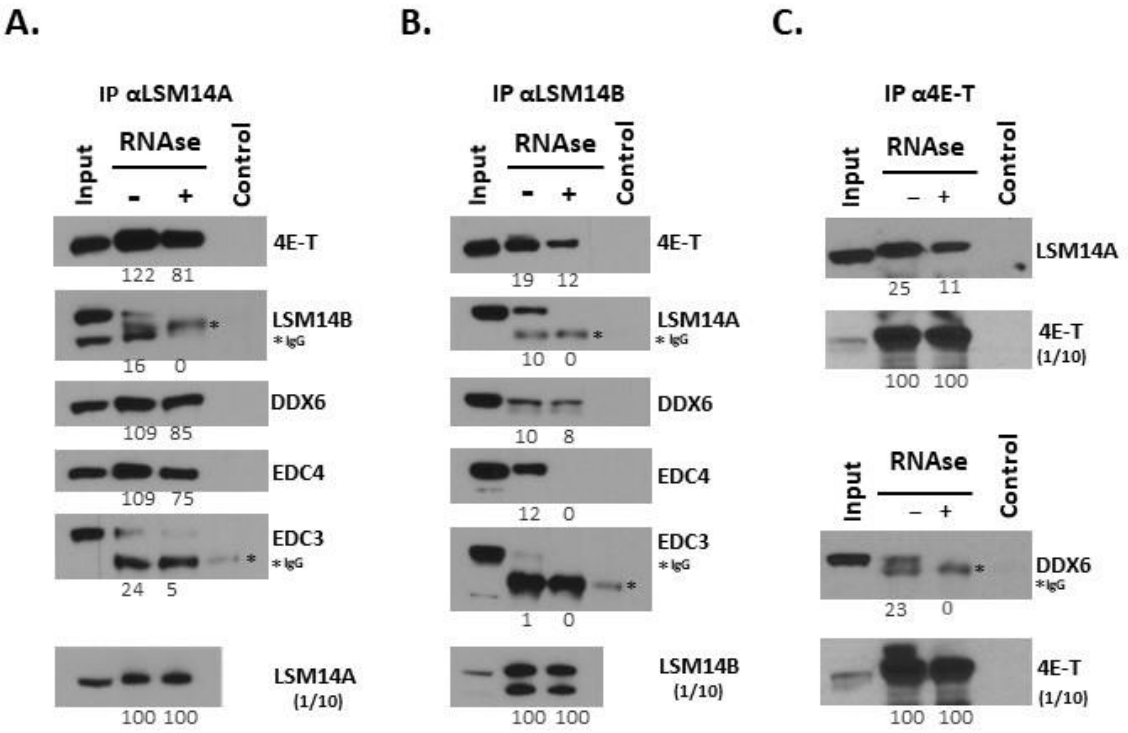

Supplemental Figure 4

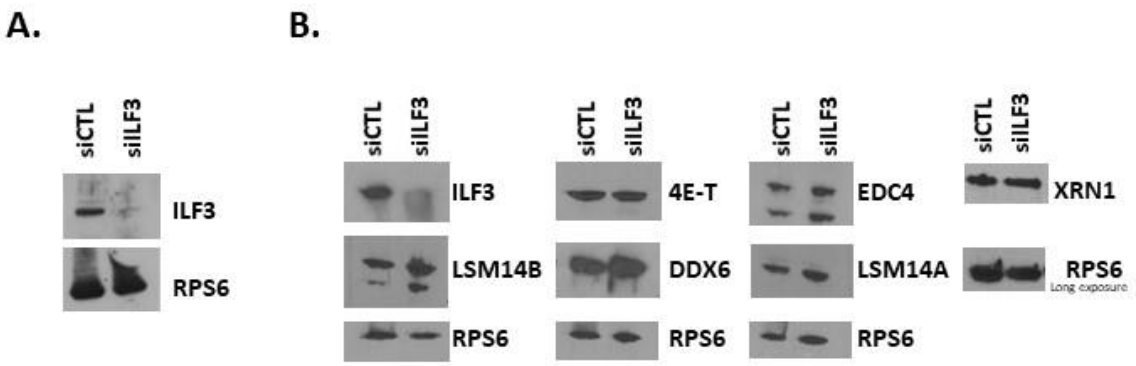

Supplemental Figure 5

A.

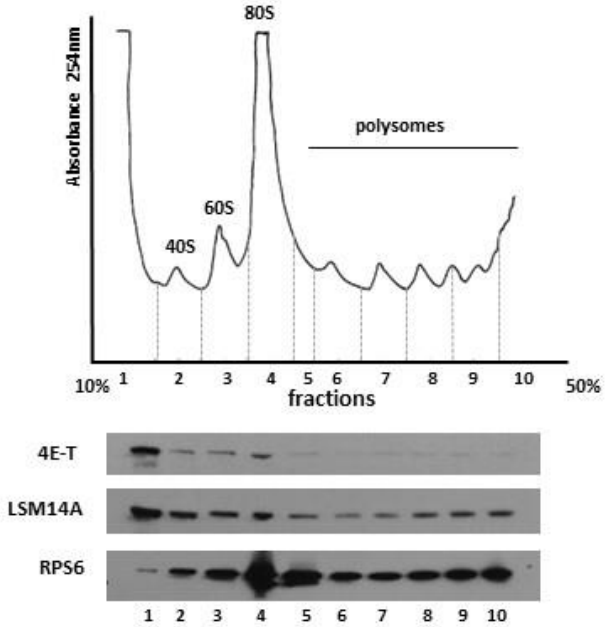

B.

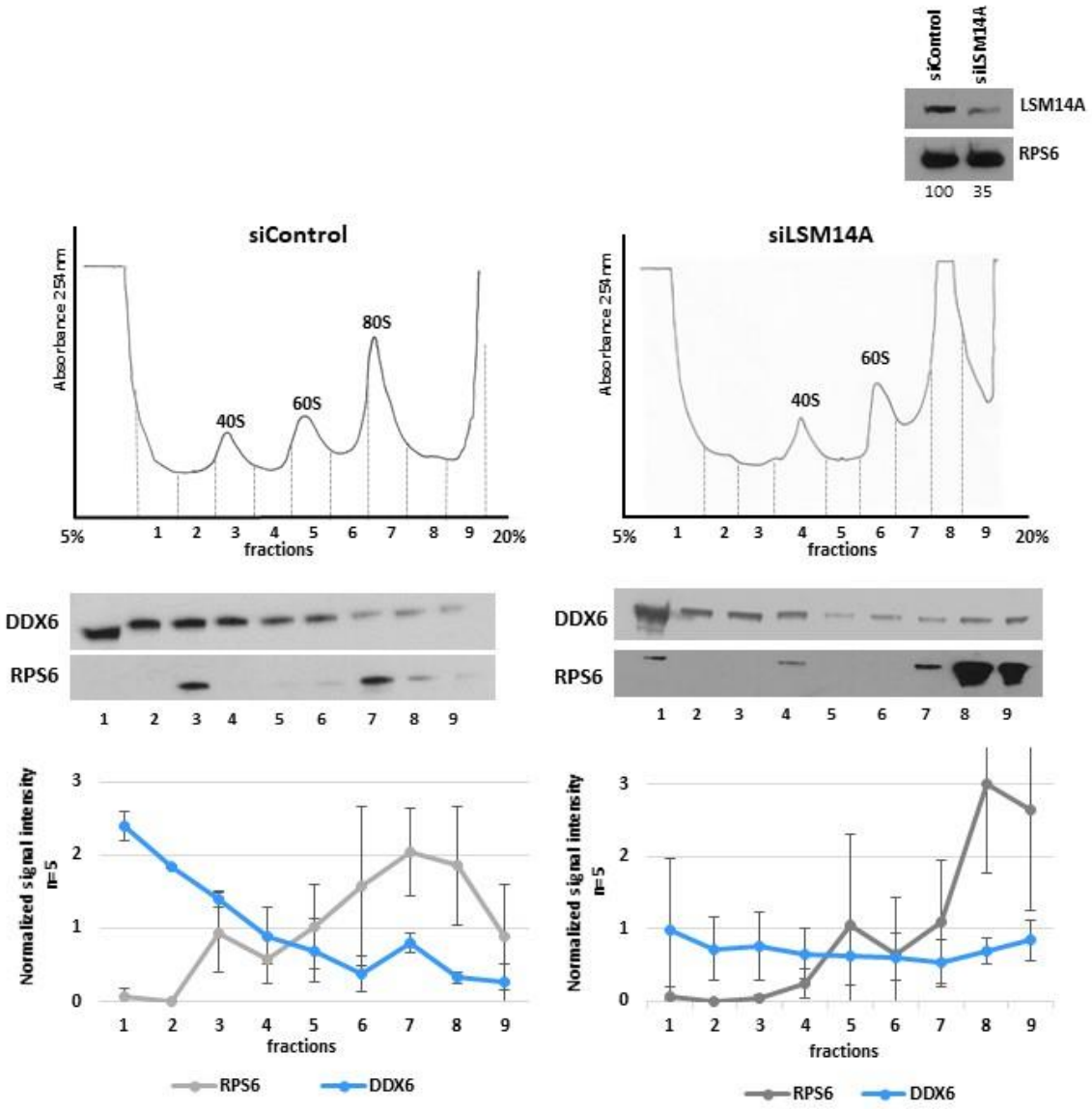
siControl
siLSM14A
LSM14A
RPS6
100
35
siControl
siLSM14A
Absorbance 254nm
40S
60S
80S
5%
20%
fractions
DDX6
RPS6
Normalized signal intensity
n=5
RPS6
DDX6

C.

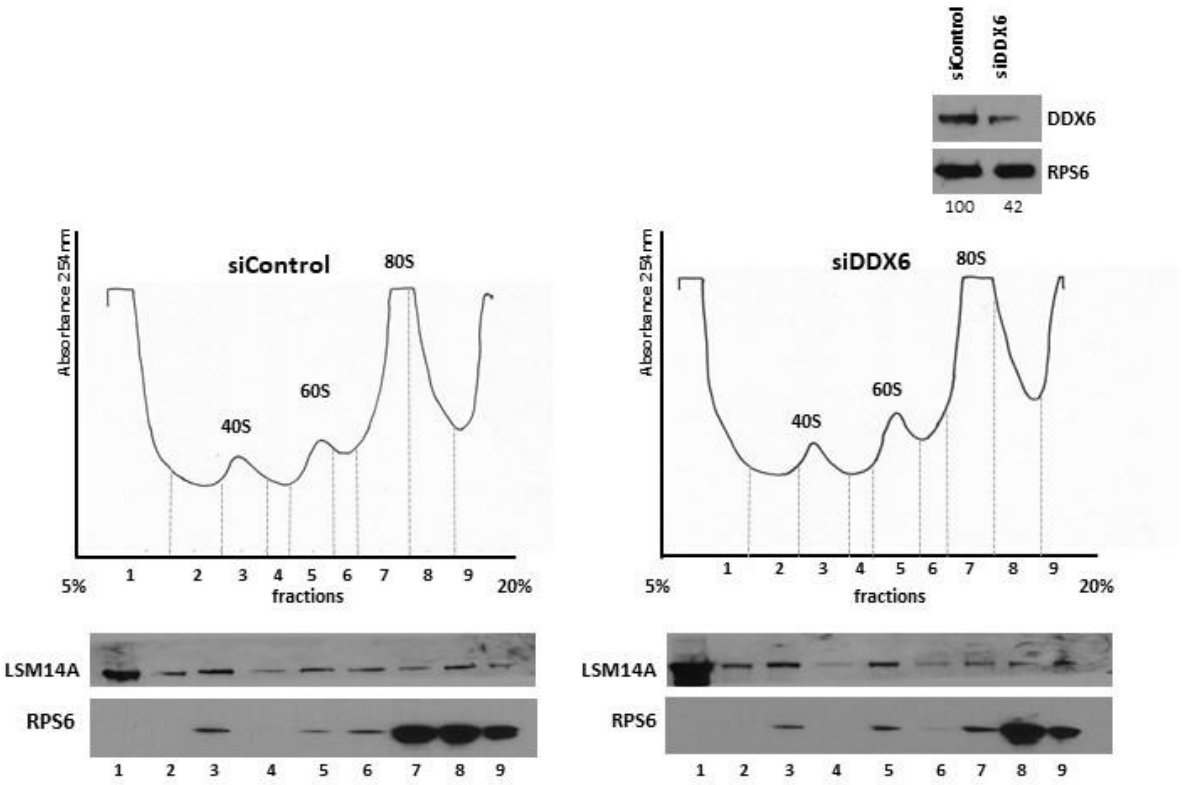
siControl
siDDX6
DDX6
RPS6
100
42
siControl
80S
60S
40S
Absorbance 254nm
5%
1 2 3 4 5 6 7 8 9
fractions
20%
siDDX6
80S
60S
40S
Absorbance 254nm
5%
1 2 3 4 5 6 7 8 9
fractions
20%
LSM14A
RPS6
1 2 3 4 5 6 7 8 9
LSM14A
RPS6
1 2 3 4 5 6 7 8 9

Supplemental table 1

Gene Name	Accession Number	Molecular Weight (kDa)	With RNAse inhibitor								With RNAse A					
			CONTROL		LSM14A		LSM14B		4E-T		LSM14A		LSM14B		4E-T	
			normalized total spectra	unique peptide	normalized total spectra	unique peptide	normalized total spectra	unique peptide	normalized total spectra	unique peptide	normalized total spectra	unique peptide	normalized total spectra	unique peptide	normalized total spectra	unique peptide
DDX6	DDX6_HUMAN	54	5,2198	3	987,09	33	637,22	34	123,83	25	1 110,8	34	316,24	30	133,54	28
EIF4A1	IF4A1_HUMAN	69	2,6099	2	100,84	33	277,65	42	0	0	53,784	22	194,14	35	58,798	25
LSM14B	LS14B_HUMAN	42	0	0	69,935	17	268,23	30	65,682	15	91,103	20	296,92	30	45,843	18
LSM14A	QSTBP5_HUMAN	27	0	0	48,482	2	195,73	2	48,531	2	0	0	221,37	2	37,87	2
HSPA1A	HS71A_HUMAN (+1)	70	33,929	15	126,05	28	160,94	33	562,07	41	140,5	31	149,34	32	244,16	37
EEF1A1	EF1A1_HUMAN	50	62,637	7	74,662	12	159,49	17	21,555	10	75,736	15	72,033	17	52,813	14
AFM	AFAM_HUMAN	69	43,063	8	28,12	2	108,02	3	0	0	0	0	0	0	0	0
TCP1	TCPA_HUMAN	60	0	0	42,664	22	106,57	29	23,689	16	37,319	22	78,182	28	29,897	20
TUBA4B	TBA4B_HUMAN	50	15,659	2	67,875	5	95,691	5	220,76	5	81,724	5	79,06	5	156,46	5
TUB5	TB5_HUMAN	50	15,659	10	68,844	20	94,241	26	226,12	27	83,419	21	85,21	23	153,47	25
PRKDC	PRKDC_HUMAN	469	2,6099	2	72,723	60	90,617	101	47,377	43	108,47	82	106,29	100	91,685	82
C1QBP	C1QBP_HUMAN	31	3,9148	2	212,35	12	87,717	10	29,072	10	158,06	11	93,994	11	4,9829	4
EEF1A2	EF1A2_HUMAN	50	0	0	0	0	86,267	4	0	0	0	0	39,55	2	0	0
LRPPRC	LRPRC_HUMAN	158	0	0	150,29	61	79,743	60	33,379	28	158,06	61	60,613	49	136,53	63
TUBB4A	TBB4A_HUMAN	50	0	0	0	0	79,743	2	175,51	5	0	0	0	0	119,59	4
MYH9	MYH9_HUMAN	227	2,6099	2	20,362	20	73,943	73	75,373	54	4,3305	6	12,298	13	5,3795	5
RPS3	RS3_HUMAN	27	35,233	12	167,75	19	73,943	18	156,13	19	220,62	20	115,08	20	176,39	20
CKAP5	CKAP5_HUMAN	226	0	0	42,664	42	73,218	71	2,1555	2	21,962	19	73,79	67	28,301	29
DYNC1H1	DYHC1_HUMAN	532	0	0	0	0	73,218	92	0	0	24,148	22	20,204	23	13,952	14
PARP1	PARP1_HUMAN	113	3,9148	3	45,573	32	73,218	45	3,2303	3	62,565	33	73,79	43	23,918	21
CCT8	TCPQ_HUMAN	60	0	0	27,15	21	68,869	34	5,3838	5	9,8786	9	48,409	27	11,993	11
MCM3	MCM3_HUMAN	91	0	0	33,937	29	68,869	38	0	0	27,441	21	59,735	35	18,935	16
R3HM10	A0A0A0MR66_HUMAN	110	0	0	39,755	27	68,144	37	0	0	36,222	25	108,05	43	38,867	28
DSP	DESP_HUMAN	332	56,113	18	117,48	63	67,419	58	60,298	46	17,562	10	133,57	95	128,56	55
EIF4G1	E9PGV1_HUMAN	167	0	0	0	0	65,244	2	0	0	0	0	0	0	0	0
EIF4G1	E7EUA6_HUMAN	172	0	0	57,205	33	65,244	47	0	0	37,319	29	60,613	41	38,867	33
CCT4	TCPD_HUMAN	58	0	0	29,089	23	64,519	27	3,2303	3	6,5857	6	33,381	23	10,962	11
TUBA1B	TBA1B_HUMAN	50	50,893	11	51,391	16	64,519	18	191,66	21	71,346	18	69,397	17	137,53	23
HSPA8	HSP7C_HUMAN	71	31,319	7	41,694	20	63,794	28	187,36	28	63,662	23	58,858	23	101,65	28
GTF2I	GTF2I_HUMAN	112	9,1346	7	217,2	56	60,894	42	12,921	11	145,98	51	69,248	45	36,873	26
HNRNPK	HNRPK_HUMAN	51	5,2198	2	14,545	11	60,894	22	9,6908	8	46,1	19	72,511	22	38,853	18
MCM4	MCM4_HUMAN	97	0	0	25,211	24	60,894	40	2,1555	2	17,562	16	25,475	21	6,9761	6
HNRNPR	HNRH3_HUMAN	89	0	0	34,367	21	60,894	28	6,4605	6	29,636	21	39,53	26	14,919	13
CCT3	TCPG_HUMAN	61	0	0	25,211	21	60,17	32	5,3838	5	15,367	12	36,895	28	10,962	10
LTF	E7EQB2_HUMAN (+4)	77	9,1346	5	27,15	16	60,17	39	11,844	6	2,1952	2	1,7569	2	2,9897	3
EIF3A	EIF3A_HUMAN	167	0	0	77,571	66	59,445	40	2,1555	2	28,538	21	58,856	36	46,839	34
DDX5	DDX5_HUMAN (+1)	69	11,744	8	89,207	26	58,72	26	35,533	17	151,47	31	124,74	29	48,829	26
CCT2	TCPB_HUMAN	57	3,9148	2	20,362	14	56,545	26	0	0	4,3305	4	33,381	21	7,9726	7
MCM5	MCM5_HUMAN	82	0	0	38,786	23	56,545	34	2,1555	2	31,831	18	61,491	34	25,911	16
NCL	NUCL_HUMAN	77	0	0	13,575	13	56,545	22	75,373	23	54,881	21	64,127	23	38,867	19
PTMTS	ANM5_HUMAN	73	11,744	7	136,72	27	55,82	23	37,686	15	216,23	30	60,613	21	21,925	14
DHX9	DHX9_HUMAN	141	5,2198	4	110,54	39	54,37	38	57,068	28	122,93	44	119,47	45	95,672	41
KIF5B	KINH_HUMAN	110	0	0	41,694	36	54,37	43	0	0	16,464	15	35,138	34	28,301	26
MYH10	MYH10_HUMAN	229	0	0	76,18	20	54,37	54	45,224	31	3,2929	3	9,6629	8	0	0
COPA	COPA_HUMAN	138	0	0	35,877	23	52,92	42	20,458	12	42,807	29	36,895	30	33,884	31
MCM6	MCM6_HUMAN	93	2,6099	2	19,393	20	52,92	32	2,1555	2	12,076	11	25,475	21	7,9726	7
PAICS	PURE_HUMAN	47	0	0	9,6964	7	52,92	20	0	0	3,2929	2	16,691	14	9,9658	9
STK38	STK38_HUMAN	56	0	0	22,302	14	52,92	22	0	0	17,562	10	28,11	18	21,925	13
HSPA5	GRP78_HUMAN	72	32,624	8	57,209	26	50,745	27	142,13	30	77,443	28	62,166	25	70,757	28
MCM7	MCM7_HUMAN	81	0	0	22,302	20	50,02	34	23,689	19	14,269	13	24,597	23	18,935	17
EIF3I	EIF3I_HUMAN	92	2,6099	2	69,452	20	49,296	26	3,2303	2	13,171	10	30,746	21	23,918	16
DDX3X	A0A087WU32_HUMAN	73	2,6099	2	69,814	29	48,571	28	15,075	10	121,84	35	86,088	33	34,88	26
IQGAP1	IQGA1_HUMAN	189	2,6099	2	74,662	53	48,571	51	52,761	40	86,955	50	78,182	57	81,719	61
CCT5	TCPE_HUMAN	60	0	0	16,484	13	47,846	31	0	0	3,2929	2	27,737	24	0	0
SNRNP200	U520_HUMAN	245	0	0	75,632	45	47,846	53	39,84	32	73,541	52	69,397	58	66,771	52
HDLBP	A0A024R4F5_HUMAN	141	0	0	15,514	16	47,121	44	0	0	2,1952	2	5,2707	6	0	0
SERBP1	PAIRB_HUMAN	45	6,5247	2	42,664	20	47,121	23	11,844	7	132,81	27	69,397	22	62,786	24
SLC25A5	ADT2_HUMAN	33	10,44	2	43,034	4	47,121	5	127,06	6	37,319	5	44,801	5	99,658	6
CCT7	TCPH_HUMAN	59	5,2198	2	19,393	14	44,221	25	3,2303	3	0	0	20,204	17	7,9726	8
ROCK1	ROCK1_HUMAN	158	0	0	29,089	29	44,221	46	0	0	6,5857	6	9,6629	9	0	0
CCT6A	TCPZ_HUMAN	58	0	0	10,666	10	42,771	20	2,1555	2	2,1952	2	20,204	15	5,3795	6
HNRNPU	HNRPU_HUMAN	91	0	0	115,39	27	42,771	21	29,072	16	217,33	33	90,48	27	68,764	25
STK38L	STK38_HUMAN	54	0	0	13,575	7	42,771	16	0	0	0	0	21,083	13	8,9692	5
SMAP2	GLYM_HUMAN	56	0	0	2,9089	3	42,096	19	0	0	7,6834	7	7,0276	8	3,9863	4
SLC25A6	ADT3_HUMAN	33	6,5247	5	40,725	12	41,321	13	111,98	16	29,636	12	36,016	14	85,706	15
DDX17	A1W2P051_HUMAN (+	80	0	0	54,3	20	40,596	18	25,842	10	103,18	24	85,21	26	40,86	17
EIF4ENIF1	4ET_HUMAN	108	2,6099	2	100,84	35	40,596	30	1 953,2	62	114,15	38	22,84	18	1 829,7	61
NAA15	NAA15_HUMAN	101	0	0	14,545	14	40,596	30	2,1555	2	14,269	12	17,569	15	4,9829	5
ATP1A1	AT1A1_HUMAN	113	0	0	16,484	10	39,871	24	6,4605	5	18,66	12	23,718	17	11,959	9
AFDN	AFAD_HUMAN	207	0	0	11,636	12	39,146	41	0	0	3,2929	3	28,11	29	38,867	35
EPRS	SYEP_HUMAN	171	0	0	19,393	20	39,146	36	6,4605	6	10,976	9	13,177	14	7,9726	8
NONO	NONO_HUMAN	54	0	0	32,068	17	39,146	17	17,228	11	57,076	19	107,17	18	55,808	19
CAD	R3VPD4_HUMAN (+1)	236	0	0	10,666	9	38,422	45	58,145	45	8,781	8	14,934	17	28,901	29
RANBP2	RBP2_HUMAN	358	0	0	6,7875	5	38,422	48	0	0	9,8786	9	17,569	18	2,9897	3
HSPA9	GRP75_HUMAN	74	15,659	5	28,12	20	37,697	28	251,96	41	77,931	33	43,922	30	113,61	39
ACLY	ACLY_HUMAN	121	0	0	3,8786	4	36,972	33	0	0	2,1952	2	7,906	9	4,9829	5
DHX15	DHX15_HUMAN	91	0	0	14,545	11	36,972	24	24,765	19	23,05	13	36,016	24	11,959	10
EIF3C	EIF3C_HUMAN	105	0	0	40,725	27	36,972	26	2,1555	2	13,171	11	29,867	22	22,921	19
MAP1	E7EVA0_HUMAN	245	0	0	14,545	13	36,972	30	0	0	6,5857	6	14,055	12	5,3795	6
TLN1	TLN1_HUMAN	270	0	0	0	0	36,247	46	0	0	0	0	1,7569	2	0	0
SFPQ	SFPQ_HUMAN	76	0	0	52,968	19	35,522	17	2,1555	2	38,417	18	75,547	22	24,914	16
TUBB6	TBB6_HUMAN	50	0	0	0	0	35,522	4	93,678	10	34,026	6	33,381	5	58,798	9
USAP2L	UBP2L_HUMAN	115	0	0	69,935	24	35,522	22	0	0	64,76	24	36,016	23	10,962	10
ATP5A1	ATPA_HUMAN	60	10,44	3	11,636	10	34,797	18	16,151	10	17,562	12	18,947	15	22,921	14
SLC25A4	ADT1_HUMAN	33	0	0	31,028	7	34,797	3	90,448	3	27,441	3	29,867	3	69,761	4
SMC3	SMC3_HUMAN	142	0	0	50,421	37	34,797	38	8,614	8	10,976	7	15,812	17	7,9726	8
SND1	SND1_HUMAN	102	0	0	3,8786	4	34,797	31	0	0	5,4881	5	11,42	13	2,9897	3
HNRNPM	HNRPM_HUMAN	78	3,9148	3	16,484	16	34,072	25	88,294	28	43,905	24	57,098	32	17,938	15
DDX1	DDX1_HUMAN	82	0	0	19,393	18	33,347	28	2,1555	2	21,962	18	31,624	25	7,9726	8
ILF3	ILF3_HUMAN	95	0	0	21,332	18	32,622	21	25,842	17	87,322	31	108,93	35	77,733	35
OTUD4	OTUD4_HUMAN	124	0	0	55,877	23	32,622	31	0	0	5,4881	4	18,447	19	0	0
UPF1	RENT1_HUMAN	124	0	0	1,9393	2	32,622	36	2,1555	2	3,2929	3	3,5138	4	0	0
VAS1	SYVC_HUMAN	140	0	0	19,393	13	32,622	27	0	0	9,8786	6	11,42	13	1,9932	2
KIF11	KIF11_HUMAN	119	0	0	0	0	31,897	34	0	0	0	0	0	0	0	0
LSM14A	LS14A_HUMAN	51	2,6099	2	658,38	40	31,897	17	68,912	21	923,1	41	29,867	16	57,802	20
PRPF8	PRP8_HUMAN	274	0	0	69,935	49	31,897	37	13,998	13	60,569	50	48,315	48	35,877	33
SF3B3	SF3B3_HUMAN	136	0	0	7,7571	6	31,897	24	10,382	14	9,8786	8	9,6629	8	4,9829	5
GCN1	GCN1_HUMAN	293	0	0	6,7875	6	31,172	40	5,3838	5	7,6834	7	20,204	22	10,962	11
PHB2	I3KPK7_HUMAN (+1)	33	2,6099	2	13,575	12	31,172	16	10,768	10	9,8786	9	21,083	16	4,9829	5
PRPF31	PRP31_HUMAN	55	0	0	34,907	16	31,172	18	13,998	11	130,62	22	141,43	20	52,682	20
SYNCRIP	HNRPQ_HUMAN	70	3,9148	2	39,877	13	31,172	14	19,382	8	126,23	22	74,668	19	36,873	15
COPB2	COPB2_HUMAN	102	0	0	14,545	12	30,447	21	5,3838	4	9,8786	9	15,812	15	12,956	13
EIF3L	EIF3L_HUMAN (+1)	71	2,6099	2	31,028	18	30,447	20	8,614	8	6,5857	6	19,326	17	19,932	16
HUWE1	HUWE1_HUMAN	482	0	0	13,575	12	30,447	41	0	0	10,976	10	36,895	39	7,9726	8
USP7	UBP7_HUMAN	128	0	0	21,332	16	30,447	36	9,6908	9	9,8786	9	16,691	18	7,9726	8
RIOK1	RIOK1_HUMAN	66	0	0	86,298	20	29,722	17	0	0	63,662	17	49,922	16	7,9726	6
RPS3A	RS3A_HUMAN	30	3,9148	3	73,771	11	29,722	14	38,763	15	37,319	16	30,746	13	12,956	10
SMC1A	SMC1A_HUMAN	143	0	0	43,034	37	29,722	33	4,307	4	28,538	25	21,961	24	13,952	12
TMPO	LAP2A_HUMAN	75	2,6099	2	11,636	6	29,722	25	0	0	14,269	6	23,718	12	12,956	8
HMGB1	HMG1_HUMAN (+1)	25	5,2198	2	4,8482	2	28,997	11	0	0	4,3305	3	9,6629	8	4,9829	4
PKP4	PKAP_HUMAN	86	0	0	20,362	16	28,997	23	22,612	17	28,538	17	29,867	25	27,804	16
CUL3	CUL3_HUMAN	89	0	0	1,9393	2	28,272	29	3,2303	3	0	0	4,3522	5	0	0
EEF2	EF2_HUMAN	95	10,44	5	15,514	13	28,272	20	5,3838	5	6,5857	6	3,5138	4	4,9829	4
SMC4	SMC4_HUMAN	147	0	0	31,028	27	28,272	27	0	0	10,976	10	8,7845	8	12,956	13
YBX1	YBOX1_HUMAN	36	0	0	31,998	11	28,272	9	11,844	7	71,346	12	37,773	12	26,908	11
CAMSAP3	CAMP3_HUMAN	135	3,9148	3	55,877	29	27,548	28	0	0	39,514	29	65,005	39	44,846	28
EIF3F	EIF3F_HUMAN	52	0	0	30,059	16	27,548	20	20,458	14	18,66	13	28,989	20	41,856	20
PSMC2	PRS7_HUMAN	49	0	0	15,514	15	27,548	20	7,5375	7	6,5857	6	18,447	16	6,9761	7
TARS	SYTC_HUMAN	83	0	0	2,9089	3	27,548	25	0	0	0	0	6,1491	7	0	0
ELP1	ELP1_HUMAN	150	0	0	3,8786	3	26,823	24	19,382	15	5,4881	5	6,1491	7	22,921	20
TMPO	LAP2B_HUMAN	51	0	0	20,362	6	26,823	8	0	0	28,538	7	30,746	7	23,918	8
ATP2A2	AT2A2_HUMAN	115	2,6099	2	14,545	10	26,098	19	10,768	8	13,171	10	10,541	9	9,9658	9
HERC1	HERC1_HUMAN	282	15,659	5	19,393	13	26,098	14	13,998	7	9,8786	5	50,072	28	300,97	38

IMPDH2	IMDH2_HUMAN	56	0	0	8,7267	8	26,098	20	3,2303	3	7,6854	7	20,204	16	9,9658	9
NSUN2	NSUN2_HUMAN	86	0	0	21,332	19	26,098	22	0	0	19,757	17	15,812	15	9,9658	9
PSMD2	PSMD2_HUMAN	100	0	0	15,514	14	26,098	23	0	0	4,3305	4	5,2707	6	0	0
RPL5	RL5_HUMAN	36	9,1348	4	10,666	9	26,098	13	0	0	29,636	13	30,746	13	0	0
SMC2	SMC2_HUMAN	136	0	0	23,271	17	26,098	35	0	0	3,2929	3	14,934	16	2,9897	3
SUPV3L	SPV3M_HUMAN	121	0	0	0	0	26,098	28	0	0	0	0	3,5138	4	0	0
TNRC6B	TNR6B_HUMAN	194	0	0	3,8786	4	26,098	30	0	0	2,1952	2	11,42	12	0	0
CASP2	E7ER18_HUMAN (+1)	166	3,9148	3	46,543	29	25,373	28	13,998	11	58,174	33	44,801	36	34,88	27
RUS	RUS_HUMAN	53	2,6099	2	29,089	11	25,373	9	5,3838	4	71,346	11	43,922	10	19,932	9
PI4KA	PI4KA_HUMAN	237	0	0	0	0	25,373	30	0	0	2,1952	2	5,2707	6	3,9863	4
PSMD3	PSMD3_HUMAN	61	0	0	5,8178	6	25,373	24	20,458	14	10,976	9	17,569	18	8,9692	9
RPS6K	KS6A_HUMAN	30	11,744	5	35,877	10	25,373	10	31,226	10	59,272	13	22,84	12	25,911	12
AP1B1	AP1B1_HUMAN	105	0	0	19,393	18	24,648	28	8,614	7	8,781	8	8,7845	10	12,956	12
CKAP4	CKAP4_HUMAN	66	0	0	20,362	15	24,648	20	36,61	21	10,976	10	38,652	23	31,891	26
HNRNPR	HNRPR_HUMAN	71	3,9148	2	22,302	14	24,648	18	16,151	12	130,62	30	87,845	32	41,856	22
MSH6	MSH6_HUMAN	153	0	0	25,211	22	24,648	25	0	0	25,245	22	14,934	16	10,962	11
PSMD1	PSMD1_HUMAN	106	0	0	9,6964	7	24,648	23	0	0	2,1952	2	2,6353	3	0	0
SF3A1	SF3A1_HUMAN	89	0	0	2,9089	3	24,648	23	0	0	0	0	3,5138	4	0	0
EIF3J	EIF3J_HUMAN	66	0	0	29,089	17	23,923	17	24,765	12	15,66	10	36,016	19	28,903	21
KLC1	KLC1_HUMAN	71	0	0	8,7267	5	23,923	17	0	0	3,2929	3	21,083	12	11,959	8
PA2G4	PA2G4_HUMAN	66	0	0	9,6964	10	23,923	17	0	0	14,269	11	18,447	14	11,959	11
SLK	STK2_HUMAN	143	0	0	13,575	14	23,923	21	0	0	8,781	8	6,1491	7	0	0
DNMT1	DNMT1_HUMAN	183	0	0	11,636	10	23,198	24	0	0	13,171	10	32,503	31	10,962	11
BTTD2	USS1_HUMAN	109	0	0	34,998	23	23,198	26	6,4605	5	20,855	16	20,204	19	7,9726	6
SF3B1	SF3B1_HUMAN	146	0	0	20,362	13	23,198	27	5,3838	5	35,124	23	25,475	23	13,952	14
SPTN1	SPTN1_HUMAN	30	0	0	9,6964	8	23,198	12	0	0	4,3305	4	19,326	12	6,9761	7
ABCF1	ABCF1_HUMAN	67	0	0	8,7267	7	22,473	16	4,307	4	14,269	11	12,298	10	5,3795	5
DSG1	DSG1_HUMAN	114	26,099	9	44,603	16	22,473	17	19,382	10	2,1952	2	36,895	22	103,64	28
IARS	SYIC1_HUMAN	132	0	0	13,575	14	22,473	27	5,3838	5	2,1952	2	5,2707	5	0	0
PSMD11	PSD11_HUMAN	47	0	0	7,7571	8	22,473	19	0	0	0	0	7,0276	8	0	0
ATAD3A	AT3A_HUMAN	71	6,5247	5	21,332	14	21,748	18	11,537	27	21,952	14	27,232	17	46,839	25
DUS4L	DUS4L_HUMAN	104	0	0	0	0	21,748	21	0	0	0	0	7,906	9	0	0
CYFIP1	CYFP1_HUMAN	145	0	0	0	0	21,748	24	0	0	0	0	0	0	0	0
EIF3I	EIF3I_HUMAN	37	0	0	24,241	12	21,748	14	0	0	15,367	10	19,326	12	0	0
EPB41L2	E41L2_HUMAN	113	0	0	39,755	27	21,748	26	0	0	38,417	24	23,718	21	6,9761	6
GART	PUR2_HUMAN	108	0	0	1,9393	2	21,748	29	0	0	0	0	0	0	0	0
MSN	MOES_HUMAN	68	2,6099	2	3,8786	4	21,748	23	0	0	0	0	13,177	12	3,9863	4
SRST	SRST_HUMAN	101	0	0	7,7571	8	21,748	23	0	0	10,976	10	17,569	19	3,9863	4
XRCC6	XRCC6_HUMAN	70	2,6099	2	12,605	12	21,748	19	6,4605	6	14,269	11	43,922	27	10,962	10
AP2B1	AP2B1_HUMAN	105	0	0	28,12	11	21,023	10	15,075	6	21,952	11	14,055	8	20,928	8
DAPH1	DAD2IH68_HUMAN (+	141	0	0	2,9089	3	21,023	24	0	0	3,2929	3	0	0	0	0
EIF2S3	IF2G_HUMAN	51	0	0	7,7571	7	21,023	14	11,844	10	24,148	14	32,503	17	24,914	15
EIF3F	EIF3F_HUMAN	58	0	0	22,302	9	21,023	11	3,2303	3	6,5857	5	15,812	8	12,956	9
FMC1	FMC1_HUMAN	112	0	0	6,8482	5	21,023	13	0	0	9,8786	9	8,7845	8	5,3795	5
KIAA0368	EBKN1G_HUMAN	224	0	0	9,6964	10	21,023	23	0	0	3,2929	3	7,0276	8	3,9863	4
LETM1	LETM1_HUMAN	85	0	0	13,575	14	21,023	20	0	0	20,855	17	25,718	19	14,949	14
G3BP1	G3BP1_HUMAN	52	0	0	22,302	13	20,298	12	2,1535	2	40,612	17	55,342	16	26,908	13
HNRNPA2B1	ROA2_HUMAN	57	6,5247	2	14,545	11	20,298	12	10,768	7	148,18	19	65,005	17	9,9658	7
MAGED2	MAGD2_HUMAN	65	0	0	15,514	12	20,298	19	9,6908	8	20,855	15	22,84	19	14,949	14
NCKAP1	NCKP1_HUMAN	129	0	0	0	0	20,298	21	0	0	0	0	1,7569	2	0	0
PTK2	FAK1_HUMAN	85	0	0	0	0	20,298	10	12,921	6	8,781	6	7,906	3	3,9658	3
RDX	RADI_HUMAN	69	0	0	1,9393	2	20,298	13	0	0	2,1952	2	9,6629	4	0	0
ROCK2	ROCK2_HUMAN	161	0	0	0	0	20,298	19	0	0	0	0	0	0	0	0
RPS5	RS5_HUMAN (+1)	22	7,8297	4	41,694	11	20,298	10	9,6908	7	40,612	10	30,746	9	22,921	10
SLC25A3	MPCP_HUMAN	40	0	0	6,7875	3	20,298	8	67,856	11	15,367	5	21,961	8	31,891	10
XRCC5	XRCC5_HUMAN	83	5,2198	4	11,636	12	20,298	15	4,307	4	13,171	11	39,53	27	1,9932	2
C11orf84	Q93UA3_SPNDC_HUM	?	0	0	2,9089	3	19,573	15	0	0	2,1952	2	14,055	12	1,9932	2
COPS1	COPS_HUMAN	107	0	0	5,8178	6	19,573	23	8,614	8	3,2929	3	9,6629	11	0	0
DIS3	RRP44_HUMAN	109	0	0	0	0	19,573	24	0	0	4,3305	4	7,0276	8	0	0
EIF2S1	IF2A_HUMAN	36	3,9148	2	13,575	9	19,573	12	8,614	6	23,05	10	21,961	15	0	0
EPB41	41_HUMAN	97	0	0	20,362	15	19,573	16	0	0	7,6854	6	7,906	6	6,9761	6
HNRNPA1	ROA1_HUMAN	39	3,9148	3	19,393	10	19,573	12	18,305	7	127,32	20	64,127	21	9,9658	6
LONP1	LONM_HUMAN	106	0	0	2,9089	3	19,573	22	0	0	3,2929	3	7,0276	8	1,9932	2
PPIB	PPIB_HUMAN	24	2,6099	2	7,7571	6	19,573	11	7,5373	7	3,2929	3	9,6629	8	7,9726	8
PRPF8	PRP8_HUMAN	107	0	0	28,12	23	19,573	22	5,3838	5	23,05	19	17,569	19	5,3795	6
TBC1D4	TBCD4_HUMAN	147	0	0	27,15	25	19,573	25	0	0	18,66	17	16,691	19	6,9761	7
USP9X	USP9X_HUMAN	292	0	0	6,8482	5	19,573	25	383,33	106	5,4881	5	2,6353	3	57,802	50
WDR77	MEP50_HUMAN	37	3,9148	3	63,077	11	19,573	8	13,998	7	86,712	11	22,84	10	0	0
XPO1	XPO1_HUMAN	123	0	0	6,8482	5	19,573	23	0	0	4,3305	4	3,5138	4	0	0
39326	SPT2_HUMAN	51	0	0	0	0	18,848	17	0	0	0	0	0	0	0	0
DHX38	PRP16_HUMAN	141	0	0	21,332	14	18,848	21	0	0	15,367	9	45,679	34	12,956	11
DNAJA1	DNJA1_HUMAN	45	0	0	10,666	7	18,848	13	17,228	10	12,074	6	16,691	12	22,921	14
HIST1H4	H4_HUMAN	80	0	0	83,389	26	18,848	15	0	0	12,074	7	8,7845	9	0	0
JUP	PLAK_HUMAN	82	26,099	5	38,786	19	18,848	13	13,998	7	4,3305	4	38,652	24	43,849	17
MTHFD1L	C1TM_HUMAN	106	0	0	10,666	11	18,848	24	0	0	2,1952	2	1,7569	2	0	0
NARS	SYNC_HUMAN	63	0	0	0	0	18,848	14	0	0	0	0	2,6353	3	0	0
POLA1	DPOLA_HUMAN	166	0	0	2,9089	3	18,848	20	0	0	0	0	12,298	13	0	0
PRMT1	ANM1_HUMAN (+2)	42	0	0	41,985	25	18,848	13	8,614	8	334,05	25	53,585	20	1,9932	2
PRKCA	PRKCA_HUMAN	229	0	0	55,877	30	18,848	25	2,1535	2	36,222	29	43,922	39	29,897	29
PTBP1	PTBP1_HUMAN	57	0	0	0	0	18,848	17	0	0	10,976	7	20,204	14	4,9829	4
AIFM1	AIFM1_HUMAN	67	0	0	2,9089	3	18,123	15	34,456	13	3,2929	3	12,298	12	31,891	19
AP3B1	AP3B1_HUMAN	121	0	0	2,9089	3	18,123	22	0	0	0	0	9,6629	11	1,9932	2
EIF3S3	EI3S3_HUMAN (+1)	42	0	0	29,089	14	18,123	13	3,2303	3	14,269	11	14,055	11	1,9932	2
FKR1	FKR1_HUMAN	70	0	0	36,846	22	18,123	17	25,842	17	109,76	35	45,044	27	24,914	22
GFM1NS	GFMIS_HUMAN	169	0	0	11,636	12	18,123	18	0	0	4,3305	4	12,298	13	10,962	11
KIF5C	KIF5C_HUMAN	109	0	0	11,636	4	18,123	8	0	0	0	0	8,7845	3	7,9726	2
KLC2	KLC2_HUMAN	69	0	0	16,545	10	18,123	21	0	0	4,3305	4	26,597	23	18,935	16
NPM1	NPM_HUMAN	33	0	0	6,7875	5	18,123	10	21,535	8	15,367	7	30,746	13	2,9897	2
PRPS1	PRPS1_HUMAN	35	0	0	1,9393	2	18,123	12	10,768	8	3,2929	2	5,5138	4	0	0
RPS16	RS16_HUMAN	16	10,44	5	30,059	10	18,123	11	19,382	10	47,198	11	26,597	11	18,935	10
RPS19	RS19_HUMAN	16	3,9148	3	24,241	11	18,123	12	7,5373	6	40,612	12	30,746	11	11,959	9
RPS2	RS2_HUMAN	31	14,354	4	62,057	12	18,123	10	30,149	12	69,15	14	21,083	12	22,921	12
SPAG9	QA0B7Q28_HUMAN (+	145	0	0	0	0	18,123	17	0	0	0	0	0	0	0	0
TAB2	TAB2_HUMAN	76	0	0	0	0	18,123	16	0	0	2,1952	2	4,3922	4	0	0
UFL1	UFL1_HUMAN	90	0	0	11,636	12	18,123	22	4,307	4	18,66	16	26,353	21	8,9692	8
AP2A1	AP2A1_HUMAN	108	0	0	22,302	22	17,398	21	19,382	16	24,148	20	14,055	16	23,918	22
EIF1C	EI1C_HUMAN	50	2,6099	2	6,7875	7	17,398	12	4,307	4	9,8786	6	10,541	9	10,962	10
PSMD12	PSD12_HUMAN	53	0	0	7,7571	5	17,398	13	0	0	2,1952	2	2,6353	3	0	0
RPL38	RL38_HUMAN	8	5,2198	2	6,7875	5	17,398	5	12,921	5	21,952	5	17,569	5	10,962	5
SRC63	SRC63_HUMAN	88	0	0	16,484	15	17,398	18	0	0	24,148	18	21,083	20	4,9829	5
ZC3HAV1	ZCCHV_HUMAN	101	0	0	1,9393	2	17,398	18	31,226	18	20,855	15	21,083	15	11,959	9
DHX30	DHX30_HUMAN (+1)	134	0	0	5,8178	5	16,673	22	21,535	17	29,636	23	17,569	18	2,9897	3
DNAJA2	DNJA2_HUMAN	46	0	0	8,7267	7	16,673	11	19,382	12	9,8786	5	14,055	10	16,942	11
DOCK7	DOCK7_HUMAN	243	0	0	11,636	10	16,673	22	0	0	3,2929	3	21,961	24	6,9761	7
EIF3C	EIF3C_HUMAN	29	0	0	17,453	12	16,673	13	3,2303	3	4,3305	3	14,055	11	5,3795	5
EIF4G3	AGADU1RQ7_HUMAN	195	0	0	10,666	5	16,673	13	0	0	0	0	14,055	7	0	0
ELAC2	RNZ2_HUMAN	92	0	0	7,7571	7	16,673	14	0	0	4,3305	4	5,2707	6	1,9932	2
HNRNPL	HNRPL_HUMAN	64	3,9148	3	12,605	9	16,673	14	3,2303	3	49,393	21	44,801	21	15,932	15
KPNA2	IMA1_HUMAN	58	0	0	6,8482	4	16,673	13	7,5373	5	10,976	8	13,177	9	8,9692	9
NAA10	NAA10_HUMAN	26	0	0	3,8786	4	16,673	15	0	0	2,1952	2	7,906	8	0	0
PHB	PHB_HUMAN	30	0	0	9,6964	10	16,673	13	6,4605	6	8,781	7	7,906	8	5,3795	5
PSMC5	PSB8_HUMAN	46	0	0	12,605	12	16,673	16	0	0	6,5857	5	11,42	11	3,9863	3
SRF1	SRSF3_HUMAN (+1)	208	0	0	18,423	13	16,673	21	13,998	13	24,148	22	30,746	31	23,918	23
TCOF1	TCOF_HUMAN	152	0	0	6,8482	4	16,673	17	0	0	9,8786	9	14,934	17	1,9932	2
TRMT10C	Q7Z7J3_TMT1C_HUM	?	0	0	19,393	15	16,673	15	0	0	26,343	16	21,961	17	0	0
TXLNA	TXLNA_HUMAN	62	0	0	7,7571	8	16,673	19	0	0	0	0	11,42	13	9,9658	9
YARS	SYYC_HUMAN	59	0	0	1,9393	2	16,673	20	0	0	0	0	7,0276	8	0	0
AP1G1	AP1G1_HUMAN	91	0	0	2,9089	3	15,949	15	0	0	0	0	0	0	0	0
AP2A2	AP2A2_HUMAN	104	0	0	16,484	9	15,949	10	0	0	12,074	3	6,1491	3	10,962	2
DARS	SYDC_HUMAN	57	0	0	2,9089	3	15,949	15	15,075	8	2,1952	2	7,906	9	2,9897	3
EIF4G2	DDX9Q9_HUMAN (+1)	102	0	0	1,9393	2	15,949	20	0	0	0	0	2,6353	3	0	0
HSPD1	CH60_HUMAN	61	32,624	13	6,7875	6	15,949	12	770,96	50	5,4881	4	7,906	9	325,88	47
MSH2	MSH2_HUMAN	105	0	0	7,7571	8	15,949	19	0	0	4,3305	4	12,298	14	3,9863	4
NONO	CYH2_HUMAN	114	0	0	3,8786	4	15,949	20	0	0	2,1952	2	5,2707	6	0	0
NCAPH	CAPH2_HUMAN	82	0	0	5,8178	6	15,949	14	0	0	0	0	1,7569	2	0	0
RAN	RAN_HUMAN	26	7,8297	5	21,332	5	15,949	6	8,614	5	18,66	5	18,447	7	10,962	5
RPLP0	RLA0_HUMAN	36	0	0	8,7267	7	15,949	11	30,149	10	18,484	8	19,326	11	0	0

TPR	TPR_HUMAN	267	0	0	0	0	0	15,949	22	0	0	0	0	0	0	0	0	0	0
CCAR1	CCAR1_HUMAN	133	0	0	10,666	9	15,224	15	0	0	0	0	0	5,2707	5	0	0		
CCAR2	CCAR2_HUMAN	103	0	0	20,362	18	15,224	18	0	0	12,074	10	10,541	11	16,942	15			
COPG2	COPG2_HUMAN	98	0	0	3,8786	4	15,224	18	3,2303	2	0	0	3,5138	3	0	0			
EIF2S2	IF2B_HUMAN	38	0	0	16,484	8	15,224	15	7,5373	7	29,636	17	35,138	17	18,935	12			
EWSR1	EWS_HUMAN	68	0	0	18,423	7	15,224	8	8,614	5	27,441	7	20,204	7	8,9692	5			
CHD1	CHD1_HUMAN	61	0	0	0	0	15,224	18	19,382	11	0	0	5,2707	6	6,3761	7			
IGF2BP1	IF2B1_HUMAN	63	0	0	11,636	11	15,224	12	31,226	15	38,417	18	48,315	24	17,938	15			
ILF2	B4DYD8_HUMAN (+1)	39	2,6099	2	13,575	10	15,224	12	23,689	11	51,588	17	75,547	18	36,873	15			
OPA1	OPA1_HUMAN	114	0	0	4,8482	5	15,224	15	0	0	2,1952	2	0	0	0	0			
PDS5A	PDS5A_HUMAN	151	0	0	16,484	14	15,224	19	0	0	17,562	11	8,7845	10	0	0			
SKIV2L2	SKI2_HUMAN	118	0	0	1,9393	2	15,224	18	0	0	3,2929	3	9,6629	11	1,9932	2			
SRPR2	SRPR2_HUMAN	75	0	0	21,332	13	15,224	14	5,3858	5	17,562	10	20,204	13	14,949	12			
ATP2B1	AT2B1_HUMAN	139	0	0	2,9089	3	14,499	13	0	0	7,6854	7	5,2707	5	4,9829	5			
CAPRIN1	CAPR1_HUMAN	78	0	0	18,423	11	14,499	11	3,2303	3	23,05	13	20,204	14	13,952	9			
EPB41L3	A0A0A0MRA8_HUMAN	102	0	0	24,241	19	14,499	17	0	0	17,562	15	43922	4	3,9863	4			
FLII	FLII_HUMAN	145	0	0	15,514	13	14,499	19	37,686	24	40,612	25	7,0276	8	27,904	23			
GFPT1	GFPT1_HUMAN	79	0	0	3,8786	4	14,499	19	0	0	0	0	5,2707	5	1,9932	2			
HADHA	ECHA_HUMAN	83	0	0	20,362	17	14,499	18	26,919	19	18,86	16	29,867	25	18,832	28			
HNRNPD	HNRPD_HUMAN	38	0	0	8,7267	7	14,499	11	0	0	40,612	12	28,11	13	15,945	9			
OSBP	OSBP1_HUMAN	89	0	0	9,6964	9	14,499	12	0	0	2,1952	2	5,2707	5	0	0			
PKM	KPYM_HUMAN	58	23,489	8	0	0	14,499	15	4,307	4	0	0	2,6353	2	2,9897	3			
PKN2	PKN2_HUMAN	112	0	0	3,8786	4	14,499	17	0	0	7,6854	7	6,1491	7	0	0			
POLD1	DPOD1_HUMAN (+1)	124	0	0	23,271	21	14,499	19	0	0	34,026	25	21,083	23	12,958	13			
PSMC1	PSA6_HUMAN	49	0	0	5,8178	5	14,499	14	0	0	0	0	7,906	7	0	0			
RNF40	BRE1B_HUMAN	114	0	0	0	0	14,499	17	0	0	0	0	0	0	0	0			
RTCB	RTCB_HUMAN	55	0	0	15,514	14	14,499	17	6,4605	5	27,441	14	20,204	16	14,949	13			
VIM	VIME_HUMAN	56	13,049	10	14,545	14	14,499	17	54,915	25	21,952	16	22,84	21	37,87	24			
WDHD1	WDHD1_HUMAN	126	0	0	0	0	14,499	16	0	0	0	0	0	0	0	0			
AMPD2	HDF360_HUMAN	99	0	0	6,7875	7	13,774	12	0	0	0	0	1,7569	2	0	0			
COPG1	COPG1_HUMAN	98	0	0	0	0	13,774	10	4,307	4	0	0	3,5138	4	0	0			
CSDE1	CSDE1_HUMAN	89	0	0	0	0	13,774	15	166,9	44	0	0	0	0	44,846	27			
DDX42	DDX42_HUMAN	103	0	0	0	0	13,774	14	0	0	0	0	43922	5	0	0			
EIF3M	EI3M_HUMAN	43	0	0	18,423	11	13,774	12	0	0	7,6854	6	13,177	9	0	0			
EIF5A	A0A87WUT6_HUMAN (+	139	0	0	1,9393	2	13,774	18	2,1535	2	27,441	22	30,746	28	8,9692	9			
HYOU1	HYOU1_HUMAN	111	0	0	2,9089	3	13,774	15	0	0	3,2929	3	6,1491	7	0	0			
LARP1	LARP1_HUMAN	124	0	0	18,423	15	13,774	17	5,3858	5	39,514	24	29,867	28	12,956	11			
LRRC59	LRC59_HUMAN	59	0	0	12,605	8	13,774	10	13,998	10	21,952	9	22,84	10	33,894	13			
NDUFS1	NDUS1_HUMAN	79	0	0	5,8178	6	13,774	19	5,3858	5	2,1952	2	5,2707	6	2,9897	3			
PRPF19	PRP19_HUMAN	55	0	0	3,8786	4	13,774	14	26,919	11	14,269	9	19,326	14	21,925	13			
PSMC4	PRS6B_HUMAN	47	0	0	5,8178	6	13,774	13	0	0	3,2929	3	43922	4	0	0			
PYCR2	PYCR2_HUMAN	34	0	0	10,666	7	13,774	7	19,382	9	13,171	8	7,0276	6	6,3761	6			
RNF20	BRE1A_HUMAN	114	0	0	1,9393	2	13,774	17	0	0	0	0	0	0	0	0			
RPS6KA3	KS6A3_HUMAN	86	0	0	0	0	13,774	16	0	0	0	0	1,7569	2	0	0			
RPS9	A0A2R4M0_HUMAN (+	23	0	0	32,968	11	13,774	10	13,998	9	40,612	13	14,055	11	8,9692	9			
RUVBL1	RUVB1_HUMAN	50	0	0	1,9393	2	13,774	13	123,83	24	9,8786	9	7,0276	8	62,781	24			
SRP68	SRP68_HUMAN	71	0	0	25,211	22	13,774	17	12,921	12	19,757	16	28,589	26	16,942	17			
YBX3	YBOX3_HUMAN	40	0	0	0	0	13,774	5	8,614	6	40,612	7	22,84	7	18,935	5			
BCAP31	BCAP1_HUMAN	106	0	0	8,7267	4	13,049	7	2,1535	2	7,6854	5	6,1491	5	2,9897	3			
CNOT1	CNOT1_HUMAN	267	0	0	0	0	13,049	18	5,3858	5	0	0	0	0	2,9897	3			
CTNND1	CTND1_HUMAN (+1)	105	0	0	1,9393	2	13,049	14	0	0	0	0	0	0	0	0			
DNAJC13	DJC13_HUMAN	254	0	0	0	0	13,049	18	0	0	0	0	0	0	0	0			
FARSA	SYFB_HUMAN (+1)	62	0	0	4,8482	4	13,049	12	17,228	9	6,5857	4	12,298	10	13,952	10			
FEN1	FEN1_HUMAN	43	0	0	6,8482	4	13,049	10	0	0	7,6854	6	12,298	10	3,9863	4			
GAPVD1	GAPD1_HUMAN	165	0	0	1,9393	2	13,049	16	0	0	0	0	5,2707	6	0	0			
HECTD1	HECD1_HUMAN	289	0	0	3,8786	2	13,049	18	0	0	0	0	6,1491	7	0	0			
HSD17B10	HCD2_HUMAN	27	0	0	3,8786	2	13,049	10	0	0	0	0	0	0	0	0			
MATR3	A8MXP9_HUMAN	100	0	0	16,484	14	13,049	15	8,614	7	85,615	31	122,98	35	99,658	31			
NCAPD2	CND1_HUMAN	157	0	0	18,423	18	13,049	16	0	0	2,1952	2	1,7569	2	0	0			
PFKM	PFKAM_HUMAN	85	0	0	5,8178	3	13,049	11	9,6908	5	9,8786	7	14,055	12	8,9692	3			
PSMC3	PRS6A_HUMAN (+1)	49	0	0	5,8178	6	13,049	15	0	0	0	0	1,7569	2	0	0			
PSMD6	PSMD6_HUMAN	46	0	0	4,8482	5	13,049	15	0	0	0	0	1,7569	2	0	0			
RARS	SYRC_HUMAN	75	0	0	3,8786	4	13,049	16	3,2303	3	0	0	14,055	16	1,9932	2			
RCC1	RCC1_HUMAN	45	0	0	2,9089	3	13,049	12	0	0	5,4881	4	7,906	8	4,9829	5			
RPL7	RL7_HUMAN	29	5,2198	2	6,7875	7	13,049	10	35,533	13	18,86	11	18,447	13	8,9692	9			
RPS14	RS14_HUMAN	16	5,2198	3	19,353	7	13,049	8	9,6908	5	16,464	7	18,447	6	4,9829	4			
SCRIB	A0A2J8X2_HUMAN (+	175	0	0	1,9393	2	13,049	17	3,2303	3	0	0	0	0	1,9932	2			
SSB	LA_HUMAN	47	0	0	3,8786	4	13,049	13	4,307	4	13,171	10	18,447	14	5,3795	6			
TCEB1	TCB1_HUMAN	124	0	0	6,7875	7	13,049	15	0	0	5,4881	5	6,1491	7	0	0			
ABCF2	ABCF2_HUMAN	71	0	0	10,666	11	12,324	14	7,5373	7	17,562	15	21,083	19	15,945	13			
ACTR3	ARP3_HUMAN	47	0	0	0	0	12,324	14	0	0	0	0	2,6353	3	0	0			
BCAP31	BAP31_HUMAN	28	0	0	5,8178	4	12,324	10	2,1535	2	2,1952	2	43922	4	3,9863	4			
CCDC47	CCD47_HUMAN	56	0	0	7,7571	8	12,324	13	0	0	9,8786	8	16,691	15	8,9692	9			
CLASP1	CLAP1_HUMAN	169	0	0	24,241	21	12,324	13	0	0	25,245	17	19,326	17	4,9829	3			
CLPX	CLPX_HUMAN	69	0	0	8,7267	7	12,324	14	0	0	4,3905	4	3,5138	4	0	0			
CUL2	A0A0M7N0_HUMAN (+	89	0	0	0	0	12,324	15	4,307	3	0	0	2,6353	3	0	0			
DDX21	DDX21_HUMAN	87	0	0	6,7875	7	12,324	15	25,842	16	29,636	20	31,624	21	11,959	12			
FLG2	FILA2_HUMAN	248	13,049	2	18,423	8	12,324	6	12,921	3	17,074	5	14,934	12	48,832	20			
HMGB2	HMGB2_HUMAN	24	0	0	4,8482	2	12,324	5	0	0	0	0	5,2707	4	0	0			
HSPA14	HSP7E_HUMAN	55	0	0	0	0	12,324	15	0	0	0	0	3,5138	4	2,9897	3			
KCD12	KCD12_HUMAN	56	0	0	6,7875	7	12,324	9	0	0	5,4881	4	8,7845	7	0	0			
KLC1	KLC1_HUMAN	69	0	0	0	0	12,324	12	0	0	0	0	9,6629	7	7,9726	4			
MTA2	MTA2_HUMAN	75	0	0	8,7267	8	12,324	14	2,1535	2	4,3905	3	16,691	18	2,9897	3			
RBM26	RBM26_HUMAN	114	0	0	16,484	12	12,324	14	0	0	13,171	11	14,934	15	4,9829	4			
RBM8	RBM8_HUMAN	129	0	0	31,998	26	12,324	16	3,2303	3	77,443	36	49,193	44	15,945	16			
RPS18	RS18_HUMAN	18	15,659	6	33,937	9	12,324	8	20,458	8	34,026	9	17,569	8	26,908	9			
SLC25A11	MCP11_HUMAN (+1)	32	0	0	7,7571	7	12,324	12	35,533	15	13,171	9	12,298	11	32,891	14			
ACACA	ACACA_HUMAN	266	0	0	0	0	11,599	16	0	0	0	0	0	0	0	0			
ACSL5	ACSL5_HUMAN	80	0	0	5,8178	6	11,599	12	5,3858	4	6,5857	5	12,298	12	14,949	10			
ARCN1	COPD_HUMAN	57	0	0	8,7267	7	11,599	15	8,614	8	3,2929	3	11,42	13	2,9897	3			
ARPC2	ARPC2_HUMAN	34	0	0	1,9393	2	11,599	9	0	0	0	0	5,2707	5	0	0			
DHX16	DHX16_HUMAN	119	0	0	1,9393	2	11,599	11	0	0	15,367	9	12,298	11	0	0			
DNAJC7	DNJC7_HUMAN	72	0	0	3,8786	4	11,599	15	0	0	0	0	6,1491	7	0	0			
EIF5	IF5_HUMAN	49	0	0	0	0	11,599	12	0	0	2,1952	2	10,541	9	5,9795	6			
FANCI	FANCI_HUMAN	149	0	0	14,545	14	11,599	15	0	0	3,2929	3	0	0	0	0			
HARS	SYHC_HUMAN (+2)	57	0	0	2,9089	3	11,599	12	0	0	3,2929	3	1,7569	2	0	0			
HNRNPUL1	HNRL1_HUMAN	96	0	0	8,7267	9	11,599	10	15,075	12	6,5857	6	3,5138	4	0	0			
MARCKS	MARCS_HUMAN	32	0	0	5,8178	6	11,599	7	0	0	0	0	6,1491	5	0	0			
PPP1R12A	MYPT1_HUMAN	115	0	0	1,9393	2	11,599	15	0	0	2,1952	2	43922	5	0	0			
PRRC2C	PRC2C_HUMAN	317	0	0	21,332	15	11,599	14	3,2303	3	20,855	19	26,353	27	15,945	16			
QARS	SYQ_HUMAN	88	0	0	0	0	11,599	15	3,2303	3	0	0	2,6353	3	0	0			
RPL17	A0A7WXM6_HUMAN (-	20	0	0	23,271	8	11,599	8	11,844	6	28,538	9	16,934	8	8,9692	7			
RPS8	RS8_HUMAN	24	0	0	22,302	9	11,599	8	10,768	7	19,757	9	11,42	7	3,9863	4			
SART3	SART3_HUMAN	110	0	0	1,9393	2	11,599	16	3,2303	3	16,464	14	9,6629	11	2,9897	3			
TAB1	TAB1_HUMAN	55	0	0	1,9393	2	11,599	16	0	0	0	0	7,0276	7	0	0			
TAF15	RBP56_HUMAN	62	0	0	6,7875	2	11,599	5	0	0	30,733	7	14,055	4	0	0			
TRMT1	TRM1_HUMAN	72	0	0	6,7875	5	11,599	12	2,1535	2	6,5857	5	12,298	12	8,9692	7			
TXLNG	TXLNG_HUMAN	61	0	0	0	0	11,599	9	0	0	0	0	6,1491	7	4,9829	5			
U2AF1	U2AF1_HUMAN (+1)	28	0	0	10,666	5	11,599	6	7,5373	4	27,441	8	22,84	8	12,956	5			
AIMP1	AIMP1_HUMAN	34	0	0	1,9393	2	10,874	11	3,2303	3	2,1952	2	6,1491	6	0	0			
AP3S	AP3S1_HUMAN	58	0	0	0	0	10,874	12	2,1535	2	0	0	6,1491	7	0	0			
ATP5C1	ATPG_HUMAN	33	3,9148	3	10,666	7	10,874	9	11,844	7	13,171	8	16,934	11	14,949	9			
CLPB	CLPB_HUMAN	79	0	0	6,7875	7	10,874	13	0	0	5,4881	5	11,42	12	6,9761	7			
CYHR1	E7EVI5_HUMAN	143	0	0	0	0	10,874	3	0	0	0	0	0	0	0	0			
DARS2	SYDM_HUMAN	74	0	0	0	0	10,874	10	0	0	0	0	43922	5	0	0			
DDB1	DDB1_HUMAN	127	0	0	3,8786	3	10,874	9	48,07	22	15,367	13	6,1491	4	8,9692	8			
DHX8	DHX8_HUMAN	115	0	0	1,9393	2	10,874	13	0	0	5,4881	3	7,906	8	3,9863	4			
DNAJB11	DJB11_HUMAN	41	0	0	2,9089	3	10,874	8	10,768	9	3,2929	3	2,6353	3	1,9932	2			
EIF3I	EIF3I_HUMAN	29	0	0	0	0	10,874	10	0	0	0	0	2,6353	3	0	0			
FBXO8	FBO8L_HUMAN	141	0	0	5,8178	6	10,874	14	0	0	5,4881	5	5,2707	5	0	0			
EZR	EZRI_HUMAN	69	0	0	0	0	10,874	4	0	0	0	0	13,177	8	3,9863	2			
GGYF2	GGYF2_HUMAN	150	0	0	12,605	12	10,874	11	3,2303	3	10,976	10	43922	4	28,901	22			
LBR	LBR_HUMAN	71	0	0	40,725	13	10,874	9	13,998	8	29,636	12	14,055	8	7,9726	8			
MAP3K7	M3K7_HUMAN	67	0	0	0	0	10,874	8	0	0	0	0	7,0276	8	0	0			
MOGS	MOGS_HUMAN	92	0	0	8,7267	9	10,874	12	6,4605	6	17,562	15	17,569	12	28,901	19			
NCBP1	NCBP1_HUMAN	92	0	0	0	0	10,874	12	0	0	0	0	5,5138	4	0	0			
PLCG1	PLCG1_HUMAN	149	0	0	0	0	10,874	15	0	0	0	0	0	0	0	0			

PSMC6	SADB7X2I1_HUMAN (+	46	0	0	9,6964	10	10,874	9	0	0	3,2929	3	7,0276	8	0	0		
PSMD13	PSD13_HUMAN	43	0	0	9,6964	9	10,874	12	0	0	0	0	3,5138	4	0	0		
PSMD4	PSMD4_HUMAN	41	0	0	7,7571	6	10,874	9	0	0	0	0	0	0	0	0		
PUF60	DADI97VP5_HUMAN (-	57	11,744	8	1,9393	2	10,874	12	21,535	15	20,855	13	33,381	19	12,958	12		
RPS11	RS11_HUMAN	18	10,44	4	20,362	9	10,874	6	12,921	8	26,343	9	8,7845	6	8,9692	7		
RPS17	RS17_HUMAN	16	2,6099	2	22,302	12	10,874	8	10,768	6	27,641	11	14,934	8	10,962	8		
RUVBL2	RUVB2_HUMAN	51	0	0	4,8482	3	10,874	9	143,21	33	9,8786	8	7,906	8	67,767	28		
SNRPD2	SMD2_HUMAN	14	3,9148	2	10,666	6	10,874	7	0	0	12,074	6	17,569	7	6,9761	5		
SRPRA	SRPRA_HUMAN	70	0	0	8,7267	9	10,874	15	0	0	7,6836	5	21,961	19	16,942	16		
U2AF2	U2AF2_HUMAN	54	0	0	7,7571	6	10,874	9	8,614	6	38,417	14	22,84	12	19,932	11		
ANKRD17	ANR17_HUMAN (+1)	274	0	0	0	0	10,149	13	0	0	5,4881	5	8,7845	10	8,9692	9		
ANLN	ANLN_HUMAN	124	0	0	2,9089	2	10,149	13	0	0	0	0	0	0	0	0		
ASCC3	ASCC3_HUMAN	251	0	0	12,605	10	10,149	14	19,382	18	41,71	35	38,652	41	33,894	30		
CALD1	CALD1_HUMAN	93	0	0	0	0	10,149	12	0	0	0	0	1,7569	2	0	0		
CAMKV	DGR9J8_HUMAN (+3)	56	0	0	1,9393	2	10,149	9	0	0	0	0	5,2707	3	0	0		
CC2D1A	C2D1A_HUMAN	104	0	0	3,8786	4	10,149	14	0	0	0	0	3,5138	4	0	0		
CLUH	K7FIG1_HUMAN	141	0	0	0	0	10,149	13	0	0	0	0	0	0	0	0		
COPE	COPE_HUMAN	54	0	0	3,8786	4	10,149	8	3,2303	3	3,2929	2	12,298	8	3,9863	4		
COTL1C	COTC_HUMAN	53	0	0	0	0	10,149	12	0	0	2,1952	2	2,6353	3	0	0		
CUL4A	CUL4A_HUMAN	88	0	0	0	0	10,149	6	0	0	0	0	5,2707	3	0	0		
DHX8	DHX8_HUMAN	41	0	0	14,545	10	10,149	12	0	0	14,269	9	14,055	12	0	0		
EEF1D	PRRVB_HUMAN (+1)	77	0	0	7,7571	6	10,149	9	0	0	3,2929	2	3,5138	3	0	0		
EML4	EMAL4_HUMAN	109	0	0	0	0	10,149	10	0	0	0	0	0	0	0	0		
EXOC7	ADAIDACMSBB_HUMAN	79	0	0	0	0	10,149	12	0	0	0	0	3,5138	4	0	0		
HBS1L	HBS1L_HUMAN	75	0	0	0	0	10,149	9	0	0	0	0	6,1491	7	0	0		
JAK1	JAK1_HUMAN	133	0	0	7,7571	5	10,149	13	0	0	18,66	11	22,84	19	13,952	11		
KIF2C	KIF2C_HUMAN	81	0	0	6,7875	7	10,149	13	0	0	3,2929	3	11,42	11	4,9829	4		
MDN1	MDN1_HUMAN	633	0	0	2,9089	3	10,149	14	6,4605	6	2,1952	2	5,2707	6	3,9863	4		
NACA	NACAM_HUMAN	205	0	0	9,6964	4	10,149	4	0	0	6,5857	3	7,0276	4	0	0		
NKRF	NKRF_HUMAN	78	0	0	3,8786	4	10,149	10	18,305	16	9,8786	8	6,1491	6	10,962	11		
PABPC1	PABP1_HUMAN	71	0	0	10,666	11	10,149	14	30,149	22	9,8786	9	18,447	20	0	0		
PRPSAP2	KPR1_HUMAN	41	0	0	2,9089	3	10,149	11	0	0	2,1952	2	4,3922	5	0	0		
RBM25	RBM25_HUMAN	100	0	0	0	0	10,149	9	0	0	4,3305	4	3,5138	4	0	0		
RPAP3	RPAP3_HUMAN	76	0	0	0	0	10,149	14	0	0	0	0	5,2707	6	0	0		
RPS6	RS6_HUMAN	29	0	0	31,998	7	10,149	5	16,151	5	23,05	10	8,7845	5	6,9761	5		
SMU1	SMU1_HUMAN	58	0	0	5,8178	4	10,149	8	5,3838	5	9,8786	6	13,177	10	4,9829	5		
SNRPB	RSMB_HUMAN	75	0	0	0	0	10,149	6	0	0	7,6836	2	13,177	6	6,9761	4		
SNRPD3	SMD3_HUMAN	14	2,6099	2	10,666	4	10,149	4	0	0	7,6836	4	14,934	4	6,9761	4		
SPTS1	SPTS_HUMAN	65	0	0	0	0	9,4241	10	0	0	0	0	0	0	0	0		
AFG32	AFG32_HUMAN	89	0	0	9,6964	10	9,4241	11	2,1555	2	6,5857	6	10,541	10	11,959	12		
AP1M1	AP1M1_HUMAN	49	0	0	1,9393	2	9,4241	10	6,4605	6	9,8786	7	8,7845	10	5,9795	6		
CDC5L	CDC5_HUMAN	92	0	0	7,7571	8	9,4241	12	17,228	14	17,562	12	14,934	15	5,9795	6		
CD.GAL1	GT251_HUMAN	72	0	0	1,9393	2	9,4241	12	0	0	0	0	5,5138	4	0	0		
CPSF7	CPSF7_HUMAN	52	0	0	3,8786	4	9,4241	10	8,614	6	15,367	9	12,298	10	9,9658	8		
CSNK2A1	E7EU96_HUMAN	45	0	0	5,8178	5	9,4241	9	0	0	5,4881	5	11,42	10	0	0		
CSNK2A2	CSK22_HUMAN	41	0	0	4,8482	4	9,4241	8	0	0	4,3305	4	12,298	10	0	0		
EXOC4	EXOC4_HUMAN	111	0	0	3,8786	4	9,4241	13	0	0	3,2929	3	2,6353	3	0	0		
HS01/812	DHB12_HUMAN	54	0	0	1,9393	2	9,4241	9	3,2303	3	4,3305	4	9,7845	9	7,9726	7		
IQT2R	MP31_HUMAN	274	0	0	0	0	9,4241	13	0	0	0	0	0	0	0	0		
KATN31	KTN31_HUMAN	72	0	0	0	0	9,4241	12	0	0	0	0	10,541	12	3,9863	4		
KHDRBS1	KHDR1_HUMAN	48	0	0	4,8482	3	9,4241	8	2,1555	2	12,074	8	12,298	8	4,9829	4		
KIF2A	KIF2A_HUMAN	80	0	0	7,7571	8	9,4241	10	0	0	6,5857	6	19,326	15	4,9829	5		
LARS	SYLC_HUMAN	134	0	0	0	0	9,4241	13	0	0	0	0	0	0	0	0		
MTCH	LYRIC_HUMAN	66	0	0	2,9089	3	9,4241	12	5,3838	5	19,757	13	18,447	17	16,942	15		
PRPF3	PRPF3_HUMAN	78	0	0	13,575	13	9,4241	12	9,6908	9	19,757	14	18,447	17	13,952	12		
PRPS2	PRPS2_HUMAN	35	0	0	0	0	9,4241	2	0	0	0	0	0	0	0	0		
PUS7	PUS7_HUMAN	75	0	0	0	0	9,4241	13	0	0	0	0	5,2707	6	0	0		
RBMX	RBMX_HUMAN	42	0	0	17,453	12	9,4241	12	13,998	11	53,784	17	28,11	15	14,949	12		
RCC2	RCC2_HUMAN	56	0	0	0	0	9,4241	12	0	0	0	0	0	0	0	0		
RECQL	RECQ1_HUMAN	73	0	0	0	0	9,4241	8	0	0	0	0	7,0276	7	0	0		
RNF219	RN219_HUMAN	81	0	0	2,9089	3	9,4241	12	5,3838	5	0	0	0	0	0	0		
RPL23	RL23_HUMAN	15	7,8297	5	13,575	5	9,4241	8	27,996	8	26,343	8	14,055	6	13,952	5		
RPN1	RPN1_HUMAN	69	0	0	2,9089	3	9,4241	8	21,535	16	3,2929	3	13,177	14	14,949	14		
RPS10	RS10_HUMAN	19	9,1346	2	14,545	7	9,4241	7	4,307	3	17,562	7	14,934	7	11,959	8		
RPS27A	RS27A_HUMAN (+2)	18	10,44	4	17,453	4	9,4241	4	11,844	3	8,781	3	8,7845	4	13,952	5		
RPS7	RS7_HUMAN	22	3,9148	3	22,302	8	9,4241	8	4,307	4	25,245	9	21,083	10	9,9658	7		
SLC25A13	CMC2_HUMAN	70	0	0	0	0	9,4241	10	63,07	21	0	0	16,691	15	3,988	19		
SPTAN1	SPTA1_HUMAN	285	0	0	0	0	9,4241	13	0	0	0	0	0	0	0	0		
SRPR8	SRPR8_HUMAN	50	0	0	7,7571	7	9,4241	10	6,4605	6	4,3305	4	12,298	11	8,9692	9		
TIP1	DADB7X0K0_HUMAN (+	188	0	0	14,907	31	9,4241	13	5,3838	5	35,124	27	16,055	13	20,928	19		
USP10	UBP10_HUMAN	87	0	0	0	0	9,4241	13	0	0	0	0	1,7569	2	0	0		
K0787	D61ER5_HUMAN (+2)	50	0	0	0	0	8,6992	5	0	0	0	0	0	0	0	0		
ANXA6	ANX6_HUMAN	629	3,9148	3	3,8786	3	8,6992	12	0	0	0	0	1,7569	2	2,9897	3		
ALYREF	ELP3G3_HUMAN	28	0	0	5,8178	5	8,6992	6	4,307	3	29,636	9	16,691	7	7,9726	6		
BUB3	BUB3_HUMAN	37	0	0	4,8482	4	8,6992	9	3,2303	3	6,5857	6	6,1491	7	0	0		
CEP170	CE170_HUMAN	175	0	0	8,7267	9	8,6992	11	16,151	15	15,367	14	16,691	19	14,949	15		
CMAS	NEUA_HUMAN	48	0	0	10,666	8	8,6992	9	3,2303	3	5,4881	4	7,906	7	6,9761	7		
CNP	CN37_HUMAN	48	0	0	3,8786	4	8,6992	11	0	0	5,4881	5	9,6629	11	7,9726	8		
CPSF6	CPSF6_HUMAN (+1)	59	0	0	1,9393	2	8,6992	6	0	0	12,074	6	11,42	11	7,9726	7		
DCTN1	DCTN1_HUMAN (+1)	142	0	0	0	0	8,6992	11	0	0	0	0	0	0	0	0		
EHD4	EHD4_HUMAN	61	0	0	0	0	8,6992	11	0	0	0	0	5,2707	6	0	0		
EIF2A	EIF2A_HUMAN	65	0	0	0	0	8,6992	11	0	0	0	0	7,0276	7	0	0		
FAM98B	FA98B_HUMAN	37	0	0	6,7875	7	8,6992	8	0	0	12,074	7	7,0276	7	2,9897	3		
FKB12	FKB2_HUMAN	26	0	0	22,302	14	8,6992	6	24,765	16	39,516	19	15,812	9	5,9795	2		
G3BP2	G3BP2_HUMAN	54	0	0	9,6964	6	8,6992	7	5,3838	3	17,562	9	26,353	12	20,928	11		
GTF2B	TF2B_HUMAN	35	0	0	2,9089	2	8,6992	9	0	0	4,3305	4	11,42	10	0	0		
KHS	SYK_HUMAN	68	0	0	0	0	8,6992	12	2,1555	2	0	0	8,7845	10	0	0		
KDM3B	KDM3B_HUMAN	192	0	0	2,9089	3	8,6992	12	0	0	0	0	2,6353	3	0	0		
LARP7	LARP7_HUMAN	67	0	0	3,8786	4	8,6992	10	2,1555	2	10,976	9	19,326	17	5,9795	5		
LMO7	LMO7_HUMAN	191	0	0	11,636	11	8,6992	12	0	0	8,781	8	16,055	14	12,956	13		
MLH1	MLH1_HUMAN	85	0	0	1,9393	2	8,6992	12	8,614	7	2,1952	2	2,6353	3	0	0		
MRTO4	MRT4_HUMAN	28	0	0	1,9393	2	8,6992	10	8,614	8	2,1952	2	9,6629	10	0	0		
MYH14	MYH14_HUMAN	228	0	0	3,8786	2	8,6992	5	0	0	0	0	0	0	0	0		
NAA16	NAA16_HUMAN	101	0	0	0	0	8,6992	4	0	0	0	0	0	0	0	0		
PPFIA1	LIPA1_HUMAN	136	0	0	17,605	12	8,6992	12	0	0	5,4881	5	8,7845	10	5,9795	6		
RAB1B	RAB1B_HUMAN	80	0	0	2,9089	3	8,6992	9	0	0	2,1952	2	5,2707	6	1,9932	2		
RPS2	RS2_HUMAN	16	7,8297	2	15,514	5	8,6992	4	8,614	5	8,781	4	8,7845	5	4,9829	3		
STRAP	DSYD24|STRAP_HUM	7	0	0	5,8178	5	8,6992	10	0	0	6,5857	6	7,906	8	3,9863	4		
SARS2	SYDND4Z_HUMAN (+1	58	0	0	2,9089	3	8,6992	10	0	0	5,4881	5	5,2707	6	7,9726	7		
SF3A3	SF3A3_HUMAN	59	0	0	0	0	8,6992	9	0	0	0	0	0	0	0	0		
SF3B2	SF3B2_HUMAN	100	0	0	5,8178	2	8,6992	6	2,1555	2	16,464	8	18,447	15	6,9761	6		
SLAIN2	SLAI2_HUMAN	63	0	0	4,8482	5	8,6992	11	0	0	2,1952	2	16,934	14	5,9795	6		
SNRPA1	RU2A_HUMAN	28	0	0	7,7571	6	8,6992	8	0	0	9,8786	8	12,298	10	7,9726	7		
SNRPB2	RU2B_HUMAN	25	0	0	2,9089	2	8,6992	5	0	0	5,4881	3	7,906	3	4,9829	3		
STX5	STX5_HUMAN	40	0	0	1,9393	2	8,6992	10	0	0	0	0	3,5138	4	0	0		
SUPT6H	SPT6H_HUMAN	199	0	0	0	0	8,6992	11	0	0	0	0	2,6353	3	0	0		
TCEA1	DA1W2PP25_HUMAN (-	36	0	0	0	0	8,6992	10	0	0	0	0	0	0	0	0		
THRAP3	TR150_HUMAN	109	0	0	11,636	7	8,6992	11	0	0	10,976	8	5,2707	4	2,9897	3		
UBE2O	Q9C0C9|UBE2O_HUM	141	0	0	12,605	12	8,6992	10	0	0	8,781	8	15,812	16	11,959	12		
VAPA	VAPA_HUMAN	28	0	0	0	0	8,6992	10	0	0	0	0	2,6353	3	0	0		
WRNIP1	WRIP1_HUMAN	72	0	0	1,9393	2	8,6992	11	2,1555	2	0	0	7,0276	7	0	0		
ZMYM1/UBI	MOQYT0_HUMAN	36	0	0	0	0	8,6992	2	0	0	0	0	0	0	0	0		
ACTR2	ARP2_HUMAN	45	0	0	0	0	7,9743	7	0	0	0	0	1,7569	2	0	0		
ANK2	ANK2_HUMAN (+1)	434	0	0	3,8786	2	7,9743	7	0	0	0	0	3,5138	3	0	0		
ATP5O	ATPO_HUMAN	23	0	0	10,666	8	7,9743	7	8,614	7	9,8786	7	9,6629	8	7,9726	7		
BTF3	BTF3_HUMAN	22	0	0	4,8482	5	7,9743	7	0	0	4,3305	4	7,0276	6	1,9932	2		
CDK12/P	CART_HUMAN	61	0	0	3,8786	4	7,9743	7	0	0	3,2929	3	6,1491	6	0	0		
DHX40	DHX40_HUMAN	89	0	0	3,8786	3	7,9743	9	2,1555	2	7,6836	6	18,447	16	7,9726	8		
DLG1	ADADC4DF13_HUMAN	100	0	0	0	0	7,9743	11	0	0	0	0	0	0	0	0		
HNRNPA3	ROA3_HUMAN	40	0	0	6,7875	5	7,9743	8	5,3838	5	63,662	17	47,436	14	11,959	6		
IMMT	MIC60_HUMAN	84	3,9148	3	3,8786	4	7,9743	10	32,305	21	0	0	5,5138	4	8,9692	9		
IMPDH1	CS1B1_HUMAN (+1)	55	0	0	0	0	7,9743	6	0	0	0	0	5,2707	4	0	0		
KIF21A	A4D0S4Z7_HUMAN (+	185	0	0	10,666	10	7,9743	10	0	0	5,4881	4	14,055	13	10,962	10		
LIG3	DNL3_HUMAN	113	0	0	3,8786	4	7,9743	10	0	0	9,8786	9	8,7845	10	2,9897	3		
LRRC47	LRC47_HUMAN	63	0	0	0	0	7,9743	8	0	0	0	0	13,177	13	0	0		
LRRFIP1	LRRF1_HUMAN	89	0	0	2,9089	3	7,9743	6	0	0	0	0	0	0	0	0		
NELFA	NADC4DFX5_HUMAN (-	59	0	0	0	0	7,9743	7	0	0	0	0	7,906	7	4,9829	5		

NELFE	NELFE_HUMAN	45	0	0	1,9393	2	7,9743	8	0	0	3,2929	2	16,055	11	4,9829	5
PA1PC4	B1AN80_HUMAN (+1)	68	0	0	0	0	7,9743	5	16,382	7	0	0	11,42	5	0	0
POLR2B	C9J2Y9_HUMAN (+1)	133	0	0	11,636	10	7,9743	11	19,382	14	10,976	10	7,0276	8	15,945	15
PSMD7	PSMD7_HUMAN	37	0	0	3,8786	4	7,9743	9	0	0	0	0	1,7569	2	0	0
RBM14	RBM14_HUMAN	69	0	0	9,6964	10	7,9743	11	13,998	11	27,441	18	30,746	21	24,914	18
RFC3	RFC3_HUMAN	41	0	0	8,7267	4	7,9743	10	8,614	6	16,464	11	16,055	11	0	0
RFC4	RFC4_HUMAN	49	0	0	4,8482	5	7,9743	10	7,5373	5	13,171	9	13,177	12	0	0
RFC5	RFC5_HUMAN	58	0	0	3,8786	4	7,9743	9	11,844	10	9,8786	8	8,7845	9	0	0
SCYL1	E9PKS9_HUMAN (+2)	86	0	0	0	0	7,9743	10	0	0	0	0	0	0	0	0
SNRPA	SNRPA_HUMAN	31	0	0	4,8482	4	7,9743	7	0	0	9,8786	7	26,353	8	8,9692	7
SNRPD1	SMD1_HUMAN	15	0	0	2,9089	2	7,9743	5	0	0	8,781	5	11,42	5	6,9761	4
SNX9	SNX9_HUMAN	67	0	0	3,8786	4	7,9743	9	0	0	2,1952	2	17,298	11	7,9726	8
XRN2	XRN2_HUMAN	109	0	0	1,9393	2	7,9743	11	0	0	12,074	11	12,298	11	3,9863	4
ZFR	ZFR_HUMAN	117	0	0	2,9089	3	7,9743	11	3,2303	3	16,464	14	17,569	17	11,959	10
37500	SEPT2_HUMAN	41	0	0	0	0	7,2493	9	0	0	0	0	1,7569	2	0	0
ABCF1	ABCF1_HUMAN	96	0	0	0	0	7,2493	10	0	0	20,855	16	22,84	17	8,9692	9
ACAP2	A0A87X1H5_HUMAN (-	88	0	0	0	0	7,2493	9	0	0	0	0	0	0	0	0
AGK	E9PC15_HUMAN	44	0	0	8,7267	9	7,2493	10	12,921	12	13,171	10	10,541	11	21,925	20
APEX1	APEX1_HUMAN	36	0	0	0	0	7,2493	8	0	0	2,1952	2	7,906	8	0	0
ARHGEF1	ARHG1_HUMAN (+1)	102	0	0	0	0	7,2493	10	0	0	0	0	0	0	0	0
ATXN2L	ATX2L_HUMAN	113	0	0	2,9089	3	7,2493	10	3,2303	3	3,2929	3	4,3922	5	0	0
CAMSAP1	CAMP1_HUMAN	178	0	0	2,9089	3	7,2493	9	0	0	0	0	6,1491	6	0	0
CCDC6	CCDC6_HUMAN	55	0	0	0	0	7,2493	9	0	0	0	0	0	0	0	0
CSNK2B	CSK2B_HUMAN (+1)	25	0	0	2,9089	3	7,2493	7	7,5373	5	0	0	4,3922	5	1,9932	2
CUL1	A0A0A0MA_HUMAN (+	87	0	0	0	0	7,2493	10	0	0	0	0	0	0	0	0
CUL5	CUL5_HUMAN	91	0	0	0	0	7,2493	10	0	0	0	0	0	0	0	0
EIF4H	EIF4H_HUMAN	36	0	0	0	0	7,2493	5	0	0	0	0	0	0	0	0
EIF4A3	IF4A3_HUMAN	47	0	0	0	0	7,2493	9	0	0	5,4881	3	6,1491	7	2,9897	2
EMR1	EMR1_HUMAN	71	0	0	16,484	8	7,2493	5	15,075	9	28,538	15	19,326	15	9,9658	6
GAK	GAK_HUMAN	143	0	0	0	0	7,2493	9	0	0	0	0	0	0	0	0
GLG1	GSLG1_HUMAN	135	0	0	18,423	17	7,2493	10	0	0	6,5857	5	3,5138	3	2,9897	3
GOLGA2	GOGA2_HUMAN	113	0	0	1,9393	2	7,2493	10	0	0	0	0	0	0	5,9795	6
HADHB	ECHB_HUMAN	51	0	0	10,666	10	7,2493	10	13,998	10	19,757	13	11,42	12	34,88	21
HMGB3	E7EQL1_HUMAN (+3)	22	0	0	0	0	7,2493	7	0	0	0	0	2,6353	3	0	0
HNRNPAD	ROAD_HUMAN	31	0	0	10,666	6	7,2493	5	6,4605	4	27,441	9	22,84	8	3,9863	3
HNRNPAB	D6R9P3_HUMAN	30	0	0	2,9089	2	7,2493	5	3,2303	2	23,05	8	21,083	7	3,9863	2
IGF2BP3	IF2S3_HUMAN	64	0	0	1,9393	2	7,2493	5	19,382	14	17,562	10	24,597	15	10,962	8
IRS2	IRS2_HUMAN	137	0	0	5,8178	6	7,2493	10	0	0	5,4881	4	0	0	1,9932	2
IRS4	IRS4_HUMAN	134	0	0	23,771	15	7,2493	8	39,84	16	25,265	18	15,812	13	25,911	20
LMNB1	LMNB1_HUMAN	66	0	0	0	0	7,2493	9	0	0	0	0	2,6353	3	0	0
MEPCE	MEPCE_HUMAN	76	0	0	2,9089	3	7,2493	9	0	0	9,8786	9	13,177	12	2,9897	3
MORC3	MORC3_HUMAN	107	0	0	0	0	7,2493	10	0	0	0	0	0	0	0	0
MRPS2	RT02_HUMAN	55	0	0	10,666	9	7,2493	9	6,4605	6	12,074	9	7,0276	8	5,9795	6
NELFB	A0A0X1KCP1_HUMAN	70	0	0	0	0	7,2493	7	0	0	3,2929	3	7,906	6	0	0
NUDT21	CPSF5_HUMAN	26	2,6099	2	3,8786	4	7,2493	8	2,1555	2	9,8786	7	12,298	7	5,9795	6
NUP205	NU205_HUMAN	228	0	0	0	0	7,2493	9	24,765	23	4,3905	4	7,906	9	6,9761	7
NUP50	NUP50_HUMAN	50	0	0	0	0	7,2493	9	0	0	0	0	0	0	0	0
PDCD4	PDCD4_HUMAN	52	0	0	0	0	7,2493	10	0	0	0	0	2,6353	3	0	0
PDIA3	PDIA3_HUMAN	156	0	0	13,575	11	7,2493	9	0	0	14,269	12	7,906	8	1,9932	2
PPIL4	PPIL4_HUMAN	57	0	0	0	0	7,2493	10	0	0	9,8786	7	23,718	11	6,9761	6
PRPSAP1	KPRA_HUMAN	39	0	0	2,9089	2	7,2493	7	0	0	3,2929	2	3,5138	3	0	0
PSPC1	PSPC1_HUMAN	59	0	0	0	0	7,2493	10	0	0	4,3905	4	9,6629	9	0	0
RANGAP1	RAGP1_HUMAN	64	0	0	3,8786	4	7,2493	9	0	0	0	0	6,1491	7	0	0
RPL12	RL12_HUMAN	18	0	0	3,8786	4	7,2493	6	15,075	5	4,3905	4	5,2707	4	1,9932	2
RPL22	RL22_HUMAN	15	3,9148	3	10,666	4	7,2493	4	2,1555	2	21,952	4	13,177	4	7,9726	4
RPS20	RS20_HUMAN	13	0	0	5,8178	3	7,2493	3	3,2303	2	7,9854	3	11,42	4	5,9795	3
RPS27	RS27_HUMAN	9	2,6099	2	13,575	4	7,2493	4	16,151	4	10,976	3	7,0276	4	15,945	5
RRBP1	RRBP1_HUMAN	152	0	0	0	0	7,2493	10	17,228	15	0	0	1,7569	2	0	0
SHMT1	GLYC_HUMAN	53	0	0	0	0	7,2493	5	0	0	0	0	0	0	0	0
SLC4A1AP	A0A87X0M4_HUMAN (+	85	0	0	0	0	7,2493	10	0	0	0	0	0	0	0	0
SLFN11	SLN11_HUMAN	103	0	0	0	0	7,2493	10	7,5373	7	0	0	1,7569	2	0	0
SMC1	SMC1B_HUMAN	189	0	0	0	0	7,2493	9	0	0	0	0	0	0	0	0
SPTAN1	A0A087WU73_HUMAN	275	0	0	0	0	7,2493	10	0	0	0	0	0	0	0	0
SRSF3	SRSF3_HUMAN	19	0	0	8,7267	4	7,2493	5	7,5373	6	12,074	6	10,541	6	4,9829	3
SUPV3L1	SUV3_HUMAN	88	0	0	0	0	7,2493	9	0	0	0	0	0	0	0	0
TECR	TECR_HUMAN	36	0	0	8,7267	5	7,2493	6	19,382	7	5,4881	4	13,177	5	29,897	10
THOC2	A0A140G8B_HUMAN (+	170	0	0	0	0	7,2493	10	0	0	8,781	8	8,7845	10	6,9761	7
TIMM44	TIM44_HUMAN	51	0	0	1,9393	2	7,2493	9	0	0	7,6854	7	5,2707	6	0	0
TRIM33	TRI33_HUMAN	123	0	0	0	0	7,2493	10	0	0	0	0	0	0	0	0
TSR1	TSR1_HUMAN	92	0	0	14,545	12	7,2493	8	5,3838	5	24,148	16	16,055	12	1,9932	2
TTC37	TTC37_HUMAN	94	0	0	0	0	7,2493	10	0	0	0	0	0	0	0	0
VCP	TERA_HUMAN	89	0	0	0	0	7,2493	7	0	0	0	0	0	0	0	0
XRN1	XRN1_HUMAN	194	0	0	20,362	14	7,2493	10	0	0	26,343	23	25,475	29	9,9658	10
ABCF3	ABCF3_HUMAN	80	0	0	0	0	6,5244	9	0	0	0	0	1,7569	2	0	0
ADD1	ADDA_HUMAN (+2)	81	0	0	0	0	6,5244	9	0	0	0	0	0	0	0	0
ANK3	ANK3_HUMAN	480	0	0	1,9393	2	6,5244	8	0	0	0	0	7,906	9	0	0
ANKHD1	ANKH1_HUMAN	269	0	0	0	0	6,5244	2	0	0	0	0	7,906	3	6,9761	2
ARHGEF2	ARHG2_HUMAN (+1)	112	0	0	9,6964	10	6,5244	8	0	0	8,781	8	7,0276	8	3,9863	4
ARPC1A	ARC1A_HUMAN	42	0	0	0	0	6,5244	2	0	0	0	0	0	0	0	0
CCDC124	CC124_HUMAN	26	0	0	2,9089	3	6,5244	6	0	0	4,3905	3	7,906	8	1,9932	2
CDK9	CDK9_HUMAN	71	0	0	0	0	6,5244	9	0	0	0	0	0	0	0	0
CDC2	A0A0Q0P7_HUMAN (+	34	0	0	1,9393	2	6,5244	6	7,5373	6	0	0	0	0	3,9863	4
DOCK11	A6NNW2_HUMAN (+1)	238	0	0	0	0	6,5244	9	0	0	0	0	11,42	13	0	0
DYNC1I2	DC1I2_HUMAN	71	0	0	0	0	6,5244	9	0	0	0	0	0	0	0	0
EDC3	EDC3_HUMAN	56	0	0	0	0	6,5244	8	10,768	9	0	0	7,0276	8	12,958	10
EDC4	EDC4_HUMAN	152	0	0	0	0	6,5244	9	0	0	0	0	0	0	0	0
EIF3E	EIF3E1_HUMAN	29	0	0	7,7571	6	6,5244	5	24,765	6	10,976	5	6,1491	4	25,911	6
FOXK1	FOXK1_HUMAN	75	0	0	2,9089	3	6,5244	7	0	0	0	0	1,7569	2	0	0
GTF2I	TF2I_HUMAN	58	0	0	1,9393	2	6,5244	8	0	0	2,1952	2	7,0276	8	0	0
HNRNPC	HNRPC_HUMAN	34	0	0	4,8482	5	6,5244	7	7,5373	4	68,955	20	60,613	22	25,911	9
HSPH1	HS105_HUMAN	97	0	0	0	0	6,5244	9	25,842	18	0	0	0	0	2,9897	3
KHSRP	KHSP_HUMAN	59	0	0	0	0	6,5244	9	6,307	4	3,2929	3	5,2707	6	1,9932	2
IPO8	IPO8_HUMAN	120	0	0	0	0	6,5244	9	0	0	0	0	0	0	0	0
KIF15	KIF15_HUMAN	160	0	0	0	0	6,5244	8	0	0	0	0	0	0	0	0
KIF3A	A0A87X011_HUMAN (+	83	0	0	4,8482	5	6,5244	9	10,768	10	4,3905	4	10,541	10	3,9863	3
KPNA1	IMA5_HUMAN	60	0	0	0	0	6,5244	8	12,921	10	2,1952	2	2,6353	3	3,9863	4
LIG1	DNL1_HUMAN (+1)	102	0	0	0	0	6,5244	9	0	0	0	0	0	0	0	0
ORC5	ORC5_HUMAN	82	0	0	0	0	6,5244	8	0	0	0	0	3,5138	4	0	0
PGAM5	PGAM5_HUMAN	32	0	0	5,8178	4	6,5244	5	5,3838	4	3,2929	3	6,1491	5	3,9863	4
PIK3CA	P3CA_HUMAN	191	0	0	2,9089	3	6,5244	9	0	0	5,4881	5	7,906	9	16,947	17
POLR1A	RPA1_HUMAN	195	0	0	9,6964	9	6,5244	8	9,6908	9	15,367	14	18,447	21	8,9692	9
POLR3E	A0A140H01_HUMAN (+	76	0	0	3,8786	4	6,5244	9	0	0	2,1952	2	9,6629	9	3,9863	4
PRRC2B	PRC2B_HUMAN	243	0	0	5,8178	5	6,5244	8	3,2303	3	17,562	16	8,7845	8	0	0
RAD50	RAD50_HUMAN	154	0	0	11,636	12	6,5244	9	3,2303	3	0	0	2,6353	3	0	0
RBM27	RBM27_HUMAN	119	0	0	7,7571	5	6,5244	3	0	0	10,976	7	7,906	5	3,9863	2
RFC2	RFC2_HUMAN	59	0	0	2,9089	3	6,5244	9	6,307	4	12,074	10	8,7845	9	0	0
RPL10	RL10_HUMAN (+1)	25	0	0	25,211	7	6,5244	4	15,075	6	20,855	8	16,934	6	9,9658	6
RPL30	RL30_HUMAN	13	0	0	7,7571	4	6,5244	5	12,921	6	30,733	8	14,934	7	5,9795	5
RPL4	RL4_HUMAN	48	0	0	11,636	6	6,5244	5	26,555	11	21,952	12	8,7845	9	10,962	9
SF01A1	B4DR61_HUMAN (+1)	53	0	0	2,9089	2	6,5244	3	5,3838	3	2,1952	2	1,7569	2	2,9897	3
SRP54	SRP54_HUMAN	56	0	0	1,9393	2	6,5244	9	0	0	5,4881	5	3,5138	4	1,9932	2
STAU1	STAU1_HUMAN	63	0	0	5,8178	6	6,5244	9	30,149	15	14,269	10	16,691	15	18,935	14
TOR1AIP1	TOIP1_HUMAN	66	0	0	0	0	6,5244	7	3,2303	2	6,5857	2	4,3922	3	5,9795	5
TTC28	TTC28_HUMAN	271	0	0	0	0	6,5244	9	22,612	21	0	0	0	0	13,952	13
UBAP2	UBAP2_HUMAN	117	0	0	0	0	6,5244	9	0	0	2,1952	2	2,6353	3	0	0
UBR4	UBR4_HUMAN	574	0	0	1,9393	2	6,5244	9	0	0	0	0	0	0	0	0
WASHC2C	A0A0B4J2C5_HUMAN (+	147	0	0	0	0	6,5244	8	0	0	0	0	0	0	0	0
WDR11	WDR11_HUMAN	137	0	0	2,9089	3	6,5244	7	0	0	0	0	0	0	2,9897	3
ZCCHC11	A0A0J9YMZ_HUMAN (+	185	0	0	23,271	22	6,5244	8	0	0	15,367	12	7,0276	7	2,9897	2
ZG16B	A0A140G4_HUMAN (+	20	0	0	5,8178	5	6,5244	5	0	0	0	0	0	0	0	0
ABI1	A0A0J9R7G_HUMAN (+	52	0	0	0	0	5,7995	7	0	0	0	0	0	0	0	0
AGO1	AGO1_HUMAN	97	0	0	0	0	5,7995	4	0	0	0	0	0	0	0	0
AP3D1	AP3D1_HUMAN	130	0	0	0	0	5,7995	8	0	0	6,5857	5	9,6629	10	2,9897	3
AP3M1	AP3M1_HUMAN	47	0	0	0	0	5,7995	7	0	0	0	0	3,5138	4	0	0
ARHGAP17	RHG17_HUMAN	95	0	0	0	0	5,7995	7	0	0	0	0	0	0	0	0
ARHGEF18	ARHG8_HUMAN	131	0	0	0	0	5,7995	8	0	0	0	0	0	0	0	0
BCS1L	BCS1_HUMAN	48	0	0	0	0	5,7995	8	0	0	5,4881	5	5,2707	5	0	0

CDK9	CDK9_HUMAN	45	0	0	5,8178	6	5,7995	6	3,2303	3	9,8786	8	8,7845	9	0	0			
CHUK	IKKA_HUMAN	85	0	0	0	0	5,7995	8	0	0	0	0	0	0	0	0			
CNOT9	CNOT9_HUMAN	54	0	0	0	0	5,7995	6	2,1555	2	0	0	0	0	0	0			
CSNK1A1	KC1A_HUMAN	39	0	0	7,7571	6	5,7995	6	3,2303	2	20,855	9	12,298	11	2,9897	3			
DDX46	DDX46_HUMAN (+	117	0	0	0	0	5,7995	8	0	0	0	0	2,6353	3	0	0			
DHX29	DHX29_HUMAN (+	155	0	0	0	0	5,7995	7	0	0	4,3305	3	3,5138	3	0	0			
DNAJA3	DNJA3_HUMAN	57	0	0	4,8482	3	5,7995	5	23,689	11	8,781	5	5,2707	4	19,332	8			
DNAJC9	DNJC9_HUMAN	30	0	0	3,8786	4	5,7995	5	2,1555	2	4,3305	4	2,6353	3	0	0			
DPM1	DPM1_HUMAN (-2)	30	0	0	6,7875	7	5,7995	8	12,921	10	7,6834	7	9,6629	9	14,949	11			
EIF3I	EIF3I_HUMAN	62	0	0	0	0	5,7995	8	13,998	12	0	0	3,5138	4	2,9897	3			
EMC2	EMC2_HUMAN	35	0	0	2,9089	3	5,7995	5	0	0	3,2929	3	4,3822	4	0	0			
FSTL3	H78K1_HUMAN	98	0	0	1,9393	2	5,7995	8	5,3838	4	3,2929	2	0	0	5,9795	6			
EXOC1	EXOC1_HUMAN	102	0	0	1,9393	2	5,7995	8	0	0	2,1952	2	0	0	1,9932	2			
EXOC5	EXOC5_HUMAN	82	0	0	0	0	5,7995	8	0	0	0	0	3,5138	4	0	0			
EXOSC2	EXOS2_HUMAN	33	0	0	0	0	5,7995	7	6,4605	5	3,2929	3	6,1491	5	1,9932	2			
HIST1H1E	H14_HUMAN	22	0	0	8,7267	4	5,7995	4	3,2303	3	4,3305	4	1,7569	2	3,9863	4			
HTT	HD_HUMAN	348	0	0	0	0	5,7995	8	0	0	0	0	0	0	0	0			
IKBKB	IKKB_HUMAN	87	0	0	0	0	5,7995	7	0	0	0	0	0	0	0	0			
NPPL1	SHP2_HUMAN	139	0	0	0	0	5,7995	8	0	0	0	0	0	0	0	0			
KIF4A	KIF4A_HUMAN	140	0	0	14,545	14	5,7995	6	0	0	14,269	11	8,7845	9	3,9863	3			
RPNA6	PSA7_HUMAN	60	0	0	0	0	5,7995	3	8,614	3	0	0	0	0	0	0			
KTN1	KTN1_HUMAN	156	0	0	6,7875	4	5,7995	6	0	0	0	0	2,6353	2	0	0			
LARP4B	LARB_HUMAN	81	0	0	3,8786	4	5,7995	5	0	0	9,8786	9	9,6629	8	2,9897	3			
MARK2	MP2K2_HUMAN	87	0	0	12,605	13	5,7995	8	6,4605	6	17,562	14	15,812	16	0	0			
MARS	SYMC_HUMAN	101	0	0	0	0	5,7995	8	0	0	0	0	0	0	0	0			
METTL13	MET13_HUMAN	79	0	0	0	0	5,7995	8	2,1555	2	0	0	0	0	1,9932	2			
MORF4L2	MO4L2_HUMAN	32	0	0	5,8178	3	5,7995	4	0	0	9,8786	6	6,1491	3	0	0			
MPO	PERM_HUMAN	84	0	0	0	0	5,7995	5	0	0	0	0	0	0	0	0			
MRPS22	DSE9VS_HUMAN (+2)	61	0	0	20,362	15	5,7995	7	8,614	7	24,148	16	10,541	11	0	0			
MRPS27	RT27_HUMAN	48	0	0	17,453	12	5,7995	7	5,3838	5	17,562	12	14,934	9	3,9863	4			
NUP42	NUP42_HUMAN	76	0	0	3,8786	4	5,7995	5	3,2303	3	4,3305	4	7,0276	7	0	0			
NUP153	NU153_HUMAN	154	0	0	11,636	12	5,7995	8	0	0	12,076	11	11,42	13	10,862	11			
OSBPL11	OSB11_HUMAN	84	0	0	0	0	5,7995	8	0	0	0	0	7,0276	8	0	0			
PAF1	PAF1_HUMAN	60	0	0	4,8482	5	5,7995	8	0	0	0	0	9,6629	11	5,9795	6			
PEG10	PEG10_HUMAN (+	40	0	0	2,9089	3	5,7995	4	4,307	4	3,2929	3	3,5138	3	2,9897	2			
PRIM2	PRI2_HUMAN	59	0	0	0	0	5,7995	8	0	0	0	0	2,6353	3	0	0			
PSMS14	PSD7_HUMAN	35	0	0	4,8482	4	5,7995	4	3,2303	3	0	0	0	0	0	0			
PTCD3	PTCD3_HUMAN	79	0	0	16,484	14	5,7995	8	2,1555	2	5,4881	5	10,541	10	2,9897	3			
PYCR1	PSCI1_HUMAN	33	0	0	3,8786	2	5,7995	5	8,614	4	3,2929	2	0	0	0	0			
QPCTL	QPCTL_HUMAN	48	0	0	5,8178	4	5,7995	4	19,382	7	8,781	7	5,2707	5	5,9795	4			
RAB35	RAB35_HUMAN	23	0	0	0	0	5,7995	3	6,4605	2	0	0	4,3822	2	0	0			
RGPD5	RGPD5_HUMAN	199	0	0	0	0	5,7995	2	6,4605	4	0	0	0	0	0	0			
RPL11	RL11_HUMAN	20	3,9148	2	10,666	5	5,7995	4	9,6908	5	16,464	6	12,298	7	2,9897	3			
RPL9	RL9_HUMAN	22	0	0	11,636	6	5,7995	6	3,2303	2	19,757	8	22,84	9	10,862	6			
RPS15A	RS15A_HUMAN	15	0	0	8,7267	4	5,7995	5	11,844	4	35,124	6	6,1491	3	3,9863	4			
SARS	SYSC_HUMAN	59	0	0	0	0	5,7995	7	0	0	0	0	0	0	0	0			
SLC16A1	MOT1_HUMAN	54	0	0	0	0	5,7995	5	4,307	4	7,6834	5	9,6629	5	9,9658	8			
SMARCC1	SMRC1_HUMAN	123	0	0	1,9393	2	5,7995	8	0	0	0	0	0	0	0	0			
TAF4	TAF4_HUMAN	110	0	0	1,9393	2	5,7995	8	0	0	0	0	0	0	0	0			
TADA1	TADA1_HUMAN	116	0	0	1,9393	2	5,7995	8	0	0	0	0	0	0	0	0			
TBL2	TBL2_HUMAN	50	0	0	7,7571	7	5,7995	8	2,1555	2	18,66	10	9,6629	11	12,956	12			
UBR5	UBR5_HUMAN	309	0	0	1,9393	2	5,7995	8	0	0	0	0	5,2707	6	1,9932	2			
VPS13A	VP13A_HUMAN	360	0	0	0	0	5,7995	8	0	0	2,1952	2	10,541	12	3,9863	4			
ZN598	ZN598_HUMAN	99	0	0	6,8482	4	5,7995	6	0	0	3,2929	3	2,6353	3	5,9795	6			
ACAT1	THIL_HUMAN	45	0	0	1,9393	2	5,0745	7	0	0	0	0	0	0	0	0			
ACSL4	ACSL4_HUMAN	79	0	0	0	0	5,0745	3	0	0	0	0	0	0	0	0			
AIMP2	AIMP2_HUMAN	35	0	0	0	0	5,0745	5	0	0	0	0	2,6353	3	0	0			
ALDH18A1	P5CS_HUMAN	87	0	0	0	0	5,0745	7	6,4605	6	0	0	0	0	0	0			
ARMCX3	ARMX3_HUMAN	43	0	0	7,7571	6	5,0745	6	11,844	10	14,269	11	11,42	12	0	0			
C7orf50	CG050_HUMAN	22	0	0	0	0	5,0745	6	5,3838	5	5,4881	5	4,3822	5	1,9932	2			
COL1A1	CO1A1_HUMAN	139	0	0	0	0	5,0745	3	6,4605	2	0	0	0	0	0	0			
CTNNA1	CTNA1_HUMAN	100	0	0	0	0	5,0745	7	0	0	0	0	0	0	0	0			
DIP2B	DIP2B_HUMAN	171	0	0	0	0	5,0745	5	0	0	0	0	0	0	0	0			
DLGAP5	DLGP5_HUMAN	95	0	0	0	0	5,0745	7	0	0	2,1952	2	1,7569	2	0	0			
DLST	ODO2_HUMAN	49	0	0	0	0	5,0745	4	0	0	0	0	0	0	0	0			
DNAJB6	DNJB6_HUMAN	36	0	0	5,8178	3	5,0745	4	9,6908	6	4,3305	3	4,3822	4	4,9829	5			
DPYSL3	DPYL3_HUMAN	62	0	0	0	0	5,0745	7	0	0	0	0	0	0	0	0			
DSC1	DSC1_HUMAN	100	6,5247	4	10,666	8	5,0745	6	4,307	4	0	0	8,7845	7	34,88	11			
DUSL	DUSL_HUMAN	75	0	0	0	0	5,0745	7	0	0	0	0	7,0276	8	0	0			
E2F7	E2F7_HUMAN	100	0	0	6,7875	7	5,0745	7	0	0	0	0	6,1491	7	0	0			
EIF1AX	IF1AX_HUMAN	16	0	0	3,8786	3	5,0745	6	0	0	4,3305	4	6,1491	4	3,9863	3			
EIF2S2	EI2S2_HUMAN	39	0	0	0	0	5,0745	6	0	0	2,1952	2	4,3822	4	0	0			
EMC3	EMC3_HUMAN	30	0	0	2,9089	3	5,0745	6	0	0	0	0	7,0276	7	0	0			
EXOC3	EXOC3_HUMAN	87	0	0	0	0	5,0745	7	0	0	0	0	3,5138	4	0	0			
EXOSC10	EXOS9_HUMAN	101	0	0	0	0	5,0745	7	5,3838	5	7,6834	7	10,541	12	0	0			
FAM126A	H2COW7_HUMAN	52	0	0	0	0	5,0745	7	0	0	0	0	0	0	0	0			
FKSPB	FKSPB_HUMAN	45	0	0	1,9393	2	5,0745	5	4,307	4	3,2929	3	4,3822	5	5,9795	6			
GIT1	ADC4GN6_HUMAN (+	83	0	0	0	0	5,0745	7	0	0	0	0	0	0	0	0			
HACD3	HACD3_HUMAN	45	2,6099	2	7,7571	6	5,0745	4	18,305	7	6,5857	5	6,1491	5	13,952	9			
HDGF	HDGF_HUMAN	27	0	0	2,9089	3	5,0745	6	0	0	3,2929	3	2,6353	3	0	0			
HEATR3	HEAT3_HUMAN	75	0	0	0	0	5,0745	7	0	0	0	0	2,6353	3	0	0			
HELLS	DADSFJ1V9_HUMAN (+	103	0	0	9,6964	10	5,0745	7	0	0	14,269	12	6,1491	7	3,9863	3			
HNRNPD	ADA087WUK2_HUMAN	40	0	0	2,9089	2	5,0745	3	0	0	17,562	6	11,42	5	0	0			
IK	RED_HUMAN	66	0	0	5,8178	6	5,0745	6	0	0	7,6834	7	15,812	15	5,9795	6			
IKZF3	DA087X8S1_HUMAN (-	48	0	0	0	0	5,0745	7	0	0	0	0	0	0	0	0			
LEMD3	MAN1_HUMAN	100	0	0	0	0	5,0745	6	0	0	0	0	0	0	0	0			
LMNB2	LMNB2_HUMAN	70	0	0	0	0	5,0745	5	0	0	0	0	2,6353	2	0	0			
LRRC8A	LRC8A_HUMAN	94	0	0	0	0	5,0745	7	0	0	0	0	0	0	0	0			
MAPKAP1	ADAD0B5EY1_HUMAN	151	0	0	7,7571	5	5,0745	6	0	0	27,441	20	10,541	9	8,9692	9			
MFAP2	MAP2_HUMAN	53	0	0	0	0	5,0745	7	0	0	0	0	0	0	0	0			
MICAL3	MICA3_HUMAN	224	0	0	1,9393	2	5,0745	7	0	0	0	0	7,906	9	0	0			
MIB1	MIB1_HUMAN	81	0	0	2,9089	3	5,0745	7	3,2303	3	0	0	5,2707	6	0	0			
MRPL37	RM37_HUMAN	48	0	0	0	0	5,0745	7	0	0	10,976	9	8,7845	7	0	0			
MRPS9	RT09_HUMAN	46	0	0	19,393	15	5,0745	7	0	0	21,952	14	10,541	11	0	0			
NAA35	NAA35_HUMAN	86	0	0	0	0	5,0745	7	0	0	0	0	0	0	0	0			
NEMF	NEMF_HUMAN	123	0	0	1,9393	2	5,0745	6	0	0	14,269	10	14,934	15	3,9863	4			
NOLC1	NOANOMRM9_HUMAN	75	0	0	0	0	5,0745	6	0	0	0	0	0	0	0	0			
PACSIN2	PACN2_HUMAN	56	0	0	0	0	5,0745	6	0	0	0	0	1,7569	2	0	0			
PAIP1	LSL_HUMAN	47	0	0	0	0	5,0745	7	0	0	0	0	0	0	0	0			
PIGR	PIGR_HUMAN	83	0	0	1,9393	2	5,0745	6	0	0	0	0	0	0	0	0			
PLOD1	PLOD1_HUMAN	84	0	0	2,9089	3	5,0745	7	0	0	8,781	8	0	0	0	0			
POLR1C	RPAC1_HUMAN	39	0	0	6,8482	4	5,0745	6	9,6908	7	8,781	7	8,7845	8	0	0			
POLR2A	RPB1_HUMAN	217	0	0	14,545	13	5,0745	7	0	0	9,8786	9	12,298	13	15,945	13			
POLR3C	RPC3_HUMAN	139	0	0	13,575	10	5,0745	7	3,2303	3	45,205	30	5,2707	6	2,9897	3			
PPP1CA	PP1A_HUMAN	38	0	0	0	0	5,0745	6	0	0	3,2929	2	9,6629	9	0	0			
PRIM1	PRI1_HUMAN	50	0	0	0	0	5,0745	6	2,1555	2	2,1952	2	2,6353	3	1,9932	2			
RAB8A	RAB8A_HUMAN	26	0	0	2,9089	2	5,0745	6	4,307	3	3,2929	3	4,3822	4	0	0			
RAVER1	DA087WZ13_HUMAN (+	78	0	0	0	0	5,0745	7	0	0	0	0	2,6353	3	0	0			
RPL15	RL15_HUMAN	26	0	0	21,332	6	5,0745	2	18,305	9	13,171	6	7,906	3	5,9795	5			
RPL23A	RL23A_HUMAN	18	0	0	20,362	8	5,0745	4	8,614	4	24,148	12	13,177	10	6,9761	4			
RPL26	RL26_HUMAN	17	0	0	12,605	5	5,0745	5	6,4605	5	13,171	6	4,3822	5	6,9761	5			
RPL3	RL3_HUMAN	46	0	0	5,8178	4	5,0745	3	37,686	14	45,205	13	20,204	10	10,862	7			
RPL31	RL31_HUMAN	14	0	0	8,7267	5	5,0745	5	9,6908	5	7,6834	5	7,0276	5	5,9795	4			
RPS15	RS15_HUMAN	17	0	0	8,7267	7	5,0745	7	9,6908	6	5,4881	4	7,0276	6	4,9829	5			
RPS15	KPIC2_HUMAN (+2)	18	0	0	12,605	3	5,0745	3	6,4605	2	29,636	4	4,3822	2	4,9829	2			
SEC22B	SC22B_HUMAN	25	0	0	1,9393	2	5,0745	6	8,614	7	0	0	4,3822	5	4,9829	4			
SERPINB12	SPB12_HUMAN	46	0	0	5,8178	4	5,0745	3	0	0	0	0	11,42	7	17,938	5			
SF3A2	SF3A2_HUMAN	49	0	0	0	0	5,0745	5	0	0	0	0	0	0	0	0			
SMARCAD1	SMHC2_HUMAN	117	0	0	0	0	5,0745	5	0	0	0	0	0	0	0	0			
SNRNP70	RU17_HUMAN	52	0	0	2,9089	2	5,0745	3	0	0	23,05	13	18,447	10	3,9863	3			
SPIN3	SPIN3_HUMAN	29	0	0	2,9089	2	5,0745	4	0	0	3,2929	2	7,906	6	0	0			
SRP14	SRP14_HUMAN	15	0	0	7,7571	5	5,0745	6	3,2303	3	7,6834	5	11,42	7	3,9863	3			
STAG2	STAG2_HUMAN	141	0	0	0	0	5,0745	7	0	0	0	0	0	0	0	0			
TPT1	TPT1_HUMAN	97	0	0	1,9393	2	5,0745	6	0	0	0	0	0	0	0	0			
TNIK	TNIK_HUMAN	155	0	0	5,8178	2	5,0745	2	0	0	15,367	8	0	0	7,9726	4			
TOMM70	TOM70_HUMAN	67	0	0	0	0	5,0745	7	0	0	2,1952	2	11,42	12	6,9761	6			
TUBGCP	TBCP_HUMAN	51	0	0	0	0	5,0745	8	2,1555	2	0	0	1,7569	2	2,9897	3			

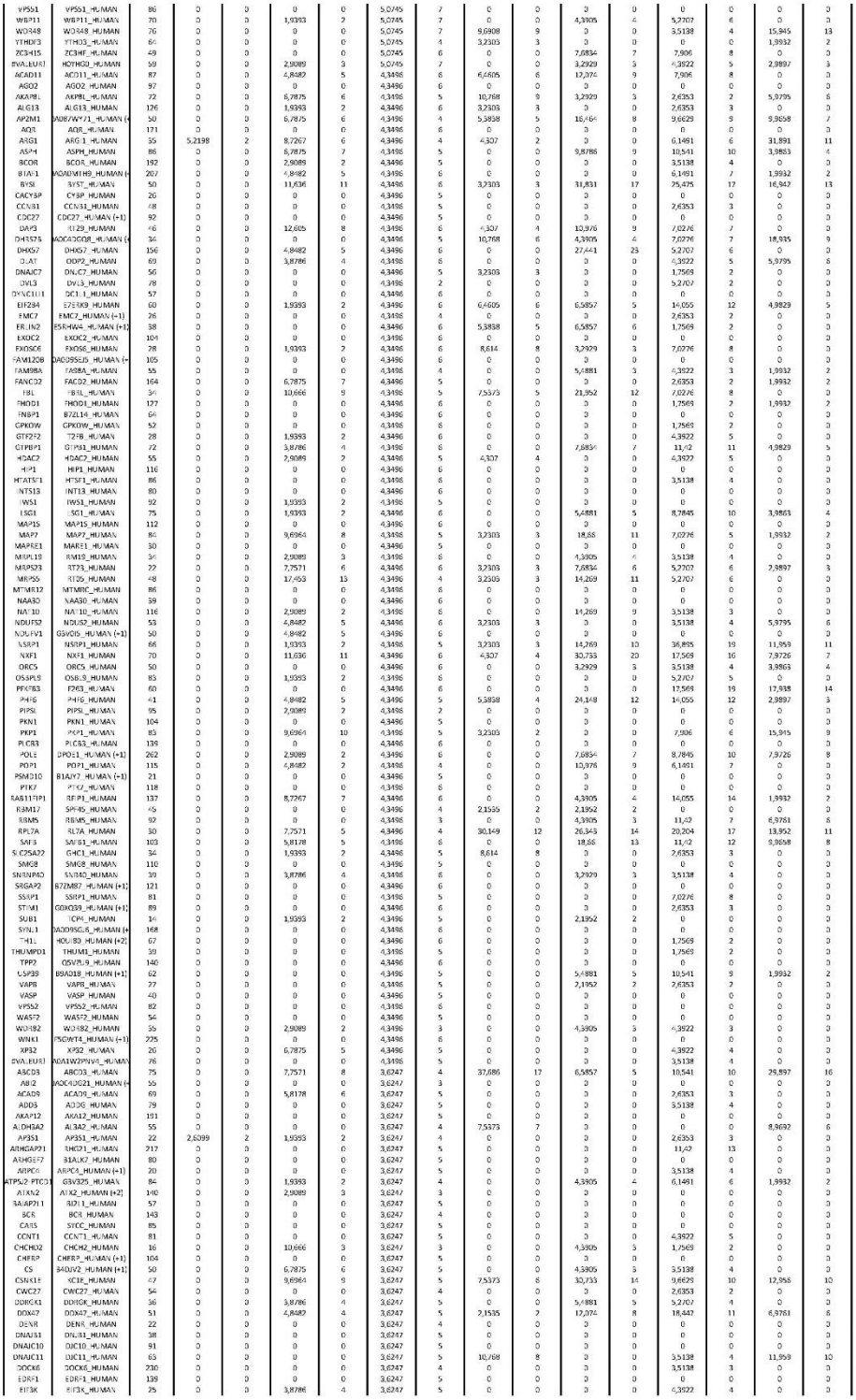

ELP2	ELP2_HUMAN	92	0	0	0	0	3,6247	2	0	0	0	0	0	0	0	0	0	0	0
FMC8	FMC8_HUMAN	26	0	0	1,9393	2	3,6247	5	0	0	0	0	1,7569	2	0	0	0	0	0
EMD	EMD_HUMAN	29	0	0	0	0	3,6247	3	20,458	13	2,1952	2	4,3922	4	8,9692	8	0	0	0
ERAL1	ERAL1_HUMAN	48	0	0	1,9393	2	3,6247	5	3,2303	3	4,3905	4	2,6353	3	0	0	0	0	0
ERC1	G8IL33_HUMAN (+1)	125	0	0	0	0	3,6247	5	0	0	0	0	0	0	0	0	0	0	0
ERI1	ERI1_HUMAN	40	0	0	3,8786	4	3,6247	5	0	0	5,4881	4	4,3922	4	0	0	0	0	0
FAM120A	FI20A_HUMAN	122	0	0	7,7571	7	3,6247	5	0	0	43,612	27	12,298	14	0	0	0	0	0
FAM91A1	F91A1_HUMAN	96	0	0	0	0	3,6247	4	0	0	0	0	0	0	0	0	0	0	0
FSD1	FSD1_HUMAN	56	0	0	0	0	3,6247	5	0	0	0	0	0	0	0	0	0	0	0
GATAD2A	P66A_HUMAN	68	0	0	1,9393	2	3,6247	4	0	0	0	0	5,2707	5	2,9897	2	0	0	0
GATAD2B	AD1BRM1_HUMAN (-	65	0	0	0	0	3,6247	5	0	0	0	0	8,7845	10	0	0	0	0	0
GTF3C5	TF3C5_HUMAN	60	0	0	2,9089	3	3,6247	5	13,998	10	2,1952	2	4,3922	4	3,9863	4	0	0	0
HDAC6	HDAC6_HUMAN	131	0	0	0	0	3,6247	4	0	0	0	0	0	0	0	0	0	0	0
HDX	HDX_HUMAN	77	0	0	0	0	3,6247	4	0	0	0	0	2,6353	2	0	0	0	0	0
HEAT1	HEAT1_HUMAN (+1)	242	0	0	0	0	3,6247	5	0	0	0	0	1,7569	2	0	0	0	0	0
HIP1R	HIP1R_HUMAN	119	0	0	0	0	3,6247	5	0	0	0	0	0	0	0	0	0	0	0
IGLC2	IGLC2_HUMAN (-1)	11	0	0	7,7571	3	3,6247	3	6,4605	2	0	0	0	0	0	0	0	0	0
ILK	MOAOMTH3_HUMAN (-	55	0	0	1,9393	2	3,6247	5	0	0	2,1952	2	0	0	1,9932	2	0	0	0
KAT6A	KAT6A_HUMAN	56	0	0	0	0	3,6247	5	2,1555	2	0	0	7,906	8	2,9897	3	0	0	0
KLC3	K7EL76_HUMAN (-1)	44	0	0	0	0	3,6247	2	0	0	0	0	0	0	0	0	0	0	0
LRPAP1	AMRP_HUMAN	41	0	0	0	0	3,6247	5	0	0	0	0	0	0	0	0	0	0	0
LRRC41	A0A0B4J2G4_HUMAN	86	0	0	1,9393	2	3,6247	4	0	0	0	0	3,5138	4	0	0	0	0	0
LRRFIP2	LRRF2_HUMAN	82	0	0	0	0	3,6247	2	0	0	0	0	1,7569	2	0	0	0	0	0
LUC7L	LUC7_HUMAN	66	0	0	10,666	3	3,6247	2	0	0	23,05	6	7,0276	2	0	0	0	0	0
MCTS1	MCTS1_HUMAN	21	0	0	0	0	3,6247	5	0	0	0	0	0	0	0	0	0	0	0
MORF4L1	E9CYM8_HUMAN	40	0	0	5,8178	6	3,6247	4	0	0	14,269	10	5,2707	5	0	0	0	0	0
MRPL11	RM11_HUMAN	21	0	0	6,7875	7	3,6247	4	5,3838	5	3,2929	3	4,3922	5	1,9932	2	0	0	0
MRPL45	A0A87X2D5_HUMAN (-	35	0	0	0	0	3,6247	4	0	0	2,1952	2	1,7569	2	0	0	0	0	0
MRPL46	RM46_HUMAN	32	0	0	2,9089	3	3,6247	3	2,1555	2	4,3905	3	7,0276	5	0	0	0	0	0
MRPS26	RT26_HUMAN	24	0	0	9,6964	8	3,6247	5	2,1555	2	9,8786	7	4,3922	5	1,9932	2	0	0	0
MTPAP	PAPD1_HUMAN	66	0	0	2,9089	3	3,6247	5	5,3838	4	5,4881	4	8,7845	9	6,9761	7	0	0	0
MYO1F	MYO1F_HUMAN	127	0	0	0	0	3,6247	5	0	0	0	0	0	0	0	0	0	0	0
NOC2L	NOC2_HUMAN	85	0	0	2,9089	3	3,6247	5	5,3838	5	0	0	3,5138	4	0	0	0	0	0
NOP58	NOP58_HUMAN	66	0	0	2,9089	3	3,6247	2	4,307	4	13,171	11	3,5138	4	0	0	0	0	0
NSUN5	NSUN5_HUMAN	47	0	0	5,8178	6	3,6247	5	0	0	9,8786	9	4,3922	4	4,9829	5	0	0	0
PHA1	PHA1_HUMAN	61	0	0	3,8786	4	3,6247	5	17,228	15	4,3905	4	10,541	11	14,949	14	0	0	0
PAXB1	PAXB1_HUMAN	105	0	0	0	0	3,6247	5	0	0	0	0	0	0	0	0	0	0	0
PCBP1	PCBP1_HUMAN	37	0	0	5,8178	6	3,6247	5	8,614	7	14,269	11	8,7845	9	0	0	0	0	0
PIKS4	PI3K4_HUMAN	153	0	0	0	0	3,6247	5	0	0	0	0	0	0	0	0	0	0	0
PNPT1	PNPT1_HUMAN	86	0	0	0	0	3,6247	5	0	0	0	0	0	0	0	0	0	0	0
PRDX2	PRDX2_HUMAN	22	0	0	4,8482	3	3,6247	3	3,2303	2	5,4881	3	0	0	14,949	6	0	0	0
PRKG1	AAKG1_HUMAN	38	0	0	1,9393	2	3,6247	5	0	0	3,2929	3	3,5138	4	0	0	0	0	0
PTS	PTPS_HUMAN	16	0	0	1,9393	2	3,6247	4	0	0	0	0	1,7569	2	0	0	0	0	0
PUS1	TRUA_HUMAN	47	0	0	7,7571	8	3,6247	5	0	0	17,582	15	13,177	14	0	0	0	0	0
PYM1	PYM1_HUMAN	23	0	0	1,9393	2	3,6247	3	0	0	2,1952	2	1,7569	2	0	0	0	0	0
RAC1	RAC1_HUMAN	21	0	0	3,8786	4	3,6247	5	4,307	4	0	0	0	0	2,9897	3	0	0	0
RBM28	RBM28_HUMAN	86	0	0	0	0	3,6247	4	12,921	12	0	0	0	0	0	0	0	0	0
RBM39	RBM39_HUMAN	59	0	0	7,7571	5	3,6247	5	0	0	18,66	6	14,055	9	12,956	9	0	0	0
RHOC	O5UI08_HUMAN (+1)	22	0	0	0	0	3,6247	3	0	0	0	0	0	0	0	0	0	0	0
RNMT	MCES_HUMAN	55	0	0	0	0	3,6247	5	0	0	3,2929	3	2,6353	3	0	0	0	0	0
RPL18	J3QQ67_HUMAN	22	0	0	4,8482	4	3,6247	4	6,4605	4	4,3905	3	3,5138	4	2,9897	3	0	0	0
RPL27A	RL27A_HUMAN	17	0	0	8,7267	4	3,6247	3	5,3838	3	6,5857	4	2,6353	2	1,9932	2	0	0	0
RRP1	RRP1_HUMAN	55	0	0	9,6964	5	3,6247	3	3,2303	3	13,171	9	5,2707	5	6,9761	6	0	0	0
SAMD1	SAMH1_HUMAN	72	0	0	0	0	3,6247	4	2,1555	2	0	0	2,6353	3	0	0	0	0	0
SCAF8	A0A0A0MT33_HUMAN	148	0	0	0	0	3,6247	4	0	0	3,2929	3	0	0	0	0	0	0	0
SDCB2	SDCB2_HUMAN	46	0	0	6,7875	3	3,6247	3	2,1555	2	9,8786	7	7,906	6	9,9658	5	0	0	0
SF1	SF01_HUMAN	68	0	0	0	0	3,6247	5	0	0	0	0	5,2707	6	0	0	0	0	0
SH3BP1	SH3B1_HUMAN	76	0	0	0	0	3,6247	5	0	0	0	0	0	0	0	0	0	0	0
SLC25A10	DIC_HUMAN	31	0	0	1,9393	2	3,6247	5	16,151	10	2,1952	2	3,5138	4	9,9658	8	0	0	0
SLC25A24	SCMC1_HUMAN	55	0	0	0	0	3,6247	4	0	0	2,1952	2	0	0	0	0	0	0	0
SMN2	A8MW2PRV5_HUMAN (-	30	0	0	2,9089	3	3,6247	3	0	0	3,2929	3	0	0	0	0	0	0	0
SMYD3	SMY3D_HUMAN	27	0	0	0	0	3,6247	4	0	0	0	0	2,6353	3	0	0	0	0	0
SNRPF	RUXF_HUMAN	11	0	0	1,9393	2	3,6247	4	0	0	4,3905	3	5,2707	4	3,9863	3	0	0	0
SNW1	SNW1_HUMAN	61	0	0	3,8786	3	3,6247	5	0	0	6,5857	4	22,84	15	10,962	10	0	0	0
SRSF1	I3KTL2_HUMAN (+1)	28	0	0	0	0	3,6247	4	13,998	10	2,1952	2	8,7845	10	0	0	0	0	0
STRAP	STRAP_HUMAN	38	0	0	0	0	3,6247	5	44,147	17	3,2929	3	1,7569	2	8,9692	8	0	0	0
SUV3	SUV3_HUMAN	80	0	0	2,9089	2	3,6247	5	2,1555	2	0	0	5,2707	5	0	0	0	0	0
SUPT16H	SP16H_HUMAN	170	0	0	0	0	3,6247	4	0	0	0	0	0	0	0	0	0	0	0
TBL1XR1	TBL1R_HUMAN	56	0	0	0	0	3,6247	5	0	0	0	0	0	0	0	0	0	0	0
TELO2	TELO2_HUMAN	92	0	0	0	0	3,6247	5	2,1555	2	0	0	0	0	0	0	0	0	0
TIMM50	TIM50_HUMAN	40	0	0	0	0	3,6247	4	12,921	7	5,4881	4	1,7569	2	0	0	0	0	0
TJP2	ZO2_HUMAN	134	0	0	32,968	25	3,6247	5	3,2303	3	37,319	24	5,2707	6	5,9795	5	0	0	0
TOP1	TOP1_HUMAN	91	0	0	6,7875	7	3,6247	5	3,2303	3	10,976	10	2,6353	3	0	0	0	0	0
TOX4	TOX4_HUMAN	66	0	0	1,9393	2	3,6247	4	0	0	0	0	4,3922	4	0	0	0	0	0
TP53	P53_HUMAN	44	0	0	5,8178	4	3,6247	3	12,921	7	8,781	6	6,1491	5	5,9795	5	0	0	0
TP53RK	P53RK_HUMAN	28	0	0	0	0	3,6247	4	0	0	5,4881	4	4,3922	4	0	0	0	0	0
TRIP10	CIP1_HUMAN	68	0	0	0	0	3,6247	5	0	0	0	0	2,6353	3	0	0	0	0	0
USP19	B5MFG5_HUMAN (+1)	150	0	0	0	0	3,6247	4	0	0	0	0	0	0	0	0	0	0	0
VPS45	VPS45_HUMAN	65	0	0	0	0	3,6247	5	5,3838	5	0	0	0	0	0	0	0	0	0
VPS50	VPS50_HUMAN	111	0	0	0	0	3,6247	5	0	0	0	0	0	0	0	0	0	0	0
WARS2	SYWM_HUMAN	49	0	0	0	0	3,6247	5	0	0	0	0	0	0	0	0	0	0	0
WASHC4	A0A87X2S6_HUMAN (+	137	0	0	0	0	3,6247	5	0	0	0	0	0	0	0	0	0	0	0
XPO5	XPO5_HUMAN	136	0	0	1,9393	2	3,6247	5	0	0	0	0	0	0	0	0	0	0	0
XPOT	XPOT_HUMAN	110	0	0	0	0	3,6247	5	5,3838	5	0	0	0	0	0	0	0	0	0
YARS2	SYYM_HUMAN	53	0	0	1,9393	2	3,6247	5	0	0	0	0	0	0	0	0	0	0	0
YME1L1	YME11_HUMAN	86	0	0	0	0	3,6247	5	24,765	18	6,5857	6	12,298	13	26,908	20	0	0	0
ABL2	ABL2_HUMAN	128	0	0	0	0	2,8997	4	0	0	0	0	0	0	0	0	0	0	0
ADD2	ADD2_HUMAN	81	0	0	0	0	2,8997	4	0	0	0	0	0	0	0	0	0	0	0
AGAP5	AGAP5_HUMAN	95	0	0	3,8786	3	2,8997	3	0	0	6,5857	5	5,2707	6	0	0	0	0	0
ANAPC7	APC7_HUMAN	67	0	0	0	0	2,8997	4	0	0	0	0	0	0	0	0	0	0	0
ANKLE2	ANKL2_HUMAN	104	0	0	0	0	2,8997	4	0	0	0	0	0	0	0	0	0	0	0
ANKZF1	ANKZ1_HUMAN (+1)	81	0	0	0	0	2,8997	4	0	0	0	0	0	0	0	0	0	0	0
APBB2	APBB2_HUMAN (+1)	72	0	0	0	0	2,8997	4	0	0	0	0	1,7569	2	0	0	0	0	0
APP	A4_HUMAN	87	0	0	0	0	2,8997	4	0	0	0	0	0	0	0	0	0	0	0
ARAF	ARAF_HUMAN (+1)	68	0	0	0	0	2,8997	4	13,998	5	4,3905	2	2,6353	2	5,9795	4	0	0	0
ARHGAP5	RHG05_HUMAN	172	0	0	0	0	2,8997	3	0	0	0	0	0	0	0	0	0	0	0
ATP13A1	AT131_HUMAN	133	0	0	0	0	2,8997	4	0	0	0	0	0	0	0	0	0	0	0
ATP5F1	ATSF1_HUMAN (+1)	29	0	0	0	0	2,8997	4	0	0	0	0	0	0	0	0	0	0	0
BAG2	BAG2_HUMAN	24	0	0	4,8482	5	2,8997	4	8,614	8	3,2929	3	2,6353	3	4,9829	5	0	0	0
BAG6	A0A0C1K2I3_HUMAN (+	119	0	0	0	0	2,8997	4	0	0	0	0	0	0	0	0	0	0	0
BCAS2	SPF27_HUMAN	26	0	0	0	0	2,8997	4	2,1555	2	0	0	0	0	0	0	0	0	0
BTD4	BRD4_HUMAN	152	0	0	0	0	2,8997	4	0	0	0	0	0	0	0	0	0	0	0
CASK	CSKP_HUMAN	105	0	0	0	0	2,8997	4	0	0	0	0	0	0	0	0	0	0	0
CCNS2	CCNS2_HUMAN	45	0	0	0	0	2,8997	4	0	0	0	0	0	0	0	0	0	0	0
CDC73	CDC73_HUMAN	61	0	0	3,8786	4	2,8997	4	5,3838	5	0	0	7,0276	8	6,9761	7	0	0	0
CDK7	CDK7_HUMAN (+1)	39	0	0	0	0	2,8997	4	0	0	0	0	0	0	0	0	0	0	0
COPS4	CSN4_HUMAN (+1)	46	0	0	0	0	2,8997	4	0	0	0	0	0	0	0	0	0	0	0
CTNNBL1	A0A87WUB9_HUMAN (-	66	0	0	0	0	2,8997	4	0	0	0	0	0	0	0	0	0	0	0
CXorf56	CX056_HUMAN	26	0	0	0	0	2,8997	4	0	0	0	0	0	0	0	0	0	0	0
CYBSR1	YB5R1_HUMAN	34	0	0	0	0	2,8997	4	0	0	0	0	0	0	0	0	0	0	0
CYC1	CY1_HUMAN	35	0	0	0	0	2,8997	4	5,3838	5	0	0	5,2707	6	4,9829	5	0	0	0
DB11	DB11_HUMAN	62	0	0	0	0	2,8997	4	0	0	0	0	3,5138	3	0	0	0	0	0
DDOST	A0C4DGS1_HUMAN (+	49	0	0	2,9089	3	2,8997	4	0	0	3,2929	3	3,5138	4	0	0	0	0	0
DDX18	DDX18_HUMAN	75	0	0	10,666	8	2,8997	4	9,6908	9	9,8786	9	9,6629	10	3,9863	4	0	0	0
DDX23	DDX23_HUMAN	96	0	0	1,9393	2	2,8997	4	0	0	7,6834	6	1,7569	2	0	0	0	0	0
DECR1	DECR_HUMAN	36	0	0	0	0	2,8997	3	0	0	0	0	1,7569	2	0	0	0	0	0
DHX	DHX_HUMAN	43	0	0	0	0	2,8997	3	0	0	9,8786	6	7,0276	6	5,9795	5	0	0	0
DHCR24	DHC24_HUMAN (+1)	60	0	0	1,9393	2	2,8997	3	0	0	0	0	0	0	2,9897	3	0	0	0
DHX37	DHX37_HUMAN	96	0	0	1,9393	2	2,8997	3	5,3838	4	4,3905	4	2,6353	3	4,9829	5	0	0	0
DIDO1	DIDO1_HUMAN	244	0	0	3,8786	3	2,8997	4	5,3838	5	18,66	16	11,42	13	10,967	11	0	0	0
DIM1	DIM1_HUMAN	35	0	0	5,8178	6	2,8997	3	4,307	4	14,269	11	7,0276	7	1,9932	2	0	0	0
DNAJC1	DNJC1_HUMAN	66	0	0	0	0	2,8997	4	0	0	0	0	4,3922	5	0	0	0	0	0
DNAJC21	DJC21_HUMAN	62	0	0	2,9089	3	2,8997	4	0	0	2,1952	2	7,0276	7	1,9932	2	0	0	0
DTD1	DTD1_HUMAN	23	0	0	1,9393	2	2,8997	4	0	0	0	0	2,6353	3	0	0	0	0	0
ECI2	A0A0C4DGA2_HUMAN	40	0	0	0	0	2,8997	4	0	0	0	0	0	0	0	0	0	0	0
EDF1	EDF1_HUMAN	16	0	0	0	0	2,8997	3	0	0	0	0	0	0	0	0	0	0	0
EIF2AK3	E2AK3_HUMAN	187	0	0	0	0	2,8997	4	0	0	0	0	0	0	0	0	0	0	0

EIF2B1	EI2BA_HUMAN	54	0	0	2,9089	2	2,8997	2	0	0	3,2929	3	9,6629	8	0	0		
EIF6P2	IF6P2_HUMAN	28	0	0	3,8786	4	2,8997	4	16,151	8	6,5857	5	2,6353	3	0,9858	7		
EIF4H	IF4H_HUMAN	27	0	0	0	0	2,8997	4	0	0	0	0	0	0	0	0		
EMG1	NEP1_HUMAN	27	0	0	2,9089	3	2,8997	4	0	0	2,1952	2	6,1491	7	0	0		
ENAH	ENAH_HUMAN	67	0	0	0	0	2,8997	3	0	0	0	0	0	0	0	0		
EXO2	EXD2_HUMAN	70	0	0	2,9089	2	2,8997	3	22,612	13	3,2929	3	6,1491	5	14,949	11		
FXD06	F7WM6_HUMAN (+1)	82	0	0	0	0	2,8997	4	0	0	0	0	0	0	0	0		
FAM50A	FA50A_HUMAN	40	0	0	0	0	2,8997	4	0	0	0	0	0	0	0	0		
FN3P1L	FBP1L_HUMAN (+1)	70	0	0	0	0	2,8997	4	0	0	0	0	0	0	0	0		
FRG1	FRG1_HUMAN	29	0	0	3,8786	4	2,8997	3	5,3838	5	7,6834	6	8,7845	6	3,9863	4		
GOLGB1	GOGB1_HUMAN	376	0	0	0	0	2,8997	4	0	0	0	0	0	0	0	0		
GPS1	CSN1_HUMAN (+1)	53	0	0	0	0	2,8997	4	0	0	0	0	0	0	0	0		
GTF3C1	TF3C1_HUMAN	236	0	0	10,666	9	2,8997	3	24,765	22	14,269	12	14,934	17	12,956	13		
HDAC1	HDAC1_HUMAN	55	0	0	0	0	2,8997	3	0	0	0	0	0	0	0	0		
HEXIM1	HEXI1_HUMAN	41	0	0	0	0	2,8997	3	0	0	0	0	1,7569	2	0	0		
HIST1H2AC	H2A1C_HUMAN (+6)	14	0	0	8,7267	2	2,8997	2	4,307	2	7,6834	2	5,2707	2	2,9897	2		
HNRNPF	HNRPF_HUMAN	46	9,1346	3	1,9393	2	2,8997	3	13,998	8	15,367	8	9,6629	5	16,942	8		
HNRNPUL2	HNRL2_HUMAN	85	0	0	17,453	15	2,8997	4	0	0	39,514	24	7,906	9	8,9692	9		
HNRPLL	D6W5I2_HUMAN (+1)	60	0	0	0	0	2,8997	4	0	0	0	0	1,7569	2	0	0		
HOOK3	HOOK3_HUMAN	83	0	0	0	0	2,8997	4	0	0	0	0	0	0	0	0		
HP	HOY300_HUMAN	49	16,964	6	1,9393	2	2,8997	3	3,2303	2	5,4881	4	1,7569	2	0	0		
IQGAP2	IQGA2_HUMAN	181	0	6	6,8482	2	2,8997	2	0	0	0	0	7,906	5	0	0		
KDM1A	KDM1A_HUMAN	95	0	0	0	0	2,8997	4	0	0	0	0	0	0	0	0		
KIF1C	KIF1C_HUMAN	123	0	0	0	0	2,8997	3	0	0	7,6834	6	1,7569	2	0	0		
KIFC1	KIFC1_HUMAN	74	0	0	0	0	2,8997	4	0	0	0	0	5,2707	6	0	0		
LARP4	LARP4_HUMAN	81	0	0	5,8178	6	2,8997	4	0	0	5,4881	5	7,0276	7	0	0		
LCN1	LCN1_HUMAN	19	0	0	1,9393	2	2,8997	3	0	0	0	0	0	0	0	0		
LEO1	LEO1_HUMAN	75	0	0	1,9393	2	2,8997	4	0	0	0	0	1,7569	2	0	0		
LIMS1	LIMS1_HUMAN	37	0	0	0	0	2,8997	4	0	0	0	0	0	0	0	0		
LRCH2	LRCH2_HUMAN	85	0	0	2,9089	3	2,8997	4	0	0	0	0	3,5138	4	0	0		
LTN1	LTN1_HUMAN	201	0	0	0	0	2,8997	4	2,1535	2	0	0	3,5138	4	4,9829	5		
MACF1	MACF1_HUMAN	86	0	0	0	0	2,8997	2	10,769	8	0	0	0	0	0	0		
MAGT1	A0B7WU53_HUMAN (+	42	0	0	4,8482	3	2,8997	2	0	0	2,1952	2	5,2707	5	3,9863	3		
MARCKS1	MRP_HUMAN	20	0	0	1,9393	2	2,8997	4	0	0	0	0	0	0	0	0		
MCAT	FABD_HUMAN	43	0	0	0	0	2,8997	4	0	0	0	0	0	0	0	0		
MICALL1	MILK1_HUMAN	95	0	0	0	0	2,8997	4	0	0	0	0	0	0	0	0		
MTM3	MTM3_HUMAN	47	0	0	0	0	2,8997	4	5,3838	5	7,6834	6	11,42	9	8,9692	8		
MRPL16	RM16_HUMAN	28	0	0	3,8786	4	2,8997	4	3,2303	3	6,5857	6	5,2707	6	1,9932	2		
MRPL44	RM44_HUMAN	38	0	0	0	0	2,8997	3	0	0	5,4881	4	4,3922	5	0	0		
MRPL53	RM53_HUMAN	12	0	0	0	0	2,8997	3	0	0	0	0	0	0	0	0		
MRPS15	RT15_HUMAN	30	0	0	6,7875	6	2,8997	4	0	0	5,4881	5	2,6353	3	0	0		
MRPS18B	RT18B_HUMAN	29	0	0	5,8178	5	2,8997	3	2,1535	2	3,2929	3	2,6353	3	0	0		
MRPS35	RT35_HUMAN	57	0	0	14,545	11	2,8997	4	0	0	8,781	8	3,5138	4	0	0		
MTA1	MTA1_HUMAN	81	0	0	0	0	2,8997	2	0	0	0	0	7,0276	5	0	0		
NDUFS3	NDUS3_HUMAN	30	0	0	2,9089	3	2,8997	4	3,2303	3	2,1952	2	2,6353	3	1,9932	2		
NHP2	D6RCS2_HUMAN (+2)	15	0	0	3,8786	4	2,8997	4	0	0	3,2929	3	4,3922	4	0	0		
NIPSNAP1	NIPS1_HUMAN	33	0	0	0	0	2,8997	3	0	0	3,2929	3	2,6353	3	1,9932	2		
NIPSNAP2	NIPS2_HUMAN	34	0	0	2,9089	3	2,8997	4	0	0	0	0	0	0	0	0		
NMT1	NMT1_HUMAN	57	0	0	0	0	2,8997	4	0	0	2,1952	2	5,2707	5	0	0		
NOA1	NOA1_HUMAN	78	0	0	4,8482	4	2,8997	4	0	0	5,4881	4	9,6629	10	0	0		
NOP58	NOP58_HUMAN	60	0	0	2,9089	3	2,8997	4	0	0	10,976	9	9,6629	9	10,962	10		
NSMCE3	NSE3_HUMAN	34	0	0	1,9393	2	2,8997	4	0	0	0	0	3,5138	4	0	0		
OS9P13	OS9L3_HUMAN	101	0	0	3,8786	4	2,8997	4	0	0	6,5857	6	3,5138	4	0	0		
PAHB	PDIA1_HUMAN	57	0	0	0	0	2,8997	4	8,614	7	0	0	1,7569	2	0	0		
PABPN1	PABP2_HUMAN	33	0	0	1,9393	2	2,8997	3	0	0	6,5857	4	3,5138	4	0	0		
PACSIN3	PACN3_HUMAN	48	0	0	0	0	2,8997	3	0	0	0	0	0	0	0	0		
PARG	PARG_HUMAN	111	0	0	0	0	2,8997	4	0	0	0	0	0	0	0	0		
PARN	PARN_HUMAN	75	0	0	0	0	2,8997	4	0	0	0	0	0	0	0	0		
PATL1	PATL1_HUMAN	87	0	0	1,9393	2	2,8997	3	31,226	17	0	0	0	0	31,891	20		
PCYT1A	CSLEJ2_HUMAN (+1)	43	0	0	0	0	2,8997	3	0	0	0	0	1,7569	2	0	0		
PDAP1	HAP28_HUMAN	21	0	0	0	0	2,8997	3	0	0	0	0	0	0	0	0		
PHAX	I3KP25_HUMAN	68	0	0	1,9393	2	2,8997	4	0	0	0	0	4,3922	4	0	0		
PHAX	PHAX_HUMAN	44	0	0	0	0	2,8997	4	0	0	0	0	4,3922	3	1,9932	2		
PIGT	A1W2PNP0_HUMAN (+	66	0	0	0	0	2,8997	4	0	0	0	0	1,7569	2	1,9932	2		
PMS1	PMS1_HUMAN	106	0	0	0	0	2,8997	4	0	0	0	0	0	0	0	0		
PNO1	PNO1_HUMAN	28	0	0	5,8178	5	2,8997	4	0	0	12,074	6	7,906	6	2,9897	3		
POLD2	A0B7WW16_HUMAN (	55	0	0	0	0	2,8997	4	0	0	0	0	0	0	0	0		
POLE2	POLE2_HUMAN	31	0	0	2,9089	3	2,8997	3	3,2303	3	3,2929	3	5,2707	3	3,9863	4		
POLR2E	A0A0M0R7_HUMAN (-	24	0	0	6,7875	6	2,8997	4	2,1535	2	0	0	6,1491	5	0	0		
POLR3B	RPC2_HUMAN	128	0	0	0	0	2,8997	4	0	0	2,1952	2	5,2707	6	0	0		
POLR3C	RPC3_HUMAN	61	0	0	0	0	2,8997	4	0	0	0	0	4,3922	5	0	0		
PRKRA	PRKRA_HUMAN	34	0	0	0	0	2,8997	4	3,2303	3	0	0	0	0	0	0		
PRPF4	PRP4_HUMAN	58	0	0	5,8178	6	2,8997	4	9,6908	9	15,367	13	20,204	19	11,959	12		
PTPRF	PTPRF_HUMAN	213	0	0	0	0	2,8997	4	0	0	0	0	0	0	0	0		
RAB12	RAB12_HUMAN	27	0	0	0	0	2,8997	3	0	0	0	0	0	0	0	0		
RFC1	RFC1_HUMAN	128	0	0	0	0	2,8997	4	3,2303	3	12,074	10	5,5138	3	4,9829	5		
RPL14	E7EP53_HUMAN (+1)	15	0	0	4,8482	3	2,8997	3	9,6908	4	5,4881	4	4,3922	3	4,9829	3		
RPL24	C9JNW5_HUMAN (+7)	18	0	0	8,7267	7	2,8997	4	6,4605	6	7,6834	6	4,3922	4	5,9795	4		
RPL28	RL28_HUMAN	16	0	0	3,8786	3	2,8997	3	6,4605	5	7,6834	5	2,6353	3	0	0		
RPL8	RL8_HUMAN	28	0	0	4,8482	3	2,8997	3	15,075	7	15,367	8	10,541	8	2,9897	3		
RPP30	Q5VU11_HUMAN (+1)	28	0	0	0	0	2,8997	4	0	0	0	0	2,6353	3	0	0		
RPS26	RS26_HUMAN	15	0	0	7,7571	3	2,8997	3	6,4605	3	3,2929	3	4,3922	3	0	0		
RRP1B	RRP1B_HUMAN	84	0	0	5,8178	6	2,8997	4	11,844	10	13,171	11	11,42	11	0	0		
RSU1	RSU1_HUMAN	32	0	0	0	0	2,8997	4	0	0	0	0	0	0	0	0		
RTCA	RTCA_HUMAN	39	0	0	0	0	2,8997	4	0	0	0	0	0	0	0	0		
SAMD4B	A0B7WZT0_HUMAN (+	72	0	0	0	0	2,8997	4	0	0	0	0	0	0	0	0		
SAP30BP	SD30Z_HUMAN	36	0	0	1,9393	2	2,8997	4	0	0	3,2929	3	4,3922	5	0	0		
SEC16A	E9QN16_HUMAN	252	0	0	0	0	2,8997	4	22,612	20	0	0	0	0	7,9726	8		
SETMAR	SETMR_HUMAN	78	0	0	0	0	2,8997	4	0	0	0	0	0	0	0	0		
SF3B6	SF3B6_HUMAN	15	0	0	1,9393	2	2,8997	3	0	0	0	0	3,5138	2	0	0		
SGPL1	SGPL1_HUMAN	64	0	0	0	0	2,8997	4	57,008	17	7,6834	4	6,1491	6	44,846	16		
SIN3A	SIN3A_HUMAN	145	0	0	2,9089	3	2,8997	4	0	0	0	0	0	0	0	0		
SLAIN1	A0A0M5S3_HUMAN (+	62	0	0	0	0	2,8997	4	0	0	0	0	2,6353	3	0	0		
SLC25A1	TXTP_HUMAN	34	0	0	1,9393	2	2,8997	4	13,998	8	4,3305	4	6,1491	5	9,9658	7		
SLIRP	SLIRP_HUMAN	12	0	0	5,8178	6	2,8997	4	3,2303	3	8,781	6	5,2707	6	7,9726	8		
SMARCE1	B4DGM3_HUMAN (+1)	45	0	0	0	0	2,8997	4	0	0	0	0	0	0	0	0		
SMCHD1	SMHD1_HUMAN	226	0	0	0	0	2,8997	4	0	0	0	0	0	0	0	0		
SPAT5	SPAT5_HUMAN	98	0	0	0	0	2,8997	2	0	0	0	0	0	0	0	0		
SRSF4	SRSF4_HUMAN	57	0	0	1,9393	2	2,8997	4	0	0	3,2929	2	7,0276	6	0	0		
STT3A	STT3A_HUMAN	96	0	0	2,9089	3	2,8997	4	3,2303	3	5,4881	5	1,7569	2	4,9829	4		
TAB3	TAB3_HUMAN	79	0	0	0	0	2,8997	3	0	0	0	0	0	0	0	0		
TARS2	SYTM_HUMAN	81	0	0	0	0	2,8997	4	5,3838	5	0	0	0	0	0	0		
TCF25	TCF25_HUMAN	77	0	0	1,9393	2	2,8997	3	2,1535	2	4,3305	4	8,7845	9	9,9658	9		
THUMPD3	THUM3_HUMAN	57	0	0	0	0	2,8997	4	0	0	0	0	0	0	0	0		
TMEM109	TM109_HUMAN	76	0	0	1,9393	2	2,8997	4	0	0	2,1952	2	1,7569	2	0	0		
TRIM25	TRI25_HUMAN	71	0	0	0	0	2,8997	4	4,307	3	0	0	0	0	0	0		
TRMT1L	TRM1L_HUMAN	82	0	0	1,9393	2	2,8997	4	7,5373	7	3,2929	3	6,1491	6	2,9897	2		
TSC2	TSC2_HUMAN	201	0	0	2,9089	2	2,8997	4	0	0	2,1952	2	2,6353	3	0	0		
TUBGCP2	GCP2_HUMAN	103	0	0	0	0	2,8997	3	0	0	0	0	0	0	0	0		
TUBGCP3	GCP3_HUMAN	104	0	0	0	0	2,8997	4	3,2303	3	0	0	0	0	0	0		
U2SURP	E7ET15_HUMAN (+1)	118	0	0	1,9393	2	2,8997	4	0	0	0	0	0	0	0	0		
VPS13C	VP13C_HUMAN	422	0	0	0	0	2,8997	4	0	0	0	0	0	0	0	0		
VWA8	VWA8_HUMAN	215	0	0	1,9393	2	2,8997	4	0	0	0	0	2,6353	3	2,9897	3		
WASHC5	WASC5_HUMAN	134	0	0	0	0	2,8997	4	0	0	0	0	0	0	0	0		
WASL	WASL_HUMAN	55	0	0	0	0	2,8997	3	0	0	0	0	1,7569	2	0	0		
WDR33	WDR33_HUMAN	146	0	0	7,7571	7	2,8997	4	0	0	9,8786	8	2,6353	3	3,9863	4		
WDR5	WDR5_HUMAN	37	0	0	0	0	2,8997	4	5,3838	4	4,3305	4	1,7569	2	0	0		
WDR92	WDR92_HUMAN	40	0	0	0	0	2,8997	4	0	0	0	0	0	0	0	0		
XAB2	SYF1_HUMAN	100	0	0	0	0	2,8997	4	0	0	0	0	0	0	0	0		
XRCC1	F5H827_HUMAN (+1)	66	0	0	0	0	2,8997	4	0	0	2,1952	2	7,0276	8	0	0		
YTHDF2	YTHD2_HUMAN	62	0	0	0	0	2,8997	2	3,2303	2	0	0	2,6353	2	3,9863	3		
YWHAC	1433C_HUMAN	28	0	0	1,9393	2	2,8997	2	8,614	6	2,1952	2	0	0	0	0		
ZC3H11A	ZC11A_HUMAN	89	0	0	2,9089	3	2,8997	4	0	0	13,171	12	16,691	18	4,9829	5		
ZCCHC9	ZCHC9_HUMAN	79	0	0	0	0	2,8997	4	0	0	0	0	0	0	0	0		
ZN326	ZN326_HUMAN	66	0	0	1,9393	2	2,8997	4	0	0	9,8786	9	8,7845	10	6,9761	7		
ZNF622	ZN622_HUMAN	54	0	0	1,9393	2	2,8997	4	0	0	3,2929	3	7,0276	8	0	0		
ZW10	ZW10_HUMAN	89	0	0	0	0	2,8997	4	0	0	0	0	0	0	0	0		

ADAR	ISRAD_HUMAN	136	0	0	0	0	2,1748	3	0	0	9,8786	9	7,906	9	6,9761	6			
AKAP8	AKAP8_HUMAN	76	0	0	2,9089	2	2,1748	2	10,768	8	13,171	10	4,3922	5	8,9692	6			
ANGEL2	ANGE2_HUMAN	62	0	0	0	0	2,1748	2	0	0	0	0	1,7569	2	0	0			
AP1S2	AP1S2_HUMAN	19	0	0	0	0	2,1748	3	0	0	0	0	0	0	0	0			
ARF4	ARF4_HUMAN	21	0	0	0	0	2,1748	2	4,307	3	0	0	2,6353	3	1,9932	2			
ATP1B1	AT1B1_HUMAN	55	0	0	0	0	2,1748	2	0	0	0	0	0	0	0	0			
ATP5H	ATP5H_HUMAN	18	0	0	0	0	2,1748	3	0	0	0	0	0	0	0	0			
AURKA	AURKA_HUMAN	46	0	0	2,9089	3	2,1748	3	3,2303	3	4,3305	4	2,6353	2	4,9829	5			
BCKDK	BCKD_HUMAN	46	0	0	4,8482	4	2,1748	3	0	0	7,6834	6	3,5138	4	0	0			
BIRC6	BIRC6_HUMAN	530	0	0	0	0	2,1748	3	0	0	0	0	0	0	0	0			
BLMH	BLMH_HUMAN	55	0	0	0	0	2,1748	2	0	0	0	0	0	0	5,9795	4			
BRD7	BA140T9F9_HUMAN (+	88	0	0	0	0	2,1748	3	0	0	0	0	0	0	0	0			
BTF3L4	BTL4_HUMAN	17	0	0	0	0	2,1748	3	0	0	0	0	0	0	0	0			
BUD23	BUD23_HUMAN	32	0	0	3,8786	4	2,1748	3	0	0	7,6834	6	3,5138	3	0	0			
C17orf75	JSUC5_HUMAN (+1)	45	0	0	2,9089	3	2,1748	3	0	0	0	0	1,7569	2	0	0			
C3orf58	DIA1_HUMAN	49	0	0	6,7875	7	2,1748	3	11,844	10	8,781	7	8,7845	9	12,956	12			
C8orf33	CH033_HUMAN	75	0	0	2,9089	3	2,1748	3	2,1535	2	0	0	4,3922	5	1,9932	2			
CADPS2	H73YR4_HUMAN	103	0	0	0	0	2,1748	3	0	0	0	0	0	0	0	0			
CAMSAP2	CAMP2_HUMAN	168	0	0	2,9089	3	2,1748	3	0	0	0	0	6,1491	7	3,9863	4			
CCDC8	CCDC8_HUMAN	59	0	0	6,7875	7	2,1748	3	4,307	4	9,8786	9	5,2707	6	0	0			
CCNK	CCNK_HUMAN	66	0	0	3,8786	3	2,1748	2	2,1555	2	2,1952	2	3,5138	4	1,9932	2			
CDC16	CDC16_HUMAN (+1)	72	0	0	0	0	2,1748	3	0	0	0	0	0	0	0	0			
CDC20	CDC20_HUMAN	55	0	0	0	0	2,1748	3	4,307	4	4,3305	4	0	0	5,9795	5			
CHCHD3	CSUI2_HUMAN (+1)	27	0	0	0	0	2,1748	3	7,5373	6	0	0	1,7569	2	1,9932	2			
CHD8	CHD8_HUMAN	291	0	0	4,8482	4	2,1748	3	0	0	10,976	10	16,691	17	11,959	12			
CHIT1B	A0A0B5I5B8_HUMAN	129	0	0	2,9089	2	2,1748	2	0	0	0	0	2,6353	3	0	0			
CIRBP	CIRBP_HUMAN	19	0	0	0	0	2,1748	2	2,1535	2	3,2929	3	3,5138	3	2,9897	2			
CISD2	CISD2_HUMAN	15	0	0	0	0	2,1748	3	0	0	0	0	1,7569	2	0	0			
CLP1	CLP1_HUMAN (+1)	48	0	0	0	0	2,1748	2	0	0	0	0	0	0	0	0			
CNOT2	CNOT2_HUMAN	60	0	0	0	0	2,1748	3	0	0	0	0	0	0	0	0			
CNOT3	CNOT3_HUMAN	82	0	0	0	0	2,1748	3	0	0	0	0	0	0	0	0			
COPS3	CSN3_HUMAN	68	0	0	0	0	2,1748	3	0	0	0	0	0	0	0	0			
COQ8A	COQ8A_HUMAN	72	0	0	0	0	2,1748	3	3,2303	3	3,2929	3	0	0	2,9897	3			
CPSF1	CPSF1_HUMAN	161	0	0	0	0	2,1748	2	0	0	8,781	8	1,7569	2	2,9897	3			
CRNKL1	QSJY65_HUMAN	99	0	0	0	0	2,1748	3	0	0	0	0	4,3922	5	0	0			
CTR9	CTR9_HUMAN	134	0	0	2,9089	2	2,1748	3	0	0	0	0	6,1491	5	0	0			
CWC22	CWC22_HUMAN	105	0	0	0	0	2,1748	2	0	0	0	0	0	0	0	0			
DBT	O2L2_HUMAN	53	0	0	0	0	2,1748	3	0	0	0	0	0	0	0	0			
DCAF7	DCAF7_HUMAN	39	0	0	2,9089	3	2,1748	3	49,531	13	4,3305	4	3,5138	4	10,962	9			
DDX49	DDX49_HUMAN	54	0	0	0	0	2,1748	2	0	0	6,5857	5	7,906	6	4,9829	5			
DIAPH2	A6NML8_HUMAN (+2)	125	0	0	0	0	2,1748	3	0	0	0	0	0	0	0	0			
DKC1	DKC1_HUMAN	58	0	0	1,9393	2	2,1748	3	0	0	7,6834	7	9,6629	9	4,9829	5			
DMXL1	F5H269_HUMAN	340	0	0	0	0	2,1748	3	0	0	0	0	0	0	0	0			
DNAJB12	DJB12_HUMAN (+1)	42	0	0	2,9089	3	2,1748	3	3,2303	3	4,3305	4	2,6353	3	2,9897	3			
DNAJC3	DNJC3_HUMAN	58	0	0	0	0	2,1748	3	0	0	0	0	0	0	0	0			
DTL	DTL_HUMAN (+1)	79	0	0	0	0	2,1748	3	6,4605	5	2,1952	2	3,5138	4	0	0			
DVL1	DVL1_HUMAN	75	0	0	0	0	2,1748	3	0	0	6,5857	6	4,3922	5	0	0			
DYNC2I1	DYHC2_HUMAN	493	0	0	0	0	2,1748	3	0	0	0	0	0	0	0	0			
EAPP	EAPP_HUMAN (+1)	33	0	0	1,9393	2	2,1748	2	0	0	0	0	3,5138	3	0	0			
EEF1E1	HOYAL7_HUMAN	35	0	0	0	0	2,1748	3	0	0	0	0	0	0	0	0			
EHD1	A0A024RS71_HUMAN	62	0	0	0	0	2,1748	2	0	0	0	0	0	0	0	0			
EIF2AK2	E2AK2_HUMAN	62	0	0	0	0	2,1748	3	0	0	0	0	1,7569	2	0	0			
EIF2B3	EI2BG_HUMAN	50	0	0	0	0	2,1748	3	0	0	0	0	7,0276	8	1,9932	2			
EIF2B5	EI2BE_HUMAN	80	0	0	0	0	2,1748	3	2,1535	2	3,2929	3	3,5138	4	0	0			
ELL	ELL_HUMAN	68	0	0	0	0	2,1748	3	0	0	0	0	0	0	0	0			
ELP4	ELP4_HUMAN	47	0	0	0	0	2,1748	3	0	0	0	0	0	0	0	0			
EMC10	EMC10_HUMAN (+1)	27	0	0	0	0	2,1748	2	0	0	0	0	0	0	0	0			
EMC4	EMC4_HUMAN	20	0	0	0	0	2,1748	2	0	0	0	0	0	0	0	0			
EP300	EP300_HUMAN	264	0	0	1,9393	2	2,1748	3	0	0	0	0	3,5138	3	0	0			
ERCC2	A8MX75_HUMAN (+2)	81	0	0	0	0	2,1748	3	2,1535	2	0	0	1,7569	2	0	0			
EXOSC2	EXOS2_HUMAN	32	0	0	0	0	2,1748	3	0	0	0	0	5,5138	4	0	0			
EXOSC8	EXOS8_HUMAN	30	0	0	0	0	2,1748	3	3,2303	3	3,2929	3	2,6353	3	0	0			
FASTKD2	FAKD2_HUMAN	81	0	0	0	0	2,1748	3	3,2303	3	0	0	0	0	0	0			
FKBP15	A0A0M7E0_HUMAN (+	136	0	0	0	0	2,1748	3	0	0	0	0	0	0	0	0			
FKBP3	FKBP3_HUMAN	25	0	0	0	0	2,1748	3	0	0	0	0	0	0	0	0			
FNDC3A	FND3A_HUMAN	132	0	0	0	0	2,1748	3	0	0	0	0	0	0	0	0			
GADD45GIP1	GI45P_HUMAN	25	0	0	0	0	2,1748	3	0	0	3,2929	3	2,6353	3	0	0			
GSF1	GSF1_HUMAN	206	0	0	0	0	2,1748	3	0	0	0	0	0	0	0	0			
GEMIN4	GEMI4_HUMAN (+1)	120	0	0	0	0	2,1748	3	2,1535	2	0	0	1,7569	2	0	0			
GNL3	GNL3_HUMAN	62	0	0	0	0	2,1748	3	18,305	11	6,5857	6	8,7845	7	4,9829	5			
GPATCH11	A0A0MSF9_HUMAN (+	33	0	0	0	0	2,1748	2	0	0	0	0	0	0	0	0			
GRAMD1A	GRM1A_HUMAN (+1)	81	0	0	0	0	2,1748	3	0	0	0	0	0	0	0	0			
GTF2E2	T2E2_HUMAN	33	0	0	3,8786	4	2,1748	3	0	0	2,1952	2	2,6353	3	0	0			
GTF2H2C	T2H2L_HUMAN	44	0	0	0	0	2,1748	3	6,4605	6	2,1952	2	1,7569	2	0	0			
GTPBP10	GTPBA_HUMAN	43	0	0	6,7875	6	2,1748	3	0	0	8,781	7	6,1491	7	0	0			
HABP4	HABP4_HUMAN	46	0	0	1,9393	2	2,1748	3	0	0	4,3305	4	0	0	0	0			
HAUS5	HAUS5_HUMAN	72	0	0	0	0	2,1748	3	2,1535	2	0	0	0	0	0	0			
HAUS6	HAUS6_HUMAN (+1)	109	0	0	0	0	2,1748	3	0	0	0	0	0	0	0	0			
HB8	HB8_HUMAN (+2)	16	0	0	5,8178	4	2,1748	3	2,1535	2	0	0	0	0	0	0			
HCG_1986216	I3L0P3_HUMAN	26	0	0	2,9089	3	2,1748	3	0	0	0	0	2,6353	3	0	0			
HIRIP3	HIRP3_HUMAN	62	0	0	0	0	2,1748	2	0	0	0	0	5,5138	4	0	0			
HOMER1	HOME1_HUMAN	40	0	0	5,8178	5	2,1748	3	0	0	0	0	0	0	0	0			
HSPA4	HSP74_HUMAN	94	0	0	0	0	2,1748	2	18,305	12	0	0	0	0	1,9932	2			
INF2	INF2_HUMAN	136	0	0	1,9393	2	2,1748	3	0	0	0	0	0	0	0	0			
IMUP	K7ERU9_HUMAN	45	0	0	0	0	2,1748	3	0	0	0	0	1,7569	2	0	0			
KIF3B	KIF3B_HUMAN	85	0	0	0	0	2,1748	3	3,2303	2	0	0	0	0	0	0			
KLC1	KLC1_HUMAN	26	0	0	0	0	2,1748	2	0	0	0	0	0	0	0	0			
KPNA3	IMA4_HUMAN	58	0	0	0	0	2,1748	3	0	0	0	0	0	0	0	0			
KRI1	KRI1_HUMAN	85	0	0	1,9393	2	2,1748	3	0	0	3,2929	3	2,6353	3	1,9932	2			
LACRT	LACRT_HUMAN	14	0	0	1,9393	2	2,1748	2	0	0	0	0	0	0	0	0			
LIN7C	LIN7C_HUMAN (+1)	19	0	0	0	0	2,1748	3	0	0	0	0	0	0	0	0			
LMF2	LMF2_HUMAN	80	0	0	0	0	2,1748	3	2,1535	2	2,1952	2	0	0	0	0			
LRWD1	LRWD1_HUMAN	71	0	0	0	0	2,1748	3	0	0	0	0	1,7569	2	1,9932	2			
LSM12	LSM12_HUMAN	22	0	0	0	0	2,1748	3	0	0	0	0	0	0	0	0			
LUC7L3	I3KPP4_HUMAN (+1)	58	0	0	0	0	2,1748	2	0	0	8,781	6	2,6353	2	3,9863	4			
MACF1	MACF1_HUMAN	838	0	0	0	0	2,1748	3	0	0	0	0	5,2707	6	3,9863	4			
MCM2	MCM2_HUMAN	102	0	0	0	0	2,1748	3	0	0	0	0	0	0	0	0			
MK2	A4IW2PPH1_HUMAN (+	61	0	0	0	0	2,1748	3	0	0	0	0	0	0	0	0			
METTL1	TRM8_HUMAN	31	0	0	1,9393	2	2,1748	2	0	0	0	0	2,6353	3	0	0			
METTL3	MTA70_HUMAN	66	0	0	0	0	2,1748	2	0	0	0	0	1,7569	2	0	0			
MICU2	MICU2_HUMAN	50	0	0	3,8786	4	2,1748	3	0	0	9,8786	7	4,3922	5	0	0			
MIPEP	RM18_HUMAN	21	0	0	0	0	2,1748	3	0	0	2,1952	2	0	0	0	0			
MRPL4	K7ES61_HUMAN (+1)	34	0	0	0	0	2,1748	2	0	0	4,3305	4	1,7569	2	0	0			
MRPL47	RM47_HUMAN	29	0	0	1,9393	2	2,1748	3	0	0	4,3305	3	0	0	1,9932	2			
MRPL48	F5H7Q7_HUMAN (+1)	13	0	0	1,9393	2	2,1748	3	0	0	2,1952	2	3,5138	3	1,9932	2			
MRPS25	RT25_HUMAN	20	0	0	4,8482	4	2,1748	3	2,1535	2	6,5857	5	3,5138	3	0	0			
MRPS31	RT31_HUMAN	45	0	0	11,636	8	2,1748	3	2,1535	2	8,781	6	4,3922	5	0	0			
MRPS34	C9JL19_HUMAN	26	0	0	11,636	6	2,1748	2	0	0	7,6834	4	3,5138	4	1,9932	2			
MRPS7	S3QLS3_HUMAN (+1)	52	0	0	12,605	9	2,1748	3	4,307	3	10,976	7	5,2707	4	5,9795	6			
MTF2	MTF2_HUMAN	81	0	0	0	0	2,1748	2	0	0	0	0	0	0	0	0			
MTOR	MTOR_HUMAN	289	0	0	0	0	2,1748	3	0	0	0	0	0	0	0	0			
MYL6	B7Z8Z6_HUMAN	27	0	0	0	0	2,1748	3	2,1535	2	0	0	0	0	0	0			
NCBP2	NCBP2_HUMAN	18	0	0	0	0	2,1748	3	0	0	0	0	0	0	0	0			
NDUFA13	B4DEZ5_HUMAN (+3)	16	0	0	1,9393	2	2,1748	3	0	0	0	0	0	0	0	0			
NDUFS4	NDUS4_HUMAN	20	0	0	0	0	2,1748	3	0	0	0	0	0	0	0	0			
NEDD1	NEDD1_HUMAN	72	0	0	0	0	2,1748	3	0	0	0	0	0	0	0	0			
NFX1	NFX1_HUMAN	36	0	0	2,9089	3	2,1748	3	0	0	8,781	5	7,0276	7	0	0			
NOP2	NOP2_HUMAN	89	0	0	0	0	2,1748	3	13,998	9	0	0	1,7569	2	0	0			
NRSC1	GCR_HUMAN	86	0	0	0	0	2,1748	3	0	0	0	0	0	0	0	0			
NSUN4	NSUN4_HUMAN	43	0	0	1,9393	2	2,1748	3	0	0	4,3305	4	2,6353	3	0	0			
NTSC2	SNTC_HUMAN	65	0	0	0	0	2,1748	2	0	0	0	0	2,6353	3	0	0			
NUB1	H3BM16_HUMAN	72	0	0	0	0	2,1748	3	0	0	0	0	0	0	0	0			
NUMB	NUMB_HUMAN	71	0	0	3,8786	4	2,1748	3	2,1535	2	7,6834	6	4,3922	5	0	0			
NUP214	NU214_HUMAN	214	0	0	0	0	2,1748	3	0	0	0	0	0	0	0	0			
ORC2	ORC2_HUMAN	66	0	0	1,9393	2	2,1748	2	0	0	0	0	1,7569	2	1,9932	2			
OS9PL8	OSL8_HUMAN	101	0	0	0	0	2,1748	3	0	0	0	0	0	0	0	0			
OXA1L	I3KNA0_HUMAN	55	0	0	0	0	2,1748	2	0	0	2,1952	2	0	0	0	0			

PARVA	E9PS87_HUMAN (+2)	26	0	0	0	0	2,1748	3	0	0	0	0	0	0	0	0	0	0
PAWR	PAWR_HUMAN	37	0	0	0	0	2,1748	3	0	0	0	0	0	0	0	0	0	0
PCF11	PCF11_HUMAN	173	0	0	0	0	2,1748	3	0	0	2,1952	2	6,1491	7	0	0	0	0
PDCD11	RIPS_HUMAN	209	0	0	0	0	2,1748	3	26,758	19	2,1952	2	2,6353	3	0	0	0	0
PDIA3	PDIA3_HUMAN	57	0	0	0	0	2,1748	3	0	0	0	0	0	0	0	0	0	0
PEX13	PX13B_HUMAN	28	0	0	0	0	2,1748	3	4,307	3	4,3905	4	2,6353	3	2,9897	3	0	0
PGD	6PGD1_HUMAN	53	0	0	1,9393	2	2,1748	3	0	0	0	0	0	0	0	0	0	0
PHKG2	J3KRN3_HUMAN (+1)	47	0	0	0	0	2,1748	3	7,5373	6	0	0	0	0	0	0	0	0
PIBF1	A0B7WUI6_HUMAN (+	85	0	0	0	0	2,1748	3	0	0	0	0	0	0	0	0	0	0
PIH1D1	PIHD1_HUMAN	32	0	0	0	0	2,1748	3	0	0	0	0	0	0	0	0	0	0
PIKSC3	A1W2P5Q5_HUMAN (+	102	0	0	0	0	2,1748	2	0	0	0	0	0	0	0	0	0	0
PIP5K1A	A6PWT7_HUMAN (+1)	61	0	0	4,8482	4	2,1748	3	5,3838	4	19,757	15	7,906	8	5,9795	5	0	0
PLK1	PLK1_HUMAN	68	0	0	0	0	2,1748	3	17,228	11	0	0	1,7569	2	27,904	17	0	0
PLRG1	PLRG1_HUMAN	57	0	0	0	0	2,1748	3	4,307	4	0	0	5,2707	5	0	0	0	0
POLD3	DPOD3_HUMAN	51	0	0	0	0	2,1748	3	0	0	4,3905	4	7,906	9	0	0	0	0
POLDIP3	PDIP3_HUMAN	46	0	0	4,8482	4	2,1748	2	0	0	26,343	17	26,353	16	17,938	15	0	0
POLR3F	RPC6_HUMAN	36	0	0	0	0	2,1748	3	0	0	0	0	3,5138	4	0	0	0	0
PPIL1	PPIL1_HUMAN	18	0	0	0	0	2,1748	2	0	0	0	0	1,7569	2	0	0	0	0
PPIP5K2	A0B7Z4V0_HUMAN (+	144	0	0	0	0	2,1748	3	0	0	0	0	0	0	0	0	0	0
PPM1D2C	PP1DC_HUMAN	85	0	0	0	0	2,1748	3	0	0	0	0	0	0	0	0	0	0
PRC1	PRC1_HUMAN	72	0	0	2,9089	2	2,1748	2	3,2303	3	2,1952	2	14,055	14	7,9726	8	0	0
PREB	PREB_HUMAN	45	0	0	0	0	2,1748	2	0	0	0	0	0	0	0	0	0	0
PRKAA1	AAPK1_HUMAN	64	0	0	0	0	2,1748	3	2,1555	2	0	0	2,6353	3	3,9863	4	0	0
PSKH1	KCP1_HUMAN	76	0	0	0	0	2,1748	3	0	0	0	0	0	0	0	0	0	0
PSMA1	PSA11_HUMAN (+1)	27	0	0	1,9393	2	2,1748	3	0	0	0	0	0	0	0	0	0	0
PSMA7	PSA7_HUMAN	28	0	0	0	0	2,1748	3	0	0	0	0	0	0	0	0	0	0
PURA	PURA_HUMAN	35	0	0	1,9393	2	2,1748	3	4,307	4	8,781	6	11,42	8	0	0	0	0
PURB	PURB_HUMAN	55	0	0	2,9089	2	2,1748	3	2,1555	2	5,4881	5	5,2707	6	0	0	0	0
QPCT	QPCT_HUMAN	41	0	0	0	0	2,1748	3	0	0	3,2929	3	3,5138	4	0	0	0	0
RAD21	RAD21_HUMAN	72	0	0	0	0	2,1748	3	0	0	0	0	0	0	0	0	0	0
RAE1	RAE1L_HUMAN	41	0	0	0	0	2,1748	3	0	0	0	0	2,6353	3	0	0	0	0
RAI14	RAI14_HUMAN	110	0	0	0	0	2,1748	3	0	0	0	0	0	0	0	0	0	0
RALA	RALA_HUMAN	24	0	0	0	0	2,1748	2	0	0	2,1952	2	2,6353	3	3,9863	3	0	0
RBM33	HOY3K6_HUMAN	100	0	0	1,9393	2	2,1748	3	0	0	3,2929	3	0	0	3,9863	4	0	0
RCOR1	RCOR1_HUMAN	53	0	0	0	0	2,1748	3	0	0	0	0	0	0	0	0	0	0
RDH13	RDH13_HUMAN	36	0	0	0	0	2,1748	3	0	0	0	0	0	0	0	0	0	0
RNASPH2B	RN2P3_HUMAN	35	0	0	0	0	2,1748	3	0	0	0	0	0	0	0	0	0	0
RNGTT	MCE1_HUMAN	69	0	0	0	0	2,1748	3	0	0	0	0	0	0	0	0	0	0
RPAP2	RPAP2_HUMAN	70	0	0	1,9393	2	2,1748	3	0	0	2,1952	2	4,3922	5	1,9932	2	0	0
RPL13A	MOQY51_HUMAN	24	0	0	0	0	2,1748	2	8,614	6	5,4881	4	4,3922	5	2,9897	3	0	0
RPL19	J3KTE4_HUMAN (+2)	23	0	0	6,7875	2	2,1748	2	2,1555	2	9,8786	6	2,6353	2	2,9897	2	0	0
RPL34	RL34_HUMAN	13	0	0	3,8786	2	2,1748	3	7,5373	4	13,171	5	7,0276	4	4,9829	3	0	0
RPP38	RPP38_HUMAN	52	0	0	0	0	2,1748	3	0	0	2,1952	2	4,3922	5	0	0	0	0
RPS26	A0A7W1S0_HUMAN (+	15	0	0	6,7875	3	2,1748	2	3,2303	2	6,5857	4	3,5138	3	0	0	0	0
RPS28	RS28_HUMAN	8	0	0	8,7267	3	2,1748	3	3,2303	3	5,4881	3	3,5138	3	1,9932	2	0	0
RRP15	RRP15_HUMAN	51	0	0	4,8482	5	2,1748	3	2,1555	2	7,6854	7	2,6353	3	0	0	0	0
RTF1	RTF1_HUMAN	80	0	0	0	0	2,1748	3	0	0	0	0	0	0	0	0	0	0
S100A8	S10A8_HUMAN	11	0	0	3,8786	2	2,1748	2	0	0	0	0	0	0	0	0	0	0
S100A9	S10A9_HUMAN	13	0	0	0	0	2,1748	2	0	0	0	0	0	0	0	0	0	0
SBNO1	SBNO1_HUMAN	154	0	0	0	0	2,1748	2	0	0	2,1952	2	0	0	0	0	0	0
SKA1	SKA1_HUMAN	29	0	0	0	0	2,1748	3	0	0	0	0	0	0	0	0	0	0
SLC1A5	AAAT_HUMAN	57	0	0	0	0	2,1748	2	0	0	3,2929	2	0	0	1,9932	2	0	0
SNAPC1	SNPC1_HUMAN	45	0	0	1,9393	2	2,1748	3	0	0	3,2929	3	0	0	0	0	0	0
SPTLC1	SPTC1_HUMAN	53	0	0	0	0	2,1748	3	9,6908	8	2,1952	2	3,5138	3	7,9726	8	0	0
SRP9	SRP09_HUMAN	10	0	0	3,8786	3	2,1748	3	0	0	2,1952	2	1,7569	2	0	0	0	0
SRRM2	SRRM2_HUMAN	300	0	0	0	0	2,1748	3	0	0	0	0	2,6353	3	1,9932	2	0	0
SRSF2	SRSF2_HUMAN	25	0	0	0	0	2,1748	2	0	0	0	0	3,5138	3	0	0	0	0
SSR1	SSRA_HUMAN	52	0	0	2,9089	3	2,1748	3	0	0	0	0	3,5138	3	0	0	0	0
STIM2	A1W2PRA1_HUMAN (+	85	0	0	0	0	2,1748	2	0	0	0	0	0	0	0	0	0	0
STK10	STK10_HUMAN	112	0	0	0	0	2,1748	3	0	0	0	0	0	0	0	0	0	0
STX18	D6RF48_HUMAN (+1)	35	0	0	0	0	2,1748	3	0	0	3,2929	3	2,6353	3	0	0	0	0
SUGP1	SUGP1_HUMAN	72	0	0	0	0	2,1748	3	0	0	0	0	0	0	0	0	0	0
SURF6	SURF6_HUMAN	30	0	0	0	0	2,1748	3	0	0	0	0	0	0	0	0	0	0
SYMPK	SYMPK_HUMAN	141	0	0	4,8482	5	2,1748	3	0	0	0	0	2,6353	2	0	0	0	0
TBRG4	TBRG4_HUMAN	71	0	0	0	0	2,1748	3	0	0	0	0	0	0	0	0	0	0
TGM1	TGM1_HUMAN	90	0	0	6,7875	5	2,1748	2	0	0	0	0	0	0	4,9829	5	0	0
TMEM21	TM21_HUMAN	28	0	0	3,8786	4	2,1748	3	4,307	4	0	0	0	0	4,9829	5	0	0
TNP2	TNP2_HUMAN	88	0	0	0	0	2,1748	3	0	0	0	0	0	0	0	0	0	0
TNRC6	TNRC6_HUMAN	104	0	0	0	0	2,1748	2	0	0	0	0	0	0	1,9932	2	0	0
TRIP12	TRIPC_HUMAN	220	0	0	0	0	2,1748	3	0	0	0	0	2,6353	3	0	0	0	0
TRIP4	TRIP4_HUMAN	66	0	0	0	0	2,1748	3	0	0	0	0	6,1491	6	4,9829	5	0	0
TRMT6	TRM6_HUMAN	56	0	0	0	0	2,1748	3	6,4605	5	2,1952	2	5,2707	5	0	0	0	0
TRMT61A	H0Y2Q1_HUMAN (+1)	21	0	0	0	0	2,1748	2	0	0	0	0	3,5138	3	0	0	0	0
TROVE2	ROE2_HUMAN	61	0	0	0	0	2,1748	3	0	0	0	0	1,7569	2	0	0	0	0
TSR3	TSR3_HUMAN	119	0	0	0	0	2,1748	2	0	0	0	0	0	0	0	0	0	0
TTK	TTK_HUMAN	97	0	0	2,9089	3	2,1748	3	2,1555	2	0	0	0	0	0	0	0	0
UBE3C	UBE3C_HUMAN	124	0	0	1,9393	2	2,1748	3	0	0	0	0	0	0	0	0	0	0
UBXN4	UBXN4_HUMAN	57	0	0	0	0	2,1748	2	0	0	0	0	0	0	0	0	0	0
UCKL1	UCKL1_HUMAN	61	0	0	0	0	2,1748	3	0	0	0	0	0	0	0	0	0	0
UNC13A	A0A1B0GUS7_HUMAN	484	0	0	0	0	2,1748	3	0	0	0	0	0	0	0	0	0	0
UNC45A	A1W2PXJ8_HUMAN (+	118	0	0	0	0	2,1748	3	0	0	0	0	0	0	0	0	0	0
UQCC1	B1AKY3_HUMAN (+2)	29	0	0	0	0	2,1748	3	0	0	0	0	0	0	0	0	0	0
USF1	USF1_HUMAN	29	0	0	0	0	2,1748	3	0	0	0	0	0	0	0	0	0	0
UVRAG	UVRAG_HUMAN	78	0	0	0	0	2,1748	3	0	0	0	0	0	0	0	0	0	0
VAC14	VAC14_HUMAN	88	0	0	0	0	2,1748	3	0	0	0	0	0	0	0	0	0	0
VPS55	VPS55_HUMAN	80	0	0	0	0	2,1748	3	0	0	0	0	0	0	0	0	0	0
VTI1B	VTI1B_HUMAN	27	0	0	1,9393	2	2,1748	3	9,6908	6	3,2929	3	3,5138	4	8,9692	7	0	0
WASF1	WASF1_HUMAN	62	0	0	0	0	2,1748	3	0	0	0	0	0	0	0	0	0	0
WASH2P	WASH2_HUMAN	50	0	0	0	0	2,1748	3	0	0	0	0	0	0	0	0	0	0
WDR6	A0A087X095_HUMAN	175	0	0	3,8786	4	2,1748	2	31,226	15	20,855	16	12,298	8	17,938	15	0	0
YTHDC2	YTDC2_HUMAN	160	0	0	0	0	2,1748	3	5,3838	5	17,562	16	4,3922	5	9,9658	8	0	0
ZBTB21	ZBT21_HUMAN	119	0	0	0	0	2,1748	2	0	0	0	0	0	0	0	0	0	0
ZFP91-CNTF	A0A0Y7C7_HUMAN (+	60	0	0	3,8786	4	2,1748	3	0	0	3,2929	3	3,5138	4	0	0	0	0
ZMYM4	ZMYM4_HUMAN	173	0	0	0	0	2,1748	3	0	0	0	0	1,7569	2	0	0	0	0
ZNF131	P2M7	CINC_HUMAN	?	0	0	0	0	2,1748	2	0	0	0	0	0	0	0	0	0	0
AAR2	A2A2Q9_HUMAN (+1)	45	0	0	0	0	1,4499	2	0	0	2,1952	2	6,1491	6	0	0	0	0
AARS2	SYAM_HUMAN	107	0	0	0	0	1,4499	2	0	0	0	0	0	0	0	0	0	0
ABL1	ABL1_HUMAN	123	0	0	0	0	1,4499	2	0	0	0	0	0	0	0	0	0	0
ACD19	ACD19_HUMAN	50	0	0	0	0	1,4499	2	0	0	0	0	0	0	0	0	0	0
ACTL6A	ACL6A_HUMAN	47	0	0	1,9393	2	1,4499	2	0	0	0	0	3,5138	4	1,9932	2	0	0
ACTR1A	ACTZ_HUMAN	43	0	0	0	0	1,4499	2	2,1555	2	0	0	0	0	0	0	0	0
ACTPBP1	CSPC1_HUMAN	138	0	0	3,8786	2	1,4499	2	0	0	4,3905	2	3,5138	4	0	0	0	0
ANAPC1	APC1_HUMAN	217	0	0	0	0	1,4499	2	0	0	0	0	0	0	0	0	0	0
APOO_	A0B7WUX8_HUMAN (+	29	0	0	0	0	1,4499	2	0	0	0	0	0	0	0	0	0	0
ARFGEF1	BIG1_HUMAN	209	0	0	0	0	1,4499	2	0	0	0	0	0	0	0	0	0	0
ARHGAP12	Q13CL9_HUMAN (+1)	91	0	0	0	0	1,4499	2	0	0	0	0	0	0	0	0	0	0
ARL6IP1	H7BZV1_HUMAN	26	0	0	0	0	1,4499	2	0	0	0	0	0	0	0	0	0	0
ARPC5L	ARPL_HUMAN	17	0	0	0	0	1,4499	2	0	0	0	0	0	0	0	0	0	0
ARRB2	ARRB2_HUMAN	46	0	0	0	0	1,4499	2	0	0	6,5857	4	3,5138	4	0	0	0	0
ASCC1	ASCC1_HUMAN (+1)	66	0	0	1,9393	2	1,4499	2	2,1555	2	2,1952	2	4,3922	4	1,9932	2	0	0
ATP1B3	AT1B3_HUMAN	32	0	0	0	0	1,4499	2	0	0	0	0	0	0	0	0	0	0
ATP5O	ATPO_HUMAN	17	0	0	0	0	1,4499	2	0	0	0	0	0	0	0	0	0	0
ATP6V1E1	VATE1_HUMAN	26	0	0	0	0	1,4499	2	0	0	0	0	0	0	0	0	0	0
AUH	AUHM_HUMAN	36	0	0	0	0	1,4499	2	0	0	0	0	0	0	0	0	0	0
AUP1	AUP1_HUMAN	53	0	0	0	0	1,4499	2	3,2303	3	0	0	0	0	0	0	0	0
BAIAP2	BIAP2_HUMAN (+1)	61	0	0	0	0	1,4499	2	0	0	0	0	0	0	0	0	0	0
BICD1	BICD1_HUMAN	111	0	0	0	0	1,4499	2	0	0	0	0	0	0	0	0	0	0
BOD1L1	BOD1L_HUMAN	330	0	0	0	0	1,4499	2	0	0	0	0	0	0	0	0	0	0
BRD8P	BRD8_HUMAN	28	0	0	0	0	1,4499	2	0	0	0	0	1,7569	2	0	0	0	0
C2CD5	C2CD5_HUMAN	110	0	0	0	0	1,4499	2	0	0	0	0	0	0	0	0	0	0
C2orf49	ASHWN_HUMAN	26	0	0	0	0	1,4499	2	0	0	0	0	3,5138	4	0	0	0	0
CA2	CAH2_HUMAN (+2)	29	0	0	0	0	1,4499	2	0	0	0	0	0	0	0	0	0	0
CC2D1B	HOY5I7_HUMAN	70	0	0	0	0	1,4499	2	0	0	0	0	0	0	0	0	0	0
CCDC22	CCD22_HUMAN	71	0	0	0	0	1,4499	2	0	0	0	0	0	0	0	0	0	0
CCDC88A	GRDN_HUMAN	216	0	0	0	0	1,4499	2	0	0	0	0	0	0	0	0	0	0
CCNA2	CCNA2_HUMAN	49	0	0	0	0	1,4499	2	0	0	0	0	0	0	0	0	0	0
CDC23	CDC23_HUMAN	69	0	0	0	0	1,4499	2	3,2303	3	0	0	0	0	0	0	0	0

CEP55	CEP55_HUMAN	56	0	0	0	0	1,4499	2	0	0	0	0	0	0	0	0	0	0	0
CEPT1	A0A0C4DGS9_HUMAN	31	0	0	0	0	1,4499	2	2,1535	2	2,1952	2	1,7569	2	0	0	0	0	0
CFAP20	CFA20_HUMAN	25	0	0	1,9393	2	1,4499	2	0	0	0	0	2,6353	3	0	0	0	0	0
CHCHD1	CHCH1_HUMAN	13	0	0	3,8786	3	1,4499	2	0	0	2,1952	2	1,7569	2	0	0	0	0	0
CHEK1	CHK1_HUMAN	54	0	0	1,9393	2	1,4499	2	4,307	3	9,8786	6	2,6353	3	4,9829	5	0	0	0
CHMP2B	CHM2B_HUMAN	24	0	0	0	0	1,4499	2	3,2303	3	0	0	0	0	0	0	0	0	0
CIPTM1	CIPT1_HUMAN	67	0	0	0	0	1,4499	2	0	0	0	0	0	0	0	0	0	0	0
CNOT10	CNO10_HUMAN	82	0	0	0	0	1,4499	2	0	0	0	0	2,6353	3	0	0	0	0	0
COPS7A	CSN7A_HUMAN	30	0	0	0	0	1,4499	2	0	0	0	0	0	0	0	0	0	0	0
CTSG	CATG_HUMAN (-2)	29	0	0	0	0	1,4499	2	0	0	0	0	0	0	0	0	0	0	0
CTU1	CTU1_HUMAN	36	0	0	1,9393	2	1,4499	2	3,2303	3	2,1952	2	2,6353	3	0	0	0	0	0
CUTC	CUTC_HUMAN	29	0	0	0	0	1,4499	2	0	0	0	0	0	0	0	0	0	0	0
DAXX	DAXX_HUMAN	81	0	0	8,7267	9	1,4499	2	2,1555	2	15,367	12	0	0	0	0	0	0	0
DCTN2	DCTN2_HUMAN	44	0	0	0	0	1,4499	2	0	0	0	0	0	0	0	0	0	0	0
DDX20	DDX20_HUMAN	92	0	0	1,9393	2	1,4499	2	3,2303	3	0	0	1,7569	2	0	0	0	0	0
DDX56	DDX56_HUMAN	62	0	0	1,9393	2	1,4499	2	5,3858	5	7,6894	7	7,0276	7	0	0	0	0	0
DIAPH3	DIAP3_HUMAN	137	0	0	0	0	1,4499	2	0	0	0	0	0	0	0	0	0	0	0
DLG3	DLG3_HUMAN (+1)	90	0	0	0	0	1,4499	2	0	0	0	0	0	0	0	0	0	0	0
DNAJC19	TIM14_HUMAN	12	0	0	1,9393	2	1,4499	2	0	0	0	0	2,6353	3	2,9897	3	0	0	0
DOCK1	A0A096LVH6_HUMAN	218	0	0	0	0	1,4499	2	0	0	0	0	0	0	0	0	0	0	0
DRAP1	C9JCC6_HUMAN (+1)	25	0	0	1,9393	2	1,4499	2	0	0	0	0	1,7569	2	0	0	0	0	0
DRG2	A8MZF9_HUMAN (+1)	38	0	0	0	0	1,4499	2	0	0	0	0	0	0	0	0	0	0	0
DTNA	DTNA_HUMAN	84	0	0	0	0	1,4499	2	0	0	0	0	0	0	0	0	0	0	0
DUS2	DUS2_HUMAN	55	0	0	0	0	1,4499	2	0	0	0	0	0	0	0	0	0	0	0
EGLN1	EGLN1_HUMAN	46	0	0	0	0	1,4499	2	0	0	0	0	1,7569	2	0	0	0	0	0
EIF2AK3	E2AK3_HUMAN	125	0	0	0	0	1,4499	2	0	0	0	0	0	0	0	0	0	0	0
EIF2S1	EIF2A_HUMAN	65	0	0	0	0	1,4499	2	0	0	0	0	0	0	0	0	0	0	0
EIPR1	A8MUM1_HUMAN (+1	46	0	0	0	0	1,4499	2	0	0	0	0	0	0	0	0	0	0	0
ELMO2	ELMO2_HUMAN (+1)	83	0	0	0	0	1,4499	2	0	0	0	0	0	0	0	0	0	0	0
EMC6	EMC6_HUMAN	12	0	0	0	0	1,4499	2	0	0	0	0	0	0	0	0	0	0	0
ENOG6	A0A1B1K686_HUMAN (+	95	0	0	0	0	1,4499	2	0	0	0	0	0	0	0	0	0	0	0
FKBP64	FKB64_HUMAN	76	0	0	0	0	1,4499	2	0	0	0	0	6,1491	6	0	0	0	0	0
FAM207A	F207A_HUMAN	25	0	0	4,8482	5	1,4499	2	0	0	9,8786	7	7,0276	7	4,9829	5	0	0	0
FAT1	FAT1_HUMAN	59	0	0	0	0	1,4499	2	16,151	11	2,1952	2	0	0	15,945	11	0	0	0
FKRP	FKRP_HUMAN	55	0	0	0	0	1,4499	2	4,307	4	0	0	0	0	0	0	0	0	0
FNBP4	FNBP4_HUMAN	110	0	0	0	0	1,4499	2	0	0	0	0	0	0	0	0	0	0	0
GAR1	GAR1_HUMAN	22	0	0	1,9393	2	1,4499	2	0	0	3,2929	3	4,3922	5	1,9932	2	0	0	0
GARS	GARS_HUMAN	83	0	0	0	0	1,4499	2	0	0	0	0	0	0	0	0	0	0	0
GNAS	GNAS1_HUMAN	111	0	0	1,9393	2	1,4499	2	0	0	0	0	3,5138	4	0	0	0	0	0
GOLGA5	GOGA5_HUMAN	85	0	0	0	0	1,4499	2	0	0	0	0	0	0	0	0	0	0	0
GRK2	ARBK1_HUMAN	80	0	0	0	0	1,4499	2	0	0	0	0	0	0	0	0	0	0	0
GTF2H1	TF2H1_HUMAN	62	0	0	0	0	1,4499	2	0	0	0	0	4,3922	5	0	0	0	0	0
GTPBP8	H8W8Y6_HUMAN (+1)	16	0	0	0	0	1,4499	2	0	0	2,1952	2	0	0	0	0	0	0	0
H1FX	H1X_HUMAN	22	0	0	0	0	1,4499	2	3,2303	2	3,2929	2	0	0	2,9897	3	0	0	0
HAT1	HAT1_HUMAN	50	0	0	0	0	1,4499	2	2,1555	2	0	0	0	0	3,9863	4	0	0	0
HAUS4	G3V5H1_HUMAN (+1)	32	0	0	0	0	1,4499	2	4,307	4	0	0	0	0	0	0	0	0	0
HMGN5	HMGN5_HUMAN (+3)	32	0	0	0	0	1,4499	2	0	0	0	0	0	0	0	0	0	0	0
HOXB6	HXB6_HUMAN	25	0	0	4,8482	4	1,4499	2	0	0	8,781	6	3,5138	3	0	0	0	0	0
HS2ST1	HS2ST_HUMAN	42	0	0	3,8786	4	1,4499	2	8,614	6	4,3905	3	4,3922	5	7,9726	6	0	0	0
HSPE1	B8ZZL8_HUMAN (+1)	11	0	0	0	0	1,4499	2	0	0	0	0	0	0	0	0	0	0	0
IARS2	SYIM_HUMAN	114	0	0	0	0	1,4499	2	0	0	0	0	0	0	0	0	0	0	0
IFT57	IFT57_HUMAN	49	0	0	0	0	1,4499	2	4,307	3	0	0	0	0	0	0	0	0	0
IFT74	IFT74_HUMAN	69	0	0	0	0	1,4499	2	4,307	4	0	0	0	0	0	0	0	0	0
ILVBL	ILVBL_HUMAN	68	0	0	0	0	1,4499	2	0	0	0	0	0	0	0	0	0	0	0
INTS10	INT10_HUMAN	82	0	0	0	0	1,4499	2	0	0	0	0	0	0	0	0	0	0	0
INTS12	INT12_HUMAN	69	0	0	0	0	1,4499	2	0	0	0	0	0	0	0	0	0	0	0
INTS3	INT3_HUMAN	118	0	0	0	0	1,4499	2	0	0	0	0	0	0	0	0	0	0	0
IPO7	IPO7_HUMAN	120	0	0	0	0	1,4499	2	0	0	0	0	0	0	0	0	0	0	0
KCTD3	KCTD3_HUMAN	89	0	0	0	0	1,4499	2	0	0	0	0	0	0	0	0	0	0	0
KIAA0100	K0100_HUMAN (+2)	254	0	0	0	0	1,4499	2	0	0	0	0	0	0	0	0	0	0	0
KIAA1468	K1468_HUMAN	135	0	0	0	0	1,4499	2	0	0	0	0	0	0	0	0	0	0	0
KIF7	KIF7_HUMAN	151	0	0	10,666	11	1,4499	2	13,998	10	5,4881	5	1,7569	2	19,932	15	0	0	0
KLC2	KLC2_HUMAN	78	2,6099	2	1,9393	2	1,4499	2	0	0	0	0	0	0	0	0	0	0	0
LANCL2	LANC2_HUMAN	51	0	0	0	0	1,4499	2	0	0	0	0	0	0	0	0	0	0	0
LCN2	NGAL_HUMAN (+1)	23	0	0	0	0	1,4499	2	0	0	0	0	0	0	0	0	0	0	0
LIMA1	LIMA1_HUMAN	85	0	0	0	0	1,4499	2	0	0	0	0	1,7569	2	0	0	0	0	0
LLGL1	A0A7WW77_HUMAN (	114	0	0	1,9393	2	1,4499	2	0	0	18,464	12	12,298	11	8,9692	9	0	0	0
LTBP1	LTBP1_HUMAN	187	0	0	0	0	1,4499	2	0	0	0	0	0	0	0	0	0	0	0
LYV1	LYV1_HUMAN	55	0	0	2,9089	2	1,4499	2	0	0	15,367	10	21,961	11	7,9726	7	0	0	0
LUC7L2	LC7L2_HUMAN	47	2,6099	2	4,8482	3	1,4499	2	0	0	18,68	8	6,1491	5	5,9795	5	0	0	0
LUZP1	LUZP1_HUMAN	120	0	0	0	0	1,4499	2	0	0	0	0	0	0	0	0	0	0	0
LYAR	LYAR_HUMAN	44	0	0	2,9089	3	1,4499	2	2,1555	2	10,976	6	4,3922	4	0	0	0	0	0
MAIP1	MAIP1_HUMAN	33	0	0	0	0	1,4499	2	3,2303	3	0	0	0	0	1,9932	2	0	0	0
MAP7D2	MA7D2_HUMAN	92	0	0	0	0	1,4499	2	0	0	0	0	1,7569	2	0	0	0	0	0
MFTC_14	MFT14_HUMAN	52	0	0	0	0	1,4499	2	2,1535	2	0	0	0	0	0	0	0	0	0
MFAP1	MFAP1_HUMAN	52	0	0	0	0	1,4499	2	7,5373	6	2,1952	2	7,0276	7	0	0	0	0	0
MKL2	MKL2_HUMAN	118	0	0	0	0	1,4499	2	0	0	0	0	0	0	0	0	0	0	0
MORC2	MORC2_HUMAN	118	0	0	0	0	1,4499	2	0	0	0	0	2,6353	3	0	0	0	0	0
MPG	3MG_HUMAN	35	0	0	3,8786	4	1,4499	2	0	0	7,6894	7	0	0	0	0	0	0	0
MRP1	RM01_HUMAN	37	0	0	0	0	1,4499	2	0	0	0	0	0	0	0	0	0	0	0
MRP10	RM10_HUMAN	29	0	0	0	0	1,4499	2	0	0	3,2929	2	1,7569	2	0	0	0	0	0
MRPL17	RM17_HUMAN	20	0	0	2,9089	3	1,4499	2	0	0	4,3905	4	2,6353	3	0	0	0	0	0
MRP2	RM02_HUMAN	33	0	0	0	0	1,4499	2	0	0	0	0	0	0	0	0	0	0	0
MRPL22	E7ESL0_HUMAN (+2)	24	0	0	2,9089	2	1,4499	2	2,1555	2	5,4881	4	2,6353	3	0	0	0	0	0
MRPL24	RM24_HUMAN	25	0	0	0	0	1,4499	2	0	0	2,1952	2	1,7569	2	0	0	0	0	0
MRPL28	A2D0C6_HUMAN (+1)	29	0	0	0	0	1,4499	2	0	0	0	0	2,6353	3	0	0	0	0	0
MRP-3	E7ETU7_HUMAN (+2)	42	0	0	0	0	1,4499	2	0	0	9,8786	8	1,7569	2	0	0	0	0	0
MRPL39	C9J687_HUMAN (+1)	34	0	0	4,8482	5	1,4499	2	0	0	10,976	7	1,7569	2	0	0	0	0	0
MRPL40	RM40_HUMAN	24	0	0	0	0	1,4499	2	0	0	0	0	1,7569	2	0	0	0	0	0
MRPL58	ICT1_HUMAN (+1)	24	0	0	0	0	1,4499	2	0	0	0	0	0	0	0	0	0	0	0
MRPS16	RT16_HUMAN	15	0	0	3,8786	4	1,4499	2	0	0	2,1952	2	0	0	0	0	0	0	0
MRPS21	RT21_HUMAN	11	0	0	3,8786	3	1,4499	2	2,1535	2	4,3905	3	2,6353	2	0	0	0	0	0
MSH3	MSH3_HUMAN	127	0	0	0	0	1,4499	2	0	0	4,3905	2	3,5138	4	0	0	0	0	0
MTERF4	MTERF4_HUMAN	44	0	0	5,8178	5	1,4499	2	0	0	5,4881	5	3,5138	4	0	0	0	0	0
MTMR3	FRWA39_HUMAN	76	0	0	1,9393	2	1,4499	2	2,1535	2	2,1952	2	8,7845	10	1,9932	2	0	0	0
MYO6	A0D96GC1_HUMAN (+	150	0	0	1,9393	2	1,4499	2	0	0	12,074	10	2,6353	3	0	0	0	0	0
NAA50	E7EQE9_HUMAN (+1)	19	0	0	0	0	1,4499	2	0	0	0	0	0	0	0	0	0	0	0
NACC1	NACC1_HUMAN	57	0	0	0	0	1,4499	2	0	0	0	0	3,5138	2	3,9863	3	0	0	0
NAA5	NAA5_HUMAN	269	0	0	0	0	1,4499	2	0	0	0	0	0	0	0	0	0	0	0
NCAPH2	A0A6Y7G7_HUMAN (+	66	0	0	0	0	1,4499	2	0	0	0	0	1,7569	2	0	0	0	0	0
NDE1	NDE1_HUMAN	39	0	0	0	0	1,4499	2	0	0	0	0	0	0	0	0	0	0	0
NDUFA9	NDUA9_HUMAN	43	0	0	2,9089	3	1,4499	2	4,307	4	4,3905	4	3,5138	4	1,9932	2	0	0	0
NDUFB10	K7ERP5_HUMAN (+1)	19	0	0	0	0	1,4499	2	0	0	0	0	0	0	1,9932	2	0	0	0
NDUFS8	NDUS8_HUMAN	24	0	0	0	0	1,4499	2	0	0	0	0	0	0	0	0	0	0	0
NFDIP	NFDIP_HUMAN (+3)	9	0	0	0	0	1,4499	2	0	0	0	0	0	0	0	0	0	0	0
NF1	NF1_HUMAN	319	0	0	0	0	1,4499	2	0	0	0	0	2,6353	3	0	0	0	0	0
NF2	MERL_HUMAN	70	0	0	0	0	1,4499	2	0	0	3,2929	3	8,7845	10	0	0	0	0	0
NHSL2	A0JPW6_HUMAN (+	90	0	0	0	0	1,4499	2	0	0	0	0	1,7569	2	0	0	0	0	0
NMD3	CSIAD8_HUMAN (+1)	60	0	0	0	0	1,4499	2	0	0	0	0	0	0	0	0	0	0	0
NOC4	NOC4L_HUMAN	58	0	0	1,9393	2	1,4499	2	6,4605	6	18,68	13	17,569	13	14,949	12	0	0	0
NOL11	NOL11_HUMAN	81	0	0	0	0	1,4499	2	0	0	0	0	0	0	0	0	0	0	0
NOL6	A0A0D9RW96_HUMAN	112	0	0	5,8178	4	1,4499	2	3,2303	3	8,781	7	0	0	0	0	0	0	0
NOSIP	NOSIP_HUMAN	33	0	0	0	0	1,4499	2	0	0	0	0	0	0	0	0	0	0	0
NR2F2	COTI2_HUMAN	46	0	0	0	0	1,4499	2	0	0	2,1952	2	0	0	2,9897	3	0	0	0
NUP93	NUP93_HUMAN	93	0	0	0	0	1,4499	2	7,5373	7	0	0	0	0	0	0	0	0	0
OBSL1	AGNN50_HUMAN	197	0	0	2,9089	3	1,4499	2	16,151	11	9,8786	8	0	0	0	0	0	0	0
OGDH	OGDHS3_HUMAN (+	113	0	0	0	0	1,4499	2	0	0	0	0	0	0	0	0	0	0	0
OGFR	OGFR_HUMAN	73	0	0	0	0	1,4499	2	0	0	0	0	0	0	0	0	0	0	0
ORC6	ORC6_HUMAN	28	0	0	0	0	1,4499	2	0	0	0	0	0	0	0	0	0	0	0
OTUD6B	A0A87X0W9_HUMAN (	37	0	0	0	0	1,4499	2	0	0	0	0	0	0	0	0	0	0	0
PARD3	PARD3_HUMAN	151	0	0	5,8178	6	1,4499	2	0	0	15,367	14	1,7569	2	1,9932	2	0	0	0
PDE12	PDE12_HUMAN (+1)	52	0	0	0	0	1,4499	2	0	0	0	0	1,7569	2	0	0	0	0	0
PDHX	ODPX_HUMAN	54	0	0	0	0	1,4499	2	0	0	0	0	0	0	0	0	0	0	0
PDK3	PDK3_HUMAN	47	0	0	0	0	1,4499	2	0	0	0	0	0	0	1,9932	2	0	0	0
PDZD8	PDZD8_HUMAN	129	0	0	0	0	1,4499	2	0	0	0	0	0	0	0	0	0	0	0
PELO	PELO_HUMAN	46	0	0	0	0	1,4499	2	5,3858	5	2,1952	2	0	0	0	0	0	0	0
PES1	B5MCY8_HUMAN (+1)	66	0	0	14,545	11	1,4499	2	4,307	4	23,25	13	13,177	14	3,9863	4	0	0	0

PHS5A	PHS5A_HUMAN	12	0	0	0	0	1.4499	2	0	0	0	0	0	0	0	0	0	0	0
PIP4K2A	PI42A_HUMAN	66	0	0	1.9393	2	1.4499	2	0	0	0	3.2929	3	2.6353	3	0	0		
PIP4K2C	PI42C_HUMAN	47	0	0	0	0	1.4499	2	0	0	0	2.1952	2	2.6353	3	0	0		
PLSC	PLSC_HUMAN	532	0	0	0	0	1.4499	2	2.1555	2	0	0	0	2.6353	3	2.9897	2		
PLEKHA1	Q5RGS4_HUMAN	44	0	0	0	0	1.4499	2	0	0	0	0	0	0	0	0	0		
PLPP6	PLPP6_HUMAN	52	0	0	0	0	1.4499	2	0	0	0	0	0	0	0	0	0		
PNPLA6	PLPL6_HUMAN	150	0	0	3.8786	3	1.4499	2	4.307	3	0	0	0	0	0	2.9897	3		
POLA2	DPOA2_HUMAN	66	0	0	0	0	1.4499	2	0	0	0	0	0	3.5138	3	0	0		
POLG	DPOG1_HUMAN	140	0	0	1.9393	2	1.4499	2	0	0	0	0	0	0	0	0	0		
POLR1E	RPA49_HUMAN	54	0	0	0	0	1.4499	2	3.2303	3	6.5857	5	0	0	3.9863	4			
POLR2H	C9JLU1_HUMAN (+1)	17	0	0	1.9393	2	1.4499	2	2.1555	2	0	0	0	2.6353	3	0	0		
PPAT	PUR1_HUMAN	57	0	0	0	0	1.4499	2	0	0	0	0	0	2.6353	3	0	0		
PPP2CA	PP2AA_HUMAN	36	0	0	0	0	1.4499	2	18.305	11	0	0	0	0	0	0	0		
PPP2R1A	2AAA_HUMAN	65	0	0	0	0	1.4499	2	68.912	24	3.2929	3	3.5138	4	10.962	11			
PQBP1	PQBP1_HUMAN	30	0	0	0	0	1.4499	2	0	0	0	0	0	0	0	0			
PRKAB2	AAKB2_HUMAN	30	0	0	0	0	1.4499	2	0	0	0	0	0	0	0	0			
PRKAR2A	KAP2_HUMAN	46	0	0	0	0	1.4499	2	0	0	0	0	0	0	0	0			
PRMT3	ANOAMSN7_HUMAN (+	55	0	0	0	0	1.4499	2	0	0	0	0	0	0	0	0			
PRPF19	PR19A_HUMAN	109	0	0	0	0	1.4499	2	0	0	0	0	0	1.7569	2	0			
PSMA4	PSA4_HUMAN	29	0	0	0	0	1.4499	2	4.307	4	0	0	0	0	0	0			
PSMD8	PSMD8_HUMAN	40	0	0	0	0	1.4499	2	0	0	0	0	0	1.7569	2	0			
PSTPIP2	PIP2_HUMAN	39	0	0	0	0	1.4499	2	0	0	0	0	0	0	0	0			
PTPN13	PTN13_HUMAN	277	0	0	0	0	1.4499	2	0	0	0	0	0	6.1491	6	12.956	13		
PYCR3	ANOAMOS1_HUMAN (+	30	0	0	6.8482	4	1.4499	2	5.3858	5	3.2929	3	2.6353	3	1.9932	2			
RAB13	RAB13_HUMAN	26	0	0	0	0	1.4499	2	0	0	0	0	0	0	0	0			
RADIL	RADIL_HUMAN	117	0	0	0	0	1.4499	2	0	0	0	0	0	0	0	0			
RAF1	RAF1_HUMAN	73	0	0	0	0	1.4499	2	11.844	11	0	0	1.7569	2	4.9829	4			
RAP1B	P5GXB2_HUMAN	16	0	0	0	0	1.4499	2	0	0	0	0	0	0	0	0			
RBBP6	RBBP6_HUMAN	68	0	0	1.9393	2	1.4499	2	2.1555	2	4.3305	4	5.2707	4	4.9829	5			
RBM34	RBM34_HUMAN	49	0	0	0	0	1.4499	2	10.768	10	4.3305	4	4.3922	5	5.9795	6			
RBSN	RBSN_HUMAN	89	0	0	0	0	1.4499	2	0	0	0	0	0	0	0	0			
RC1	SC11_HUMAN	41	0	0	0	0	1.4499	2	0	0	8.781	7	6.1491	7	0	0			
RIF1	RIF1_HUMAN	274	0	0	2.9089	3	1.4499	2	0	0	0	0	2.6353	3	0	0			
RIOK2	RIOK2_HUMAN	63	0	0	6.8482	5	1.4499	2	6.307	4	13.171	11	12.298	11	2.9897	3			
RIOX1	RIOX1_HUMAN	71	0	0	3.8786	4	1.4499	2	3.2303	3	3.2929	3	1.7569	2	0	0			
RNASEH2A	RNH2A_HUMAN	35	0	0	0	0	1.4499	2	0	0	0	0	0	0	0	0			
RNF2	RING2_HUMAN	38	0	0	0	0	1.4499	2	0	0	0	0	0	0	0	0			
RPL15	RL15_HUMAN	24	0	0	0	0	1.4499	2	5.3858	2	5.4881	2	1.7569	2	1.9932	2			
RPL18A	MOSJA7_HUMAN (+1)	17	0	0	2.9089	3	1.4499	2	6.307	3	4.3305	4	1.7569	2	2.9897	3			
RPL35A	RL35A_HUMAN	13	0	0	0	0	1.4499	2	2.1555	2	3.2929	2	2.6353	2	1.9932	2			
RPL37A	C9J423_HUMAN (+1)	8	0	0	2.9089	2	1.4499	2	6.307	4	4.3305	4	1.7569	2	0	0			
RPLP2	RLA2_HUMAN	12	0	0	0	0	1.4499	2	0	0	0	0	2.6353	3	0	0			
RPN2	RPN2_HUMAN	69	0	0	0	0	1.4499	2	0	0	0	0	0	0	0	0			
RPRD1A	RPR1A_HUMAN	37	0	0	0	0	1.4499	2	0	0	0	0	0	0	0	0			
RPRD2	RPRD2_HUMAN	156	0	0	0	0	1.4499	2	0	0	0	0	0	0	0	0			
RPS25	RS25_HUMAN	16	0	0	7.7571	4	1.4499	2	2.1555	2	7.6854	5	1.7569	2	0	0			
RSL1D1	RL1D1_HUMAN	55	0	0	0	0	1.4499	2	0	0	8.781	6	1.7569	2	0	0			
SACM1L	E9PGZ6_HUMAN (+1)	56	0	0	0	0	1.4499	2	0	0	0	0	0	0	0	0			
SAP18	SAP18_HUMAN (+1)	18	0	0	0	0	1.4499	2	0	0	0	0	1.7569	2	0	0			
SCRIB1	SCB1D1_HUMAN	10	0	0	0	0	1.4499	2	0	0	0	0	0	0	0	0			
SCRIB2	SCB1D2_HUMAN	10	0	0	0	0	1.4499	2	0	0	0	0	0	0	0	0			
SCRIB2	SCB2A1_HUMAN	11	0	0	0	0	1.4499	2	0	0	0	0	0	0	0	0			
SCO1	J3QL56_HUMAN (+1)	30	0	0	0	0	1.4499	2	0	0	2.1952	2	2.6353	3	2.9897	3			
SCO2	SCO2_HUMAN	30	0	0	0	0	1.4499	2	3.2303	2	0	0	0	0	2.9897	2			
SDA01	SDA1_HUMAN	80	0	0	5.8178	6	1.4499	2	0	0	5.4881	4	6.1491	7	0	0			
SEC11A	H0YN05_HUMAN (+3)	16	0	0	0	0	1.4499	2	0	0	0	0	0	0	0	0			
SEC61G	SC61G_HUMAN	10	0	0	1.9393	2	1.4499	2	2.1555	2	2.1952	2	2.6353	3	1.9932	2			
SERPINB3	SPB3_HUMAN	45	0	0	4.8482	3	1.4499	2	0	0	0	0	3.5138	4	4.9829	5			
SHOC2	SHOC2_HUMAN	65	0	0	0	0	1.4499	2	0	0	0	0	0	0	0	0			
SLC12A2	G3XAL9_HUMAN (+1)	125	0	0	0	0	1.4499	2	0	0	0	0	0	0	0	0			
SLC25A15	ORNT1_HUMAN	33	0	0	0	0	1.4499	2	5.3858	5	0	0	0	0	0	0			
SLC25A23	O3C2_HUMAN	33	0	0	0	0	1.4499	2	6.7605	6	0	0	1.7569	2	4.9829	5			
SLC30A9	ZNT9_HUMAN	62	0	0	0	0	1.4499	2	0	0	3.2929	3	0	0	5.9795	4			
SLPI	SLPI_HUMAN	14	0	0	1.9393	2	1.4499	2	0	0	0	0	0	0	0	0			
SMAD2	SMAD2_HUMAN	52	0	0	0	0	1.4499	2	0	0	0	0	0	0	0	0			
SMAD5	SMAD5_HUMAN	52	0	0	0	0	1.4499	2	0	0	0	0	0	0	0	0			
SMARCA4	A0A0A0MT49_HUMAN	189	0	0	0	0	1.4499	2	2.1555	2	10.976	10	5.2707	6	0	0			
SMARCA5	SMCA5_HUMAN	122	0	0	0	0	1.4499	2	0	0	3.2929	3	0	0	0	0			
SMG9	SMG9_HUMAN	58	0	0	0	0	1.4499	2	0	0	0	0	0	0	0	0			
SNTB2	SNTB2_HUMAN	58	0	0	0	0	1.4499	2	0	0	0	0	0	0	0	0			
SNX18	SNX18_HUMAN	69	0	0	1.9393	2	1.4499	2	0	0	4.3305	4	5.2707	6	1.9932	2			
SPAST	SPAST_HUMAN	67	0	0	0	0	1.4499	2	0	0	0	0	0	0	0	0			
SPATS2	SPS2L_HUMAN	62	0	0	0	0	1.4499	2	3.2303	3	0	0	3.5138	4	0	0			
SPIN2A	SPI2A_HUMAN (+1)	29	0	0	0	0	1.4499	2	0	0	0	0	0	0	0	0			
SRPK1	SRPK1_HUMAN	76	0	0	0	0	1.4499	2	5.3858	4	3.2929	3	0.6629	3	3.9863	3			
SRSF11	SRS11_HUMAN	54	0	0	0	0	1.4499	2	0	0	4.3305	4	3.5138	4	2.9897	3			
SRSF9	SRSF9_HUMAN	26	0	0	0	0	1.4499	2	3.2303	3	5.4881	5	4.3922	5	0	0			
STRN4	F5GYK2_HUMAN (+1)	69	0	0	0	0	1.4499	2	0	0	0	0	0	0	0	0			
SYX3B	SYX3B_HUMAN	68	0	0	0	0	1.4499	2	0	0	0	0	0	0	0	0			
SUMO1	B4Z7V8_HUMAN (+3)	17	0	0	0	0	1.4499	2	0	0	0	0	0	0	0	0			
TAF12	TAF12_HUMAN	18	0	0	0	0	1.4499	2	0	0	0	0	0	0	0	0			
TAF9B	TAF9B_HUMAN	28	0	0	0	0	1.4499	2	0	0	0	0	0	0	0	0			
TAMM41	TAM41_HUMAN	51	0	0	0	0	1.4499	2	0	0	0	0	0	0	0	0			
TANC1	TANC1_HUMAN	202	0	0	0	0	1.4499	2	0	0	0	0	3.5138	4	0	0			
TBC1D23	TBD23_HUMAN	110	0	0	0	0	1.4499	2	0	0	0	0	0	0	0	0			
TFAM	TFAM_HUMAN	29	0	0	0	0	1.4499	2	0	0	7.6854	5	6.1491	6	1.9932	2			
TIBTM	TIBTM_HUMAN	40	0	0	7.7571	8	1.4499	2	2.1555	2	21.952	16	6.1491	6	0	0			
THOC1	A0B7W9S1_HUMAN (+	76	0	0	0	0	1.4499	2	0	0	0	0	0	0	0	0			
THOC5	THOC5_HUMAN	79	0	0	0	0	1.4499	2	0	0	0	0	0	0	0	0			
TIMELESS	TIM_HUMAN	139	0	0	7.7571	7	1.4499	2	0	0	0	0	2.6353	3	0	0			
TIMMDC1	TIDC1_HUMAN	52	0	0	0	0	1.4499	2	2.1555	2	0	0	1.7569	2	1.9932	2			
TMA16	H0Y9K1_HUMAN (+1)	28	0	0	1.9393	2	1.4499	2	2.1555	2	0	0	0.6629	3	1.9932	2			
TMEM33	TMM33_HUMAN	28	0	0	0	0	1.4499	2	6.4605	5	2.1952	2	0	0	3.9863	3			
TMEM43	TMM43_HUMAN	45	0	0	0	0	1.4499	2	0	0	0	0	0	0	0	0			
TNRC6A	TNR6A_HUMAN	210	0	0	1.9393	2	1.4499	2	2.1555	2	0	0	2.6353	3	2.9897	3			
TOMM20	TOM20_HUMAN	16	0	0	0	0	1.4499	2	0	0	0	0	0	0	3.9863	2			
TPI1	TPIS_HUMAN	31	23.489	8	1.9393	2	1.4499	2	0	0	0	0	1.7569	2	0	0			
TRIP13	PCH2_HUMAN	49	0	0	0	0	1.4499	2	9.6908	8	0	0	1.7569	2	6.9761	7			
TTI1	Q9BSD1 (TTI1_HUM/	7	0	0	0	0	1.4499	2	0	0	0	0	0	0	0	0			
TRMT2A	F2Z2W7_HUMAN (+1)	71	0	0	0	0	1.4499	2	0	0	6.5857	6	0.6629	11	0	0			
TRMT61B	TR61B_HUMAN	55	0	0	0	0	1.4499	2	0	0	0	0	0	0	0	0			
TRRAP	TRRAP_HUMAN	438	0	0	0	0	1.4499	2	2.1555	2	0	0	0	0	0	0			
TRUB1	TRUB1_HUMAN	37	0	0	0	0	1.4499	2	0	0	0	0	0	0	0	0			
TSEN2	SEN2_HUMAN	55	0	0	0	0	1.4499	2	0	0	0	0	0	0	0	0			
TSN	HYCD4_HUMAN	71	0	0	0	0	1.4499	2	0	0	0	0	0	0	0	0			
TTC21B	TT21B_HUMAN	151	0	0	0	0	1.4499	2	0	0	0	0	0	0	0	0			
TTC27	TTC27_HUMAN	97	0	0	0	0	1.4499	2	7.5373	6	0	0	0	0	0	0			
TTC37	TTC37_HUMAN	175	0	0	0	0	1.4499	2	0	0	0	0	0	0	0	0			
TTI2	TTI2_HUMAN	130	0	0	0	0	1.4499	2	0	0	0	0	0	0	0	0			
TUFM	EFTU_HUMAN	50	0	0	2.9089	2	1.4499	2	18.305	16	13.171	10	14.934	14	26.908	17			
UPF3B	RENB_HUMAN	58	0	0	3.8786	4	1.4499	2	4.307	4	12.074	10	11.42	12	7.9726	8			
UPF3	A0A0MR15_HUMAN (+	31	0	0	0	0	1.4499	2	0	0	0	0	0	0	0	0			
UQCRC2	QCR2_HUMAN	48	0	0	1.9393	2	1.4499	2	4.307	4	0	0	0	0	2.9897	3			
URGCP	URGCP_HUMAN	105	0	0	0	0	1.4499	2	0	0	0	0	0	0	0	0			
URI1	RMP_HUMAN	60	0	0	0	0	1.4499	2	0	0	0	0	0	0	0	0			
USP16	UBP16_HUMAN	96	0	0	0	0	1.4499	2	0	0	0	0	0	0	0	0			
USP48	UBP48_HUMAN	119	0	0	0	0	1.4499	2	0	0	0	0	0	0	0	0			
UTRN	UTRO_HUMAN	394	0	0	0	0	1.4499	2	0	0	0	0	0	0	0	0			
VANGL1	VANG1_HUMAN	60	0	0	0	0	1.4499	2	0	0	6.5857	6	3.5138	4	2.9897	3			
VARS2	A0A0MTG1_HUMAN (+	118	0	0	0	0	1.4499	2	0	0	0	0	0	0	0	0			
VRK1	VRK1_HUMAN	45	0	0	0	0	1.4499	2	0	0	0	0	0	0	0	0			
WAC	WAC_HUMAN	71	0	0	0	0	1.4499	2	0	0	0	0	0	0	0	0			
WDR36	WDR36_HUMAN	105	0	0	0	0	1.4499	2	3.2303	3	0	0	2.6353	3	0	0			
WIS1	WIS1_HUMAN	100	0	0	0	0	1.4499	2	0	0	4.3305	4	3.5138	4	2.9897	3			
WIPI1	WIPI1_HUMAN	51	0	0	0	0	1.4499	2	0	0	0	0	0	0	0	0			
WIZ	B9EGQ5_HUMAN (+1)	89	0	0	1.9393	2	1.4499	2	0	0	2.1952	2	0	0	0	0			
WTAP	FL2D_HUMAN	66	0	0	0	0	1.4499	2	3.2303	3	0	0	1.7569	2	0	0			

XRCC4	XRCC4_HUMAN	38	0	0	0	0	1,4499	2	0	0	0	0	1,7569	2	0	0			
YIPM1	YIPM1_HUMAN	220	0	0	0	0	1,4499	2	0	0	0	0	16,055	16	5,9795	5			
ZC2HC1A	ZC21A_HUMAN	35	0	0	3,8786	4	1,4499	2	2,1555	2	5,4881	5	2,6353	3	0	0			
ZC3H7A	ZC3H7A_HUMAN	111	0	0	0	0	1,4499	2	0	0	0	0	0	0	0	0			
ZGPAT	ZGPAT_HUMAN	57	0	0	0	0	1,4499	2	0	0	0	0	1,7569	2	0	0			
3B961	B1AM52_HUMAN (+1)	49	0	0	0	0	0	0	0	0	0	0	0	0	0	0			
AAT7	AAT7_HUMAN	63	0	0	0	0	0	0	0	0	0	0	2,6353	3	0	0			
ABC810	ABC8A_HUMAN	79	0	0	0	0	0	0	0	0	0	0	1,7569	2	0	0			
ABH012	ABD12_HUMAN	45	0	0	0	0	0	0	4,307	4	3,2929	2	0	0	5,9795	5			
ABRAXAS2	ABRX2_HUMAN	47	0	0	0	0	0	0	3,2303	3	0	0	0	0	0	0			
ABT1	ABT1_HUMAN	51	0	0	3,8786	3	0	0	0	0	5,4881	5	1,7569	2	0	0			
ABTB1	ABTB1_HUMAN	56	0	0	0	0	0	0	6,4605	6	0	0	0	0	0	0			
ACADVL	ACADV_HUMAN	70	0	0	0	0	0	0	0	0	0	0	0	0	0	0			
ACAT2	THIC_HUMAN	41	0	0	0	0	0	0	15,075	13	0	0	0	0	1,9932	2			
ACBD3	GCP60_HUMAN	61	0	0	0	0	0	0	2,1535	2	0	0	0	0	0	0			
ACBD5	ACBD5_HUMAN	60	0	0	0	0	0	0	5,3858	5	0	0	1,7569	2	0	0			
ACIN1	ACINU_HUMAN (+2)	152	0	0	0	0	0	0	0	0	0	0	2,6353	3	0	0			
ACOT8	ACOT8_HUMAN	36	0	0	0	0	0	0	3,2303	3	0	0	0	0	0	0			
ADNP	ADNP_HUMAN	124	0	0	0	0	0	0	0	0	0	0	2,6353	3	0	0			
AGPS	AGAS_HUMAN	73	0	0	0	0	0	0	0	0	0	0	0	0	0	0			
AHCY	SAHH_HUMAN	48	0	0	0	0	0	0	0	0	0	0	0	0	1,9932	2			
AHCY11	SAHH2_HUMAN	59	0	0	0	0	0	0	5,3858	5	0	0	0	0	0	0			
ALDH9A1	ALSA1_HUMAN	54	0	0	0	0	0	0	0	0	0	0	0	0	2,9897	3			
ALG1	ALG1_HUMAN	53	0	0	1,9393	2	0	0	0	0	0	0	0	0	1,9932	2			
ALG3	ALG3_HUMAN (+1)	50	0	0	0	0	0	0	0	0	0	0	0	0	1,9932	2			
ALKBH5	ALKB5_HUMAN	44	0	0	0	0	0	0	0	0	3,2929	3	1,7569	2	2,9897	3			
AMD1	DCAM_HUMAN	38	0	0	0	0	0	0	2,1535	2	0	0	0	0	0	0			
ANGEL1	ANGE1_HUMAN	75	0	0	6,7875	7	0	0	0	0	21,952	12	0	0	0	0			
APTX	APTX_HUMAN	41	0	0	0	0	0	0	0	0	3,2929	3	0	0	0	0			
ARF1	ARF1_HUMAN (+1)	21	0	0	0	0	0	0	5,3858	2	0	0	2,6353	2	0	0			
ARHGAP18	RHG18_HUMAN	75	0	0	0	0	0	0	0	0	0	0	0	0	0	0			
ARHGAP19	RHG19_HUMAN	56	0	0	0	0	0	0	0	0	2,1952	2	0	0	0	0			
ARHGEF39	ARG39_HUMAN	58	0	0	0	0	0	0	0	0	4,3305	3	0	0	0	0			
ARID4B	ARI4B_HUMAN	148	0	0	1,9393	2	0	0	0	0	0	0	0	0	0	0			
ARL1	ARL1_HUMAN (+1)	20	0	0	0	0	0	0	2,1535	2	0	0	0	0	0	0			
ARMC6	ARMC6_HUMAN	50	0	0	0	0	0	0	4,307	4	0	0	0	0	0	0			
ARMC9	ARMC9_HUMAN	66	0	0	0	0	0	0	0	0	0	0	2,6353	3	0	0			
ARPC3	ARPC3_HUMAN	21	0	0	0	0	0	0	0	0	0	0	0	0	0	0			
ARPC5	ARPC5_HUMAN	16	0	0	0	0	0	0	0	0	0	0	0	0	0	0			
ASCC2	ASCC2_HUMAN	86	0	0	0	0	0	0	0	0	5,4881	4	3,5138	4	2,9897	3			
ASF1A	ASF1A_HUMAN	23	0	0	0	0	0	0	0	0	3,2929	3	1,7569	2	0	0			
ASPSV1	APSV1_HUMAN	37	0	0	1,9393	2	0	0	0	0	0	0	0	0	0	0			
ASPSCR1	ASPC1_HUMAN	60	0	0	0	0	0	0	0	0	0	0	0	0	0	0			
ASTE1	ASTE1_HUMAN (+1)	77	0	0	0	0	0	0	0	0	0	0	1,7569	2	0	0			
ATAD3A	HDX2W2_HUMAN	64	0	0	0	0	0	0	104,45	2	0	0	26,353	2	40,86	2			
ATAD3B	AT03B_HUMAN	73	0	0	0	0	0	0	89,371	7	0	0	0	0	34,88	5			
ATF1	B5GXF4_HUMAN	58	0	0	0	0	0	0	0	0	0	0	0	0	0	0			
ATP6V1D	VATD_HUMAN	28	0	0	0	0	0	0	0	0	0	0	1,7569	2	0	0			
ATP6V1H	VATH_HUMAN	56	0	0	0	0	0	0	4,307	4	0	0	0	0	0	0			
ATXN10	ATX10_HUMAN	53	0	0	0	0	0	0	0	0	0	0	0	0	2,9897	3			
AURKB	AURKB_HUMAN	39	0	0	0	0	0	0	7,5373	4	8,781	5	1,7569	2	0	0			
AVEN	AVEN_HUMAN	39	0	0	0	0	0	0	0	0	3,2929	2	0	0	0	0			
B3GALNT2	B3GL2_HUMAN	57	0	0	0	0	0	0	3,2303	3	0	0	0	0	0	0			
B3GALT6	B3GT6_HUMAN	37	0	0	0	0	0	0	7,5373	5	3,2929	2	1,7569	2	0	0			
BAG4	BAG4_HUMAN	50	0	0	0	0	0	0	6,4605	4	0	0	0	0	0	0			
BAG5	BAG5_HUMAN	51	0	0	0	0	0	0	3,2303	3	0	0	0	0	1,9932	2			
BCAP29	BAP29_HUMAN	28	0	0	0	0	0	0	2,1535	2	0	0	0	0	1,9932	2			
BECN1	BECN1_HUMAN	52	0	0	0	0	0	0	0	0	0	0	0	0	0	0			
BIVM-ERCC5	A1W2PSB5_HUMAN (+	159	0	0	1,9393	2	0	0	0	0	0	0	0	0	0	0			
BLM	BLM_HUMAN	159	0	0	0	0	0	0	2,1535	2	0	0	0	0	0	0			
BMS1	BMS1_HUMAN	146	0	0	0	0	0	0	0	0	10,976	10	4,3922	3	4,9829	5			
BN_P1	SHCD2_HUMAN	26	0	0	0	0	0	0	0	0	0	0	3,5138	4	0	0			
BOP1	BOP1_HUMAN	84	0	0	1,9393	2	0	0	0	0	9,8786	9	4,3922	5	0	0			
BRIX1	BRX1_HUMAN	41	0	0	0	0	0	0	0	0	5,4881	4	2,6353	3	0	0			
C19orf47	CSD47_HUMAN	45	0	0	0	0	0	0	0	0	2,1952	2	4,3922	4	0	0			
CALML5	CALL5_HUMAN	16	0	0	0	0	0	0	0	0	0	0	2,6353	2	0	0			
CAPN1	CAN1_HUMAN	82	0	0	0	0	0	0	3,2303	3	0	0	0	0	0	0			
CAPN7	B1AK87_HUMAN (+1)	29	0	0	0	0	0	0	3,2303	3	0	0	0	0	0	0			
CASC3	CASC3_HUMAN	76	0	0	0	0	0	0	0	0	3,2929	3	1,7569	2	0	0			
CBSL	CBSL_HUMAN (+1)	61	0	0	0	0	0	0	2,1535	2	0	0	0	0	0	0			
CBWD2	CBWD2_HUMAN (+2)	42	0	0	0	0	0	0	3,2303	3	0	0	0	0	0	0			
CBX8	CBX8_HUMAN	43	0	0	0	0	0	0	0	0	4,3305	3	0	0	0	0			
CCDC125	CC125_HUMAN (+1)	59	0	0	0	0	0	0	2,1535	2	0	0	0	0	0	0			
CCDC138	CC138_HUMAN	76	0	0	0	0	0	0	0	0	0	0	1,7569	2	2,9897	3			
CCDC50	CCD50_HUMAN	36	0	0	0	0	0	0	0	0	0	0	0	0	0	0			
CCDC59	TAP26_HUMAN	29	0	0	2,9089	3	0	0	0	0	4,3305	4	0	0	0	0			
CCDC85B	CC85B_HUMAN	22	0	0	0	0	0	0	4,307	4	0	0	0	0	0	0			
CCDC85C	CC85C_HUMAN	45	0	0	0	0	0	0	18,305	11	0	0	0	0	9,9658	8			
CCDC9	CCDC9_HUMAN	60	0	0	0	0	0	0	0	0	4,3305	3	2,6353	3	0	0			
CCDC93	CCD93_HUMAN	73	0	0	0	0	0	0	0	0	0	0	0	0	0	0			
CCNT2	CCNT2_HUMAN	81	0	0	0	0	0	0	0	0	0	0	2,6353	3	0	0			
CD3EAP	RPA34_HUMAN	55	0	0	0	0	0	0	0	0	0	0	2,6353	3	0	0			
CDC40	O55RN1_HUMAN	61	0	0	0	0	0	0	0	0	0	0	2,6353	3	0	0			
CDC42	CDC42_HUMAN	21	0	0	0	0	0	0	3,2303	2	0	0	0	0	0	0			
CDC42EP1	BORG5_HUMAN	40	0	0	0	0	0	0	0	0	4,3305	4	0	0	1,9932	2			
CDC45	CDC45_HUMAN	66	0	0	0	0	0	0	20,458	11	0	0	0	0	0	0			
CDC6	CDC6_HUMAN	63	0	0	0	0	0	0	8,814	8	0	0	0	0	0	0			
CDC7	CDC7_HUMAN	64	0	0	0	0	0	0	11,844	9	0	0	1,7569	2	3,9863	4			
CDK9	CDK9_HUMAN (+1)	26	0	0	0	0	0	0	6,4605	2	2,1952	2	0	0	3,9863	3			
CDK11B	A0A0B9SEI3_HUMAN	89	0	0	0	0	0	0	0	0	4,3305	4	0	0	0	0			
CDK2	CDK2_HUMAN (+1)	34	0	0	0	0	0	0	3,2303	2	0	0	0	0	0	0			
CDK4	CDK4_HUMAN	36	0	0	0	0	0	0	5,3858	5	0	0	0	0	0	0			
CDK5	CDK5_HUMAN	33	0	0	0	0	0	0	0	0	0	0	3,5138	3	0	0			
CDK5RAP1	CK5P1_HUMAN	68	0	0	0	0	0	0	3,2303	2	0	0	0	0	0	0			
CDKAL1	CDKAL_HUMAN	65	0	0	0	0	0	0	3,2303	3	0	0	1,7569	2	1,9932	2			
CDSN	CDSN_HUMAN (+2)	52	0	0	1,9393	2	0	0	0	0	0	0	4,3922	3	12,956	4			
CENPB	CENPB_HUMAN	65	0	0	0	0	0	0	8,814	7	0	0	0	0	0	0			
CENPJ	CENPJ_HUMAN	153	0	0	1,9393	2	0	0	0	0	0	0	0	0	0	0			
CEP120	CE120_HUMAN	113	0	0	0	0	0	0	7,5373	7	0	0	0	0	0	0			
CEP131	CP131_HUMAN	122	0	0	1,9393	2	0	0	2,1535	2	0	0	0	0	0	0			
CEP41	CEP41_HUMAN	41	0	0	0	0	0	0	0	0	0	0	0	0	0	0			
CEP57	CEP57_HUMAN (+1)	57	0	0	0	0	0	0	3,2303	3	0	0	0	0	0	0			
CEP78	A8MST6_HUMAN (+1)	78	0	0	0	0	0	0	3,2303	3	0	0	0	0	0	0			
CERS2	CERS2_HUMAN (+1)	45	0	0	0	0	0	0	0	0	3,2929	2	0	0	1,9932	2			
CFAP97	CFA97_HUMAN	59	0	0	0	0	0	0	0	0	0	0	1,7569	2	0	0			
CHAF1B	CAF1B_HUMAN	61	0	0	0	0	0	0	0	0	0	0	0	0	0	0			
CHD4	A0A0G0G9_HUMAN (+	220	0	0	0	0	0	0	0	0	0	0	8,7845	10	0	0			
CHPF2	CHPF2_HUMAN (+1)	86	0	0	0	0	0	0	2,1535	2	0	0	0	0	0	0			
CHST14	CHST E_HUMAN (+1)	43	0	0	1,9393	2	0	0	0	0	3,2929	2	0	0	0	0			
CHTOP	CHTOP_HUMAN	26	0	0	2,9089	2	0	0	3,2303	2	9,8786	5	0	0	1,9932	2			
CIAP2	CIAP2_HUMAN	77	0	0	0	0	0	0	2,1555	2	0	0	2,6353	2	0	0			
CLCN7	CLCN7_HUMAN	89	0	0	0	0	0	0	0	0	3,2929	3	0	0	0	0			
CLINT1	EPN4_HUMAN	68	0	0	0	0	0	0	7,5373	7	0	0	0	0	1,9932	2			
CLNS1A	ES1P1_HUMAN (+3)	20	0	0	0	0	0	0	0	0	2,1952	2	0	0	0	0			
CLSPN	CLSPN_HUMAN	151	0	0	0	0	0	0	0	0	0	0	2,6353	3	0	0			
CLTC	A0A87WVQ6_HUMAN (	192	7,8297	5	0	0	0	0	24,765	21	0	0	0	0	11,959	12			
CMSS1	CSI3B4_HUMAN	26	0	0	0	0	0	0	0	0	5,4881	5	5,2707	4	0	0			
CNOT11	CNO11_HUMAN	55	0	0	1,9393	2	0	0	0	0	0	0	1,7569	2	1,9932	2			
COIL	COIL_HUMAN	63	0	0	0	0	0	0	0	0	3,2929	2	5,2707	6	0	0			
COL18A1	COIA1_HUMAN	178	0	0	1,9393	2	0	0	0	0	0	0	0	0	0	0			
COMTD1	CMTD1_HUMAN	29	0	0	0	0	0	0	2,1555	2	0	0	0	0	1,9932	2			
COQ8B	COQ8B_HUMAN	60	0	0	0	0	0	0	4,307	4	0	0	0	0	0	0			
COROT_PAM16	A0A0A0EYY4_HUMAN	114	0	0	1,9393	2	0	0	0	0	3,2929	3	1,7569	2	2,9897	3			
COX15	COX15_HUMAN	46	0	0	0	0	0	0	0	0	0	0	0	0	3,9863	4			
CPNE1	O95D59_HUMAN	73	0	0	0	0	0	0	2,1535	2	0	0	0	0	0	0			
CPSF4	CPSF4_HUMAN	30	0	0	0	0	0	0	2,1555	2	3,2929	3	2,6353	3	0	0			
CPT1A	CPT1A_HUMAN	88	0	0	0	0	0	0	2,1535	2	0	0	0	0	0	0			

CPVL	CPVL_HUMAN	56	0	0	0	0	0	0	57,068	10	0	0	0	0	0	26,308	9
CAPBP	CBP_HUMAN	265	0	0	0	0	0	0	0	0	0	0	4,3922	2	0	0	0
CRTAP	CSLP16_HUMAN (+1)	41	0	0	0	0	0	0	2,1555	2	0	0	0	0	0	0	0
CSNK1D	KC1D_HUMAN	67	0	0	5,8178	2	0	0	0	0	13,171	2	7,0276	3	9,9858	3	
CSNK1G1	U3KQB3_HUMAN	54	0	0	0	0	0	0	0	0	0	0	2,6353	3	1,9932	2	
CSTB	CYTM_HUMAN	17	0	0	0	0	0	0	0	0	0	0	0	0	1,9932	2	
CSTA	CYTA_HUMAN	11	0	0	0	0	0	0	0	0	0	0	3,5138	4	5,9795	5	
CSTF1	CSTF1_HUMAN	48	0	0	0	0	0	0	2,1555	2	0	0	0	0	0	0	
CSTF3	CSTF3_HUMAN	83	0	0	0	0	0	0	0	0	0	0	0	0	0	0	
CTPS1	PYRG1_HUMAN	67	0	0	0	0	0	0	0	0	0	0	0	0	0	0	
CTSB	CATB_HUMAN	38	0	0	0	0	0	0	2,1555	2	0	0	0	0	0	0	
CTSC	CATC_HUMAN	52	0	0	0	0	0	0	0	0	0	0	0	0	1,9932	2	
CUL7	CUL7_HUMAN	191	0	0	0	0	0	0	13,998	12	0	0	0	0	0	0	
DCAF10	A0A0M0T4_HUMAN (+	43	0	0	0	0	0	0	2,1535	2	0	0	0	0	0	0	
DCAF11	DCA11_HUMAN	62	0	0	0	0	0	0	5,3858	5	0	0	0	0	0	0	
DCAF13	A0A087WV20_HUMAN	68	0	0	0	0	0	0	0	0	2,1952	2	0	0	0	0	
DCAF4	DCAF4_HUMAN	56	0	0	0	0	0	0	2,1535	2	2,1952	2	0	0	0	0	
DCAF6	DCAF6_HUMAN	96	0	0	0	0	0	0	2,1555	2	0	0	0	0	0	0	
DCAF8	DCAF8_HUMAN (+1)	67	0	0	0	0	0	0	8,614	5	0	0	0	0	0	0	
DDB2	DDB2_HUMAN	48	0	0	0	0	0	0	0	0	0	0	2,6353	3	0	0	
DDX10	DDX10_HUMAN (+1)	101	0	0	0	0	0	0	0	0	8,781	7	0	0	0	0	
DDX24	DDX24_HUMAN (+1)	96	0	0	0	0	0	0	3,2303	2	2,1952	2	0	0	0	0	
DDX27	B7Z6D5_HUMAN (+1)	87	0	0	1,9393	2	0	0	2,1555	2	3,2929	3	0	0	0	0	
DDX28	DDX28_HUMAN	60	0	0	2,9089	3	0	0	6,4605	4	18,68	12	0	0	2,9897	2	
DDX50	DDX50_HUMAN	83	0	0	7,7571	7	0	0	6,4605	3	9,8786	6	14,055	10	0	0	
DDX51	DDX51_HUMAN	72	0	0	0	0	0	0	0	0	0	0	1,7569	2	0	0	
DDX52	DDX52_HUMAN	68	0	0	0	0	0	0	3,2303	3	2,1952	2	6,1481	4	0	0	
DDX54	DDX54_HUMAN	99	0	0	2,9089	2	0	0	0	0	9,8786	6	0	0	0	0	
DDX55	DDX55_HUMAN (+1)	69	0	0	0	0	0	0	2,1535	2	2,1952	2	1,7569	2	0	0	
DDX60	DDX60_HUMAN	198	0	0	0	0	0	0	0	0	0	0	2,6353	3	0	0	
DENND4A	A0A0U1RQZ7_HUMAN (+	215	0	0	0	0	0	0	0	0	0	0	2,6353	3	1,9932	2	
DGAT1	A0A0D9R7K7_HUMAN	36	0	0	0	0	0	0	0	0	0	0	0	0	2,9897	3	
DGKE	DGKE_HUMAN	64	0	0	0	0	0	0	20,458	9	0	0	0	0	13,952	8	
DHFR	DYR_HUMAN	21	0	0	0	0	0	0	2,1535	2	0	0	0	0	0	0	
DHPS	DHPS_HUMAN	41	0	0	0	0	0	0	2,1555	2	0	0	0	0	0	0	
DHRS13	DHR13_HUMAN	41	0	0	0	0	0	0	0	0	2,1952	2	0	0	0	0	
DHX33	DHX33_HUMAN	79	0	0	0	0	0	0	2,1535	2	0	0	0	0	0	0	
DHX34	DHX34_HUMAN	128	0	0	0	0	0	0	0	0	2,1952	2	0	0	0	0	
DHX35	DHX35_HUMAN	79	0	0	0	0	0	0	3,2303	3	0	0	0	0	0	0	
DICER1	DICER_HUMAN	219	0	0	0	0	0	0	3,2303	3	0	0	0	0	0	0	
DLD	DLDH_HUMAN (+1)	56	0	0	0	0	0	0	0	0	2,1952	2	0	0	0	0	
DMAP1	DMAP1_HUMAN	53	0	0	0	0	0	0	0	0	0	0	1,7569	2	0	0	
DMD	EBPON5_HUMAN	426	0	0	0	0	0	0	0	0	0	0	0	0	1,9932	2	
DNAJC16	DJC16_HUMAN	91	0	0	0	0	0	0	3,2303	3	0	0	0	0	0	0	
DNAJC30	DJC30_HUMAN	26	0	0	0	0	0	0	2,1555	2	0	0	0	0	1,9932	2	
DNAJC8	DNJC8_HUMAN	30	0	0	0	0	0	0	0	0	0	0	0	0	0	0	
DNM2	DYN2_HUMAN	98	0	0	0	0	0	0	0	0	0	0	0	0	0	0	
DNTTIP1	TDIF1_HUMAN	57	0	0	0	0	0	0	0	0	2,1952	2	0	0	0	0	
DPY19L1	A0A1B0GWQ5_HUMAN	85	0	0	1,9393	2	0	0	0	0	0	0	0	0	2,9897	3	
DPYS-2	DHCY09_HUMAN (+	74	0	0	0	0	0	0	0	0	0	0	0	0	0	0	
DROSHA	RNC_HUMAN	159	0	0	0	0	0	0	0	0	2,1952	2	0	0	0	0	
DSC3	DSC3_HUMAN	100	0	0	0	0	0	0	0	0	0	0	1,7569	2	13,952	6	
DUSP11	DUS11_HUMAN	39	0	0	0	0	0	0	0	0	10,976	6	0	0	0	0	
DYRK1A	DYR1A_HUMAN	86	0	0	0	0	0	0	30,149	19	0	0	0	0	24,914	13	
DYRK1B	DYR1B_HUMAN	69	0	0	0	0	0	0	16,151	3	0	0	0	0	15,945	5	
EBP3	CO53_HUMAN	65	0	0	0	0	0	0	0	0	3,2929	2	3,5138	4	0	0	
EBNA1BP2	EBP2_HUMAN (+1)	35	0	0	0	0	0	0	4,307	4	6,5857	5	3,5138	4	0	0	
ECSIT	ECSIT_HUMAN	49	0	0	1,9393	2	0	0	0	0	0	0	2,6353	3	1,9932	2	
ECT2	ECT2_HUMAN	104	0	0	0	0	0	0	0	0	3,2929	3	0	0	0	0	
EED	EED_HUMAN	50	0	0	0	0	0	0	0	0	0	0	1,7569	2	0	0	
EEF1B2	EF1B_HUMAN	25	0	0	0	0	0	0	0	0	0	0	2,6353	3	0	0	
EEF1E1	SCLB_HUMAN	65	0	0	0	0	0	0	0	0	2,1952	2	9,6629	10	8,9692	6	
EFL1	EFL1_HUMAN	125	0	0	0	0	0	0	0	0	0	0	0	0	0	0	
EGFL7	EGFL7_HUMAN	30	0	0	0	0	0	0	2,1555	2	2,1952	2	0	0	0	0	
EHHADH	ECHP_HUMAN	79	0	0	0	0	0	0	0	0	0	0	1,7569	2	0	0	
EI24	EI24_HUMAN	59	0	0	0	0	0	0	4,307	3	0	0	0	0	2,9897	3	
ELAVL1	ELAV1_HUMAN	36	0	0	0	0	0	0	0	0	3,2929	3	3,5138	4	0	0	
ELOC	ELOC_HUMAN (+2)	10	0	0	0	0	0	0	0	0	0	0	1,7569	2	0	0	
EPB41L3	E41L3_HUMAN	100	0	0	0	0	0	0	0	0	3,2929	3	0	0	0	0	
EPB41L5	E41L5_HUMAN	82	0	0	0	0	0	0	0	0	3,2929	3	0	0	0	0	
EPPK1	DA0758I30_HUMAN (+	553	0	0	0	0	0	0	0	0	0	0	5,2707	2	0	0	
ERBIN	ERBIN_HUMAN	158	0	0	0	0	0	0	3,2303	2	0	0	0	0	0	0	
ERCC3	ERCC3_HUMAN	89	0	0	0	0	0	0	0	0	0	0	3,5138	3	2,9897	3	
ERCC6	ERCC6_HUMAN	168	0	0	0	0	0	0	0	0	9,8786	9	1,7569	2	0	0	
FBXP1	FZR1Z7_HUMAN (+1)	93	0	0	0	0	0	0	0	0	0	0	1,7569	2	0	0	
ESF1	ESF1_HUMAN	99	0	0	0	0	0	0	0	0	0	0	3,5138	4	0	0	
ESYT1	ESYT1_HUMAN	123	0	0	0	0	0	0	0	0	0	0	0	0	0	0	
EXOC8	EXOC8_HUMAN	82	0	0	0	0	0	0	3,2303	3	0	0	0	0	0	0	
EXOG	EXOG_HUMAN	41	0	0	0	0	0	0	21,555	11	3,2929	3	1,7569	2	4,9829	5	
EXOSC3	EXOS3_HUMAN	30	0	0	0	0	0	0	7,5373	6	0	0	1,7569	2	4,9829	5	
EXOSC5	EXOS5_HUMAN	25	0	0	0	0	0	0	0	0	0	0	3,5138	4	0	0	
EXOSC9	EXOS9_HUMAN	49	0	0	0	0	0	0	4,307	4	0	0	0	0	0	0	
FAF2	FAF2_HUMAN	53	0	0	0	0	0	0	4,307	3	0	0	0	0	2,9897	3	
FAM120C	F120C_HUMAN	121	0	0	0	0	0	0	0	0	6,5857	2	0	0	0	0	
FAM76B	F76D9_HUMAN (+1)	39	0	0	0	0	0	0	0	0	0	0	1,7569	2	0	0	
FAR2	FACR2_HUMAN	59	0	0	0	0	0	0	6,4605	6	0	0	0	0	5,9795	5	
FARP2	FARP2_HUMAN	120	0	0	0	0	0	0	0	0	3,2929	3	0	0	0	0	
FBXO21	FBX21_HUMAN (+1)	72	0	0	0	0	0	0	2,1535	2	0	0	0	0	0	0	
FBXW11	FBW1B_HUMAN	62	0	0	2,9089	3	0	0	0	0	4,3305	4	0	0	0	0	
FBXW8	FBXW8_HUMAN	67	0	0	0	0	0	0	3,2303	3	0	0	0	0	0	0	
FHL1	A0D9SF30_HUMAN (+	37	0	0	0	0	0	0	0	0	0	0	0	0	0	0	
FIBP	FIBP_HUMAN	42	0	0	0	0	0	0	0	0	2,1952	2	3,5138	4	0	0	
FIGL1	FIGL1_HUMAN	74	0	0	0	0	0	0	2,1535	2	0	0	0	0	0	0	
FIP1L1	FIP1_HUMAN	67	0	0	0	0	0	0	0	0	0	0	5,2707	6	0	0	
FKBP4	FKBP4_HUMAN	52	0	0	0	0	0	0	0	0	0	0	0	0	0	0	
FLG	FILA_HUMAN	435	0	0	0	0	0	0	0	0	0	0	2,6353	3	24,914	13	
FMNL2	FMNL2_HUMAN	123	0	0	0	0	0	0	0	0	2,1952	2	0	0	0	0	
FMR1	A8MQ38_HUMAN (+1)	66	0	0	0	0	0	0	0	0	31,851	2	18,447	2	0	0	
FOXRED1	FXRD1_HUMAN	56	0	0	0	0	0	0	0	0	0	0	0	0	4,9829	5	
FTSJ1	TRM7_HUMAN	36	0	0	0	0	0	0	0	0	6,5857	5	0	0	0	0	
FUBP3	FUBP3_HUMAN	62	0	0	0	0	0	0	3,2303	3	0	0	0	0	0	0	
FYTTD1	UIF_HUMAN	36	0	0	0	0	0	0	0	0	3,2929	3	0	0	0	0	
GALK1	GALK1_HUMAN	42	0	0	0	0	0	0	4,307	4	0	0	0	0	0	0	
GCDH	GCDH_HUMAN	48	0	0	0	0	0	0	3,2303	3	0	0	0	0	1,9932	2	
GEMIN2	GEMI2_HUMAN	32	0	0	0	0	0	0	0	0	0	0	2,6353	3	0	0	
GID8	GID8_HUMAN	27	0	0	0	0	0	0	2,1555	2	0	0	0	0	0	0	
GIGYF1	GGYF1_HUMAN	115	0	0	0	0	0	0	0	0	6,5857	6	0	0	2,9897	3	
GLYR1	GLYR1_HUMAN (+1)	61	0	0	0	0	0	0	3,2303	3	0	0	0	0	0	0	
GNA12	GNA12_HUMAN	44	0	0	0	0	0	0	0	0	3,2929	2	0	0	0	0	
GNB1	GBB1_HUMAN	37	0	0	0	0	0	0	2,1535	2	0	0	0	0	0	0	
GNL1	GNL1_HUMAN	69	0	0	1,9393	2	0	0	0	0	0	0	6,1481	7	0	0	
GNL2	NOC2_HUMAN	86	0	0	0	0	0	0	0	0	2,1952	2	0	0	0	0	
GNL3L	GNL3L_HUMAN	66	0	0	0	0	0	0	5,3858	4	5,4881	4	7,906	9	0	0	
GNPAI	GNPAI_HUMAN	27	0	0	0	0	0	0	3,2303	3	0	0	0	0	0	0	
GOPC	GOPC_HUMAN	51	0	0	0	0	0	0	10,768	6	0	0	0	0	0	0	
GOSR1	E9PCW1_HUMAN (+1)	28	0	0	1,9393	2	0	0	0	0	0	0	0	0	2,9897	3	
GPAM	GPAT1_HUMAN	96	0	0	0	0	0	0	18,305	14	0	0	0	0	7,9725	6	
GPAT4	GPAT4_HUMAN	52	0	0	0	0	0	0	0	0	0	0	0	0	1,9932	2	
GPATCH1	GPTC1_HUMAN	50	0	0	0	0	0	0	0	0	2,1952	2	0	0	0	0	
GPATCH8	GPTC8_HUMAN	164	0	0	0	0	0	0	0	0	2,1952	2	0	0	0	0	
GPN3	GPN3_HUMAN	35	0	0	0	0	0	0	2,1555	2	0	0	0	0	0	0	
GPRS0	MTR1_HUMAN	67	0	0	1,9393	2	0	0	0	0	0	0	0	0	1,9932	2	
GRB10	GRB10_HUMAN	67	0	0	0	0	0	0	0	0	0	0	0	0	0	0	
GRK6	KBWSW2_HUMAN (+1)	62	0	0	0	0	0	0	0	0	0	0	1,7569	2	0	0	
GRN	GRN_HUMAN	64	0	0	0	0	0	0	3,2303	3	0	0	0	0	0	0	
GRWD1	GRWD1_HUMAN	49	0	0	0	0	0	0	8,614	8	7,6854	7	4,3922	5	2,9897	3	
GSDMA	GSDMA_HUMAN	49	0	0	2,9089	2	0	0	0	0	0	0	0	0	0	0	

GSPT1	ERF3A_HUMAN	56	0	0	0	0	0	0	0	0	0	0	0	0	0	0	0	0	0
GSTP1	ARMX4_HUMAN (+3)	19	0	0	0	0	0	0	0	0	0	0	0	0	1,7569	2	0	0	0
GTF2H4	TF2H4_HUMAN	52	0	0	0	0	0	0	0	0	0	0	2,1952	2	5,2707	5	3,9863	4	0
GTF3C2	TF3C2_HUMAN	101	0	0	5,8178	5	0	0	0	0	0	0	7,6834	6	3,5138	4	0	0	0
GTF3C3	TF3C3_HUMAN	101	0	0	1,9393	2	0	0	0	15,075	13	5,4881	5	4,3822	5	1,9932	2	0	0
GTF3C4	TF3C4_HUMAN	92	0	0	0	0	0	0	0	4,307	4	0	0	1,7569	2	0	0	0	0
GTPBP2	GTPB2_HUMAN	66	0	0	0	0	0	0	0	2,1535	2	0	0	0	0	1,9932	2	0	0
GTPBP4	NOG1_HUMAN	74	0	0	0	0	0	0	0	5,3838	5	10,976	9	6,1491	7	0	0	0	0
GTPBP6	GTPB6_HUMAN (+1)	57	0	0	0	0	0	0	0	2,1535	2	8,781	6	1,7569	2	1,9932	2	0	0
GTSE1	GTSE1_HUMAN	77	0	0	0	0	0	0	0	0	0	4,3905	4	0	0	0	0	0	0
GUF1	GUF1_HUMAN	74	0	0	0	0	0	0	0	0	0	0	0	4,3822	5	0	0	0	0
GYS1	GYS1_HUMAN	86	0	0	0	0	0	0	0	5,3838	5	0	0	0	0	0	0	1,9932	2
HAL	HUTH_HUMAN	73	0	0	0	0	0	0	0	0	0	0	0	0	0	0	0	0	0
HARS2	SYHM_HUMAN	57	0	0	0	0	0	0	0	0	0	5,4881	5	0	0	0	0	0	0
HAUS1	HAUS1_HUMAN	32	0	0	0	0	0	0	0	2,1535	2	0	0	0	0	0	0	0	0
HAX1	HAX1_HUMAN	32	0	0	0	0	0	0	0	3,2303	3	0	0	0	0	0	0	0	0
HBA1	HBA_HUMAN (+2)	15	3,9148	2	1,9393	2	0	0	0	0	0	0	0	0	0	0	0	0	0
HCG_20434026	FGDS0_HUMAN	54	0	0	0	0	0	0	0	0	0	0	0	0	0	0	0	0	0
HDDC2	HDDC2_HUMAN	76	0	0	0	0	0	0	0	0	0	0	0	0	0	0	0	0	0
HELZ2	HELZ2_HUMAN	295	0	0	0	0	0	0	0	3,2303	2	5,4881	5	0	0	0	0	0	0
HERC2	HERC2_HUMAN	527	0	0	0	0	0	0	0	13,998	13	0	0	0	0	0	0	0	0
HERC5	HERC5_HUMAN	117	0	0	0	0	0	0	0	0	0	0	0	1,7569	2	0	0	0	0
HLA-C	1C07_HUMAN (+1)	41	0	0	0	0	0	0	0	3,2303	3	0	0	0	0	0	0	0	0
HLTF	SMC4OA6_HUMAN (+	114	0	0	2,9089	3	0	0	0	0	0	7,6834	7	5,2707	5	0	0	0	0
HNRNPH2	HNRH2_HUMAN	49	0	0	0	0	0	0	0	0	0	17,562	2	0	0	11,959	4	0	0
HNRNPH3	HNRH3_HUMAN	57	0	0	0	0	0	0	0	2,1535	2	13,057	7	1,7569	2	0	0	0	0
HOMER3	HOMR3_HUMAN	40	0	0	1,9393	2	0	0	0	0	0	0	0	0	0	0	0	0	0
HOXA10	HXA10_HUMAN	42	0	0	0	0	0	0	0	0	0	2,1952	2	0	0	1,9932	2	0	0
HOXA5	HXA5_HUMAN	29	0	0	5,8178	3	0	0	0	0	0	9,8786	3	2,6353	3	0	0	0	0
HOXB8	HXB8_HUMAN (+2)	28	0	0	0	0	0	0	0	0	0	4,3905	2	0	0	0	0	0	0
HOXB9	HXB9_HUMAN	28	0	0	0	0	0	0	0	0	0	4,3905	2	0	0	0	0	0	0
HRAS	RASH_HUMAN (+3)	21	0	0	0	0	0	0	0	0	0	0	0	1,7569	2	0	0	0	0
HSDL2	HSDL2_HUMAN	45	0	0	0	0	0	0	0	0	0	0	0	0	0	0	0	0	0
HSPA1L	HS71L_HUMAN	70	0	0	0	0	0	0	0	189,51	3	0	0	0	0	0	0	0	0
HSPA4L	HS74L_HUMAN	95	0	0	0	0	0	0	0	16,151	11	0	0	0	0	2,9897	2	0	0
HSPB1	HSPB1_HUMAN	25	0	0	1,9393	2	0	0	0	3,2303	3	0	0	4,3822	4	2,9897	2	0	0
ICMT	ICMT_HUMAN	32	0	0	0	0	0	0	0	2,1535	2	0	0	0	0	0	0	0	0
IDE	IDE_HUMAN	118	0	0	0	0	0	0	0	0	0	0	0	1,7569	2	0	0	0	0
IDH2	IDHP_HUMAN	51	0	0	1,9393	2	0	0	0	0	0	0	0	0	0	0	0	0	0
IFRD1	IFRD1_HUMAN	50	0	0	0	0	0	0	0	0	0	0	0	1,7569	2	0	0	0	0
IFT140	IF140_HUMAN	165	0	0	0	0	0	0	0	2,1535	2	0	0	0	0	0	0	0	0
IFT172	IF172_HUMAN	198	0	0	0	0	0	0	0	30,149	27	0	0	0	0	4,9829	5	0	0
IFT81	IFT81_HUMAN	80	0	0	0	0	0	0	0	5,3838	5	0	0	0	0	0	0	0	0
IGF2BP2	IF2B2_HUMAN (+1)	67	0	0	0	0	0	0	0	10,768	8	0	0	7,306	4	4,9829	2	0	0
IGHMBP2	SMBP2_HUMAN	109	0	0	0	0	0	0	0	0	0	0	0	1,7569	2	0	0	0	0
IMMT	CHI60_HUMAN	73	0	0	0	0	0	0	0	30,149	2	0	0	0	0	0	0	0	0
INA	AINX_HUMAN	55	0	0	0	0	0	0	0	7,5373	7	0	0	0	0	0	0	0	0
INPPL1	INPSK_HUMAN	51	0	0	0	0	0	0	0	3,2303	2	0	0	0	0	0	0	0	0
INVS	INVS_HUMAN	118	0	0	0	0	0	0	0	2,1535	2	0	0	0	0	0	0	0	0
IPO11	IPO11_HUMAN	50	0	0	0	0	0	0	0	0	0	2,1952	2	0	0	0	0	0	0
IPO9	IPO9_HUMAN	101	0	0	0	0	0	0	0	2,1535	2	0	0	0	0	0	0	0	0
IQCB1	IQCB1_HUMAN	69	0	0	0	0	0	0	0	6,4605	4	3,2929	3	0	0	2,9897	3	0	0
IQCC	IQCC_HUMAN	55	0	0	0	0	0	0	0	2,1535	2	0	0	0	0	0	0	0	0
IQGAP3	IQGA3_HUMAN	185	0	0	0	0	0	0	0	78,603	46	5,4881	3	6,1491	4	48,832	42	0	0
IQSEC1	A0B7W8_HUMAN (+	124	0	0	0	0	0	0	0	6,4605	5	0	0	0	0	0	0	0	0
ITAX1	D3Y1B5_HUMAN (+1)	76	0	0	0	0	0	0	0	4,307	4	0	0	1,7569	2	2,9897	3	0	0
IRF2BP1	I2BP1_HUMAN	62	0	0	0	0	0	0	0	3,2303	3	0	0	0	0	1,9932	2	0	0
ITPRIPL1	H2C0T2_HUMAN (+1)	67	0	0	0	0	0	0	0	3,2303	3	0	0	0	0	0	0	0	0
JPH1	JPH1_HUMAN	72	0	0	1,9393	2	0	0	0	8,614	8	0	0	2,6353	3	7,9726	8	0	0
JUN	JUN_HUMAN	36	0	0	0	0	0	0	0	0	0	2,1952	2	1,7569	2	0	0	0	0
KCTD5	KCTD5_HUMAN	26	0	0	0	0	0	0	0	3,2303	3	0	0	0	0	0	0	0	0
KDM4B	KDM4B_HUMAN (+	122	0	0	0	0	0	0	0	0	0	2,1952	2	0	0	0	0	0	0
KHDRBS3	KHDR3_HUMAN	39	0	0	0	0	0	0	0	0	0	6,5857	4	3,5138	4	0	0	0	0
KIF14	KIF14_HUMAN	186	0	0	0	0	0	0	0	0	0	0	0	1,7569	2	0	0	0	0
KIF23	KIF23_HUMAN	110	0	0	0	0	0	0	0	2,1535	2	0	0	0	0	0	0	0	0
KIF3C	KIF3C_HUMAN (+2)	76	0	0	0	0	0	0	0	2,1535	2	0	0	0	0	0	0	0	0
KIFAP3	KIFA3_HUMAN	91	0	0	0	0	0	0	0	6,4605	6	0	0	0	0	0	0	0	0
KIN	KIN17_HUMAN	45	0	0	0	0	0	0	0	0	0	0	0	1,7569	2	0	0	0	0
KLHDC2	KLDC2_HUMAN	46	0	0	0	0	0	0	0	2,1535	2	0	0	0	0	0	0	0	0
KLHL21	KLH21_HUMAN	67	0	0	0	0	0	0	0	3,2303	2	0	0	0	0	0	0	0	0
KLHL23	KLH23_HUMAN	64	0	0	0	0	0	0	0	4,307	4	0	0	0	0	0	0	0	0
KPNA4	IMA3_HUMAN	58	0	0	0	0	0	0	0	0	0	0	0	0	0	0	0	0	0
KPNB1	IMB1_HUMAN	97	0	0	0	0	0	0	0	2,1535	2	2,1952	2	1,7569	2	0	0	0	0
KRR1	KRR1_HUMAN	44	0	0	0	0	0	0	0	2,1535	2	3,2929	3	5,2707	6	2,9897	3	0	0
LSM12	LSM12_HUMAN	79	0	0	0	0	0	0	0	5,3838	5	0	0	0	0	2,9897	3	0	0
LANCL1	LANL1_HUMAN (+1)	22	0	0	0	0	0	0	0	0	0	2,1952	2	0	0	0	0	0	0
LAT1	LAT1_HUMAN	127	0	0	0	0	0	0	0	0	0	2,1952	2	0	0	0	0	0	0
LDHA	LDHA_HUMAN	37	11,744	5	1,9393	2	0	0	0	0	0	0	0	0	0	0	0	0	0
LEMD2	LEMD2_HUMAN	57	0	0	0	0	0	0	0	0	0	0	0	0	0	3,9863	4	0	0
LENG8	A0A7A7T7_HUMAN (+	86	0	0	0	0	0	0	0	0	0	3,2929	3	0	0	0	0	0	0
LETM1	RBVZA2_HUMAN (+1)	84	0	0	0	0	0	0	0	2,1535	2	0	0	0	0	0	0	0	0
LGALS3BP	LG3BP_HUMAN	65	0	0	0	0	0	0	0	2,1535	2	0	0	0	0	0	0	0	0
LGALS7	LEG7_HUMAN	15	0	0	0	0	0	0	0	0	0	0	0	4,3822	4	2,9897	3	0	0
LIAT1	LIAT1_HUMAN	50	0	0	0	0	0	0	0	0	0	2,1952	2	2,6353	3	0	0	0	0
LIN28B	A13GVD3_HUMAN (+	28	0	0	0	0	0	0	0	2,1535	2	0	0	0	0	0	0	0	0
LLGL2	LGORV5_HUMAN (+1)	113	0	0	0	0	0	0	0	0	0	2,1952	2	0	0	0	0	0	0
LOR	LORI_HUMAN	26	2,6099	2	1,9393	2	0	0	0	0	0	0	0	0	0	0	0	0	0
LPCAT1	PCAT1_HUMAN	59	0	0	0	0	0	0	0	3,2303	2	3,2929	2	0	0	3,9863	4	0	0
LRCH4	LRCH4_HUMAN	75	0	0	0	0	0	0	0	0	0	0	0	1,7569	2	0	0	0	0
LRRC15	LRC15_HUMAN	66	0	0	2,9089	3	0	0	0	0	0	0	0	0	0	0	0	0	0
LRRC40	LRC40_HUMAN	68	0	0	0	0	0	0	0	0	0	0	0	0	0	0	0	0	0
LSM1	LSM1_HUMAN	15	0	0	0	0	0	0	0	0	0	0	0	0	0	1,9932	2	0	0
LSM11	LSM11_HUMAN	40	0	0	1,9393	2	0	0	0	0	0	0	0	1,7569	2	0	0	0	0
LSM2	LSM2_HUMAN	11	0	0	1,9393	2	0	0	0	3,2303	2	0	0	0	0	3,9863	3	0	0
LSM4	LSM4_HUMAN	15	0	0	0	0	0	0	0	3,2303	3	0	0	0	0	6,9761	4	0	0
LSM6	LSM6_HUMAN	9	0	0	0	0	0	0	0	2,1535	2	0	0	0	0	2,9897	3	0	0
LSM7	LSM7_HUMAN	12	0	0	0	0	0	0	0	2,1535	2	0	0	0	0	0	0	0	0
LZTS2	LZTS2_HUMAN	73	0	0	0	0	0	0	0	3,2303	3	0	0	0	0	0	0	0	0
MA2C1L	MO2C1_HUMAN	24	0	0	0	0	0	0	0	3,2303	3	0	0	0	0	0	0	0	0
MAFA	F7F5C7_HUMAN (+3)	49	0	0	0	0	0	0	0	2,1535	2	0	0	0	0	0	0	0	0
MAP2K7	MP2K7_HUMAN	47	0	0	1,9393	2	0	0	0	0	0	0	0	1,7569	2	0	0	0	0
MAPK20	M3K20_HUMAN	91	0	0	0	0	0	0	0	0	0	2,1952	2	0	0	0	0	0	0
MAPK4	F5H4R3_HUMAN (+3)	163	0	0	0	0	0	0	0	0	0	0	0	2,6353	3	0	0	0	0
MAP7D3	MA7D3_HUMAN	98	0	0	0	0	0	0	0	0	0	8,781	8	0	0	0	0	0	0
MAPK9	MK09_HUMAN	41	0	0	0	0	0	0	0	6,4605	5	0	0	0	0	0	0	0	0
MAPK9	MK09_HUMAN	45	0	0	0	0	0	0	0	6,4605	2	0	0	0	0	0	0	0	0
MAPKAP1	SIN1_HUMAN	59	0	0	0	0	0	0	0	2,1535	2	0	0	0	0	0	0	0	0
MARCH7	F5H6W4_HUMAN	70	0	0	0	0	0	0	0	6,4605	6	0	0	0	0	0	0	0	0
MARK3	ADAOM123_HUMAN (+	84	0	0	6,7875	4	0	0	0	5,3838	4	10,976	4	4,3822	2	0	0	0	0
MAT	I3L2P5_HUMAN	22	0	0	0	0	0	0	0	0	0	4,3905	3	1,7569	2	0	0	0	0
MBD4	MBD4_HUMAN	66	0	0	0	0	0	0	0	0	0	2,1952	2	0	0	0	0	0	0
MCM10	MCM10_HUMAN (+1)	98	0	0	0	0	0	0	0	0	0	2,1952	2	0	0	0	0	0	0
MCM3P	MCM3P_HUMAN	73	0	0	0	0	0	0	0	0	0	0	0	0	0	0	0	0	0
MCM4	MCM4_HUMAN	96	0	0	6,7875	7	0	0	0	0	0	2,1952	2	0	0	0	0	0	0
MERTK	F8WHX8_HUMAN (+1)	91	0	0	0	0	0	0	0	0	0	4,3905	2	0	0	0	0	0	0
MESD	MESD_HUMAN	26	0	0	0	0	0	0	0	0	0	0	0	0	0	0	0	0	0
METTL15	METL5_HUMAN	68	0	0	2,9089	3	0	0	0	0	0	4,3905	2	1,7569	2	0	0	0	0
METTL16	METL16_HUMAN	64	0	0	1,9393	2	0	0	0	0	0	3,2929	2	5,2707	6	1,9932	2	0	0
METTL17	METL7_HUMAN	51	0	0	1,9393	2	0	0	0	0	0	8,781	6	4,3822	5	3,9863	4	0	0
MGAT2	MGAT2_HUMAN	52	0	0	0	0	0	0	0	0	0	0	0	0	0	1,9932	2	0	0
MICU1	A0A0U1RRK1_HUMAN	55	0	0	0	0	0	0	0	2,1535	2	5,4881	5	5,2707	3	4,9829	5	0	0
MID1	TRI18_HUMAN	75	0	0	0	0	0	0	0	0	0	0	0	0	0	0	0	0	0
MINK1	MINK1_HUMAN	150	0	0	0	0	0	0	0	0	0	10,976	4	0	0	0	0	0	0
MIS1	MIS1_HUMAN	65	0	0	0	0	0	0	0	2,1535	2	0	0	0	0	0	0	0	0
MIF2	MIF2_HUMAN	28	0	0	0	0	0	0	0	3,2303	2	0	0	0	0	0	0	0	0
MMTAG2	MMTA2_HUMAN	29	0	0	0	0	0	0	0	0	0	4,3905	2	1,7569	2	0	0	0	0
MOV10	MOV10_HUMAN (+1)	114	0	0	0	0	0	0	0	5,3838	5	6,5857	6	0	0	1,9932	2	0	0

MPHOSPH10	MPP10_HUMAN	79	0	0	0	0	0	0	0	2,1555	2	2,1952	2	0	0	0	0
MPP6	A8K7G1_HUMAN (+1)	49	0	0	0	0	0	0	0	0	0	0	0	0	0	0	0
MRPL14	RM14_HUMAN	16	0	0	1,9393	2	0	0	0	0	0	0	0	0	0	0	0
MRPL15	RM15_HUMAN	33	0	0	0	0	0	0	0	0	0	7,8836	6	0	0	0	0
MRPL21	RM21_HUMAN	23	0	0	0	0	0	0	0	0	0	2,1952	2	1,7569	2	0	0
MRPL38	RM38_HUMAN	45	0	0	0	0	0	0	0	0	0	2,1952	2	1,7569	2	0	0
MRPL41	RM41_HUMAN	15	0	0	0	0	0	0	0	0	0	2,1952	2	0	0	0	0
MRPL43	B1AL05_HUMAN (+2)	21	0	0	0	0	0	0	0	0	0	0	0	1,7569	2	0	0
MRPL55	RM55_HUMAN	15	0	0	0	0	0	0	0	0	0	0	0	1,7569	2	0	0
MRPS9	RMO5_HUMAN	30	0	0	0	0	0	0	0	0	0	8,781	6	4,3922	4	1,9932	2
MRPS10	RT10_HUMAN	25	0	0	1,9393	2	0	0	0	0	0	2,1952	2	5,5138	3	0	0
MRPS11	RT11_HUMAN	21	0	0	4,8482	4	0	0	0	0	0	0	0	0	0	0	0
MRPS12	RT12_HUMAN	15	0	0	0	0	0	0	0	0	0	2,1952	2	1,7569	2	0	0
MRPS14	RT14_HUMAN	15	0	0	2,9089	2	0	0	0	0	0	0	0	0	0	0	0
MRPS18A	RT18A_HUMAN	22	0	0	0	0	0	0	0	0	0	3,2929	3	0	0	0	0
MRPS28	RT28_HUMAN	21	0	0	3,8786	3	0	0	0	0	0	0	0	1,7569	2	1,9932	2
MRPS30	RT30_HUMAN	50	0	0	0	0	0	0	0	0	0	0	0	1,7569	2	3,9863	4
MRPS6	RT06_HUMAN	14	0	0	5,8178	6	0	0	0	0	0	0	0	0	0	0	0
MRRF	RRFM_HUMAN	29	0	0	0	0	0	0	0	0	0	0	0	0	0	0	0
MRS2	A0A0M0X2_HUMAN (+	44	0	0	0	0	0	0	0	2,1555	2	0	0	0	0	0	0
MSH6	A0A2R8VB_HUMAN (+	95	0	0	0	0	0	0	0	0	0	0	0	1,7569	2	0	0
MT-CO2	COX2_HUMAN	26	0	0	0	0	0	0	0	2,1555	2	0	0	0	0	0	0
MTG2	MTG2_HUMAN (+1)	44	0	0	0	0	0	0	0	0	0	3,2929	3	0	0	0	0
MTM1	MTM1_HUMAN	70	0	0	0	0	0	0	0	0	0	0	0	0	0	0	0
MTX2	MTX2_HUMAN	30	0	0	0	0	0	0	0	6,4605	5	0	0	0	0	0	0
MUT	MUTA_HUMAN	85	0	0	0	0	0	0	0	0	0	0	0	0	0	0	0
MYBBP1A	MBB1A_HUMAN	148	0	0	5,8178	6	0	0	0	9,6908	9	75,736	36	30,746	25	24,914	19
MYL12A	J3QR53_HUMAN (+2)	20	0	0	0	0	0	0	0	2,1555	2	0	0	0	0	0	0
MYO1D	A0A0M0X1_HUMAN (+	236	0	0	0	0	0	0	0	9,6908	9	0	0	0	0	0	0
MYO9A	MYO9A_HUMAN	293	0	0	0	0	0	0	0	2,1555	2	0	0	0	0	0	0
MYO9B	M0R0P8_HUMAN (+2)	243	0	0	0	0	0	0	0	8,614	8	4,3305	4	5,2707	6	0	0
NAA25	NAA25_HUMAN	117	0	0	0	0	0	0	0	0	0	0	0	0	0	0	0
NAGK	H7C5G9_HUMAN (+1)	57	0	0	0	0	0	0	0	2,1555	2	0	0	0	0	0	0
NAP1L1	P54636_HUMAN (+7)	45	0	0	0	0	0	0	0	0	0	0	0	2,6353	2	0	0
NAP1L4	C9J7I7_HUMAN (+1)	32	0	0	1,9393	2	0	0	0	0	0	0	0	0	0	0	0
NAT14	NAT14_HUMAN	22	0	0	0	0	0	0	0	2,1555	2	0	0	0	0	0	0
NAV1	A0A0M8R3_HUMAN (+	197	0	0	0	0	0	0	0	0	0	0	0	2,6353	3	0	0
NCBP3	NCBP3_HUMAN	71	0	0	1,9393	2	0	0	0	0	0	3,2929	3	9,6629	10	0	0
NCCRP1	FBXS0_HUMAN	31	0	0	0	0	0	0	0	0	0	0	0	0	0	1,9932	2
NCOA5	NCOA5_HUMAN	66	0	0	0	0	0	0	0	0	0	5,4881	4	8,7845	8	1,9932	2
NDC1	NDC1_HUMAN	76	0	0	0	0	0	0	0	0	0	3,2929	3	0	0	0	0
NDC80	NDC80_HUMAN	74	0	0	0	0	0	0	0	0	0	0	0	0	0	0	0
NDUFA4	NDUA4_HUMAN	9	0	0	0	0	0	0	0	2,1555	2	0	0	0	0	0	0
NDUFS5	NDUS5_HUMAN	13	0	0	0	0	0	0	0	0	0	0	0	1,7569	2	0	0
NDUFS7	PSRC1_HUMAN (+2)	25	0	0	1,9393	2	0	0	0	2,1555	2	2,1952	2	1,7569	2	0	0
NEFL	NFL_HUMAN	62	0	0	0	0	0	0	0	8,614	8	0	0	5,5138	3	5,9795	4
NEK1	NEK1_HUMAN	143	0	0	5,8178	6	0	0	0	0	0	3,2929	3	0	0	0	0
NEK4	NEK4_HUMAN	95	0	0	0	0	0	0	0	0	0	2,1952	2	1,7569	2	0	0
NHP2	NHP2_HUMAN	42	0	0	0	0	0	0	0	0	0	0	0	0	0	2,9897	3
NIBL4	I3L100_HUMAN (+2)	153	0	0	0	0	0	0	0	4,307	3	0	0	0	0	0	0
NIIC	NIIC_HUMAN (+1)	56	0	0	0	0	0	0	0	0	0	2,1952	2	1,7569	2	0	0
NFKBIL1	A0A0M8T5_HUMAN (+	41	0	0	0	0	0	0	0	0	0	2,1952	2	0	0	0	0
NFS1	NFS1_HUMAN	50	0	0	0	0	0	0	0	0	0	0	0	0	0	0	0
NFX1	NFX1_HUMAN	124	0	0	0	0	0	0	0	0	0	2,1952	2	0	0	0	0
NFXL1	NFXL1_HUMAN	101	0	0	1,9393	2	0	0	0	0	0	0	0	0	0	2,9897	3
NGDN	NGDN_HUMAN	36	0	0	0	0	0	0	0	0	0	3,2929	3	1,7569	2	0	0
NIP7	NIP7_HUMAN	20	0	0	0	0	0	0	0	2,1555	2	0	0	0	0	0	0
NKX2-5	NKX25_HUMAN	35	0	0	2,9089	3	0	0	0	0	0	0	0	0	0	0	0
NOB1	NOB1_HUMAN	47	0	0	2,9089	3	0	0	0	0	0	0	0	0	0	0	0
NOM1	NOM1_HUMAN	96	0	0	1,9393	2	0	0	0	3,2303	3	5,4881	5	0	0	0	0
NOP14	NOP14_HUMAN	98	0	0	3,8786	4	0	0	0	0	0	20,855	16	4,3922	5	2,9897	3
NOP16	NOP16_HUMAN	21	0	0	0	0	0	0	0	0	0	3,2929	3	0	0	0	0
NOP53	NOP53_HUMAN	54	0	0	0	0	0	0	0	2,1555	2	2,1952	2	0	0	0	0
NOP9	NOP9_HUMAN	69	0	0	0	0	0	0	0	0	0	6,5857	5	0	0	0	0
NPLOC4	NPL4_HUMAN	68	0	0	0	0	0	0	0	0	0	0	0	0	0	0	0
NRDE2	NRDE2_HUMAN	133	0	0	0	0	0	0	0	0	0	0	0	2,6353	3	0	0
NSF	I3L0N3_HUMAN (+1)	82	0	0	0	0	0	0	0	0	0	0	0	0	0	0	0
NT5DC2	NT5D2_HUMAN	61	0	0	0	0	0	0	0	6,4605	5	0	0	0	0	3,9863	4
NTHL1	NTH1_HUMAN	54	0	0	1,9393	2	0	0	0	0	0	3,2929	3	0	0	0	0
NUMA1	NUMA1_HUMAN	238	0	0	11,636	12	0	0	0	9,6908	8	6,5857	5	0	0	0	0
NUMBL	NUMBL_HUMAN	65	0	0	0	0	0	0	0	0	0	0	0	1,7569	2	0	0
NUP133	NU133_HUMAN	129	0	0	0	0	0	0	0	2,1555	2	0	0	0	0	0	0
NUP160	G3V198_HUMAN	148	0	0	0	0	0	0	0	3,2303	3	0	0	0	0	0	0
NUP188	NU188_HUMAN	196	0	0	0	0	0	0	0	2,1555	2	0	0	0	0	0	0
NUP37	NUP37_HUMAN	37	0	0	0	0	0	0	0	3,2303	3	0	0	0	0	0	0
NUP85	J3QL54_HUMAN (+2)	62	0	0	0	0	0	0	0	3,2303	3	0	0	0	0	0	0
NUSAP1	NUSAP_HUMAN	49	0	0	1,9393	2	0	0	0	2,1555	2	0	0	2,6353	3	0	0
OGFOD3	OGFD3_HUMAN	36	0	0	0	0	0	0	0	0	0	2,1952	2	0	0	0	0
OGT	OGT1_HUMAN	117	0	0	0	0	0	0	0	2,1555	2	0	0	0	0	0	0
PDH1	PDH1_HUMAN	83	0	0	0	0	0	0	0	4,307	3	0	0	0	0	0	0
PAHA2	PAHA2_HUMAN	61	0	0	0	0	0	0	0	3,2303	3	0	0	0	0	0	0
PAK1	PAK1_HUMAN	66	0	0	0	0	0	0	0	0	0	0	0	3,5138	3	0	0
PAN4	PAN4_HUMAN	86	0	0	0	0	0	0	0	2,1555	2	0	0	0	0	0	0
PARP2	G3V167_HUMAN (+1)	60	0	0	0	0	0	0	0	0	0	3,2929	3	0	0	0	0
PCBP2	F8VZK2_HUMAN (+2)	34	0	0	0	0	0	0	0	7,5373	7	5,4881	5	5,2707	6	0	0
PCID2	PCID2_HUMAN	46	0	0	1,9393	2	0	0	0	2,1555	2	6,5857	6	4,3922	5	0	0
PCNA	PCNA_HUMAN	29	0	0	0	0	0	0	0	2,1555	2	0	0	0	0	0	0
PCSK6	A0A7W4Y8_HUMAN (+	107	0	0	0	0	0	0	0	4,307	3	0	0	0	0	0	0
PDCD7	PDCD7_HUMAN	55	0	0	0	0	0	0	0	0	0	0	0	1,7569	2	0	0
PDF	DEFM_HUMAN	27	0	0	0	0	0	0	0	2,1555	2	5,4881	5	3,5138	4	8,9692	8
PDIA4	PDIA4_HUMAN	73	0	0	0	0	0	0	0	0	0	0	0	0	0	0	0
PEX3	PEX3_HUMAN	42	0	0	0	0	0	0	0	0	0	2,1952	2	0	0	0	0
PFKFB2	PFK2_HUMAN	58	0	0	0	0	0	0	0	0	0	0	0	7,906	6	7,9726	4
PGM5	A0A7W7Z7_HUMAN (+	49	0	0	0	0	0	0	0	3,2303	3	0	0	0	0	0	0
PHF10	PHF10_HUMAN (+1)	56	0	0	0	0	0	0	0	0	0	5,4881	3	1,7569	2	0	0
PHF3	PHF3_HUMAN	229	0	0	0	0	0	0	0	0	0	3,2929	3	5,2707	6	1,9932	2
PHKB	KPB3_HUMAN	125	0	0	0	0	0	0	0	3,2303	3	0	0	0	0	0	0
PHLDB3	PHLB3_HUMAN	72	0	0	0	0	0	0	0	5,3838	5	0	0	0	0	0	0
PI5P4	PI5P4_HUMAN	62	0	0	0	0	0	0	0	0	0	0	0	1,7569	2	0	0
PIK3C3	P85A_HUMAN	86	0	0	0	0	0	0	0	0	0	0	0	2,6353	3	0	0
PINX1	PINX1_HUMAN	57	0	0	0	0	0	0	0	0	0	2,1952	2	2,6353	2	0	0
PIP4P1	PPIP1_HUMAN	29	0	0	0	0	0	0	0	7,5373	6	0	0	0	0	5,9795	5
PIP4P2	PP4P2_HUMAN	28	0	0	0	0	0	0	0	3,2303	2	0	0	0	0	0	0
PIP5K1C	PI5IC_HUMAN	73	0	0	0	0	0	0	0	0	0	0	0	3,5138	2	0	0
PITX1	PITX1_HUMAN	34	0	0	0	0	0	0	0	0	0	2,1952	2	0	0	0	0
PITX2	PITX2_HUMAN	35	0	0	1,9393	2	0	0	0	0	0	3,2929	2	1,7569	2	0	0
PKN3	PKN3_HUMAN	99	0	0	0	0	0	0	0	0	0	4,3305	2	0	0	0	0
PKP2	PKP2_HUMAN	97	0	0	0	0	0	0	0	5,3838	5	0	0	0	0	0	0
PLA1	TPA_HUMAN	65	0	0	3,8786	4	0	0	0	0	0	2,1952	2	0	0	0	0
PLBD2	PLBD2_HUMAN	65	0	0	0	0	0	0	0	12,971	7	2,1952	2	0	0	0	0
PLD2	PLD2_HUMAN	106	0	0	0	0	0	0	0	3,2303	3	0	0	0	0	5,9795	6
PLD6	PLD6_HUMAN	28	0	0	0	0	0	0	0	5,3838	5	0	0	0	0	3,9863	4
PLEKHA5	PKHA5_HUMAN	127	0	0	3,8786	4	0	0	0	0	0	6,5857	5	3,5138	4	0	0
PMPCA	MPPA_HUMAN	58	0	0	0	0	0	0	0	0	0	3,2929	3	0	0	0	0
PMPCB	G3V0F4_HUMAN (+1)	56	0	0	0	0	0	0	0	2,1555	2	0	0	0	0	0	0
PNKD	PNKD_HUMAN	46	0	0	0	0	0	0	0	3,2303	3	0	0	0	0	0	0
PNKP	MOOTH2_HUMAN (+1)	56	0	0	0	0	0	0	0	0	0	0	0	0	0	0	0
PNMA2	PNMA2_HUMAN	42	0	0	0	0	0	0	0	35,533	13	15,367	8	1,7569	2	0	0
PNN	PININ_HUMAN	82	0	0	0	0	0	0	0	0	0	4,3305	3	0	0	0	0
PNP	PNPH_HUMAN	32	0	0	0	0	0	0	0	0	0	0	0	0	0	1,9932	2
POC1A	POC1A_HUMAN	45	0	0	0	0	0	0	0	3,2303	3	0	0	0	0	3,9863	4
POF1B	POF1B_HUMAN	68	0	0	0	0	0	0	0	0	0	0	0	5,2707	5	0	0
POLB	HDAB0_HUMAN	27	0	0	0	0	0	0	0	0	0	2,1952	2	0	0	0	0
POLD2P2	POLD2_HUMAN	42	0	0	7,7571	7	0	0	0	0	0	13,171	11	0	0	0	0
POLE2	DPOE2_HUMAN	60	0	0	0	0	0	0	0	0	0	0	0	2,6353	3	0	0
POLR1B	RPA2_HUMAN	128	0	0	2,9089	3	0	0	0	4,307	4	6,5857	6	5,5138	3	3,9863	4
POLR3D	RPC4_HUMAN	44	0	0	0	0	0	0	0	0	0	0	0	4,3922	5	3,9863	4

POMGNT2	PMGT2_HUMAN	67	0	0	0	0	0	0	24,765	12	0	0	1,7569	2	23,918	14			
POP4	K7ER37_HUMAN (+1)	21	0	0	0	0	0	0	0	0	0	0	1,7569	2	0	0			
PPAN-P2RY11	A0A0A0J1V8_HUMAN	88	0	0	0	0	0	0	4,307	4	3,2929	2	0	0	0	0			
PPIA	PPIA_HUMAN (+2)	18	0	0	1,9393	2	0	0	0	0	0	0	0	0	0	0			
PPP1R10	PP1RA_HUMAN	99	0	0	0	0	0	0	0	0	0	0	2,6353	3	0	0			
PPP2CB	PP2AB_HUMAN	36	0	0	0	0	0	0	17,228	2	0	0	0	0	0	0			
PPP2R1B	2AAB_HUMAN	66	0	0	0	0	0	0	11,866	3	0	0	0	0	0	0			
PPP2R2A	2AAA_HUMAN	52	0	0	0	0	0	0	53,858	16	3,2929	3	0	0	18,935	13			
PPP2R2D	2AB2_HUMAN	52	0	0	0	0	0	0	17,228	2	0	0	0	0	0	0			
PPP2R5E	2A5E_HUMAN	55	0	0	0	0	0	0	0	0	0	0	0	0	0	0			
PPP5C	HOTDU8_HUMAN	55	0	0	0	0	0	0	0	0	0	0	0	0	0	0			
PRCC	PRCC_HUMAN	57	0	0	0	0	0	0	0	0	0	0	0	0	0	0			
PRDX3	PRDX3_HUMAN	28	0	0	0	0	0	0	7,5373	5	0	0	0	0	0	0			
PRICKLE1	PRIC1_HUMAN	96	0	0	0	0	0	0	4,307	4	0	0	0	0	0	0			
PRICKLE3	PRIC3_HUMAN	69	0	0	0	0	0	0	5,3858	3	0	0	0	0	0	0			
PRKCI	KPCI_HUMAN	68	0	0	0	0	0	0	0	0	0	0	4,3922	5	0	0			
PRKCZ	KPCZ_HUMAN	68	0	0	0	0	0	0	0	0	0	0	2,6353	2	0	0			
PSKD3	KPCD3_HUMAN	100	0	0	2,9089	3	0	0	0	0	3,2929	3	0	0	0	0			
PSPC1BB	PS1BB_HUMAN	66	0	0	0	0	0	0	0	0	2,1952	2	0	0	0	0			
PRPF39	PRP39_HUMAN	78	0	0	0	0	0	0	7,5373	7	0	0	0	0	0	0			
PSPH-IS	PSPH3_HUMAN	117	0	0	0	0	0	0	0	0	0	0	0	0	1,9932	2			
PRP4	PRP4_HUMAN	56	0	0	0	0	0	0	8,614	2	0	0	0	0	0	0			
PSIP1	PSIP1_HUMAN	60	0	0	0	0	0	0	0	0	0	0	5,5138	4	0	0			
PSMA5	PSA5_HUMAN	26	0	0	0	0	0	0	0	0	0	0	0	0	3,9863	3			
PSMA6	G3V2P5_HUMAN (+2)	23	0	0	0	0	0	0	0	0	0	0	0	0	0	0			
PSMB2	PSB2_HUMAN	23	0	0	0	0	0	0	0	0	0	0	0	0	1,9932	2			
PSMB4	PSB4_HUMAN	29	0	0	0	0	0	0	3,2303	3	0	0	0	0	0	0			
PSMB5	H0YM88_HUMAN	15	0	0	0	0	0	0	0	0	0	0	0	0	1,9932	2			
PSMB6	PSB6_HUMAN	25	0	0	0	0	0	0	0	0	0	0	0	0	1,9932	2			
PSME4	PSME4_HUMAN	211	0	0	0	0	0	0	0	0	0	0	2,6353	3	0	0			
PTDSS1	PTSS1_HUMAN	56	0	0	0	0	0	0	0	0	0	0	0	0	2,9897	3			
PTGES2	A6NHH0_HUMAN	71	0	0	0	0	0	0	7,1535	7	0	0	0	0	0	0			
PTOV1	PTOV1_HUMAN	47	0	0	3,8786	2	0	0	17,228	8	5,4881	5	1,7569	2	5,9795	5			
PTPIK	E9PGC5_HUMAN (+1)	166	0	0	0	0	0	0	13,998	12	0	0	0	0	0	0			
PUM3	PUM3_HUMAN	74	0	0	0	0	0	0	0	0	4,3305	3	10,541	10	2,9897	3			
PUSL1	PUSL1_HUMAN	55	0	0	0	0	0	0	2,1555	2	2,1952	2	0	0	0	0			
PWP1	PWP1_HUMAN	56	0	0	0	0	0	0	4,307	4	4,3305	4	3,5138	4	0	0			
RAB11FIP2	RFIP2_HUMAN	58	0	0	0	0	0	0	4,307	3	2,1952	2	0	0	0	0			
RAB13	RAB13_HUMAN	23	0	0	3,8786	2	0	0	0	0	0	0	0	0	0	0			
RAB14	RAB14_HUMAN	24	0	0	0	0	0	0	5,3858	3	0	0	0	0	0	0			
RAB32	RAB32_HUMAN	25	0	0	0	0	0	0	3,2303	3	0	0	0	0	0	0			
RACGAP1	RGAP1_HUMAN	71	0	0	0	0	0	0	0	0	0	0	2,6353	3	0	0			
RACK1	RACK1_HUMAN	35	0	0	0	0	0	0	9,6908	8	0	0	0	0	0	0			
RAD17	A0A0Z1V6_HUMAN (+	57	0	0	0	0	0	0	0	0	0	0	1,7569	2	0	0			
RAD54L2	ARIP4_HUMAN	163	0	0	1,9393	2	0	0	0	0	0	0	5,2707	6	3,9863	4			
RADX	I6NSN8_HUMAN	?	0	0	0	0	0	0	3,2303	3	0	0	0	0	0	0			
RALY	RALY_HUMAN	32	0	0	0	0	0	0	3,2303	2	15,367	11	9,6629	11	1,9932	2			
RANBP10	A0A096LUL5_HUMAN (+	67	0	0	0	0	0	0	2,1555	2	0	0	0	0	0	0			
RARS2	SYRM_HUMAN	66	0	0	0	0	0	0	10,768	9	0	0	1,7569	2	5,9795	4			
RBBP6	RBBP6_HUMAN	202	0	0	0	0	0	0	0	0	4,3305	3	1,7569	2	0	0			
RBFA	RBFA_HUMAN	38	0	0	0	0	0	0	0	0	2,1952	2	2,6353	3	0	0			
RBM15	A0A7WWP4_HUMAN (-	102	0	0	0	0	0	0	0	0	3,2929	3	4,3922	5	0	0			
RBM15B	RB15B_HUMAN	97	0	0	1,9393	2	0	0	0	0	0	0	0	0	0	0			
RBM19	RBM19_HUMAN	107	0	0	0	0	0	0	0	0	2,1952	2	0	0	0	0			
RBM22	RBM22_HUMAN	47	0	0	0	0	0	0	0	0	4,3305	4	0	0	1,9932	2			
RBM23	RBM23_HUMAN	49	0	0	0	0	0	0	0	0	2,1952	2	0	0	0	0			
RBM4	F8WBS1_HUMAN (+2)	26	0	0	0	0	0	0	3,2303	3	2,1952	2	0	0	0	0			
RBM42	K7EPS0_HUMAN (+1)	48	0	0	0	0	0	0	0	0	0	0	4,3922	4	0	0			
RBM45	RBM45_HUMAN	56	0	0	0	0	0	0	0	0	0	0	0	0	1,9932	2			
RBPJ	SUH_HUMAN	56	0	0	0	0	0	0	0	0	0	0	0	0	0	0			
RCC1L	RCC1L_HUMAN	50	0	0	0	0	0	0	0	0	2,1952	2	0	0	0	0			
RCC01	RCC01_HUMAN	40	0	0	0	0	0	0	2,1555	2	0	0	0	0	0	0			
RCN1	RCN1_HUMAN	39	0	0	0	0	0	0	2,1535	2	0	0	0	0	0	0			
RCN2	RCN2_HUMAN	57	0	0	0	0	0	0	11,866	8	0	0	5,5138	4	6,9761	7			
RECQL4	A0A087WZ30_HUMAN	133	0	0	1,9393	2	0	0	0	0	8,781	7	0	0	0	0			
REEP4	E5RGS2_HUMAN (+1)	28	0	0	0	0	0	0	0	0	0	0	0	0	2,9897	3			
TBB1	A0A0M8R0E_HUMAN (+	21	0	0	0	0	0	0	0	0	2,1952	2	0	0	2,9897	2			
RFST	RFST_HUMAN	122	0	0	0	0	0	0	0	0	0	0	1,7569	2	0	0			
REXO4	REXO4_HUMAN	47	0	0	0	0	0	0	3,2303	3	5,4881	5	2,6353	3	0	0			
RFWD2	RFW02_HUMAN	80	0	0	0	0	0	0	11,866	7	0	0	0	0	0	0			
RFX5	F8W089_HUMAN (+1)	65	0	0	0	0	0	0	0	0	0	0	1,7569	2	0	0			
RHOBTB3	RHBT3_HUMAN	69	0	0	0	0	0	0	3,2303	3	0	0	0	0	0	0			
RHOT1	MIRO1_HUMAN	71	0	0	0	0	0	0	8,614	8	0	0	0	0	0	0			
RHOT2	H3BSI5_HUMAN (+2)	25	0	0	0	0	0	0	2,1555	2	0	0	0	0	2,9897	3			
RICTOR	RICTR_HUMAN	192	0	0	0	0	0	0	17,228	16	0	0	1,7569	2	3,9863	4			
RIOK3	B4E1Q4_HUMAN (+1)	57	0	0	0	0	0	0	2,1555	2	0	0	0	0	0	0			
RIOX2	RIOX2_HUMAN	55	0	0	0	0	0	0	0	0	0	0	1,7569	2	0	0			
RLIM	RNF12_HUMAN	69	0	0	0	0	0	0	0	0	0	0	0	0	3,9863	4			
RMDN3	RMD3_HUMAN	52	0	0	0	0	0	0	3,2303	3	0	0	0	0	0	0			
RMND5A	RM35A_HUMAN	44	0	0	0	0	0	0	7,1535	7	0	0	0	0	0	0			
RNASEH1	RNH1_HUMAN	32	0	0	2,9089	3	0	0	0	0	4,3305	4	0	0	0	0			
RNASEL	RNSL_HUMAN	86	0	0	0	0	0	0	3,2303	3	0	0	0	0	0	0			
RNF113A	R113A_HUMAN	39	0	0	0	0	0	0	0	0	0	0	0	0	0	0			
RNH1	RNH1_HUMAN	50	0	0	0	0	0	0	3,2303	3	0	0	0	0	0	0			
RPA1	RFA1_HUMAN	68	0	0	0	0	0	0	0	0	0	0	0	0	0	0			
RPL21	RL21_HUMAN	19	0	0	0	0	0	0	0	0	5,4881	4	2,6353	2	0	0			
RPL22L1	C9JYQ9_HUMAN (+2)	16	0	0	0	0	0	0	0	0	3,2929	3	0	0	0	0			
RPL32	D3YTB1_HUMAN	16	0	0	0	0	0	0	4,307	3	5,4881	4	0	0	0	0			
RPL35	I2J388_HUMAN (+1)	11	0	0	5,8178	2	0	0	0	0	4,3305	2	0	0	0	0			
RPL36	RL36_HUMAN	12	0	0	1,9393	2	0	0	4,307	3	5,4881	3	1,7569	2	0	0			
RPL36A	J3KQN4_HUMAN (+1)	16	0	0	7,7571	3	0	0	0	0	4,3305	3	0	0	0	0			
RPL7L1	RL7L_HUMAN	29	0	0	0	0	0	0	0	0	3,2929	3	0	0	0	0			
RPN2	RPN2_HUMAN	42	0	0	0	0	0	0	0	0	0	0	1,7569	2	0	0			
RPS6KA1	E9PGT3_HUMAN (+1)	81	0	0	0	0	0	0	0	0	0	0	0	0	0	0			
RPUSD3	RUSD3_HUMAN	38	0	0	2,9089	2	0	0	0	0	0	0	0	0	0	0			
RPUSD4	RUSD4_HUMAN	42	0	0	1,9393	2	0	0	2,1555	2	13,171	9	1,7569	2	0	0			
RRP12	RRP12_HUMAN	144	0	0	3,8786	3	0	0	0	0	10,976	9	3,5138	3	1,9932	2			
RRP7A	RRP7A_HUMAN	32	0	0	2,9089	3	0	0	2,1535	2	3,2929	3	0	0	0	0			
RRP9	U3IP2_HUMAN	52	0	0	0	0	0	0	0	0	0	0	1,7569	2	0	0			
TRS1	TRS1_HUMAN	41	0	0	0	0	0	0	0	0	0	0	1,7569	2	0	0			
S100A14	S10AE_HUMAN	12	0	0	2,9089	2	0	0	0	0	0	0	0	0	0	0			
S100A7	S10A7_HUMAN	11	0	0	1,9393	2	0	0	0	0	0	0	0	0	0	0			
SAFB2	SAFB2_HUMAN	107	0	0	0	0	0	0	0	0	0	0	7,906	2	0	0			
SAMD1	SAMD1_HUMAN	56	0	0	0	0	0	0	0	0	0	0	1,7569	2	0	0			
SAMM50	SAMM2_HUMAN	57	0	0	0	0	0	0	9,6908	9	0	0	0	0	2,9897	3			
SAPCD2	SAPC2_HUMAN	43	0	0	1,9393	2	0	0	4,307	4	2,1952	2	1,7569	2	5,9795	5			
SART1	SNUT1_HUMAN	90	0	0	0	0	0	0	0	0	7,6836	6	8,7845	9	2,9897	3			
SAV1	SAV1_HUMAN	45	0	0	0	0	0	0	2,1555	2	0	0	0	0	3,9863	4			
SBDS	A0A87X020_HUMAN (+	29	0	0	1,9393	2	0	0	0	0	0	0	0	0	0	0			
SBSN	SBSN_HUMAN	61	0	0	0	0	0	0	0	0	0	0	0	0	8,9692	5			
SCAF4	SFR15_HUMAN	126	0	0	0	0	0	0	0	0	5,4881	3	0	0	0	0			
SCCPDH	SCPDL_HUMAN	47	0	0	1,9393	2	0	0	6,4605	6	7,6836	6	1,7569	2	5,9795	5			
SDC1	SDC1_HUMAN	32	0	0	0	0	0	0	2,1555	2	0	0	0	0	0	0			
SDE2	SDE2_HUMAN	50	0	0	0	0	0	0	0	0	0	0	0	0	0	0			
SDHA	SDHA_HUMAN	73	0	0	0	0	0	0	3,2303	3	0	0	0	0	0	0			
SEC13	SEC13_HUMAN	36	0	0	0	0	0	0	3,2303	3	0	0	0	0	0	0			
SEMG1	SEMG1_HUMAN	52	0	0	0	0	0	0	0	0	0	0	0	0	0	0			
SEMG2	SEMG2_HUMAN	65	0	0	0	0	0	0	0	0	0	0	0	0	0	0			
SENP1	SENP1_HUMAN	73	0	0	0	0	0	0	2,1555	2	0	0	0	0	0	0			
SFNP2	SFNP2_HUMAN	68	0	0	0	0	0	0	0	0	2,1952	2	0	0	0	0			
SEPSECS	SPCS_HUMAN	56	0	0	0	0	0	0	0	0	0	0	1,7569	2	0	0			
SESTD1	SESD1_HUMAN	79	0	0	0	0	0	0	7,5373	7	0	0	0	0	0	0			
SETD2	SETD2_HUMAN	288	0	0	0	0	0	0	0	0	2,1952	2	1,7569	2	0	0			
SFXN2	SFXN2_HUMAN	36	0	0	0	0	0	0	2,1555	2	0	0	0	0	0	0			
SFXN4	SFXN4_HUMAN	38	0	0	0	0	0	0	7,5373	6	0	0	0	0	2,9897	2			
SGK3	SGK3_HUMAN	57	0	0	0	0	0	0	2,1555	2	0	0	0	0	0	0			
SH3BH	A0A0S2FM0_HUMAN (+	193	0	0	0	0	0	0	0	0	4,3305	4	7,0276	8	4,9829	5			

SHQ1N1	SHQ1_HUMAN	72	0	0	0	0	0	0	0	0	0	0	0	0	0	0	0	0	0
SKIV2L	SKIV2_HUMAN	138	0	0	0	0	0	0	0	0	0	0	0	0	0	0	0	0	0
SLAIN2	DGRIF6_HUMAN	45	0	0	0	0	0	0	0	0	0	0	0	0	12,298	2	0	0	0
SLC25A12	CMC1_HUMAN	75	0	0	0	0	0	0	0	36,61	15	0	0	0	9,6629	5	26,908	13	
SLC25A14	T65L11_HUMAN (+1)	32	0	0	0	0	0	0	0	2,1535	2	0	0	0	0	0	0	0	
SLC25A17	B0QYW5_HUMAN (+2)	26	0	0	0	0	0	0	0	0	0	2,1952	2	0	0	0	2,9897	3	
SLC25A19	TPC_HUMAN	36	0	0	0	0	0	0	0	6,4305	6	0	0	1,7569	2	3,9863	3		
SLC25A33	S2533_HUMAN	35	0	0	0	0	0	0	0	4,307	3	0	0	0	0	1,9932	2		
SLC27A1	S27A1_HUMAN	71	0	0	0	0	0	0	0	6,307	3	0	0	0	0	0	0		
SLC27A4	S27A4_HUMAN	72	0	0	0	0	0	0	0	51,684	23	4,3305	4	0	0	32,887	24		
SLC27A6	S27A6_HUMAN	70	0	0	0	0	0	0	0	2,1555	2	0	0	0	0	0	0		
SLC35F1	H7C1D_HUMAN (+1)	38	0	0	0	0	0	0	0	2,1535	2	0	0	0	0	0	0		
SLIT2	SLIT2_HUMAN (+1)	170	0	0	2,9089	3	0	0	0	2,1555	2	3,2929	3	1,7569	2	2,9897	2		
SLTM	SLTM_HUMAN	117	0	0	0	0	0	0	0	0	0	2,1952	2	0	0	0	0		
SLU7	SLU7_HUMAN	68	0	0	0	0	0	0	0	0	0	0	0	6,1491	7	0	0		
SMAD3	SMAD3_HUMAN	48	0	0	0	0	0	0	0	0	0	2,1952	2	0	0	3,9863	4		
SMG6	EST1A_HUMAN	160	0	0	0	0	0	0	0	0	0	5,4881	5	6,1491	7	0	0		
SMTN	A0A87WVP4_HUMAN (+	105	0	0	0	0	0	0	0	2,1555	2	0	0	0	0	0	0		
SNAP47	A0A87X087_HUMAN (+	67	0	0	0	0	0	0	0	7,5373	7	0	0	0	0	0	0		
SNAPC2	SNPC2_HUMAN	36	0	0	2,9089	3	0	0	0	0	0	0	0	0	0	0	0		
SNAPC4	SNPC4_HUMAN	159	0	0	4,8482	5	0	0	0	0	0	2,1952	2	3,5138	4	0	0		
SNRPC	A0A0MR37_HUMAN (+	20	0	0	0	0	0	0	0	0	0	0	0	1,7569	2	0	0		
SNRPF	RUXF_HUMAN	10	0	0	0	0	0	0	0	0	0	2,1952	2	2,6353	2	0	0		
SNRPG	RUXG_HUMAN	8	0	0	0	0	0	0	0	0	0	0	0	2,6353	2	0	0		
SNU13	B1AHD1_HUMAN (+1)	15	0	0	0	0	0	0	0	0	0	0	0	1,7569	2	0	0		
SNX33	H3BPI3_HUMAN (+1)	36	0	0	0	0	0	0	0	0	0	0	0	1,7569	2	0	0		
SNX6	A0A0MR72_HUMAN (+	48	0	0	0	0	0	0	0	2,1535	2	0	0	0	0	0	0		
SOGA1	HOYDM2_HUMAN (+1)	142	0	0	0	0	0	0	0	2,1555	2	0	0	0	0	0	0		
SORT1	SORT_HUMAN	92	0	0	0	0	0	0	0	5,3838	4	0	0	0	0	0	0		
SPIN4	SPN4_HUMAN (-1)	29	0	0	0	0	0	0	0	0	0	0	0	1,7569	2	0	0		
SPNS1	HS3MF9_HUMAN	61	0	0	0	0	0	0	0	2,1535	2	0	0	0	0	0	0		
SPOUT1	C11K_HUMAN	42	0	0	1,9393	2	0	0	0	0	0	8,781	4	3,5138	4	0	0		
SPR1A	SPR1A_HUMAN	10	0	0	3,8786	2	0	0	0	0	0	0	0	1,7569	2	0	0		
SPR2E	SPR2E_HUMAN	8	0	0	1,9393	2	0	0	0	2,1535	2	2,1952	2	1,7569	2	1,9932	2		
SPR3	B1AN48_HUMAN (+1)	17	0	0	2,9089	3	0	0	0	0	0	0	0	3,5138	4	0	0		
SPTLC2	SPTC2_HUMAN	65	0	0	0	0	0	0	0	4,307	4	2,1952	2	2,6353	3	2,9897	3		
SRFK1	SRFK1_HUMAN	59	0	0	0	0	0	0	0	0	0	3,2929	3	1,7569	2	0	0		
SRP19	SRP19_HUMAN	49	0	0	0	0	0	0	0	0	0	6,5857	6	3,5138	4	1,9932	2		
SRM	SPE3_HUMAN	36	0	0	0	0	0	0	0	2,1535	2	0	0	0	0	0	0		
SRRM1	A9Z1X7_HUMAN (+1)	103	0	0	1,9393	2	0	0	0	0	0	3,2929	3	1,7569	2	0	0		
SRSF10	Q5JSI3_HUMAN	21	0	0	0	0	0	0	0	0	0	2,1952	2	0	0	0	0		
SRSF5	SRSF5_HUMAN	31	0	0	0	0	0	0	0	0	0	0	0	5,2707	3	0	0		
SRSF7	SRSF7_HUMAN	27	0	0	0	0	0	0	0	5,3838	3	8,781	4	8,7845	3	6,9761	3		
SSAP1	SSRL_HUMAN	17	7,8297	2	1,9393	2	0	0	0	8,614	5	2,1952	2	0	0	4,9829	4		
SSR4	SSRD_HUMAN	19	0	0	0	0	0	0	0	3,2303	2	0	0	0	0	0	0		
STAU2	E9PHS2_HUMAN (+1)	59	0	0	0	0	0	0	0	5,3838	2	0	0	3,5138	2	0	0		
STK11	K7EPS8_HUMAN (+1)	48	0	0	0	0	0	0	0	0	0	2,1952	2	0	0	0	0		
STK3	STK3_HUMAN	56	0	0	0	0	0	0	0	7,5373	6	0	0	0	0	4,9829	5		
STK4	STK4_HUMAN	56	0	0	0	0	0	0	0	7,5373	3	0	0	0	0	0	0		
STK40	STK40_HUMAN	49	0	0	0	0	0	0	0	3,2303	3	0	0	0	0	0	0		
STRBP	STRBP_HUMAN	76	0	0	0	0	0	0	0	0	0	29,636	12	36,895	17	21,925	8		
STT3A	STT3A_HUMAN	81	0	0	0	0	0	0	0	3,2303	2	3,2929	2	1,7569	2	1,9932	2		
STUB1	CHIP_HUMAN	35	0	0	0	0	0	0	0	4,307	4	0	0	0	0	0	0		
STX10	K7ERY4_HUMAN (+3)	26	0	0	0	0	0	0	0	3,2303	2	0	0	0	0	0	0		
STX12	STX12_HUMAN	32	0	0	0	0	0	0	0	4,307	4	0	0	0	0	0	0		
STX17	STX17_HUMAN	33	0	0	0	0	0	0	0	3,2303	3	0	0	0	0	0	0		
STX6	STX6_HUMAN	29	0	0	0	0	0	0	0	4,307	4	0	0	0	0	0	0		
STX7	STX7_HUMAN	30	0	0	0	0	0	0	0	9,6908	8	0	0	0	0	1,9932	2		
STX8	STX8_HUMAN	27	0	0	0	0	0	0	0	9,6908	7	0	0	0	0	3,9863	4		
SUGP2	M0R229_HUMAN (+1)	122	0	0	0	0	0	0	0	3,2303	3	10,976	10	10,541	12	1,9932	2		
SURF4	Q9BRL5_HUMAN (+1)	21	0	0	0	0	0	0	0	0	0	0	0	0	0	1,9932	2		
SURF6	SURF6_HUMAN	41	0	0	0	0	0	0	0	0	0	2,1952	2	0	0	0	0		
TAPS1	TAPS_HUMAN	66	0	0	0	0	0	0	0	2,1535	2	0	0	0	0	0	0		
TAFEL	TAFEL_HUMAN	68	0	0	0	0	0	0	0	5,3838	3	0	0	0	0	0	0		
TAB1P1	TAB1I_HUMAN	182	0	0	0	0	0	0	0	0	0	2,1952	2	0	0	9,8658	10		
TAD3IP	TADBP_HUMAN	45	0	0	1,9393	2	0	0	0	3,2303	3	0	0	1,7569	2	2,9897	3		
TBC1D10B	T1010_HUMAN	87	0	0	2,9089	3	0	0	0	0	0	6,5857	5	0	0	0	0		
TBP	Q37MV6_HUMAN (+1)	32	0	0	1,9393	2	0	0	0	2,1535	2	2,1952	2	2,6353	3	0	0		
TCAF1	TCAF1_HUMAN	102	0	0	0	0	0	0	0	3,2303	3	0	0	0	0	6,9761	6		
TCEB3	A0A0A6AC6_HUMAN (+	87	0	0	0	0	0	0	0	2,1535	2	2,1952	2	2,6353	3	0	0		
TDRD3	TDRD3_HUMAN	75	0	0	3,8786	4	0	0	0	0	0	10,976	10	3,5138	4	0	0		
TEFM	TEFM_HUMAN	42	0	0	0	0	0	0	0	0	0	3,2929	3	0	0	0	0		
TERF2	TERF2_HUMAN	60	0	0	0	0	0	0	0	5,3838	4	2,1952	2	3,5138	4	3,9863	4		
TEX10	TEX10_HUMAN	106	0	0	0	0	0	0	0	2,1555	2	0	0	0	0	0	0		
TFA2A	C9JXZ2_HUMAN	35	0	0	0	0	0	0	0	0	0	2,1952	2	0	0	0	0		
TFB2M	TFB2M_HUMAN	45	0	0	0	0	0	0	0	0	0	0	0	1,7569	2	0	0		
TFCP2	F8VWL0_HUMAN (+1)	66	0	0	0	0	0	0	0	0	0	0	0	0	0	0	0		
TFPT	TFPT_HUMAN	28	0	0	0	0	0	0	0	0	0	3,2929	3	0	0	0	0		
THAP11	THA11_HUMAN	54	0	0	0	0	0	0	0	0	0	3,2929	2	0	0	0	0		
THEMI	THEM6_HUMAN	26	0	0	0	0	0	0	0	2,1535	2	0	0	0	0	0	0		
THOC3	THOC3_HUMAN	39	0	0	1,9393	2	0	0	0	0	0	2,1952	2	1,7569	2	0	0		
TIAM1	TIAM1_HUMAN	178	0	0	0	0	0	0	0	0	0	4,3305	4	1,7569	2	1,9932	2		
TIMM13	TIM13_HUMAN	11	3,9148	2	0	0	0	0	0	35,533	6	0	0	0	0	16,942	5		
TIMM23	TIM23_HUMAN	22	0	0	0	0	0	0	0	3,2303	2	0	0	0	0	0	0		
TIMM29	TIM29_HUMAN	29	0	0	0	0	0	0	0	5,3838	5	0	0	0	0	5,3795	5		
TIMM8A	TIM8A_HUMAN	11	0	0	0	0	0	0	0	10,768	5	0	0	0	0	3,9863	4		
TIMM8B	C9JWJ8_HUMAN	11	0	0	0	0	0	0	0	13,998	5	0	0	0	0	5,3795	5		
TMCO1	J9JIF6_HUMAN (-1)	27	0	0	2,9089	3	0	0	0	0	0	2,1952	2	0	0	0	0		
TMEM120B	T120B_HUMAN	40	0	0	0	0	0	0	0	3,2303	3	0	0	0	0	1,9932	2		
TMEM214	TM214_HUMAN	77	0	0	0	0	0	0	0	0	0	0	0	3,5138	4	0	0		
TMEM57	MACOI_HUMAN	76	0	0	0	0	0	0	0	2,1555	2	0	0	0	0	0	0		
TMLHE	TMLH_HUMAN	50	0	0	0	0	0	0	0	2,1535	2	0	0	0	0	0	0		
TNP2	TNP2_HUMAN	49	0	0	0	0	0	0	0	23,089	15	0	0	0	0	10,962	10		
TOE1	TOE1_HUMAN	57	0	0	0	0	0	0	0	0	0	0	0	0	0	0	0		
TONSL	TONSL_HUMAN	151	0	0	1,9393	2	0	0	0	0	0	0	0	0	0	0	0		
TOP3B	TOP3B_HUMAN	97	0	0	1,9393	2	0	0	0	0	0	9,8786	9	1,7569	2	0	0		
TOPBP1	TOPB1_HUMAN	171	0	0	1,9393	2	0	0	0	0	0	0	0	5,2707	6	1,9932	2		
TPM3	A0A087WWL8_HUMAN	26	0	0	0	0	0	0	0	0	0	0	0	0	0	1,9932	2		
TRA2B	TRA2B_HUMAN	54	0	0	0	0	0	0	0	0	0	5,4881	5	4,3922	5	0	0		
TRAF2	TRAF2_HUMAN	56	0	0	0	0	0	0	0	0	0	0	0	1,7569	2	18,935	15		
TRAF4	TRAF4_HUMAN	54	0	0	0	0	0	0	0	0	0	0	0	6,1491	6	0	0		
TRAF7	TRAF7_HUMAN	75	0	0	0	0	0	0	0	18,305	13	0	0	0	0	1,9932	2		
TRAFD1	TRAD1_HUMAN	65	0	0	0	0	0	0	0	0	0	0	0	1,7569	2	0	0		
TRIM14	TRI14_HUMAN	50	0	0	0	0	0	0	0	0	0	3,2929	3	0	0	0	0		
TRIM24	TRI24_HUMAN	62	0	0	0	0	0	0	0	0	0	0	0	0	0	0	0		
TRIM27	TRI27_HUMAN	58	0	0	0	0	0	0	0	8,614	8	0	0	0	0	3,9863	4		
TRIM32	TRI32_HUMAN	72	0	0	0	0	0	0	0	2,1535	2	0	0	0	0	0	0		
TRIM35	TRI35_HUMAN	57	0	0	0	0	0	0	0	3,2303	2	0	0	0	0	0	0		
TRIM56	TRI56_HUMAN	81	0	0	0	0	0	0	0	2,1555	2	0	0	0	0	0	0		
TRIO	TRIO_HUMAN	347	0	0	0	0	0	0	0	9,6908	9	0	0	1,7569	2	11,959	12		
TSN12	TS112_HUMAN	14	0	0	1,9393	2	0	0	0	0	0	2,1952	2	1,7569	2	0	0		
TRNAU1AP	TSAP1_HUMAN	32	0	0	0	0	0	0	0	3,2303	2	0	0	0	0	0	0		
TRPT1	F5H8A0_HUMAN (+1)	21	0	0	0	0	0	0	0	0	0	2,1952	2	0	0	0	0		
TRUB2	TRUB2_HUMAN	57	0	0	0	0	0	0	0	0	0	4,3305	4	0	0	0	0		
TSPY11	TSY11_HUMAN	49	0	0	0	0	0	0	0	5,3838	3	6,5857	6	2,6353	3	0	0		
TSR3	TSR3_HUMAN	54	0	0	1,9393	2	0	0	0	0	0	9,8786	8	0	0	0	0		
TSSC4	C9JVL1_HUMAN (+1)	22	0	0	1,9393	2	0	0	0	0	0	5,4881	4	3,5138	4	0	0		
TTC19	TTC19_HUMAN	42	0	0	0	0	0	0	0	4,307	4	0	0	0	0	0	0		
TTC26	IFT56_HUMAN	66	0	0	0	0	0	0	0	8,614	7	0	0	0	0	0	0		
TTC31	TTC31_HUMAN	57	0	0	0	0	0	0	0	3,2303	3	0	0	0	0	2,9897	3		
TUBB2B	TBB2B_HUMAN	50	0	0	0	0	0	0	0	150,59	5	68,055	5	66,762	4	127,56	6		
TUSC3	TUSC3_HUMAN	50	0	0	0	0	0	0	0	150,75	2	0	0	0	0	107,61	2		
TUSC1	TUSC1_HUMAN	23	0	0	0	0	0	0	0	0	0	2,1952	2	0	0	0	0		
TXNDC5	TXND5_HUMAN	48	0	0	0	0	0	0	0	0	0	2,1952	2	0	0	0	0		
TYK2	TYK2_HUMAN	134	0	0	2,9089	3	0	0	0	36,61	24	2,1952	2	0	0	7,9726	8		
UBAC2	UBAC2_HUMAN	59	0	0	0	0	0	0	0	0	0	0	0	0	0	5,9795	6		
UBE2S	UBE2S_HUMAN	24	0	0	0	0	0	0	0	0	0	0	0	0	0	0	0		

UBR2	UBR2_HUMAN	201	0	0	0	0	0	0	2,1555	2	0	0	0	0	0	0	0
UBXN6	UBXN6_HUMAN	50	0	0	0	0	0	0	0	0	0	0	0	0	0	0	0
UGT8	CGT_HUMAN	61	0	0	0	0	0	0	2,1555	2	0	0	0	0	0	0	0
UHMK1	UHMK1_HUMAN	67	0	0	0	0	0	0	2,1555	2	0	0	0	0	0	0	0
UHRF1	UHRF1_HUMAN	90	0	0	1,9393	2	0	0	0	0	4,3305	4	2,6353	3	0	0	0
UPF2	RENT2_HUMAN	148	0	0	0	0	0	0	0	0	9,8786	9	7,0276	8	9,9658	10	
URB1	NPA1P_HUMAN	254	0	0	0	0	0	0	2,1535	2	0	0	0	0	0	0	
USMG5	USMG5_HUMAN	6	0	0	0	0	0	0	2,1555	2	0	0	0	0	1,9932	2	
USP30	B3KU55_HUMAN (+1)	55	0	0	0	0	0	0	0	0	0	0	0	0	1,9932	2	
USP46	H7BZK6_HUMAN (+1)	40	0	0	0	0	0	0	3,2303	3	0	0	0	0	0	0	
USP8	USP8_HUMAN	128	0	0	0	0	0	0	0	0	0	0	0	0	0	0	
USP9Y	USP9Y_HUMAN	291	0	0	0	0	0	0	162,59	2	0	0	0	0	0	0	
UTP14A	UTP14A_HUMAN	88	0	0	1,9393	2	0	0	2,1555	2	8,781	8	0	0	0	0	
UTP15	UTP15_HUMAN	58	0	0	0	0	0	0	11,866	8	0	0	5,2707	6	4,9829	5	
UTP18	UTP18_HUMAN	62	0	0	0	0	0	0	4,307	4	0	0	2,6353	3	0	0	
UTP20	UTP20_HUMAN	318	0	0	0	0	0	0	0	0	3,2929	3	0	0	0	0	
UTP4	H0Y5H7_HUMAN	78	0	0	2,9089	2	0	0	0	0	2,1952	2	0	0	1,9932	2	
UTP6	UTP6_HUMAN	70	0	0	0	0	0	0	2,1555	2	0	0	0	0	0	0	
UXS1	UXS1_HUMAN	68	0	0	0	0	0	0	2,1535	2	0	0	0	0	0	0	
VCL	VINC_HUMAN	124	0	0	0	0	0	0	0	0	0	0	0	0	3,9863	4	
VPS16	VPS16_HUMAN	95	0	0	0	0	0	0	4,307	4	0	0	0	0	0	0	
VPS18	VPS18_HUMAN	110	0	0	0	0	0	0	4,307	2	0	0	0	0	0	0	
VPS33B	PSH008_HUMAN	68	0	0	0	0	0	0	0	0	0	0	0	0	0	0	
VPS35	VPS35_HUMAN	92	0	0	0	0	0	0	3,2303	3	0	0	0	0	0	0	
VTA1	A0A7A4Y5S_HUMAN (+	31	0	0	0	0	0	0	0	0	0	0	0	0	0	0	
VTI1A	VTI1A_HUMAN	25	0	0	0	0	0	0	4,307	4	0	0	0	0	0	0	
WAPL	WAPL_HUMAN	133	0	0	1,9393	2	0	0	0	0	3,2929	3	0	0	0	0	
WDR12	WDR12_HUMAN	48	0	0	3,8786	4	0	0	0	0	7,6854	7	5,2707	4	4,9829	5	
WDR18	A0A0M0Q0_HUMAN (	67	0	0	0	0	0	0	3,2303	2	0	0	0	0	0	0	
WDR20	WDR20_HUMAN	63	0	0	0	0	0	0	3,2303	3	0	0	0	0	3,9863	3	
WDR26	WDR26_HUMAN	72	0	0	0	0	0	0	13,998	10	0	0	0	0	1,9932	2	
WDR3	WDR3_HUMAN	106	0	0	0	0	0	0	0	0	0	0	2,6353	3	0	0	
WDR4	WDR4_HUMAN	45	0	0	0	0	0	0	0	0	0	0	1,7569	2	0	0	
WDR61	WDR61_HUMAN	34	0	0	0	0	0	0	0	0	0	0	2,6353	3	0	0	
WDR70	WDR70_HUMAN	73	0	0	0	0	0	0	0	0	0	0	0	0	0	0	
WDR74	WDR74_HUMAN	42	0	0	0	0	0	0	0	0	0	0	1,7569	2	0	0	
WDR75	WDR75_HUMAN	95	0	0	0	0	0	0	0	0	0	0	0	0	1,9932	2	
WDTC1	WDTC1_HUMAN	76	0	0	0	0	0	0	6,4605	5	0	0	0	0	0	0	
WNT5A	WNT5A_HUMAN	42	0	0	0	0	0	0	2,1535	2	0	0	0	0	0	0	
Y8EY	Y8EY_HUMAN	19	0	0	1,9393	2	0	0	0	0	0	0	0	0	0	0	
YPEL5	YPEL5_HUMAN	34	0	0	0	0	0	0	3,2303	3	0	0	0	0	0	0	
YTHDC1	YTDC1_HUMAN	85	0	0	1,9393	2	0	0	0	0	4,3305	4	0	0	0	0	
YTHDF1	YTHD1_HUMAN	61	0	0	0	0	0	0	0	0	0	0	0	0	0	0	
YWHAB	1433B_HUMAN	28	0	0	0	0	0	0	8,614	3	0	0	0	0	0	0	
YWHAH	1433F_HUMAN	28	0	0	0	0	0	0	6,4605	3	0	0	0	0	0	0	
YWHAQ	1433T_HUMAN	28	0	0	0	0	0	0	9,8908	5	0	0	0	0	0	0	
YWHAZ	1433Z_HUMAN	28	0	0	0	0	0	0	6,4605	3	0	0	0	0	3,9863	2	
YY1	YY1_HUMAN	45	0	0	0	0	0	0	0	0	3,2929	3	3,5138	4	1,9932	2	
ZBED5	ZBED5_HUMAN	79	0	0	0	0	0	0	0	0	0	0	4,3922	5	0	0	
ZBTB10	ZBTB_HUMAN	95	0	0	0	0	0	0	0	0	4,3305	4	0	0	0	0	
ZBTB24	ZBTB2_HUMAN	78	0	0	0	0	0	0	0	0	0	0	3,5138	4	0	0	
ZC3H14	G3V256_HUMAN (-1)	68	0	0	0	0	0	0	0	0	0	0	0	0	0	0	
ZC3H4	ZC3H4_HUMAN	140	0	0	2,9089	2	0	0	0	0	5,4881	5	3,5138	3	8,9692	9	
ZC3H8	A0A0G2F1_HUMAN (+	36	0	0	0	0	0	0	0	0	7,6854	6	2,6353	3	0	0	
ZCCHC3	ZCHC3_HUMAN	44	0	0	0	0	0	0	0	0	6,5857	4	5,2707	5	0	0	
ZCCHC9	ZCHC9_HUMAN	59	0	0	0	0	0	0	0	0	2,1952	2	0	0	0	0	
ZCCHC8	TUT1_HUMAN	171	0	0	4,8482	5	0	0	0	0	17,562	16	26,353	27	14,949	15	
ZDHHC17	ZDH17_HUMAN	75	0	0	0	0	0	0	0	0	0	0	0	0	1,9932	2	
ZFP1	ZFP1_HUMAN	48	0	0	0	0	0	0	2,1535	2	0	0	0	0	0	0	
ZFP64	A2A2N5_HUMAN (+1)	25	0	0	0	0	0	0	3,2303	3	3,2929	3	0	0	0	0	
ZKSCAN1	ZKSC1_HUMAN	64	0	0	0	0	0	0	2,1535	2	0	0	0	0	1,9932	2	
ZN121	ZN121_HUMAN	45	0	0	0	0	0	0	0	0	0	0	0	0	1,9932	2	
ZN146	OZF_HUMAN	33	0	0	0	0	0	0	3,2303	3	0	0	0	0	0	0	
ZN187	A0A24RCN4_HUMAN (+	55	0	0	0	0	0	0	0	0	2,1952	2	0	0	0	0	
ZN207	J3QTS8_HUMAN (-2)	53	0	0	0	0	0	0	0	0	0	0	0	0	0	0	
ZN239	ZN239_HUMAN	52	0	0	0	0	0	0	6,4605	3	0	0	0	0	1,9932	2	
ZN24	ZNT2C_HUMAN	42	0	0	0	0	0	0	0	0	2,1952	2	2,6353	3	0	0	
ZN275	ZN275_HUMAN	68	0	0	0	0	0	0	0	0	2,1952	2	0	0	0	0	
ZN316	ZN316_HUMAN	108	0	0	0	0	0	0	0	0	2,1952	2	0	0	0	0	
ZN346	ZN346_HUMAN	33	0	0	1,9393	2	0	0	0	0	9,8786	5	2,6353	3	0	0	
ZN391	ZN391_HUMAN	41	0	0	0	0	0	0	0	0	0	0	1,7569	2	0	0	
ZN48	A0A87WV71_HUMAN (+	54	0	0	0	0	0	0	2,1555	2	0	0	0	0	0	0	
ZN629	ZN629_HUMAN	97	0	0	0	0	0	0	0	0	4,3305	4	1,7569	2	0	0	
ZN638	ZN638_HUMAN	221	0	0	0	0	0	0	0	0	9,8786	9	1,7569	2	0	0	
ZN655	ZN655_HUMAN	57	0	0	0	0	0	0	5,3838	3	0	0	0	0	0	0	
ZN768	ZN768_HUMAN	60	0	0	7,7571	8	0	0	5,3838	5	13,171	11	3,5138	4	3,9863	4	
ZN771	ZN771_HUMAN	36	0	0	2,9089	3	0	0	0	0	10,976	8	1,7569	2	0	0	
ZN787	A0A087WU31_HUMAN	40	0	0	0	0	0	0	0	0	3,2929	2	0	0	0	0	
ZNH12	ZNH12_HUMAN	45	0	0	0	0	0	0	0	0	0	0	0	0	0	0	
ZNHIT6	HIC1_HUMAN	56	0	0	0	0	0	0	0	0	5,4881	5	1,7569	2	2,9897	3	
ZRANB2	ZRAB2_HUMAN	57	0	0	0	0	0	0	0	0	0	0	3,5138	4	0	0	

Supplemental table 2

	Gene name	molecular excess over LSM14A	molecular excess over LSM14B	molecular excess over 4E-T
mRNA REPRESSION	CYFIP1	0,23	2,42	5,20
	DDX6	2,01	20,75	44,70
	4E-T	0,04	0,46	1,00
	FMR1	0,1143	1,1804	2,5430
	FXR1	0,86	8,85	19,06
	FXR2	0,24	2,49	5,37
	GIGYF1	0,04	0,44	0,95
	GIGYF2	0,16	1,62	3,48
	LSM14A	1,00	10,33	22,25
	LSM14B	0,10	1,00	2,15
	NUFIP1	0,00	0,03	0,07
	NUFIP2	0,57	5,94	12,79
DECAPPING/DECAY	DCP1A	0,19	1,91	4,12
	DCP1B	0,03	0,29	0,63
	DCP2	0,02	0,18	0,40
	EDC3	0,16	1,69	3,64
	EDC4	0,32	3,27	7,05
	LSM1	1,78	18,40	39,64
	LSM11	0,02	0,24	0,53
	LSM12	0,97	10,06	21,68
	LSM3	4,62	47,72	102,81
	LSM4	1,24	12,79	27,56
	PAT1B	0,14	1,46	3,15
	XRN1	0,04	0,43	0,92
RNA interference	AGO1	0,03	0,33	0,71
	AGO2	0,05	0,57	1,22
	ATXN2L	0,68	7,03	15,15
	ATXN2	0,10	0,99	2,13
	MOV10	0,17	1,75	3,76
	TNRC6A	0,00	0,02	0,04
	TNRC6B	0,03	0,35	0,76
CCR4-NOT complex	CNOT2	0,34	3,55	7,64
	CNOT3	0,27	2,82	6,07
	CNOT8	0,22	2,24	4,83
	CNOT6L	0,11	1,13	2,44
	CNOT4	0,04	0,39	0,84
	CNOT10	0,03	0,29	0,62
	CNOT1	0,00	0,05	0,10
	CNOT6	0,00	0,02	0,05
INITIATION of TRANSLATION	EIF2B4	0,14	1,40	3,02
	EIF2B5	0,16	1,65	3,55
	EIF3A	1,13	11,72	25,24
	EIF3B	1,57	16,20	34,91
	EIF3D	2,40	24,83	53,50
	EIF3F	1,69	17,46	37,62
	EIF3G	4,38	45,21	97,40
	EIF3I	4,21	43,51	93,75
	EIF3J	0,19	1,98	4,27
	EIF3K	4,64	47,92	103,24
	EIF4A2	0,16	1,64	3,53
	EIF4EBP2	0,01	0,13	0,28
	EIF4G1	0,09	0,94	2,03
OTHER	ATAD3A	2,84	29,28	63,08
	DHX9	2,20	22,70	48,90
	G3BP1	9,51	98,21	211,57
	HNRNPU	10,11	104,42	224,96
	ILF3	0,42	4,33	9,32
	PRMT1	0,98	10,15	21,87
	SLC25A5	22,08	228,00	491,18
	SLC25A6	2,16	22,35	48,16
	SYNCRIP	0,06	0,60	1,30
	FUS	3,67	37,92	81,69
	YBX1	12,43	128,31	276,42
	IGF2BP1	1,19	12,33	26,56

Figure Legends

Figure 1: Purification of LSM14A, LSM14B and 4E-T cytoplasmic complexes by TAP-tag.

HEK293 cells were transfected with plasmids coding either FLAG-LSM14A-HA, FLAG-LSM14B-HA, FLAG-4E-T-HA or FLAG-HA as a control.

(A) 48 h after transfection, cells were stained with anti-FLAG (red) and anti-EDC4 (green) antibodies to detect respectively the exogenous proteins and PBs. Scale bar: 10 µm.

(B) Exogenous proteins were analyzed by Western blotting with anti-FLAG-M2 antibody (left panel). For comparison, the endogenous proteins were analysed in untransfected HEK293 cells with anti-LSM14A, anti-LSM14B, anti-4E-T and anti-RPS6 antibodies as indicated (right panel).

(C) 1/10th of each elution obtained after TAP-tag in RNAse and RNAse inhibitor conditions, in cells expressing either FLAG-HA, FLAG-LSM14A-HA, FLAG-LSM14B-HA or FLAG-4E-T-HA was migrated on a denaturing gel along with a molecular weight marker (MW) and silver stained. Yellow stars indicate fusion proteins according to their expected size.

Figure 2: Functional description of LSM14A, LSM14B and 4E-T partners identified by mass spectrometry.

(A) Venn diagrams showing the number and corresponding percentages of partners identified in RNAse and/or RNAse inhibitor-conditions. In order to reduce the dataset complexity, only partners scoring above 20 were considered.

(B) Distribution into functional categories of LSM14A, LSM14B and 4E-T partners based on the literature. Proteins partners categorized in RNA metabolism (left panel) were subcategorized into seven classes: RNA localization/mRNA decay/repression of mRNA translation/mRNA translation effectors/RNA splicing factors/ tRNA metabolism/ others. (right panel). Note that arbitrary choices had to be made for partners involved in several pathways like some repressors of translation which can also act as decapping activators.

(C) Dot graph representing MS scores of LSM14A (upper panel), LSM14B (middle panel) and 4E-T (lower panel) partners from TAP-tag purification in RNAse (y axis) and RNAse inhibitor (x axis)-treated samples. Orange dots correspond to repressors of translation and red dots to

decay & decapping factors. Circles indicate main mRNP complexes related to repression of translation or mRNA decay.

Figure 3: Identification of potential new PB assembly factors.

(A) Venn diagram showing distribution of LSM14A, LSM14B, 4E-T and DDX6 partners identified from RNAse-treated lysates. Common partners that were also significantly enriched (p-value < 0,05) in the PB proteome dataset from (Hubstenberger et al., 2017) are listed on the right.

(B) Role of ILF3 in PB maintenance. HeLa cells transfected for 48h with siILF3 or siCTL and were analysed by immunofluorescence images using anti-EDC4 (upper panel), anti-XRN1(middle panel), or anti-DDX6(lower panel) antibodies to detect PBs. Scale bar 10 µm.

(C) Quantification of ILF3 contribution to PB maintenance. PBs visualized by immunofluorescence imaging as described in (B) were counted using EDC4, XRN1 and DDX6 as PB marker in n=20 to 36 cells, in 2 independent experiments. **p-value<0.05, two-tailed paired t-test.

(D) Role of ILF3 in PB assembly after arsenite treatment. HeLa cells transfected for 48h with siILF3 or siCTL and were treated with arsenite 30 min before fixation and analysed by immunofluorescence images using anti-EDC4 (upper panel), anti-XRN1(middle panel), or anti-DDX6(lower panel) antibodies to detect PBs. Scale bar 10 µm.

(E) Quantification of ILF3 contribution to PB assembly after arsenite treatment. PBs immunostained as described in (D) were counted for each PB marker in n=18 to 34 cells, in 2 independent experiments. n.s: non significative at threshold 0.95, two-tailed paired t-test.

Figure 4: Characterisation of LSM14A association to the translation initiation complex.

(A). Translation initiation factors and ribosomal proteins identified by mass spectrometry among LSM14A partners. In the upper panel, dot plot represents MS scores of RNA-independent (y axis) and RNA-dependent (x axis) LSM14A protein partners. mRNA translation factors are plotted in green. eIF3 subunits are labelled in pink and eIF2 subunits in purple. Table in the lower panel recapitulates distribution of 40S and 60S ribosomal proteins scoring above 20, across the MS dataset.

(B) Interaction of endogenous LSM14A with components of the translation initiation complex. **Left panel:** HEK293 cytoplasmic lysates treated with RNAse or RNAse inhibitor were

immunoprecipitated with anti-LSM14A antibodies and analysed by Western blotting for translation initiation factors eIF3a, eIF4E, LSM14A and the mitochondrial protein COXIV as a negative control. Immunoprecipitation efficiency estimated as described in Materials and methods is indicated below as percent values. **Right panel**: Reciprocal immunoprecipitation was carried out by analysing immunoprecipitation by anti-eIF3a antibody of LSM14A and RPS6 proteins.

(C) 2 mg of HEK293 cytoplasmic extracts were treated with RNAse and purified on agarose beads coated either with m^7GTP or GTP as a control. Purified proteins were analysed by western blotting for LSM14A and DDX6 proteins, canonical cap-binding proteins eIF4E and 4E-T as well as COXIV as a negative control

(D) HEK293 cytoplasmic lysates were separated by ultra-centrifugation on 5-20% sucrose gradients for 2h45min. **Upper panel:** Absorbance profile of separated lysates was analysed by optical densitometry at 254nm. **Middle panel:** Proteins were extracted from the collected fractions and abundance of LSM14A, DDX6, RPS6 and 4E-T proteins in each fraction was analysed by Western blot (representative western blots are presented here)**. Lower panel:** Quantification of LSM14A, DDX6, RPS6 and 4E-T distribution along the gradient was achieved by calculating for each protein, the average normalized signal densities associated to each band over n= 2 to 5 independent experiments, as described in Materials and Methods. ** p-value < 0.05, two tailed paired t-test comparing fractions sub 40S and 40S.

Figure 5: Investigating LSM14A partners involved in LSM14A association to the translation initiation complex.

(A) Cytoplasmic lysates from HEK293 cells transfected with si4E-T or siControl were separated by ultra-centrifugation on 5-20% sucrose gradients. Inset shows verification of 4E-T silencing by Western blot analysis 48h post transfection **Upper panels**: Absorbance profile of separated lysates was analysed by optical densitometry at 254nm. **Middle panels**: representative western blots showing abundance of LSM14A and RPS6 proteins in each fraction. **Lower panels:** Quantification of LSM14A and RPS6 distribution along the gradient as described in Figure 4D.

(B) HEK293 cells were transfected either with si4E-T or siControl for 48h. **Left panel:** 4E-T silencing was verified by western blotting and efficiency of 4E-T silencing normalized to RPS6

expression is indicated below as percentages. **Right panel**: Cytosolic lysates from HEK293 cells transfected either with si4E-T or siControl for 48h treated with RNAseA were used for immunoprecipitation by anti-LSM14A antibody. Immunoprecipitates were analysed by Western blotting with eIF3a antibody.

Supplemental Figure 1: TAP-tag experimental strategy

(A). Cytoplasmic lysates from HEK293 cells transiently transfected for 48h with a plasmid coding either FLAG-LSM14A-HA, FLAG-LSM14B-HA, FLAG-4E-T-HA or FLAG-HA (control) were lysed in the presence of RNase inhibitor or RNAse. Lysates were immunoprecipitated using FLAG-M2 antibody coupled to magnetic beads. Bound proteins were eluted with M2 peptide, immunoprecipitated using HA-agarose beads and eluted in Laemmli. 9/10th of the elution was migrated on a denaturing gel for subsequent mass spectrometry analysis.

(B). Protein partners purified by TAP tag were separated using SDS-PAGE, gel was stained with Coomassie blue. Gel was cut in 5 lanes each one corresponding to a sample. These lanes were individually trypsinized and peptides obtained were identified by LC-MS/MS mass spectrometry in the Cambridge Centre for Proteomics.

Supplemental Figure 2: Comparison of TAP tag results to proteomes from the literature

(A) Dot graph representing MS scores of DDX6 partners from TAP-tag purification in RNAse (y axis) and RNAse inhibitor (x axis) treated samples according to results published in (Ayache et al., 2015). Orange dots correspond to repressors of translation and red dots to decay & decapping factors. Circles indicate main mRNP complexes related to repression of translation or mRNA decay.

(B). Dot plot representing MS scores of LSM14A or 4E-T partners from RNAse treated-lysates and the Fold Change values associated to LSM14A or 4E-T protein partners identified by BioID (*proximity*-dependent biotin identification) approach from (Youn et al., 2018). Blue dots represent significant interactions (FDR < 0,05) in the BioID dataset. Proteins functionally related to either degradation, repression of translation, CCR4-NOT complex, RNA interference or mRNP granules formation are labelled in the indicated colours.

(C) Dot plot representing MS scores of 4E-T partners from our TAP tag purification in RNAse conditions (y axis) and MS scores of 4E-T partners from an independent FLAG affinity-purification (Kamenska et al., 2016) (x axis). Orange dots represent top 50 partners in the MS

analysis from Kamenska and colleagues. Repressors of translation are labelled in brown, translation factors in purple and chaperone proteins in green.

Supplemental Figure 3: Protein interactions in untransfected cells

Protein partners co-immunoprecipitating with endogenous LSM14A **(A)**, LSM14B **(B)** or 4E-T **(C)** and related to mRNA decapping (EDC4, EDC3) or repression of translation (4E-T, LSM14A, LSM14B, DDX6). HEK293 cytoplasmic lysates were treated with RNAse or RNAse out prior to immunoprecipitation as indicated. To avoid saturation, only $1/10^{th}$ of the immunoprecipitate was loaded on the gel for LSM14A in **(A)**, LSM14B in **(B)** and 4E-T in **(C)**. Control: no antibody. Immunoprecipitation efficiency was calculated a described in Materials and Methods and indicated below each signal as percent values. Immunoprecipitations presented in this panel were performed by Michèle Ernoult-Lange.

Supplemental Figure 4: Control experiments for experiments described in Figures 3

(A) Verification of ILF3 silencing in HeLa cells 48h after siRNA transfection.

(B) Western blot analysis of EDC4, XRN1, LSM14A, LSM14B 4E-T and RPS6 (loading control) expression in HeLa cells, 48h after transfection with siILF3 or siControl.

Supplemental Figure 5: Investigating LSM14A partners involved in LSM14A association to the translation initiation complex.

(A) Cytoplasmic lysates from HEK293 cells were separated by ultra-centrifugation on 10-50% sucrose gradients for 2h45min. **Upper panels**: Absorbance profile of separated lysates was analysed by optical densitometry at 254nm. **Lower panels**: representative western blots showing abundance of LSM14A and RPS6 proteins in each fraction.

(B) Cytoplasmic lysates from HEK293 cells transfected with siLSM14A or siControl were separated by ultra-centrifugation on 5-20% sucrose gradients for 2h45. Inset shows verification of LSM14A silencing by Western blot analysis 48h post transfection. **Upper panels** : Absorbance profiles of separated lysates was analysed by optical densitometry at 254nm. **Middle panels**: Representative western blots showing abundance of DDX6 and RPS6 proteins in each fraction. **Lower panels** Quantification of DDX6 and RPS6 distribution along the gradients was performed as described in Figure 4D.

(C). Cytoplasmic lysates from HEK293 cells transfected with siDDX6 or siControl were separated by ultra-centrifugation on 5-20% sucrose gradients for 2h45. Inset shows verification of DDX6 silencing by Western blot analysis 48h post transfection **Upper panels**: Absorbance profile of separated lysates was analysed by optical densitometry at 254nm. **Lower panels**: western blot showing abundance of LSM14A and RPS6 proteins in each fraction.

Supplemental Table 1 Mass spectrometry results

Table of mass spectrometry data (filtering details are described in Materials & Methods section), indicating for each identified protein normalized spectrum count (hereafter referred to as MS scores) and number of exclusive unique peptides from which proteins were identified.

Supplemental Table 2 Quantitative expression of relevant proteins

Expression relative to either LSM14A, LSM14B or 4E-T of several proteins relevant regarding our analysis was calculated from the quantitative proteomic analysis of human HeLa cells performed by Nagaraj and colleagues (Nagaraj et al., 2011).

Discussion

1) Mass spectrometry analysis of LSM14A LSM14B and 4E-T proteome highlights repressive complexes rather than degradation complexes

In order to better understand the mechanism of PB assembly, we undertook tandem-affinity purification coupled to high-resolution mass spectrometry identification of LSM14A, LSM14B and 4E-T protein partners. Characterization of LSM14A LSM14B and 4E-T interactome in human epithelial found DDX6 and the other components of the CPEB-like complex among top interacting partners, which was expected from studies on this complex in Xenopus (Minshall et al., 2007) and human cells (Ayache et al., 2015). However, while we previously showed that DDX6 was equally distributed between the decapping and the CPEB-like complex (Ayache et al., 2015), we did not detect any components of the decapping complex except for EDC3 in LSM14B and 4E-T interactomes. Concerning LSM14A, this is in contradiction with results from another approach that found all decapping activators interacting with LSM14A (Youn et al., 2018). Indeed, proximity-dependent labelling approach used by Youn and colleagues can detect interactions with higher sensitivity than our TAP-tag purification, hence we hypothesize that absence of decapping factors in our TAP tag might result from the transient nature of these interactions.

In parallel, we found components of several repressive complexes co-purified with LSM14A, LSM14B and 4E-T. These complexes included the FMRP (Fragile-X Mental retardation protein) complex composed of FMR1 and its partners FXR1, FXR2 CYFIP and NUFIP (Bardoni and Mandel, 2002; Bardoni et al., 2006), and the CRD (coding region instability determinant)-mediated complex composed of six RBPs: YBX1, HNRNPU, SYNCRIP, DHX9, IGF2BP1 and ILF3. In agreement with this finding, characterization of recombinant FMRP-TAD (Tandem Agenet Domain) interactors in HEK293 cells identified a hundredth of partners including LSM14A. *In vitro*, the interaction between FMRP and LSM14A is sensitive to mutations of the methyl-binding pocket of FMRP TAD domain and to deletion of RGG/RG motifs in LSM14A, suggesting that methylated RGG motif of LSM14A can mediate the interaction (He and Ge, 2017).

Speculating on how and why LSM14A could contribute to these repressive complexes, a possibility is that LSM14A could bind to mRNA 3’ UTR and would therefore enable the

formation of repressive protein complexes with diverse composition. Another possibility would be that LSM14A coats the mRNA possibly with others RBPs hence sequestering mRNA from ribosomes and facilitating mRNA recruitment to RNA granules. Several points support this coating model and include that LSM14A possesses all the features of a multivalent RNA-binding protein: it contains a Lsm domain and two RGG motifs. (Tanaka et al., 2006) as well as PPI motifs (Brandmann et al., 2018). Moreover, LSM14A is more abundant than most of its partners which enables its binding in multiple copies along mRNA. Of note, such a "packaging model" has been described for LSM14A partner's, FMRP (Ivanyi-Nagy et al., 2005). An interesting prospect would be to assess whether and how these two RBP coordinate to regulate translation.

2) Comparison of PB assembly factors proteome reveals new candidates for PB formation

Liquid-liquid phase separation (LLPS), which is the physical principle currently thought to underly P-bodies assembly, is mainly mediated through multivalent interactions of RNA-binding proteins composed of structured folded domains, modular RNA-binding domains and disordered regions associating with mRNA molecules (Banani et al., 2017; Brangwynne et al., 2009). In human cells, three multivalent RBPs, DDX6, LSM14A and 4E-T, are able to interact one with another and have in common to be indispensable for PB assembly. Also, they are at the crossroad of several post-transcriptional regulation pathways including RNA-interference, general and targeted repression of translation, general and targeted mRNA decay whose molecular components are also found in PBs. The question is then how can contribution of DDX6, LSM14A and 4E-T to several translationally repressed mRNPs contribute to their concentration in supramolecular aggregates like PBs? In line with this question, two main scenari can be distinguished. On the one hand, DDX6, LSM14A, 4E-T possibly together with others yet unknown partners could form a nucleating PB complex to which other repressed mRNP complexes would aggregate to form PBs. On the other hand, contribution of DDX6 LSM14A and 4E-T to PB assembly could rely on their ability to achieve complete repression of translation of a large amount of transcripts possibly *via* different repression pathways and which would allow these mRNAs to condense into PBs.

To progress on this issue, we first tried to find other indispensable PB assembly factors by crossing proteomes of DDX6, LSM14A and 4E-T with PB proteome. Doing so we identified proteins of the CPEB-like complex which corroborates its central role in PB formation in epithelial cell lines (Ayache et al., 2015). Several other candidates emerged from this approach and included three RBPs related to mRNA metabolism: ILF3, DHX9 and HNRNPU, two ribosomal proteins RPS3 and RPS4X and three mitochondrial proteins ATAD3, SLC25A5 and SLC25A6. Looking for these proteins in a contaminant repository database for affinity purification mass spectrometry data (Mellacheruvu et al., 2013) did not find them among common contaminants suggesting that these proteins are not classical contaminant and could have a plausible biological importance with regards to PB formation.

Concerning the two ribosomal proteins, RPS3 and RPS4X, it is at first difficult to understand how ribosomal proteins could assemble PBs while the translation machinery is massively excluded from PBs and that repression of translation seems a prerequisite for PB recruitment. Yet in yeast, RPS3 has the particularity to be located at mRNA entry channel of the 40S subunit where it contacts mRNA (Dong et al., 2017). Moreover, RPS3 has been functionally characterized to act in a coordinated fashion with eIF3 to control translation termination (Poncová et al., 2019). However, if these proteins can bind mRNA in context of the ribosome, it is not known whether this happens with free cytosolic ribosomal RPS3 and RPS4X which would be a prerequisite for their involvement in PB assembly.

The three mitochondrial proteins ATAD3, SLC25A5 and SLC25A6 also present in our list of potential PB assembly factors have in common to be encoded by the nuclear genome, synthesized by cytoplasmic ribosomes and imported from cytosol to the inner mitochondria membrane (Ogunbona and Claypool, 2019; Pfanner et al., 2019), where they play a central role in the regulation of ATP production (Willis et al., 2018). Several studies based on RNA interactome capture [6] unvealed RNA-binding activities in proteins lacking classical RBD nor a predicted IDR like metabolic enzymes (Baltz et al., 2012; Castello et al., 2012, 2015). In agreement with these experiments it is possible that ATAD3, SLC25A5 and SLC25A6 are also

[6] In RNA interactome capture, protein-RNA interactions are crosslinked by applying ultraviolet (UV) light to cultured cells which induces short-lived free radicals at the nucleotide base that can attack amino acids in close proximity. Because proteins do not efficiently absorb UV light at these wavelengths, protein-protein cross-linking is not detectable. After irradiation, stringent purification of polyadenylated (poly(A)) RNA is performed under denaturing conditions. Finally, co purified cross-linked proteins are identified by quantitative mass spectrometry (Hentze et al., 2018).

bifunctional and have a post-transcriptional regulative activity. Yet we noted that these proteins were absent from a recent RNA interactome performed in HEK293 (Trendel et al., 2019). Moreover, such an activity would require that a fraction of these proteins is not imported in mitochondria and can effectively be located to PB which remains to be demonstrated.

Coming to the 3 other candidates ILF3, DHX9, HNRNPU, we noted that these three RBP contain arginine/glycine (RGG) rich domains methylated by PRMT1 (Kiledjian and Dreyfuss, 1992; Lee and Pelletier, 2016; Tang et al., 2000). RGG domains are intrinsically disordered RNA binding domains commonly found in eucaryotes (Chong et al., 2018; Järvelin et al., 2016). Due to their disordered nature, they display a conformational plasticity and adaptability in the absence of RNA that may facilitate targeting to a variety of RNAs. Moreover, RGG domains enhance the binding affinity of other RNA Binding motifs *in vitro* which is known as an "avidity effect" (Ozdilek et al., 2017). Several RGG containing proteins including hnRNPs can self-assemble into large RNA-rich granules *in vitro* (Lin et al., 2015b; Patel et al., 2015). *In vivo*, methylation of LSM14A by PRMT1 is required for LSM14A localization to PBs. Thus, an engaging prospect would be to further assess importance of these RGG domains as well as the influence of post-translational modifications by methylation on PB formation *in vivo*.

Since localization of ILF3 to PBs had previously been confirmed by immunofluorescence we focused on the role of this protein in PB maintenance and assembly. We showed that ILF3 silencing decreased the number of PBs of 40% without affecting expression of indispensable PB assembly factors DDX6 LSM14A and 4E-T levels nor the expression of PB proteins XRN1 and EDC4 we demonstrated that ILF3 contributes to PB maintenance. Moreover, we showed that ILF3 had no influence on PB de novo assembly following arsenite treatment indicating that ILF3 is not involved in PB formation. Similar behaviour was observed for other PB proteins such as PAT1B (Ayache et al., 2015).

Concerning the possible mechanisms by which ILF3 can contribute to PB maintenance, several features of ILF3 are to be considered. First, ILF3 is a RBP associated to RNA by two RNA binding motifs (Parrott et al., 2007) plus an recently identified RBM UUUUUGAGA (Dotu et al., 2018).Additionally, ILF3 has a large number of cellular targets (2849 targets) as identified by CLIP approach in the CLIP dataset from POSTAR2 database (Zhu et al., 2019). Thus, it would be

possible that ILF3 contributes to PB maintenance by simultaneously targeting a large number of mRNAs there. This hypothesis could be investigated further on by comparing ILF3 CLIP results with our PB transcriptome.

3) LSM14A is present in a subcomplex at the initiation complex

Unexpectedly, mass spectrometry analysis unveiled interaction of LSM14A with several components of the translation machinery including ribosomal proteins from the small sub-unit and translation initiation factors which at first glance seems to contradict a function of LSM14A in repression of mRNA translation or mRNA decay. Aiming to confirm those interactions *in vivo*, we found that a fraction of LSM14A co-immunoprecipitated with eIF3a, eIF4E and RPS6. However, we did not find that LSM14A co-immunoprecipitated with eIF4G as it has been shown in *S.cerevisiae* from *in vitro* experiments (Rajyaguru et al., 2012b). Among the possible explanations, we can speculate either that endogenous eIF4G is not abundant enough and/or that the fraction of eIF4G interacting with LSM14A is too weak to be detected by a co immunoprecipitation approach. Though, similar co immunoprecipitation technique was successful at detecting interaction in yeast. We therefore speculate that mechanism of interaction of LSM14A with the initiation complex is different between yeast and human .Interestingly, we noted from polysome gradient approach that LSM14A association to 40S could depend on 4E-T which is absent in yeast and binds to the same eIF4E as eIF4G in metazoans (Peter et al., 2015). A tempting hypothesis would be that 4E-T targets eIF4E and could subsequently accommodate LSM14A bound to the 43S before its binding to mRNA, thus strengthening the repressive mechanism by affecting different stages of translation initiation: eIF4F assembly and 48S formation. (Figure 6)

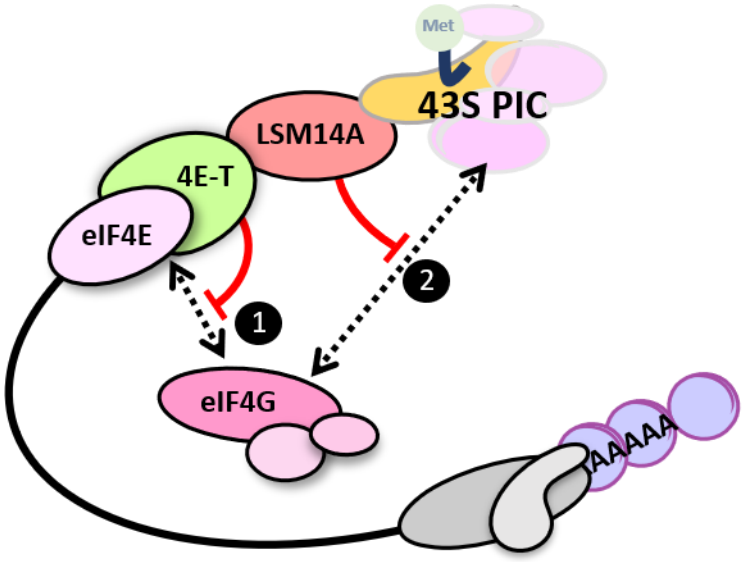

Figure 6 Model of translation initiation control by LSM14A and 4E-T

Interaction of 4E-T with eIF4E prevents formation of eIF4F complex (1) while interaction of LSM14A with 43S prevents its assembly on mRNA (2) thus strengthening repression of the initiation step.

In order to test this hypothesis experiments are in progress at the laboratory. I intend to assess whether recombinant LSM14A proteins deleted for either 4E-T interacting domain or for the RGG motif can be immunoprecipitated together with 4E-T and eIF3a with the same efficiency as full length LSM14A.

Materials and methods

Plasmids, Cell culture and transfection

Human embryonic kidney HEK293 and epithelioid carcinoma HeLa cells were cultivated in DMEM (Dulbecco's Modified Eagle's Medium)-glutamax (Invitrogen™) supplemented with 10% (v/v) fetal calf serum and 100U.mL^{-1} penicillin/streptomycin, at 37°C, 5% CO2.

For PB induction, arsenite 0.5 mM was added to the culture medium for 30 min at 37°C.

For tandem-affinity purification, HEK293 cells were transfected with 45 µg plasmid DNA per 150-mm-diameter dish using a standard calcium phosphate procedure. Human 4E-T, LSM14A open reading frame (ORF) were subcloned into pcDNA3-FLAG vector (BamHI/NotI restriction sites). The HA tag was then introduced downstream and in-frame with DDX6 ORF, using the In-Fusion Advantage PCR cloning kit (Clontech). LSM14B ORF was subcloned into a pcDNA3-FLAG vector with a PSV40 promotor.

For siRNA reverse transfection, cells were transfected with 1.5 µg siRNA per 35-mm-diameter dish using Lullaby (*OZ Biosciences*) according to the manufacturer's protocol. 48 h after transfection, cells were fixed in MetOH for immunofluorescence analysis or scrapped for subsequent protein extraction.

Following oligonucleotides were used for reverse transfection:

siRNA	Sequence (5'->3')
si4E-T	(AGACUCUUCUCCCACUACA)TT
siDDX6	(GGAACUA MGAAGACUUAAATT)TTT
siLSM14A	(UCA MGGUCC MGAACAU MGA)TT
siLSM14B	(CUAC MGAAG MGGCGCAUAA)TT
siILF3	(GAAGUAU MGAUAACACCAA)TT
siControl	(UAA MGUAU MGGAACGCAUA) TT

Immunofluorescence

Cells grown on glass coverslips were fixed in MetOH for 3 min at −20°C. After rehydration in PBS, cells were incubated with the primary antibody for 1h, rinsed with PBS, incubated with

the fluorochrome-conjugated secondary antibody for 45 min, and stained with DAPI, all steps being performed at room temperature. Slides were mounted in Citifluor (Citifluor). Microscopy was performed on a Leica DMR microscope using a 63 × 1.32 oil-immersion objective. Photographs were taken using a Micromax CCD camera (Princeton Scientific Instruments, Monmouth Junction, NJ) driven by MetaMorph software (Molecular Devices, Sunnyvale, CA). Images were processed with the open bioimage informatics software Icy (http://icy.bioimageanalysis.org; de Chaumont et al., 2012). P-bodies were counted manually.

Western blot

Proteins were separated on a NuPage 4–12% gel (Invitrogen, Life Technologies) and transferred to a nitrocellulose membrane (Perkin Elmer). After blocking in PBS containing 5% non-fat dry milk (wt/vol) for 30 min at room temperature, the membrane was incubated with the primary antibody over night at 4°C, rinsed in PBS, blocked again in PBS-milk for 30 min and incubated with HRP (HorseRadish Peroxidase)–conjugated secondary antibody for 1 h at room temperature. After 3 washing steps in PBS, immune complexes were detected using the Supersignal West Pico Chemiluminescent Signal kit (Pierce, Life Technologies) and visualized by exposure to CL-XPosure film (Pierce).

Following primary antibodies were used for western blot and immunofluorescence analysis:

antigen	species	type	source	dilution IF	dilution WB
COX IV	mouse	monoclonal	Life Technology A21348		1/500
4E-T	goat	polyclonal	Abcam ab6034	1/250	1/400
4E-T	rabbit	polyclonal	Abcam ab95030 (1mg/ml)		1/2500
GFP	mouse	Monoclonal JL8	Clontech		1/1000
EDC4	mouse	monoclonal	Santa Cruz sc-8416	1/1000	1/3000

eIF3a	mouse	Monoclonal	Santa Cruz sc-9976		1/1000
eIF4E (P2)	mouse	monoclonal	Santa Cruz sc-365789		1/1000
eIF4G1	mouse	monoclonal	Santa Cruz sc-373892		1/1000
Flag HA	mouse	monoclonal clone 7	Sigma H3663	1/1000	1/4000
LSM14A	rabbit	polyclonal	Millipore ABE37	1/1000	1/5000
LSM14A	rabbit	polyclonal	Bethyl A305-102A	1/1000	1/5000
LSM14B	rabbit	polyclonal	Sigma HPA041274	1/300	1/1000
Flag M2	mouse	monoclonal	Sigma F3165	1/1000	1/4000
DDX6 (D2)	rabbit	polyclonal	Bethyl BL2142	1/2000	1/15000
RPS6	rabbit	polyclonal	Cell signaling ref 2217		1/5000
XRN1	mouse	monoclonal	Sigma sc-165985	1/250	1/1000

Secondary antibodies Goat Anti-Mouse IgG coupled to horseradish-peroxidase (Jackson ImmunoResearch, 115-035-003) or Goat Anti rabbit IgG coupled to Horseradish peroxidase (Jackson ImmunoResearch, 111-035-144) were used in a 1/10000 dilution.

Immunoprecipitation

Cytoplasmic proteins were extracted as described previously (Ernoult-Lange et al., 2008) from HEK293 cytoplasmic lysates. For immunoprecipitations, HEK293 cytoplasmic protein extracts were incubated at 4°C for 1 h with antibodies according to the following proportions in lysis buffer supplemented with either 65 U/ml RNaseOut recombinant ribonuclease inhibitor (Promega) or 20 µg/ml RNAse A (Euromedex).

Antibody	Antibody quantity (µg)	HEK293 cytoplasmic extract (mg)
Anti DDX6	1	3
Anti LSM14A (Bethyl)	5	4.5

Anti LSM14B	3	1.5
Anti eIF3a3	5	4.5
Anti 4-ET	4	2.5

Twenty-five microliters of Dynabeads protein A magnetic beads (Life Technologies) was added per sample. After 2h at 4°C with constant rotation, beads were washed three times in 500 µL lysis buffer. Associated proteins were eluted in 30µL Laemmli 1.5X and separated by SDS PAGE along with 30 µg cytoplasmic lysate as input. Fraction of each protein immunoprecipitated was estimated from OD profiles established from scanned X-ray films using Gel Analyse plugin of ImageJ software (ImageJ, Fiji, version 2.0.0-rc-49/1.51e, https://fiji.sc/), standardized for the amount of input and immunoprecipitated proteins loaded on the gel, and expressed as a percentage of protein immunoprecipitated by the antibody used in the same experiment.

Tandem-affinity purification and mass spectrometry

HEK293 cells were lysed in a NET buffer containing 50 mM Tris-HCl (pH 7.4), 150 mM NaCl, 1 mM EDTA, 1mM EGTA, 0.5% NP-40, and 1 mM dithiothreitol (DTT), supplemented with a protease inhibitor cocktail without EDTA (Roche Diagnostic), for 30 min on ice, in the presence of either 65 U/ml RNaseOut recombinant ribonuclease inhibitor (Promega) or 20 µg/ml RNAse A (Euromedex). Nuclei and cytoplasm were separated by centrifugation at 500g for 5 min at 4°C. Cytoplasmic proteins were quantified by Coomassie protein assay (Thermo Scientific). 35 mg of proteins were mixed with 150 µL of anti-FLAG M2 Magnet resin (Sigma) for 2 h at 4°C. After beads were washed in the lysis buffer lacking NP-40, bound complexes were eluted twice in 5mL of lysis buffer supplemented with 250 µg/ml M2 peptide (Sigma-Aldrich) for 30 min at 4°C with constant rotation. Complexes were then incubated overnight with 120 µl of 50% slurry of the monoclonal anti-HA agarose (Sigma-Aldrich). After beads were washed, bound proteins were eluted in Laemmli 1.5X. One-tenth of each sample was separated on a Nu-PAGE 4%–12% Bis-Tris gel and stained with the Pierce Silver stain kit (Thermo Scientific). The remainder was briefly migrated on a Nu-PAGE 4%–12% Bis-Tris gel and stained with SimplyBlue SafeStain (Life Technologies). Each lane was sliced in 6 bands and processed for liquid chromatography–tandem mass spectrometry (LC-MS/MS) analysis in the Cambridge

Center for Proteomics, at the University of Cambridge (UK). A Mascot search algorithm (Matrix Science, London, UK) was used to search against the UniProt human database using a fixed modification of carbamidomethyl (C), a variable modification of oxidation (M), and a peptide tolerance of 25 ppm.

Scaffold proteome software (Scaffold, version4.4.7) was used to calculate normalized total spectra counts and to filter results. For each protein and peptide, False Discovery Rate was calculated by Scaffold using ProteinProphet algorithm based on assigned protein and peptides probabilities. Proteins with FDR < 0.2% and identified from at least 2 peptides with FDR < 0.1% and that did not correspond to common contaminants such as keratins, immunoglobins and several proteins of cytoskeleton were conserved for subsequent analysis.

m^7GTP affinity chromatography

HEK293 cells were lysed for 30 min on ice with NET buffer supplemented with protease inhibitor, 20 µg/ml RNAse A (Euromedex), DTT and 0.1 mM GTP. Lysates were centrifugedfor 15 minutes at 500g. 30 µL of m^7GTP-agarose beads or 30 µL of GTP-agarose beads (Jena Bioscience) were incubated with 2mg of cytoplasmic extract for 1h at 4°C with constant rotation. Beads were washed with NET buffer supplemented with GTP 1mM. Associated proteins were eluted in 30µL Laemmli 1.5X and separated by SDS PAGE along with 30 µg cytoplasmic lysate as input.

Polysome gradients

Cells grown to ~80% confluency were rinsed and scrapped in ice-cold PBS supplemented with cycloheximide 100 µg/mL. Cell pellets were lysed in ice-cold lysis buffer (20 mM HEPES, pH 7.5, 250 mM KCl, 10 mM $MgCl_2$, 5 mM DTT, 1 mM EDTA, 0.5% NP-40), supplemented with protease inhibitors and 65 U/ml of RNaseOut ribonuclease inhibitor (Promega), for 5 min. After centrifugation at 500g, supernatants were layered onto 5-20% or 10–50% sucrose gradients in Beckman centrifuge tubes 331372 and centrifuged at 39,000 rpm for 2h45min at 4°C in a Beckman SW41-Ti rotor. Equivalent volume of the first fraction was removed from the top of the gradient before collecting, and discarded to avoid contamination of following fractions by components that did not enter into the gradient. Optical density at 254 nm was monitored using a density gradient fractionator (Teledyne Isco, Lincoln, NE). For fraction collection, gradients were pushed up with FluorInert with the following settings: pump flow:

30, paper scroll rate: 60 $cm.h^{-1}$, sensitivity 0.2, running 40s/fraction. Collected fractions were precipitated in 2 equivalent volumes of EtOH and freezed overnight at -80°C. Fractions were subsequently centrifuged at 15000 r.p.m for 30min at 4°C. Pellets were rinsed with EtOH 70%, centrifuged at 15000 r.p.m and dried at 37°C for at least 4h. Proteins were resuspended in 15µL Laemmli 1X and denaturated for 5 min at 100°C. Fractions were then pooled into pairs and separated by SDS PAGE.

For quantitation, signals associated to each pooled fraction of a given protein were quantified by densitometry from scanned X-ray films, using Gel Analyze pl µgin of ImageJ software and expressed as a percentage of total signal associated to the protein in the sedimentation profile.

Part 2: Influence of mRNA GC content on mRNA localization to PBs and on its cytoplasmic post-transcriptional regulations

Analysis presented here details personal contribution to (Courel et al., 2019) (see Annexe).

Introduction

Post-transcriptional regulation of gene expression in eukaryotes relies on a balance between translation, storage and mRNA turnover. Some of these steps occur in specific places in the cytoplasm. For instance secreted proteins are locally translated at the surface of the endoplasmic reticulum (ER), which enables nascent peptides to translocate through the ER membrane and enter into the endomembrane system to be secreted (Aviram and Schuldiner, 2017). As another example, mRNAs excluded from the translation machinery transiently concentrate in mRNP granules called P-bodies (PBs). Recent purification of these granules by FAPS (Fluorescent Activated Particle Sorting) in human cells revealed that they store one third of the coding transcriptome with a striking prevalence of AU-rich transcripts, and hundreds of proteins among which a majority of RBPs, mainly involved in general and targeted repression of translation pathways including the miRNA pathway (Hubstenberger et al., 2017). Three of these proteins: LSM14A, the RNA helicase DDX6 and repressor of translation 4E-T, are of particular interest with regards to cytoplasmic post-transcriptional regulations. While in yeast these three factors are dispensable to form PBs, they are essential to PB assembly in human cells. Indeed, absence of one of these factors leads to PB disassembly and prevents their reinduction. (Ayache et al., 2015; Brandmann et al., 2018; Kamenska et al., 2016).

DDX6 is an abundant cytoplasmic protein, highly concentrated in PBs and able to bind single-stranded RNA molecules with high affinity and no sequence specificity *in vitro* (Ernoult-Lange et al., 2012). In yeast, its deletion results in the accumulation of full-length deadenylated mRNAs and leads to strong defects in mRNA decapping (Coller and Parker, 2005). Moreover, DDX6 specifically targets mRNAs containing suboptimal codons to decay (Presnyak et al., 2015). Recent transcriptome analysis in *patl1Δ, lsm1Δ, dhh1Δ or dcp2Δ* yeast strains found that rather than being global activators of decapping, Pat1, Lsm1, and Dhh1 directly regulate

specific subsets of mRNAs and have suggested that Dhh1 and Pat1/Lsm1-7 respectively form a distinct decapping complex (He et al. 2018). Once the cap cleaved by Dcp1/2, mRNAs are decayed by the 5'-3' exonuclease Xrn1. Yet, Xrn1 can also act co-translationally (Heck and Wilusz, 2018; Hu et al., 2009) and Dhh1 is thought to couple translation and mRNA stability by sensing elongation rates (Radhakrishnan and Green, 2016). In mammalian cells as in yeast, DDX6 interacts with the enhancers of decapping DCP1/2, EDC3, PAT1B and the LSM1-7 heptamer ring (Ayache et al., 2015; Sharif et al., 2013; Vindry et al., 2017; Wu et al., 2014). As a regulator of translation, DDX6 takes part to the repressive CPEB1 complex in Xenopus oocytes (Minshall et al., 2007a) and to a "CPEB-like complex" in human epithelial cells along with LSM14A and 4E-T (Ayache et al., 2015). In Drosophila it is also involved in an SRE (Smaug Recognition Element)-dependent repressor complex where it oligomerizes along *nos* mRNA in association with Tral (LSM14A) (Amadei et al., 2015; Götze et al., 2017).

DDX6 partner, LSM14A, is also conserved from yeast to human (Marnef et al., 2009). Its yeast homolog Scd6 enhances decapping (Coller and Parker, 2005) and represses translation *in vitro* by associating to eIF4G *via* its methylated RGG motifs (Rajyaguru et al., 2012). Translational repression activity of LSM14A has been reported by tether assays in Xenopus (Tanaka et al., 2006c), Arabidopsis (Xu and Chua, 2009) and human (Brandmann et al., 2018).

The third PB assembly factor, 4E-T, is a global repressor of translation conserved among vertebrates whose repression mechanism relies on eIF4E-sequestering from the eIF4F complex (Ferraiuolo et al., 2005; Kamenska et al., 2014; Waghray et al., 2015). Yet, tether assays showed that full length 4E-T and a mutated version of 4E-T that cannot bind eIF4E both repress translation in human cells (Kamenska et al., 2014). Similar results were observed for the insect-specific 4E-BP CUP in Drosophila S2 cells (Igreja and Izaurralde, 2011), suggesting that 4E-T can repress translation in an eIF4E-dependent and eIF4E-independent ways. 4E-T also interacts with CNOT1 *via* DDX6 (Ozgur et al., 2015b; Waghray et al., 2015) and directly *via* additional binding sites (Räsch et al., 2020). Its interaction with CNOT1 promotes CCR4-NOT-mediated deadenylation of 4E-T-bound mRNAs, which can subsequently be stored in a repressed form in PBs (Räsch et al., 2020).

Among the selective gene expression silencing pathways, miRNA interference can regulate expression of 60% of the human transcriptome (Friedman et al., 2009). After being processed by DICER enzymes in the cytoplasm, mature miRNAs bind specific mRNA sequences known as

MRE (miRNA Responsive Elements), through imperfect base-pairing interactions. Of note, the 5' portion of miRNA sequence from 2–7nt, called the "seed", is particularly important for miRNA recognition of its targets (Bartel, 2018). These base-pairing interactions miRNA/mRNA take place in a miRISC complex (miRNA RNA-Induced Silencing Complex) that also includes one of the 4 AGOs paralogs and TNRC6A or TNRC6B. Depending on the RBPs further recruited by the miRISC complex, miRNA targeted mRNAs can be either translationally repressed and/or degraded (Duchaine and Fabian, 2019) though determinants of these two outcomes remain poorly understood. There has been extensive debates about whether miRNAs primarily inhibit translation or induce destabilization of their mRNA targets (Iwakawa and Tomari, 2015; Jonas and Izaurralde, 2015). Currently, it is quite consensual that translational repression of miRNA targets is either the cause of mRNA destabilization or at least occurs ahead of mRNA decay (Djuranovic et al., 2012; Radhakrishnan and Green, 2016). Among molecular downstream effectors of silencing, DDX6 and 4E-T are thought to play a central role in miRNA-mediated regulations through the CCR4-NOT/ 4E-T/DDX6 complex (Chen et al., 2014b; Kuzuoğlu-Öztürk et al., 2016; Rouya et al., 2014). Moreover, interaction of 4E-T with DDX6 is required to repress translation of a miRNA reporter (Kamenska et al., 2016). Interestingly, in mouse embryonic stem cells where *Dgcr8* (DiGeorge syndrome chromosomal region 8, required for miRNA biogenesis*)* has been inactivated and which consequently lack all mature miRNAs, both inhibition of translation repression and mRNA destabilization of miRNA targets were observed whereas in ESCs inactivated for *Ddx6*, translation of the same miRNA targets was upregulated without simultaneous changes in mRNA stability (Freimer et al., 2018). These observations suggest that DDX6 is an essential effector for miRNA-driven translational repression, but not mRNA degradation in ESCs. Recently, it was also observed that 4E-T depletion prevented the accumulation of mRNA reporter artificially bound to TNRC6B hence suggesting that 4E-T recruitment protects miRNA targets from decay (Räsch et al., 2020)

In the context of this study, I took advantage of PBs, siDDX6, siDICER, siPAT1B and siXRN1 transcriptomes as well as other datasets including DDX6 and AGO CLIPs, and 4E-T RIP to address the following questions : (1) Which RBP could be responsible for the accumulation of AU-rich mRNAs in PBs considering as relevant candidates the 3 PB assembly factors DDX6, 4E-T and LSM14A; (2) what can be learnt from global localization of miRNA targets in/out PB in regards to relative importance of repression of translation versus decay in the miRNA pathway

?; (3) which other parameters apart from mRNA GC content could influence mRNA localization to PBs?

Results

1) Nucleotide preference and PB localization of mRNAs bound by PB assembly factors

mRNAs bound by DDX6 and 4E-T are GC-biased and display opposite PB localization patterns

PBs store a large number of transcripts, more than 1/5th of the human transcriptome. Looking for broad determinants of mRNA localization in PBs, we considered mRNA GC content of human PB transcripts. PB localization strongly correlates (Rs= -0.57; p-value < 0.0001) with mRNA GC content, AU-rich transcripts (further defined as transcripts whose GC content is inferior to the median GC content of all HEK293 mRNAs, that is to say 49%) being the most enriched in PBs (Figure 1A, left panel). Moreover, a detailed analysis evidenced that CDS and 3'UTR GC contents similarly contribute to PB enrichment (Rs= -0.57 and Rs= -0.55 respectively; p-value< 0.0001 for both). By contrast, nucleotide composition of 5'UTR seems less influential (Rs= -0.22; p-value< 0.0001) (Figure 1A, right panel). A complementary analysis established that the GC bias of PB mRNAs occurs independently of several parameters including PB mRNA length, mRNA expression, genomic context and gene conservation (Courel et al., 2019). Thus, being AU-rich is a prime determinant of PB mRNAs.

PB formation relies on mRNA recruitment by RBPs and in human, three RBPs, DDX6 LSM14A and 4E-T, were demonstrated to be particularly important for PB *de novo* assembly. To assess whether one of these PB assembly factors may have a nucleotide preference that could account for accumulation of AU-rich transcripts in PBs, we took advantage of DDX6 eCLIP in the human myelogenous leukemia cell line K562, generated from the ENCODE dataset (accession codes ENCSR893EFU, see material and methods for further details) and 4E-T RIP (Yang et al., 2014b). For the DDX6 eCLIP, we considered transcripts present in our HEK293 transcriptome dataset and with a DDX6 eCLIP enrichment > 1 (n=4555 bound mRNAs). Concerning the 4E-T RIP, as the experiment was performed in mouse E12 cortex cells, we selected mouse transcripts significantly enriched in 4E-T RIP (FC > 1.5) and retained as 4E-T-bound mRNAs, their human homologues expressed in HEK293 cells (n=967 bound mRNAs). For both DDX6 eCLIP and 4E-T RIP datasets, we defined as "non bound mRNAs" all the

transcripts expressed in HEK cells that were not identified as physically associated to either DDX6 or 4E-T (further defined as “bound mRNAs”). We observed that DDX6-bound mRNAs and 4E-T-bound mRNAs display opposite features: while DDX6 preferentially binds GC-rich transcripts, 4E-T associates with AU-rich transcripts (Figure 1A). In terms of cytoplasmic localization, DDX6-clipped mRNAs are mainly excluded from PBs whereas 4E-T-bound mRNAs are particularly enriched in these granules (Figure 1B).

mRNAs bound by DDX6 and 4E-T are regulated in translation by DDX6 and in stability by PAT1B

DDX6 is a multifunctional protein that plays an evolutionary conserved role in translational repression and activation of mRNA decapping before degradation by XRN1(Carroll et al., 2011; Coller and Parker, 2005; Coller et al., 2001; Ernoult-Lange et al., 2012b; Fenger-Grøn et al., 2005; Minshall and Standart, 2004). Moreover, it is one of 4E-T main protein partners (Kamenska et al., 2016). In order to assess how DDX6 and 4E-T-bound mRNAs are regulated in terms of stability and translation, DDX6 eCLIP and 4E-T RIP datasets were crossed with : transcriptome after siDDX6 in HEK293 cells, transcriptome after siXRN1 in HeLa cells, transcriptome after siPAT1B in HEK293T cells and polysome profiling after siDDX6 in HEK293 cells (see materials and methods for details on these datasets)(Figure 1D). Compared to all mRNAs, transcripts bound by DDX6 are stabilized after DDX6 knockdown while stability of 4E-T-bound transcripts is not affected by DDX6 depletion .In parallel, 4E-T-bound mRNAs are translationally derepressed after DDX6 knockdown which is not the case of DDX6 bound-mRNAs. Moreover, we noted that 4E-T-bound mRNAs are only weakly bound by DDX6 (Figure 1E). Overall these observations suggest that DDX6 and 4E-T-bound globally to distinct mRNAs subsets : GC-rich transcripts, excluded from PBs are preferentially targeted by DDX6 and regulated at the level of stability by DDX6, whereas AU-rich transcripts including 4E-T targets are more prone to be regulated at the level of translation by DDX6. Interestingly, we noted that DDX6 and 4E-T targets have opposite stability regulation patterns: DDX6 targets are stabilized after siXRN1 whereas 4E-T targets are destabilized. Conversely 4E-T targets are stabilized after PAT1B knockdown while DDX6 targets are not. This last observation might be consistent with 4E-T binding to the 5’ extremity of mRNA and precluding its access to decapping enzymes.

LSM14A binds mRNA independently of its CDS GC content

In regards to the third PB assembly factor, LSM14A, we investigated influence of nucleotide composition on LSM14A RNA binding by performing RIP on cytoplasmic lysates from HEK293 cells that transiently co-expressed two versions of Renilla luciferase mRNA : a version with an AU-rich CDS (36 %GC) and a version with a GC-rich CDS (55% GC). To make sure that these reporters could recapitulate behaviour of endogenous transcripts with respect to PB localization, Marianne Bénard analysed their cellular localization by smiFISH (single molecule inexpensive Fluorescent In Situ Hybridation) using probes specific of the AU-rich or the GC-rich reporter and concomitantly immuno-stained cells with DDX6 antibody to detect PBs. We observed that the GC-rich reporter is homogeneously distributed throughout cytoplasm and excluded from PBs (Figure 2A, left panel). In comparison, the AU-rich reporter also has a cytoplasmic expression but tend to cluster more often in PBs (Figure 2A, middle panel). Quantification from two independent experiments indicate that around 20% of PBs contain clusters of AU-rich reporter mRNAs (Figure 2A, right panel). These experiments confirmed that CDS GC content is sufficient to influence mRNA localization to PBs *in vivo*. It also indicates that these reporter mRNAs could be used to assess LSM14A sequence binding preference. To do so, we co-transfected plasmids encoding the 2 versions of Renilla luciferase in HEK293 cells. After 40hrs expression, transfection efficiency was checked by measuring luciferase activity (Supplemental Figure 1A). Then, mRNP complexes associated to LSM14A were immunoprecipitated by an anti-LSM14A antibody from HEK293 cytoplasmic lysates co-expressing both reporter mRNAs. In parallel, mRNP complexes associated to DDX6 were immunoprecipitated by an anti-DDX6 antibody. Immunoprecipitation with IgG was used to control immunoprecipitation specificity. Quantification of the amount of co-precipitated reporter mRNAs by qRT-PCR showed that GC-rich reporter is immunoprecipitated twice as efficiently as AU-rich reporter by DDX6 antibody (Figure 2B). This observation is consistent with the DDX6 eCLIP dataset showing that DDX6 preferentially targets GC-rich transcripts. However, AU-rich and GC-rich reporters were immunoprecipitated with the same efficiency by LSM14A antibody (Figure 2B). Hence, CDS GC content seems not to influence LSM14A association while DDX6 preferentially binds mRNAs with a GC-rich CDS.

In conclusion, out of the three proteins analysed, only 4E-T could be responsible of recruitment of AU-rich transcripts to PBs.

2) Influence of GC content on PB localization and post-transcriptional regulations of miRNA-targets

mRNAs targeted by miRNAs can be translationally repressed and/or/then degraded (Jakymiw et al., 2005) and these regulations involve DDX6 (Rouya et al., 2014). Moreover in human cells, PBs store repressed mRNAs protected from 5'->3' decay (Hubstenberger et al., 2017) including miRNA targets (Bhattacharyya et al., 2006; Liu et al., 2005; Pillai et al., 2005b). In order to assess if localization of miRNA targets in/out PBs is related to mRNA fate in terms of translational repression versus degradation, we compared GC content and PB localization of mRNAs targeted by the 22 most abundant miRNAs in HEK293 cells (19 from Hafner et al., 2010 and 3 from Patrick Brest quantitation's). Concomitantly, we analysed mRNAs bound to AGO 1,2,3 or 4 identified in CLIP experiments (Yang et al., 2015) and mRNA stabilized after DICER depletion in HEK293 cells (Rybak-Wolf et al., 2014). Compared to all mRNAs, targets of 18 out of the 22 miRNAs analysed are AU-rich, exceptions concerning targets of miR-10b-5p, miR 99a-5p and miR 99b-5p which have the same nucleotide GC content as all mRNAs (Figure 3A). Moreover, miRNA targets are overall enriched in PBs though to different extents, from targets of miR-99-5p which enrichment in PBs does not reach statistical significance to miR 21-5p targets which are the most enriched in PBs (Figure 3B). AGO 1,2, 3 and 4 targets display the same features: they are overall AU-rich (Figure 3A) and enriched in PBs (Figure 3B), though number of AGO4 targets is too small to reach statistical significance. Overall, these results evidence that miRNA targets tend to be AU-rich and accumulate in PBs.

In order to assess how these miRNA-targets are regulated in terms of translation and decay, we looked at their behaviour in siDDX6, siPAT1B, siXRN1 transcriptomes datasets and in DDX6 eCLIP dataset (Figure 3C). Neither stability of AGO 1,3,4 targets is sensible to DDX6 depletion nor are AGO 1,3,4 targets directly bound by DDX6. However, AGO2 targets are slightly bound by DDX6 and regulated in stability by this protein. Conversely, translation rate of AGOs targets is DDX6-dependant. Finally, AGO targets display opposite behaviour in XRN1 and PAT1B transcriptomes: they are destabilized after XRN1 depletion but stabilized after PAT1B knockdown (Figure 3C). We concluded from these results that AGO targets which reflects behaviour of miRNA targeted mRNAs, are regulated like other mRNAs enriched in PBs: DDX6

regulates their translation but not their stability except for AGO2 targets and PAT1B regulates their stability.

In parallel, we observed that mRNAs whose stability was enhanced following DICER depletion tend to be also stabilized after DROSHA silencing (Rp=0.44, p-value < 0.0001) (Supplemental Figure 2A), which suggests that mRNAs upregulated after siDICER are miRNA-regulated mRNAs and not passive DICER mRNA targets Transcripts upregulated after siDICER are slightly more GC-rich (Figure 3A) and less enriched in PBs compared to all transcripts (Figure 3B). Moreover, transcripts upregulated after siDICER are targeted by DDX6, stabilised after siDDX6 and after XRN1 silencing but are neither translationally upregulated following DDX6 depletion nor stabilised after PAT1B silencing (Figure 3C). Yet, magnitude of the observed effects is very weak (for instance mRNAs stabilized after siDICER are less than 1 point more GC-rich than all mRNAs) which makes interpretation of these results difficult.

Investigating whether the observed effects may depend on the miRNA itself, we noticed that median %GC content of miRNAs strongly correlates with median %GC content of their targets (Rp = 0.74, p-value < 0.0001) (Figure 4A). Moreover, the more AU-rich is the miRNA, the more its targets are enriched in PBs (Figure 4B). Thus, AU-rich miRNAs tended to target mRNAs themselves AU-rich and enriched in PBs and effect intensity seems proportional to the miRNA GC content. Because miRNAs bind their targets *via* Watson–Crick base-pairing where the miRNA seed sequence is particularly important for target selection, we wondered whether the correlation would be stronger when considering GC content of the seed sequence instead of the miRNA median GC content. Actually, it is not the case : correlation between GC content of the seed and GC content of the miRNA targets is weaker than between miRNAs and targets GC contents, presumably because the very short length of the seed sequence allows a limited number of seed GC content values (Figure 4C). Though, identical slopes (Figure 4A and Figure 4C) suggest similar influences of the miRNA GC content or GC content of the seed sequence with regards to miRNA targets GC content. However, pairwise correlations between GC contents of the miRNA seed and 3'UTR of miRNA targets is stronger than between GC contents of miRNA seed and CDS of miRNA targets. We also noted that median length of targets 3'UTR is not significantly different compared to other variables (Figure 4D). These observations indicate that 3'UTR GC content of the miRNA target is an important determinant of their post transcriptional regulation by miRNAs.

To assess whether miRNA GC content also affected post-transcriptional regulations we analysed behaviour of the 3 most AU-rich miRNAs (let7f, miR-101-3p, miR-301-3p) and the 3 most GC-rich miRNAs (miR 92a-3p, miR-24a-3p and miR-99b-5p) in the different silencing datasets (Figure 4E). Compared to all mRNAs, targets of the 6 miRNAs are not stabilized following DDX6 silencing except for miR-99b-5p nor bound by DDX6. Also, targets of the 6 miRNAs are destabilized after XRN1 silencing. In contrast, targets of the three most AU-rich miRNAs are up-translated after siDDX6 depletion while translation of the 3 most GC rich miRNA is unaffected by DDX6 silencing. mRNA targets of AU-rich miRNAs are also slightly more stabilized after PAT1B silencing than targets of GC-rich miRNAs. Thus, targets of AU-rich miRNAs recapitulate overall regulations of AU-rich mRNAs enriched in PBs: they are regulated in translation by DDX6 and in stability by PAT1B. Hence, miRNA GC bias contributes to orientate miRNA targets fate in terms of PB localization and regulations by general post-transcriptional factors DDX6, XRN1 and PAT1B.

3) Localization of AU-rich mRNAs transcripts

GC content is a parameter strongly correlated with mRNA localization to PBs. Indeed, distribution of HEK293 transcripts according to their GC content evidenced that 61% of AU-rich mRNAs selectively accumulate in PBs (Figure 5A). To investigate other determinants of mRNA localization, we considered the AU-rich transcripts excluded from PBs and compared them to all AU-rich mRNAs in a Gene Ontology overrepresentation test using the Cellular Component categories. Noteworthily, AU-rich transcripts excluded from PBs are enriched in transcripts coding proteins related to membranous organelles, such as mitochondria, ER, lysosomes, secretory granules, and to ribosomes (Figure 5B). According to the PB purification protocol, PBs were sorted from a cytoplasmic lysate centrifuged at 10000g hence containing organelle-and that was further used as a reference for PB enrichment analysis (Hubstenberger et al., 2017). This observation suggests that to be recruited to PBs, a given mRNA should be preferentially AU-rich and not be retained on membranous organelles and/or on ribosomes.

Figures

Figure 1

A.

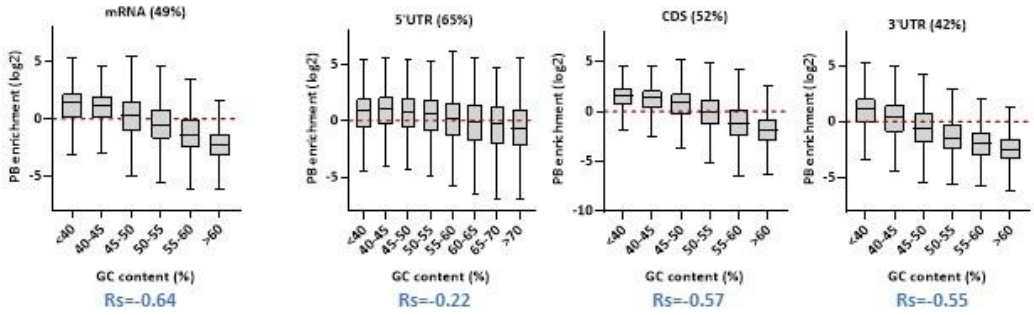

B.

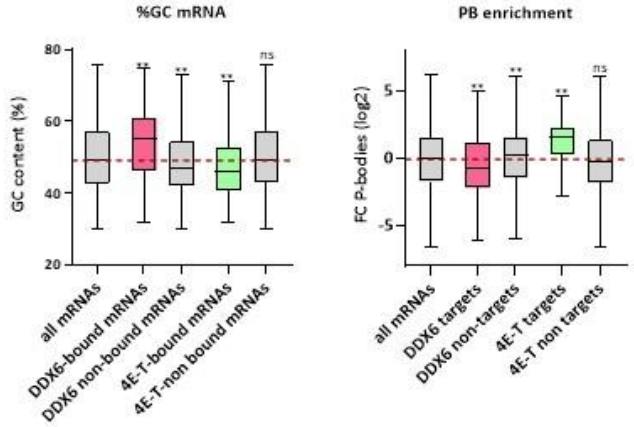

C.

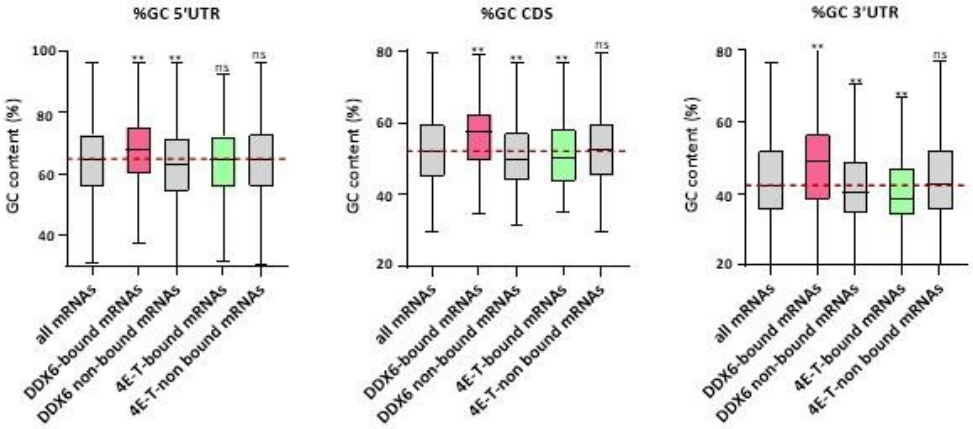

D.

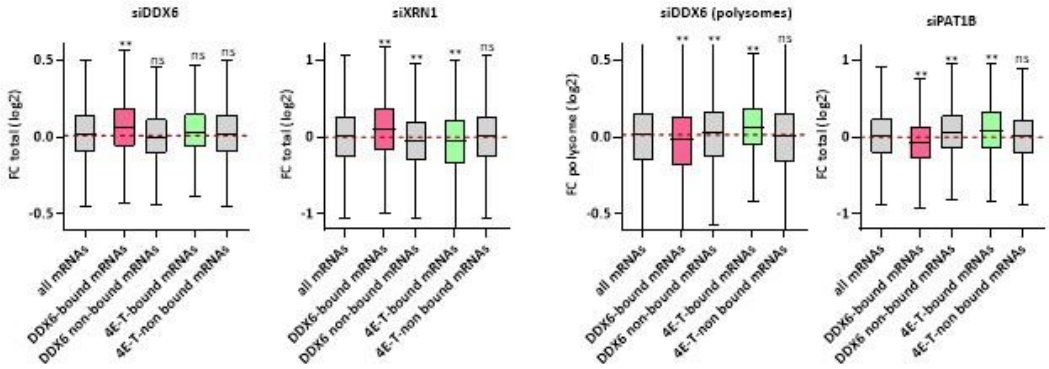
siDDX6
siXRN1
siDDX6 (polysomes)
siPAT1B
FC total (log2)
FC polysome (log2)
all mRNAs
DDX6-bound mRNAs
DDX6 non-bound mRNAs
4E-T-bound mRNAs
4E-T-non bound mRNAs
**
ns
*

E.

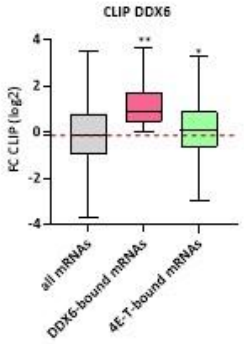
CLIP DDX6
FC CLIP (log2)
all mRNAs
DDX6-bound mRNAs
4E-T-bound mRNAs
**
*

Figure 2

A.

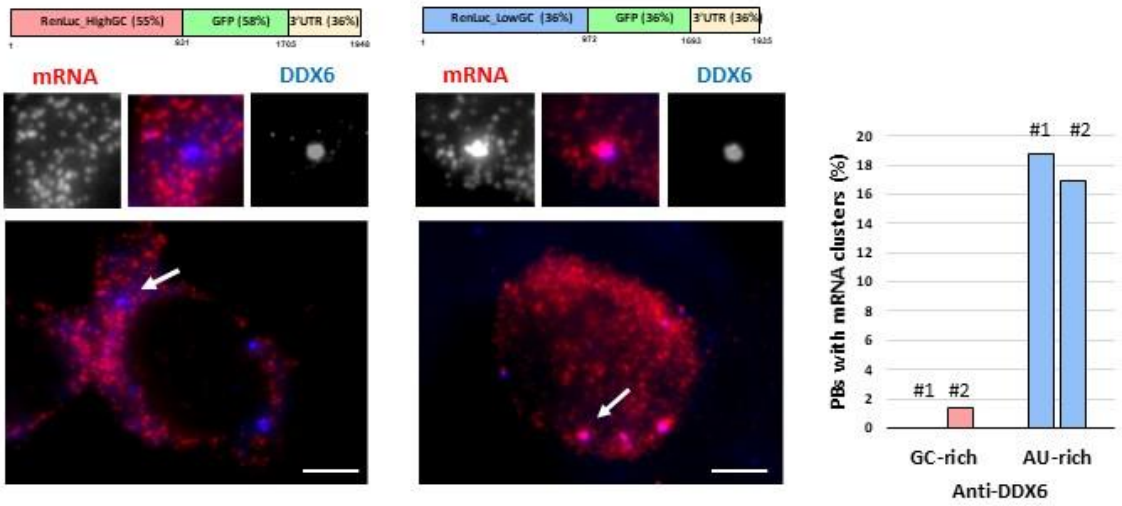
RenLuc_HighGC (55%)
GFP (58%)
3'UTR (36%)
RenLuc_LowGC (36%)
GFP (36%)
3'UTR (36%)
mRNA
DDX6
mRNA
DDX6
PBs with mRNA clusters (%)
#1 #2
#1 #2
GC-rich
AU-rich
Anti-DDX6

B.

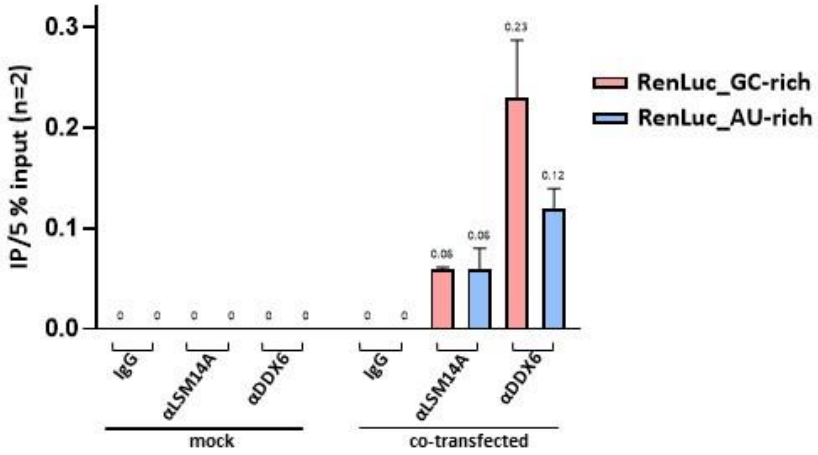
IP/5 % input (n=2)
RenLuc_GC-rich
RenLuc_AU-rich
0.23
0.12
0.06
0.06
IgG
αLSM14A
αDDX6
IgG
αLSM14A
αDDX6
mock
co-transfected

Figure 3

A.

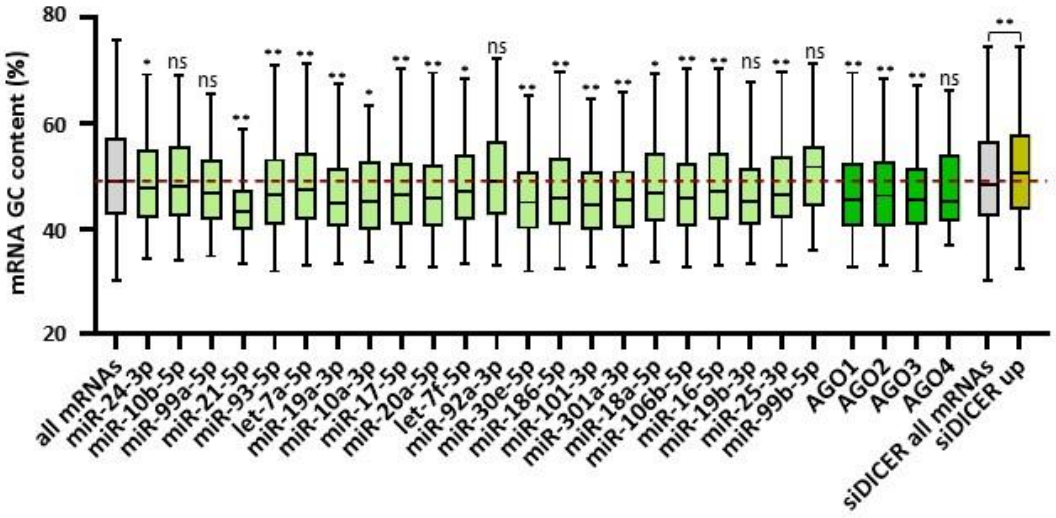
mRNA GC content (%)
80
60
40
20
ns
all mRNAs
miR-24-3p
miR-10b-5p
miR-99a-5p
miR-21-5p
miR-93-5p
let-7a-5p
miR-19a-3p
miR-10a-3p
miR-17-5p
miR-20a-5p
let-7f-5p
miR-92a-3p
miR-30e-5p
miR-186-5p
miR-101-3p
miR-301a-3p
miR-18a-5p
miR-106b-5p
miR-16-5p
miR-19b-3p
miR-25-3p
miR-99b-5p
AGO1
AGO2
AGO3
AGO4
siDICER all mRNAs
siDICER up

B.

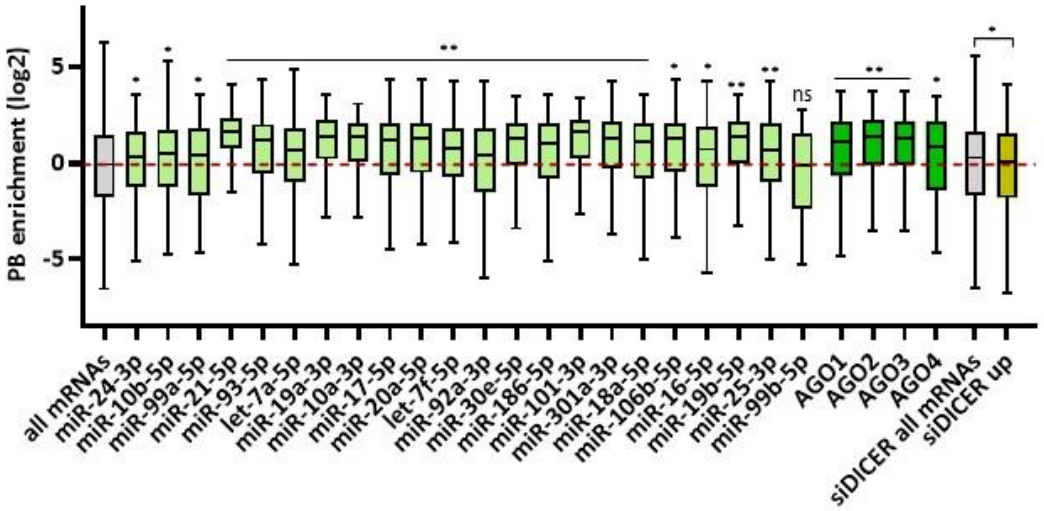
PB enrichment (log2)
5
0
-5
ns
all mRNAs
miR-24-3p
miR-10b-5p
miR-99a-5p
miR-21-5p
miR-93-5p
let-7a-5p
miR-19a-3p
miR-10a-3p
miR-17-5p
miR-20a-5p
let-7f-5p
miR-92a-3p
miR-30e-5p
miR-186-5p
miR-101-3p
miR-301a-3p
miR-18a-5p
miR-106b-5p
miR-16-5p
miR-19b-5p
miR-25-3p
miR-99b-5p
AGO1
AGO2
AGO3
AGO4
siDICER all mRNAs
siDICER up

C.

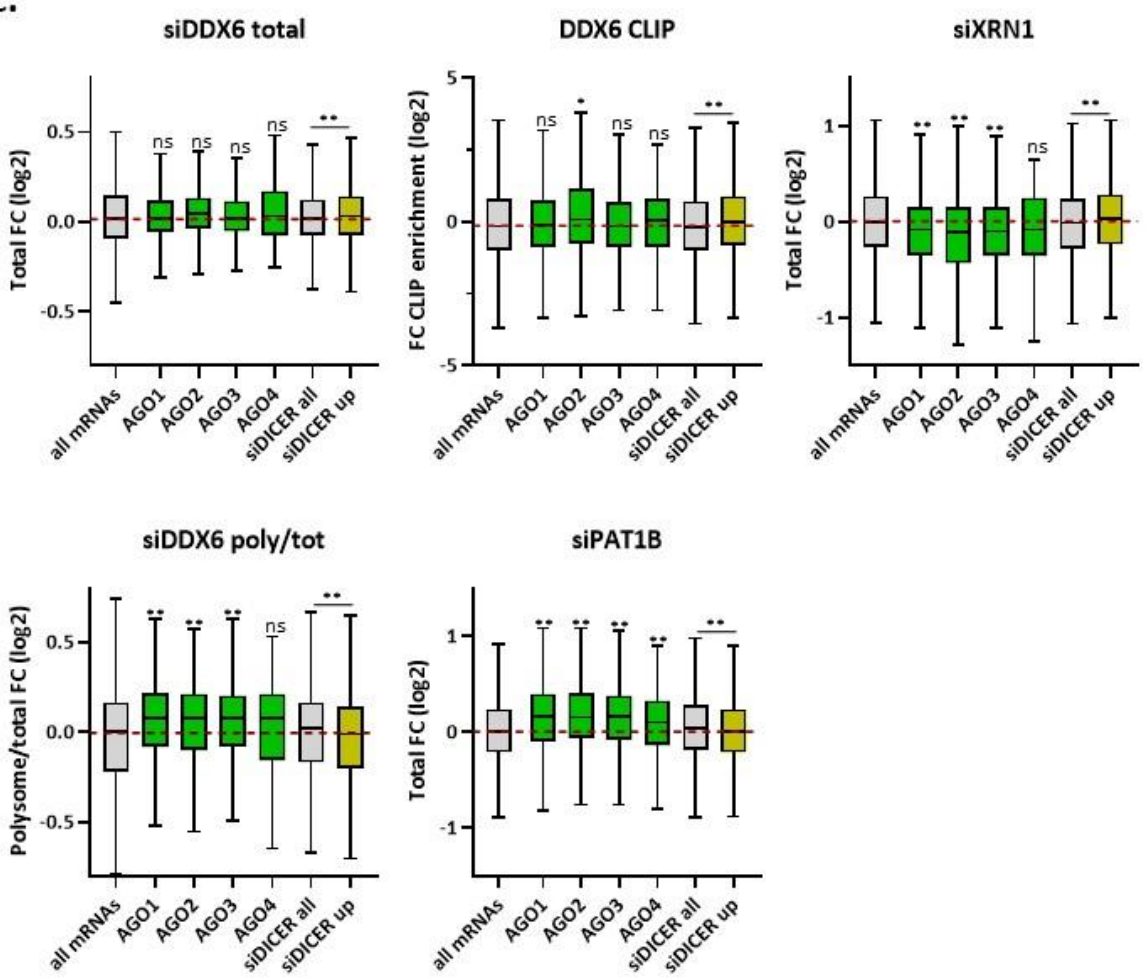

D.

miRNA	number of targets
miR-24-3p	758
miR-10b-5p	280
miR-99a-5p	121
miR-21-5p	553
miR-93-5p	1096
let-7a-5p	576
miR-19a-3p	524
miR-10a-3p	59
miR-17-5p	1041
miR-20a-5p	956
let-7f-5p	355
miR-92a-3p	1261
miR-30e-5p	321
miR-186-5p	659
miR-101-3p	356
miR-301a-3p	358
miR-18a-5p	237
miR-106b-5p	913
miR-16-5p	1399
miR-25-3p	455
miR-99b-5p	49
miR-19b-3p	714

CLIP	Number of targets
AGO1	1018
AGO2	413
AGO3	977
AGO4	96

RNAseq	Number of mRNAs
siDICER (all)	9209
siDICER (up)	4552

Figure 4

A.

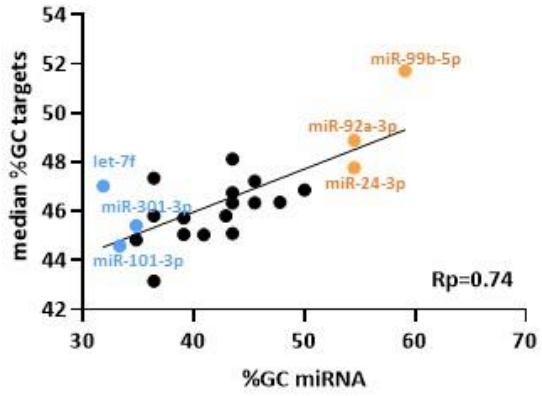

B.

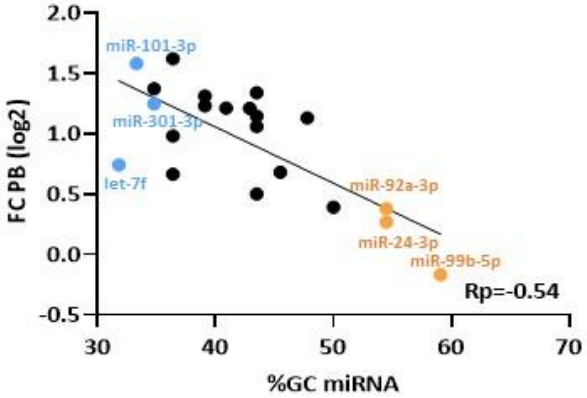

C.

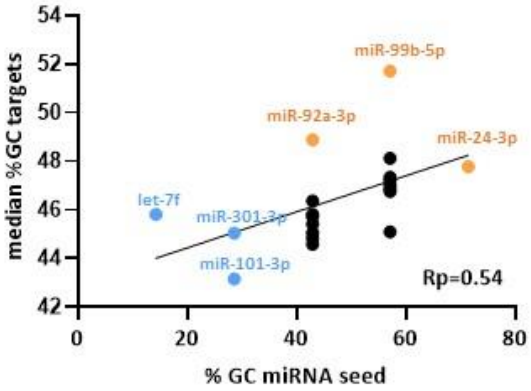

D.

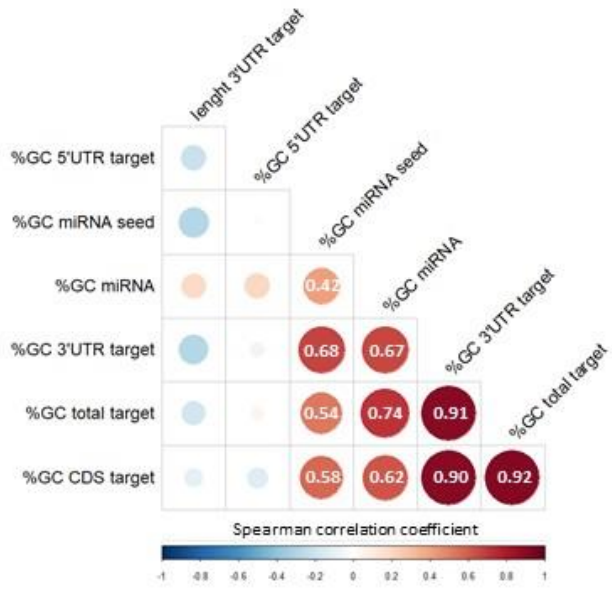

E.

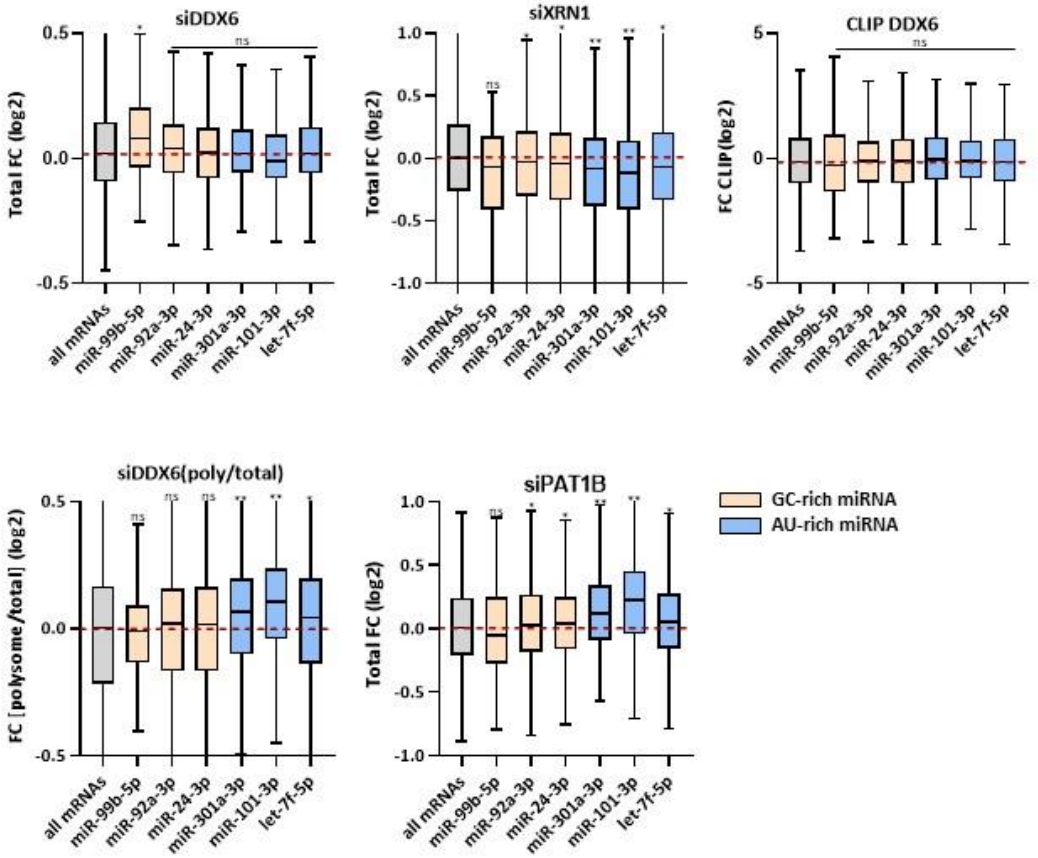
siDDX6
siXRN1
CLIP DDX6
siDDX6(poly/total)
siPAT1B
Total FC (log2)
FC CLIP (log2)
FC [polysome/total] (log2)
ns
all mRNAs
miR-99b-5p
miR-92a-3p
miR-24-3p
miR-301a-3p
miR-101-3p
let-7f-5p
GC-rich miRNA
AU-rich miRNA

Figure 5

A.

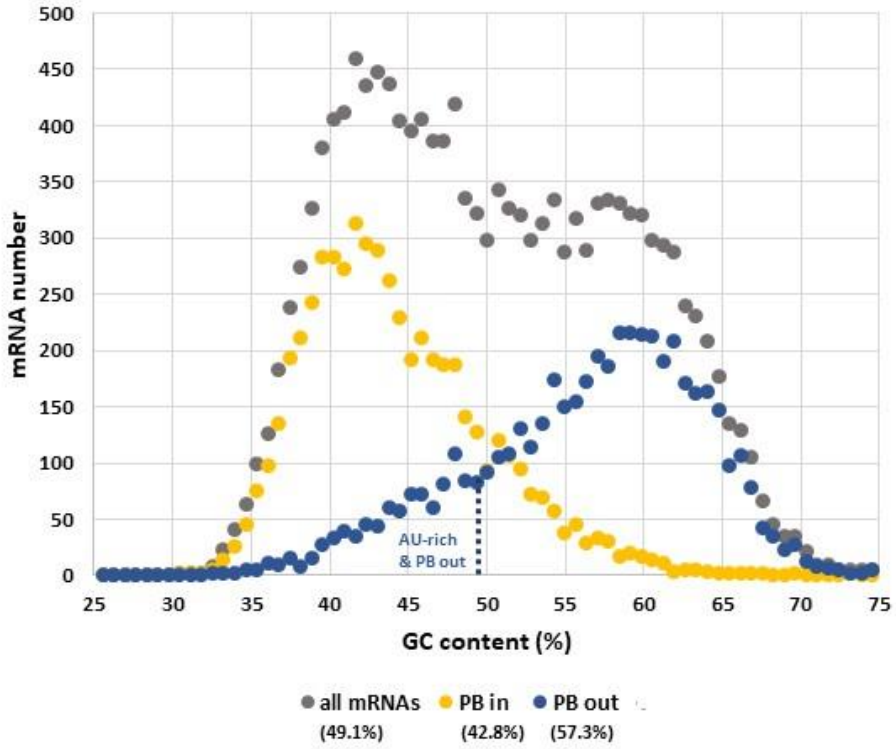
mRNA number
GC content (%)
AU-rich
& PB out
all mRNAs
(49.1%)
PB in
(42.8%)
PB out
(57.3%)

B.

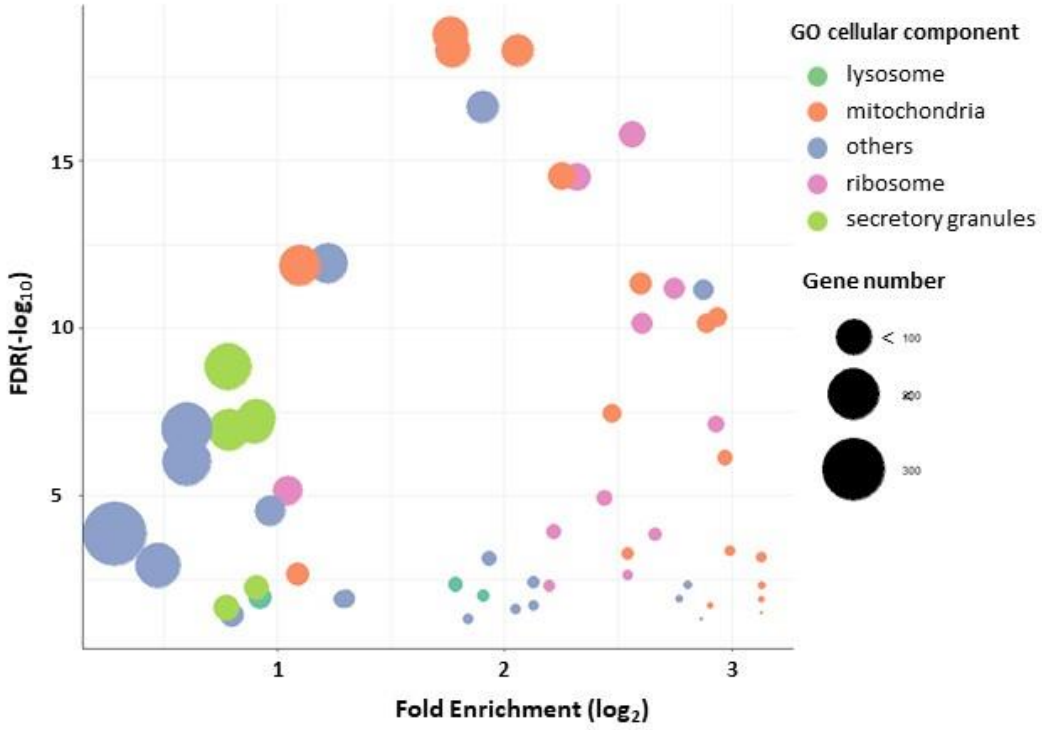
FDR(-log10)
Fold Enrichment (log2)
GO cellular component
lysosome
mitochondria
others
ribosome
secretory granules
Gene number
< 100
300

Supplemental Figure 1

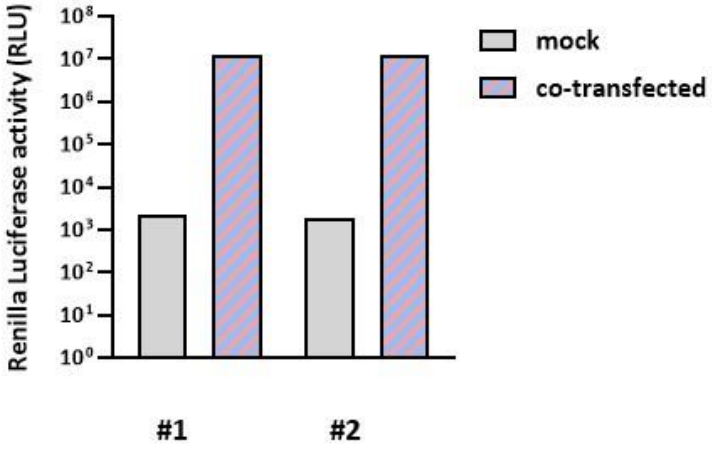

Supplemental Figure 2

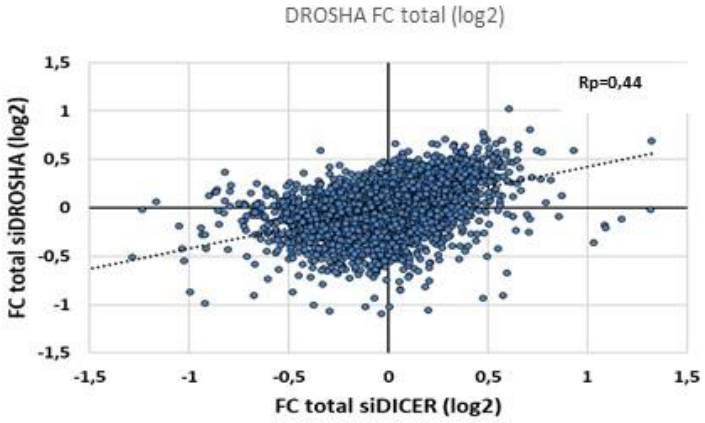

Figure Legends

Figure 1: **PB localization and post-transcriptional regulations of DDX6 and 4E-T-bound mRNAs**

(A). GC content of mRNAs and PB localization in human cells. Transcripts expressed in HEK293 (n=14490) were subdivided into six to seven classes according to their mRNA GC content (from < 40% to >60%). Boxplots show mRNA enrichment in PBs according to either mRNA, 5'UTR, CDS or 3'UTR mRNA %GC content in HEK293 transcriptome. Boxes represent the 25-75 percentile and whiskers the [min-max] interval. Median of each class is indicated by horizontal bar inside boxes. Red dashes indicate median of the 14490 transcripts ("all mRNAs") analysed. Median %GC content of the whole dataset is indicated into brackets. Rs: Spearman correlation coefficient.

(B). GC bias and PB enrichment of DDX6 and 4E-T-bound mRNAs. Boxplots show enrichment in PB transcriptome dataset and mRNA %GC content of DDX6 (n=4555, pink boxes), 4E-T (n= 967, green boxes) targets from CLIP and RIP experiments (see material and methods for datasets details). For comparison, all mRNAs (n=14490), DDX6 non-bound (n=9935) and 4E-T non-bound (n=13523) are represented in grey. Red dashes indicate median of all mRNAs. Median of each class was compared to all mRNAs and statistical significance assessed by two-tail Mann-Whitney test. n.s: non significative. **: p-value < 0.0001. *: 0.0001<p-value < 0.05.

(C). Detail of nucleotide composition of DDX6 and 4E-T-bound mRNAs. Boxplots show GC content of 5'UTR, CDS, and 3'UTR sequences of DDX6 or 4E-T-bound mRNAs. Analysis is similar to Figure 1B.

(D). Translational regulation by DDX6 and regulation in stability by DDX6, XRN1 and PAT1B of DDX6 and 4E-T-bound mRNAs. Boxplots show behaviour of DDX6 and 4E-T-bound mRNAs in the following transcriptomes datasets: siDDX6 (polysome profiling), siDDX6, siXRN1 and siPAT1B. Analysis is similar to Figure 1B.

(E). Influence of 4E-T on DDX6 RNA binding. Boxplots show behaviour of DDX6 and 4E-T-bound mRNAs in DDX6 CLIP dataset. Analysis is similar to Figure 1B.

Figure 2: Influence of nucleotide composition on LSM14A and DDX6 RNA-binding

(A). Preferential localization of AU-rich reporter mRNA in PBs. HEK293 cells were transfected with the GC-rich (left panel) or the AU-rich (middle panel) Renilla luciferase reporter construct. After 24hr, cells were analysed by smiFISH to localize GC or AU probe sets (red) and simultaneously by immunofluorescence with anti-DDX6 antibody (blue) to localize PBs White arrows indicate zoomed area. Scale bar: 5µm. Quantifications (right panel) indicate percentage of PBs containing clusters of Renilla luciferase mRNA in two independent experiments (#1, #2). Experience #1: 32 PBs were counted from 19 cells; Experience #2: 83 PBs counted from 41 cells.

(B). Comparison of DDX6 and LSM14A nucleotide preference. RNA-immunoprecipitation from HEK293 cytoplasmic lysates co-transfected or not with both AU-rich and GC rich Renilla luciferase reporter constructs was performed using antibodies against LSM14A or DDX6, or IgG as a negative control. In each immunoprecipitate, respective amounts of AU-rich and GC-rich Renilla luciferase reporters were quantified by qRT-PCR in two independent experiments. Enrichment was calculated comparatively to the amount of reporter mRNA extracted from 5% of the input used for the immunoprecipitation (see material and methods).

Figure 3: GC bias, PB enrichment and post-transcriptional regulations of miRNA targets

(A). GC content of human miRNA targets. Boxplot graphs show mRNA %GC content distribution of mRNAs targeted by the 22 most abundantly expressed miRNAs in HEK293, of AGO1-4 targets and of all and up-regulated transcripts following DICER depletion by RNA interference. For comparison we used transcripts from the PB transcriptome (“all mRNA”, n = 14490). Analysis is performed similarly to Figure 1B.

(B). Storage in PBs of human miRNA targets. Boxplot graphs show PB enrichment of miRNA targets, AGO1-4 targets, all and upregulated mRNAs from the siDICER transcriptome. Analysis is performed similarly to Figure 1B.

(C) Regulation in translation by DDX6 and in stability by DDX6, XRN1 and PAT1B of AGO 1,2,3,4 and DICER mRNA targets. Boxplot graphs show regulation in translation by DDX6, regulation in stability by PAT1B, XRN1, DDX6, and direct binding by DDX6 of AGO1-4 targets and of transcripts up-regulated following DICER silencing. Analysis is similar to Figure 1B.

(D) Analysed mRNAs targeted by the miRNA pathway. Table recapitulating number of transcripts analysed in each dataset.

Figure 4: Effect of miRNA nucleotide composition on miRNA activity

(A). Dot plot graph showing median GC content of miRNA targets according to miRNA GC content. The 3 most AU-rich miRNAs are in blue and the 3 most-GC-rich miRNAs in orange. Rp : Pearson correlation coefficient.

(B). Dot plot graph showing enrichment in PBs of miRNA targets according to miRNA GC content.

(C). Dot plot graph showing GC content of miRNA targets according to miRNA seed GC content.

(D). Correlogram representing pairwise Spearman correlations between GC content of the 22 most abundantly expressed miRNAs, GC content of miRNA seed, median GC content of mRNA, CDS or UTRs of the targets of the 22 miRNAs and 3'UTR length of the targets. Statistically significant correlations (confidence interval 0.95) are written in white.

(E). Boxplot graphs showing regulation at the translation level by DDX6, regulation in stability by PAT1B, XRN1, DDX6, DICER and direct binding by DDX6 of the 3 most AU-rich miRNAs and the 3 most-GC-rich miRNAs. Analysis is similar to Figure 1B.

Figure 5: Concurrent cytoplasmic localizations of AU-rich mRNAs

(A). Distribution of all mRNAs (n=14490), mRNAs enriched in PBs ("PB-in", n= 5380), mRNAs excluded from PBs ("PB out", n=5014) according to their GC content binned by 0.7 % GC increment. Blue pointed line is drawn at GC= 49.1%. Median %GC content are indicated in brackets below each group.

(B). Volcano plot recapitulating Gene Ontology overrepresentation-test. Complete categories of Gene Ontology cellular components were used to compare PB-excluded and AU-rich mRNAs (%GC < 49.1 % and FC PB > 1, 579 mRNAs annotated) to all AU-rich mRNAs (%GC < 49.1%, 7164 mRNAs annotated). Enriched categories are represented by dots whose size is proportional to the number of genes related to each category. Category "others" includes miscellaneous GO annotations mostly related to membranes such as membrane protein complex (GO 0098796), vesicle (GO 0031982).

Supplemental Figure 1: Dosage of luciferase activity of AU-rich and GC-rich Renilla luciferase proteins

Cells co-transfected or not (mock) with RenLuc_GC-rich and RenLuc_AU-rich plasmids were harvested 40h after transfection and an aliquot was processed for protein luciferase quantification. Luciferase protein activity was measured with the Dual Glo Luciferase assay kit (Promega) according to the manufacturer's instructions. Relative light determinations were obtained in a Lumat LB 9507 luminometer (Berthold). #1 and #2 represent two independent transfections. RLU: Relative Light Unit.

Supplemental Figure 2: Transcriptome following DICER silencing

Dot plots representing total fold change after DROSHA silencing as a function of mRNA fold change following DICER silencing. Rp: Pearson coefficient correlation.

Discussion

1) Out of the 3 PB assembly factors, only 4E-T has a preference for AU-rich mRNAs

Having noticed that CDS and 3'UTR GC content is a prime determinant of mRNA enrichment in PBs, we investigated whether RNA-binding preference of one of the 3 PB assembly factors, DDX6, LSM14A and 4E-T, could explain concentration of AU-rich mRNAs in PBs. From DDX6 eCLIP, we found that DDX6 binds GC-rich mRNAs mainly excluded from PBs. Concerning LSM14A, no large-scale transcriptomic analysis has yet been performed in human cells, thus we assessed LSM14A RNA-binding preference by RIP on two reporter mRNAs with a different CDS nucleotide composition. While GC-rich reporter was immunoprecipitated more efficiently with DDX6 than the AU-rich RenLuc mRNA, both reporters were immunoprecipitated by anti-LSM14A with the same efficiency, suggesting that LSM14A has no nucleotide preference. Finally, analysis of 4E-T RIP showed that 4E-T-bound-mRNAs are AU-rich including in their CDS and 3'UTR and enriched in PBs. This observation is compatible with a nucleotide preference of 4E-T involved in accumulation of AU-rich mRNAs in PBs. Yet, this statement calls for some nuance. Indeed, 4E-T is an "indirect RBP" since it has no RBD but interacts with the mRNA *via* eIF4E. Moreover, RIP approach does not discriminate between direct targets (*i.e* mRNAs physically bound to the RBP), and mRNAs bound indirectly *via* another protein partner. Thus, the observed effect may not directly come from 4E-T but from one of its partners, possibly a fourth PB assembly factor, that would display a nucleotide binding preference for AU-rich mRNAs. In light of this comment, our conclusion concerning LSM14A should similarly be tempered. Consequently, prospects to properly address the issue of a nucleotide binding preference of LSM14A and 4E-T include to identify their endogenous and directly bound mRNA targets in human cells, for instance by a CLIPseq approach.

Association of a RBP to RNA does not always correlate with direct regulation by this RBP. On these grounds, we looked at the post -transcriptional regulations of DDX6 and 4E-T-bound mRNAs. We noted that GC-rich mRNAs bound by DDX6 and mostly excluded from PBs are stabilized after DDX6 silencing, as well as after XRN1 silencing. This suggests that DDX6-bound mRNAs are mainly regulated in stability *via* a cytoplasmic and XRN1-dependent pathway. Existence of such a pathway would be consistent with data in yeast demonstrating that XRN1

can physically interact with 80S ribosome (Tesina et al., 2019), and also mediate co-translational 5'-3' decay (Antic et al., 2015; Hu et al., 2009). Whether this pathway is conserved in human, as well as details of DDX6 implication in this process remain an issue for further investigation.

In parallel, we observed that 4E-T-bound mRNAs are derepressed after siDDX6 and regulated in stability by PAT1B, like most PB mRNAs. Actually, mRNA localization in PBs is intimately linked with mRNA translation status. Indeed, mRNAs from different repression pathways such as ARE-containing mRNAs targeted by ARE BP like TTP and BRF (Franks and Lykke-Andersen, 2007) and also targets of the miRNA pathway (Bhattacharyya et al., 2006; Pillai et al., 2005b; Pitchiaya et al., 2019) concentrate in PBs. Moreover, human AU-rich mRNAs are less efficiently translated due to their biased codon usage (Courel et al., 2019). Thus they could be more accessible to 4E-T, which would repress their translation and stabilize them by preventing access of decapping activators to the cap. Overall, this repression would favour concentration of AU-rich mRNAs in PBs. Overall, in addition to nucleotide binding preference, the repressive function of DDX6 and 4E-T also contributes to mRNA recruitment to PBs.

Looking for another hypothesis explaining the GC bias of PB mRNAs, it was demonstrated that helicase activity of DDX6 is necessary to form PBs *in vivo* (Minshall et al., 2009). This suggests that formation of these mRNP granules relies on mRNA and/or mRNP complex remodelling. An interesting issue to address is whether remodelling mRNA intermolecular interactions, for instance with helicases like those enriched in PBs, could preferentially favour phase separation of AU-rich mRNAs.

2) 3'UTR nucleotide composition of miRNA targets is a key parameter of their localization and repression into PBs

miRNAs mediate gene silencing through the miRISC complex, composed of several RBPs, including AGO1,2,3 or 4 and TNRC6A/B or C. Within this complex, the miRNA pairs to MRE site via a 7nt sequences called the seed sequence and which is evolutionary conserved across metazoan (Lewis et al., 2005). Meanwhile, AGO interacts with TNRC6, which recruits the PAN2/PAN3 and the CCR4/NOT déadénylation complexes to the target mRNA (Duchaine and Fabian, 2019). Consequences of CCR4/NOT recruitment can entail direct degradation or a prior translational repression stage. Different mechanisms have been proposed to explain miRNA-

mediated translational repression, involving interference with translation initiation (Humphreys et al., 2005; Meijer et al., 2013; Pillai et al., 2005), inhibition of ribosome elongation (Petersen et al., 2006) and ribosome drop-off (Nottrott et al., 2006).

In order to assess whether PB localization of miRNA targets could be informative in regards to the relative importance of repression of translation versus decay in the miRNA pathway, we analysed PB localization and general post-transcriptional regulations of mRNAs targeted by the 22 miRNAs most expressed in HEK293 and of AGO1-4 targets. We noted that miRNAs and AGO1,2,3,4 targets tend to be AU-rich. and preferentially enriched in PBs. Moreover AGO1-4 targets are regulated in translation by DDX6 and in stability by PAT1B, similarly as mRNAs enriched in PB. These observations are therefore not compatible with the hypothesis of GC content or localization in/out PBs of miRNA targets defining their fate towards either decay by DDX6 and XRN1 or translational repression by DDX6 and decay by PAT1B. Hence, we investigated whether outcome of miRNA-dependent regulations would depend on the miRNA itself. We observed that targets of the 3 most AU-rich miRNAs are translationally more active after DDX6 silencing while translation of targets of the 3 most GC-rich miRNAs were not sensible to DDX6 silencing. Targets of AU-rich and targets of GC-rich miRNAs are not affected by DDX6 nor XRN1 silencing in terms of stability. Thus, our observations suggest a model where AU-rich miRNAs target AU-rich mRNAs which are preferentially enriched in PBs and translationally repressed by DDX6 (Figure 6)

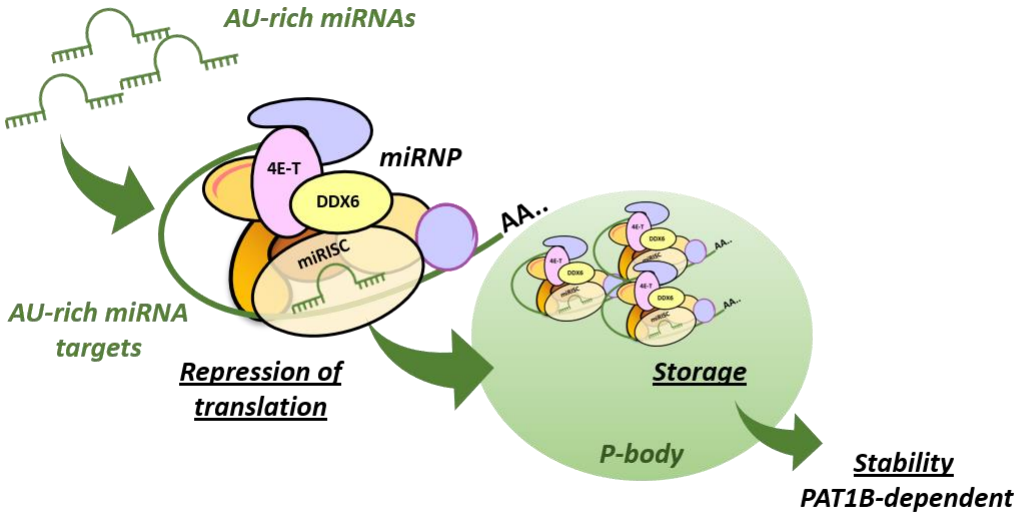

Figure 6 Model of translational repression miRNA-dependent

The biased GC content observed among miRNA targets was unexpected. Indeed since 60% of the genes can be regulated by the miRNA pathway (Friedman et al., 2009), we could have thought that GC content and PB localization of the studied population of miRNA targets would have reflected effects observed for all transcripts.

Trying to explain this GC bias, we considered the following points. First human AU-rich mRNAs correspond to AU-rich genes (Courel et al., 2019) which appeared earlier throughout Evolution than the GC-rich part of the human genome (Duret et al., 2002). Then, these AU-rich mRNAs tend to be targeted by AU-rich miRNAs (this study). Moreover, it was noted that most recent miRNA tend to be expressed at low levels, while more ancient miRNAs are expressed at higher levels (Liang and Li, 2009; Meunier et al., 2013). On these grounds, it would be interesting to assess whether GC content of the miRNAs (or at least GC content of their seed sequences which are well conserved throughout Evolution) also reflects their conservation throughout Evolution. If yes, we could speculate on a "target avoidance" model. According to this model, genes co-expressed with a miRNA evolve to avoid sites that are targeted by more recent miRNAs because they could perturb established regulatory networks (Iwama et al., 2018).

Interestingly, miRNA- binding sites are located near AU-rich sequences of 3'UTR (Lewis et al., 2005) which are more efficiently targeted by miRNAs possibly because structures in these regions have a lower stability and may be thus more accessible to miRNA (Farh et al., 2005; Grimson et al., 2007).Thus a second hypothesis concerning functional consequences of the GC bias observed in miRNA targets may imply increased efficiency of mRNA targeting.

3) PB-excluded and AU-rich mRNAs are localized transcripts

Concentration to PBs concerns most AU-rich mRNAs. Nonetheless, 20% of AU- rich transcripts (940 mRNAs) escape this general trend and are significantly excluded from PBs. Our Gene Ontology analysis of this subset of transcripts reveals that most of them correspond to mRNAs encoding proteins related to membranous organelles, such as mitochondria, ER, lysosomes, secretory granules, or ribosomes. Since translation of mRNAs coding secreted or trans membranous proteins occurs on endoplasmic reticulum membrane and that translation of several mitochondrial proteins occurs on mitochondria membrane, we hypothesize that localization of these mRNAs onto membranous organelles prevents their recruitment to PBs.

In support of this hypothesis, a protein/mRNA screen based on a BAComics approach in HeLa cells found that *Hsp90b1* which is an AU-rich mRNA (42.4 %GC) significantly excluded from PBs (logFC =-0.495, p value <0.05) and encoding a resident ER protein, actually colocalizes with its protein in a translation-dependant way (*i.e* general translation inhibition by puromycin disrupts colocalization between *Hsp90b1* mRNA and its protein) (Chouaib et al., 2020). Prospects related to this issue may include to verify the colocalization between mRNA and protein, as well as the translation dependency of a larger number of AU-rich transcripts excluded from PBs.

Materials and methods

Cell culture and transfection

Human embryonic kidney HEK293 and epithelioid carcinoma HeLa cells were cultivated in DMEM (Dulbecco's Modified Eagle's Medium)-glutamax (Invitrogen™) supplemented with 10% (v/v) fetal calf serum and 100U.mL^{-1} penicillin/streptomycin, at 37°C, 5% CO_2.

For RNA immunoprecipitation assays, HEK293 cells were co-transfected with 12 µg hRluc-GFP-GC-rich plasmid and 12 µg of Rluc-GFP-AU-rich plasmid per 150-mm-diameter dish using GenJet Plus DNA (SignaGen Laboratories) according to the manufacturer's protocol. See (Courel et al., 2019) for details on plasmids design.

RNA Immunoprecipitation

Cells were scrapped 40h after transfection. Expression of plasmids Rluc-GFP-AU-rich and hRluc-GFP-GC-rich was checked by luciferase protein assay performed on a Lumat LB 9507 luminometer (Berthold)with the Dual Glo Luciferase assay kit (Promega) according to the manufacturer's instructions. Cytoplasmic lysates were prepared in NET buffer supplemented with RNAseOut 65U/mL as described in Material and methods part 1, section immunoprecipitation. 5 mg of cytoplasmic extract were incubated with either 2µg anti-DDX6 antibody, 4.5 µg anti-LSM14A antibody or 4.5 µg IgG as control for 1h at 4°C with constant rotation. 50 µL of protein A Dynabeads were added to the samples and incubated for 2 hrs at 4°C with constant rotation. Beads were washed with RIP buffer containing 50 mM Tris-HCl (pH 7.4), 150 mM NaCl, 1mM $MgCl_2$, 1mM EGTA, 0.5% NP-40 and nucleic acids were eluted in RIP buffer supplemented with 0.1%, SDS 0.1%, 80U/mL RNAseOut and 30 µg/mL proteinase K for 30 min at 65°C.

RT-qPCR

Total RNA was extracted using standard Trizol /Choroform procedure. Purified RNAs were treated with DNAse using Turbo DNA free kit (Life Technologies). For reverse transcription, 135 ng of total RNA were pre amorced with random primers, sense oligonucleotides hRluc-GFP-GC-rich and Rluc-GFP-AU-rich and denaturated for 5min at 65°C. RT mix containing (10mM dNTP, Superscript II buffer 1X, 10 mM DTT, RNAse out 8U, Superscript II 8U) was added and the following thermal cycle was applied: 10 min at 30°C, 50 min at 42°C and 15 minutes

at 75 °C. RT product was diluted 10x and 2 µL of the dilution was analysed in duplicate by qPCR on Light Cycler apparatus with the following primers pairs

qPCR primer	SENS	SEQUENCE
RLuc-highGC	forward	CGAGAACGCCGTGATTTT
	reverse	GACGTGCCTCCACAGGTAG
RLuc-lowGC	forward	CCAGGATTCTTTTCCAATGC
	reverse	CTTGCGAAAAATGAAGACCTTT

qPCR results were analysed with LightCycler®480 software and Cp were obtained *via* the 2d derivative method.

Primers efficiency (E) was calculated from the standards. RNA immunoprecipitation efficiency was calculated as the relative quantity of reporter mRNA between IP and 5% input sample and is given by the expression : $\frac{(RNA\ total\ extracted\ in\ IP}{RNA\ total\ extracted\ in\ 5\%\ input} * E^{-(Cp\ IP - Cp\ input)}$

Bioinformatic analysis

Datasets used in the bioinformatic analysis came from the following sources

dataset	reference
DDX6 CLIP (K562)	ENCODE Project Consortium, 2012 (analysis: A. Hubstenberger)
4E-T RIP (mouse E12 cortex cells)	(Yang et al., 2014a)
AGO1,2,3 ,4 CLIP (HEK293 cells)	(Yang et al., 2015)
PAT1B transcriptome (HEK 293T cells)	(Vindry et al., 2017b)
DICER transcriptome (HEK293 cells)	(Rybak-Wolf et al., 2014)
DROSHA transcriptome (HEK293 cells)	(Rybak-Wolf et al., 2014)
XRN1 transcriptome (HeLa cells)	(Courel et al., 2019) from P.Brest lab
DDX6 transcriptome (HEK293 cells)	(Courel et al., 2019)
DDX6 polysome profiling (HEK293 cells)	(Courel et al., 2019)
P-body transcriptome	(Hubstenberger et al., 2017)
miRNA targets	miRTarBase (Hsu et al., 2014)

For each dataset we considered transcripts that were present in the HEK293 transcriptome. When replicates were available, we used mean of replicates.

For GC content, transcripts fasta sequences were downloaded from ENSEMBL and GC content of mRNA, CDS, 3'UTR, 5'UTR contents were obtained using the seqinr R package (https://cran.r-project.org/web/packages/seqinr/seqinr.)

Boxplot representations and statistical tests were performed using the GraphPad Prism software (GraphPad software, Inc) and the R packages corrr (https://github.com/tidymodels/corrr) and corrplot (htttps://github.com/taiyun/corrplot). Pearson correlation coefficient was computed for near linear relationships (e.g. miRNA and targets GC contents) and Spearman correlation for non-linear relationships. Other graphical representations were generated using Excel.

The enrichment of the GO Complete Cellular component categories in AU-rich mRNA excluded from PB (Input database: 940 gene IDs, 579 annotated in GO categories) compared to AU-rich transcripts from the HEK293 transcriptome (Input database: 7266 gene IDs, 7164 annotated in GO categories) was assessed with PANTHER overrepresentation Test (http://pantherdb.org/, Mi et al., 2013). R package ggplot (https://ggplot2.tidyverse.org) was used for graphical representation.

Annexe: article

eLIFE elifesciences.org

RESEARCH ARTICLE

GC content shapes mRNA storage and decay in human cells

Maïté Courel[1], Yves Clément[2], Clémentine Bossevain[1], Dominika Foretek[3], Olivia Vidal Cruchez[4], Zhou Yi[5], Marianne Bénard[1], Marie-Noëlle Benassy[1], Michel Kress[1], Caroline Vindry[6], Michèle Ernoult-Lange[1], Christophe Antoniewski[7], Antonin Morillon[3], Patrick Brest[4], Arnaud Hubstenberger[5], Hugues Roest Crollius[2], Nancy Standart[6], Dominique Weil[1]*

[1]Sorbonne Université, CNRS, Institut de Biologie Paris Seine (IBPS), Laboratoire de Biologie du Développement, Paris, France; [2]Ecole Normale Supérieure, Institut de Biologie de l'ENS, IBENS, Paris, France; [3]ncRNA, Epigenetic and Genome Fluidity, Institut Curie, PSL Research University, CNRS UMR 3244, Sorbonne Université, Paris, France; [4]Université Côte d'Azur, CNRS, INSERM, IRCAN, FHU-OncoAge, Nice, France; [5]Université Côte d'Azur, CNRS, INSERM, iBV, Nice, France; [6]Department of Biochemistry, University of Cambridge, Cambridge, United Kingdom; [7]Sorbonne Université, CNRS, Institut de Biologie Paris Seine (IBPS), ARTbio Bioinformatics Analysis Facility, Paris, France

Abstract mRNA translation and decay appear often intimately linked although the rules of this interplay are poorly understood. In this study, we combined our recent P-body transcriptome with transcriptomes obtained following silencing of broadly acting mRNA decay and repression factors, and with available CLIP and related data. This revealed the central role of GC content in mRNA fate, in terms of P-body localization, mRNA translation and mRNA stability: P-bodies contain mostly AU-rich mRNAs, which have a particular codon usage associated with a low protein yield; AU-rich and GC-rich transcripts tend to follow distinct decay pathways; and the targets of sequence-specific RBPs and miRNAs are also biased in terms of GC content. Altogether, these results suggest an integrated view of post-transcriptional control in human cells where most translation regulation is dedicated to inefficiently translated AU-rich mRNAs, whereas control at the level of 5' decay applies to optimally translated GC-rich mRNAs.

***For correspondence:** dominique.weil@upmc.fr

Competing interests: The authors declare that no competing interests exist.

Funding: See page 26

Received: 26 June 2019
Accepted: 18 December 2019
Published: 19 December 2019

Reviewing editor: Karsten Weis, ETH Zurich, Switzerland

Introduction

Translation, storage, localization and decay of mRNAs in the cytoplasm are closely coupled processes, which are governed by a large number of RNA-binding proteins (RBPs) (***Hentze et al., 2018***). These RBPs have to act in a coordinated manner to give rise to a proteome both coherent with cellular physiology and responsive to new cellular needs. mRNA fate is also intimately linked with their localization in membrane-less organelles, such as P-bodies (PBs). We recently identified the transcriptome and proteome of PBs purified from human cells. Their analysis showed that human PBs are broadly involved in mRNA storage rather than decay (***Hubstenberger et al., 2017***; ***Standart and Weil, 2018***), as also observed using fluorescent decay reporters (***Horvathova et al., 2017***). However, the mechanism underlying the large but specific targeting of mRNAs to PBs is still unknown, though it clearly results in the co-recruitment of particular RBPs (***Hubstenberger et al., 2017***).

In mammalian cells, the RNA helicase DDX6, known for its involvement in mRNA decay and translation repression, is a key factor in PB assembly (**Minshall et al., 2009**). Patients with neurodevelopmental delay caused by heterozygous DDX6 missense mutations were recently identified, and their skin fibroblasts show a PB defect (**Balak et al., 2019**). Human DDX6 interacts with both translational repressors, and the decapping enzyme DCP1/2 and its activators (**Ayache et al., 2015**; **Bish et al., 2015**). Its yeast homologue Dhh1 is a cofactor of DCP2, as well as a translational repressor (**Coller and Parker, 2005**). The RBP PAT1B has also been defined as an enhancer of decapping, as it interacts with DDX6, the LSM1-7 heptamer ring and the decapping complex in mammalian cells (**Vindry et al., 2017**), while in yeast Pat1p activates Dcp2 directly (**Nissan et al., 2010**) and its deletion results in deadenylated but capped intact mRNA (**Bonnerot et al., 2000**; **Bouveret et al., 2000**). DDX6 and PAT1B interact with the CCR4-NOT deadenylase complex and the DDX6-CNOT1 interaction is required for miRNA silencing (**Vindry et al., 2017**; **Chen et al., 2014**; **Mathys et al., 2014**; **Ozgur et al., 2015**). DDX6 also binds the RBP 4E-T, another key factor in PB assembly, which in turn interacts with the cap-binding factor eIF4E and inhibits translation initiation, including that of miRNA target mRNAs (**Kamenska et al., 2016**). Altogether, DDX6 and PAT1B have been proposed to link deadenylation/translational repression with decapping. Finally, the 5′−3′ exonuclease XRN1 decays RNAs following decapping by DCP1/2, a step triggered by deadenylation mediated by PAN2/3 and CCR4-NOT or by exosome activity (**Łabno et al., 2016**).

A number of RBPs also control mRNA fate in a sequence-specific manner, some of them localizing in PBs as well. For instance, the CPEB complex, best described in *Xenopus* oocytes (**Minshall et al., 2007**), binds the CPE motif in the 3′ untranslated region (UTR) of maternal transcripts through CPEB1, thus controlling their storage and their translational activation upon hormone stimulation (**Standart and Minshall, 2008**). Additional examples include the proteins which bind 3′UTR AU-rich elements (ARE), such as HuR and TTP, to control translation and decay, and play key roles in inflammation, apoptosis and cancer (**Wells et al., 2017**). Protein-binding motifs are generally not unique and rather defined as consensus sequence elements. In the case of RISC, binding specificity is given by a guide miRNA, which also hybridizes with some flexibility with complementary mRNA sequences. A variety of techniques have therefore been developed to identify the effective RNA targets of such factors, ranging from affinity purification (such as RIP or CLIP) to transcriptome and polysome profiling after RBP silencing, providing the groundwork to address systematic questions about post-transcriptional regulation.

In this study, we searched for broad determinants of mRNA storage and decay in unstressed human cell lines, using our transcriptome of purified PBs and several transcriptomic analyses performed after silencing of general translation and decay regulatory factors, including DDX6, PAT1B and XRN1. We also used datasets available from the literature, including a transcriptomic analysis after DDX6 silencing, a DDX6-CLIP experiment and various lists of RBP and miRNA targets. Their combined analysis revealed the central role of mRNA GC content which, by impacting codon usage, PB targeting and RBP binding, influences mRNA fate and contributes to the coordination between two opposite processes: decay and storage. Reporter mRNAs varying in their GC content confirmed that AU-rich mRNAs have a lower protein yield than GC-rich ones, that they preferentially localize to PBs, and that they have an enhanced capacity to form RNP granules in vitro.

Results

PBs mostly accumulate AU-rich mRNAs

We have previously shown that PBs store one third of the coding transcriptome in human epithelial HEK293 cells (**Hubstenberger et al., 2017**). Such a large transcript number led us to search for general distinctive sequence features that could be involved in PB targeting. We first analyzed transcript length, as it was reported to be key for mRNA accumulation in stress granules (**Khong et al., 2017**). When mRNAs were subdivided into six classes ranging from <1.5 kb to >10 kb, longer mRNAs appeared more enriched in PBs than shorter ones, with a moderate correlation between length and PB enrichment (Spearman r (r_s) = 0.39, p<0.0001) (**Figure 1A**, **Figure 1—figure supplement 1A,B**). However, their increased length in PBs was less striking than previously observed for stress granule mRNAs (**Khong et al., 2017**) (**Figure 1—figure supplement 1C**).

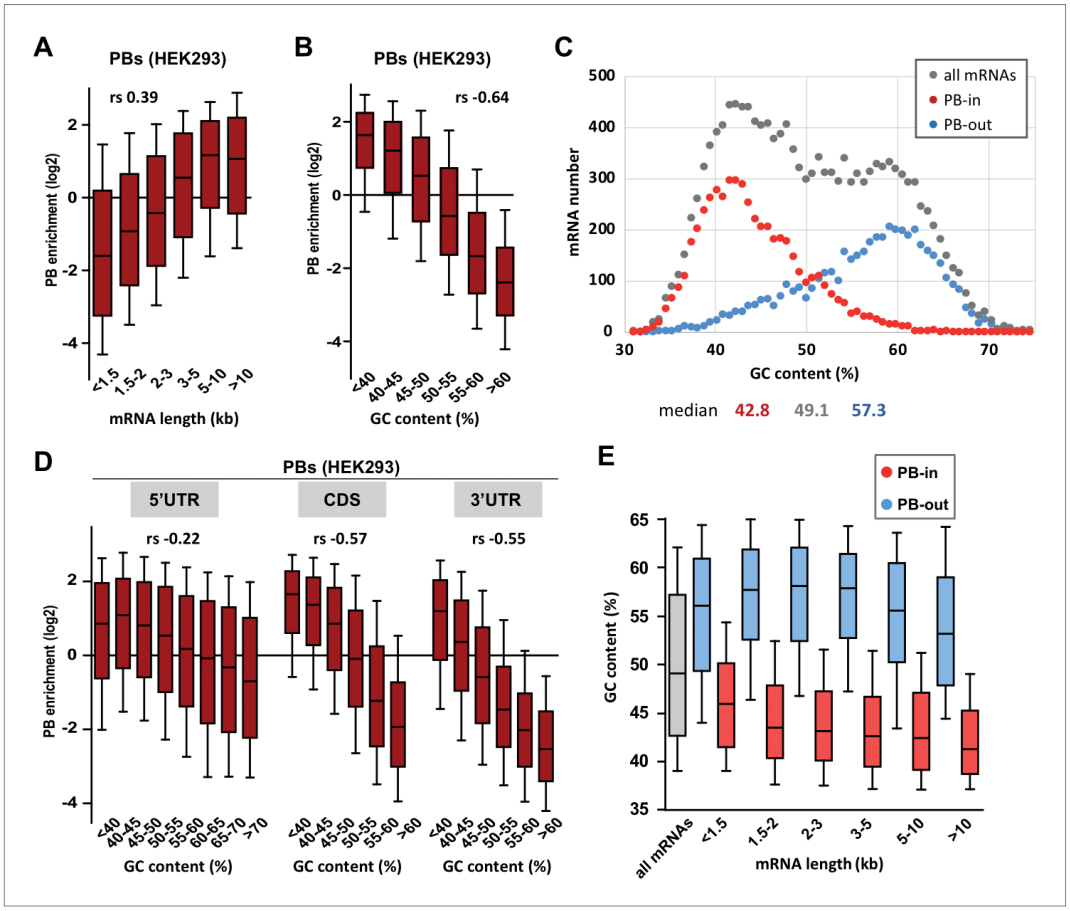

Figure 1. PB mRNAs are AU-rich and longer than average. (**A**) Long mRNAs are particularly enriched in PBs. Transcripts were subdivided into six classes depending on their length (from <1.5 kb to >10 kb). The boxplots represent the distribution of their respective enrichment in PBs. The boxes represent the 25–75 percentiles and the whiskers the 10–90 percentiles. rs, Spearman correlation coefficient. (**B**) AU-rich mRNAs are particularly enriched in PBs. Transcripts were subdivided into six classes depending on their GC content (from <40 to >60%) and analyzed as in (**A**). (**C**) PBs mostly contain the AU-rich fraction of the transcriptome. The human transcriptome was binned depending on its GC content (0.7% GC increments). The graph represents the number of PB-enriched (PB-in, $p<0.05$, n = 5200) and PB-excluded (PB-out, $p<0.05$, n = 4669) transcripts in each bin. The distribution of all transcripts is shown for comparison (n = 14443). The median GC value is indicated below for each group. (**D**) mRNA localization in PBs mostly depends on the GC content of their CDS and 3'UTR. The analysis was repeated as in (**B**) using the GC content of the 5'UTR, CDS or 3'UTR, as indicated. For 5'UTRs, the >60% class was subdivided into three classes to take into account their higher GC content compared to CDSs and 3'UTRs. −0.57 and −0.55 are not significantly different ($p=0.17$), while −0.22 and −0.55 are ($p<0.0001$) (**E**) GC content is lower in PB-enriched mRNAs than PB-excluded ones independently of their length. The GC content distribution of PB-enriched (PB-in, $p<0.05$) and PB-excluded (PB-out, $p<0.05$) mRNAs was analyzed as in (**B**).

The online version of this article includes the following figure supplement(s) for figure 1:

Figure supplement 1. PB-enriched mRNAs tend to be long and AU-rich.

Most remarkably, mRNA accumulation in PBs was dependent on their global nucleotide composition, with a strong correlation between GC content and PB localization (r_s = −0.64, p<0.0001). When transcripts were subdivided into six classes ranging from <40% to >60% GC, PB enrichment was predominant for those <45% GC (***Figure 1B***, ***Figure 1—figure supplement 1D,E***). While reminiscent of the low GC content reported for stress granule mRNAs in HEK293 cells (***Khong et al., 2017***), our reanalysis of the published dataset indicated that stress granule localization correlated weakly with the gene GC content (r_s = −0.12, p<0.0001) and almost not at all with the mRNA GC content (r_s = −0.06, p<0.0001). Indeed, comparing the GC content distribution of the transcripts that are enriched or excluded from PBs with all HEK293 cell transcripts, revealed that mRNA storage in PBs is confined to the AU-rich fraction of the transcriptome (***Figure 1C***).

As these transcripts also correspond to AU-rich genes (***Figure 1—figure supplement 1F***), it raised the possibility that the impact of GC content on PB enrichment resulted indirectly from the genomic context of the genes. To address this issue, we looked at the link between PB enrichment and meiotic recombination, which can influence GC content through GC-biased gene conversion (***Duret and Galtier, 2009***). The correlation between PB enrichment and meiotic recombination was much weaker than between PB enrichment and mRNA GC content (r_s = −0.16 vs −0.64, p<0.0001 for both, significantly different from each other, p<0.0001). Moreover, the latter was almost unchanged when controlling for meiotic recombination (r_s = −0.65 vs −0.64, p<0.0001). Finally, it was still significant when controlling for intronic or flanking GC content (r_s = −0.33 and −0.45 respectively, all p<0.0001), showing that mRNA base composition and PB enrichment are associated independently of meiotic recombination or the genomic context. We also computed partial correlations to verify that the correlation between PB enrichment and GC content was not secondary to the correlation that exists between GC content and expression level, or between GC content and gene conservation (***Figure 1—figure supplement 1G***).

To refine the link between mRNA accumulation in PBs and their GC content, we analyzed separately the influence of their CDS and UTRs. Interestingly, mRNA accumulation in PBs correlated strongly with the GC content of both their CDS and 3'UTR (r_s = −0.57 and −0.55, respectively, p<0.0001 for both), and weakly with the one of their 5'UTR (r_s = −0.22, p<0.0001) (***Figure 1D***, ***Figure 1—figure supplement 1E***). Moreover, the lower GC content of PB-enriched mRNAs compared to PB-excluded ones was a feature independent of their length, since it was observed in all length ranges (***Figure 1E***, ***Figure 1—figure supplement 1B***). Conversely, the longer length of PB mRNAs was a feature independent of their GC content (***Figure 1—figure supplement 1E,H***).

In conclusion, while PB mRNAs tend to be longer than average, their most striking feature is that they correspond to an AU-rich subset of the transcriptome.

GC bias in PBs impacts codon usage and protein yield

The strong GC bias in the CDS of PB mRNAs prompted us to compare the coding properties of PB-stored and PB-excluded mRNAs. Consistently, we found that the frequency of amino acids encoded by GC-rich codons (Ala, Gly, Pro) was lower in PB-stored than in PB-excluded mRNAs, while the frequency of those encoded by AU-rich codons (Lys, Asn) was higher (***Figure 2A***). The difference could be striking, as illustrated by Lys, whose median frequency in PB-excluded mRNAs was 32% lower than in PB-enriched mRNAs, thus ranging within the lower 17th centile of their distribution (***Figure 2—figure supplement 1A***). In addition to different amino acid usage, we observed dramatic variation in codon usage between the two mRNA subsets. For all amino acids encoded by synonymous codons, the relative codon usage in PBs versus out of PBs was systematically biased towards AU-rich codons (log2 of the ratio >0, ***Figure 2B***). For example, among the six Leu codons, AAU was used 4-fold more frequently in PB-enriched than in PB-excluded mRNAs, whereas CUG was used 2-fold less frequently. This systematic trend also applied to Stop codons. Some additional codon bias independent of base composition (NNA/U or NNG/C) was also observed for 4 and 6-fold degenerated codons (***Figure 2—figure supplement 1B,C***). For instance, Leu was encoded twice more often by CUU than CUA in PB-enriched mRNAs, whereas the use of both codons was low in PB-excluded mRNAs. Similarly, Gly was encoded more often by GGG than GGC in PB mRNAs, whereas the use of both codons was similar in PB-excluded mRNAs (***Figure 2C***).

In human, 22 out of the 29 synonymous codons that are less frequently used (normalized relative usage <1) end with an A or U, and were therefore overrepresented in PB mRNAs (***Figure 2—figure supplement 1D***). Considering for each amino acid the codon with the lowest usage (called low

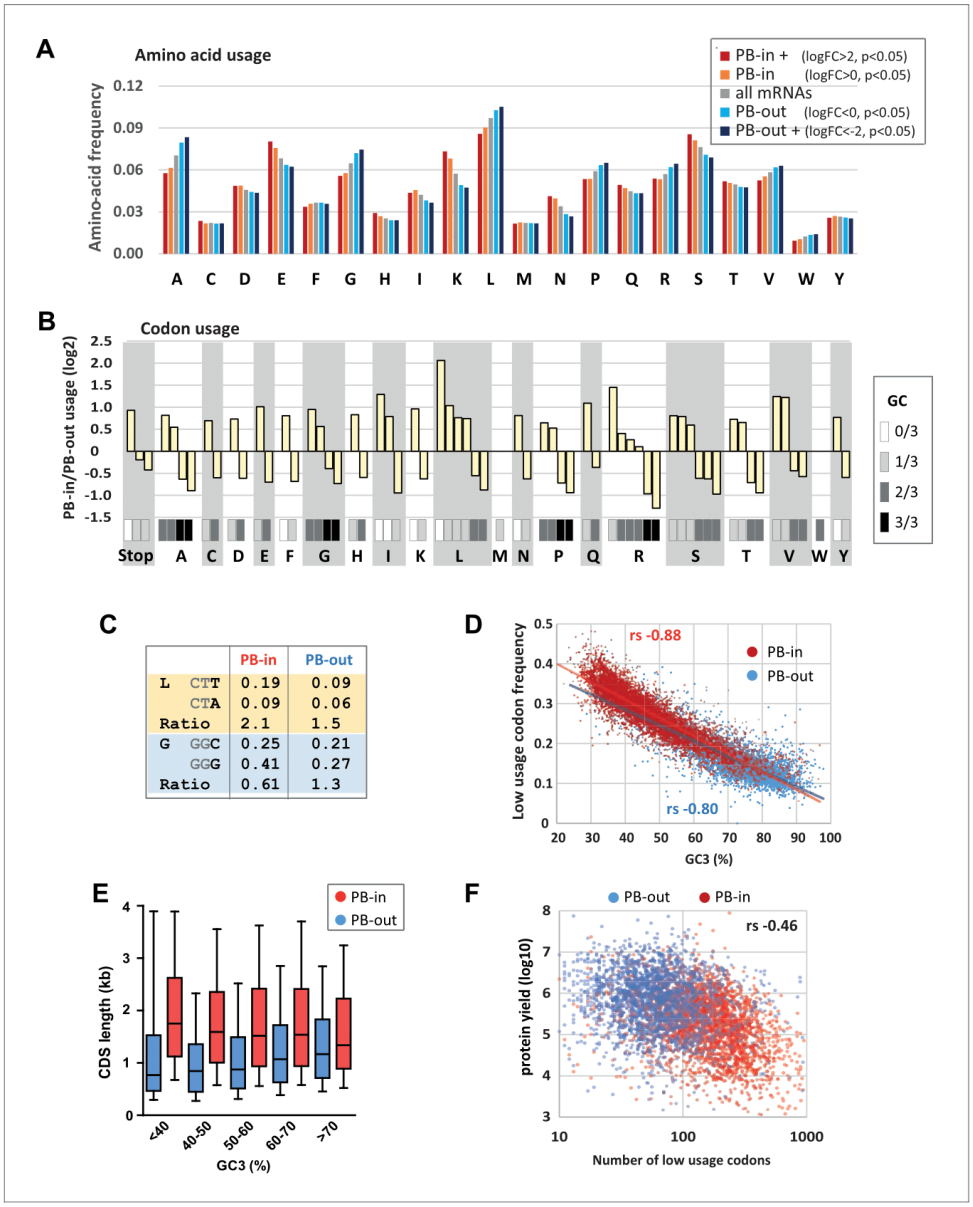

Figure 2. Codon usage is strongly biased in PBs. (**A**) PB mRNAs and PB-excluded mRNAs encode proteins with different amino acid usage. The graph represents the frequency of each amino acid in the proteins encoded by mRNAs enriched or excluded from PBs, using the indicated PB enrichment thresholds. (**B**) Codon usage bias in and out of PBs follows their GC content. The relative codon usage for each amino acid was calculated in PB-enriched (PB-in) and PB-excluded (PB-out) mRNAs, using a PB enrichment threshold of +/- 1 (in log2). The graph represents the log2 of their ratio (PB-

Figure 2 continued on next page

Figure 2 continued

in/PB-out) and was ranked by decreasing values for each amino acid. The GC content of each codon is gray-coded below, using the scale indicated on the right. (**C**) The usage of some codons is biased independently of their GC content. Two examples are shown encoding Leucine (L) and Glycine (G). (**D**) The frequency of low usage codons strongly correlates with the GC content of the CDS, independently of their PB localization. The frequency of low usage codons was calculated for mRNAs excluded (PB-out) and enriched (PB-in) in PBs using a PB enrichment threshold of +/- 1 (in log2). It was expressed as a function of the CDS GC content at position 3 (GC3). Note that the slopes of the tendency curves are similar for PB-enriched and PB-excluded transcripts. The difference between the Spearman correlation coefficients (rs) are nevertheless statistically significant (p<0.0001). (**E**) PB mRNAs have longer CDS than PB-excluded mRNAs. The analysis was performed as in ***Figure 1E***. (**F**) The number of low usage codons per CDS is a good determinant of both protein yield and PB localization. The protein yield was expressed as a function of the number of low usage codons for PB-enriched (PB-in) and PB-excluded (PB-out) mRNAs. rs, Spearman correlation coefficient.
The online version of this article includes the following figure supplement(s) for figure 2:

Figure supplement 1. Amino acid usage and codon usage biases in PBs.
Figure supplement 2. Codon usage biases and abundance of amino-acylated tRNA.

usage codon thereafter), 14 out of 18 are NNA or NNU, with the exception of Thr, Ser, Pro, Ala. We calculated the frequency of low usage codons for each CDS, and plotted it as a function of the GC content at the third position (GC3) to avoid any confounding effects of the amino acid bias. As expected, the frequency of low usage codons correlated strongly and negatively with GC3, with AU-rich CDS having a higher frequency of low usage codons than GC-rich CDS (***Figure 2D***). According to their distinct GC content, PB mRNAs had a higher frequency of low usage codons than PB-excluded mRNAs. However, the correlation coefficient between frequency of low usage codons and GC3 was very close for both mRNA subsets (r_s = −0.88 for PB-enriched; −0.80 for PB-excluded mRNAs, p<0.0001 for both), meaning that their different frequency of low usage codons could be largely explained by their GC bias alone.

We previously reported that protein yield, defined as the ratio between protein and mRNA abundance in HEK293 cells, was 20-times lower for PB-enriched than PB-excluded mRNAs. This was not due to translational repression within PBs, as the proportion of a given mRNA in PBs hardly exceeded 15%, but rather to some intrinsic mRNA property (***Hubstenberger et al., 2017***). In this respect, the frequency of low usage codons correlated more with PB localization (r_s = 0.59, p<0.0001) than with protein yield (r_s = −0.21, p<0.0001, significantly different from 0.59, p<0.0001) (***Figure 2—figure supplement 1E***). Conversely, the CDS length correlated more with protein yield (r_s = −0.43, p<0.0001) than with PB localization (r_s = 0.26, p<0.0001, significantly different from −0.43, p<0.0001). Nevertheless, the length of the CDS and its GC content contributed independently to PB localization (***Figure 2E***). Finally, combining the frequency of low usage codons with the CDS length, that is, considering the absolute number of low usage codons per CDS, was a shared parameter of both protein yield (r_s = −0.46, p<0.0001, ***Figure 2F***) and PB localization (r_s = 0.49, p<0.0001). Strikingly, CDS with more than 100 low usage codons were particularly enriched in PBs, while those under 100 were mostly excluded (***Figure 2F***). One of the mechanisms linking codon usage to translation yield could be the abundance of cognate tRNAs (***Novoa and Ribas de Pouplana, 2012***). However, codon usage in PB-excluded mRNAs was not more adapted to the abundance of amino-acylated tRNAs (***Evans et al., 2017***) than codon usage in PB-enriched mRNAs (***Figure 2—figure supplement 2***). In conclusion, the strong GC bias in PB mRNAs results in both a biased amino acid usage in encoded proteins and a biased codon usage. Furthermore, the high number of low usage codons in PB mRNAs is a likely determinant of their low protein yield.

The PB assembly factor DDX6 has opposite effects on mRNA stability and translation rate depending on their GC content

In human, the DDX6 RNA helicase is key for PB assembly (***Minshall et al., 2009***). It associates with a variety of proteins involved in mRNA translation repression and decapping (***Ayache et al., 2015***; ***Bish et al., 2015***), suggesting that it plays a role in both processes. To investigate how DDX6 activity is affected by mRNA GC content, we conducted a polysome profiling experiment in HEK293 cells transfected with DDX6 or control β-globin siRNAs for 48 hr. In these conditions, DDX6 expression decreased by 90% compared to control cells (***Figure 3—figure supplement 1A***). The polysome profile was largely unaffected by DDX6 silencing, implying that DDX6 depletion did not grossly disturb global translation (***Figure 3—figure supplement 1B***). Polysomal RNA isolated from the sucrose

gradient fractions (***Figure 3—figure supplement 1B***) and total RNA were used to generate libraries using random hexamers to allow for poly(A) tail-independent amplification. As expected, both total and polysomal DDX6 mRNA was markedly decreased (by 72%) following DDX6 silencing (***Figure 3—figure supplement 1C–E***; ***Supplementary file 1***, sheet1). Since DDX6 is cytoplasmic (***Ernoult-Lange et al., 2009***) and has a role in mRNA decay, we assumed that changes in total mRNA accumulation generally reflected an increased stability of the transcripts, though we cannot exclude altered transcription levels for some of them. As polysomal accumulation can result from both regulated translation and a change in total RNA without altered translation, we then used the polysomal to total mRNA ratio as a proxy measurement of translation rate. Nevertheless, for few transcripts, polysomal enrichment may reflect an elongation block rather than an increased rate of initiation. Analysis of the whole transcriptome showed a link between mRNA fate following DDX6 depletion and their GC content, but, intriguingly, the correlation was positive for changes in total RNA (r_s = 0.45, p<0.0001; ***Figure 3—figure supplement 1F***) and negative for changes in polysomal RNA (r_s = −0.32, p<0.0001; ***Figure 3—figure supplement 1G***). Therefore, DDX6 depletion affected different mRNA subsets in total and polysomal RNA.

The extent of mRNA stabilization steadily increased with the GC content and became predominant for transcripts with >50% GC (***Figure 3A***, left panel, ***Figure 3—figure supplement 2A***). This analysis was repeated on an independent dataset available from the ENCODE project (***ENCODE Project Consortium, 2012***), obtained in a human erythroid cell line, K562, following induction of a stably transfected DDX6 shRNA, and using an oligo(dT)-primed library. Despite the differences in cell type, depletion procedure and sequencing methods, again, mRNA stabilization preferentially concerned those with high GC content (r_s = 0.59, p<0.0001; ***Figure 3A***, right panel, ***Figure 3—figure supplement 2A***; ***Supplementary file 1***, sheet2). In contrast, following DDX6 silencing in HEK293 cells, the translation rate predominantly increased for transcripts with less than 45% GC (r_s = −0.53, p<0.0001; ***Figure 3B***, ***Figure 3—figure supplement 2A***). As a result, mRNAs with the most upregulated translation rate were the least stabilized, and conversely (***Figure 3—figure supplement 2B***).

To investigate how DDX6 activity was related to its binding to RNA, we used the CLIP dataset of K562 cells, also available from the ENCODE project. In both HEK293 and K562 cells, the mRNAs clipped to DDX6 were particularly stabilized after DDX6 knockdown, as compared to all mRNAs

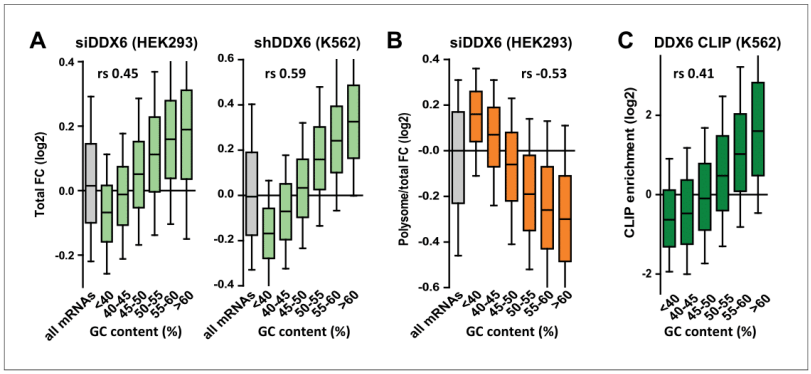

Figure 3. DDX6 silencing has opposite effects on mRNA fate depending on their GC content. (**A**) mRNA stabilization after DDX6 silencing in HEK293 and K562 cells applies to GC-rich mRNAs. The fold-changes (FC) in mRNA accumulation were analyzed as in ***Figure 1B***. (**B**) mRNA translation derepression after DDX6 silencing in HEK293 cells applies to AU-rich mRNAs. The fold-changes in translation rate (polysomal/total mRNA ratio) were analyzed as in (**A**). (**C**) GC-rich mRNAs are particularly enriched in the DDX6 CLIP experiment.
The online version of this article includes the following figure supplement(s) for figure 3:

Figure supplement 1. Polysome profiling following DDX6 silencing.
Figure supplement 2. Impact of DDX6 binding and mRNA length on DDX6 dependency.
Figure supplement 3. Impact of the GC content on DDX6-dependency.

(*Figure 3—figure supplement 2C*; *Supplementary file 1*, sheet3), while they were not translationally derepressed in HEK293 cells (*Figure 3—figure supplement 2D*). In agreement, mRNAs with a high GC content were preferentially enriched in the DDX6 CLIP experiment (r_s = 0.41, p<0.0001; *Figure 3C*, *Figure 3—figure supplement 2A*). Then, as we previously showed that DDX6 can oligomerize along repressed transcripts (*Ernoult-Lange et al., 2012*), we also considered mRNA length. While DDX6-dependent decay had a marginal preference for short transcripts (r_s = −0.09, p<0.0001), as a combined effect of CDS and 3'UTR length (*Figure 3—figure supplement 2E,F*), DDX6-dependent translation repression was independent of the CDS length but higher on mRNAs with long 3'UTRs (r_s = 0.16, p<0.0001; *Figure 3—figure supplement 2E,G*). Interestingly, the GC content of the CDS and the 3'UTR were similarly predictive of DDX6 sensitivity, whether for mRNA stability (r_s = 0.42 and 0.40 for CDS and 3'UTR, respectively, p<0.0001 for both) or for translation repression (r_s = −0.53 and −0.52, respectively, p<0.0001 for both), while the 5'UTR was less significant (r_s = 0.18 and −0.15 for stability and translation repression, respectively, p<0.0001 for both; *Figure 3—figure supplement 3A–C*).

Altogether, we showed that DDX6 knockdown affected differentially the mRNAs depending on the GC content of both their CDS and 3'UTR, with the most GC-rich mRNAs being preferentially regulated at the level of stability and the most AU-rich mRNAs at the level of translation.

DDX6/XRN1 and PAT1B decrease the stability of separate sub-classes of mRNAs with distinct GC content

DDX6 acts as an enhancer of decapping to stimulate mRNA decay, upstream of RNA degradation by the XRN1 5'−3' exonuclease. To investigate whether XRN1 targets are similarly GC-rich, we performed XRN1 silencing experiments in two cell lines. HeLa cells were transfected with XRN1 siRNA (*Figure 4—figure supplement 1A*; *Supplementary file 1*, sheet4), while HCT116 cells stably transfected with an inducible XRN1 shRNA were induced with doxycyclin (*Figure 4—figure supplement 1B*; *Supplementary file 1*, sheet5), both for 48 hr. In both cell lines, XRN1-dependent decay preferentially acted on mRNAs which were GC-rich (r_s = 0.41 for HeLa and 0.49 for HCT116, p<0.0001 for both; *Figure 4A*, *Figure 4—figure supplement 1A*) and localized out of PBs (r_s = −0.35, p<0.0001; *Figure 4—figure supplement 1C*), as observed for DDX6.

PAT1B is a well-characterized direct DDX6 partner known for its involvement in mRNA decay (*Vindry et al., 2017*; *Braun et al., 2010*; *Ozgur et al., 2010*; *Vindry et al., 2019*). As for DDX6, we assume that changes in steady-state mRNAs following PAT1B silencing generally reflect their increased stability (though, again, we cannot exclude some changes at the transcription level). However, using our previous PAT1B silencing experiment in HEK293 cells (*Vindry et al., 2017*), we surprisingly found a negative correlation between mRNA stabilization after PAT1B and after DDX6 silencing (r_s = −0.31, p<0.0001; *Figure 4—figure supplement 1D*; *Supplementary file 1*, sheet6), suggesting that they largely target separate sets of mRNAs. Unexpectedly, the correlation was however positive with translational derepression after DDX6 silencing (r_s = 0.45, p<0.0001; *Figure 4—figure supplement 1E*), indicating that PAT1B preferentially targets mRNAs that are translationally repressed by DDX6. Accordingly, these transcripts are prone to PB storage (r_s = 0.49, p<0.0001; *Figure 4—figure supplement 1F*), as reported previously (*Vindry et al., 2017*). Indeed, in contrast to DDX6 and XRN1 decay targets, PAT1B targets tended to be AU-rich (r_s = −0.50, p<0.0001; *Figure 4B*, *Figure 4—figure supplement 1A*). To gain insight into the mechanism of regulation by PAT1B, we analyzed the read coverage in the PAT1B silencing experiment (*Figure 4C*) and found it to be unchanged over the whole transcriptome. In contrast, following XRN1 silencing, the 5' coverage was higher, confirming that such an analysis can reveal 5' decay (*Figure 4D*). Of note, in control cells PAT1B target mRNAs had a higher 5' coverage than average (*Figure 4C*), while XRN1 targets had a lower 5' coverage than average (*Figure 4D*). These results suggest that mRNA accumulation in the absence of PAT1B does not result from their 5' end protection.

In conclusion, DDX6 and PAT1B decrease the stability of distinct mRNA subsets, which strongly differ in their GC content. The results suggest that DDX6 is a cofactor of XRN1 5'−3' exonuclease, whereas PAT1B affects 3' to 5' degradation.

To obtain a global visualization of the results we conducted a clustering analysis of the various datasets (*Figure 4E*). Note that to avoid clustering interdependent datasets, we included the changes in polysomal RNA after DDX6 silencing rather than in the polysomal/total RNA ratio. Altogether, the heatmap shows that GC-rich mRNAs are excluded from PBs and tend to be decayed by

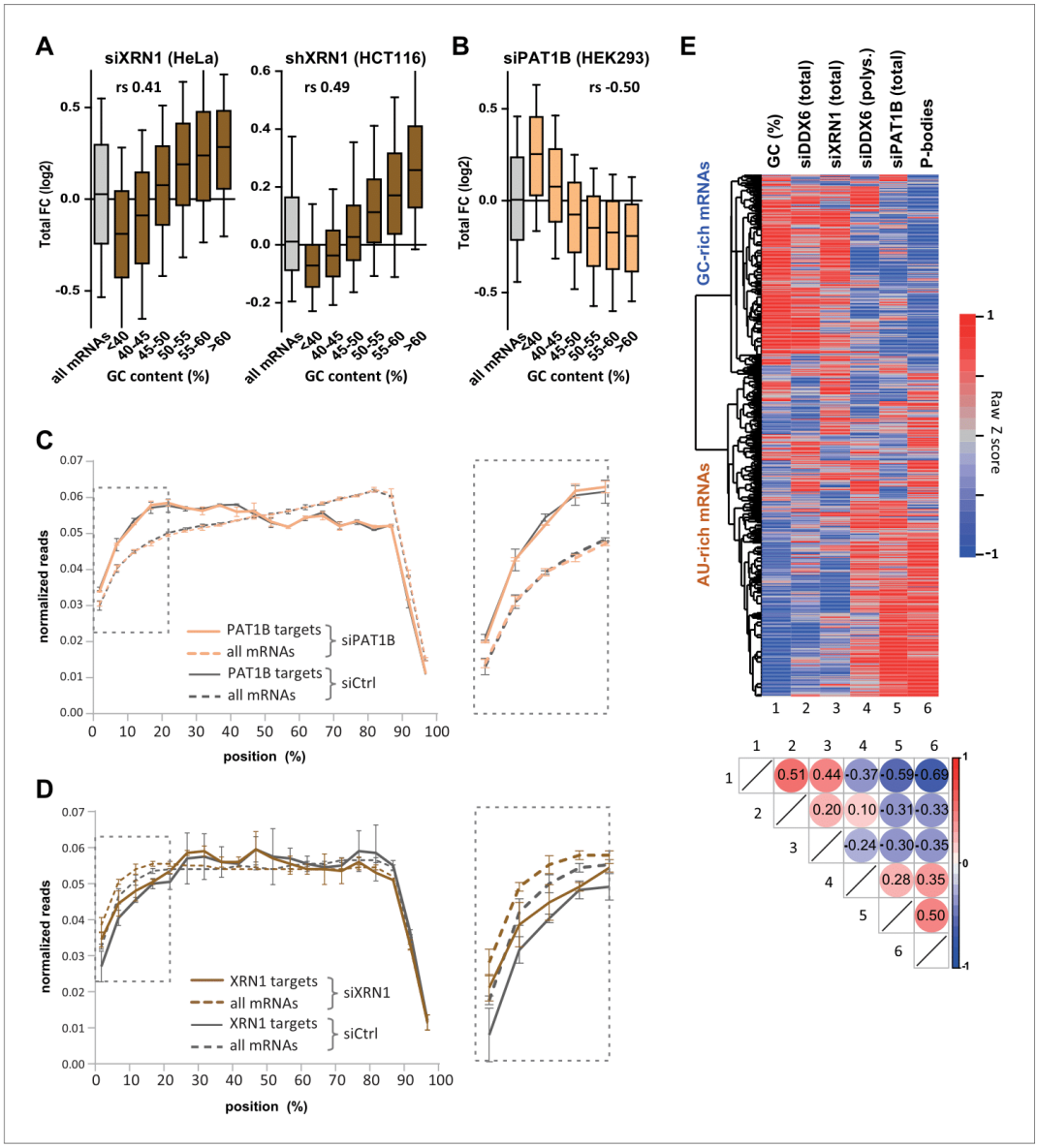

Figure 4. XRN1 and PAT1B targets have distinct GC content. (**A**) mRNA stabilization after XRN1 silencing in HeLa and HCT116 cells applies to GC-rich mRNAs. The analysis was performed as in ***Figure 1B***. The GC content distribution for all mRNAs is presented for comparison (in gray). (**B**) mRNA stabilization after PAT1B silencing in HEK293 cells applies to AU-rich mRNAs. The analysis was performed as in (**A**). (**C**) Read coverage of PAT1B targets (FC >0.7, n = 330, solid lines) and all mRNAs (n = 16000, dashed lines) in the siPAT1B dataset. The read coverage was analyzed in each duplicate experiment and normalized as described in Materials and methods. The average value in control cells (gray lines) and after PAT1B silencing (peach

Figure 4 continued on next page

Figure 4 continued

lines) was plotted, with the bars representing the duplicate values. An expanded view of the dashed box is presented on the right panel. (**D**) Read coverage of XRN1 targets (FC >0.8, n = 199, solid lines) and all mRNAs (n = 13760, dashed lines) in the siXRN1 dataset. The data were analyzed as in (**C**). (**E**) Clustering analysis of mRNAs depending on their GC content, their differential expression after silencing DDX6, XRN1 or PAT1B, and their enrichment in PBs. Raw GC content and log2 transformed ratio of the other datasets were used for the clustering of both transcripts (lines) and datasets (columns). The values were color-coded as indicated on the right scale, and the Spearman correlation matrix is presented below (all $p<10^{-48}$). The heatmap highlights the distinct fate of GC-rich and AU-rich mRNAs.

The online version of this article includes the following figure supplement(s) for figure 4:

Figure supplement 1. Transcriptome analysis following XRN1 and PAT1B silencing.

a mechanism involving DDX6 and XRN1, while AU-rich mRNAs are recruited in PBs, they undergo DDX6-dependent translation repression and their stability depends on PAT1B.

Specific mRNA decay factors and translation regulators target mRNAs with distinct GC content

Having shown that GC content is a distinctive feature of DDX6 and XRN1 versus PAT1B targets, we investigated the link between this global sequence determinant and a variety of sequence-specific post-transcriptional regulators for which relevant genome-wide datasets are available (***Figure 5—figure supplement 1A***).

On the mRNA decay side (group I lists), we considered the Nonsense Mediated Decay (NMD) pathway, taking as targets the mRNAs cleaved by SMG6 (***Schmidt et al., 2015***), and the m^6A-associated decay pathways, using the targets of the YTHDF2 reader defined by CLIP (***Wang et al., 2014***; ***Yang et al., 2015***). We also analyzed mRNAs with a 5'UTR-located G4 motif, which have been shown to be preferential substrates of murine XRN1 in vitro (***Bashkirov et al., 1997***). On the translation regulation side (group II lists), we analyzed the TOP mRNAs, whose translation is controlled by a TOP motif at the 5' extremity (***Thoreen et al., 2012***), and targets of various PB proteins and/or DDX6 partners (***Hubstenberger et al., 2017***; ***Ayache et al., 2015***): FXR1-2, FMR1, PUM1-2, IGF2BP1-3, the helicase MOV10, ATXN2, 4E-T, ARE-containing mRNAs and the targets of the two ARE-binding proteins HuR and TTP. We also included mRNAs with a CPE motif, since DDX6 is a component of the CPEB complex that binds CPEs (***Minshall et al., 2007***). Of note, among the group II factors, some are known to also affect mRNA half-life, as exemplified by the ARE-binding proteins (***Wells et al., 2017***). G4, ARE and CPE motifs have been defined in silico, while the targets of the various factors originate from RIP and CLIP approaches in human cells or mouse studies in the case of TOP mRNAs (see Materials and methods).

Intriguingly, compared to all mRNAs, group I list mRNAs were GC-rich, as well as TOP mRNAs and ATXN2 targets, whereas all other group II lists were AU-rich (***Figure 5A***). Furthermore, they shared common behavior in the various experiments. This is summarized in ***Figure 5B*** in a heatmap representing their median value in each dataset, while ***Figure 5—figure supplements 1*** and ***2*** provide detailed analysis, as described below.

Group I list mRNAs tended to be dependent on DDX6 and XRN1 but not on PAT1B for stability (***Figure 5—figure supplement 1B–D***), with nevertheless some variation between cell lines, as only SMG6 targets were sensitive to XRN1 depletion in HeLa cells (***Figure 5—figure supplement 1C***, upper panel). They did not accumulate in PBs and their translation rate was independent of DDX6 (***Figure 5—figure supplement 2A,B***). These results were consistent with their high GC content and our global analysis above. However, surprisingly, within PB-excluded mRNAs, there was little or no additional effect of being a SMG6 target, an YTHDF2 target or containing a G4 motif, neither for DDX6- nor for XRN1-dependent decay (***Figure 5—figure supplement 2C,D***).

Group II list mRNAs, except TOP mRNAs, ATXN2 and 4E-T targets, had the exact mirror fate compared to group I lists: they were stabilized following PAT1B silencing (***Figure 5—figure supplement 1D***), as previously reported for ARE-containing mRNAs and the targets of the ARE-BPs HuR and TTP (***Vindry et al., 2017***), but not following DDX6 or XRN1 silencing (***Figure 5—figure supplement 1B,C***); they were enriched in PBs and translationally more active after DDX6 silencing (***Figure 5—figure supplement 2A,B***), which is consistent with the reported presence of most of these regulatory proteins in PBs (***Hubstenberger et al., 2017***; ***Franks and Lykke-Andersen, 2007***).

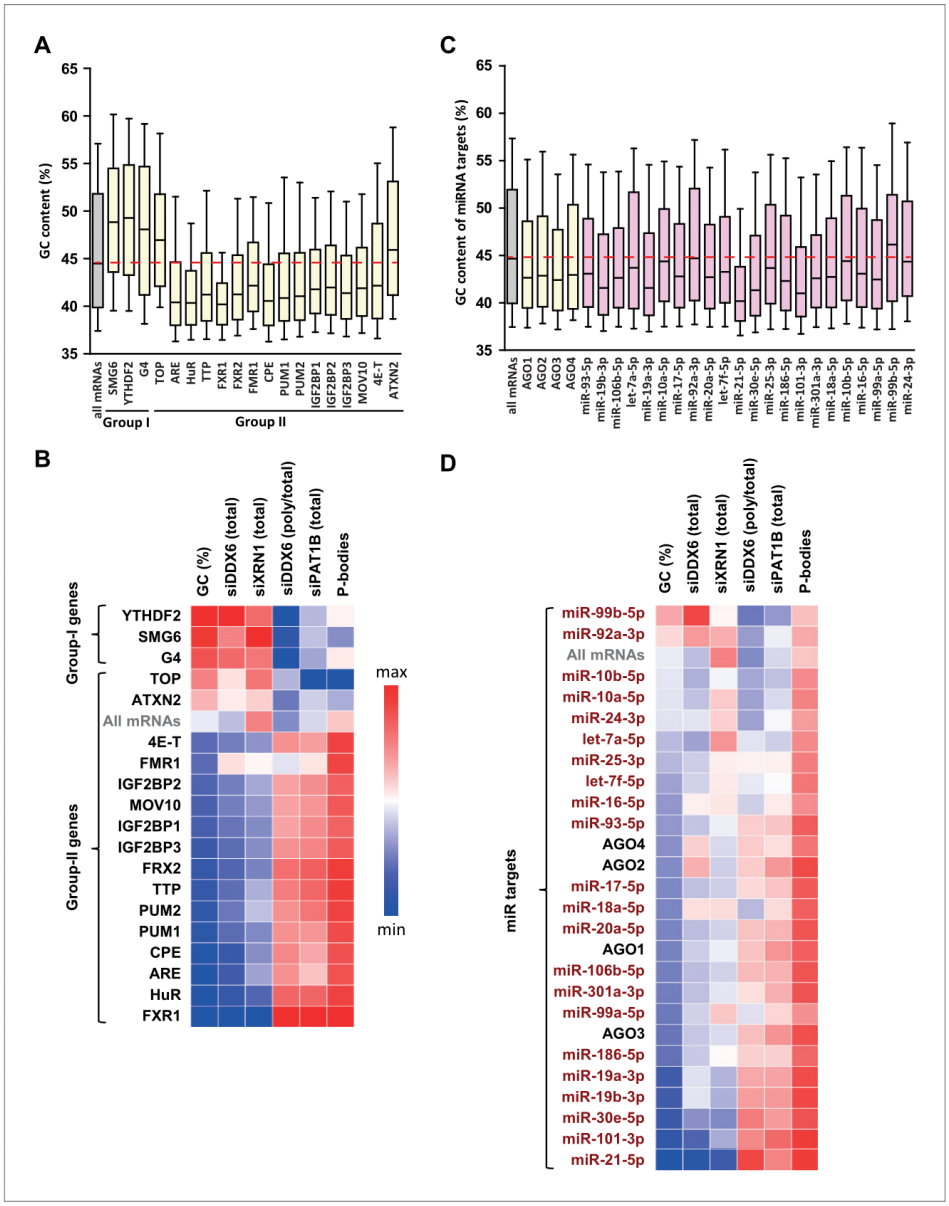

Figure 5. GC biases in the targets of various RNA decay factors, translation regulators and miRNAs. (**A**) GC content biases in the targets of various RBPs. The targets of the indicated factors were defined using CLIP experiments or motif analysis (see Materials and methods). The boxplots represent the distribution of the GC content of their gene. The distribution for all mRNAs is presented for comparison (in gray) and the red dashed line indicates its median value. (**B**) Heatmap representation of the different factors depending on the behavior of their mRNA targets in the different datasets. The

Figure 5 continued on next page

XRN1-dependent decay (***Figure 6—figure supplement 1A***). However they were not more sensitive to DDX6-dependent decay (***Figure 6—figure supplement 1B***). This suggested that XRN1 preference for GC-rich mRNAs is at least in part related to their exclusion from PBs, whereas DDX6 has a true preference for GC-rich mRNAs.

Interestingly, these PB-excluded AU-rich mRNAs were strongly enriched in mRNAs encoding secreted proteins and proteins associated with membranous organelles, with GO categories related to mitochondria, intracellular organelles and extracellular matrix proteins representing up to 36% of the transcripts (***Figure 6—figure supplement 1C***). Thus, while mRNA localization in PBs is highly influenced by their GC content, it may also be outcompeted by retention on membranous organelles and plasma membrane.

Contribution of both the CDS and 3'UTR GC content to PB localization

The next major issue was to distinguish which of the CDS or 3'UTR is more important for PB localization, since they have very similar GC contents (r_s = 0.72, p<0.0001).

As a first approach, we analyzed PB localization of long non-coding RNAs (lncRNAs) (***Hubstenberger et al., 2017***). The correlation between their GC content and PB accumulation was significant (r_s = −0.20, p<0.0001), but much weaker than that observed for mRNAs (−0.64, ***Figure 1B***) or 3'UTRs (−0.55, ***Figure 1D***) (−0.20 and −0.55 are significantly different, p<0.0001). In fact, AU-rich lncRNAs poorly accumulated in PBs, while GC-rich lncRNAs were excluded (***Figure 6—figure supplement 1D,E***). This suggested that the coding capacity of mRNAs was important for PB localization. As a second approach, we directly analyzed the respective contribution of the GC content of CDS and 3'UTR to PB localization. On one side, we analyzed transcripts by groups of similar 3'UTR GC content. Their GC3 was systematically much lower in PB mRNAs than in PB-excluded mRNAs, with differences ranging between 9% and 13% GC (***Figure 6A***, ***Figure 6—figure supplement 1E***). In a mirror analysis, we analyzed groups of transcripts with similar GC3. The importance of the 3'UTR GC content became visible only for GC3 higher than 50% GC (note that GC3 median value is 59% GC), with AU-rich 3'UTR allowing for their accumulation in PBs despite a GC-rich CDS (***Figure 6B***, ***Figure 6—figure supplement 1E***). We concluded that both the CDS and the 3'UTR GC content are important for PB localization, with the CDS being the primary feature.

We speculate that suboptimal translation of AU-rich CDS makes mRNAs optimal targets for translation regulation, since any control mechanism has to rely on a limiting step. Conversely, optimally translated transcripts would be better controlled at the level of stability. One prediction is that proteins produced in limiting amounts, such as those encoded by haplo-insufficiency genes, are more likely to be encoded by PB mRNAs. Genome-wide haplo-insufficiency prediction scores have been defined for human genes, using diverse genomic, evolutionary, and functional properties trained on known haplo-insufficient and haplo-sufficient genes (***Huang et al., 2010***; ***Steinberg et al., 2015***). Using these scores, we found that haplo-insufficient mRNAs were indeed significantly enriched in PBs (***Figure 6C***).

To add experimental support to the importance of GC content for PB assembly, we conducted two assays. First, we analyzed the localization of reporter transcripts that differ only by the GC content of their CDS. HEK293 cells stably expressing the PB marker GFP-LSM14A (***Hubstenberger et al., 2017***) were transfected with plasmids containing an AU-rich (36% GC) or GC-rich (58% GC) CDS that encodes the same Renilla luciferase (Rluc) protein. After 24 h cells were analyzed for luciferase activity and transcript localization. In agreement with our previous analyses, Rluc protein yield was considerably reduced (4.5-fold) using the AU-rich rather than the GC-rich version of the CDS, despite similar mRNA levels (***Figure 6D***). The localization of the Rluc transcripts was then analyzed by smiFISH using AU-rich or GC-rich specific probes (***Figure 6—figure supplement 2A***, ***Supplementary file 2***) (***Tsanov et al., 2016***). PBs containing clusters of Rluc mRNA molecules were five times more frequent using the AU-rich than the GC-rich version of the CDS (***Figure 6E,F***). A similar result was obtained in HEK293 cells after PB immunostaining with DDX6 antibodies (***Figure 6F***, ***Figure 6—figure supplement 2B***). Therefore, simply changing the GC content of this medium-size CDS (564 codons) was sufficient to modify mRNA localization in PBs.

Second, we tested the capacity of AU-rich and GC-rich RNA to form granules independently of translation. To this aim, we set-up a cell-free assay using HEK293 cells expressing GFP-LSM14A to monitor the formation of fluorescent PB-like granules and count them by flow cytometry, as previously performed for PBs (***Hubstenberger et al., 2017***). After lysis and elimination of preexisting PBs

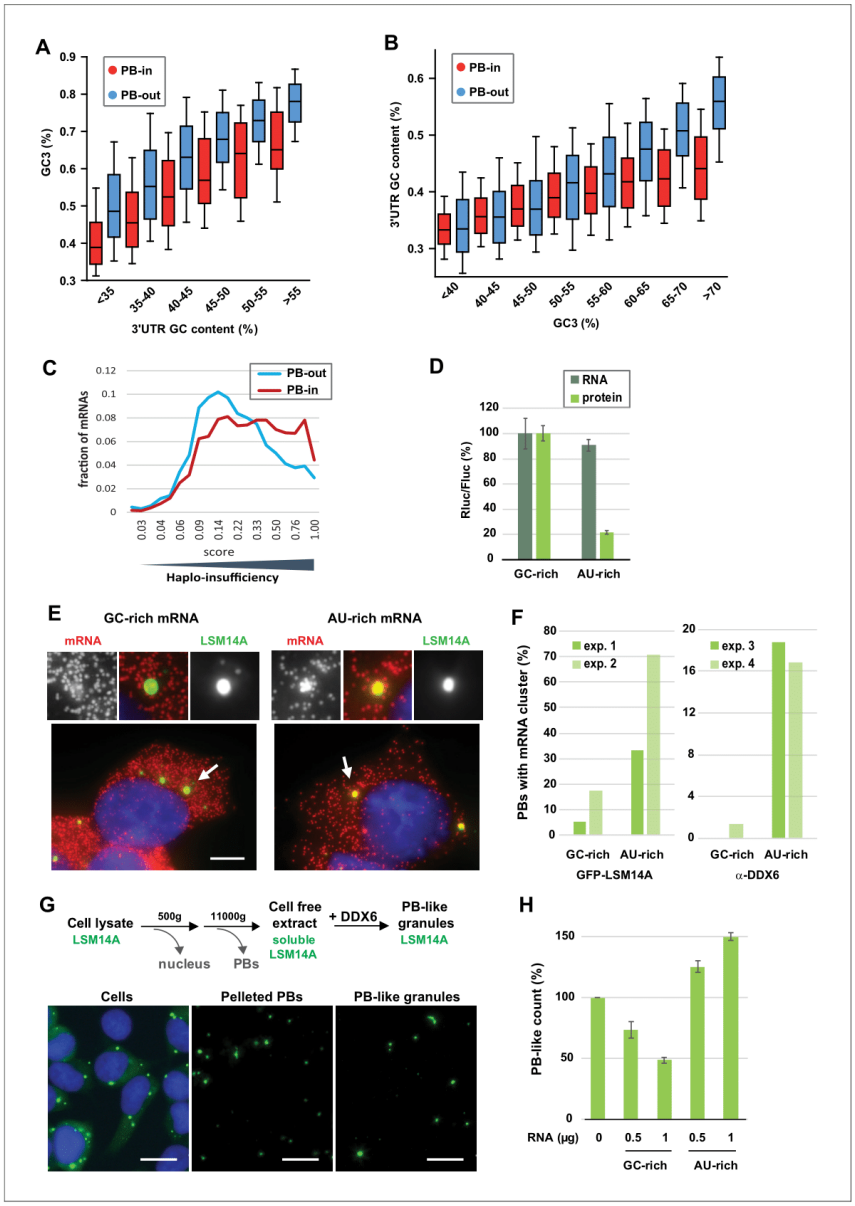

Figure 6. The GC content of the CDS and the 3'UTR both contribute to PB localization. (**A**) General importance of the CDS. Transcripts were subdivided into six classes depending on the GC content of their 3'UTR (from <40 to >55%). The boxplots represent the distribution of their CDS GC content at position 3 (GC3) in PB-enriched (PB-in) and PB-excluded (PB-out) mRNAs. (**B**) Importance of the 3'UTR for GC-rich CDSs. Transcripts were subdivided into eight classes depending on their GC3 (from <40 to >70%). The boxplots represent the distribution of their 3'UTR GC content in PB-

Figure 6 continued on next page

Figure 6 continued

enriched (PB-in) and PB-excluded (PB-out) mRNAs. (**C**) The transcripts of haplo-insufficiency genes are enriched in PBs. The haplo-insufficiency score is the probability that a gene is haplo-insufficient, as taken from the ***Huang et al. (2010)*** study. The analysis was performed for PB-enriched (PB-in, n = 4646, median score 0.26) and PB-excluded (PB-out, n = 4205, median score 0.17) mRNAs. The difference of distribution of haplo-insufficiency scores was statistically significant using a two tail Mann-Whitney test: $p<0.0001$. The results were similar using ***Steinberg et al. (2015)*** scores. (**D**) Protein yield is higher from a GC-rich than an AU-rich CDS. HEK293 cells were transfected with Rluc reporters differing by the GC content of their CDS, along with a control Fluc plasmid. After 24 hr, mRNA levels were measured by qPCR and protein levels by luciferase activity. The Rluc to Fluc ratio for the GC-rich reporter was set to 100 (n = 3). Error bars, SD. (**E, F**) Preferential localization of AU-rich transcripts in PBs. HEK293 cells expressing GFP-LSM14A were transfected with the AU-rich and GC-rich Rluc reporters and the localization of the Rluc transcripts (in red) was analyzed by smiFISH. Representative cells are shown in (**E**). Bar, 5 µm. Arrows indicate the PBs enlarged above. The experiment was performed in duplicate (exp. 1 and 2) and repeated in HEK293 cells where PBs were immunostained using DDX6 antibodies (exp. 3 and 4). The percentage of PBs containing clusters of Rluc transcripts in the four experiments is represented in (**F**). Exp.1: 56/75 PBs from 21/27 cells; exp.2: 87/75 PBs from 38/35 cells; exp.3: 31/32 PBs from 15/19 cells; exp.4: 72/83 PBs from 34/41 cells (**G**) Assembly of PB-like granules in cell-free extracts from HEK293 cells expressing GFP-LSM14A. The scheme recapitulates the main steps of the assay. Fluorescence microscopy images show that PBs in cells, PBs after cell lysis, and reconstituted PB-like granules have similar size. Bar, 10 µm. (**H**) AU-rich RNA favors the formation of PB-like granules. PB-like granules were assembled in cell-free extracts in the presence of AU-rich or GC-rich RNA, and counted by flow cytometry. Their number in the absence of added RNA was set to 100 (n = 3 experiments in duplicate, using two independent cell-free extracts and RNA preparations). Error bars, SD.
The online version of this article includes the following figure supplement(s) for figure 6:

Figure supplement 1. Role of PB localization in XRN1 and DDX6 sensitivity and importance of the coding property for PB localization.
Figure supplement 2. The GC content of reporters RNAs is key for PB localization.

by centrifugation, addition of recombinant DDX6 triggered the formation of new granules on ice, in a dose-dependent manner (***Figure 6—figure supplement 2C–E***). These granules had a similar size to endogenous PBs (***Figure 6G***, ***Figure 6—figure supplement 2D***). This reconstitution assay was surprisingly efficient, as granule formation required rather low concentrations of both the lysate components (about 100-fold lower than in cells, see Materials and methods) and recombinant DDX6 (0.17 µM versus 3.3 µM in cells, ***Ernoult-Lange et al., 2012***). Next, the cell-free extract was briefly treated with micrococcal nuclease to decrease the amount of cellular RNA, and the assay was repeated with or without addition of an either AU-rich or GC-rich 1700 nt-long synthetic RNA (***Figure 6H***, ***Figure 6—figure supplement 2F***). The AU-rich RNA increased the number of PB-like granules in a dose-dependent manner, while GC-rich RNA prevented their formation. Therefore, in the complex lysate environment and at 0˚C, uncapped non-polyadenylated AU-rich RNA specifically favor the condensation of granules that are DDX6-dependent and contain LSM14A, two proteins that play a major role in the assembly of cellular PBs.

We conclude from these experimental data and our previous analyses that both the CDS and the 3'UTR contribute to PB localization. Low GC content in the CDS likely acts, at least in part, through codon usage and low translation efficiency. In the 3'UTR low GC content could allow for the binding of RBPs with affinity for AU-rich motifs and/or influence RNA secondary structure.

Discussion

An integrated model of post-transcriptional regulation

Our combined analysis of the transcriptome of purified PBs together with transcriptomes following the silencing of broadly-acting storage and decay factors, including DDX6, XRN1 and PAT1B, provided a general landscape of post-transcriptional regulation in human cells, where mRNA GC content plays a central role. As schematized in ***Figure 7***, GC-rich mRNAs are excluded from PBs and mostly controlled at the mRNA level by a mechanism involving the helicase DDX6 and the 5'−3' exonuclease XRN1. In contrast, AU-rich mRNAs are enriched in PBs and rather controlled at the level of translation by a mechanism also involving DDX6, while their accumulation tend to depend on a mechanism involving the DDX6 partner PAT1B and most likely 3' decay. Accordingly, NMD and m6A-associated mRNA decay pathways tend to target GC-rich mRNAs, while most sequence-specific translation regulators and miRNAs tend to target AU-rich mRNAs. The distinct fate of GC-rich and AU-rich mRNAs correlates with a contrasting protein yield resulting from both different codon usage and CDS length. Thus, 5' mRNA decay appears to control preferentially mRNAs with optimal

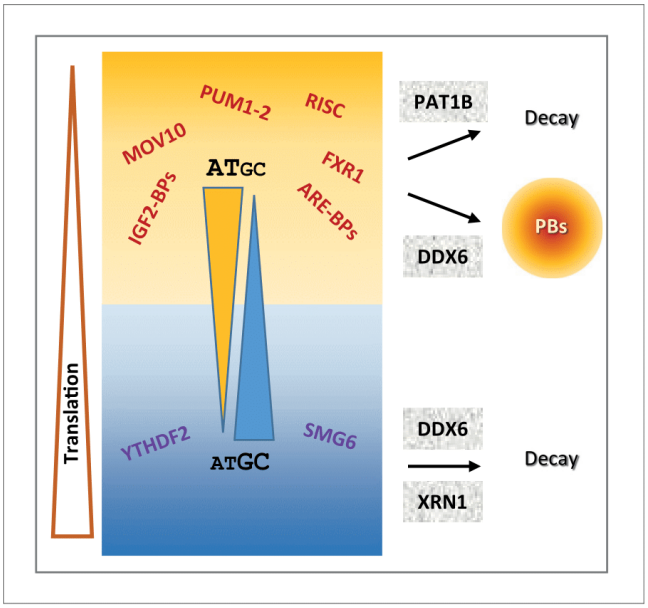

Figure 7. Schematic representation recapitulating the features of mRNA post-transcriptional regulation depending on their GC content.
The online version of this article includes the following figure supplement(s) for figure 7:

Figure supplement 1. Distribution of the gene GC content in various eukaryotic genomes.

translation, which are mostly GC-rich, whereas translation regulation is mostly used to control mRNAs with limiting translational efficiency, which are AU-rich.

It should be stressed that this model only applies to post-transcriptional regulation pathways that involve PBs, XRN1, DDX6 and PAT1B. Moreover, while the analysis was consistent in proliferating cells of various origins, giving rise to a general model, it is possible that changes in cell physiology, for instance at particular developmental stages or during differentiation, rely on a different mechanism. In addition, our analysis focused on trends common to most transcripts, which does not preclude that particular mRNAs could be exceptions to the general model, being GC-rich and translationally controlled, or AU-rich and regulated by 5' decay. In terms of translation yield and PB localization, this model is strongly supported by our experiments using AU-rich and GC-rich RNAs: AU-rich reporter mRNAs have a low protein yield compared to GC-rich ones, they preferentially localize in PBs in cells, and they enhance the formation of PB-like granules in a cell free extract.

GC content and codon usage

While the redundancy of the genetic code should enable amino acids to be encoded by synonymous codons of different base composition, the wide GC content variation between PB-enriched and PB-excluded mRNAs has consequences on the amino acid composition of encoded proteins. It also strongly impacts the identity of the wobble base: in PB mRNAs, the increased frequency of A/U at position 3 of the codon mechanically results in an increased use of low usage codons. As CDS are also longer in PB mRNAs, it further increases the number of low usage codons per CDS in these mRNAs. Interestingly, we showed that the absolute number of low usage codons per CDS best correlates with low protein yield. Thus, these results provide a molecular mechanism to a previously unexplained feature of PB mRNAs, that is, their particularly low protein yield, which we reported was

an intrinsic property of these mRNAs and not simply the result of their sequestration in PBs (**Hubstenberger et al., 2017**). Interestingly, the mRNAs of haplo-insufficiency genes, which by definition are expected to have a limited protein yield, are indeed enriched in PBs (**Figure 6C**).

In addition to the GC-dependent codon bias, we also observed some GC-independent codon bias in PB-enriched mRNAs. Interestingly, some important post-transcriptional regulation programs involve codon usage. This was shown for proliferation- versus differentiation-specific transcripts in human cells (**Gingold et al., 2014**) and for maternal mRNA clearance during the maternal-to-zygotic transition in zebrafish, *Xenopus*, mouse, and *Drosophila* (**Bazzini et al., 2016**). Codon usage could also enable the regulation of small subsets of mRNAs, depending on cellular requirements. In man, half of GO sets show more variability in codon usage than expected by chance (**Rudolph et al., 2016**). Based on GO analysis, we previously demonstrated that PB mRNAs tend to encode regulatory proteins, while PB-excluded mRNAs encode basic functions. Furthermore, proteins of the same complexes tended to be encoded by mRNAs co-regulated in or out of PBs, in so-called post-transcriptional regulons (**Hubstenberger et al., 2017**; **Standart and Weil, 2018**). We speculate that specific codon usage could also underlie these post-transcriptional regulons.

Distinct mechanisms of mRNA stability control

Our analysis distinguished separate modes of stability control, depending on mRNA GC content. Interestingly, our previous analysis of the read coverage of PB and non-PB RNAs alsosuggested the existence of distinct decay pathways related to 3′ and 5′ extremities, respectively (**Hubstenberger et al., 2017**). Part of the triage towards the PAT1B versus the DDX6/XRN1-dependent pathway could be somehow associated with the capacity of the transcripts to condense in PBs, since, among the AU-rich mRNAs, only the ones enriched in PBs were affected by PAT1B silencing (not shown). Nevertheless, PBs do not directly mediate the triage, since (i) TOP mRNAs were strongly excluded from PBs, but unaffected by either DDX6 or XRN1 silencing, and (ii) while PBs disappeared after DDX6 silencing (**Minshall et al., 2009**), causing the release of AU-rich mRNAs into the cytosol, only GC-rich mRNAs were stabilized.

Focusing on DDX6-dependent decay, the minor impact of the 5′UTR GC content, compared to CDS and 3′UTR, indicates that this helicase is not simply involved in allowing XRN1 access to the 5′ end. It is tempting to propose rather that, by unwinding GC-rich double-stranded regions over the entire length of the mRNA, DDX6 facilitates XRN1 progression. UPF1, another RNA helicase involved in mRNA decay, has also been shown to preferentially affect the decay of GC-rich mRNAs (**Imamachi et al., 2017**). The same observation was made for targets of the NMD pathway, which involves UPF1, SMG6 and SMG7 (**Colombo et al., 2017**). Although the bias in these cases was restricted to the 3′UTR regions, it suggests that DDX6 could act in concert with other helicases for decay of GC-rich mRNAs. For AU-rich mRNAs, either such an active unfolding would be dispensable, or it would rely on other helicases that remain to be identified, with potential candidates being those enriched in purified PBs (**Hubstenberger et al., 2017**). Noteworthily, in agreement with the present study in cell lines, skin fibroblasts from patients with DDX6 missense mutations also showed significant accumulation of GC-rich mRNAs (**Balak et al., 2019**).

Concerning XRN1, we showed that it preferentially acts on PB-excluded mRNAs, that is, on GC-rich mRNAs but also, to a lesser extent, on a subset of AU-rich mRNAs (**Figure 6—figure supplement 1A**). While XRN1 is described as a general decay factor, there is evidence that 5′ decay shows some specificity in vivo. In *Drosophila*, mutations in XRN1 have specific phenotypes, including wound healing, epithelial closure and stem cell renewal in testes, suggesting that it specifically degrades a subset of mRNAs (**Pashler et al., 2016**). Of particular relevance, a recent study showed that yeast XRN1 associates with ribosomes and decays mRNAs during translation (**Tesina et al., 2019**). If the mechanism is conserved in human, it would explain why XRN1 preferentially acts on GC-rich mRNAs, since they are the most actively translated mRNAs.

Turning to PAT1B, we showed that its silencing did not affect the same mRNAs as DDX6 silencing. A recent yeast study also showed that Dhh1/DDX6 and Pat1/PAT1B decay targets poorly overlap, suggesting the existence of two separate pathways in yeast as well (**He et al., 2018**). However, the underlying mechanisms may differ in the two organisms, since both Pat1 and Dhh1 targets were poorly translated in yeast, while only PAT1B targets were poorly translated in our study. Previous studies reported that tethered PAT1B decreases the abundance of a reporter mRNA in human cells, as a result of enhanced deadenylation and decapping (**Ozgur et al., 2010**; **Kamenska et al., 2014**;

Totaro et al., 2011). However, we did not find any significant evidence of PAT1B-enhanced 5′ to 3′ decay in our read coverage analysis. Interestingly, genome-wide evidence in yeast too suggests that following decapping a significant fraction of the transcripts up-regulated in cells lacking Pat1 or Lsm1 is efficiently decayed from 3′ to 5′, rather than by the 5′−3′ Xrn1 exonuclease (*He et al., 2018*). Moreover, CLIP experiments in yeast showed a preference for Pat1 and Lsm1 binding to the 3′ end of mRNAs (*Mitchell et al., 2013*). Altogether, we therefore favor the possibility that the mechanism by which PAT1B affects mRNA stability in human cells relies prominently on 3′ to 5′ decay. It could involve the CCR4/CNOT deadenylase and the LMS1-7 complexes, as, despite their low abundance or small size, CNOT1 and LSM2/4 had high scores in our previous PAT1B interactome analysis (*Vindry et al., 2017*; *Vindry et al., 2019*).

PAT1B showed a strong preference for AU-rich targets, including those containing AREs. Many studies have demonstrated a link between AREs and mRNA stability, and its striking importance for processes such as inflammation (*Wells et al., 2017*). Most ARE-BPs promote mRNA destabilization while some ARE-BPs, such as HuR (*Lebedeva et al., 2011*; *Mukherjee et al., 2011*) and AUF1 for a subset of mRNAs (*Yoon et al., 2014*), can stabilize mRNAs. Altogether, these observations raise the possibility that ARE-BPs behave either as enhancers or inhibitors of PAT1B activity in mRNA decay. Similarly, the miRNA pathway could activate this PAT1B activity.

Translation repression and PB accumulation

DDX6 activity in translation repression has been documented in a variety of biological contexts. In *Xenopus* oocytes, DDX6 contributes to the repression of maternal mRNAs, as a component of the well characterized CPEB complex (*Minshall et al., 2007*). In *Drosophila*, Me31B/DDX6 represses the translation of thousands of mRNAs during the early stages of the maternal to zygotic transition (*Wang et al., 2017*). It also collaborates with FMRP and AGO proteins for translation repression in fly neurons (*Barbee et al., 2006*). In mammals, DDX6 is a general co-factor of the miRNA pathway (*Chen et al., 2014*; *Mathys et al., 2014*; *Kamenska et al., 2016*; *Chu and Rana, 2006*). The intriguing finding of our analysis was that the targets of most tested translation regulators (FRX1-2, FMR1, PUM1-2, most miRNAs. . .) were AU-rich and had a median behavior in all datasets similar to other mRNAs of same GC content. While the GC bias of the targets of the various RBPs and miRNAs are likely to reflect their sequence preference, some RBPs may not reach sufficient concentration to occupy a significant number of binding sites. Moreover binding does not mean activity, and these factors could require cofactors or post-translational modifications to become 'productive' in terms of mRNA regulation. Of note, while TOP mRNAs clearly constituted an exception in terms of GC content, they are particular too in terms of their translation repression mechanism, with a regulatory sequence located at the 5′ end.

PBs add another layer to translation regulation, by storing translationally repressed mRNAs. It was already known that ARE-containing mRNAs bound to ARE-BPs such as TTP and BRF were recruited to PBs (*Franks and Lykke-Andersen, 2007*) and that miRNA targets accumulate in PBs upon miRNA binding in a reversible manner (*Bhattacharyya et al., 2006*; *Liu et al., 2005*). As DDX6 and 4E-T are key factors in PB assembly in mammalian cells (*Minshall et al., 2009*; *Ayache et al., 2015*; *Kamenska et al., 2014*; *Ferraiuolo et al., 2005*), it raises the question of whether these proteins contribute to translation repression by triggering the recruitment of arrested mRNA to PBs, or by mediating translation arrest, which then results in mRNA recruitment to PBs. While we have no answer for DDX6, we observed that 4E-T targets were particularly enriched in PBs, though rather insensitive to DDX6 or PAT1B depletion. First, this suggests that 4E-T function in PBs is partly independent of DDX6, agreeing with the previous observation that some PBs can still form when the DDX6 interaction domain of 4E-T is mutated (*Kamenska et al., 2016*). Second, it indicates that PB localization and translation repression by DDX6 can be separated, at least to some extent.

In addition to their high AU content, we observed that PB mRNAs were longer than mRNAs excluded from PBs. Long CDS could favor mRNA recruitment in PBs by decreasing translation efficiency, and hence increasing the fraction of polysome-free mRNAs. Long 3′UTR should increase the probability of binding translation regulators, contributing also to PB recruitment. In agreement, it is interesting that DDX6 preferentially repressed the translation of mRNAs with long 3′UTR, while the CDS length was irrelevant (*Figure 3—figure supplement 2G*). It is also possible that protein binding over the entire length of mRNA may contribute to PB recruitment. This would explain why the GC content of the 5′UTR has little impact as it is considerably shorter than CDS and 3′UTR. In this

regard, it is interesting to note that we and others have previously proposed from biochemical experiments and electron microscopy imaging that DDX6 and its partner LSM14A coat repressed mRNAs at multiple positions, according to their length (***Ernoult-Lange et al., 2012***; ***Götze et al., 2017***).

Evolutionary issues

Our results raise intriguing issues in terms of evolution. While PBs have been observed in very diverse eukaryotes, animal and vegetal, the GC-rich part of the human genome only emerged in amniotes (the ancestor of birds and mammals) (***Duret et al., 2002***). In more distant organisms, such as yeast, *C. elegans*, *Drosophila* or *Xenopus*, genes have a narrow GC content distribution, most often AU-rich (***Figure 7—figure supplement 1***). Thus, despite the conservation of the DDX6, XRN1 and to a lesser extent PAT1B proteins in eukaryotes, distinct modes of mRNA stability control depending on GC content may have evolved more recently. Moreover, the enzymatic properties of DDX6 could have adapted to the higher GC content of human transcripts.

The GC-rich part of the human genome was acquired through GC-biased gene conversion (gBGC), a non-selective process linked with meiotic recombination affecting GC content evolution (***Duret and Galtier, 2009***). We considered the possibility that meiotic recombination occurred more frequently in genomic regions containing genes involved in basic functions, leading to stronger gBGC and, consequently, to higher GC content of PB-excluded mRNA. However, our analysis showed that mRNA base composition and PB enrichment are associated independently of meiotic recombination or the genomic context. We therefore put forward a model where the genome of higher eukaryotes has evolved partly to facilitate the control of regulators at the translation level, by limiting their protein yield. Regardless, the overall outcome of our study is that in human the GC content, a feature written in the genome, shapes in part mRNA fate and its control in a strikingly coherent system.

Materials and methods

Key resources table

Reagent type (species) or resource	Designation	Source or reference	Identifiers	Additional information
Cell line (*Homo sapiens*)	HEK293	ATCC	Cat# PTA-4488, RRID:CVCL_0045	
Cell line (*Homo sapiens*)	HeLa	ATCC	Cat# CCL-2, RRID:CVCL_0030	
Cell line (*Homo sapiens*)	HCT116	ATCC	Cat# CCL-247, RRID:CVCL_0291	
Cell line (*Homo sapiens*)	HEK293 expressing GFP-LSM14A	***Hubstenberger et al., 2017***	PMID:28965817	
Transfected construct (rabbit)	siβ-Globin	***Serman et al., 2007***	PMID:17604308	GGUGAAUGUGGAAGAAGUUdTdT siRNA used as negative control for the siDDX6 expt.
Transfected construct (human)	siDDX6	***Minshall et al., 2009***	PMID:19297524	GGAACUAUGAAGACUUAAAdTdT
Transfected construct (human)	siXRN1	Thermofisher	Cat# AM16708A	ID125199
Transfected construct (human)	siRNA negative control	Thermofisher	Cat# 4390843	siRNA used as a negative control for the siXRN1 expt.
Transfected construct (human)	shXRN1	Thermofisher	Cat# RHS 4696–99704634	Lentiviral 'TRIPZ' construct to transfect and express the XRN1 shRNA.
Transfected construct (human)	Non-silencing shRNA	Thermofisher	Cat# RHS 4743	Lentiviral 'TRIPZ' construct to transfect and express the control shRNA.

Continued on next page

Continued

Reagent type (species) or resource	Designation	Source or reference	Identifiers	Additional information
Antibody	anti DDX6 (rabbit polyclonal)	Novus biological	Cat# NB200-191, RRID:AB_10003156	WB (1:15000), IF (1:2000)
Antibody	Anti XRN1 (rabbit polyclonal)	Novus Biosciences	Cat# NB 500–191, RRID:AB_527572	WB (1:5000)
Antibody	Anti XRN1 (rabbit polyclonal)	Bethyl	Cat# A300-443A, RRID:AB_2219047	WB (1:1000)
Antibody	Anti ribosomal S6 (rabbit monoclonal)	Cell signalling technologies	Cat# 2217, RRID:AB_331355	WB (1:5000)
Antibody	Anti Pol II (rabbit polyclonal)	Santa Cruz	Cat# sc-899, RRID:AB_632359	WB (1:100)
Antibody	Anti tubulin (mouse monoclonal)	Sigma-Aldrich	Cat# T9026, RRID:AB_477593	WB (1:30000)
Recombinant DNA reagent	hRluc-GFP-GC-rich	This paper		phRL-CMV vector bearing an Rluc-GFP GC-rich insert, used in PB-like reconstitution, smiFISH and luciferase reporter expts.
Recombinant DNA reagent	Rluc-GFP-AU-rich	This paper		phRL-CMV vector bearing an Rluc-GFP GC-rich insert, used in PB-like reconstitution, smiFISH and luciferase reporter expts.
Sequence-based reagent	ACTB qPCR primers	This paper		Fwd: TCCCTGGAGAAGAGCTACGA Rev: AGCACTGTGTTGGCGTACAG
Sequence-based reagent	APP qPCR primers	Gift from R. Blaise		Fwd: acttgcatgactacggc Rev: actcttcagtgtcaaagttgt
Sequence-based reagent	BACE1 qPCR primers	Gift from R. Blaise		Fwd: ctttgtggagatggtggac Rev: aaagttactgctgcctgtat
Sequence-based reagent	LSM14A qPCR primers	This paper		Fwd: AGCAGTTTGGTGCTGTTGGT Rev: AACCGCACTACTTTGGGGTA
Sequence-based reagent	LSM14B qPCR primers	This paper		Fwd: CGACAACATCTCTTCTGAACTCAA Rev: GTGTTGAGCTTCCTCTCTTCG
Sequence-based reagent	MFN2 qPCR primers	This paper		Fwd: GAACCTGGAGCAGGAAATTG Rev: AACCAACCGGCTTTATTCCT
Sequence-based reagent	PNRC1 qPCR primers	This paper		Fwd: CCCCCTCAGGAAAGAGGTTTT Rev: ACAAGTGTATACCATGAACAAGCTG
Sequence-based reagent	TIMP2 qPCR primers	***Blaise et al., 2012***	PMID:22260497	Fwd: gaagagcctgaaccacaggt Rev: cggggaggagatgtagcac
Sequence-based reagent	TRIB1 qPCR primers	This paper		Fwd: ACCTGAAGCTTAGGAAGTTCGT Rev: CTGACAAAGCATCATCTTCCCC
Sequence-based reagent	HPRT1 qPCR primers	This paper		Fwd: TAATTGACACTGGCAAAACAATGCAGACT Rev: GGGCATATCCTACAACAAACTTGTCTGGA
Sequence-based reagent	REN-lowGC qPCR primers	This paper		Fwd: CCAGGATTCTTTTCCAATGC Rev: CTTGCGAAAAATGAAGACCTTT
Sequence-based reagent	REN-highGC qPCR primers	This paper		Fwd: CGAGAACGCCGTGATTTT Rev: GACGTGCCTCCACAGGTAG
Sequence-based reagent	FIREfly qPCR primers	This paper		Fwd: TGAGTACTTCGAAATGTCCGTTC Rev: GTATTCAGCCCATATCGTTTCAT
Sequence-based reagent	RenGFP-lowGC-24 DNA probe	This paper		Set of 24 primary probes specific of the RenGFP lowGC mRNA used in smiFISH expts. (See ***Supplementary file 2***)

Continued on next page

Continued

Reagent type (species) or resource	Designation	Source or reference	Identifiers	Additional information
Sequence-based reagent	RenGFP-highGC-24 DNA probe	This paper		Set of 24 primary probes specific of the RenGFP highGC mRNA used in smiFISH expts. (see ***Supplementary file 2***)
Sequence-based reagent	FLAP-Y-Cy3 DNA probe	***Tsanov et al., 2016***	PMID:27599845	AA TGC ATG TCG ACG AGG TCC GAG TGT AA Secondary probe conjugated to two Cy3 moieties at the 5' and 3' termini. Used in smiFISH expts.
Peptide, recombinant protein	CBP-DDX6-HIS	***Ernoult-Lange et al., 2012***	PMID:22836354	
Commercial assay or kit	miRNeasy Mini kit	Qiagen	Cat# 217004	
Commercial assay or kit	TruSeq Stranded Total RNA kit	Illumina	Cat# RS-122–2201	
Commercial assay or kit	Dual-Glo Luciferase assay system	Promega	Cat# E2920	
Chemical compound, drug	Micrococcal Nuclease	Thermo Scientific	Cat# 88216	
Software, algorithm	Cluster 3.0	http://www.eisenlab.org/eisen/?page_id=42	RRID:SCR_013505	
Software, algorithm	Java Treeview	https://sourceforge.net/projects/jtreeview/	RRID:SCR_016916)	
Software, algorithm	Morpheus	https://software.broadinstitute.org/morpheus	RRID: SCR_017386	
Software, algorithm	Icy	http://icy.bioimageanalysis.org/	RRID:SCR_010587	
Software, algorithm	WebGestalt	http://www.webgestalt.org/	RRID:SCR_006786	

Cell culture and transfection

Human embryonic kidney HEK293 cells, epithelioid carcinoma HeLa cells and colorectal carcinoma HCT116 cells were obtained from ATCC. All cells were tested negative for mycoplasma contamination. HEK293 and HeLa cells were maintained in DMEM supplemented with 10% (v/v) fetal calf serum. HCT116 cells were grown in McCoy's 5A modified medium supplemented with 10% (v/v) fetal bovine serum, 5% (v/v) sodium pyruvate and 5% (v/v) non-essential amino acids. The HEK293 cell line stably expressing GFP-LSM14A (***Hubstenberger et al., 2017***) was maintained under selection using 500 µg/ml Geneticin (Gibco, Life Technology).

For DDX6 silencing, 7.10^5 cells were transfected at the time of their plating (reverse transfection) with 50 pmoles DDX6 or control β-globin siRNAs (***Minshall et al., 2009***) per 3 cm diameter well, using Lipofectamine 2000 (Life Technologies, France), and split in two 24 hr later. Cells were lyzed 48 hr after transfection.

For XRN1 silencing with siRNAs, 2.10^5 cells/well were plated in 6-well plates and transfected 24 hr later with 50 nM siRNA negative Control or Silencer Pre-designed siRNA XRN1 (Thermofisher), using Lipofectamine RNAiMAX (Life Technologies). Cells were lyzed 48 hr after transfection.

For XRN1 silencing with shRNA, a doxycycline inducible construct provided by Thermofisher (TRIPZ) with shRNA against XRN1 or non-silencing shRNA was introduced by lentiviral transduction (MOI 0.5). After 10 days of puromycin selection, cells were tested for expression of the construct. For shRNA induction cells were grown to 30% confluency in 10 cm plates before adding 1 µg/ml doxycycline. After 24 hr, cells were split in three and doxycycline was maintained until 48 hr.

For smiFISH experiments and luciferase reporter expression, 2.10^5 cells were plated in 35 mm diameter dish and transfected 24 hr later with 100 ng of hRluc-GFP-GC-rich or Rluc-GFP-AU-rich plasmids using GenJet Plus DNA (SignaGen Laboratories). For luciferase reporter assay, a Firefly luciferase plasmid (150 ng) was added for normalization. All transfection mixes were made up to 1 µg with pUC19. Cells were processed 24 hr after transfection.

Construction of DNA plasmids

All plasmids were obtained using the InFusion Advantage PCR cloning kit (Clontech). To obtain medium-size CDS, we cloned the Rluc CDS in frame with the one of GFP. An AU-rich CDS of GFP was amplified from the pUC57-GFP(opt) plasmid (generous gift from N. Campo, ***Martin et al., 2010***) and cloned in place of GFP into the BamHI/NotI sites of the pEGFP-N1 plasmid (Clontech) to generate the pGFP(opt)-N1 plasmid. The AU-rich CDS of Rluc was taken from the pRL-TK vector (Promega) and cloned in frame into the pGFP(opt)-N1 plasmid to obtain pRL-GFP(opt) plasmid. The GC-rich CDS of Rluc (hRluc) was taken from the phRL-CMV vector (Promega) and cloned in-frame into the pEGFP-N1 to obtain the phRL-EGFP plasmid. Finally, hRluc-EGFP-GC-rich and Rluc-GFP-AU-rich CDS were cloned into the NheI/NotI sites of the T7 promotor-containing phRL-CMV vector to generate hRluc-GFP-GC-rich and Rluc-GFP-AU-rich plasmids, respectively. The resulting plasmids differ by their AU-rich or GC-rich CDS but encode the same Rluc-GFP fusion protein.

CBP-DDX6-HIS protein purification

E.*E. coli* BL21-CodonPlus (Novagen) transformed with the CBP-p54-His expression vector (***Ernoult-Lange et al., 2012***) were induced in MagicMedia (Invitrogen) at 16˚C during 72 hr to produce the CBP-DDX6-HIS protein. Crude protein extract was prepared and sequentially purified as described previously (***Ernoult-Lange et al., 2012***).

In vitro transcription and RNA purification

GC-rich and AU-rich RNAs (1707 and 1714 bp, respectively) were transcribed with T7 RNA polymerase (Promega) from linearized (NotI) hRluc-GFP-GC-rich and Rluc-GFP-AU-rich plasmids, purified using the Nucleospin RNA clean-up XS (Macherey-Nagel), quantified with Quantus Fluorometer (Promega) and visualized on 1% agarose gel in 1XTAE buffer containing ethidium bromide.

Cell-free extract preparation

Stable GFP-LSM14A HEK293 cells grown to 80–90% confluency in 15 cm plates were collected in PBS, cell pellets were frozen in liquid nitrogen and stored at −80˚C. Pellets were resuspended in lysis buffer (50 mM Tris, pH 7.4, 1 mM EDTA, 150 mM NaCl, 0,2% Triton X-100) containing 65 U/mL RNaseOut ribonuclease inhibitor (Promega) and EDTA-free protease inhibitor cocktail (Roche Diagnostics), incubated 20 min on ice and centrifuged at 500 xg for 5 min at 4˚C to deplete nuclei. The cytoplasmic lysate was half diluted to 75 mM NaCl with buffer containing 50 mM Tris, pH 7.4, 1 mM EDTA, 10 mM CaCl2, 0,2% Triton X-100, and treated with 1000 u/ml of micrococcal nuclease (Thermo Scientific) for 15 min at 37˚C. The micrococcal nuclease was inactived by adding EGTA, pH 8.0 to a final concentration of 20 mM. The cytoplasmic lysate was further spun at 11000 xg for 7 min at 4˚C to obtain a surpernatant depleted of endogenous P-bodies. This supernatant containing the GFP-LSM14A soluble protein, called cell free extract, was quantified by the Coomassie protein assay (Thermo Scientific).

In vitro reconstitution assay of P-body like granules

To reconstitute P-body like granules, 1 µg of purified CBP-DDX6-HIS protein was added to 200 µg of cell free extract, mixed or not with RNA, in a 100 µL reaction volume. After 2 hr on ice, 90 µL of the reactions were run through a MACSQuant analyzer (Miltenyi Biotec). Particles were detected according to their Forward-scattered light (FSC) and their green fluorescence using the 488 nm excitation laser and counted in the total volume. We have previously reported that in HeLa cells, 15 µg proteins (corresponding to 53,000 cells) contain 8.6 ng DDX6, and that DDX6 concentration is 0.56 mM in PBs and 3.3 µM in cells (170-fold less) (***Ernoult-Lange et al., 2012***). In the assay, CBP-DDX6-HIS concentration is 0.17 µM (1 µg in 100 µl, 61 kDa), and therefore about 20 fold less concentrated than in a cell, while the cell content (15 µg/53000 cells, 1000 μm^3/cell, leading to 200 µg/0.7 µl) is diluted about 100 fold (200 µg in 100 µl).

For imaging experiments, the reactions were centrifuged at 11000 xg for 7 min at 4˚C, resuspended in 5 µL of Mowiol (PolySciences) mounting medium, mixed by vortexing and mounted between glass slide and coverslip. Microscopy was performed on a Leica DMR microscope (Leica) using a 63 × 1.32 oil-immersion objective. Photographs were taken using a Micromax CCD camera

(Princeton Scientific Instruments) driven by MetaMorph software (Molecular Devices). Images were processed with NIH ImageJ software.

smiFISH experiments

Cells transfected for 24 hr with hRluc-GFP-GC-rich or Rluc-GFP-AU-rich plasmids were fixed with 4% paraformaldehyde for 20 min at RT and permeabilized in 70% ethanol overnight at 4˚C. The sets of transcript-specific probes (***Supplementary file 2***) and the secondary Cy3 FLAP probe were designed, purchased and hybridized as previously described (***Tsanov et al., 2016***). Of note, none of the AU-rich probes and only 7 out of the 24 GC-rich probes hybridize to the GFP-LSM14A transcripts, resulting in either no signal or a faint signal which was easy to discriminate from the Rluc-GFP mRNA signal. Cells were further processed for immunostaining using rabbit polyclonal anti-DDX6 (1:2000; Novus Biological) and goat anti-rabbit Alexa Fluor 350 (1:300, Thermofisher) antibodies. Epifluorescence microscopy was performed on an inverted Zeiss Z1 microscope equipped with a motorized stage using a 63 × 1.32 oil immersion objective. Images were processed with Icy software.

Luciferase reporter assay

Cells transfected for 24 hr with Firefly control plasmid and hRluc-GFP-GC-rich or Rluc-GFP-AU-rich plasmids were harvested and processed for RNA (4/5) and protein (1/5) luciferase quantification. Total RNA was purified using Trizol (Invitrogen) and DNAse-treated (Turbo DNAse, Invitrogen). qRT-PCR was carried out as described in the corresponding section, and Renilla mRNA levels were normalized to the Firefly control. Luciferase protein assay was performed with the Dual Glo Luciferase assay kit (Promega) according to the manufacturer's instructions. Relative light determinations were measured in a Lumat LB 9507 luminometer (Berthold).

Western blot analysis

Total cell lysates were obtained as described previously (***Courel et al., 2006***). Proteins were separated on SDS-PAGE on 4–12% polyacrylamide gel (NuPage, Invitrogen) and transferred onto nitrocellulose membrane (PerkinElmer, France). After blocking in 5% (w/v) nonfat dry milk in PBS for 30 min at RT, the membrane was incubated for 1 hr at 37˚C with primary antibodies. After washing in PBS containing 0.05% (v/v) tween-20, blots were incubated for 40 min at RT with horseradish peroxidase-conjugated secondary anti-rabbit antibody (1:10000; Jackson Immunoresearch Laboratories). Immunoreactive bands were visualized by chemiluminescence detection of peroxidase activity (SuperSignal West Pico, Pierce) and exposure to CL-XPosure film (Pierce). Protein expression was evaluated by densitometry (NIH ImageJ).

For the shRNA XRN1 experiment, proteins were isolated using RIPA buffer with Halt Protease and Phosphatase Inhibitor Cocktail (Thermo Scientific), precipitated with acetone and separated on Tris-Acetate 3–8% polyacrylamide gel (NuPage, Invitrogen) before transfer to nitrocellulose membrane (GE Healthcare). After blocking with 5% (w/v) nonfat dry milk in TBST for 30 min at RT the membrane was incubated for 1 hr at RT or o/n at 4˚C with primary antibodies. After washing in TBST, blots were subsequently incubated for 1 hr at RT with horseradish peroxidase-conjugated secondary anti-rabbit/mouse antibodies (1:10000; Sigma). Immunoreactive bands were visualized by chemiluminescence detection of peroxidase activity (SuperSignal West Dura, Pierce) and imaged using ImageQuant LAS 4000 (GE Healthcare). Protein expression was evaluated by densitometry (NIH ImageJ).

Primary antibodies were: rabbit polyclonal anti-DDX6 (1:15000; Novus Biological), rabbit polyclonal anti-ribosomal S6 (1:5000; Cell Signaling Technology), rabbit polyclonal anti-XRN1 (1:1000, Bethyl Laboratories, and 1:5000 Novus Bioscience), rabbit polyclonal anti-Pol II (1:100, Santa Cruz), mouse monoclonal anti-tubulin (1:30000, Sigma-Aldrich). *q-RT-PCR analysis* Total RNA (1 µg) was reverse transcribed for 1 hr at 50˚C using the SuperScript II First-Strand Synthesis System for RT-PCR (Invitrogen) with 1 µg random primers (Promega). Reverse primers for Firefly and Renilla luciferases were also added for the luciferase reporter assay. No amplification was detected in negative controls omitting the reverse transcriptase. qPCR amplifications (12 µl) were done in duplicates using 1 µl of cDNA and the GoTaq Probe 2X Master Mix (Promega) on a LightCycler 480 (Roche), programmed as follows: 5 min, 95˚C; 40 cycles [10 s, 95˚C; 15 s, 60˚C; 10 s, 72˚C]. A last step (5 min progressive

95˚C to 72˚C) calculating the qPCR product Tm allowed for reaction specificity check. Primers for ACTB, APP, BACE1, LSM14A, LSM14B, MFN2, PNRC1, TIMP2, TRIB1, HPRT1, REN-low-GC, REN-high-GC and FIREfly were either gifts from R. Blaise or designed using the Primer three software (***Untergasser et al., 2012***). The results were normalized using either HPRT1 or FIREfly.

Library preparation and RNA-Seq data processing

For polysome profiling after DDX6 silencing and transcriptome after PAT1B silencing in HEK293 cells, rRNA was depleted using the Ribo-Zero kit Human/Mouse/Rat (Epicentre), and libraries were prepared using random priming. Triplicate and duplicate libraries were generated from three and two independent experiments, respectively, and processed as detailed previously (***Hubstenberger et al., 2017***; ***Vindry et al., 2017***).

For the transcriptome after XRN1 silencing in HeLa cells, libraries were prepared from 500 ng of total RNAs and oligo(dT) primed using TruSeq Stranded Total RNA kit (Illumina) with two technical replicates for each sample. Libraries were then quantified with KAPA Library Quantification kit (Kapa Biosystems) and pooled. 4 nM of this pool were loaded on a high output flowcell and sequenced on a NextSeq500 platform (Illumina) with 2 × 75 nt paired-end chemistry.

For the shRNA XRN1 experiment RNA was isolated using Quiazol and miRNeasy Mini Kit (Quiagen), next subjected to DNase treatment (Quiagen) and quality control with Bioanalyzer. The rRNA was removed using rRNA Removal Mix. Libraries were prepared from 1 ug of RNA following TruSeq Stranded Total RNA kit (Illumina) with two technical replicates for each sample. 100nt paired-end RNA-Seq was performed on HiSeq - Rapid Run (Illumina). The results were aligned using hg19 genome and DESeq2, with standard settings, was used for determining FC and p-values.

For PB enrichment, libraries were prepared without prior elimination of rRNA and using random priming. Triplicate libraries were generated from three independent experiments and processed using the same pipeline as for DDX6 silencing (***Hubstenberger et al., 2017***).

For the transcriptome after induction of a stably transfected DDX6 shRNA for 48 hr in K562 cells, the .fastq files from experiments ENCSR119QWQ (DDX6 shRNA) and ENCSR913CAE (control shRNA) were processed according to the same pipeline as DDX6 silencing, except that the control and DDX6 shRNA experiments were not paired to compute the corrected p-values of RNA differential expression in EdgeR_3.6.2.

The ENCODE dataset of mRNAs clipped to DDX6 in K562 cells was generated using ENCODE . bam files aligned on the hg19 genome corresponding to (i) the DDX6 eClip experiment ENCSR893EFU, and (ii) the total RNA-seq of K562 experiment ENCSR109IQO. The enrichment in the CLIP dataset compared to the total RNA sample was calculated as in the DDX6 shRNA experiment.

Bioinformatic analysis

Briefly, the read coverage was computed as follows. Raw reads were processed using trimmomatics. Alignment was performed on the longest transcript isoforms of Ensembl annotated genes with bowtie2 aligner. Isoforms shorter than 500 nucleotides were not considered. Only unique mapped reads were qualified for counting. Each transcript was subdivided in 20 bins from transcription start site (TSS) to transcript end site (TES) and the proportion of reads for each bin was computed. For the metagene analysis, the average distribution of reads along transcript length was computed so that each gene had the same weight independently of it expression level.

The protein yield was calculated as the ratio between protein abundance in HEK293 cells, taken from ***Geiger et al. (2012)***, and mRNA abundance in HEK293 cells, taken from the control sample of our DDX6 polysome profiling experiment. The translation rate was defined as the polysomal to total mRNA ratio, since polysome accumulation can result from both regulated translation and a change in total RNA without altered translation.

For GC profiling of the transcripts in various organisms (***Figure 7—figure supplement 1***), transcripts were downloaded from ENSEMBL (version 92) with their associated gene GC content.

Boxplot representations and statistical tests were performed using the GraphPad Prism software (GraphPad software, Inc) and the R suite (https://www.R-project.org) (R Core Team 2018. R: A language and environment for statistical computing. R Foundation for Statistical Computing, Vienna, Austria). We chose to systematically use the Spearman correlation in the interest of consistency, since the variables under consideration showed both nearly linear (e.g. accumulation in PBs and GC

content of the mRNA) and non-linear (e.g. accumulation in PBs and mRNA length) relationships. Statistical tests for differences between Spearman correlation coefficients were performed using the R package cocor and the 'meng1992' test. Partial correlations were computed using the ppcor package. Other graphical representations were generated using Excel and the Excel Analysis ToolPak (Microsoft). Hierarchical clustering of all transcripts in ***Figure 4E*** was performed using the Cluster 3.0/Treeview softwares (Kendall's tau distance, average linkage, ***de Hoon et al., 2004***). Heatmap representation of the targets of the various regulators in ***Figure 5B and D*** was performed online using Morpheus (https://software.broadinstitute.org/morpheus).

Gene meiotic recombination rates were computed as crossover rates between gene start and gene end using the genetic map from the HapMap project (***Frazer et al., 2007***). Rates were computed as the weighted average of crossover rates of chromosomal regions that overlap the window.

The enrichment of the GO SLIM categories of cellular component in AU-rich mRNA excluded from PB (Input database: 881 gene IDs, 558 annotated in GO categories) was assessed using the WebGestalt enrichment analysis web tool (***Liao et al., 2019***).

Datasets used in the bioinformatics analysis

The following datasets were downloaded from the supplementary material of the corresponding papers: 1) For mRNAs containing cis-regulatory motifs: (i) in silico identification: AREs (***Halees et al., 2008***); (ii) experimental determination: CPEs (***Piqué et al., 2008***), G4-containing (***Huppert et al., 2008***) and TOP mRNAs (***Thoreen et al., 2012***). G4-containing genes were restricted to those harboring a G4 in 5'UTR. 2) For RBP targets: (i) PARE in HeLa cells: SMG6 (mRNAs actually cleaved by SMG6) (***Schmidt et al., 2015***) (ii) CLIP in HEK293 cells: HuR and TTP (***Mukherjee et al., 2011***; ***Mukherjee et al., 2014***); (iii) CLIP in HeLa cells: YTHDF2 (***Wang et al., 2014***); (iv) RIP-CHIP in HeLa cells: PUM1 (***Galgano et al., 2008***); (v) RIP-CHIP in mouse neurons: 4E-T (***Yang et al., 2014***). In the case of HuR, the transcripts clipped only in 5'UTR/CDS/introns were removed, and the target list was restricted to transcripts clipped more than once. In the case of TTP, the transcripts clipped only in introns were removed.

For other RBP targets (ATXN2, MOV10, IGF2BP1-3, PUM2, FMR1, FXR1-2, AGO1-4, YTHDF2), CLIP data from different laboratories were previously processed through the same pipeline in the CLIPdb 1.0 database using the Piranha method (***Yang et al., 2015***). We retained those performed in epithelial cells (HeLa, HEK293, HEK293T). Moreover, when replicates were available, we selected the RNA-protein interactions detected in at least 50% of the replicates. Except for FXR1-2 targets, we determined whether protein-RNA interactions occurred in UTR or CDS by intersecting coordinates of the read peaks with the v19 gencode annotation, and we removed the transcripts clipped in their CDS.

For miRNA targets, we extracted the list of all experimentally documented targets from miRTarBase (http://mirtarbase.mbc.nctu.edu.tw/php/index.php) (***Hsu et al., 2014***), and selected the targets of the 22 miRNAs of interest.

Acknowledgements

We thank Marina Pinskaya and Marc Gabriel for scientific discussions and technical assistance. We also thank Virginie Magnone, Kevin Lebrigand (NGS platform, UCA Genomix), Sylvain Baulande, Patricia Legoix-Né, Virginie Raynal (NGS platform, Institut Curie), Nathalie Campo (LMGM, Toulouse) and Régis Blaise (IBPS, Paris).

Additional information

Funding

Funder	Grant reference number	Author
Association pour la Recherche sur le Cancer	Subvention Fixe	Dominique Weil
Agence Nationale de la Recherche	ANR-14-CE09-0013-01	Dominique Weil

European Research Council	DARK consolidator grant	Antonin Morillon
Agence Nationale de la Recherche	ANR-11-LABX-0028-01	Antonin Morillon
Canceropôle PACA		Patrick Brest
Biotechnology and Biological Sciences Research Council		Nancy Standart
Isaac Newton Trust		Nancy Standart
Fondation Philippe Wiener - Maurice Anspach		Nancy Standart

The funders had no role in study design, data collection and interpretation, or the decision to submit the work for publication.

Author contributions

Maïté Courel, Marianne Bénard, Conceptualization, Formal analysis, Supervision, Validation, Investigation, Visualization, Writing - original draft, Writing - review and editing; Yves Clément, Dominika Foretek, Olivia Vidal Cruchez, Michèle Ernoult-Lange, Conceptualization, Formal analysis, Validation, Investigation, Visualization, Writing - original draft, Writing - review and editing; Clémentine Bossevain, Conceptualization, Formal analysis, Investigation, Visualization, Writing - original draft, Writing - review and editing; Zhou Yi, Conceptualization, Software, Formal analysis, Validation, Investigation, Writing - original draft, Writing - review and editing; Marie-Noëlle Benassy, Formal analysis, Validation, Investigation, Visualization, Writing - original draft, Writing - review and editing; Michel Kress, Conceptualization, Formal analysis, Supervision, Validation, Investigation, Writing - original draft, Writing - review and editing; Caroline Vindry, Conceptualization, Formal analysis, Validation, Investigation, Writing - original draft, Writing - review and editing; Christophe Antoniewski, Conceptualization, Resources, Formal analysis, Writing - original draft, Writing - review and editing; Antonin Morillon, Patrick Brest, Nancy Standart, Conceptualization, Supervision, Funding acquisition, Writing - original draft, Writing - review and editing; Arnaud Hubstenberger, Conceptualization, Supervision, Writing - original draft, Writing - review and editing; Hugues Roest Crollius, Conceptualization, Formal analysis, Supervision, Writing - original draft, Writing - review and editing; Dominique Weil, Conceptualization, Formal analysis, Supervision, Funding acquisition, Validation, Investigation, Visualization, Writing - original draft, Project administration, Writing - review and editing

Author ORCIDs

Yves Clément http://orcid.org/0000-0002-5932-9412
Christophe Antoniewski http://orcid.org/0000-0001-7709-2116
Antonin Morillon http://orcid.org/0000-0002-0575-5264
Hugues Roest Crollius http://orcid.org/0000-0002-8209-173X
Dominique Weil https://orcid.org/0000-0001-7630-1772

Decision letter and Author response

Decision letter https://doi.org/10.7554/eLife.49708.sa1
Author response https://doi.org/10.7554/eLife.49708.sa2

Additional files

Supplementary files

- Supplementary file 1. Transcriptome datasets. Sheet1: polysome profiling after siDDX6 in HEK293 cells. Sheet2: transcriptome after shDDX6 in K562 cells. Sheet3: DDX6 CLIP in K562 cells. Sheet4: transcriptome after siXRN1 in HeLa cells. Sheet5: transcriptome after shXRN1 in HCT116 cells. Sheet6: transcriptome after siPAT1B in HEK293 cells.
- Supplementary file 2. SmiFISH probes sets. Sheet1: AU-rich probes Sheet2: GC-rich probes.
- Transparent reporting form

Data availability

RNA-Seq gene data have been deposited in SRA under accession codes E-MTAB-4091 for the polysome profiling after DDX6 silencing, E-MTAB-5577 for the transcriptome after PAT1B silencing, and E-MTAB-5477 for the PB transcriptome, all in HEK293 cells. RNA-Seq gene data have been deposited in GEO under accession codes GSE115471 and GSE114605 for the transcriptome after XRN1 silencing in HeLa and HCT116 cells, respectively. ENCODE datasets are available at https://www.encodeproject.org under accession codes ENCSR893EFU for the DDX6 eClip experiment, and ENCSR109IQO for the transcriptome after DDX6 silencing in K562 cells. All data generated or analyzed during this study are included in Supplementary file 1.

The following datasets were generated:

Author(s)	Year	Dataset title	Dataset URL	Database and Identifier
Courel M, Weil D	2017	Large-scale study of total and polysomial mRNA after DDX6 depletion in HEK293 cells	https://www.ebi.ac.uk/arrayexpress/experiments/E-MTAB-4091/	ArrayExpress, E-MTAB-4091
Vindry C	2017	RNA-seq of HEK293T cells treated with control b-globin siRNA and Pat1b siRNA	https://www.ebi.ac.uk/arrayexpress/experiments/E-MTAB-5577/	ArrayExpress, E-MTAB-5577
Hubstenberger A	2017	RNA-Seq of purified P-bodies from HEK293 cells	https://www.ebi.ac.uk/arrayexpress/experiments/E-MTAB-5477/	ArrayExpress, E-MTAB-5477

References

Ayache J, Bénard M, Ernoult-Lange M, Minshall N, Standart N, Kress M, Weil D. 2015. P-body assembly requires DDX6 repression complexes rather than decay or Ataxin2/2L complexes. *Molecular Biology of the Cell* **26**: 2579–2595. DOI: https://doi.org/10.1091/mbc.E15-03-0136, PMID: 25995375

Balak C, Benard M, Schaefer E, Iqbal S, Ramsey K, Ernoult-Lange M, Mattioli F, Llaci L, Geoffroy V, Courel M, Naymik M, Bachman KK, Pfundt R, Rump P, Ter Beest J, Wentzensen IM, Monaghan KG, McWalter K, Richholt R, Le Béchec A, et al. 2019. Rare de novo missense variants in RNA helicase DDX6 cause intellectual disability and dysmorphic features and lead to P-Body defects and RNA dysregulation. *The American Journal of Human Genetics* **105**:509–525. DOI: https://doi.org/10.1016/j.ajhg.2019.07.010, PMID: 31422817

Barbee SA, Estes PS, Cziko AM, Hillebrand J, Luedeman RA, Coller JM, Johnson N, Howlett IC, Geng C, Ueda R, Brand AH, Newbury SF, Wilhelm JE, Levine RB, Nakamura A, Parker R, Ramaswami M. 2006. Staufen- and FMRP-containing neuronal RNPs are structurally and functionally related to somatic P bodies. *Neuron* **52**:997–1009. DOI: https://doi.org/10.1016/j.neuron.2006.10.028, PMID: 17178403

Bashkirov VI, Scherthan H, Solinger JA, Buerstedde JM, Heyer WD. 1997. A mouse cytoplasmic exoribonuclease (mXRN1p) with preference for G4 tetraplex substrates. *The Journal of Cell Biology* **136**:761–773. DOI: https://doi.org/10.1083/jcb.136.4.761, PMID: 9049243

Bazzini AA, Del Viso F, Moreno-Mateos MA, Johnstone TG, Vejnar CE, Qin Y, Yao J, Khokha MK, Giraldez AJ. 2016. Codon identity regulates mRNA stability and translation efficiency during the maternal-to-zygotic transition. *The EMBO Journal* **35**:2087–2103. DOI: https://doi.org/10.15252/embj.201694699, PMID: 27436874

Bhattacharyya SN, Habermacher R, Martine U, Closs EI, Filipowicz W. 2006. Relief of microRNA-mediated translational repression in human cells subjected to stress. *Cell* **125**:1111–1124. DOI: https://doi.org/10.1016/j.cell.2006.04.031, PMID: 16777601

Bish R, Cuevas-Polo N, Cheng Z, Hambardzumyan D, Munschauer M, Landthaler M, Vogel C. 2015. Comprehensive protein interactome analysis of a key RNA helicase: detection of novel stress granule proteins. *Biomolecules* **5**:1441–1466. DOI: https://doi.org/10.3390/biom5031441, PMID: 26184334

Blaise R, Mateo V, Rouxel C, Zaccarini F, Glorian M, Bérériat G, Golubkov VS, Limon I. 2012. Wild-type amyloid beta 1-40 peptide induces vascular smooth muscle cell death independently from matrix metalloprotease activity. *Aging Cell* **11**:384–393. DOI: https://doi.org/10.1111/j.1474-9726.2012.00797.x, PMID: 22260497

Bonnerot C, Boeck R, Lapeyre B. 2000. The two proteins Pat1p (Mrt1p) and Spb8p interact in vivo, are required for mRNA decay, and are functionally linked to Pab1p. *Molecular and Cellular Biology* **20**:5939–5946. DOI: https://doi.org/10.1128/MCB.20.16.5939-5946.2000, PMID: 10913177

Bouveret E, Rigaut G, Shevchenko A, Wilm M, Séraphin B. 2000. A Sm-like protein complex that participates in mRNA degradation. *The EMBO Journal* **19**:1661–1671. DOI: https://doi.org/10.1093/emboj/19.7.1661, PMID: 10747033

Braun JE, Tritschler F, Haas G, Igreja C, Truffault V, Weichenrieder O, Izaurralde E. 2010. The C-terminal alpha-alpha superhelix of pat is required for mRNA decapping in metazoa. *The EMBO Journal* **29**:2368–2380. DOI: https://doi.org/10.1038/emboj.2010.124, PMID: 20543818

Chan LY, Mugler CF, Heinrich S, Vallotton P, Weis K. 2018. Non-invasive measurement of mRNA decay reveals translation initiation as the major determinant of mRNA stability. *eLife* **7**:e32536. DOI: https://doi.org/10.7554/eLife.32536, PMID: 30192227

Chen Y, Boland A, Kuzuoğlu-Öztürk D, Bawankar P, Loh B, Chang CT, Weichenrieder O, Izaurralde E. 2014. A DDX6-CNOT1 complex and W-binding pockets in CNOT9 reveal direct links between miRNA target recognition and silencing. *Molecular Cell* **54**:737–750. DOI: https://doi.org/10.1016/j.molcel.2014.03.034, PMID: 24768540

Chu CY, Rana TM. 2006. Translation repression in human cells by MicroRNA-Induced gene silencing requires RCK/p54. *PLOS Biology* **4**:e210. DOI: https://doi.org/10.1371/journal.pbio.0040210, PMID: 16756390

Coller J, Parker R. 2005. General translational repression by activators of mRNA decapping. *Cell* **122**:875–886. DOI: https://doi.org/10.1016/j.cell.2005.07.012, PMID: 16179257

Colombo M, Karousis ED, Bourquin J, Bruggmann R, Mühlemann O. 2017. Transcriptome-wide identification of NMD-targeted human mRNAs reveals extensive redundancy between SMG6- and SMG7-mediated degradation pathways. *RNA* **23**:189–201. DOI: https://doi.org/10.1261/rna.059055.116, PMID: 27864472

Courel M, Rodemer C, Nguyen ST, Pance A, Jackson AP, O'connor DT, Taupenot L. 2006. Secretory granule biogenesis in sympathoadrenal cells: identification of a granulogenic determinant in the secretory prohormone chromogranin A. *The Journal of Biological Chemistry* **281**:38038–38051. DOI: https://doi.org/10.1074/jbc.M604037200, PMID: 17032650

de Hoon MJ, Imoto S, Nolan J, Miyano S. 2004. Open source clustering software. *Bioinformatics* **20**:1453–1454. DOI: https://doi.org/10.1093/bioinformatics/bth078, PMID: 14871861

Duret L, Semon M, Piganeau G, Mouchiroud D, Galtier N. 2002. Vanishing GC-rich isochores in mammalian genomes. *Genetics* **162**:1837–1847. PMID: 12524353

Duret L, Galtier N. 2009. Biased gene conversion and the evolution of mammalian genomic landscapes. *Annual Review of Genomics and Human Genetics* **10**:285–311. DOI: https://doi.org/10.1146/annurev-genom-082908-150001, PMID: 19630562

ENCODE Project Consortium. 2012. An integrated encyclopedia of DNA elements in the human genome. *Nature* **489**:57–74. DOI: https://doi.org/10.1038/nature11247, PMID: 22955616

Ernoult-Lange M, Wilczynska A, Harper M, Aigueperse C, Dautry F, Kress M, Weil D. 2009. Nucleocytoplasmic traffic of CPEB1 and accumulation in Crm1 nucleolar bodies. *Molecular Biology of the Cell* **20**:176–187. DOI: https://doi.org/10.1091/mbc.e08-09-0904, PMID: 18923137

Ernoult-Lange M, Baconnais S, Harper M, Minshall N, Souquere S, Boudier T, Bénard M, Andrey P, Pierron G, Kress M, Standart N, le Cam E, Weil D. 2012. Multiple binding of repressed mRNAs by the P-body protein rck/p54. *RNA* **18**:1702–1715. DOI: https://doi.org/10.1261/rna.034314.112, PMID: 22836354

Evans ME, Clark WC, Zheng G, Pan T. 2017. Determination of tRNA aminoacylation levels by high-throughput sequencing. *Nucleic Acids Research* **45**:e133. DOI: https://doi.org/10.1093/nar/gkx514, PMID: 28586482

Ferraiuolo MA, Basak S, Dostie J, Murray EL, Schoenberg DR, Sonenberg N. 2005. A role for the eIF4E-binding protein 4E-T in P-body formation and mRNA decay. *The Journal of Cell Biology* **170**:913–924. DOI: https://doi.org/10.1083/jcb.200504039, PMID: 16157702

Franks TM, Lykke-Andersen J. 2007. TTP and BRF proteins nucleate processing body formation to silence mRNAs with AU-rich elements. *Genes & Development* **21**:719–735. DOI: https://doi.org/10.1101/gad.1494707, PMID: 17369404

Frazer KA, Ballinger DG, Cox DR, Hinds DA, Stuve LL, Gibbs RA, Belmont JW, Boudreau A, Hardenbol P, Leal SM, Pasternak S, Wheeler DA, Willis TD, Yu F, Yang H, Zeng C, Gao Y, Hu H, Hu W, Li C, et al. 2007. A second generation human haplotype map of over 3.1 million SNPs. *Nature* **449**:851–861. DOI: https://doi.org/10.1038/nature06258, PMID: 17943122

Freimer JW, Hu TJ, Blelloch R. 2018. Decoupling the impact of microRNAs on translational repression versus RNA degradation in embryonic stem cells. *eLife* **7**:e38014. DOI: https://doi.org/10.7554/eLife.38014, PMID: 30044225

Galgano A, Forrer M, Jaskiewicz L, Kanitz A, Zavolan M, Gerber AP. 2008. Comparative analysis of mRNA targets for human PUF-family proteins suggests extensive interaction with the miRNA regulatory system. *PLOS ONE* **3**:e3164. DOI: https://doi.org/10.1371/journal.pone.0003164, PMID: 18776931

Geiger T, Wehner A, Schaab C, Cox J, Mann M. 2012. Comparative proteomic analysis of eleven common cell lines reveals ubiquitous but varying expression of most proteins. *Molecular & Cellular Proteomics* **11**:M111.014050. DOI: https://doi.org/10.1074/mcp.M111.014050, PMID: 22278370

Gingold H, Tehler D, Christoffersen NR, Nielsen MM, Asmar F, Kooistra SM, Christophersen NS, Christensen LL, Borre M, Sørensen KD, Andersen LD, Andersen CL, Hulleman E, Wurdinger T, Ralfkiær E, Helin K, Grønbæk K, Ørntoft T, Waszak SM, Dahan O, et al. 2014. A dual program for translation regulation in cellular proliferation and differentiation. *Cell* **158**:1281–1292. DOI: https://doi.org/10.1016/j.cell.2014.08.011, PMID: 25215487

Götze M, Dufour J, Ihling C, Rammelt C, Pierson S, Sambrani N, Temme C, Sinz A, Simonelig M, Wahle E. 2017. Translational repression of the *Drosophila Nanos* mRNA involves the RNA helicase Belle and RNA coating by Me31B and Trailer hitch. *RNA* **23**:1552–1568. DOI: https://doi.org/10.1261/rna.062208.117, PMID: 28701521

Hafner M, Landthaler M, Burger L, Khorshid M, Hausser J, Berninger P, Rothballer A, Ascano M, Jungkamp AC, Munschauer M, Ulrich A, Wardle GS, Dewell S, Zavolan M, Tuschl T. 2010. Transcriptome-wide identification of RNA-binding protein and microRNA target sites by PAR-CLIP. *Cell* **141**:129–141. DOI: https://doi.org/10.1016/j.cell.2010.03.009, PMID: 20371350

Halees AS, El-Badrawi R, Khabar KS. 2008. ARED organism: expansion of ARED reveals AU-rich element cluster variations between human and mouse. *Nucleic Acids Research* **36**:D137–D140. DOI: https://doi.org/10.1093/nar/gkm959, PMID: 17984078

He F, Celik A, Wu C, Jacobson A. 2018. General decapping activators target different subsets of inefficiently translated mRNAs. *eLife* **7**:e34409. DOI: https://doi.org/10.7554/eLife.34409, PMID: 30520724

Hentze MW, Castello A, Schwarzl T, Preiss T. 2018. A brave new world of RNA-binding proteins. *Nature Reviews Molecular Cell Biology* **19**:327–341. DOI: https://doi.org/10.1038/nrm.2017.130, PMID: 29339797

Horvathova I, Voigt F, Kotrys AV, Zhan Y, Artus-Revel CG, Eglinger J, Stadler MB, Giorgetti L, Chao JA. 2017. The dynamics of mRNA turnover revealed by Single-Molecule imaging in single cells. *Molecular Cell* **68**:615–625. DOI: https://doi.org/10.1016/j.molcel.2017.09.030, PMID: 29056324

Hsu SD, Tseng YT, Shrestha S, Lin YL, Khaleel A, Chou CH, Chu CF, Huang HY, Lin CM, Ho SY, Jian TY, Lin FM, Chang TH, Weng SL, Liao KW, Liao IE, Liu CC, Huang HD. 2014. miRTarBase update 2014: an information resource for experimentally validated miRNA-target interactions. *Nucleic Acids Research* **42**:D78–D85. DOI: https://doi.org/10.1093/nar/gkt1266, PMID: 24304892

Huang N, Lee I, Marcotte EM, Hurles ME. 2010. Characterising and predicting haploinsufficiency in the human genome. *PLOS Genetics* **6**:e1001154. DOI: https://doi.org/10.1371/journal.pgen.1001154, PMID: 20976243

Hubstenberger A, Courel M, Bénard M, Souquere S, Ernoult-Lange M, Chouaib R, Yi Z, Morlot JB, Munier A, Fradet M, Daunesse M, Bertrand E, Pierron G, Mozziconacci J, Kress M, Weil D. 2017. P-Body purification reveals the condensation of repressed mRNA regulons. *Molecular Cell* **68**:144–157. DOI: https://doi.org/10.1016/j.molcel.2017.09.003, PMID: 28965817

Huppert JL, Bugaut A, Kumari S, Balasubramanian S. 2008. G-quadruplexes: the beginning and end of UTRs. *Nucleic Acids Research* **36**:6260–6268. DOI: https://doi.org/10.1093/nar/gkn511, PMID: 18832370

Imamachi N, Salam KA, Suzuki Y, Akimitsu N. 2017. A GC-rich sequence feature in the 3' UTR directs UPF1-dependent mRNA decay in mammalian cells. *Genome Research* **27**:407–418. DOI: https://doi.org/10.1101/gr.206060.116, PMID: 27940950

Kamenska A, Lu WT, Kubacka D, Broomhead H, Minshall N, Bushell M, Standart N. 2014. Human 4E-T represses translation of bound mRNAs and enhances microRNA-mediated silencing. *Nucleic Acids Research* **42**:3298–3313. DOI: https://doi.org/10.1093/nar/gkt1265, PMID: 24335285

Kamenska A, Simpson C, Vindry C, Broomhead H, Bénard M, Ernoult-Lange M, Lee BP, Harries LW, Weil D, Standart N. 2016. The DDX6-4E-T interaction mediates translational repression and P-body assembly. *Nucleic Acids Research* **44**:6318–6334. DOI: https://doi.org/10.1093/nar/gkw565, PMID: 27342281

Khong A, Matheny T, Jain S, Mitchell SF, Wheeler JR, Parker R. 2017. The stress granule transcriptome reveals principles of mRNA accumulation in stress granules. *Molecular Cell* **68**:808–820. DOI: https://doi.org/10.1016/j.molcel.2017.10.015, PMID: 29129640

Łabno A, Tomecki R, Dziembowski A. 2016. Cytoplasmic RNA decay pathways - Enzymes and mechanisms. *Biochimica Et Biophysica Acta (BBA) - Molecular Cell Research* **1863**:3125–3147. DOI: https://doi.org/10.1016/j.bbamcr.2016.09.023, PMID: 27713097

Lebedeva S, Jens M, Theil K, Schwanhäusser B, Selbach M, Landthaler M, Rajewsky N. 2011. Transcriptome-wide analysis of regulatory interactions of the RNA-binding protein HuR. *Molecular Cell* **43**:340–352. DOI: https://doi.org/10.1016/j.molcel.2011.06.008, PMID: 21723171

Liao Y, Wang J, Jaehnig EJ, Shi Z, Zhang B. 2019. WebGestalt 2019: gene set analysis toolkit with revamped UIs and APIs. *Nucleic Acids Research* **47**:W199–W205. DOI: https://doi.org/10.1093/nar/gkz401, PMID: 31114916

Liu J, Valencia-Sanchez MA, Hannon GJ, Parker R. 2005. MicroRNA-dependent localization of targeted mRNAs to mammalian P-bodies. *Nature Cell Biology* **7**:719–723. DOI: https://doi.org/10.1038/ncb1274, PMID: 15937477

Martin B, Granadel C, Campo N, Hénard V, Prudhomme M, Claverys JP. 2010. Expression and maintenance of ComD-ComE, the two-component signal-transduction system that controls competence of *Streptococcus pneumoniae*. *Molecular Microbiology* **75**:1513–1528. DOI: https://doi.org/10.1111/j.1365-2958.2010.07071.x, PMID: 20180906

Mathys H, Basquin J, Ozgur S, Czarnocki-Cieciura M, Bonneau F, Aartse A, Dziembowski A, Nowotny M, Conti E, Filipowicz W. 2014. Structural and biochemical insights to the role of the CCR4-NOT complex and DDX6 ATPase in microRNA repression. *Molecular Cell* **54**:751–765. DOI: https://doi.org/10.1016/j.molcel.2014.03.036, PMID: 24768538

Minshall N, Reiter MH, Weil D, Standart N. 2007. CPEB interacts with an ovary-specific eIF4E and 4E-T in early xenopus oocytes. *The Journal of Biological Chemistry* **282**:37389–37401. DOI: https://doi.org/10.1074/jbc.M704629200, PMID: 17942399

Minshall N, Kress M, Weil D, Standart N. 2009. Role of p54 RNA helicase activity and its C-terminal domain in translational repression, P-body localization and assembly. *Molecular Biology of the Cell* **20**:2464–2472. DOI: https://doi.org/10.1091/mbc.e09-01-0035, PMID: 19297524

Mitchell SF, Jain S, She M, Parker R. 2013. Global analysis of yeast mRNPs. *Nature Structural & Molecular Biology* **20**:127–133. DOI: https://doi.org/10.1038/nsmb.2468, PMID: 23222640

Mukherjee N, Corcoran DL, Nusbaum JD, Reid DW, Georgiev S, Hafner M, Ascano M, Tuschl T, Ohler U, Keene JD. 2011. Integrative regulatory mapping indicates that the RNA-binding protein HuR couples pre-mRNA processing and mRNA stability. *Molecular Cell* **43**:327–339. DOI: https://doi.org/10.1016/j.molcel.2011.06.007, PMID: 21723170

Mukherjee N, Jacobs NC, Hafner M, Kennington EA, Nusbaum JD, Tuschl T, Blackshear PJ, Ohler U. 2014. Global target mRNA specification and regulation by the RNA-binding protein ZFP36. *Genome Biology* **15**:R12. DOI: https://doi.org/10.1186/gb-2014-15-1-r12, PMID: 24401661

Nissan T, Rajyaguru P, She M, Song H, Parker R. 2010. Decapping activators in Saccharomyces cerevisiae act by multiple mechanisms. *Molecular Cell* **39**:773–783. DOI: https://doi.org/10.1016/j.molcel.2010.08.025, PMID: 20832728

Nonhoff U, Ralser M, Welzel F, Piccini I, Balzereit D, Yaspo ML, Lehrach H, Krobitsch S. 2007. Ataxin-2 interacts with the DEAD/H-box RNA helicase DDX6 and interferes with P-bodies and stress granules. *Molecular Biology of the Cell* **18**:1385–1396. DOI: https://doi.org/10.1091/mbc.e06-12-1120, PMID: 17392519

Novoa EM, Ribas de Pouplana L. 2012. Speeding with control: codon usage, tRNAs, and ribosomes. *Trends in Genetics* **28**:574–581. DOI: https://doi.org/10.1016/j.tig.2012.07.006, PMID: 22921354

Ozgur S, Chekulaeva M, Stoecklin G. 2010. Human Pat1b connects deadenylation with mRNA decapping and controls the assembly of processing bodies. *Molecular and Cellular Biology* **30**:4308–4323. DOI: https://doi.org/10.1128/MCB.00429-10, PMID: 20584987

Ozgur S, Basquin J, Kamenska A, Filipowicz W, Standart N, Conti E. 2015. Structure of a human 4E-T/DDX6/CNOT1 complex reveals the different interplay of DDX6-Binding proteins with the CCR4-NOT complex. *Cell Reports* **13**:703–711. DOI: https://doi.org/10.1016/j.celrep.2015.09.033, PMID: 26489469

Pashler AL, Towler BP, Jones CI, Newbury SF. 2016. The roles of the exoribonucleases DIS3L2 and XRN1 in human disease. *Biochemical Society Transactions* **44**:1377–1384. DOI: https://doi.org/10.1042/BST20160107, PMID: 27911720

Piqué M, López JM, Foissac S, Guigó R, Méndez R. 2008. A combinatorial code for CPE-mediated translational control. *Cell* **132**:434–448. DOI: https://doi.org/10.1016/j.cell.2007.12.038, PMID: 18267074

Radhakrishnan A, Chen YH, Martin S, Alhusaini N, Green R, Coller J. 2016. The DEAD-Box protein Dhh1p couples mRNA decay and translation by monitoring Codon optimality. *Cell* **167**:122–132. DOI: https://doi.org/10.1016/j.cell.2016.08.053, PMID: 27641505

Rudolph KL, Schmitt BM, Villar D, White RJ, Marioni JC, Kutter C, Odom DT. 2016. Codon-Driven translational efficiency is stable across diverse mammalian cell states. *PLOS Genetics* **12**:e1006024. DOI: https://doi.org/10.1371/journal.pgen.1006024, PMID: 27166679

Schmidt SA, Foley PL, Jeong DH, Rymarquis LA, Doyle F, Tenenbaum SA, Belasco JG, Green PJ. 2015. Identification of SMG6 cleavage sites and a preferred RNA cleavage motif by global analysis of endogenous NMD targets in human cells. *Nucleic Acids Research* **43**:309–323. DOI: https://doi.org/10.1093/nar/gku1258, PMID: 25429978

Serman A, Le Roy F, Aigueperse C, Kress M, Dautry F, Weil D. 2007. GW body disassembly triggered by siRNAs independently of their silencing activity. *Nucleic Acids Research* **35**:4715–4727. DOI: https://doi.org/10.1093/nar/gkm491, PMID: 17604308

Standart N, Minshall N. 2008. Translational control in early development: cpeb, P-bodies and germinal granules. *Biochemical Society Transactions* **36**:671–676. DOI: https://doi.org/10.1042/BST0360671, PMID: 18631138

Standart N, Weil D. 2018. P-Bodies: cytosolic droplets for coordinated mRNA storage. *Trends in Genetics* **34**:612–626. DOI: https://doi.org/10.1016/j.tig.2018.05.005, PMID: 29908710

Steinberg J, Honti F, Meader S, Webber C. 2015. Haploinsufficiency predictions without study Bias. *Nucleic Acids Research* **43**:e101. DOI: https://doi.org/10.1093/nar/gkv474, PMID: 26001969

Tesina P, Heckel E, Cheng J, Fromont-Racine M, Buschauer R, Kater L, Beatrix B, Berninghausen O, Jacquier A, Becker T, Beckmann R. 2019. Structure of the 80S ribosome-Xrn1 nuclease complex. *Nature Structural & Molecular Biology* **26**:275–280. DOI: https://doi.org/10.1038/s41594-019-0202-5, PMID: 30911188

Thoreen CC, Chantranupong L, Keys HR, Wang T, Gray NS, Sabatini DM. 2012. A unifying model for mTORC1-mediated regulation of mRNA translation. *Nature* **485**:109–113. DOI: https://doi.org/10.1038/nature11083, PMID: 22552098

Totaro A, Renzi F, La Fata G, Mattioli C, Raabe M, Urlaub H, Achsel T. 2011. The human Pat1b protein: a novel mRNA deadenylation factor identified by a new immunoprecipitation technique. *Nucleic Acids Research* **39**:635–647. DOI: https://doi.org/10.1093/nar/gkq797, PMID: 20852261

Tsanov N, Samacoits A, Chouaib R, Traboulsi AM, Gostan T, Weber C, Zimmer C, Zibara K, Walter T, Peter M, Bertrand E, Mueller F. 2016. smiFISH and FISH-quant - a flexible single RNA detection approach with super-resolution capability. *Nucleic Acids Research* **44**:e165. DOI: https://doi.org/10.1093/nar/gkw784, PMID: 27599845

Untergasser A, Cutcutache I, Koressaar T, Ye J, Faircloth BC, Remm M, Rozen SG. 2012. Primer3–new capabilities and interfaces. *Nucleic Acids Research* **40**:e115. DOI: https://doi.org/10.1093/nar/gks596, PMID: 22730293

Vindry C, Marnef A, Broomhead H, Twyffels L, Ozgur S, Stoecklin G, Llorian M, Smith CW, Mata J, Weil D, Standart N. 2017. Dual RNA processing roles of Pat1b via cytoplasmic Lsm1-7 and nuclear Lsm2-8 complexes. *Cell Reports* **20**:1187–1200. DOI: https://doi.org/10.1016/j.celrep.2017.06.091, PMID: 28768202

Vindry C, Weil D, Standart N. 2019. Pat1 rna-binding proteins: multitasking shuttling proteins. *Wiley Interdisciplinary Reviews. RNA* **10**:e1557. DOI: https://doi.org/10.1002/wrna.1557, PMID: 31231973

Wang X, Lu Z, Gomez A, Hon GC, Yue Y, Han D, Fu Y, Parisien M, Dai Q, Jia G, Ren B, Pan T, He C. 2014. N6-methyladenosine-dependent regulation of messenger RNA stability. *Nature* **505**:117–120. DOI: https://doi.org/10.1038/nature12730, PMID: 24284625

Wang M, Ly M, Lugowski A, Laver JD, Lipshitz HD, Smibert CA, Rissland OS. 2017. ME31B globally represses maternal mRNAs by two distinct mechanisms during the *Drosophila* maternal-to-zygotic transition. *eLife* **6**: e27891. DOI: https://doi.org/10.7554/eLife.27891, PMID: 28875934

Wells ML, Perera L, Blackshear PJ. 2017. An ancient family of RNA-Binding proteins: still important!. *Trends in Biochemical Sciences* **42**:285–296. DOI: https://doi.org/10.1016/j.tibs.2016.12.003, PMID: 28096055

Yang G, Smibert CA, Kaplan DR, Miller FD. 2014. An eIF4E1/4E-T complex determines the genesis of neurons from precursors by translationally repressing a proneurogenic transcription program. *Neuron* **84**:723–739. DOI: https://doi.org/10.1016/j.neuron.2014.10.022, PMID: 25456498

Yang YC, Di C, Hu B, Zhou M, Liu Y, Song N, Li Y, Umetsu J, Lu ZJ. 2015. CLIPdb: a CLIP-seq database for protein-RNA interactions. *BMC Genomics* **16**:51. DOI: https://doi.org/10.1186/s12864-015-1273-2, PMID: 25652745

Yoon JH, De S, Srikantan S, Abdelmohsen K, Grammatikakis I, Kim J, Kim KM, Noh JH, White EJ, Martindale JL, Yang X, Kang MJ, Wood WH, Noren Hooten N, Evans MK, Becker KG, Tripathi V, Prasanth KV, Wilson GM, Tuschl T, et al. 2014. PAR-CLIP analysis uncovers AUF1 impact on target RNA fate and genome integrity. *Nature Communications* **5**:5248. DOI: https://doi.org/10.1038/ncomms6248, PMID: 25366541

Bibliographie

Adivarahan, S., Livingston, N., Nicholson, B., Rahman, S., Wu, B., Rissland, O.S., and Zenklusen, D. (2018). Spatial Organization of Single mRNPs at Different Stages of the Gene Expression Pathway. Mol. Cell *72*, 727-738.e5.

Afroz, T., Cienikova, Z., Cléry, A., and Allain, F.H.T. (2015). Chapter Nine - One, Two, Three, Four! How Multiple RRMs Read the Genome Sequence. In Methods in Enzymology, S.A. Woodson, and F.H.T. Allain, eds. (Academic Press), pp. 235–278.

Aizer, A., Kalo, A., Kafri, P., Shraga, A., Ben-Yishay, R., Jacob, A., Kinor, N., and Shav-Tal, Y. (2014). Quantifying mRNA targeting to P-bodies in living human cells reveals their dual role in mRNA decay and storage. J Cell Sci *127*, 4443–4456.

Alberti, S. (2017). Phase separation in biology. Current Biology *27*, R1097–R1102.

Albrecht, M., and Lengauer, T. (2004). Novel Sm-like proteins with long C-terminal tails and associated methyltransferases. FEBS Letters *569*, 18–26.

Alekhina, O.M., Terenin, I.M., Dmitriev, S.E., and Vassilenko, K.S. (2020). Functional Cyclization of Eukaryotic mRNAs. Int J Mol Sci *21*.

Algire, M.A., Maag, D., and Lorsch, J.R. (2005). Pi release from eIF2, not GTP hydrolysis, is the step controlled by start-site selection during eukaryotic translation initiation. Mol. Cell *20*, 251–262.

Amadei, G., Zander, M.A., Yang, G., Dumelie, J.G., Vessey, J.P., Lipshitz, H.D., Smibert, C.A., Kaplan, D.R., and Miller, F.D. (2015). A Smaug2-Based Translational Repression Complex Determines the Balance between Precursor Maintenance versus Differentiation during Mammalian Neurogenesis. J Neurosci *35*, 15666–15681.

Andrei, M.A. (2005). A role for eIF4E and eIF4E-transporter in targeting mRNPs to mammalian processing bodies. RNA *11*, 717–727.

Änkö, M.-L., Müller-McNicoll, M., Brandl, H., Curk, T., Gorup, C., Henry, I., Ule, J., and Neugebauer, K.M. (2012). The RNA-binding landscapes of two SR proteins reveal unique functions and binding to diverse RNA classes. Genome Biol *13*, R17.

Antic, S., Wolfinger, M.T., Skucha, A., Hosiner, S., and Dorner, S. (2015). General and MicroRNA-Mediated mRNA Degradation Occurs on Ribosome Complexes in Drosophila Cells. Molecular and Cellular Biology *35*, 2309–2320.

Araki, Y., Takahashi, S., Kobayashi, T., Kajiho, H., Hoshino, S., and Katada, T. (2001). Ski7p G protein interacts with the exosome and the Ski complex for 3'-to-5' mRNA decay in yeast. EMBO J *20*, 4684–4693.

Archer, S.K., Shirokikh, N.E., Hallwirth, C.V., Beilharz, T.H., and Preiss, T. (2015). Probing the closed-loop model of mRNA translation in living cells. RNA Biol *12*, 248–254.

Arribas-Layton, M., Wu, D., Lykke-Andersen, J., and Song, H. (2013). Structural and functional control of the eukaryotic mRNA decapping machinery. Biochim Biophys Acta *1829*, 580–589.

Ascano, M., Hafner, M., Cekan, P., Gerstberger, S., and Tuschl, T. (2012). Identification of RNA-protein interaction networks using PAR-CLIP. Wiley Interdiscip Rev RNA *3*, 159–177.

Aslam, A., Mittal, S., Koch, F., Andrau, J.-C., and Winkler, G.S. (2009). The Ccr4–Not Deadenylase Subunits CNOT7 and CNOT8 Have Overlapping Roles and Modulate Cell Proliferation. Mol Biol Cell *20*, 3840–3850.

Aviram, N., and Schuldiner, M. (2017). Targeting and translocation of proteins to the endoplasmic reticulum at a glance. J. Cell. Sci. *130*, 4079–4085.

Ayache, J., Bénard, M., Ernoult-Lange, M., Minshall, N., Standart, N., Kress, M., and Weil, D. (2015). P-body assembly requires DDX6 repression complexes rather than decay or Ataxin2/2L complexes. Mol. Biol. Cell *26*, 2579–2595.

Baek, D., Villén, J., Shin, C., Camargo, F.D., Gygi, S.P., and Bartel, D.P. (2008). The impact of microRNAs on protein output. Nature *455*, 64–71.

Bah, A., and Forman-Kay, J.D. (2016). Modulation of Intrinsically Disordered Protein Function by Post-translational Modifications. J Biol Chem *291*, 6696–6705.

Bah, A., Vernon, R.M., Siddiqui, Z., Krzeminski, M., Muhandiram, R., Zhao, C., Sonenberg, N., Kay, L.E., and Forman-Kay, J.D. (2015). Folding of an intrinsically disordered protein by phosphorylation as a regulatory switch. Nature *519*, 106–109.

Balak, C., Benard, M., Schaefer, E., Iqbal, S., Ramsey, K., Ernoult-Lange, M., Mattioli, F., Llaci, L., Geoffroy, V., Courel, M., et al. (2019). Rare De Novo Missense Variants in RNA Helicase DDX6 Cause Intellectual Disability and Dysmorphic Features and Lead to P-Body Defects and RNA Dysregulation. Am J Hum Genet *105*, 509–525.

Baltz, A.G., Munschauer, M., Schwanhäusser, B., Vasile, A., Murakawa, Y., Schueler, M., Youngs, N., Penfold-Brown, D., Drew, K., Milek, M., et al. (2012). The mRNA-Bound Proteome and Its Global Occupancy Profile on Protein-Coding Transcripts. Molecular Cell *46*, 674–690.

Banani, S.F., Lee, H.O., Hyman, A.A., and Rosen, M.K. (2017). Biomolecular condensates: organizers of cellular biochemistry. Nature Reviews Molecular Cell Biology *18*, 285–298.

Bardoni, B., and Mandel, J.-L. (2002). Advances in understanding of fragile X pathogenesis and FMRP function, and in identification of X linked mental retardation genes. Current Opinion in Genetics & Development *12*, 284–293.

Bardoni, B., Davidovic, L., Bensaid, M., and Khandjian, E.W. (2006). The fragile X syndrome: exploring its molecular basis and seeking a treatment. Expert Rev. Mol. Med. *8*, 1–16.

Barreau, C., Paillard, L., and Osborne, H.B. (2005). AU-rich elements and associated factors: are there unifying principles? Nucleic Acids Res *33*, 7138–7150.

Bartel, D.P. (2018). Metazoan MicroRNAs. Cell *173*, 20–51.

Bashkirov, V.I., Scherthan, H., Solinger, J.A., Buerstedde, J.-M., and Heyer, W.-D. (1997). A Mouse Cytoplasmic Exoribonuclease (mXRN1p) with Preference for G4 Tetraplex Substrates. J Cell Biol *136*, 761–773.

Beckmann, B.M., Horos, R., Fischer, B., Castello, A., Eichelbaum, K., Alleaume, A.-M., Schwarzl, T., Curk, T., Foehr, S., Huber, W., et al. (2015). The RNA-binding proteomes from yeast to man harbour conserved enigmRBPs. Nature Communications *6*, 10127.

Behm-Ansmant, I., Rehwinkel, J., Doerks, T., Stark, A., Bork, P., and Izaurralde, E. (2006). mRNA degradation by miRNAs and GW182 requires both CCR4:NOT deadenylase and DCP1:DCP2 decapping complexes. Genes Dev. *20*, 1885–1898.

Béthune, J., Artus-Revel, C.G., and Filipowicz, W. (2012). Kinetic analysis reveals successive steps leading to miRNA-mediated silencing in mammalian cells. EMBO Rep *13*, 716–723.

Beznosková, P., Wagner, S., Jansen, M.E., von der Haar, T., and Valášek, L.S. (2015). Translation initiation factor eIF3 promotes programmed stop codon readthrough. Nucleic Acids Res. *43*, 5099–5111.

Bhandari, D., Raisch, T., Weichenrieder, O., Jonas, S., and Izaurralde, E. (2014). Structural basis for the Nanos-mediated recruitment of the CCR4-NOT complex and translational repression. Genes Dev. *28*, 888–901.

Bhattacharyya, S.N., Habermacher, R., Martine, U., Closs, E.I., and Filipowicz, W. (2006). Relief of microRNA-mediated translational repression in human cells subjected to stress. Cell *125*, 1111–1124.

Boeynaems, S., Alberti, S., Fawzi, N.L., Mittag, T., Polymenidou, M., Rousseau, F., Schymkowitz, J., Shorter, J., Wolozin, B., Van Den Bosch, L., et al. (2018). Protein Phase Separation: A New Phase in Cell Biology. Trends in Cell Biology *28*, 420–435.

Borja, M.S., Piotukh, K., Freund, C., and Gross, J.D. (2011). Dcp1 links coactivators of mRNA decapping to Dcp2 by proline recognition. RNA *17*, 278–290.

Bounedjah, O., Desforges, B., Wu, T.-D., Pioche-Durieu, C., Marco, S., Hamon, L., Curmi, P.A., Guerquin-Kern, J.-L., Piétrement, O., and Pastré, D. (2014). Free mRNA in excess upon polysome dissociation is a scaffold for protein multimerization to form stress granules. Nucleic Acids Res *42*, 8678–8691.

Bouveret, E., Rigaut, G., Shevchenko, A., Wilm, M., and Séraphin, B. (2000). A Sm-like protein complex that participates in mRNA degradation. EMBO J *19*, 1661–1671.

Brandmann, T., Fakim, H., Padamsi, Z., Youn, J.-Y., Gingras, A.-C., Fabian, M.R., and Jinek, M. (2018). Molecular architecture of LSM14 interactions involved in the assembly of mRNA silencing complexes. The EMBO Journal *37*, e97869.

Brangwynne, C.P. (2013). Phase transitions and size scaling of membrane-less organelles. The Journal of Cell Biology *203*, 875–881.

Brangwynne, C.P., Eckmann, C.R., Courson, D.S., Rybarska, A., Hoege, C., Gharakhani, J., Jülicher, F., and Hyman, A.A. (2009). Germline P Granules Are Liquid Droplets That Localize by Controlled Dissolution/Condensation. Science *324*, 1729–1732.

Brangwynne, C.P., Tompa, P., and Pappu, R.V. (2015). Polymer physics of intracellular phase transitions. Nature Phys *11*, 899–904.

Braun, J.E., Huntzinger, E., Fauser, M., and Izaurralde, E. (2011). GW182 proteins directly recruit cytoplasmic deadenylase complexes to miRNA targets. Mol. Cell *44*, 120–133.

Braun, J.E., Truffault, V., Boland, A., Huntzinger, E., Chang, C.-T., Haas, G., Weichenrieder, O., Coles, M., and Izaurralde, E. (2012). A direct interaction between DCP1 and XRN1 couples mRNA decapping to 5′ exonucleolytic degradation. Nat Struct Mol Biol *19*, 1324–1331.

Brengues, M., Teixeira, D., and Parker, R. (2005). Movement of Eukaryotic mRNAs Between Polysomes and Cytoplasmic Processing Bodies. Science *310*, 486–489.

Bulbrook, D., Brazier, H., Mahajan, P., Kliszczak, M., Fedorov, O., Marchese, F.P., Aubareda, A., Chalk, R., Picaud, S., Strain-Damerell, C., et al. (2018). Tryptophan-Mediated Interactions between Tristetraprolin and the CNOT9 Subunit Are Required for CCR4-NOT Deadenylase Complex Recruitment. J. Mol. Biol. *430*, 722–736.

Buxbaum, A.R., Haimovich, G., and Singer, R.H. (2015). In the right place at the right time: visualizing and understanding mRNA localization. Nat. Rev. Mol. Cell Biol. *16*, 95–109.

Calvo, S.E., Pagliarini, D.J., and Mootha, V.K. (2009). Upstream open reading frames cause widespread reduction of protein expression and are polymorphic among humans. Proc. Natl. Acad. Sci. U.S.A. *106*, 7507–7512.

Caput, D., Beutler, B., Hartog, K., Thayer, R., Brown-Shimer, S., and Cerami, A. (1986). Identification of a common nucleotide sequence in the 3'-untranslated region of mRNA molecules specifying inflammatory mediators. Proceedings of the National Academy of Sciences *83*, 1670–1674.

Carroll, J.S., Munchel, S.E., and Weis, K. (2011). The DExD/H box ATPase Dhh1 functions in translational repression, mRNA decay, and processing body dynamics. J Cell Biol *194*, 527–537.

Castello, A., Fischer, B., Eichelbaum, K., Horos, R., Beckmann, B.M., Strein, C., Davey, N.E., Humphreys, D.T., Preiss, T., Steinmetz, L.M., et al. (2012). Insights into RNA Biology from an Atlas of Mammalian mRNA-Binding Proteins. Cell *149*, 1393–1406.

Castello, A., Hentze, M.W., and Preiss, T. (2015). Metabolic Enzymes Enjoying New Partnerships as RNA-Binding Proteins. Trends in Endocrinology & Metabolism *26*, 746–757.

Castello, A., Fischer, B., Frese, C.K., Horos, R., Alleaume, A.-M., Foehr, S., Curk, T., Krijgsveld, J., and Hentze, M.W. (2016). Comprehensive Identification of RNA-Binding Domains in Human Cells. Mol Cell *63*, 696–710.

Cerutti, H., and Casas-Mollano, J.A. (2006). On the origin and functions of RNA-mediated silencing: from protists to man. Curr Genet *50*, 81–99.

Chang, C.-T., Bercovich, N., Loh, B., Jonas, S., and Izaurralde, E. (2014). The activation of the decapping enzyme DCP2 by DCP1 occurs on the EDC4 scaffold and involves a conserved loop in DCP1. Nucleic Acids Res. *42*, 5217–5233.

Chang, C.-T., Muthukumar, S., Weber, R., Levdansky, Y., Chen, Y., Bhandari, D., Igreja, C., Wohlbold, L., Valkov, E., and Izaurralde, E. (2019). A low-complexity region in human XRN1 directly recruits deadenylation and decapping factors in 5'-3' messenger RNA decay. Nucleic Acids Res. *47*, 9282–9295.

Chapat, C., Jafarnejad, S.M., Matta-Camacho, E., Hesketh, G.G., Gelbart, I.A., Attig, J., Gkogkas, C.G., Alain, T., Stern-Ginossar, N., Fabian, M.R., et al. (2017). Cap-binding protein 4EHP effects translation silencing by microRNAs. PNAS.

Charenton, C., Taverniti, V., Gaudon-Plesse, C., Back, R., Séraphin, B., and Graille, M. (2016). Structure of the active form of Dcp1–Dcp2 decapping enzyme bound to m7GDP and its Edc3 activator. Nat Struct Mol Biol *23*, 982–986.

Chen, C.Y., and Shyu, A.B. (1995). AU-rich elements: characterization and importance in mRNA degradation. Trends Biochem. Sci. *20*, 465–470.

Chen, S., and Gao, G. (2017). MicroRNAs recruit eIF4E2 to repress translation of target mRNAs. Protein Cell *8*, 750–761.

Chen, C.Y., Gherzi, R., Ong, S.E., Chan, E.L., Raijmakers, R., Pruijn, G.J., Stoecklin, G., Moroni, C., Mann, M., and Karin, M. (2001). AU binding proteins recruit the exosome to degrade ARE-containing mRNAs. Cell *107*, 451–464.

Chen, C.-Y.A., Zheng, D., Xia, Z., and Shyu, A.-B. (2009). Ago-TNRC6 triggers microRNA-mediated decay by promoting two deadenylation steps. Nat. Struct. Mol. Biol. *16*, 1160–1166.

Chen, Y., Boland, A., Kuzuoğlu-Öztürk, D., Bawankar, P., Loh, B., Chang, C.-T., Weichenrieder, O., and Izaurralde, E. (2014). A DDX6-CNOT1 complex and W-binding pockets in CNOT9 reveal direct links between miRNA target recognition and silencing. Mol. Cell *54*, 737–750.

Chew, G.-L., Pauli, A., and Schier, A.F. (2016). Conservation of uORF repressiveness and sequence features in mouse, human and zebrafish. Nature Communications *7*, 11663.

Chin, A., and Lécuyer, E. (2017). RNA localization: Making its way to the center stage. Biochim Biophys Acta Gen Subj *1861*, 2956–2970.

Chong, P.A., Vernon, R.M., and Forman-Kay, J.D. (2018). RGG/RG Motif Regions in RNA Binding and Phase Separation. Journal of Molecular Biology *430*, 4650–4665.

Chouaib, R., Safieddine, A., Pichon, X., Imbert, A., Kwon, O.S., Samacoits, A., Traboulsi, A.-M., Robert, M.-C., Tsanov, N., Coleno, E., et al. (2020). A localization screen reveals translation factories and widespread co-translational RNA targeting. BioRxiv 2020.05.20.106989.

Chu, C., and Rana, T.M. (2006). Translation Repression in Human Cells by MicroRNA-Induced Gene Silencing Requires RCK/p54. PLOS Biology *4*, e210.

Chu, D., Kazana, E., Bellanger, N., Singh, T., Tuite, M.F., and von der Haar, T. (2014). Translation elongation can control translation initiation on eukaryotic mRNAs. EMBO J. *33*, 21–34.

Clemens, M.J. (2001). Initiation factor eIF2 alpha phosphorylation in stress responses and apoptosis. Prog. Mol. Subcell. Biol. *27*, 57–89.

Coller, J., and Parker, R. (2004). Eukaryotic mRNA decapping. Annu. Rev. Biochem. *73*, 861–890.

Coller, J., and Parker, R. (2005). General Translational Repression by Activators of mRNA Decapping. Cell *122*, 875–886.

Coller, J.M., Tucker, M., Sheth, U., Valencia-Sanchez, M.A., and Parker, R. (2001). The DEAD box helicase, Dhh1p, functions in mRNA decapping and interacts with both the decapping and deadenylase complexes. RNA *7*, 1717–1727.

Colombo, M., Karousis, E.D., Bourquin, J., Bruggmann, R., and Mühlemann, O. (2017). Transcriptome-wide identification of NMD-targeted human mRNAs reveals extensive redundancy between SMG6- and SMG7-mediated degradation pathways. RNA *23*, 189–201.

Cordin, O., Banroques, J., Tanner, N.K., and Linder, P. (2006). The DEAD-box protein family of RNA helicases. Gene *367*, 17–37.

Corley, M., Burns, M.C., and Yeo, G.W. (2020). How RNA-Binding Proteins Interact with RNA: Molecules and Mechanisms. Mol. Cell *78*, 9–29.

Cougot, N., Babajko, S., and Séraphin, B. (2004). Cytoplasmic foci are sites of mRNA decay in human cells. J. Cell Biol. *165*, 31–40.

Courel, M., Clément, Y., Bossevain, C., Foretek, D., Vidal Cruchez, O., Yi, Z., Bénard, M., Benassy, M.-N., Kress, M., Vindry, C., et al. (2019). GC content shapes mRNA storage and decay in human cells. ELife *8*, e49708.

Darling, A.L., Liu, Y., Oldfield, C.J., and Uversky, V.N. (2018). Intrinsically Disordered Proteome of Human Membrane-Less Organelles. Proteomics *18*, 1700193.

Daubner, G.M., Cléry, A., and Allain, F.H.-T. (2013). RRM-RNA recognition: NMR or crystallography…and new findings. Curr. Opin. Struct. Biol. *23*, 100–108.

Decker, C.J., and Parker, R. (2012). P-bodies and stress granules: possible roles in the control of translation and mRNA degradation. Cold Spring Harb Perspect Biol *4*, a012286.

Decker, C.J., Teixeira, D., and Parker, R. (2007). Edc3p and a glutamine/asparagine-rich domain of Lsm4p function in processing body assembly in Saccharomyces cerevisiae. Journal of Cell Biology *179*, 437–449.

Dever, T.E., Kinzy, T.G., and Pavitt, G.D. (2016). Mechanism and Regulation of Protein Synthesis in Saccharomyces cerevisiae. Genetics *203*, 65–107.

Dhote, V., Sweeney, T.R., Kim, N., Hellen, C.U.T., and Pestova, T.V. (2012). Roles of individual domains in the function of DHX29, an essential factor required for translation of structured mammalian mRNAs. Proc Natl Acad Sci U S A *109*, E3150–E3159.

van Dijk, E., Cougot, N., Meyer, S., Babajko, S., Wahle, E., and Séraphin, B. (2002). Human Dcp2: a catalytically active mRNA decapping enzyme located in specific cytoplasmic structures. EMBO J. *21*, 6915–6924.

Djuranovic, S., Nahvi, A., and Green, R. (2012). miRNA-mediated gene silencing by translational repression followed by mRNA deadenylation and decay. Science *336*, 237–240.

D'Lima, N.G., Ma, J., Winkler, L., Chu, Q., Loh, K.H., Corpuz, E.O., Budnik, B.A., Lykke-Andersen, J., Saghatelian, A., and Slavoff, S.A. (2017). A human microprotein that interacts with the mRNA decapping complex. Nat Chem Biol *13*, 174–180.

Dong, J., Aitken, C.E., Thakur, A., Shin, B.-S., Lorsch, J.R., and Hinnebusch, A.G. (2017). Rps3/uS3 promotes mRNA binding at the 40S ribosome entry channel and stabilizes preinitiation complexes at start codons. Proc Natl Acad Sci U S A *114*, E2126–E2135.

Dostie, J., Ferraiuolo, M., Pause, A., Adam, S.A., and Sonenberg, N. (2000). A novel shuttling protein, 4E-T, mediates the nuclear import of the mRNA 5' cap-binding protein, eIF4E. EMBO J. *19*, 3142–3156.

Dotu, I., Adamson, S.I., Coleman, B., Fournier, C., Ricart-Altimiras, E., Eyras, E., and Chuang, J.H. (2018). SARNAclust: Semi-automatic detection of RNA protein binding motifs from immunoprecipitation data. PLOS Computational Biology *14*, e1006078.

Dresios, J., Chappell, S.A., Zhou, W., and Mauro, V.P. (2006). An mRNA-rRNA base-pairing mechanism for translation initiation in eukaryotes. Nature Structural & Molecular Biology *13*, 30–34.

Duchaine, T.F., and Fabian, M.R. (2019). Mechanistic Insights into MicroRNA-Mediated Gene Silencing. Cold Spring Harb Perspect Biol *11*.

Durand, S., Cougot, N., Mahuteau-Betzer, F., Nguyen, C.-H., Grierson, D.S., Bertrand, E., Tazi, J., and Lejeune, F. (2007). Inhibition of nonsense-mediated mRNA decay (NMD) by a new chemical molecule reveals the dynamic of NMD factors in P-bodies. J Cell Biol *178*, 1145–1160.

Duret, L., Semon, M., Piganeau, G., Mouchiroud, D., and Galtier, N. (2002). Vanishing GC-Rich Isochores in Mammalian Genomes. Genetics *162*, 1837–1847.

Dutta, A., Zheng, S., Jain, D., Cameron, C.E., and Reese, J.C. (2011). Intermolecular Interactions within the Abundant DEAD-box Protein Dhh1 Regulate Its Activity in Vivo. J Biol Chem *286*, 27454–27470.

Eberle, A.B., Lykke-Andersen, S., Mühlemann, O., and Jensen, T.H. (2009). SMG6 promotes endonucleolytic cleavage of nonsense mRNA in human cells. Nat. Struct. Mol. Biol. *16*, 49–55.

Eichhorn, S.W., Guo, H., McGeary, S.E., Rodriguez-Mias, R.A., Shin, C., Baek, D., Hsu, S., Ghoshal, K., Villén, J., and Bartel, D.P. (2014). mRNA Destabilization Is the Dominant Effect of Mammalian MicroRNAs by the Time Substantial Repression Ensues. Molecular Cell *56*, 104–115.

Eliseev, B., Yeramala, L., Leitner, A., Karuppasamy, M., Raimondeau, E., Huard, K., Alkalaeva, E., Aebersold, R., and Schaffitzel, C. (2018). Structure of a human cap-dependent 48S translation pre-initiation complex. Nucleic Acids Res *46*, 2678–2689.

Ernoult-Lange, M., Baconnais, S., Harper, M., Minshall, N., Souquere, S., Boudier, T., Bénard, M., Andrey, P., Pierron, G., Kress, M., et al. (2012). Multiple binding of repressed mRNAs by the P-body protein Rck/p54. RNA *18*, 1702–1715.

Eulalio, A., Rehwinkel, J., Stricker, M., Huntzinger, E., Yang, S.-F., Doerks, T., Dorner, S., Bork, P., Boutros, M., and Izaurralde, E. (2007a). Target-specific requirements for enhancers of decapping in miRNA-mediated gene silencing. Genes Dev. *21*, 2558–2570.

Eulalio, A., Behm-Ansmant, I., and Izaurralde, E. (2007b). P bodies: at the crossroads of post-transcriptional pathways. Nature Reviews Molecular Cell Biology *8*, 9–22.

Eystathioy, T., Jakymiw, A., Chan, E.K.L., Séraphin, B., Cougot, N., and Fritzler, M.J. (2003). The GW182 protein colocalizes with mRNA degradation associated proteins hDcp1 and hLSm4 in cytoplasmic GW bodies. RNA *9*, 1171–1173.

F, Z., Ak, S., Bs, S., J, N., and Ag, H. (2015). Conformational Changes in the P Site and mRNA Entry Channel Evoked by AUG Recognition in Yeast Translation Preinitiation Complexes (Nucleic Acids Res).

Faehnle, C.R., Walleshauser, J., and Joshua-Tor, L. (2014). Mechanism of Dis3l2 substrate recognition in the Lin28-let-7 pathway. Nature *514*, 252–256.

Fairman-Williams, M.E., Guenther, U.-P., and Jankowsky, E. (2010). SF1 and SF2 helicases: family matters. Curr. Opin. Struct. Biol. *20*, 313–324.

Farh, K.K.-H., Grimson, A., Jan, C., Lewis, B.P., Johnston, W.K., Lim, L.P., Burge, C.B., and Bartel, D.P. (2005). The widespread impact of mammalian MicroRNAs on mRNA repression and evolution. Science *310*, 1817–1821.

Fenger-Grøn, M., Fillman, C., Norrild, B., and Lykke-Andersen, J. (2005). Multiple Processing Body Factors and the ARE Binding Protein TTP Activate mRNA Decapping. Molecular Cell *20*, 905–915.

Feoktistova, K., Tuvshintogs, E., Do, A., and Fraser, C.S. (2013). Human eIF4E promotes mRNA restructuring by stimulating eIF4A helicase activity. PNAS *110*, 13339–13344.

Fernández, I.S., Bai, X.-C., Hussain, T., Kelley, A.C., Lorsch, J.R., Ramakrishnan, V., and Scheres, S.H.W. (2013). Molecular architecture of a eukaryotic translational initiation complex. Science *342*.

Fernández-Miranda, G., and Méndez, R. (2012). The CPEB-family of proteins, translational control in senescence and cancer. Ageing Res. Rev. *11*, 460–472.

Ferraiuolo, M.A., Basak, S., Dostie, J., Murray, E.L., Schoenberg, D.R., and Sonenberg, N. (2005). A role for the eIF4E-binding protein 4E-T in P-body formation and mRNA decay. J. Cell Biol. *170*, 913–924.

Fonseca, B.D., Zakaria, C., Jia, J.-J., Graber, T.E., Svitkin, Y., Tahmasebi, S., Healy, D., Hoang, H.-D., Jensen, J.M., Diao, I.T., et al. (2015). La-related Protein 1 (LARP1) Represses Terminal Oligopyrimidine (TOP) mRNA Translation Downstream of mTOR Complex 1 (mTORC1). J. Biol. Chem. *290*, 15996–16020.

Ford, L., Ling, E., Kandel, E.R., and Fioriti, L. (2019). CPEB3 inhibits translation of mRNA targets by localizing them to P bodies. PNAS *116*, 18078–18087.

Franks, T.M., and Lykke-Andersen, J. (2007). TTP and BRF proteins nucleate processing body formation to silence mRNAs with AU-rich elements. Genes Dev. *21*, 719–735.

Freimer, J.W., Hu, T., and Blelloch, R. (2018). Decoupling the impact of microRNAs on translational repression versus RNA degradation in embryonic stem cells. ELife *7*, e38014.

Friedman, R.C., Farh, K.K.-H., Burge, C.B., and Bartel, D.P. (2009). Most mammalian mRNAs are conserved targets of microRNAs. Genome Res *19*, 92–105.

Fromm, S.A., Truffault, V., Kamenz, J., Braun, J.E., Hoffmann, N.A., Izaurralde, E., and Sprangers, R. (2012). The structural basis of Edc3- and Scd6-mediated activation of the Dcp1:Dcp2 mRNA decapping complex. EMBO J. *31*, 279–290.

Fukao, A., Mishima, Y., Takizawa, N., Oka, S., Imataka, H., Pelletier, J., Sonenberg, N., Thoma, C., and Fujiwara, T. (2014). MicroRNAs trigger dissociation of eIF4AI and eIF4AII from target mRNAs in humans. Mol. Cell *56*, 79–89.

Gallie, D.R. (1991). The cap and poly(A) tail function synergistically to regulate mRNA translational efficiency. Genes Dev. *5*, 2108–2116.

García-García, C., Frieda, K.L., Feoktistova, K., Fraser, C.S., and Block, S.M. (2015). Factor-dependent processivity in human eIF4A DEAD-box helicase. Science *348*, 1486–1488.

Garcia-Jove Navarro, M., Kashida, S., Chouaib, R., Souquere, S., Pierron, G., Weil, D., and Gueroui, Z. (2019). RNA is a critical element for the sizing and the composition of phase-separated RNA–protein condensates. Nat Commun *10*, 3230.

des Georges, A., Dhote, V., Kuhn, L., Hellen, C.U.T., Pestova, T.V., Frank, J., and Hashem, Y. (2015). Structure of mammalian eIF3 in the context of the 43S preinitiation complex. Nature *525*, 491–495.

Giess, A., Torres Cleuren, Y.N., Tjeldnes, H., Krause, M., Bizuayehu, T.T., Hiensch, S., Okon, A., Wagner, C.R., and Valen, E. (2020). Profiling of Small Ribosomal Subunits Reveals Modes and Regulation of Translation Initiation. Cell Rep *31*, 107534.

Gilks, N., Kedersha, N., Ayodele, M., Shen, L., Stoecklin, G., Dember, L.M., and Anderson, P. (2004). Stress granule assembly is mediated by prion-like aggregation of TIA-1. Mol. Biol. Cell *15*, 5383–5398.

Gingras, A.-C., Raught, B., and Sonenberg, N. (1999). eIF4 Initiation Factors: Effectors of mRNA Recruitment to Ribosomes and Regulators of Translation. Annu. Rev. Biochem. *68*, 913–963.

Godwin, A.R., Kojima, S., Green, C.B., and Wilusz, J. (2013). Kiss your tail goodbye: the role of PARN, Nocturnin, and Angel deadenylases in mRNA biology. Biochim. Biophys. Acta *1829*, 571–579.

Gomes, E., and Shorter, J. (2019). The molecular language of membraneless organelles. J. Biol. Chem. *294*, 7115–7127.

Gönczy, P. (2012). Towards a molecular architecture of centriole assembly. Nat. Rev. Mol. Cell Biol. *13*, 425–435.

Gosselin, P., Martineau, Y., Morales, J., Czjzek, M., Glippa, V., Gauffeny, I., Morin, E., Le Corguillé, G., Pyronnet, S., Cormier, P., et al. (2013). Tracking a refined eIF4E-binding motif reveals Angel1 as a new partner of eIF4E. Nucleic Acids Research *41*, 7783–7792.

Götze, M., Dufourt, J., Ihling, C., Rammelt, C., Pierson, S., Sambrani, N., Temme, C., Sinz, A., Simonelig, M., and Wahle, E. (2017). Translational repression of the Drosophila nanos mRNA involves the RNA helicase Belle and RNA coating by Me31B and Trailer hitch. RNA *23*, 1552–1568.

Grimson, A., Farh, K.K.-H., Johnston, W.K., Garrett-Engele, P., Lim, L.P., and Bartel, D.P. (2007a). MicroRNA Targeting Specificity in Mammals: Determinants Beyond Seed Pairing. Mol Cell *27*, 91–105.

Grob, A., Colleran, C., and McStay, B. (2014). Construction of synthetic nucleoli in human cells reveals how a major functional nuclear domain is formed and propagated through cell division. Genes Dev. *28*, 220–230.

Grüner, S., Peter, D., Weber, R., Wohlbold, L., Chung, M.-Y., Weichenrieder, O., Valkov, E., Igreja, C., and Izaurralde, E. (2016). The Structures of eIF4E-eIF4G Complexes Reveal an Extended Interface to Regulate Translation Initiation. Molecular Cell *64*, 467–479.

Guca, E., and Hashem, Y. (2018). Major structural rearrangements of the canonical eukaryotic translation initiation complex. Current Opinion in Structural Biology *53*, 151–158.

von der Haar, T., Gross, J.D., Wagner, G., and McCarthy, J.E.G. (2004). The mRNA cap-binding protein eIF4E in post-transcriptional gene expression. Nat Struct Mol Biol *11*, 503–511.

Hafner, M., Landthaler, M., Burger, L., Khorshid, M., Hausser, J., Berninger, P., Rothballer, A., Ascano, M., Jungkamp, A.-C., Munschauer, M., et al. (2010). Transcriptome-wide Identification of RNA-Binding Protein and MicroRNA Target Sites by PAR-CLIP. Cell *141*, 129–141.

Haghandish, N., Baldwin, R.M., Morettin, A., Dawit, H.T., Adhikary, H., Masson, J.-Y., Mazroui, R., Trinkle-Mulcahy, L., and Côté, J. (2019). PRMT7 methylates eukaryotic translation initiation factor 2α and regulates its role in stress granule formation. Mol Biol Cell *30*, 778–793.

Haimov, O., Sehrawat, U., Harush, A.T.-B., Bahat, A., Uzonyi, A., Will, A., Hiraishi, H., Asano, K., and Dikstein, R. (2018). Dynamic Interaction of Eukaryotic Initiation Factor 4G1 (eIF4G1) with eIF4E and eIF1 Underlies Scanning-Dependent and -Independent Translation. Molecular and Cellular Biology *38*.

Halstead, J.M., Lionnet, T., Wilbertz, J.H., Wippich, F., Ephrussi, A., Singer, R.H., and Chao, J.A. (2015). Translation. An RNA biosensor for imaging the first round of translation from single cells to living animals. Science *347*, 1367–1671.

Hanson, G., and Coller, J. (2018). Codon optimality, bias and usage in translation and mRNA decay. Nat Rev Mol Cell Biol *19*, 20–30.

Harvey, R.F., Smith, T.S., Mulroney, T., Queiroz, R.M.L., Pizzinga, M., Dezi, V., Villenueva, E., Ramakrishna, M., Lilley, K.S., and Willis, A.E. (2018). Trans-acting translational regulatory RNA binding proteins. Wiley Interdiscip Rev RNA *9*.

Hashem, Y., des Georges, A., Dhote, V., Langlois, R., Liao, H.Y., Grassucci, R.A., Hellen, C.U.T., Pestova, T.V., and Frank, J. (2013). Structure of the Mammalian Ribosomal 43S Preinitiation Complex Bound to the Scanning Factor DHX29. Cell *153*, 1108–1119.

He, Q., and Ge, W. (2017). The tandem Agenet domain of fragile X mental retardation protein interacts with FUS. Scientific Reports *7*.

He, C., Sidoli, S., Warneford-Thomson, R., Tatomer, D.C., Wilusz, J.E., Garcia, B.A., and Bonasio, R. (2016). High-Resolution Mapping of RNA-Binding Regions in the Nuclear Proteome of Embryonic Stem Cells. Mol. Cell *64*, 416–430.

He, F., Celik, A., Wu, C., and Jacobson, A. (2018). General decapping activators target different subsets of inefficiently translated mRNAs. Elife *7*.

Heck, A.M., and Wilusz, J. (2018). The Interplay between the RNA Decay and Translation Machinery in Eukaryotes. Cold Spring Harb Perspect Biol *10*, a032839.

Helfer, S., Schott, J., Stoecklin, G., and Förstemann, K. (2012). AU-Rich Element-Mediated mRNA Decay Can Occur Independently of the miRNA Machinery in Mouse Embryonic Fibroblasts and Drosophila S2-Cells. PLoS One *7*.

Hentze, M.W., Castello, A., Schwarzl, T., and Preiss, T. (2018). A brave new world of RNA-binding proteins. Nat. Rev. Mol. Cell Biol. *19*, 327–341.

Herrmannová, A., Prilepskaja, T., Wagner, S., Šikrová, D., Zeman, J., Poncová, K., and Valášek, L.S. (2020). Adapted formaldehyde gradient cross-linking protocol implicates human eIF3d and eIF3c, k and l subunits in the 43S and 48S pre-initiation complex assembly, respectively. Nucleic Acids Research *48*, 1969–1984.

Hershey, J.W.B., Sonenberg, N., and Mathews, M.B. (2019). Principles of Translational Control. Cold Spring Harb Perspect Biol *11*, a032607.

Hia, F., Yang, S.F., Shichino, Y., Yoshinaga, M., Murakawa, Y., Vandenbon, A., Fukao, A., Fujiwara, T., Landthaler, M., Natsume, T., et al. (2019). Codon bias confers stability to human mRNAs. EMBO Rep. *20*, e48220.

Hilliker, A. (2021). mRNA Localization and Localized Translation. In Molecular Life Sciences: An Encyclopedic Reference, E. Bell, ed. (New York, NY: Springer), pp. 1–3.

Hinnebusch, A.G. (2014). The scanning mechanism of eukaryotic translation initiation. Annu. Rev. Biochem. *83*, 779–812.

Hinnebusch, A.G., and Lorsch, J.R. (2012). The mechanism of eukaryotic translation initiation: new insights and challenges. Cold Spring Harb Perspect Biol *4*.

Hinnebusch, A.G., Ivanov, I.P., and Sonenberg, N. (2016). Translational control by 5′-untranslated regions of eukaryotic mRNAs. Science *352*, 1413–1416.

Hofweber, M., and Dormann, D. (2019). Friend or foe—Post-translational modifications as regulators of phase separation and RNP granule dynamics. J. Biol. Chem. *294*, 7137–7150.

Hondele, M., Sachdev, R., Heinrich, S., Wang, J., Vallotton, P., Fontoura, B.M.A., and Weis, K. (2019). DEAD-box ATPases are global regulators of phase-separated organelles. Nature *573*, 144–148.

Horman, S.R., Janas, M.M., Litterst, C., Wang, B., MacRae, I.J., Sever, M.J., Morrissey, D.V., Graves, P., Luo, B., Umesalma, S., et al. (2013). Akt-mediated phosphorylation of argonaute 2 downregulates cleavage and upregulates translational repression of MicroRNA targets. Mol. Cell *50*, 356–367.

Horvathova, I., Voigt, F., Kotrys, A.V., Zhan, Y., Artus-Revel, C.G., Eglinger, J., Stadler, M.B., Giorgetti, L., and Chao, J.A. (2017). The Dynamics of mRNA Turnover Revealed by Single-Molecule Imaging in Single Cells. Molecular Cell *68*, 615-625.e9.

Hu, W., Sweet, T.J., Chamnongpol, S., Baker, K.E., and Coller, J. (2009). Co-translational mRNA decay in Saccharomyces cerevisiae. Nature *461*, 225–229.

Huang, Y.-S., Kan, M.-C., Lin, C.-L., and Richter, J.D. (2006). CPEB3 and CPEB4 in neurons: analysis of RNA-binding specificity and translational control of AMPA receptor GluR2 mRNA. EMBO J. *25*, 4865–4876.

Hubstenberger, A., Cameron, C., Noble, S.L., Keenan, S., and Evans, T.C. (2015). Modifiers of solid RNP granules control normal RNP dynamics and mRNA activity in early development. The Journal of Cell Biology *211*, 703–716.

Hubstenberger, A., Courel, M., Bénard, M., Souquere, S., Ernoult-Lange, M., Chouaib, R., Yi, Z., Morlot, J.-B., Munier, A., Fradet, M., et al. (2017). P-Body Purification Reveals the Condensation of Repressed mRNA Regulons. Molecular Cell *68*, 144-157.e5.

Hug, N., Longman, D., and Cáceres, J.F. (2016). Mechanism and regulation of the nonsense-mediated decay pathway. Nucleic Acids Res *44*, 1483–1495.

Humphreys, D.T., Westman, B.J., Martin, D.I.K., and Preiss, T. (2005). MicroRNAs control translation initiation by inhibiting eukaryotic initiation factor 4E/cap and poly(A) tail function. Proc. Natl. Acad. Sci. U.S.A. *102*, 16961–16966.

Huntzinger, E., Kashima, I., Fauser, M., Saulière, J., and Izaurralde, E. (2008). SMG6 is the catalytic endonuclease that cleaves mRNAs containing nonsense codons in metazoan. RNA *14*, 2609–2617.

Hyman, A.A., and Brangwynne, C.P. (2011). Beyond Stereospecificity: Liquids and Mesoscale Organization of Cytoplasm. Developmental Cell *21*, 14–16.

Hyman, A.A., Weber, C.A., and Jülicher, F. (2014). Liquid-Liquid Phase Separation in Biology. Annual Review of Cell and Developmental Biology *30*, 39–58.

Igreja, C., and Izaurralde, E. (2011). CUP promotes deadenylation and inhibits decapping of mRNA targets. Genes Dev. *25*, 1955–1967.

Igreja, C., Peter, D., Weiler, C., and Izaurralde, E. (2014). 4E-BPs require non-canonical 4E-binding motifs and a lateral surface of eIF4E to repress translation. Nat Commun *5*, 4790.

Imamachi, N., Salam, K.A., Suzuki, Y., and Akimitsu, N. (2017). A GC-rich sequence feature in the 3' UTR directs UPF1-dependent mRNA decay in mammalian cells. Genome Res. *27*, 407–418.

Imataka, H., Gradi, A., and Sonenberg, N. (1998). A newly identified N-terminal amino acid sequence of human eIF4G binds poly(A)-binding protein and functions in poly(A)-dependent translation. EMBO J. *17*, 7480–7489.

Ingelfinger, D., Arndt-Jovin, D.J., Luhrmann, R., and Achsel, T. The human LSm1-7 proteins colocalize with the mRNA-degrading enzymes Dcp1/2 and Xrnl in distinct cytoplasmic foci. 14.

Ingolia, N.T. (2014). Ribosome profiling: new views of translation, from single codons to genome scale. Nat. Rev. Genet. *15*, 205–213.

Ingolia, N.T., Ghaemmaghami, S., Newman, J.R.S., and Weissman, J.S. (2009). Genome-Wide Analysis in Vivo of Translation with Nucleotide Resolution Using Ribosome Profiling. Science *324*, 218–223.

Ingolia, N.T., Lareau, L.F., and Weissman, J.S. (2011). Ribosome profiling of mouse embryonic stem cells reveals the complexity and dynamics of mammalian proteomes. Cell *147*, 789–802.

Ivanyi-Nagy, R., Davidovic, L., Khandjian, E.W., and Darlix, J.-L. (2005). Disordered RNA chaperone proteins: from functions to disease. CMLS, Cell. Mol. Life Sci. *62*, 1409–1417.

Ivshina, M., Lasko, P., and Richter, J.D. (2014). Cytoplasmic polyadenylation element binding proteins in development, health, and disease. Annu. Rev. Cell Dev. Biol. *30*, 393–415.

Iwakawa, H., and Tomari, Y. (2015). The Functions of MicroRNAs: mRNA Decay and Translational Repression. Trends in Cell Biology *25*, 651–665.

Iwama, H., Kato, K., Imachi, H., Murao, K., and Masaki, T. (2018). Human microRNAs preferentially target genes with intermediate levels of expression and its formation by mammalian evolution. PLOS ONE *13*, e0198142.

Jackson, R.J., Hellen, C.U.T., and Pestova, T.V. (2010). The mechanism of eukaryotic translation initiation and principles of its regulation. Nat. Rev. Mol. Cell Biol. *11*, 113–127.

Jacobson, A., He, F., and Celik, A. (2018). General decapping activators target different subsets of inefficiently translated mRNAs.

Jain, S., Wheeler, J.R., Walters, R.W., Agrawal, A., Barsic, A., and Parker, R. (2016). ATPase-Modulated Stress Granules Contain a Diverse Proteome and Substructure. Cell *164*, 487–498.

Jakymiw, A., Lian, S., Eystathioy, T., Li, S., Satoh, M., Hamel, J.C., Fritzler, M.J., and Chan, E.K.L. (2005). Disruption of GW bodies impairs mammalian RNA interference. Nat. Cell Biol. *7*, 1267–1274.

Januszyk, K., and Lima, C.D. (2014). The eukaryotic RNA exosome. Curr Opin Struct Biol *0*, 132–140.

Järvelin, A.I., Noerenberg, M., Davis, I., and Castello, A. (2016). The new (dis)order in RNA regulation. Cell Commun. Signal *14*, 9.

Jennings, M.D., and Pavitt, G.D. (2010). eIF5 has GDI activity necessary for translational control by eIF2 phosphorylation. Nature *465*, 378–381.

Jennings, M.D., and Pavitt, G.D. (2014). A new function and complexity for protein translation initiation factor eIF2B. Cell Cycle *13*, 2660–2665.

Jennings, M.D., Kershaw, C.J., Adomavicius, T., and Pavitt, G.D. (2017). Fail-safe control of translation initiation by dissociation of eIF2α phosphorylated ternary complexes. ELife *6*, e24542.

Jinek, M., Fabian, M.R., Coyle, S.M., Sonenberg, N., and Doudna, J.A. (2010). Structural insights into the human GW182-PABC interaction in microRNA-mediated deadenylation. Nat. Struct. Mol. Biol. *17*, 238–240.

Jinek, M., Coyle, S.M., and Doudna, J.A. (2011). Coupled 5′ Nucleotide Recognition and Processivity in Xrn1-Mediated mRNA Decay. Molecular Cell *41*, 600–608.

Jing, Q., Huang, S., Guth, S., Zarubin, T., Motoyama, A., Chen, J., Di Padova, F., Lin, S.-C., Gram, H., and Han, J. (2005). Involvement of microRNA in AU-rich element-mediated mRNA instability. Cell *120*, 623–634.

Johnstone, T.G., Bazzini, A.A., and Giraldez, A.J. (2016). Upstream ORFs are prevalent translational repressors in vertebrates. EMBO J *35*, 706–723.

Jonas, S., and Izaurralde, E. (2013). The role of disordered protein regions in the assembly of decapping complexes and RNP granules. Genes & Development *27*, 2628–2641.

Jonas, S., and Izaurralde, E. (2015). Towards a molecular understanding of microRNA-mediated gene silencing. Nature Reviews Genetics *16*, 421–433.

Jones, C.I., Zabolotskaya, M.V., and Newbury, S.F. (2012). The 5′ → 3′ exoribonuclease XRN1/Pacman and its functions in cellular processes and development. WIREs RNA *3*, 455–468.

Joshi, B., Cameron, A., and Jagus, R. (2004). Characterization of mammalian eIF4E-family members. Eur. J. Biochem. *271*, 2189–2203.

Kahvejian, A., Roy, G., and Sonenberg, N. (2001). The mRNA closed-loop model: the function of PABP and PABP-interacting proteins in mRNA translation. Cold Spring Harb. Symp. Quant. Biol. *66*, 293–300.

Kaibara, K., Okazaki, T., Bohidar, H.B., and Dubin, P.L. (2000). pH-Induced Coacervation in Complexes of Bovine Serum Albumin and Cationic Polyelectrolytes. Biomacromolecules *1*, 100–107.

Kakumani, P.K., Harvey, L.-M., Houle, F., Guitart, T., Gebauer, F., and Simard, M.J. (2020). CSDE1 controls gene expression through the miRNA-mediated decay machinery. Life Science Alliance *3*.

Kamenska, A., Lu, W.-T., Kubacka, D., Broomhead, H., Minshall, N., Bushell, M., and Standart, N. (2014). Human 4E-T represses translation of bound mRNAs and enhances microRNA-mediated silencing. Nucleic Acids Research *42*, 3298–3313.

Kamenska, A., Simpson, C., Vindry, C., Broomhead, H., Bénard, M., Ernoult-Lange, M., Lee, B.P., Harries, L.W., Weil, D., and Standart, N. (2016). The DDX6–4E-T interaction mediates translational repression and P-body assembly. Nucleic Acids Research *44*, 6318–6334.

Kapp, L.D., and Lorsch, J.R. (2004). GTP-dependent Recognition of the Methionine Moiety on Initiator tRNA by Translation Factor eIF2. Journal of Molecular Biology *335*, 923–936.

Kato, M., Han, T.W., Xie, S., Shi, K., Du, X., Wu, L.C., Mirzaei, H., Goldsmith, E.J., Longgood, J., Pei, J., et al. (2012). Cell-free formation of RNA granules: low complexity sequence domains form dynamic fibers within hydrogels. Cell *149*, 753–767.

Kedersha, N., Stoecklin, G., Ayodele, M., Yacono, P., Lykke-Andersen, J., Fritzler, M.J., Scheuner, D., Kaufman, R.J., Golan, D.E., and Anderson, P. (2005). Stress granules and processing bodies are dynamically linked sites of mRNP remodeling. J. Cell Biol. *169*, 871–884.

Kervestin, S., and Jacobson, A. (2012). NMD: a multifaceted response to premature translational termination. Nat Rev Mol Cell Biol *13*, 700–712.

Kiledjian, M., and Dreyfuss, G. (1992). Primary structure and binding activity of the hnRNP U protein: binding RNA through RGG box. EMBO J. *11*, 2655–2664.

Kim, J.H., and Richter, J.D. (2006). Opposing polymerase-deadenylase activities regulate cytoplasmic polyadenylation. Mol. Cell *24*, 173–183.

King, H.A., Cobbold, L.C., and Willis, A.E. (2010). The role of IRES trans-acting factors in regulating translation initiation. Biochem. Soc. Trans. *38*, 1581–1586.

Koga, H., Kaushik, S., and Cuervo, A.M. (2011). Protein Homeostasis and Aging: the importance of exquisite quality control. Ageing Res Rev *10*, 205–215.

Komar, A.A., and Hatzoglou, M. (2011). Cellular IRES-mediated translation. Cell Cycle *10*, 229–240.

Kozak, M. (1986). Point mutations define a sequence flanking the AUG initiator codon that modulates translation by eukaryotic ribosomes. Cell *44*, 283–292.

Kozak, M. (1987). At least six nucleotides preceding the AUG initiator codon enhance translation in mammalian cells. Journal of Molecular Biology *196*, 947–950.

Kramer, S., Queiroz, R., Ellis, L., Hoheisel, J.D., Clayton, C., and Carrington, M. (2010). The RNA helicase DHH1 is central to the correct expression of many developmentally regulated mRNAs in trypanosomes. J Cell Sci *123*, 699–711.

Kumar, P., Hellen, C.U.T., and Pestova, T.V. (2016b). Toward the mechanism of eIF4F-mediated ribosomal attachment to mammalian capped mRNAs. Genes Dev. *30*, 1573–1588.

Kuzuoğlu-Öztürk, D., Bhandari, D., Huntzinger, E., Fauser, M., Helms, S., and Izaurralde, E. (2016). miRISC and the CCR4–NOT complex silence mRNA targets independently of 43S ribosomal scanning. The EMBO Journal e201592901.

Łabno, A., Tomecki, R., and Dziembowski, A. (2016). Cytoplasmic RNA decay pathways - Enzymes and mechanisms. Biochim. Biophys. Acta *1863*, 3125–3147.

Ladomery, M., and Sommerville, J. (2015). The Scd6/Lsm14 protein xRAPB has properties different from RAP55 in selecting mRNA for early translation or intracellular distribution in Xenopus oocytes. Biochimica et Biophysica Acta (BBA) - Gene Regulatory Mechanisms *1849*, 1363–1373.

Lahr, R.M., Fonseca, B.D., Ciotti, G.E., Al-Ashtal, H.A., Jia, J.-J., Niklaus, M.R., Blagden, S.P., Alain, T., and Berman, A.J. (2017). La-related protein 1 (LARP1) binds the mRNA cap, blocking eIF4F assembly on TOP mRNAs. ELife *6*, e24146.

Lau, N.-C., Kolkman, A., van Schaik, F.M.A., Mulder, K.W., Pijnappel, W.W.M.P., Heck, A.J.R., and Timmers, H.T.M. (2009). Human Ccr4-Not complexes contain variable deadenylase subunits. Biochem. J. *422*, 443–453.

Lavut, A., and Raveh, D. (2012). Sequestration of highly expressed mRNAs in cytoplasmic granules, P-bodies, and stress granules enhances cell viability. PLoS Genet. *8*, e1002527.

Lebreton, A., Tomecki, R., Dziembowski, A., and Séraphin, B. (2008). Endonucleolytic RNA cleavage by a eukaryotic exosome. Nature *456*, 993–996.

Lee, T., and Pelletier, J. (2016). The biology of DHX9 and its potential as a therapeutic target. Oncotarget *7*, 42716–42739.

Lee, Y., Jeon, K., Lee, J.-T., Kim, S., and Kim, V.N. (2002). MicroRNA maturation: stepwise processing and subcellular localization. EMBO J *21*, 4663–4670.

Leppek, K., Das, R., and Barna, M. (2018). Functional 5′ UTR mRNA structures in eukaryotic translation regulation and how to find them. Nat Rev Mol Cell Biol *19*, 158–174.

Lerner, R.S., and Nicchitta, C.V. (2006). mRNA translation is compartmentalized to the endoplasmic reticulum following physiological inhibition of cap-dependent translation. RNA *12*, 775–789.

Leung, A.K.L., Calabrese, J.M., and Sharp, P.A. (2006). Quantitative analysis of Argonaute protein reveals microRNA-dependent localization to stress granules. Proc Natl Acad Sci U S A *103*, 18125–18130.

Lewis, B.P., Burge, C.B., and Bartel, D.P. (2005). Conserved seed pairing, often flanked by adenosines, indicates that thousands of human genes are microRNA targets. Cell *120*, 15–20.

Li, J.J., Bickel, P.J., and Biggin, M.D. (2014). System wide analyses have underestimated protein abundances and the importance of transcription in mammals. PeerJ *2*, e270.

Li, P., Banjade, S., Cheng, H.-C., Kim, S., Chen, B., Guo, L., Llaguno, M., Hollingsworth, J.V., King, D.S., Banani, S.F., et al. (2012). Phase transitions in the assembly of multivalent signalling proteins. Nature *483*, 336–340.

Li, X.-H., Chavali, P.L., Pancsa, R., Chavali, S., and Babu, M.M. (2018). Function and Regulation of Phase-Separated Biological Condensates. Biochemistry *57*, 2452–2461.

Liang, H., and Li, W.-H. (2009). Lowly expressed human microRNA genes evolve rapidly. Mol. Biol. Evol. *26*, 1195–1198.

Lin, Y., Protter, D.S.W., Rosen, M.K., and Parker, R. (2015). Formation and Maturation of Phase-Separated Liquid Droplets by RNA-Binding Proteins. Molecular Cell *60*, 208–219.

Liu, J., Valencia-Sanchez, M.A., Hannon, G.J., and Parker, R. (2005). MicroRNA-dependent localization of targeted mRNAs to mammalian P-bodies. Nat. Cell Biol. *7*, 719–723.

Loh, B., Jonas, S., and Izaurralde, E. (2013). The SMG5-SMG7 heterodimer directly recruits the CCR4-NOT deadenylase complex to mRNAs containing nonsense codons via interaction with POP2. Genes Dev. *27*, 2125–2138.

Lomakin, I.B., and Steitz, T.A. (2013). The initiation of mammalian protein synthesis and mRNA scanning mechanism. Nature *500*, 307–311.

Lomakin, I.B., Kolupaeva, V.G., Marintchev, A., Wagner, G., and Pestova, T.V. (2003). Position of eukaryotic initiation factor eIF1 on the 40S ribosomal subunit determined by directed hydroxyl radical probing. Genes Dev. *17*, 2786–2797.

Lui, J., Castelli, L.M., Pizzinga, M., Simpson, C.E., Hoyle, N.P., Bailey, K.L., Campbell, S.G., and Ashe, M.P. (2014). Granules Harboring Translationally Active mRNAs Provide a Platform for P-Body Formation following Stress. Cell Reports *9*, 944–954.

Lykke-Andersen, J. (2002). Identification of a Human Decapping Complex Associated with hUpf Proteins in Nonsense-Mediated Decay. Mol Cell Biol *22*, 8114–8121.

Lykke-Andersen, J., and Bennett, E.J. (2014). Protecting the proteome: Eukaryotic cotranslational quality control pathways. J Cell Biol *204*, 467–476.

Lykke-Andersen, J., and Wagner, E. (2005). Recruitment and activation of mRNA decay enzymes by two ARE-mediated decay activation domains in the proteins TTP and BRF-1. Genes Dev. *19*, 351–361.

Mackereth, C.D., and Sattler, M. (2012). Dynamics in multi-domain protein recognition of RNA. Current Opinion in Structural Biology *22*, 287–296.

Mader, S., Lee, H., Pause, A., and Sonenberg, N. (1995). The Translation Initiation Factor eIF-4E Binds to a Common Motif Shared by the Translation Factor eIF-4 and the Translational Repressors 4E-Binding Proteins. MOL. CELL. BIOL. *15*, 8.

Mancera-Martínez, E., Brito Querido, J., Valasek, L.S., Simonetti, A., and Hashem, Y. (2017). ABCE1: A special factor that orchestrates translation at the crossroad between recycling and initiation. RNA Biology *14*, 1279–1285.

Mangus, D.A., Evans, M.C., and Jacobson, A. (2003). Poly(A)-binding proteins: multifunctional scaffolds for the post-transcriptional control of gene expression. Genome Biol. *4*, 223.

Marcotrigiano, J., Gingras, A.-C., Sonenberg, N., and Burley, S.K. (1997). Cocrystal Structure of the Messenger RNA 5′ Cap-Binding Protein (eIF4E) Bound to 7-methyl-GDP. Cell *89*, 951–961.

Marnef, A., and Standart, N. (2010). Pat1 proteins: a life in translation, translation repression and mRNA decay. Biochem Soc Trans *38*, 1602–1607.

Marnef, A., Sommerville, J., and Ladomery, M.R. (2009). RAP55: Insights into an evolutionarily conserved protein family. The International Journal of Biochemistry & Cell Biology *41*, 977–981.

Matheny, T., Rao, B.S., and Parker, R. (2019). Transcriptome-Wide Comparison of Stress Granules and P-Bodies Reveals that Translation Plays a Major Role in RNA Partitioning. Molecular and Cellular Biology *39*.

Mathys, H., Basquin, J., Ozgur, S., Czarnocki-Cieciura, M., Bonneau, F., Aartse, A., Dziembowski, A., Nowotny, M., Conti, E., and Filipowicz, W. (2014). Structural and Biochemical Insights to the Role of the CCR4-NOT Complex and DDX6 ATPase in MicroRNA Repression. Molecular Cell *54*, 751–765.

Matsumoto, K., Nakayama, H., Yoshimura, M., Masuda, A., Dohmae, N., Matsumoto, S., and Tsujimoto, M. (2012). PRMT1 is required for RAP55 to localize to processing bodies. RNA Biol *9*, 610–623.

Mauxion, F., Prève, B., and Séraphin, B. (2013). C2ORF29/CNOT11 and CNOT10 form a new module of the CCR4-NOT complex. RNA Biol *10*, 267–276.

McSwiggen, D.T., Mir, M., Darzacq, X., and Tjian, R. (2019). Evaluating phase separation in live cells: diagnosis, caveats, and functional consequences. Genes Dev. *33*, 1619–1634.

Meijer, H.A., Kong, Y.W., Lu, W.T., Wilczynska, A., Spriggs, R.V., Robinson, S.W., Godfrey, J.D., Willis, A.E., and Bushell, M. (2013). Translational repression and eIF4A2 activity are critical for microRNA-mediated gene regulation. Science *340*, 82–85.

Meijer, H.A., Schmidt, T., Gillen, S.L., Langlais, C., Jukes-Jones, R., de Moor, C.H., Cain, K., Wilczynska, A., and Bushell, M. (2019). DEAD-box helicase eIF4A2 inhibits CNOT7 deadenylation activity. Nucleic Acids Res *47*, 8224–8238.

Melero, R., Hug, N., López-Perrote, A., Yamashita, A., Cáceres, J.F., and Llorca, O. (2016). The RNA helicase DHX34 functions as a scaffold for SMG1-mediated UPF1 phosphorylation. Nature Communications *7*, 10585.

Mélèse, T., and Xue, Z. (1995). The nucleolus: an organelle formed by the act of building a ribosome. Curr. Opin. Cell Biol. *7*, 319–324.

Mellacheruvu, D., Wright, Z., Couzens, A.L., Lambert, J.-P., St-Denis, N.A., Li, T., Miteva, Y.V., Hauri, S., Sardiu, M.E., Low, T.Y., et al. (2013). The CRAPome: a contaminant repository for affinity purification–mass spectrometry data. Nature Methods *10*, 730–736.

Mendez, R., and Richter, J.D. (2001). Translational control by CPEB: a means to the end. Nat Rev Mol Cell Biol *2*, 521–529.

Merrick, W.C., and Pavitt, G.D. (2018). Protein Synthesis Initiation in Eukaryotic Cells. Cold Spring Harb Perspect Biol *10*, a033092..

Meunier, J., Lemoine, F., Soumillon, M., Liechti, A., Weier, M., Guschanski, K., Hu, H., Khaitovich, P., and Kaessmann, H. (2013). Birth and expression evolution of mammalian microRNA genes. Genome Res. *23*, 34–45.

Meyer, K.D., Patil, D.P., Zhou, J., Zinoviev, A., Skabkin, M.A., Elemento, O., Pestova, T.V., Qian, S.-B., and Jaffrey, S.R. (2015). 5′ UTR m6A Promotes Cap-Independent Translation. Cell *163*, 999–1010.

Meyuhas, O., and Kahan, T. (2015). The race to decipher the top secrets of TOP mRNAs. Biochim. Biophys. Acta *1849*, 801–811.

Mi, H., Muruganujan, A., Casagrande, J.T., and Thomas, P.D. (2013). Large-scale gene function analysis with the PANTHER classification system. Nat Protoc *8*, 1551–1566.

Miller, J.E., Zhang, L., Jiang, H., Li, Y., Pugh, B.F., and Reese, J.C. (2017). Genome-Wide Mapping of Decay Factor–mRNA Interactions in Yeast Identifies Nutrient-Responsive Transcripts as Targets of the Deadenylase Ccr4. G3 (Bethesda) *8*, 315–330.

Minshall, N., and Standart, N. (2004). The active form of Xp54 RNA helicase in translational repression is an RNA-mediated oligomer. Nucleic Acids Res *32*, 1325–1334.

Minshall, N., Reiter, M.H., Weil, D., and Standart, N. (2007). CPEB Interacts with an Ovary-specific eIF4E and 4E-T in Early Xenopus Oocytes. J. Biol. Chem. *282*, 37389–37401.

Minshall, N., Kress, M., Weil, D., and Standart, N. (2009). Role of p54 RNA helicase activity and its C-terminal domain in translational repression, P-body localization and assembly. Molecular Biology of the Cell *20*, 2464–2472.

Mitchell, P., Petfalski, E., Shevchenko, A., Mann, M., and Tollervey, D. (1997). The exosome: a conserved eukaryotic RNA processing complex containing multiple 3'-->5' exoribonucleases. Cell *91*, 457–466.

Moon, S.L., Morisaki, T., Khong, A., Lyon, K., Parker, R., and Stasevich, T.J. (2019). Multicolour single-molecule tracking of mRNA interactions with RNP granules. Nature Cell Biology *21*, 162.

Morisaki, T., Lyon, K., DeLuca, K.F., DeLuca, J.G., English, B.P., Zhang, Z., Lavis, L.D., Grimm, J.B., Viswanathan, S., Looger, L.L., et al. (2016). Real-time quantification of single RNA translation dynamics in living cells. Science *352*, 1425–1429.

Mugridge, J.S., Coller, J., and Gross, J.D. (2018). Structural and molecular mechanisms for the control of eukaryotic 5'–3' mRNA decay. Nat Struct Mol Biol *25*, 1077–1085.

Muhlrad, D., and Parker, R. (1992). Mutations affecting stability and deadenylation of the yeast MFA2 transcript. Genes Dev. *6*, 2100–2111.

Müller-McNicoll, M., and Neugebauer, K.M. (2013). How cells get the message: dynamic assembly and function of mRNA–protein complexes. Nature Reviews Genetics *14*, 275–287.

Nadler-Holly, M., Breker, M., Gruber, R., Azia, A., Gymrek, M., Eisenstein, M., Willison, K.R., Schuldiner, M., and Horovitz, A. (2012). Interactions of subunit CCT3 in the yeast chaperonin CCT/TRiC with Q/N-rich proteins revealed by high-throughput microscopy analysis. Proc Natl Acad Sci U S A *109*, 18833–18838.

Nakashima, K.K., Vibhute, M.A., and Spruijt, E. (2019). Biomolecular Chemistry in Liquid Phase Separated Compartments. Front. Mol. Biosci. *6*.

Nandagopal, N., and Roux, P.P. (2015). Regulation of global and specific mRNA translation by the mTOR signaling pathway. Translation (Austin) *3*, e983402.

Napoli, I., Mercaldo, V., Boyl, P.P., Eleuteri, B., Zalfa, F., De Rubeis, S., Di Marino, D., Mohr, E., Massimi, M., Falconi, M., et al. (2008). The Fragile X Syndrome Protein Represses Activity-Dependent Translation through CYFIP1, a New 4E-BP. Cell *134*, 1042–1054.

Narula, A., Ellis, J., Taliaferro, J.M., and Rissland, O.S. (2019). Coding regions affect mRNA stability in human cells. RNA *25*, 1751–1764.

Nicastro, G., Taylor, I.A., and Ramos, A. (2015). KH-RNA interactions: back in the groove. Curr. Opin. Struct. Biol. *30*, 63–70.

Niewidok, B., Igaev, M., Pereira da Graca, A., Strassner, A., Lenzen, C., Richter, C.P., Piehler, J., Kurre, R., and Brandt, R. (2018). Single-molecule imaging reveals dynamic biphasic partition of RNA-binding proteins in stress granules. J Cell Biol *217*, 1303–1318.

Nishimura, T., Padamsi, Z., Fakim, H., Milette, S., Dunham, W.H., Gingras, A.-C., and Fabian, M.R. (2015). The eIF4E-Binding Protein 4E-T Is a Component of the mRNA Decay Machinery that Bridges the 5' and 3' Termini of Target mRNAs. Cell Reports *11*, 1425–1436.

Nissan, T., Rajyaguru, P., She, M., Song, H., and Parker, R. (2010). Decapping Activators in Saccharomyces cerevisiae Act by Multiple Mechanisms. Molecular Cell *39*, 773–783.

Noriega, T.R., Chen, J., Walter, P., and Puglisi, J.D. (2014). Real-time observation of signal recognition particle binding to actively translating ribosomes. ELife *3*, e04418.

Nott, T.J., Petsalaki, E., Farber, P., Jervis, D., Fussner, E., Plochowietz, A., Craggs, T.D., Bazett-Jones, D.P., Pawson, T., Forman-Kay, J.D., et al. (2015). Phase Transition of a Disordered Nuage Protein Generates Environmentally Responsive Membraneless Organelles. Mol Cell *57*, 936–947.

Nott, T.J., Craggs, T.D., and Baldwin, A.J. (2016). Membraneless organelles can melt nucleic acid duplexes and act as biomolecular filters. Nat Chem *8*, 569–575.

Nottrott, S., Simard, M.J., and Richter, J.D. (2006). Human let-7a miRNA blocks protein production on actively translating polyribosomes. Nat. Struct. Mol. Biol. *13*, 1108–1114.

Ogunbona, O.B., and Claypool, S.M. (2019). Emerging Roles in the Biogenesis of Cytochrome c Oxidase for Members of the Mitochondrial Carrier Family. Front. Cell Dev. Biol. *7*.

Orr, M.W., Mao, Y., Storz, G., and Qian, S.-B. (2020). Alternative ORFs and small ORFs: shedding light on the dark proteome. Nucleic Acids Res *48*, 1029–1042.

Otsuka, H., Fukao, A., Funakami, Y., Duncan, K.E., and Fujiwara, T. (2019). Emerging Evidence of Translational Control by AU-Rich Element-Binding Proteins. Front. Genet. *10*.

Ozdilek, B.A., Thompson, V.F., Ahmed, N.S., White, C.I., Batey, R.T., and Schwartz, J.C. (2017). Intrinsically disordered RGG/RG domains mediate degenerate specificity in RNA binding. Nucleic Acids Res *45*, 7984–7996.

Ozgur, S., Chekulaeva, M., and Stoecklin, G. (2010). Human Pat1b connects deadenylation with mRNA decapping and controls the assembly of processing bodies. Mol. Cell. Biol. *30*, 4308–4323.

Ozgur, S., Buchwald, G., Falk, S., Chakrabarti, S., Prabu, J.R., and Conti, E. (2015a). The conformational plasticity of eukaryotic RNA-dependent ATPases. The FEBS Journal *282*, 850–863.

Ozgur, S., Basquin, J., Kamenska, A., Filipowicz, W., Standart, N., and Conti, E. (2015b). Structure of a Human 4E-T/DDX6/CNOT1 Complex Reveals the Different Interplay of DDX6-Binding Proteins with the CCR4-NOT Complex. Cell Reports *13*, 703–711.

Pak, C.W., Kosno, M., Holehouse, A.S., Padrick, S.B., Mittal, A., Ali, R., Yunus, A.A., Liu, D.R., Pappu, R.V., and Rosen, M.K. (2016). Sequence Determinants of Intracellular Phase Separation by Complex Coacervation of a Disordered Protein. Mol. Cell *63*, 72–85.

Pakos-Zebrucka, K., Koryga, I., Mnich, K., Ljujic, M., Samali, A., and Gorman, A.M. (2016). The integrated stress response. EMBO Rep. *17*, 1374–1395.

Palade, G. (1975). Intracellular aspects of the process of protein synthesis. Science *189*, 347–358.

Parker, R., and Sheth, U. (2007). P Bodies and the Control of mRNA Translation and Degradation. Molecular Cell *25*, 635–646.

Parrott, A.M., Walsh, M.R., and Mathews, M.B. (2007). Analysis of RNA:protein interactions in vivo: identification of RNA-binding partners of nuclear factor 90. Meth. Enzymol. *429*, 243–260.

Patel, A., Lee, H.O., Jawerth, L., Maharana, S., Jahnel, M., Hein, M.Y., Stoynov, S., Mahamid, J., Saha, S., Franzmann, T.M., et al. (2015). A Liquid-to-Solid Phase Transition of the ALS Protein FUS Accelerated by Disease Mutation. Cell *162*, 1066–1077.

Pause, A., Belsham, G.J., Gingras, A.C., Donzé, O., Lin, T.A., Lawrence, J.C., and Sonenberg, N. (1994). Insulin-dependent stimulation of protein synthesis by phosphorylation of a regulator of 5'-cap function. Nature *371*, 762–767.

Pavitt, G.D. (2005). eIF2B, a mediator of general and gene-specific translational control. Biochem. Soc. Trans. *33*, 1487–1492.

Pechmann, S., and Frydman, J. (2013). Evolutionary conservation of codon optimality reveals hidden signatures of cotranslational folding. Nat. Struct. Mol. Biol. *20*, 237–243.

Pelletier, J., and Sonenberg, N. (2019). The Organizing Principles of Eukaryotic Ribosome Recruitment. Annual Review of Biochemistry *88*, 307–335.

Peran, I., and Mittag, T. (2020). Molecular structure in biomolecular condensates. Current Opinion in Structural Biology *60*, 17–26.

Peter, D., Igreja, C., Weber, R., Wohlbold, L., Weiler, C., Ebertsch, L., Weichenrieder, O., and Izaurralde, E. (2015). Molecular Architecture of 4E-BP Translational Inhibitors Bound to eIF4E. Molecular Cell *57*, 1074–1087.

Petersen, C.P., Bordeleau, M.-E., Pelletier, J., and Sharp, P.A. (2006). Short RNAs repress translation after initiation in mammalian cells. Mol. Cell *21*, 533–542.

Pfanner, N., Warscheid, B., and Wiedemann, N. (2019). Mitochondrial proteins: from biogenesis to functional networks. Nature Reviews Molecular Cell Biology *20*, 267–284.

Philippe, L., Vasseur, J.-J., Debart, F., and Thoreen, C.C. (2018). La-related protein 1 (LARP1) repression of TOP mRNA translation is mediated through its cap-binding domain and controlled by an adjacent regulatory region. Nucleic Acids Res *46*, 1457–1469.

Piao, X., Zhang, X., Wu, L., and Belasco, J.G. (2010). CCR4-NOT deadenylates mRNA associated with RNA-induced silencing complexes in human cells. Mol. Cell. Biol. *30*, 1486–1494.

Pilkington, G.R., and Parker, R. (2008). Pat1 contains distinct functional domains that promote P-body assembly and activation of decapping. Mol. Cell. Biol. *28*, 1298–1312.

Pillai, R.S. (2005). MicroRNA function: multiple mechanisms for a tiny RNA? RNA *11*, 1753–1761.

Pillai, R.S., Bhattacharyya, S.N., Artus, C.G., Zoller, T., Cougot, N., Basyuk, E., Bertrand, E., and Filipowicz, W. (2005). Inhibition of translational initiation by Let-7 MicroRNA in human cells. Science *309*, 1573–1576.

Piqué, M., López, J.M., Foissac, S., Guigó, R., and Méndez, R. (2008). A combinatorial code for CPE-mediated translational control. Cell *132*, 434–448.

Pisarev, A.V., Kolupaeva, V.G., Yusupov, M.M., Hellen, C.U., and Pestova, T.V. (2008). Ribosomal position and contacts of mRNA in eukaryotic translation initiation complexes. EMBO J *27*, 1609–1621.

Pitchiaya, S., Mourao, M.D.A., Jalihal, A.P., Xiao, L., Jiang, X., Chinnaiyan, A.M., Schnell, S., and Walter, N.G. (2019). Dynamic Recruitment of Single RNAs to Processing Bodies Depends on RNA Functionality. Molecular Cell.

Poncová, K., Wagner, S., Jansen, M.E., Beznosková, P., Gunišová, S., Herrmannová, A., Zeman, J., Dong, J., and Valášek, L.S. (2019). uS3/Rps3 controls fidelity of translation termination and programmed stop codon readthrough in co-operation with eIF3. Nucleic Acids Res. *47*, 11326–11343.

Poornima, G., Shah, S., Vignesh, V., Parker, R., and Rajyaguru, P.I. (2016). Arginine methylation promotes translation repression activity of eIF4G-binding protein, Scd6. Nucleic Acids Res *44*, 9358–9368.

Pop, C., Rouskin, S., Ingolia, N.T., Han, L., Phizicky, E.M., Weissman, J.S., and Koller, D. (2014). Causal signals between codon bias, mRNA structure, and the efficiency of translation and elongation. Mol. Syst. Biol. *10*, 770.

Preiss, T., and Hentze, M.W. (1998). Dual function of the messenger RNA cap structure in poly(A)-tail-promoted translation in yeast. Nature *392*, 516–520.

Presnyak, V., and Coller, J. (2013). The DHH1/RCKp54 family of helicases: An ancient family of proteins that promote translational silencing. Biochim Biophys Acta *1829*, 817–823.

Presnyak, V., Alhusaini, N., Chen, Y.-H., Martin, S., Morris, N., Kline, N., Olson, S., Weinberg, D., Baker, K.E., Graveley, B.R., et al. (2015). Codon optimality is a major determinant of mRNA stability. Cell *160*, 1111–1124.

Proud, C.G. (2018). Phosphorylation and Signal Transduction Pathways in Translational Control. Cold Spring Harb Perspect Biol a033050.

Radhakrishnan, A., and Green, R. (2016). Connections Underlying Translation and mRNA Stability. J. Mol. Biol. *428*, 3558–3564.

Rajyaguru, P., She, M., and Parker, R. (2012). Scd6 targets eIF4G to repress translation: RGG motif proteins as a class of eIF4G-binding proteins. Mol. Cell *45*, 244–254.

Räsch, F., Weber, R., Izaurralde, E., and Igreja, C. (2020). 4E-T-bound mRNAs are stored in a silenced and deadenylated form. Genes Dev. *34*, 847–860.

Reijns, M.A.M., Alexander, R.D., Spiller, M.P., and Beggs, J.D. (2008). A role for Q/N-rich aggregation-prone regions in P-body localization. J. Cell. Sci. *121*, 2463–2472.

Rhoads, R.E. (2009). eIF4E: New Family Members, New Binding Partners, New Roles. J. Biol. Chem. *284*, 16711–16715.

Rissland, O.S., Subtelny, A.O., Wang, M., Lugowski, A., Nicholson, B., Laver, J.D., Sidhu, S.S., Smibert, C.A., Lipshitz, H.D., and Bartel, D.P. (2017). The influence of microRNAs and poly(A) tail length on endogenous mRNA–protein complexes. Genome Biology *18*.

Rolfe, D.F., and Brown, G.C. (1997). Cellular energy utilization and molecular origin of standard metabolic rate in mammals. Physiol. Rev. *77*, 731–758.

Roux, K.J. (2013). Marked by association: techniques for proximity-dependent labeling of proteins in eukaryotic cells. Cell. Mol. Life Sci. *70*, 3657–3664.

Rouya, C., Siddiqui, N., Morita, M., Duchaine, T.F., Fabian, M.R., and Sonenberg, N. (2014). Human DDX6 effects miRNA-mediated gene silencing via direct binding to CNOT1. RNA *20*, 1398–1409.

Rüdel, S., Wang, Y., Lenobel, R., Körner, R., Hsiao, H.-H., Urlaub, H., Patel, D., and Meister, G. (2011). Phosphorylation of human Argonaute proteins affects small RNA binding. Nucleic Acids Res. *39*, 2330–2343.

Rybak-Wolf, A., Jens, M., Murakawa, Y., Herzog, M., Landthaler, M., and Rajewsky, N. (2014). A variety of dicer substrates in human and C. elegans. Cell *159*, 1153–1167.

Safaee, N., Kozlov, G., Noronha, A.M., Xie, J., Wilds, C.J., and Gehring, K. (2012). Interdomain allostery promotes assembly of the poly(A) mRNA complex with PABP and eIF4G. Mol. Cell *48*, 375–386.

Sawicka, K., Bushell, M., Spriggs, K.A., and Willis, A.E. (2008). Polypyrimidine-tract-binding protein: a multifunctional RNA-binding protein. Biochem. Soc. Trans. *36*, 641–647.

Scheper, G.C., van Kollenburg, B., Hu, J., Luo, Y., Goss, D.J., and Proud, C.G. (2002). Phosphorylation of Eukaryotic Initiation Factor 4E Markedly Reduces Its Affinity for Capped mRNA. J. Biol. Chem. *277*, 3303–3309.

Schirle, N.T., Sheu-Gruttadauria, J., and MacRae, I.J. (2014). Structural basis for microRNA targeting. Science *346*, 608–613.

Schirle, N.T., Sheu-Gruttadauria, J., Chandradoss, S.D., Joo, C., and MacRae, I.J. (2015). Water-mediated recognition of t1-adenosine anchors Argonaute2 to microRNA targets. Elife *4*.

Schmidt, H.B., and Görlich, D. (2016). Transport Selectivity of Nuclear Pores, Phase Separation, and Membraneless Organelles. Trends Biochem. Sci. *41*, 46–61.

Schütz, S., Nöldeke, E.R., and Sprangers, R. (2017). A synergistic network of interactions promotes the formation of in vitro processing bodies and protects mRNA against decapping. Nucleic Acids Res *45*, 6911–6922.

Schwanhäusser, B., Busse, D., Li, N., Dittmar, G., Schuchhardt, J., Wolf, J., Chen, W., and Selbach, M. (2011). Global quantification of mammalian gene expression control. Nature *473*, 337–342.

Selbach, M., Schwanhäusser, B., Thierfelder, N., Fang, Z., Khanin, R., and Rajewsky, N. (2008). Widespread changes in protein synthesis induced by microRNAs. Nature *455*, 58–63.

Serman, A., Le Roy, F., Aigueperse, C., Kress, M., Dautry, F., and Weil, D. (2007). GW body disassembly triggered by siRNAs independently of their silencing activity. Nucleic Acids Research *35*, 4715–4727.

Sharif, H., and Conti, E. (2013). Architecture of the Lsm1-7-Pat1 Complex: A Conserved Assembly in Eukaryotic mRNA Turnover. Cell Reports *5*, 283–291.

Sharif, H., Ozgur, S., Sharma, K., Basquin, C., Urlaub, H., and Conti, E. (2013a). Structural analysis of the yeast Dhh1-Pat1 complex reveals how Dhh1 engages Pat1, Edc3 and RNA in mutually exclusive interactions. Nucleic Acids Res. *41*, 8377–8390.

She, M., Decker, C.J., Svergun, D.I., Round, A., Chen, N., Muhlrad, D., Parker, R., and Song, H. (2008). Structural Basis of Dcp2 Recognition and Activation by Dcp1. Molecular Cell *29*, 337–349.

Sheth, U., and Parker, R. (2003). Decapping and Decay of Messenger RNA Occur in Cytoplasmic Processing Bodies. Science *300*, 805–808.

Shin, Y., and Brangwynne, C.P. (2017). Liquid phase condensation in cell physiology and disease. Science *357*.

Shoemaker, C.J., and Green, R. (2012). Translation drives mRNA quality control. Nat Struct Mol Biol *19*, 594–601.

Simonetti, A., Brito Querido, J., Myasnikov, A.G., Mancera-Martinez, E., Renaud, A., Kuhn, L., and Hashem, Y. (2016). eIF3 Peripheral Subunits Rearrangement after mRNA Binding and Start-Codon Recognition. Molecular Cell *63*, 206–217.

Simonetti, A., Guca, E., Bochler, A., Kuhn, L., and Hashem, Y. (2020). Structural Insights into the Mammalian Late-Stage Initiation Complexes. Cell Reports *31*.

Slavoff, S.A., Mitchell, A.J., Schwaid, A.G., Cabili, M.N., Ma, J., Levin, J.Z., Karger, A.D., Budnik, B.A., Rinn, J.L., and Saghatelian, A. (2013). Peptidomic discovery of short open reading frame-encoded peptides in human cells. Nat. Chem. Biol. *9*, 59–64.

Smillie, D.A., and Sommerville, J. RNA helicase p54 and mRNP assembly. 13.

Sokabe, M., and Fraser, C.S. (2014). Human eukaryotic initiation factor 2 (eIF2)-GTP-Met-tRNAi ternary complex and eIF3 stabilize the 43 S preinitiation complex. J. Biol. Chem. *289*, 31827–31836.

Sokabe, M., and Fraser, C.S. (2018). Toward a Kinetic Understanding of Eukaryotic Translation. Cold Spring Harb Perspect Biol a032706.

Sonenberg, N., and Hinnebusch, A.G. (2009). Regulation of Translation Initiation in Eukaryotes: Mechanisms and Biological Targets. Cell *136*, 731–745.

Sonenberg, N., Morgan, M.A., Merrick, W.C., and Shatkin, A.J. (1978). A polypeptide in eukaryotic initiation factors that crosslinks specifically to the 5'-terminal cap in mRNA. Proc. Natl. Acad. Sci. U.S.A. *75*, 4843–4847.

Sonenberg, N., Rupprecht, K.M., Hecht, S.M., and Shatkin, A.J. (1979). Eukaryotic mRNA cap binding protein: purification by affinity chromatography on sepharose-coupled m7GDP. Proceedings of the National Academy of Sciences *76*, 4345–4349.

Soto-Rifo, R., Rubilar, P.S., Limousin, T., de Breyne, S., Décimo, D., and Ohlmann, T. (2012). DEAD-box protein DDX3 associates with eIF4F to promote translation of selected mRNAs. EMBO J. *31*, 3745–3756.

Souquere, S., Mollet, S., Kress, M., Dautry, F., Pierron, G., and Weil, D. (2009). Unravelling the ultrastructure of stress granules and associated P-bodies in human cells. J. Cell. Sci. *122*, 3619–3626.

Stadler, M., and Fire, A. (2011). Wobble base-pairing slows in vivo translation elongation in metazoans. RNA *17*, 2063–2073.

Standart, N., and Weil, D. (2018). P-Bodies: Cytosolic Droplets for Coordinated mRNA Storage. Trends Genet. *34*, 612–626.

Staudacher, J.J., Naarmann-de Vries, I.S., Ujvari, S.J., Klinger, B., Kasim, M., Benko, E., Ostareck-Lederer, A., Ostareck, D.H., Bondke Persson, A., Lorenzen, S., et al. (2015). Hypoxia-induced gene expression results from selective mRNA partitioning to the endoplasmic reticulum. Nucleic Acids Res. *43*, 3219–3236.

Stoecklin, G., Mayo, T., and Anderson, P. (2006). ARE-mRNA degradation requires the 5'–3' decay pathway. EMBO Rep *7*, 72–77.

Stoneley, M., and Willis, A.E. (2004). Cellular internal ribosome entry segments: structures, trans-acting factors and regulation of gene expression. Oncogene *23*, 3200–3207.

Sweet, T., Kovalak, C., and Coller, J. (2012). The DEAD-box protein Dhh1 promotes decapping by slowing ribosome movement. PLoS Biol. *10*, e1001342.

Tanaka, K.J., Ogawa, K., Takagi, M., Imamoto, N., Matsumoto, K., and Tsujimoto, M. (2006). RAP55, a Cytoplasmic mRNP Component, Represses Translation in *Xenopus* Oocytes. J. Biol. Chem. *281*, 40096–40106.

Tang, J., Kao, P.N., and Herschman, H.R. (2000). Protein-arginine methyltransferase I, the predominant protein-arginine methyltransferase in cells, interacts with and is regulated by interleukin enhancer-binding factor 3. J. Biol. Chem. *275*, 19866–19876.

Tani, H., Mizutani, R., Salam, K.A., Tano, K., Ijiri, K., Wakamatsu, A., Isogai, T., Suzuki, Y., and Akimitsu, N. (2012). Genome-wide determination of RNA stability reveals hundreds of short-lived noncoding transcripts in mammals. Genome Res. *22*, 947–956.

Tanner, N.K., Cordin, O., Banroques, J., Doère, M., and Linder, P. (2003). The Q motif: a newly identified motif in DEAD box helicases may regulate ATP binding and hydrolysis. Mol. Cell *11*, 127–138.

Tarun, S.Z., and Sachs, A.B. (1995). A common function for mRNA 5' and 3' ends in translation initiation in yeast. Genes Dev. *9*, 2997–3007.

Tarun, S.Z., Wells, S.E., Deardorff, J.A., and Sachs, A.B. (1997). Translation initiation factor eIF4G mediates in vitro poly(A) tail-dependent translation. Proc Natl Acad Sci U S A *94*, 9046–9051.

Tauber, D., Tauber, G., Khong, A., Van Treeck, B., Pelletier, J., and Parker, R. (2020). Modulation of RNA Condensation by the DEAD-Box Protein eIF4A. Cell *180*, 411-426.e16.

Teixeira, D., and Parker, R. (2007). Analysis of P-Body Assembly in Saccharomyces cerevisiae. Mol Biol Cell *18*, 2274–2287.

Teixeira, D., Sheth, U., Valencia-Sanchez, M.A., Brengues, M., and Parker, R. (2005). Processing bodies require RNA for assembly and contain nontranslating mRNAs. RNA *11*, 371–382.

Tesina, P., Heckel, E., Cheng, J., Fromont-Racine, M., Buschauer, R., Kater, L., Beatrix, B., Berninghausen, O., Jacquier, A., Becker, T., et al. (2019a). Structure of the 80S ribosome–Xrn1 nuclease complex. Nat Struct Mol Biol *26*, 275–280.

Tharun, S., He, W., Mayes, A.E., Lennertz, P., Beggs, J.D., and Parker, R. (2000). Yeast Sm-like proteins function in mRNA decapping and decay. Nature *404*, 515–518.

Trendel, J., Schwarzl, T., Horos, R., Prakash, A., Bateman, A., Hentze, M.W., and Krijgsveld, J. (2019). The Human RNA-Binding Proteome and Its Dynamics during Translational Arrest. Cell *176*, 391-403.e19.

Tritschler, F., Eulalio, A., Helms, S., Schmidt, S., Coles, M., Weichenrieder, O., Izaurralde, E., and Truffault, V. (2008). Similar modes of interaction enable Trailer Hitch and EDC3 to associate with DCP1 and Me31B in distinct protein complexes. Mol. Cell. Biol. *28*, 6695–6708.

Tritschler, F., Braun, J.E., Eulalio, A., Truffault, V., Izaurralde, E., and Weichenrieder, O. (2009). Structural Basis for the Mutually Exclusive Anchoring of P Body Components EDC3 and Tral to the DEAD Box Protein DDX6/Me31B. Molecular Cell *33*, 661–668.

Tutucci, E., Vera, M., Biswas, J., Garcia, J., Parker, R., and Singer, R.H. (2018). An improved MS2 system for accurate reporting of the mRNA life cycle. Nat. Methods *15*, 81–89.

Uchida, N., Hoshino, S.-I., and Katada, T. (2004). Identification of a human cytoplasmic poly(A) nuclease complex stimulated by poly(A)-binding protein. J. Biol. Chem. *279*, 1383–1391.

Ustianenko, D., Hrossova, D., Potesil, D., Chalupnikova, K., Hrazdilova, K., Pachernik, J., Cetkovska, K., Uldrijan, S., Zdrahal, Z., and Vanacova, S. (2013). Mammalian DIS3L2 exoribonuclease targets the uridylated precursors of let-7 miRNAs. RNA *19*, 1632–1638.

Uversky, V.N. (2017). Intrinsically disordered proteins in overcrowded milieu: Membrane-less organelles, phase separation, and intrinsic disorder. Current Opinion in Structural Biology *44*, 18–30.

Uversky, V.N., Kuznetsova, I.M., Turoverov, K.K., and Zaslavsky, B. (2015). Intrinsically disordered proteins as crucial constituents of cellular aqueous two phase systems and coacervates. FEBS Letters *589*, 15–22.

Van Treeck, B., Protter, D.S.W., Matheny, T., Khong, A., Link, C.D., and Parker, R. (2018). RNA self-assembly contributes to stress granule formation and defining the stress granule transcriptome. Proceedings of the National Academy of Sciences *115*, 2734–2739.

Vessey, J.P., Vaccani, A., Xie, Y., Dahm, R., Karra, D., Kiebler, M.A., and Macchi, P. (2006). Dendritic localization of the translational repressor Pumilio 2 and its contribution to dendritic stress granules. J. Neurosci. *26*, 6496–6508.

Vindry, C., Marnef, A., Broomhead, H., Twyffels, L., Ozgur, S., Stoecklin, G., Llorian, M., Smith, C.W., Mata, J., Weil, D., et al. (2017). Dual RNA Processing Roles of Pat1b via Cytoplasmic Lsm1-7 and Nuclear Lsm2-8 Complexes. Cell Rep *20*, 1187–1200.

Waghray, S., Williams, C., Coon, J.J., and Wickens, M. (2015). Xenopus CAF1 requires NOT1-mediated interaction with 4E-T to repress translation in vivo. RNA *21*, 1335–1345.

Wahle, E., and Winkler, G.S. (2013). RNA decay machines: deadenylation by the Ccr4-not and Pan2-Pan3 complexes. Biochim. Biophys. Acta *1829*, 561–570.

Wang, C., Schmich, F., Srivatsa, S., Weidner, J., Beerenwinkel, N., and Spang, A. Context-dependent deposition and regulation of mRNAs in P-bodies. ELife *7*.

Wang, X., Flynn, A., Waskiewicz, A.J., Webb, B.L.J., Vries, R.G., Baines, I.A., Cooper, J.A., and Proud, C.G. (1998). The Phosphorylation of Eukaryotic Initiation Factor eIF4E in Response to Phorbol Esters, Cell Stresses, and Cytokines Is Mediated by Distinct MAP Kinase Pathways. J. Biol. Chem. *273*, 9373–9377.

Wang, Z., Jiao, X., Carr-Schmid, A., and Kiledjian, M. (2002). The hDcp2 protein is a mammalian mRNA decapping enzyme. Proc. Natl. Acad. Sci. U.S.A. *99*, 12663–12668.

Webster, M.W., Chen, Y.-H., Stowell, J.A.W., Alhusaini, N., Sweet, T., Graveley, B.R., Coller, J., and Passmore, L.A. (2018). mRNA Deadenylation Is Coupled to Translation Rates by the Differential Activities of Ccr4-Not Nucleases. Molecular Cell *70*, 1089-1100.e8.

Webster, M.W., Stowell, J.A., and Passmore, L.A. (2019). RNA-binding proteins distinguish between similar sequence motifs to promote targeted deadenylation by Ccr4-Not. ELife *8*, e40670.

Weidensdorfer, D., Stöhr, N., Baude, A., Lederer, M., Köhn, M., Schierhorn, A., Buchmeier, S., Wahle, E., and Hüttelmaier, S. (2009). Control of c-myc mRNA stability by IGF2BP1-associated cytoplasmic RNPs. RNA *15*, 104–115.

Weingarten-Gabbay, S., Elias-Kirma, S., Nir, R., Gritsenko, A.A., Stern-Ginossar, N., Yakhini, Z., Weinberger, A., and Segal, E. (2016). Systematic discovery of cap-independent translation sequences in human and viral genomes. Science *351*, aad4939.

Wells, S.E., Hillner, P.E., Vale, R.D., and Sachs, A.B. (1998). Circularization of mRNA by eukaryotic translation initiation factors. Mol. Cell *2*, 135–140.

Weston, A., and Sommerville, J. (2006). Xp54 and related (DDX6-like) RNA helicases: roles in messenger RNP assembly, translation regulation and RNA degradation. Nucleic Acids Res. *34*, 3082–3094.

Wethmar, K. (2014). The regulatory potential of upstream open reading frames in eukaryotic gene expression. WIREs RNA *5*, 765–768.

Wilczynska, A., Aigueperse, C., Kress, M., Dautry, F., and Weil, D. (2005). The translational regulator CPEB1 provides a link between dcp1 bodies and stress granules. J. Cell. Sci. *118*, 981–992.

Wilczynska, A., Gillen, S.L., Schmidt, T., Meijer, H.A., Jukes-Jones, R., Langlais, C., Kopra, K., Lu, W.-T., Godfrey, J.D., Hawley, B.R., et al. (2019). eIF4A2 drives repression of translation at initiation by Ccr4-Not through purine-rich motifs in the 5'UTR. Genome Biol *20*, 262.

Willis, W., Miranda-Grandjean, D., Hudgens, J., Willis, E., Finlayson, J., De Filippis, E., Bustos, R.Z., Langlais, P., Mielke, C., and Mandarino, L. (2018). Dominant and Sensitive Control of Oxidative Flux by the ATP-ADP Carrier in Human Skeletal Muscle Mitochondria: Effect of Lysine Acetylation. Arch Biochem Biophys *647*, 93–103.

Winter, J., Jung, S., Keller, S., Gregory, R.I., and Diederichs, S. (2009). Many roads to maturity: microRNA biogenesis pathways and their regulation. Nat. Cell Biol. *11*, 228–234.

Wu, D., Muhlrad, D., Bowler, M.W., Jiang, S., Liu, Z., Parker, R., and Song, H. (2014). Lsm2 and Lsm3 bridge the interaction of the Lsm1-7 complex with Pat1 for decapping activation. Cell Research *24*, 233–246.

Wu, K., He, J., Pu, W., and Peng, Y. (2018). The Role of Exportin-5 in MicroRNA Biogenesis and Cancer. Genomics, Proteomics & Bioinformatics *16*, 120–126.

Wu, Q., Medina, S.G., Kushawah, G., DeVore, M.L., Castellano, L.A., Hand, J.M., Wright, M., and Bazzini, A.A. (2019). Translation affects mRNA stability in a codon-dependent manner in human cells. ELife *8*, e45396.

Xing, W., Muhlrad, D., Parker, R., and Rosen, M.K. (2020). A quantitative inventory of yeast P body proteins reveals principles of composition and specificity. BioRxiv 489658.

Xu, J., and Chua, N.-H. (2009). Arabidopsis Decapping 5 Is Required for mRNA Decapping, P-Body Formation, and Translational Repression during Postembryonic Development. Plant Cell *21*, 3270–3279.

Yamashita, A., Chang, T.-C., Yamashita, Y., Zhu, W., Zhong, Z., Chen, C.-Y.A., and Shyu, A.-B. (2005). Concerted action of poly(A) nucleases and decapping enzyme in mammalian mRNA turnover. Nat. Struct. Mol. Biol. *12*, 1054–1063.

Yan, X., Hoek, T.A., Vale, R.D., and Tanenbaum, M.E. (2016). Dynamics of Translation of Single mRNA Molecules In Vivo. Cell *165*, 976–989.

Yanagiya, A., Svitkin, Y.V., Shibata, S., Mikami, S., Imataka, H., and Sonenberg, N. (2009). Requirement of RNA binding of mammalian eukaryotic translation initiation factor 4GI (eIF4GI) for efficient interaction of eIF4E with the mRNA cap. Mol. Cell. Biol. *29*, 1661–1669.

Yanagiya, A., Suyama, E., Adachi, H., Svitkin, Y.V., Aza-Blanc, P., Imataka, H., Mikami, S., Martineau, Y., Ronai, Z.A., and Sonenberg, N. (2012). Translational Homeostasis via the mRNA Cap-Binding Protein, eIF4E. Molecular Cell *46*, 847–858.

Yang, W.-H. (2006). RNA-associated protein 55 (RAP55) localizes to mRNA processing bodies and stress granules. RNA *12*, 547–554.

Yang, Z. (2004). GW182 is critical for the stability of GW bodies expressed during the cell cycle and cell proliferation. Journal of Cell Science *117*, 5567–5578.

Yang, Y., and Wang, Z. (2019). IRES-mediated cap-independent translation, a path leading to hidden proteome. J Mol Cell Biol *11*, 911–919.

Yang, G., Smibert, C.A., Kaplan, D.R., and Miller, F.D. (2014). An eIF4E1/4E-T Complex Determines the Genesis of Neurons from Precursors by Translationally Repressing a Proneurogenic Transcription Program. Neuron *84*, 723–739.

YANG, W.-H., YU, J.H., GULICK, T., BLOCH, K.D., and BLOCH, D.B. (2006). RNA-associated protein 55 (RAP55) localizes to mRNA processing bodies and stress granules. RNA *12*, 547–554.

Yang, Y.-C.T., Di, C., Hu, B., Zhou, M., Liu, Y., Song, N., Li, Y., Umetsu, J., and Lu, Z. (2015). CLIPdb: a CLIP-seq database for protein-RNA interactions. BMC Genomics *16*, 51.

Yanniotis, S., Skaltsi, S., and Karaburnioti, S. (2006). Effect of moisture content on the viscosity of honey at different temperatures. Journal of Food Engineering *72*, 372–377.

Ye, Y., Liang, Y., Yu, Q., Hu, L., Li, H., Zhang, Z., and Xu, X. (2015). Analysis of human upstream open reading frames and impact on gene expression. Hum. Genet. *134*, 605–612.

Yi, H., Park, J., Ha, M., Lim, J., Chang, H., and Kim, V.N. (2018). PABP Cooperates with the CCR4-NOT Complex to Promote mRNA Deadenylation and Block Precocious Decay. Molecular Cell *70*, 1081-1088.e5.

Yoshizawa, T., Nozawa, R.-S., Jia, T.Z., Saio, T., and Mori, E. (2020). Biological phase separation: cell biology meets biophysics. Biophys Rev *12*, 519–539.

Youn, J.-Y., Dunham, W.H., Hong, S.J., Knight, J.D.R., Bashkurov, M., Chen, G.I., Bagci, H., Rathod, B., MacLeod, G., Eng, S.W.M., et al. (2018). High-Density Proximity Mapping Reveals the Subcellular Organization of mRNA-Associated Granules and Bodies. Molecular Cell *69*, 517-532.e11.

Yu, C.-H., Dang, Y., Zhou, Z., Wu, C., Zhao, F., Sachs, M.S., and Liu, Y. (2015). Codon Usage Influences the Local Rate of Translation Elongation to Regulate Co-translational Protein Folding. Mol. Cell *59*, 744–754.

Yu, Y., Marintchev, A., Kolupaeva, V.G., Unbehaun, A., Veryasova, T., Lai, S.-C., Hong, P., Wagner, G., Hellen, C.U.T., and Pestova, T.V. (2009). Position of eukaryotic translation initiation factor eIF1A on the 40S ribosomal subunit mapped by directed hydroxyl radical probing. Nucleic Acids Res *37*, 5167–5182.

Zayat, V., Balcerak, A., Korczynski, J., Trebinska, A., Wysocki, J., Sarnowska, E., Chmielarczyk, M., Macech, E., Konopiński, R., Dziembowska, M., et al. (2015). HAX-1: A Novel P-Body Protein. DNA Cell Biol *34*, 43–54.

ze, A.R., Feoktistova, K., Avanzino, B.C., and Fraser, C.S. (2011). Duplex Unwinding and ATPase Activities of the DEAD-Box Helicase eIF4A Are Coupled by eIF4G and eIF4B. Journal of Molecular Biology *412*, 674–687.

Zeidan, Q., He, F., Zhang, F., Zhang, H., Jacobson, A., and Hinnebusch, A.G. (2018). Conserved mRNA-granule component Scd6 targets Dhh1 to repress translation initiation and activates Dcp2-mediated mRNA decay in vivo. PLoS Genet *14*.

Zekri, L., Huntzinger, E., Heimstädt, S., and Izaurralde, E. (2009). The silencing domain of GW182 interacts with PABPC1 to promote translational repression and degradation of microRNA targets and is required for target release. Mol. Cell. Biol. *29*, 6220–6231.

Zhou, T., Weems, M., and Wilke, C.O. (2009). Translationally Optimal Codons Associate with Structurally Sensitive Sites in Proteins. Mol Biol Evol *26*, 1571–1580.

Zhu, Y., Xu, G., Yang, Y.T., Xu, Z., Chen, X., Shi, B., Xie, D., Lu, Z.J., and Wang, P. (2019). POSTAR2: deciphering the post-transcriptional regulatory logics. Nucleic Acids Res. *47*, D203–D211.

Zimmermann, R., Eyrisch, S., Ahmad, M., and Helms, V. (2011). Protein translocation across the ER membrane. Biochimica et Biophysica Acta (BBA) - Biomembranes *1808*, 912–924.

Zwicker, D., Decker, M., Jaensch, S., Hyman, A.A., and Jülicher, F. (2014). Centrosomes are autocatalytic droplets of pericentriolar material organized by centrioles. PNAS *111*, E2636–E2645.

A proximity biotinylation map of a human cell | bioRxiv.